Using low temperature calorimetry and moisture fixation method to study the pore structure of cement based materials

Wu, Min

Publication date:
2014

Document Version
Publisher's PDF, also known as Version of record

Using low temperature calorimetry and moisture fixation method to study the pore structure of cement based materials

Min Wu

PhD Thesis

Department of Civil Engineering

Technical University of Denmark

2014

Supervisors:

Associate Prof. Björn Johannesson[1]
Prof. Mette Rica Geiker[2]

Assessment committee:

Associate Prof. Lisbeth M. Ottosen[1]
Prof. Lars Wadsö[3]
Prof. Geert De Schutter [4]

[1]Dept. of Civil Engineering, Technical University of Denmark, Denmark
[2]Dept. of Structural Engineering, Norwegian University of Science and Technology, Norway
[3]Division of Building Materials, Lund University, Sweden
[4]Dept. of Structural Engineering, Ghent University, Belgium

Preface

This thesis is submitted by Min Wu, as a partial fulfilment of the requirements for the Danish PhD degree at the Technical University of Denmark. The thesis is based on the investigations conducted for Project 10 "*Cryoporometry characterization for cement based materials*" of the Marie Curie Initial Training Network (MC ITN) TRANSCEND programme. This programme consists of 15 PhD projects and is financed by the European Community (Framework Programme 7), aiming at understanding water transport in concrete structures. The TRANSCEND programme is divided into three principal themes: theme A is about modeling of water dynamics in cement pastes; theme B concerns experimental work to provide input data to the modeling and theme C is about experimental work to validate the modeling. The present work is a part of the theme B. The thesis consists of the following three parts:

Part I Introduction and summary
Part II Appendices
Part III Appended papers

Part I introduces the general background, some fundamentals of cement based materials and summarizes the studies conducted in this PhD project. The six appendices collected in **Part II** are materials supporting the experimental and analysis methods used in this research. **Part III** is a collection of a part of the papers completed during the PhD project.

The principal supervisor of this PhD project was Associate Professor Björn Johannesson from the Department of Civil Engineering of the Technical University of Denmark (DTU Byg) and the co-supervisor was Professor Mette Rica Geiker from the Department of Structural Engineering of Norwegian University of Science and Technology (NTNU). Dr. Jeffrey Chen and Dr. Ellis Gartner from Lafarge Centre de Recherche (LCR) France were the industrial advisors. The experimental work related to the moisture fixation method was carried out at DTU Byg and the experimental work of low temperature calorimetry was mainly conducted at the Building Materials Laboratory of Lund University.

Kongens Lyngby, 28th March 2014
Min Wu

Acknowledgments

I would like to extend my deepest gratitude to my supervisors Björn Johannesson at DTU and Mette Geiker at NTNU for their kind guidance, constructive suggestions, consistent support and teaching throughout the course of my PhD study. I also would like to express my sincere thanks to my industrial advisors, Jeffrey Chen and Ellis Gartner, at Lafarge Centre de Recherche for stimulating discussions, advice and the kind arrangements for my visits to Lafarge. Thanks to all of your kind help, I have gained a lot of invaluable experience and knowledge during my PhD study period, not only scientifically but also on many other aspects.

I owe my thanks to the staff at the Division of Building Materials of Lund University. I really appreciate the kind welcome I received each time when I visited the Division. Moreover, I enjoyed the discussions with Dr. Katja Fridh on low temperature calorimetry, which were really stimulating and fruitful. Additionally, I would like to thank Dr. Katja Fridh and Stefan Backe for their great help in performing some of the experiments on low temperature calorimetry.

I am truly grateful to have chances to meet the professors, researchers, fellow PhD students and friends in the Marie Curie Initial Training Network TRANSCEND and Nanocem consortium. This is really a treasure during my PhD study and I believe it is going to be the most important network in my whole life. Meanwhile, I also want to sincerely thank my colleagues at the Section of Construction Materials at DTU Byg for their kind and great help with my work and my life in Denmark.

With respect to financial contributions, I am grateful to the funding received from the European Union Seventh Framework Programme (FP7/2007-2013) under grant agreement 264448. Also, I acknowledge the contribution from Otto Mønsted's Fund, which partially sponsored expenses of conference participation.

Very importantly, I would like to acknowledge my family for their unconditional support and continuous encouragement, even though it is from a long distance. I feel my family is always with me no matter where I am and what I do. Also I wish to extend my gratitude to the friends I meet here in Denmark, who make my work and life in this foreign country much better. I will always be grateful to all of you.

Abstract

Pore structure is one of the most important characteristics of cement based materials. This PhD study focused on using a low (micro-)temperature calorimetry (LTC) and a moisture fixation method to study the pore structure of cement based materials, especially at the nanometric level. Special attention was devoted to investigating important factors influencing the analysis of measured LTC data and using LTC to characterize the pore structure of cement based materials. Besides, the moisture fixation method was selected as a comparison and complementary method to the LTC. Attempts have been made to correlate the porosity characteristics determined by the two different techniques.

The experimental investigations were mainly conducted on a mono-sized model material MCM-41 and samples of two types of well hydrated cement pastes made from CEM I 32.5 R and CEM III/B 42.5 N, respectively. The primary consideration of including the model material in this investigation was to validate the applicability of the chosen methods in the context of pore size determination. In addition, data from literature were used.

LTC investigations conducted in this PhD study include the ice content determination from measured data, the impact of sample saturation on the detected porosity, the effect of frost damage on the pore size distribution determination by LTC, the effect of preconditioning the cement paste samples on the freezing and melting behavior of the pore solution, the impact of sample crushing and a preliminary exploration of the influence of ions present in cement pore solution during measurements on the porosity determination by LTC.

Important results of the LTC investigations can be summarized as follows: (1) Two factors are of paramount importance in the analysis of measured LTC data, i.e., the baseline determination of the measured heat flow and the values adopted for the heat of fusion for the water/ice confined in pores. (2) Sample saturation has an impact on the porosity determination by LTC. The freezing/melting point of the water/ice in a non-fully saturated pore system is lower compared with the case when the system is fully saturated. Using non-fully saturated samples, some pores will be misinterpreted in the sense that they are estimated to be too small. (3) Frost damage may take place in the used cylinder samples of the studied cement pastes. It was concluded that frost damage potentially changes the pore connectivity while it has limited effect

on changing the interior size distribution of the meso-pores. (4) Hardened cement paste samples were preconditioned in a big amount or in a small amount of saturated limewater for a relatively long time. The results indicate that the two preconditioning cases have very limited influence on the freezing and melting behaviors of the pore solution in the studied cement paste samples. (5) Two types of samples, i.e., in the form of powders and cylinders, of two types of cement pastes (CEM I and CEM III) were used to study the impact of sample crushing on the porosity determination by LTC. For the CEM I samples, the results indicate that sample crushing only changes the pore connectivity while it has limited effect on the pore (interior) size distribution and the total pore volume. For the CEM III samples, however, sample crushing not only changes the pore connectivity but also the pore (interior) size distribution and the total pore volume. (6) Thermodynamic modeling using the program PHREEQC was performed on relevant cement paste samples. The results suggest that for the studied paste samples, the temperature depression caused by the ions present in the pore solution only affects the determination of the pore size distribution by LTC to a limited extent.

Moisture fixation behaviors of the materials were studied by the "dynamic (water) vapor sorption" (DVS) measurements at the hygroscopic range and pressure plate measurements at the over-hygroscopic range.

Key points of the sorption studies can be summarized as follows: (1) A resaturation study was used to investigate the possible pore structure changes at low relative humidities (RHs). The results showed that the drying at low RHs does not cause any microstructure changes or, alternatively, that the absorption process must have been able to fully restore the pore structure of hardened cement paste samples, indicating the possible microstructure changes are reversible. (2) A study on sorption isotherms suggests that the differences between the sorption isotherms measured at different temperatures are mainly a consequence of the temperature dependent properties of water. The pronounced impact of temperature on desorption isotherms of cement based materials as reported in some references in literature were not found in this study. (3) The calculated specific surface areas were very much dependent on the type of equations used for describing multilayer adsorption, indicating that the calculated specific surface area may not represent the "real" geometrical surface area. (4) The important factors influencing the analyzed pore size distribution (PSD) results using sorption data were reviewed. For the studied hardened cement pastes CEM I and CEM III, three characteristic peaks with the radii of about 1.4, 1.8 and 3.0 nm were found in the calculated PSD curves from the desorption isotherms. The peak at 1.4 nm was missing in the PSD curves calculated from the absorption isotherm. The network theory, suggesting desorption is controlled by the pore entry sizes while absorption is controlled by the interior pore sizes, tends to be of great relevance in explaining the results.

The PSD results determined by the LTC and the water vapor sorption method were compared and only a certain degree of agreement has been found. Due to the uncertainties and many unsolved factors involved in the data analysis, it is concluded that probably none of these two methods can deliver the "true" (actual) pore size distribution information. That is, before the uncertainties and unsolved factors being solved, both methods are only semi-quantitative and meaningful for comparison purposes.

Resumé (in Danish)

Porestrukturen er en af de vigtigste karakteristika ved cement baserede materialer. Dette PhD studium har fokuseret på brugen af lav (mikro-)temperatur calorimetri (LTC) og en fugt fikserings metode til bestemmelse af porestrukturen i cement baserede materialer, specielt på nano-skala. Der er specielt lagt vægt på undersøgelser af faktorer, som har indflydelse på analysen af målte data og brugen af LTC til at karakterisere porestrukturen i cement baserede materialer. Fugt fikserings metoden blev valgt både for at sammenligne med og komplementere LTC. Det skal hertil siges, at begge metoder kan anvendes på prøver og forudsætter således ikke tørring af prøver inden analyserne. Der er forsøgt at etablere en korrelation imellem porøsitets karakteristika bestemt ved de to anvendte metoder.

De eksperimentelle undersøgelser var hovedsagelig udført på et model materiale MCM-41med een veldefineret porestørrelse og prøver af to typer vel hydratiserede cement pastaer lavet af henholdsvis CEM I 32,5 R og CEM III/B 42,5 N. De primære formål med brugen af model materialet i undersøgelserne var at validere anvendeligheden af de valgte metoder til porestørrelses karakterisering. Endvidere blev data fra litteraturen anvendt.

LTC undersøgelser udført i dette PhD studium inkluderer is mængden bestemt fra målte data, indflydelsen af prøvens mætningsgrad, effekten af forkonditionering af cement pasta prøverne på fryse og tø processen i pore opløsningen, effekten af knuste prøve emner og en foreløbig undersøgelse af indflydelsen af ioner i cementpastaens pore opløsning på målinger af porøsitet bestemt ved LTC.

Vigtige resultaterne fra LTC undersøgelserne kan summeres som følgende: (1) To faktorer har væsentlig betydning for analysen af målte LTC data: bestemmelsen af basislinjen af den målte varmestrøm og værdierne for entalpi for vand/is i porerne. (2) Mætningsgrad af prøveemnet har en indflydelse på porøsiteten bestemt ved LTC. Smelte-/frysepunktet for vand/is i et ikke vandmættet poresystem er lavere, sammenlignet med et fuldt vandmættet system. Ved brugen af ikke-vandmættede prøver, vil nogle porer bestemt til at mindre end deres faktiske størrelse. (3) Frostskader forekommer muligvis i de cylinder formede cement pasta prøver. Det blev konkluderet at frostskader muligvis kunne ændre pore sammenhængen, imens det har begrænset effekt på ændringen af den indre porestørrelses fordeling af meso-porene. (4) Hærdede cement pasta prøver var pre-konditionerede i en stor mænge eller lille mængde mættet

kalkvand i relativt lang tid. Resultatet indikerede, at de to forkonditionerings metoder havde en begrænset effekt på fryse og tø egenskaber af pore opløsningen for de undersøgte cement pasta prøver. (5) To typer af prøver, i form af pulver og cylindre af to typer cement (CEM I og CEM III) blev brugt til at studere indflydelsen af knusning af prøveemner på porøsiteten bestemt ved LTC. For CEM I prøverne, havde knusning af prøverne alene indflydelse på sammenhængsgraden af porerne, imens den indre porestørrelses fordeling kun blev ændret i et begrænset omfang. For CEM III prøverne blev bådesammenhængsgraden af porerne, den indre porestørrelses fordeling og det totale porevolumen påvirket. (6) Termodynamisk modellering med PHREEQC blev foretaget for relevante cement pasta prøver. Resultaterne indikerede, for de undersøgte pasta prøver, at temperatur sænkningen forårsaget af tilstædeværeslen af ioner i poreopløsningen kun har begrænset effekt på porestørrelses fordelingen bestemt med LTC.

Fugt fiksering i materialerne blev undersøgt med "dynamisk vanddamp sorption (DVS)" målinger i det hygroskopiske område og trykplade målinger i det overhygroskopiske område.

Nøglepunkter i sorptions studierne kan sammenfattes således: (1) En genopfugtnings undersøgelse blev brugt til at undersøge mulige porestruktur ændringer ved lave relative fugtigheder (RF). Resultaterne viste, at udtørring ved lav RF ikke forårsaget mikrostruktur ændringer, eller alternativt, at absorptions processen måtte have været i stand til at genskabe porestrukturen i hærdede cement pasta prøver, som kunne indikere, at mikrostruktur ændreinger er reversible. (2) En undersøgelse af sorptions isotermer viste at forskellen imellem sorptions isotermer målt ved forskellige temperaturer hovedsagelig er en konsekvens af vands temperatur afhængige egenskaber. Indflydelsen af temperaturen på desorptions isotermer for cement baserede materialer som det er reporteret i referencer fra litteraturen blev ikke fundet i dette studie. (3) Det beregnede specifikke overflade areal var meget afhængig af det valgte matematiske udtryk for beskrivelsen af multi-lags adsorption, hvilket indikerer at det beregnede overflade areal ikke er repræsentativt for det eksakte geometriske areal. (4) De vigtige faktorer som har indflydelse på de analyserede porestørrelse fordelings (PSD) resultater, ved hjælp af sorptions data blev opsummeret. For de undersøgte cement pastaer CEM I og CEM III, blev tre karakteristiske toppunkter med radius pa omkring 1,4, 1,8 og 3,0 nm fundet i de beregnede PSD-kurver fra desorption isotermerne. Toppunktet ved 1.4 nm blev ikke fundet på PSD-kurven for den beregnede absorptions isoterm. Netværks teorien, som foreslår at desorption er kontrolleret af pore åbnings størrelsen imens absorption er kontrolleret af de interne porestørrelser, synes at have stor relevans ved forklaringen af resultaterne.

PSD-resultaterne bestemt ved LTC og vanddamp sorptions metoden blev sammenlignet og delvis overensstemmelse blev fundet. På grund af usikkerheder og mangelfuld beskrivelse af flere faktorer involveret i data analysen, er det konkluderet, at

sandsynligvis ingen af de to metoder kan gengive den information om porestørrelses fordelingen korrekt. Dette betyder, at før usikkerhederne og uløste faktorer er løst, er begge metoder semi-kvantitative med meningsfyldte til sammenlignings.

Contents

List of Symbols **xix**

List of Abbreviations **xxi**

I Introduction and summary **1**

1 Introduction **3**
1.1 Background 3
1.2 Scope and objectives 6
1.3 Organization of contents 6

2 Fundamentals of cement based materials **9**
2.1 Introduction 9
2.2 Manufacturing process of Portland cement 10
2.3 Hydration process of Portland cement 11
2.3.1 Cement composition and minerals 11
2.3.2 Chemical reactions involved in hydration 12
2.3.3 Hydration process and the heat evolution 13
2.4 Microstructure of cement based materials 14
2.4.1 Hydration products 15
2.4.2 Pore structure 17
2.4.3 Water in hydrated cement paste 18
2.4.4 C-S-H models 19
2.5 Porosity characterization 21
2.5.1 Microscopy techniques 22
2.5.2 Mercury intrusion porosimetry (MIP) 23
2.5.3 Gas adsorption and desorption 24
2.5.4 Low temperature calorimetry (LTC) 25
2.5.5 Nuclear magnetic resonance (NMR) 26

3 Low temperature calorimetry on cement based materials **29**
3.1 Introduction 29

3.2 Summary of low temperature calorimetry investigations 30
3.2.1 Overview of the LTC investigations 30
3.2.2 Summary of the LTC investigations 32
3.2.2.1 Ice content determination 32
3.2.2.2 Impact of sample saturation 34
3.2.2.3 Frost damage on the porosity determination 35
3.2.2.4 Sample preconditioning on the freezing/melting behaviors 36
3.2.2.5 Sample crushing on the porosity determination 37
3.2.2.6 Ions effect on the porosity determination 38

4 Moisture fixation on cement based materials 41
4.1 Introduction 41
4.2 Measurement of sorption isotherms 42
4.2.1 Measurement methods 42
4.2.1.1 Salt solution method 42
4.2.1.2 Dynamic vapor sorption (DVS) method 43
4.2.1.3 Pressure plate method 44
4.2.2 Measurements on studied materials 45
4.3 Summary of moisture fixation studies 46
4.3.1 Overview of moisture fixation studies 46
4.3.2 Summary of moisture fixation studies 46
4.3.2.1 Determined sorption isotherms 46
4.3.2.2 Possible pore structure changes at low relative humidities 50
4.3.2.3 Temperature dependent isotherms 51
4.3.2.4 Specific surface area 52
4.3.2.5 Pore size distribution 53

5 Comparison of porosity by LTC and water vapor sorption method 57
5.1 Introduction 57
5.2 General comparison 57
5.3 Porosity results determined by LTC and water vapor sorption method . 59

6 Conclusions and future studies 65
6.1 Conclusions 65
6.2 Future studies 69

II Appendices 73
A Freezing/melting point and pore size 74
B Cooling/heating rate stability on the ice content calculation 78

C Equations for multilayer adsorption 87

D Kelvin equation and Kelvin-Laplace equation 98

E Calculation of pore size distribution 102

F Thermodynamic database of PHREEQC-CEMDATA07 107

Bibliography **119**

III Appended Papers 135

Paper I

Determination of ice content in hardened concrete by low-temperature calorimetry: influence of baseline calculation and heat of fusion of confined water

M. Wu, B. Johannesson, M. Geiker

Published in: *Journal of Thermal Analysis and Calorimetry, 2014* 137

Paper II

Impact of sample saturation on the detected porosity of hardened concrete using low temperature calorimetry

M. Wu, B. Johannesson

Published in: *Thermochimica Acta, 2014* 161

Paper III

Influence of frost damage and sample preconditioning in studying the porosity of cement based materials using low temperature calorimetry

M. Wu, K. Fridh, B. Johannesson, M. Geiker

Submitted to: *Construction and Building Materials, 2014* 177

Paper IV

Impact of sample crushing on porosity characterization of hardened cement pastes by low temperature calorimetry: comparison of powder and cylinder samples

M. Wu, K. Fridh, B. Johannesson, M. Geiker

Submitted to: *Journal of Thermal Analysis and Calorimetry, 2014* 203

Paper V

A preliminary study of the influence of ions in the pore solution of hardened cement pastes on the porosity determination by low temperature calorimetry

M. Wu, B. Johannesson, M. Geiker

Published in: *Thermochimica Acta, 2014* 225

Paper VI

A study of the water vapor sorption isotherms of hardened cement pastes: possible pore structure changes at low relative humidity and the impact of temperature on isotherms

M. Wu, B. Johannesson, M. Geiker

Published in: *Cement and Concrete Research, 2014* 239

Paper VII

Application of water vapor sorption measurement for porosity characterization of hardened cement pastes

M. Wu, B. Johannesson, M. Geiker

Accepted by: *Construction and Building Materials, 2014* 251

List of Symbols

Symbols

A	m^2	Area
A_m	$Å^2$	The area occupied by one water molecule
A, B, A', a	-	Constants
a_i, b_i	-	Material constants in adsorption
a^0, b	-	Parameters for ionic species
b, c	-	Two-layer BET equation constants
C_p	J/kg/K	Heat capacity
$\mathbf{c}$	mol	Oxide composition vector of a hydrated cement
c	mol/kgW	Concentration
c	-	BET equation constant
c, k	-	GAB equation constants
d	nm	Thickness of a monolayer water molecules
E_i	J	Heat of adsorption
G	J/mol	Gibbs free energy
$\triangle G$	J/mol	Gibbs free energy of a reaction
$\triangle_r G^\Theta$	J/mol	Standard Gibbs free energy of a reaction
g	-	Constant for adsorption
H	J/mol	Enthalpy
$\triangle H$	J/mol	Enthalpy of a reaction
$\triangle_r H^\Theta$	J/mol	Standard enthalpy of a reaction
$\triangle H_{fus}$	J/mol	Heat of fusion
h	J	Heat
$\triangle h$	J/g	Specific heat of fusion
K_a	-	Thermodynamic equilibrium constant
K_1, K_2, K_3	-	Constants for hydration rate predication
l	m	Length
M	kg/mol	Molecular weight
M, N	-	Number of components, species
m	kg	Mass of a substance
N_A	/mol	Avogadro constant
N_1, N_3		Constants for hydration rate predication
n	mol	Amount of substance
n_i	-	Stoichiometric coefficient
P, p	Pa	Pressure
$\mathbf{p}$	-	Oxide content vector of a cement

Q	J/g	Heat flow
q	K/s [°C/s]	Cooling/heating rate
$\mathbf{R}$	-	Matrix for Bogue calculation
R	J/mol/K	Ideal gas constant
R_p	m	Pore size
R_t	-	Rate of hydration
r	m	Radius of the interfacial curvature
r_k	m	Kelvin radius
S	m^2/g	Specific surface area
S	J/mol/K	Entropy
$\triangle S$	J/mol/K	Entropy of a reaction
$\triangle_r S^{\Theta}$	J/mol/K	Standard entropy of a reaction
s	J/g/K	Specific entropy
s_i	m^2/g	Surface area occupied by layers of adsorbed molecules
T	K	Temperature
ΔT	K	Temperature depression
t	s	Time
t	m	Thickness of adsorbed layer
V	m^3	Volume
v	m^3/g	Specific volume
v	m^3/g	Volume of adsorbed vapor
v_m	g/g	Monolayer capacity
W_{aq}	kg	Mass of water
$\mathbf{x}$	mol	Mineral content vector of a cement
x	-	Mole fraction
x	-	Relative pressure (humidity)
y, z	-	Parameters for adsorption
z_i	-	Ionic charge of aqueous species
α	-	Hydration degree
γ	N/m	Surface tension of an interface
γ	-	Activity coefficient of ions
δ	nm	Thickness of un-freezable layer
λ	-	Activity coefficient of solid solution component
μ	mol/kgW	Ionic strength
μ	J/mol	Chemical potential
θ	°C	Temperature
ρ	kg/m^3	Density
ϕ	-	Relative humidity

Indicia:

0	reference or initial state
f, m	freezing, melting
l	liquid phase
$g(v)$	gas (vapor) phase
s	solid phase
w	water
fus	fusion

List of Abbreviations

Abbreviations

AFM	Atomic Force Microscopy
AFm	monosulfate aluminate hydrate
AFt	ettringite
ASTM	American Society for Testing and Materials
BET	Brunauer, Emmett and Teller
BJH	Barrett, Joyner and Halenda
BSE	Back Scattered Electrons
C_2S	dicalcium silicate $2\,CaO \cdot SiO_2$
C_4AF	calcium ferroaluminate $4\,CaO \cdot Al_2O_3 \cdot Fe_2O_3$
C_3A	tricalcium aluminate $3\,CaO \cdot Al_2O_3$
C_3S	tricalcium silicate $3\,CaO \cdot SiO_2$
CH	Calcium Hydroxide
CEMHYD3D	Three Dimensional CEMent HYDration model
C-S-H	Calcium-Silicate-Hydrates
DVS	Dynamic (water) Vapor Sorption
EDS	Energy Dispersive Spectroscopy
HEB	HEat of fusion of Bulk water
HEBT	HEat of fusion of Bulk water but corrected for Temperature dependence
HEMC	HEat of fusion of water Modified for Cylindrical pores
HEMS	HEat of fusion of water Modified for Spherical pores
HYMOSTRUC	HYdration, MOrphology and STRUCture formation
HydratiCA	Hydration model applying Cellular Automata
IUPAC	International Union of Pure and Applied Chemistry
LTC	Low Temperature Calorimetry
MC ITN	Marie Curie Initial Training Network
MIP	Mercury Intrusion Porosimetry
NAD	Nitrogen Adsorption/Desorption
NMR	Nuclear Magnetic Resonance
OPC	Ordinary Portland Cement
PSD	Pore Size Distribution
PHREEQC	PH (pH), RE (redox), EQ (equilibrium) and C (program written in C)

RH	Relative Humidity
SAXS	Small Angle X-ray Scattering
SANS	Small Angle Neutron Scattering
SCM	Supplementary Cementitious Materials
SE	Secondary Electrons
SEM	Scanning Electron Microscopy
TEM	Transmission Electron Microscopy
TRANSCEND	understanding TRANSport for Concrete which is Eco friendly iNnovative and Durable
w/c	water to cement ratio
XRD	X-ray Diffraction
XRF	X-ray Florescence Spectroscopy

Part I

Introduction and summary

Chapter 1

Introduction

1.1 Background

Concrete is the single most widely used construction material in the world. The production scale of concrete is huge, which is on the order of several billion tonnes per year [USGS Mineral Commodities Summary 2013, Chemistry World 2008]. One important reason for the large use of concrete is perhaps its cheap price. Figure 1.1 compares the price of some commonly used materials and the annual production. There are other factors which make concrete easy to use, including, e.g., the availability of raw materials, the ease of transport, the ease of constructability (complex equipment are not required on the construction site) and the flexibility in its use (it can fill into almost any shape and can set and harden at different environments) [Valori 2009].

Cement is the primary binding component of concrete. Due to the huge demand on concrete, consequently the amount of cement produced each year is huge. It is well known that the cement industry consumes a large quantity of energy. This fact perhaps creates a misconception in common sense that cement industry is quite energy intensive. Actually, the energy consumption of producing one unit mass (or volume) of cement is relatively low. The production energy of cement and concrete is compared with other construction materials as presented in Figure 1.2. It is essentially the huge amount of cement produced yearly worldwide that results in a high total energy consumption.

Greenhouse gas emission and its in pact on the environment is a great challenge for human beings. Due to the huge amount of production, cement industry is responsible for about $5 \sim 7$ % of global man-made CO_2 emission, making it an important target for CO_2 emission mitigation strategies. The difficulty in reducing the emission is partly because only small improvements can be made with better combustion techniques or by using alternative fuels. The cement manufacture process is believed to be close to 80 % efficient in terms of heat recovery and fuel optimization [Scrivener 2006,

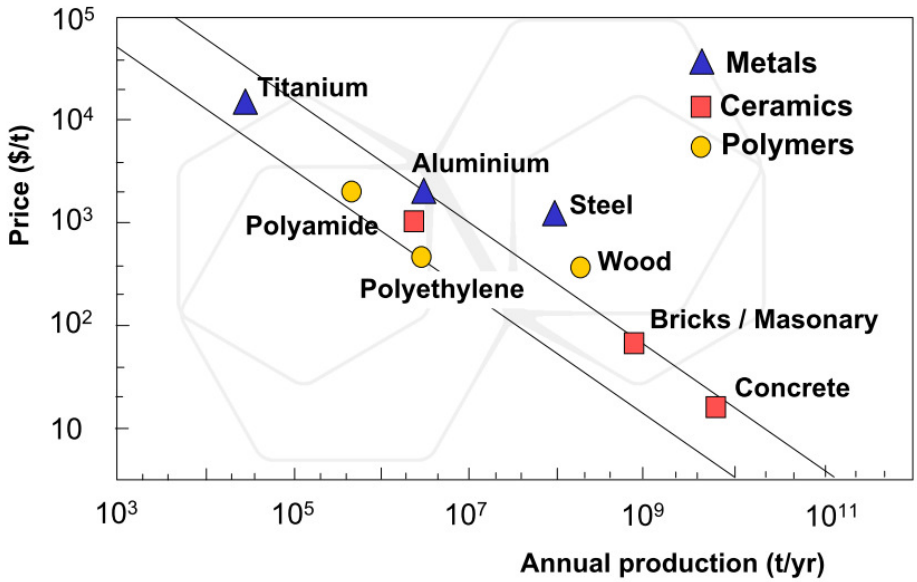

Figure 1.1: Price of some of the commonly used materials versus the annual production (after [Mercier et al. 1999]).

Valori 2009]. It should be observed, however, that more than half of the CO_2 associated with cement manufacture comes from the breakdown of limestone into calcium oxide and carbon dioxide [Scrivener 2011]. That is, in order to drastically reduce the emission, a different chemistry must be adopted in terms of the raw materials used [Scrivener 2011]. Even though a change in the basic manufacturing chemistry and types of raw materials used to produce cement are not foreseeable in the near future, a present useful trend is the using of Supplementary Cementitious Materials (SCM), such as fly ash and granulated blast furnace slag [Valori 2009, Scrivener 2011].

The cement industry urgently requires more sustainable cement based products with equal or better performance to current materials over the life time of buildings and infra-structures (∼100 years) [Scrivener 2011]. A major obstacle to the introduction of new and more sustainable cementitious materials is the lack of understanding on the underlying degradation mechanisms of the materials [MC ITN TRANSCEND Website]. Thus, important properties and processes related to the degradation of cement based materials must be understood to ensure durability, which in turn will allow the introduction of new and more sustainable and environmentally friendly cementitious materials [MC ITN TRANSCEND Website].

Porosity is one of the most, if not the most, important characteristics of cement based materials. It is the main parameter which determines strength and influences transport properties and permeability. Moreover, it is also a major parameter determining durability.

It is generally acknowledged that there exist different types of pores with different pore sizes in a cement based material. There are deliberately entrained air voids with diameters in the order of 50–100 μm used for frost protection [Powers 1949, Pi-

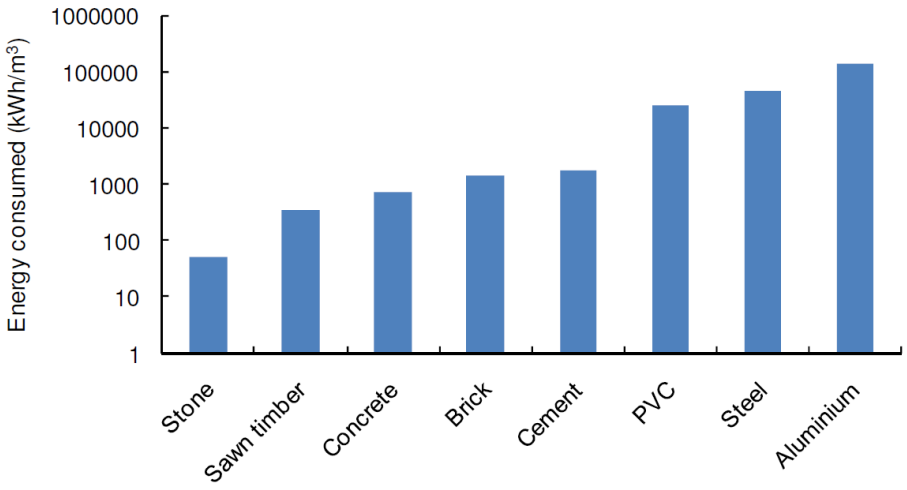

Figure 1.2: Production energy of cement, concrete and other construction materials (after [Kirby 2008]).

geon and Pleau 1995]. Mixing and casting often entrap air voids whose size can reach the millimeter scale [Kosmatka and Panarese 2002]. Also, there are nano-microscale "capillary pores" that are remnants of the interstitial spaces between the unhydrated cement grains [Powers and Brownyard 1947]. Additionally, as described, e.g., in [Jennings 2008, McDonald et al. 2010], there are interlayer spaces, or "gel pores" at the nanometric level between the primary particles of the hydration products calcium-silicate-hydrates (C-S-H). It is also demonstrated that the transport properties of mature cement based materials are dominated by the mesopores [Scherer et al. 2007], with characteristic sizes between 2 and 50 nm according to the IUPAC definition [Sing et al. 1985].

Because of the paramount importance of porosity to the performances of cement based materials, considerable efforts have been devoted to understanding the pore structure. Many methods for porosity characterization have been developed and applied to cement based materials [Feldman 1989, Thomas et al. 1999, Strange et al. 2003, Baroghel-Bouny 2007, Kjeldsen and Geiker 2008, Sun and Scherer 2010], e.g., nitrogen adsorption/desorption (NAD), mercury intrusion porosimetry (MIP), scanning electron microscopy (SEM), small angle scattering using X-rays or neutrons, low (micro-)temperature calorimetry (LTC), nuclear magnetic resonance (NMR), moisture fixation, etc. The background of some of the methods mentioned above are summarized in *Chapter 2*. A discussion of the comparison with respect to the strengths and limitations of some of the methods can be found in the appended *Paper II*.

It is noted that most of the porosity characterization methods are indirect approaches. One aim of this PhD study was by investigating the selected experimental and analysis methods, the characterized pore structure of cement based materials, especially at the nanometric level, is expected to be better understood.

1.2 Scope and objectives

Two methods, i.e., the LTC and the moisture fixation method, have been chosen to investigate the pore structure of cement based materials, especially at the nanometric level. Compared with traditional methods for porosity characterization, e.g., NAD, MIP and SEM, a major advantage of using the LTC and the moisture fixation method to characterize cement based materials is that the measurements can be conducted on virgin samples without any pre-drying treatment [Bager 1984, Hansen et al. 1997, Janz and Johannesson 2001, Baroghel-Bouny 2007, Kjeldsen and Geiker 2008, Sun and Scherer 2010]. That is because the pre-drying treatment often results in an alteration of cement based materials [Villadsen 1992]. Since both selected methods, i.e., the LTC and the moisture fixation method, are indirect methods for porosity characterization, special attention has to be paid to the factors influencing the measured data and the data analysis.

The experimental investigations were mainly conducted on a mono-sized model material MCM-41 and the samples of two types of well hydrated cement pastes made from CEM I 32.5 R and CEM III/B 42.5 N, respectively. The primary consideration of including the model material in this investigation was to validate the applicability of the chosen methods in the context of pore size determination. In addition, measurement data from the literature were used.

The main objectives of this research were:

- To investigate factors influencing the analysis of measured LTC data.
- To study effects due to, e.g., saturation state of the pore system, possible frost damage, sample preconditioning and the ions presented in cement pore solution, on the porosity determination using the LTC.
- To understand important aspects of the freezing behavior of the pore liquid in cement based materials.
- To better understand the porosity determined by the moisture fixation method.
- To compare the porosity characteristics determined by the LTC and the moisture fixation method.

1.3 Organization of contents

This thesis is divided into three parts, including:

Part I Introduction and summary This part introduces the general background, some fundamentals of cement based materials and mainly summarizes the studies conducted in this PhD project. It constitutes important underlying information to the included papers of this thesis, materials which are not suited for

papers but still important for the overall context. This part consists of six chapters.

Chapter 1 is a general description of the PhD project, containing the background, the scope and objectives and the organization of the contents.

Chapter 2 introduces some fundamentals of cement based materials based on literature study, including the basics of cement chemistry, hydration, microstructure development and pore structure characterization.

Chapter 3 summarizes the LTC studies conducted in this research, including: (1) the ice content determination; (2) the impact of sample saturation on the detected porosity; (3) the effect of frost damage on the pore size distribution determination by LTC; (4) the effect of preconditioning the cement paste samples on the freezing and melting behaviors of the cement pore solution; (5) the impact of sample crushing on the porosity determination by LTC and (6) a preliminary exploration of the influence of ions presented in cement pore solution on the porosity determination by LTC.

Chapter 4 gives a summary of the moisture fixation studies conducted in this research.

Chapter 5 compares the porosity results of the studied materials determined by LTC and moisture fixation method.

Chapter 6 summarizes the main conclusions of this research and provides some suggestions for further studies.

In the **Part I** of this PhD thesis, efforts haven been made to minimize the repetition and special attention has been paid to the details not described in the appended papers. Nevertheless, some repetition of the contents in the thesis may be necessary to make the message clear in all parts.

Part II Appendices The six appendices are important supporting materials to understand the experimental and analysis methods used in this thesis. Appendix A describes the adopted thermodynamic relation used between the depressed freezing/melting point and the pore size. In Appendix B, the impact of cooling and heating rate fluctuation or drift on the ice content calculation by LTC is discussed. Different sets of measurement data are used for these purposes. Appendix C concerns the detailed derivation of equations for multilayer adsorption. Appendix D presents the detailed derivations of the Kelvin equation and the Kelvin-Laplace equation, which are central in the evaluation methods using sorption measurements. In Appendix E, the main concepts of determining

pore size distribution using sorption data following the Barret, Joyner and Halenda (BJH) model is presented. Appendix F is the thermodynamic database for the aqueous species and the mineral phases used in the chemical equilibrium program PHREEQC and its calculation of this study.

Part III Appended papers This part consists a part of the papers completed during the PhD project, including five on the LTC and two on the moisture fixation method.

Chapter 2

Fundamentals of cement based materials

2.1 Introduction

Cement based materials have been used for a long time and are still widely used around the world. Scientific research work about the underlying chemistry of cement production and especially the hydration process started about 200 years ago [Johannesson 2011a]. Powers, who might be considered as the first modern cement scientist [Jennings et al. 2008], together with his co-workers did systematic studies on cement based systems since the 1940s, e.g., see [Powers and Brownyard 1947, Powers 1955, 1958, 1960], which greatly improved the understanding of cement based materials. Due to the increased awareness about the importance and the development of modern instruments and techniques, great advances have been made during the past decades. In modern cement and concrete research, computed based modeling becomes more and more useful and important, in which the notable representatives include thermodynamic modeling, e.g., see [Lothenbach and Winnefeld 2006, Lothenbach 2010, Damidot et al. 2011, Hosokawa et al. 2011, Kulik 2011], and the mathematical or geometric based modeling, e.g., the HYMOSTRUC model [van Breugel 1991], the CEMHYD3D model [Bentz 1997] and the HydratiCA model [Bullard 2007]. Knowledge about the fundamentals of cement based materials helps to understand the properties and performances of the materials. Moreover, it helps to understand and improve existing research methods (models) and to develop new ones.

In this chapter, some fundamentals of cement based materials are introduced. Firstly, the manufacturing and the hydration process of Portland cement are shortly described. Secondly, the microstructure of cement based materials, including the solid hydration products, pore structure and the state of water, are briefly summarized. A special focus is given to the structure models proposed for the principal binding phase, calcium silicate hydrate, at different length scales. Finally, since porosity

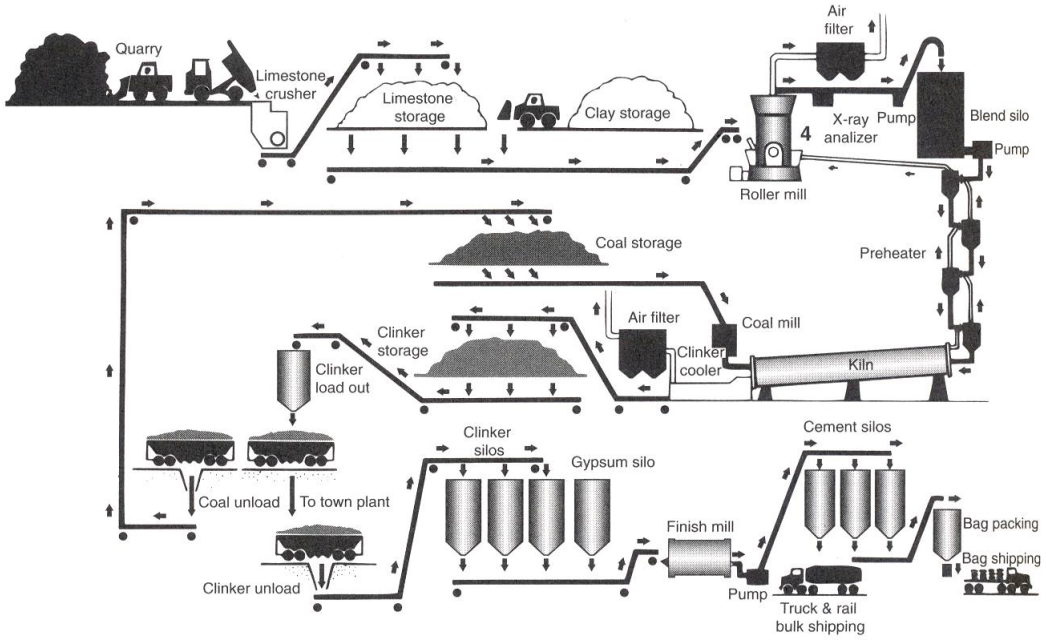

Figure 2.1: Schematic flow chart of the dry process of manufacturing Portland cement (after [Metha and Monteiro 2005]).

characterization is the main topic of this study, some of the techniques developed for this purpose and applied to cement based materials are reviewed and shortly discussed.

2.2 Manufacturing process of Portland cement

The modern cement manufacturing involves numerous complex processes and requires enormous equipment and machineries. The most common type of cement is Portland cement. Figure 2.1 schematically shows the flow of the so-called dry process of manufacturing Portland cement. A short summary of the manufacturing process is described in the following.

Raw materials containing calcium and silica are necessary in the manufacturing of Portland cement. Materials such as limestone, chalk, marl and sea-shells are the sources for calcium while silica mainly come from sand, clay and shale. The addition of other materials is often required to obtain the correct raw material composition. The raw materials are crushed, ground and blended in order to obtain a homogenized mix. The powdered raw mix is then fed into a rotary kiln which has a slope and allows the materials to move slowly from the highest part towards the lower parts. The powdered limestone, $CaCO_3$(s) is firstly calcined to break it down to free lime, CaO and CO_2(g) which is emitted to the environment. In the high temperature zone of the kiln, which is on the order of 1450 °C to 1550 °C, the chemical reactions forming the Portland cement compounds are completed. The formed compounds are cement clinkers. At the end of the manufacturing line, the hot clinkers are cooled down

and then finely ground into powders. Gypsum is usually added in the final grinding process to regulate the setting time of the produced cement when mixed with water.

2.3 Hydration process of Portland cement

2.3.1 Cement composition and minerals

The chemical composition of cement clinker is often expressed as weight percentage of oxides. Oxides of main importance in the clinker of Portland cement are CaO, SiO_2, Al_2O_3 and Fe_2O_3. The oxides do not occur in the cement clinker structure as suggested by the chemical formulas but in forms of different clinker minerals (phases). There are four main minerals in the sintered clinker, i.e., tricalcium silicate $3\,CaO \cdot SiO_2$, dicalcium silicate $2\,CaO \cdot SiO_2$, tricalcium aluminate $3\,CaO \cdot Al_2O_3$ and calcium ferroaluminate $4\,CaO \cdot Al_2O_3 \cdot Fe_2O_3$. In cement chemistry, short notation is usually used in which the four minerals are denoted as C_3S, C_2S, C_3A and C_4AF, respectively. Cement is a mixture of a clinker and the added gypsum $CaSO_4 \cdot 2\,H_2O$ ($C\underline{S}H_2$).

The oxide composition is important for the characteristics of the cement and can be experimentally determined by, e.g., X-ray florescence spectroscopy (XRF) [ASTM C114, Anzelmo 2009], X-ray diffraction (XRD) [Redler 1991, Struble 1991] and energy dispersive spectroscopy (EDS) [Lin et al. 1997]. With the known composition of the oxides, the amount of each mineral can be calculated using the Bogue equations, e.g., see [Taylor 1989, ASTM C150]. There are two sets of equations, based on the ratio of Al_2O_3/Fe_2O_3 (A/F) in the cement in question:

If $A/F \geq 0.64$

$$\begin{aligned} C_3S &= 4.071CaO - 7.600SiO_2 - 6.718Al_2O_3 - 1.430Fe_2O_3 - 2.852SO_3 \\ C_2S &= 2.867SiO_2 - 0.754C_3S \\ C_3A &= 2.650Al_2O_3 - 1.692Fe_2O_3 \\ C_4AF &= 3.043Fe_2O_3 \end{aligned} \tag{2.1}$$

or if $A/F < 0.64$[1]

$$\begin{aligned} C_3S &= 4.071CaO - 7.600SiO_2 - 4.479Al_2O_3 - 2.859Fe_2O_3 - 2.852SO_3 \\ C_2S &= 2.867SiO_2 - 0.754C_3S \\ C_3A &= 0 \\ ss(C_4AF + C_2F) &= 2.100Al_2O_3 + 1.702Fe_2O_3 \end{aligned} \tag{2.2}$$

[1]In this case, a calcium aluminoferrite solid solution (expressed as $ss(C_4AF + C_2F)$ is formed.

It should be mentioned that the Bogue calculation provides a quick but somewhat rough estimation with respect to the amount of the minerals. Discussions about the accuracy of the Bogue calculation can be found, e.g., in [Scrivener et al. 2004, Scrivener 2011].

2.3.2 Chemical reactions involved in hydration

When cement is mixed with water, a number of chemical reactions start to take place. The chemical reactions of cement minerals with water are usually called hydration. In most studies, pure individual minerals are used to investigate the hydration mechanisms. However, it should be noted that the hydration of Portland cement is rather complex because water reacts with C_3S, C_2S, C_3A and C_4AF simultaneously to form different hydration products. The reactions of the different minerals with water do not take place independently but are coupled to some extent. Nevertheless, in most cases, the hydration of Portland cement can be approximated as the sum of the hydration effects of the individual minerals [Taylor 1997, van Odler 1998]. The chemical reactions of the individual minerals have been described, e.g., in [van Odler 1998, Mindess et al. 2003, Jennings et al. 2002, Johannesson 2011b] and a summarized description is given as follows:

- Tricalcium silicate C_3S and dicalcium silicate C_2S react with water to produce calcium silicate hydrate, calcium hydroxide (CH). The reactions are

$$C_3S + (1.3 + x)H \rightarrow C_{1.7}SH_x + 1.3CH \tag{2.3}$$

$$C_2S + (0.3 + x)H \rightarrow C_{1.7}SH_x + 0.3CH \tag{2.4}$$

  The main hydration product, calcium silicate hydrate, does not have a well-defined composition. The x in reaction (2.3) and (2.4) indicates that the chemically bound water in the calcium silicate hydrate is not fixed. For this reason, the calcium silicate hydrate is often denoted as C-S-H. A typical formula for a water saturated C-S-H is $C_{1.7}SH_{4.0}$. The calcium hydroxide CH is also called portlandite.

- In the initial period of hydration, tricalcium aluminate C_3A reacts with gypsum $CaSO_4 \cdot 2\,H_2O$ ($C\underline{S}H_2$) and water to produce ettringite (AFt). The reaction can be expressed as

$$C_3A + 3C\underline{S}H_2 + 26H \rightarrow C_6A\underline{S}_3H_{32} \tag{2.5}$$

  When the gypsum is consumed up in reaction (2.5), the formed AFt becomes unstable and would react with any remaining C_3A to form monosulfate aluminate

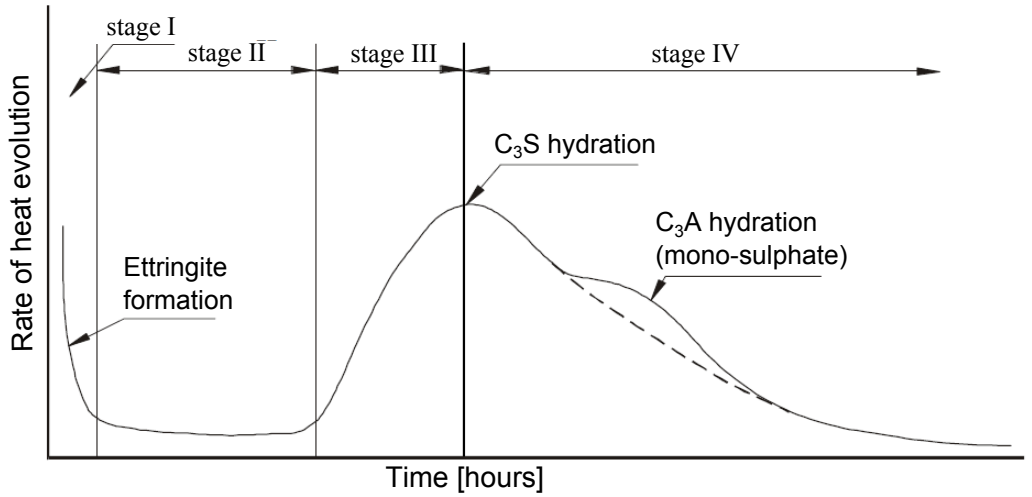

Figure 2.2: A typical heat evolution curve during the hydration of Portland cement (after [Mindess et al. 2003]).

hydrate (AFm), which is

$$2\,C_3A + C_6A\underline{S_3}H_{32} + 4H \rightarrow 3\,C_4A\underline{S}H_{12} \tag{2.6}$$

The formed AFm is only stable under sulfate-deficient conditions and it can be transformed back into AFt in the presence of sulfates, which is referred to delayed AFt formation. Another possible reaction for C_3A is

$$C_3A + 6H \rightarrow C_3AH_6 \tag{2.7}$$

- For the calcium ferroaluminate C_4AF, firstly it reacts with gypsum and water to form ettringite, portlandite and alumina hydroxide; and secondly, it further reacts with the formed ettringite in reaction (2.8) to produce garnets. The reactions can be expressd as

$$C_4AF + 3C\underline{S}H_2 + 30H \rightarrow C_6(A,F)\underline{S_3}H_{32} + (A,F)H_3 + CH \tag{2.8}$$

$$C_4AF + C_6(A,F)\underline{S_3}H_{32} + 2CH + 23H \rightarrow 3\,C_4(A,F)\underline{S}H_{18} + (A,F)H_3 \tag{2.9}$$

2.3.3 Hydration process and the heat evolution

Cement hydration process involves heat evolution and the heat evolution can indicate information about chemical reactions taking place during the hydration [Mindess et al. 2003, Scrivener 2011]. A typical heat evolution curve for the hydration of Portland cement is shown in Figure 2.2. Based on the heat evolution behavior, the hydration process of Portland cement may be divided into several different stages [Mindess et al. 2003, Scrivener 2011].

- Stage I: Pre-induction stage
  Cement hydration initiates immediately after mixing with water. Calcium and hydroxide ions are released from the surface of cement grains. Together with other released ions, e.g., Na^+ and K^+, the alkalinity of the solution rises. During this initiating stage, C_3A is the most active mineral. The duration of this stage is on the order of minutes.

- Stage II: Induction (dormant) stage
  After the rapid reactions in the first few minutes (stage I), the rate of hydration slows down. The reasons for the slowing down of the hydration at this stage include, e.g., the "protective layer theory" and the "delayed nucleation and growth theory" [van Breugel 1991, Taylor 1997, Scrivener 2004]. The duration of this stage is about 2-4 hours, depending on, e.g., the fineness, chemical composition of the cement and the hydration temperature.

- Stage III: Acceleration stage
  The rate of hydration increases and reaches a maximum value at the end of stage III. During this period, the hydration rate of C_3S accelerates and the hydration of C_2S starts to become noticeable [van Odler 1998]. This is the period in which final set is completed and the early hardening begins. The duration of this stage is on the order of hours.

- Stage IV: Post-acceleration stage
  The rate of hydration decreases gradually in this stage. The hydration product C-S-H continues to grow and the contribution from the less reactive mineral C_2S increases. This period could last for a long time, even years [Taylor 1997]. It is also noted that some authors, e.g., see [Nelson and Guillot 2006], divide the stage IV described here further into two stages: deceleration stage and steady-state (diffusion limited) stage.

2.4 Microstructure of cement based materials

Cement based materials have complex and multi-component structure at multiscales with a high degree of heterogeneity. The structure starts to form from the beginning of hydration and continues to evolve with time. The microstructure is of vital importance in the overall understanding of the behavior of cement based materials, since all the properties of a material can be related to its microstructure to some extent [Scrivener 1989].

When cement particles and water are mixed, the microstructure starts to develop. At the very beginning, cement particles are separated and suspended in the mixing water. Then the hydration products (solid phases) are produced either on the

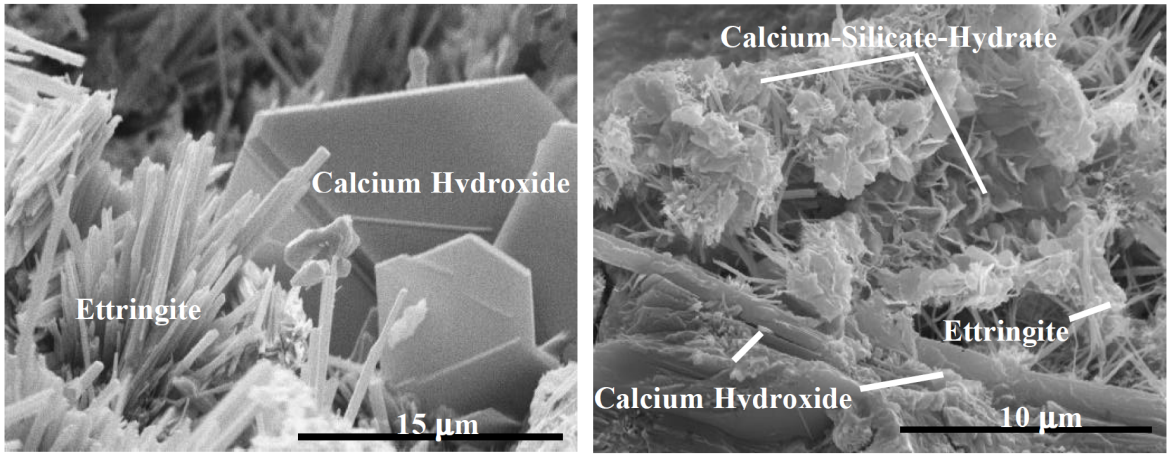

(a) (b)

Figure 2.3: The main hydration products of Portland cement observed under a scanning electron microscope. Type I and Type II C-S-H are in fine bundles. CH is plate-like crystalline and AFt is in the form of needles (after [Stutzman 2000]).

surface of cement particles or precipitated in the water filled spaces surrounding the cement particles. Since the volume of the hydration products is smaller than the initial volume of cement powders and water from which they are formed, a pore system is generated. As the hydration goes on, more and more solids are formed and they start to connect each other. Afterwards, there comes a period in which the hydration products increase rapidly. At the late age of hydration, all the hydration products are connected and the remaining unreacted materials hydrate slowly by a solid state mechanism resulting into only a slow increase of the solid phases. A detained description of the microstructural development in hydrating cement based materials can be found, e.g., in [Locher et al. 1976, Scrivener 1984, Taylor 1997, van Odler 1998].

In this section, the microstructure of a cement paste, including the hydration products and the pore structure, is briefly introduced. It should be mentioned that a lot of attention has been paid to the state of water in cement structure because it plays a key role in most (if not all) of the processes from hardening to degradation, e.g., see [Powers 1958, Jennings et al. 2002, Metha and Monteiro 2005]. For this reason, water has been suggested to be considered as a part of the cement structure [Valori 2009]. Besides, a short summary about several models in literature describing the structure of the principal hydration product C-S-H, is given.

2.4.1 Hydration products

Calcium silicate hydrate (C-S-H), calcium hydroxide (CH), ettringite (AFt) and monosulfate aluminate (AFm) are the main hydration products of Portland cement. Figure 2.3 shows an example of the hydration products observed using a scanning electron microscope.

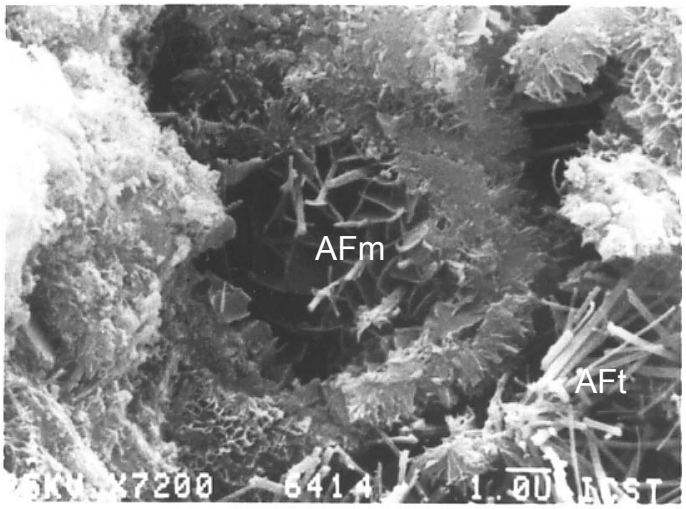

Figure 2.4: Morphologies of ettringite (AFt) and monosulfate aluminate (AFm) observed in a 7-day hardened cement paste (after [Scrivener 2011]).

C-S-H is in many respects the most important hydration product. As mentioned before, the stoichiometric composition of C-S-H varies. The C-S-H products with different stoichiometry are usually collectively mentioned as C-S-H gel. It has been reported that several morphologies of C-S-H gel are formed during cement hydration [Lachowski and Diamond 1983, Taylor 1997]. C-S-H gel of Type I and Type II, with acicular and honeycomb morphology, respectively, are formed in the first few days. The C-S-H gel formed at the early stage has been described as long fibers by Locher et al. [1976]. After several days, Type III C-S-H in the form of small disks or spheres can be observed, which was described as short fibers (in opposite to long fibers) in [Locher et al. 1976]. The C-S-H gel has also been classified into "outer" product (formed in the originally water-filled spaces) and "inner" product (formed within the boundaries of the original anhydrous cement particles) [Scrivener 1984, van Breugel 1991, Richardson and Groves 1993], middle and late products [Jennings et al. 1981], phenograins and groundmass [Diamond and Bonen 1993], and more recently high density and low density C-S-H [Jennings 2000, Tennis and Jennings 2000, Jennings 2008]. The structure of the C-S-H gel will be dealt with in a more detailed manner in Section 2.4.4.

The hydration product CH is a hexagonal plate-like shaped crystals (see Figure 2.3), which is formed by precipitation from solution and fills water filled and empty spaces during hydration.

As is the case of CH, AFt is also a crystalline product. It is typically visible in microscopes as long needles with a length up to 10 μm to 25 μm [Stutzman 2000], e.g., see Figure 2.3. As mentioned in Section 2.3.2, AFt would convert into AFm when the sulphate ions are deficient. The morphology of AFm crystals is different from that of AFt and has many similarities with that of CH [Scrivener 1984], i.e., in

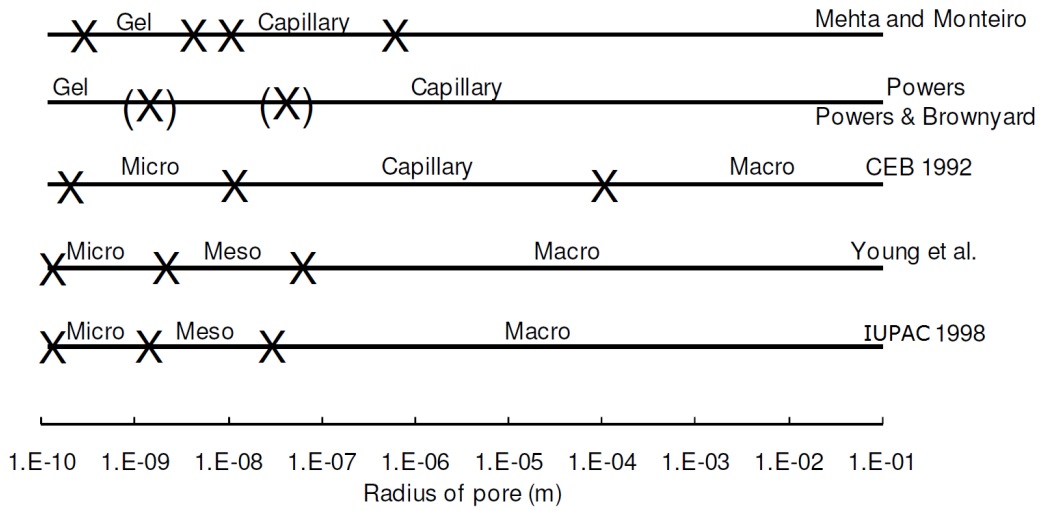

Figure 2.5: Nomenclature with respect to pore types used in different references (after [Geiker 2011]).

the form of hexagonal plates. Figure 2.4 shows the different morphologies of ettringite and monosulfate aluminate hydrate observed in a hardened cement paste.

2.4.2 Pore structure

Cement based materials are intrinsically porous. Including entrapped and intentionally entrained air voids, the pore size in cement based materials can range from nanometer to millimeter [Neville 1995, Diamond 1999]. According to the size, pores can be classified into different types. It should be noted, however, that the nomenclature used for the pore types varies widely in literature. Figure 2.5 gives a rough idea about the variability. Nevertheless, capillary pores and gel pores are considered to be the two main types in studying cement based materials [Powers and Brownyard 1947, Mindess et al. 2003, Jennings et al. 2002, Metha and Monteiro 2005].

The initially water occupied spaces which are not filled by solid hydration products are traditionally called capillary pores. The volume of capillary pores depends on the water/cement ratio and the extent of hydration. According to Jennings et al. [2002], the capillary pores mainly affect the properties, such as strength, permeability and shrinkage.

Gel pores are present in the principal hydration product C-S-H gel (Section 2.4.4). They are very small in size compared to the capillary pores but the volume is significant [Jennings et al. 2008]. Diamond and co-workers [Lachowski and Diamond 1983, Diamond and Bonen 1993] suggested that open gel pores (pores with diameter $\sim$5 nm) exist in the "outer" C-S-H product and dense gel pores (pores with diameter $<$0.5 nm) exist in the "inner" C-S-H product. According to Jennings and co-workers [Jennings 2000, Tennis and Jennings 2000, Jennings 2008], the specific surface and pores in low density C-S-H can be accessed by experiments using nitrogen; while in

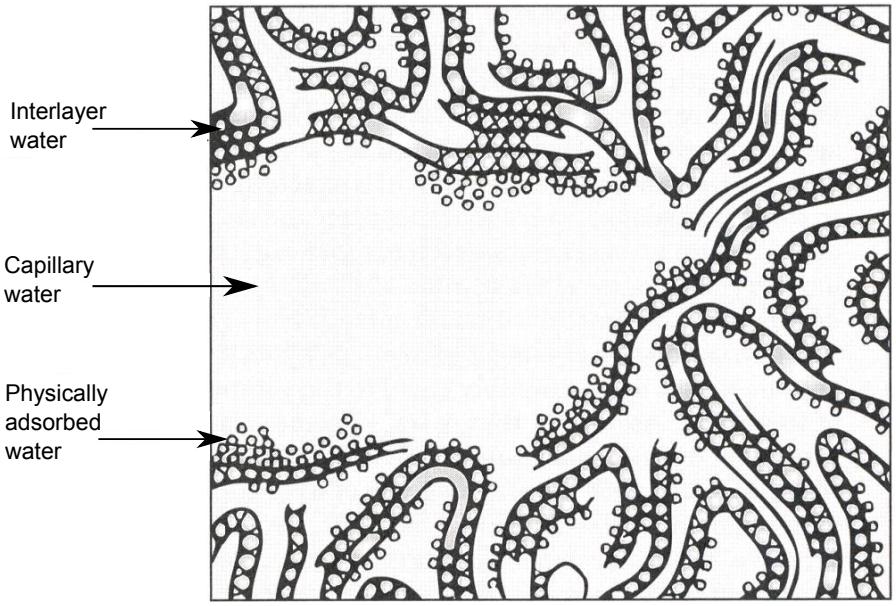

Figure 2.6: Different types of water presented in a C-S-H gel (after [Metha and Monteiro 2005]).

high density C-S-H, the surface and pores are not accessible by nitrogen. The properties that can be affected by gel pores including, e.g., shrinkage and creep [Jennings et al. 2002]. It should be mentioned that the size distinction between capillary and gel pores is somewhat arbitrary since the spectrum of pore sizes continuous. Hence, the distinction of gel pores and capillary pores are rather defined by the way they are formed and not directly related to their characteristic pore size.

There is another type of pores present being smaller than the gel and capillary pores, i.e., interlayer pores. Interlayer pores are the spaces between the sheets of the C-S-H gel (e.g., see Section 2.4.4) where water molecules can reside [Jennings et al. 2002, Metha and Monteiro 2005, Jennings et al. 2008, McDonald et al. 2010]. Since interlayer pores are also in the structure of C-S-H gel, the distinction between interlayer and gel pores is somewhat ambiguous. A more detailed discussion can be found, e.g., in [Jennings et al. 2008].

2.4.3 Water in hydrated cement paste

The state of water in hydrated cement based materials is predominantly determined by the pores in which it is retained [Metha and Monteiro 2005, Valori 2009] and it can be divided into several categories, including capillary water, physically adsorbed water, interlayer water and chemically bound water. Figure 2.6 schematically shows the different types of water presented in a C-S-H gel.

Water present in pores larger than about 50 nm (diameter) is referred to as free water and it can be removed from the hydrated cement paste without altering its volume. Capillary condensed water will here be referred to the water present

in pores with diameter from about 5 nm to 50 nm, and is held in the structure by capillary tension forces. The removal of capillary condensed water may result in drying shrinkage of the material. Adsorbed water is characterized to be close to the solid surfaces of hydration products held in the structure by direct adsorption forces being different from the capillary tension forces valid for the capillary condensed water. Interlayer water is held in the C-S-H structure by hydrogen bonding. Adsorbed and interlayer water are collectively referred to as gel water. Chemically bound water is a part of the various hydration products and is defined as water still remaining after a drying process (e.g., using 11% relative humidity) [Metha and Monteiro 2005]. Related and more detailed discussions about water in the C-S-H structure can be found, e.g., in [McDonald et al. 2010].

2.4.4 C-S-H models

The most important binding phase in cement based materials is the C-S-H gel and it is highly variable in chemical composition, nanostructure and morphology, which makes it difficult to establish its exact nature. It is generally agreed that the C-S-H gel can only be related to crystalline structures at the short range while there is no well defined order at the long range [Scrivener 2011]. That is, the C-S-H gel tends to be amorphous at the long range. A lot of efforts have been devoted to studying the structures of C-S-H gel and debates are still ongoing.

The structure of the C-S-H can be described at different length scales. At the atomic level, the C-S-H structure is to a large extent analogous to the natural mineral 1.4 nm Tobermorite [Taylor 1997, Scrivener 2011]. Figure 2.7 shows a schematic illustration of the layered structure of 1.4 nm Tobermorite. Silicate tetrahedra are attached to Ca-O layers (sheets), with the spacing between two Ca-O layers being 1.4 nm. The Ca-O layer to some extent serves as chemical bridging between the neighboring silicate tetrahedrons.

At the so-called meso level (IUPAC definition) [Scrivener 2011], several models have been proposed for the structure of the C-S-H gel. Based mainly on sorption and pore volume studies, Powers and co-workers [Powers and Brownyard 1947, Powers 1958, 1960] suggested that cement hydration products are assemblage of particles about 3 nm to 4 nm in size. Figure 2.8a shows a schematic illustration of the Powers model for the structure of hydration products. It should be noted that Powers model does not distinguish between different solid phases in the hydration products and the hydration products are collectively referred to as “cement gel”. And it is further deduced that there is an intrinsic “gel” porosity, which is about 26 % to 28 % [Scrivener 2011]. An important step in studying the hydration products of Portland cement is that they were separated into distinct phases and the principal product C-S-H was studied separately. Unlike Powers model in which the hydration products are

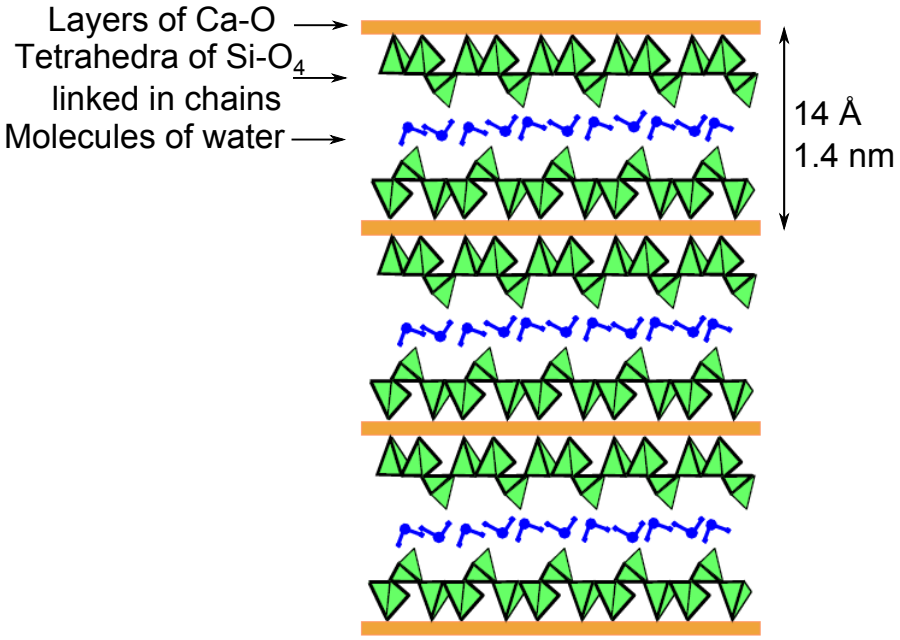

Figure 2.7: Schematic illustration of the layered structure of 1.4 nm Tobermorite (after [Scrivener 2011]).

considered to be made of colloid-scale particles [Jennings et al. 2008], Feldman and Sereda [1968] proposed the sheet like structure for the C-S-H, see Figure 2.8b. It is claimed that the behavior of water in the interlayer spaces can explain many properties including drying shrinkage and creep [Feldman and Sereda 1968].

Recently, Jennings and co-workers proposed a colloidal model [Jennings and Tennis 1994, Jennings 2000, Tennis and Jennings 2000, Jennings 2004, Thomas and Jennings 2006] and later refined it [Jennings 2008]. In the original Jennings model, the basic spherical units cluster together (flocculate) to make globules with a diameter of about 5 nm. The globules of the C-S-H clusters, which is referred to as the building

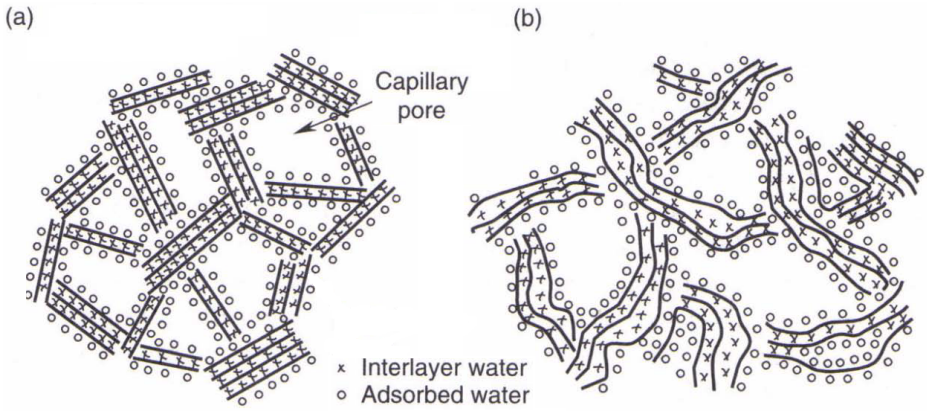

Figure 2.8: Schematic illustration of (a) Powers model for the structure of cement gel and (b) Feldman-Sereda model for the C-S-H structure (adapted from [Scrivener 2011]).

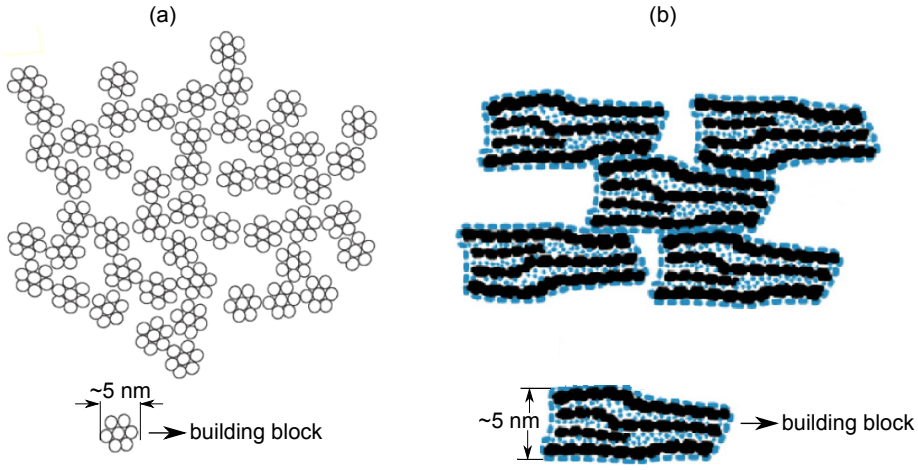

Figure 2.9: Jennings model for the C-S-H structure: (a) original and (b) refined (adapted from [Jennings 2000] and [Jennings 2008]).

blocks, pack together in two packing densities, known as high density C-S-H and low density C-S-H. Later the authors refined the model and claimed that the basic building blocks are not formed by spherical units but rather having an internal sheet like structure. Each of the refined building block is about 4 nm to 5 nm across and a few layers thick [Jennings 2008]. The original and the refined Jennings model for the C-S-H structure are shown in Figure 2.9. There are some other models proposed for gel pores, e.g., the Munich model [Wittmann 1979]. However, they do not explicitly address the structure of the C-S-H porosity [Jennings et al. 2008]. Therefore, they are not discussed further here.

It is concluded that more and more studies suggest that the C-S-H gel has nanocrystalline regions with a layered (or sheet like) structure and the main remaining open question is that whether they are discrete (granules, independent blobs) or linked by sheets [Scrivener 2011]. With the results obtained by a nuclear magnetic resonance (NMR) technique, some of the proposed models are critically discussed in a recent study [Muller et al. 2012].

The structure of the C-S-H at a greater length scale than the meso level, which is usually mentioned as microstructure or morphology, has already been shortly described in Section 2.4.1.

2.5 Porosity characterization

The importance of porosity to cement based materials can never be overestimated. The parameters related to porosity include, e.g., total pore volume, specific surface area, pore shape, pore size distribution, pore connectivity and tortuosity. Due to the complexity and in order to better describe the pore system in cement based

materials, several parameters are often combinedly used in the porosity characterization.

A number of general measuring techniques have been developed in the past decades and most of them have been applied to cement based materials. In this section, some of the most commonly used porosity characterization techniques are shortly summarized. It should be noted that each technique described in the following has its limitations and it is always good practice to use more than one technique for the porosity characterization purpose. In this work, both low temperature calorimetry and sorption measurements using water vapor are adopted.

2.5.1 Microscopy techniques

Microscopy techniques enable direct observation of the particles and features of studied materials. Optical microscopy and scanning electron microscopy (SEM) are commonly used to study the pore structure in cement based materials. Optical microscopy involves passing visible light transmitted through or reflected from the sample through a single or multiple lenses to allow a magnified view of the sample. SEM uses a high energy beam of electrons to scan the sample and images can be created based on the collected fingerprint signals. Using SEM, some important pore structure parameters can be quantified using image analysis techniques combined with stereological methods [Scrivener 2004]. Stereology is the science of establishing information for a three-dimensional (3D) object from measurements or observations of two-dimensional (2D) planes [Aligizaki 2006].

One advantage of microscopy techniques is that they are relatively easy to use and not very expensive. Besides, the pore shape can be detected along with the characteristic pore sizes. Compared with optical microscopy, the pores that SEM can resolve are considerably smaller [Aligizaki 2006]. Another main advantage of SEM compared to optical approaches is that it does not limit the analysis to porosity. Using different models, SEM can give spatially resolved chemical composition via back-scattered electrons (BSE) and morphological surface information using the secondary electrons (SE) [Scrivener 2004].

The disadvantages of SEM and most other microscopy techniques include mainly the difficulties of sample preparation. The samples must be sectioned into pieces, dried, vacuumed and impregnated with a resin to fill the pores. Additionally, the samples need to be carefully polished to ensure good resolution. The sample preparation is time consuming and requires skill. Moreover, the sample preparation may cause damage to the studied pore system even if care is taken. Other limitations are that microscopy techniques gives a 2D section which does not allow the complete determination of the pore connectivity. Further, the smallest detectable pore size is

limited (for optical microscopy, the resolution is in the order of micrometer and for SEM, about 100 nm) [Taylor 1997, Aligizaki 2006, Geiker 2011].

With the development of advanced instruments and techniques, e.g., transmission electron microscopy (TEM) and atomic force microscopy (AFM), the length scale that can be studied by a microscopy is expanded. With modern techniques, it is possible to obtain important information at the nanometric level [Aligizaki 2006, Geiker 2011].

2.5.2 Mercury intrusion porosimetry (MIP)

Mercury intrusion porosimetry (MIP) has been widely used in porosity characterization of different types of porous materials. The technique is based on the fact that mercury, a non-wetting liquid, is forced into the pores of a solid by applying an external pressure. Mercury can penetrate into relatively large pores at low applied pressures and for smaller pores, high pressures need to be applied. The volume of the intruded mercury is measured at different applied pressure levels and the information is used to derive the characteristics of the studied pore system. By assuming cylinder pore shape, the relation between the pore size and the applied pressure is given by the Washburn equation as

$$d = -4\gamma\cos\theta/p \tag{2.10}$$

where d is the pore diameter; γ is the surface tension of mercury; θ is the contact angle of mercury-solid interface and p is the applied external pressure. For mercury the common value adopted for the contact angle is in the range of 117^o to 140^o. However, it is noted that values up to 180^o have been proposed [Good and Mikhail 1981]. In order to detect relatively small pores, the applied pressure needed is up to several hundred MPa. The pore size that can be studied by MIP are from about 2.5 nm to 100 μm according to [Aligizaki 2006] and from about 2 nm to 200 μm according to [Geiker 2011].

Compared with other techniques, MIP is conceptually simpler, experimentally faster and has the ability to evaluate a wide range of pore sizes [Aligizaki 2006]. Besides, due to its wide use on cement based materials, extensive amount of data have been produced in the past years, which makes this technique valuable for comparison purposes.

There are several disadvantages of the MIP technique. The samples must be dried before measurements and the drying may cause damage to the samples [Villadsen 1992]. Moreover, different drying methods can be used and the results obtained using different drying methods are often different [Taylor 1997]. As mentioned earlier, high pressures must be applied in the measurements, which is likely to damage the pore structure of the studied material. More importantly, the technique measures the pore entry sizes rather than the pore interior sizes, which means the sizes of big pores

with small entries (the so-called "ink-bottle" pores) are underestimated. Additionally, mercury is a hazardous substance and using a large amount of liquid mercury may cause environmental issues.

2.5.3 Gas adsorption and desorption

This technique measures the mass of gas in the studied porous material as a function of the gas pressure. With the obtained sorption data, the specific surface area and the pore size distribution can be estimated. Following the classic BET theory [Brunauer et al. 1938], the specific surface area can be calculated as

$$S_{BET} = \frac{A_m N_A}{M} v_m \tag{2.11}$$

where S_{BET} is the BET specific surface area; v_m is the mass of the adsorbed gas when the surface of the material is completely covered by a monolayer molecules (the so-called monolayer capacity); N_A is the Avogadro constant; M is the molar mass of the gas and A_m is the area occupied by one gas molecule.

The pore size distribution of the studied material can be derived following the BJH model [Barrett et al. 1951]. Based on the Kelvin equation, the pore radius can be characterized by using the following expression

$$\frac{2}{r_k} = -\frac{RT\rho}{M\gamma_{lg}} \ln(p/p_0) \tag{2.12}$$

where r_k is the Kelvin radius; M, γ and ρ is the molecular weight, surface tension of the liquid-gas interface and the density of the gas, respectively; p is the pressure and p_0 is the saturated vapor pressure; R is the universal gas constant and T is the temperature in Kelvin degree.

Different gases can be used in sorption measurements and nitrogen and water are the mostly commonly used ones. One advantage of the overall technique is that the procedures are well established and defined with international standards. One disadvantage of applying the gas adsorption/desorption technique to cement based materials is that it requires pre-drying of the samples if the gas used is not water and, as mentioned before, the pre-drying may potentially alter the cement pore structure [Villadsen 1992]. Besides, the measured surface area and the porosity of a same material determined by using different gases are usually different and the reasons for this type of differences are not fully understood. Figure 2.10 gives an example showing the different values of the specific surface areas of hardened cement pastes as determined by using different gases. The difference between the measured results in terms of the surface area and the porosity determined by water and nitrogen sorption has been attributed to that the size of the nitrogen molecule is bigger than that of water, e.g., in [Powers and Brownyard 1947, Hagymassy et al. 1969, Thomas et al.

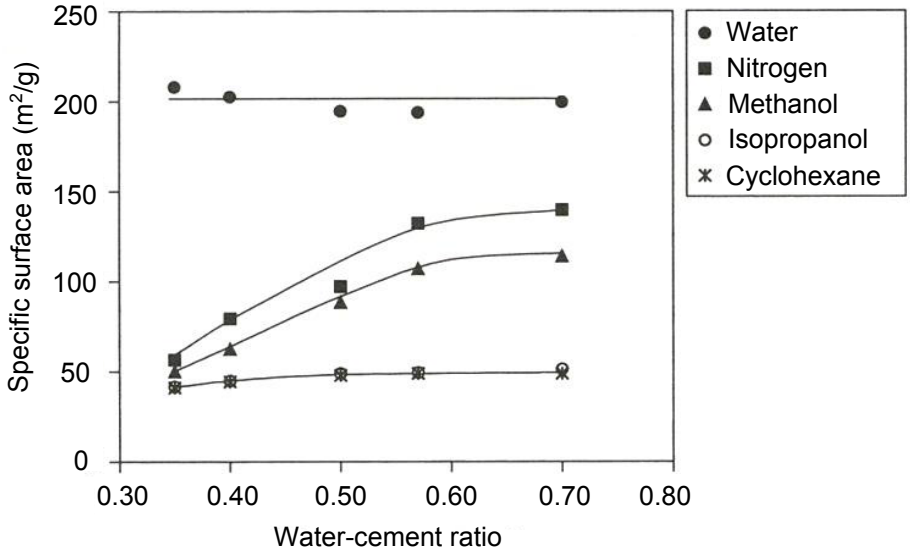

Figure 2.10: Different values of the specific surface areas of hardened cement pastes determined by the use of different types of measuring gases (after [Aligizaki 2006]).

1999, Geiker 2011]. However, other arguments such as energetic reasons were discussed [Feldman and Sereda 1968, Jennings et al. 2008]. Other disadvantages include that sorption measurement is time consuming, since it typically takes a relatively long time for the needed equilibrium conditions to be established. For cement based materials, hydration may take place during the measurement using water, which alters the pore characteristics on samples not being sufficiently hydrated before the performed test.

2.5.4 Low temperature calorimetry (LTC)

Low temperature calorimetry (LTC), also known as thermoporometry, is based on the fact that the freezing/melting point of the liquid/solid phase of a substance confined in small pores is lowered compared with that in bulk. Typically a fully saturated sample is subjected to cooling and heating at a constant rate. By monitoring the heat evolution which partly is due to the phase transition process, the pore entry sizes can be estimated from the freezing process and the pore interior sizes can be estimated from the melting process. Water and other liquids such as organic solvents can be used as the probe liquid. Water is the most commonly used probe liquid in the context of analyzing porosity of cement based materials.

For cement based materials, one main advantage of LTC is that it can be applied to virgin samples without any pre-drying treatment (using water as the probe liquid). That is, the risk that pre-drying changes the cement pore structure can be avoided [Kjeldsen and Geiker 2008]. However, one important concern of using LTC to cement based materials is the frost damage which may change the pore structure of the studied materials to a certain extent. Considerable amount of work has been conducted to study the frost damage in cement based materials, e.g., see [Powers 1949, Powers and

Helmuth 1953, Fagerlund 1977, 1991, 1997, Scherer and Valenza II 2005, Fridh 2005]. Additionally, as an indirect method for porosity characterization, the analysis of the LTC experimental data is not that straightforward. The factors which influence the accurate interpretation of the results include, e.g., the baseline calculation, the heat of fusion for water/ice confined in small pores, the supercooling effect, the ions in the pore solution, the thickness of a water layer very close to the pore walls, temperature lag between the thermopile of the instrument and the sample tested. More details in this context will be presented in *Chapter 3*.

2.5.5 Nuclear magnetic resonance (NMR)

Nuclear magnetic resonance (NMR) techniques can be used to study characteristics of porous materials including the pore volume and the pore size distribution. NMR techniques are based on the fact that most types of atomic nuclei have a non-zero spin state. The rate at which the spins align themselves with a static magnetic field (spin-lattice NMR) or the response of the materials to an oscillating magnetic field (spin-spin NMR) provides information about the chemical and physical environment of the nuclei [Kimmich 1997]. The proton (^{1}H) NMR is of particular relevance in studying the porosity of cement based materials. Several techniques based on NMR have been developed and the mostly used ones include:

- NMR relaxometry
  By applying a radio frequency pulse to a water saturated sample, relaxation times can be measured. The relaxation times of the proton in a solid and in a liquid are significantly different, which makes it possible to determine the occurrence of the two different phases in the sample in question. The relaxation times, especially the spin-spin relaxation time, have been proven to be sensitive to pore confinement [Valori 2009, McDonald et al. 2010] in which increased relaxation times are observed for liquid confined in small pores. Based on the obtained data of relaxation times, it is possible to estimate the total pore volume, pore size distribution and the pore connectivity of the studied sample [Valori 2009, McDonald et al. 2010].

- NMR cryporometry
  The principle of NMR cryoporometry is essentially the same as that of LTC, i.e., both methods are based on the fact that the freezing/melting point of the liquid/solid phase of a substance confined in small pores is lowered (depressed). That is, like the case of LTC, the samples used in NMR cryporometry also need to be saturated and then exposed to freezing and melting. The difference between LTC and NMR cryoporometry is that the content of the solid (or the liquid) phase is determined using different methods. In LTC, the solid content is determined based on the heat response recorded during the phase transition

while in the case of NMR cryoporometry, it is determined by analyzing relaxation times of proton nuclei in the solid phase and the liquid phase [Mitchell et al. 2008, Petrov and Furó 2009].

- NMR imaging
  In this approach, the samples are exposed to a linear magnetic field gradient in order to relate the response from the NMR measurements to a position in a sample. By creating an orthogonal magnetic field in three dimensions with different field gradients, the position of detected nuclei within the sample can be determined [Aligizaki 2006]. However, it should be mentioned that NMR imaging itself is a technique with rather limited resolution; as a "rule of thumb", it is usually compared to the human eye resolution, which makes this technique absolutely unsuitable to detect water within the nanometric structure of hydrated cement. But it can, however, be of great use in measuring macroscopic water ingress or in detecting cracks in samples [Valori 2009].

One important advantage of NMR techniques is that the samples not necessarily need to be dried before measurements. Furthermore, NMR techniques provide the possibility to monitor some processes in a non-destructive manner, e.g., the drying process in fresh concrete and the development of early age strength [Aligizaki 2006]. There are some drawbacks of the NMR techniques, which include [Aligizaki 2006]: the presence of paramagnetic impurities in cement based materials may generate internal field gradients, which complicates the data analysis; the liquid present in the pores of cement based materials are not pure water but contains certain types of ions, which influences the obtained NMR results and the data analysis as well; the complex geometry of the pore system in cement based materials makes the interpretation of the measured data difficult.

Chapter 3

Low temperature calorimetry on cement based materials

3.1 Introduction

The freezing point of the liquid phase, or the melting point of the solid phase, of a substance (among which, water is one of the mostly used) confined in small pores of materials is lower than that of the bulk state. The magnitude of this freezing/melting temperature depression is closely related to the size of the pores in which the phase transition takes place. If a porous material is saturated with a substance, the amount of the substance confined in the porous material is a measure of the pore volume. By studying the amount of the substance undergoing phase transition under different freezing/melting temperatures in a test, it is possible to estimate the pore volume assigned to each temperature interval considered. Thus, the total pore volume is the sum of all pore volumes detected at all temperature intervals considered under the condition that the whole temperature domain of relevance is used. Moreover, thermodynamically there is a relation between the freezing/melting temperature of the confined substance and the pore size. That is, by making some important assumptions regarding the surface energies and its geometrical configurations, the pore size corresponding to each freezing/melting temperature can be determined. In other words, the pore size distribution, can be obtained by introducing certain assumptions. The detailed description of the thermodynamic considerations used in this context is presented in *Appendix A*. Based on the above described principles, cryoporometry has been developed to characterize the pore volume and the pore size distribution of porous materials.

Cryoporometry is, in fact, a general term for several techniques. It can be further divided into different methods according to the techniques employed to detect the amount of the substance undergoing phase transition in a test [Wikipeida]. Low temperature calorimetry or LTC, which is also called thermoporosimetry or ther-

moporometry, is a calorimetric method for porosity characterization by analyzing the transient heat flow during the phase transition process, i.e., the freezing process is exothermic and the melting process is endothermic. Compared with traditional methods for porosity characterization, e.g., nitrogen adsorption/desorption (NAD), mercury intrusion porosimetry (MIP), scanning electron microscopy (SEM), the most remarked advantage of using LTC to study cement based materials is that virgin samples can be used without any pre-drying treatment [Sellevold and Bager 1985, Kjeldsen and Geiker 2008, Caunt 2011]. The pre-drying treatment often results into an alteration of the pore structure of cement based materials [Bager and Sellevold 1986b, Villadsen 1992].

Using LTC to study porous materials dates back to the 1950s [Kuhn et al. 1955]. LTC has been widely adopted to investigate cement based materials, e.g., see [Fagerlund 1973a, Bager 1984, Sellevold and Bager 1985, Bager and Sellevold 1986a, Villadsen 1992, Kjeldsen and Geiker 2008, Johannesson 2010, Caunt 2011]. The state of art of using LTC to study the porosity of cement based materials has been summarized and presented in the appended papers, i.e., *Paper I* to *Paper V*. Discussions concerning the limitations of the LTC method for porosity characterization will be presented in some detail in *Chapter 5*. General discussions about the application of LTC to porous materials can be found, e.g., in [Riikonen et al. 2011a,b].

This chapter summarizes important aspects of the LTC investigations conducted in this PhD study, including ice content determination from measured LTC data, impact of sample saturation on the detected porosity, effect of frost damage on the pore size distribution determination by LTC, effect of preconditioning the cement paste samples on the freezing and melting behaviors of the pore solution, impact of sample crushing and a preliminary exploration of the influence of ions presented in cement pore solution during measurements on the porosity determination by LTC. Details of these investigations are presented in the appended papers.

3.2 Summary of low temperature calorimetry investigations

3.2.1 Overview of the LTC investigations

An overview of the conducted LTC investigations is shown in Table 3.1. It lists the factors investigated together with short descriptions of the investigations. Additionally, it also indicates in which paper (*Paper I* to *Paper V*) the investigations are presented.

Table 3.1: An overview of the conducted LTC investigations.

Investigation	Description	In paper
Ice content determination	Two main factors influencing the determined ice contents were studied: (1) baseline calculation and (2) the adopted values of heat of fusion of pore water/ice.	*I*
Impact of sample saturation on the calculated porosity	The freezing/melting point of the water/ice in a non-fully saturated pore is lower compared with the case where the pore is fully saturated. Using the same type of calculations regarding the pore size determination for the non-fully and fully saturated case, some pores may be misinterpreted as smaller pores (using non-fully saturated samples) than those based on the fully saturated condition.	*II*
Effect of frost damage on the porosity determination	Frost damage potentially takes place in the studied cylinder paste samples. From the investigations performed, it was concluded that frost damage changes the pore connectivity. On the other hand, it has limited effects on changing the interior size distribution of the meso-pores.	*III*
Effect of sample preconditioning on the freezing or melting behaviors of cement pore solution	Cement paste samples were preconditioned in a big amount and a small amount of limewater for a relatively long time. The obtained results indicate that the preconditioning has limited influence on the freezing and melting behaviors of the pore solution in the studied cement paste samples.	*III*
Impact of sample crushing on the porosity determination	Two types of samples, i.e., in the form of powders and cylinders, of two types of cements (CEM I and CEM III) were used to study the impact of sample crushing on the porosity determination by LTC. For the CEM I, the results indicate that sample crushing only changes the pore connectivity while it has limited effects on the pore (interior) size distribution and the total pore volume. For the CEM III, however, it was shown that sample crushing not only changes the pore connectivity but also the pore (interior) size distribution and the total pore volume.	*IV*
Effect of ions present in cement pore solution on the porosity determination	Thermodynamic modeling using the program PHREEQC were performed on the cement paste samples. The results obtained indicate that the temperature depression caused by the ions present in the pore solution affects the determination of the pore size distribution by LTC to a limited extent.	*V*

3.2.2 Summary of the LTC investigations

3.2.2.1 Ice content determination

An accurate analysis of the measured LTC data, e.g., ice content determination, is totally central for an accurate estimation of the pore volume and pore size distribution for a porous material. Two fundamental aspects are crucial in this context: the baseline calculation of the measured heat flow and the values of the heat of fusion of the water/ice confined in pores.

The heat flow measured by a LTC instrument consists of two parts: (1) the contribution from the heat capacity of the system (including water and ice in the concrete sample, and also the concrete skeleton matrix), which is referred to as the "heat flow baseline" or simply "baseline" in this discussion; and (2) the contribution due to the phase transition. Hence, in order to calculate the ice content, one needs to know how much energy goes to form or melt ice at each temperature level, which basically is obtained by subtracting the baseline from the measured total heat flow. During each test, the ice in the pores of the concrete will be continuously forming/melting as the temperatures decreases/increases (due to the relative wide distribution of the pore sizes in concrete), which means that the baseline of the heat flow is continuously changing due to the change in the proportion of ice and liquid water confined in the pores. Additionally, the heat capacities of water, ice and the solid matrix are temperature dependent, which makes it even more difficult to accurately determine the baseline.

Two different methods for baseline and ice content calculations were studied. The 'J-baseline' method was adapted from [Johannesson 2010], which is a recently proposed method based on extrapolation by using the accumulated heat curves measured in the freezing and the melting process. The 'C-baseline' was adapted from [Sun and Scherer 2010], which considers the heat capacity of both water and ice and the phase changing behavior under the different testing temperatures. The current study showed that both methods can be used for the baseline and the ice content calculations if due attention is paid. Results obtained using the 'J-baseline' method are not affected by the uncertainties of the heat capacity of water and ice under very low temperatures and the possible fluctuations of the cooling and heating rate during testing. The 'C-baseline' is capable of delivering accurate results due to its relatively stringent theoretical basis, provided that the thermodynamic parameters included in the model can be identified correctly, which in fact is not easy. Useful information can be gained by using the two methods complementarily.

It should be noted that the water/ice under study in this case is the water/ice confined in small pores. Although bulk water/ice is relatively well studied, there is no general agreement on how to obtain the important temperature dependence of the heat of fusion of water/ice confined in small pores. Based on the literature studies, the

values of the heat of fusion of water confined in pores used for the analysis of LTC data can be divided into two groups: (1) as that of bulk water, but corrected based on the depressed freezing/melting temperature of the confined water, e.g., see Ishikiriyama et al. [Ishikiriyama et al. 1995, Ishikiriyama and Todoki 1995a,b, Ishikiriyama et al. 1996]; (2) modified by taking into account two correction terms, i.e., the lowered pressure of the liquid water and the water-ice interface formation, e.g., see Brun et al. [1973, 1977].

Comparison studies were performed to demonstrate the influence of the different values of the heat of fusion commonly adopted on the calculated ice content for the studied concrete samples using the 'C-baseline' method. The results showed that for the studied concrete samples, the relative difference of the maximum ice content determined from one freezing and melting cycle could differ up to 27 % solely due to using different values of the heat of fusion presented in literature. Using the heat of fusion of bulk water but corrected for the depressed freezing/melting temperature of the pore water resulted in the smallest difference between the maximum ice content calculated from the measured heat flow during freezing and melting in one cycle. This is an adequate result since the ice formed during the freezing process is the ice melted during the melting process in one measurement cycle. That is, the maximum ice content calculated from the freezing process should be equal to that calculated from the melting process. If this criterion is adopted in the 'C-baseline' method for identifying the soundness of the results, it suggests that it makes more sense to use the heat of fusion of bulk water but corrected for the depressed freezing/melting point of the pore water for the analysis.

The details of using the 'J-baseline'and the 'C-baseline' methods to calculate ice contents from measured LTC data are presented in *Paper I*.

Additionally, it should be mentioned that the cooling or heating rate is normally set at constant target values in LTC measurements. It has been noticed, however, that the cooling/heating rate may fluctuate or drift during a measurement, in which the magnitude of the fluctuation and drift. essentially are depending on the precision of the instrument used. This is especially true when a measurement covers a large temperature range. To demonstrate the impact of cooling and heating rate fluctuation and drift on the ice content determination, three sets of LTC data measured by different types of instruments were analyzed. Of the three sets of data, two were measured under stable cooling/heating condition and one under relatively big fluctuation of cooling/heating rate. That is, a less stable performing instrument was used in this latter case. The analyzed results showed that reasonable freezing and melting curves of ice content could be calculated from the data measured under relatively stable cooling/heating conditions; while for the data measured under cooling/heating rates with relatively big fluctuation, the calculated ice content curves were subjected to important errors. The main conclusion of this investigation is that the calorimetric

instrument used needs to be checked for fluctuation and drift issues. The details of this discussion are presented in *Appendix B*.

3.2.2.2 Impact of sample saturation on the detected porosity

For LTC measurements aiming at determining the complete range of pore sizes of a material, the samples to be tested need to be fully saturated with water before testing it in a calorimeter. Under the condition that a sample is not fully saturated, the pores which are not filled with water will not be detected and as a result, the total pore volume will be underestimated. Furthermore, the correlation between the pore size and the depressed freezing/melting temperature used in the context of pore size determination is normally based on the prerequisite that the pores under study are fully saturated, e.g., see Brun et al. [1973, 1977]. However, a careful examination of the theoretical background emphasized that the thermodynamic description for fully saturated pores is different from that for non-fully saturated pores. Moreover, the thermodynamic description for a non-fully saturated system is much more complicated compared with the case of fully saturated conditions. Indeed, it is extremely difficult to quantitatively characterize a non-saturated system, if it is still possible. Hence, it was concluded that it is inadequate to use the thermodynamic relations as derived based on the fully saturation assumption for tests using non-fully saturated samples.

Based on the experimental data measured on hardened concrete samples with different w/c ratios and nominal air contents conditioned by capillary saturation (samples submerged in water) and vacuum saturation, the ice content, pore volume and pore size distribution were calculated to demonstrate the impact of sample saturation on the porosity analysis. The obtained results could be summarized as follows:

1. The ice content calculated from the capillary saturated sample was obtained to be lower than that from the vacuum saturated sample for the same concrete mix and the difference becomes bigger as the nominal air content increases. This implies that the capillary saturation may not be able to saturate all the pores, especially the entrained air voids, in the concrete samples. For this case, part of the water in some of the initially fully saturated small pores (at the nanometric level) before freezing may be sucked out by the cryo-suction force during the freezing process, leaving some of the small pores non-fully saturated.

2. The proportion of the calculated pores with small radii was higher in the capillary saturated samples than that in the vacuum saturated samples, using the same calculation method. The reason is probably that for the capillary saturated samples, not all of the pores under study are fully saturated during the freezing/melting process and consequently the corresponding phase transition temperatures for the water/ice confined in these pores are further depressed.

Of this reason, the pore radii are wrongly interpreted because the full saturation is explicitly assumed when calculating the pore sizes. Since no reliable quantitative relation exists for the non-fully saturated pores, it is questionable whether the capillary saturated sample preparation should be adopted for pore size characterization using LTC.

3. The hysteresis behavior observed between the freezing and melting ice content curves was shown to be more dominant in the capillary saturated samples compared with that observed in the vacuum saturated samples. Possibly, the difference in hysteresis behavior is related to the further depressed phase transition temperatures for the water/ice in the non-fully saturated pores.

The details of this study are presented in *Paper II*.

3.2.2.3 Impact of frost damage on the pore size distribution determination

For water saturated porous materials, frost damage may potentially take place as the pore water freezes, especially when water in very small pores freezes [Scherer 1993]. The frost damage may change the pore structure of the studied materials to a certain extent. The frost damage on the porosity determination is not fully clear. The present study tried to explore the impact of frost damage on the porosity determination using LTC, especially the impact related to the meso-pores (IUPAC definition).

One mono-sized model material MCM-41 and two types of hardened cement pastes were studied in this investigation. The MCM-41 was in powder form and the cement paste samples were in the form of cylinders ($\sim \phi 15 \times 45$ mm). Three freezing and melting cycles were applied on a same sample of the MCM-41 and two cycles were applied on a same sample of each of the two cement pastes. If the heat flow curves of freezing and melting change after each cycle, it may be an indication of frost damage changing the pore structure.

The measured results showed that for the model material MCM-41, the heat flow curves of freezing and melting after each cycle were almost the same. For the two cement paste samples, the heat flow curves of freezing changed significantly after one cycle of measurement and the change was most evident at very low temperatures; while the heat flow curves of melting were almost not affected after one cycle of measurement.

The results suggest that the pressure generated during freezing and melting measurements does not change the pore structure of the MCM-41 samples. As for the studied cylinder cement paste samples, frost damage most probably takes place resulting in changes in the pore connectivity while it has limited effects on changing the interior size distribution of the meso-pores. These conclusions were drawn based

on the characteristics of the freezing measurements (changed form after a cycle of measurement) and the melting measurements (remained almost the same after a cycle of measurement).

The details of this study are described in *Paper III*.

3.2.2.4 Impact of sample preconditioning on the freezing/melting behavior of cement pore solution

The pore liquid in cement based materials is not pure water but contains ionic species including calcium, sodium, potassium and hydroxide ions, etc. [Taylor 1997]. The presence of ionic species in pure water influences the freezing and melting behaviors of the solution. To minimize the effect of the ions on the data analysis in LTC studies, water cured samples have been suggested to be used. In this approach it is assumed that the alkalies leach out of the sample and then allowing the pore liquid to be approximated to be dilute [Fagerlund 1973a]. In a study conducted by Sun and Scherer [2010], mortar samples ($\sim 20 \times 30 \times 100$ mm) were stored in a relatively big amount of saturated limewater ($\sim$ 48 liters) for about 6 months; then it was suggested that the alkalies would likely to have diffused out during the curing and the pores contained a solution very similar to saturated limewater. Since saturated limewater solution is rather dilute ($\sim$ 2 g calcium hydroxide/liter water), they further concluded that the freezing and melting behaviors of the pore solution in the limewater treated mortar samples could be approximated to that of pure water [Sun and Scherer 2010]. However, it is noted that due to a relatively big buffering capacity of the cement hydrates as demonstrated in thermodynamic modeling studies, e.g., see [Lothenbach and Winnefeld 2006, Lothenbach 2010, Setunge et al. 2009], the ionic concentrations in the pore solution of the samples cured in limewater might not necessarily be significantly changed, not even in cases where a big amount of saturated limewater is used.

Comparison measurements were performed on cement paste samples of the same recipe but preconditioned in a relatively small amount and a relatively big amount of saturated limewater. The hardened cement paste cylinders ($\sim \phi 15 \times 45$ mm) were demoulded after one day of sealed curing at room temperature (about 20 °C) and then placed into slightly bigger plastic flasks ($\sim \phi 25 \times 60$ mm) filled with saturated limewater for curing at room temperature. After about three months, the paste samples were divided into two groups: the first group was left curing in the slightly bigger plastic flasks (denoted as preconditioned in a small amount of saturated limewater); and the second group was cured in a big bucket filled with saturated limewater ($\sim$ 40 liters) (denoted as preconditioned in a big amount of saturated limewater) until the calorimetric measurements.

The measured results on the above described different preconditioned samples showed that there was almost no difference in the heat flow curves of freezing and

melting between the samples preconditioned in a small amount and a big amount of saturated limewater, indicating that either the curing in a big amount of limewater does not change the concentration of the pore solution to any significant level (e.g., due to the buffering effect of the cement hydrates) or the leaching of ions from cement hydrates had limited influence on the freezing and melting behaviors of the pore solution in the studied cement paste samples.

The details of this study are presented in *Paper III*.

3.2.2.5 Influence of sample crushing on the porosity determination

It is noted that in LTC studies on cement based materials, the sample size used is either relatively small (with the mass in the order of tens of milligrams), e.g., see [Bentz and Stutzman 2006], or relatively big (with the mass in the order of several grams), e.g, see [Bager 1984, Kjeldsen and Geiker 2008, Johannesson 2010], depending on the instrument adopted. For LTC measurements on the samples with relatively small size, crushing or even grinding is needed in sample preparation. It is noted that the procedure of crushing and/or grinding the studied samples is also needed in sorption studies using a "dynamic vapor sorption" (DVS) instrument. In sorption studies, it is normally assumed that the crushing and/or grinding of the cement paste samples do not change the pore structure at the nanometric level, e.g., see [Åhs 2011, Baroghel-Bouny 2007]. Meanwhile, it should be mentioned that there are NMR cryoporometry studies, e.g., [Perkins et al. 2008, Shiko et al. 2012], compared the measurements on a same porous material but in different forms, i.e., big integral pieces and crushed samples. The investigation showed that the pore connectivity is changed by the sample crushing. It was also concluded that the interior pore size distribution is unaffected by the crushing procedure. The impact of sample crushing, i.e., using different size of samples, on the porosity determination of cement pastes using LTC measurements is further explored in this work.

Two types of cements were used to prepare the pastes, denoted as CEM I and CEM III. For each hardened cement paste, two types of samples, i.e., in the form of powders and cylinders, were used. The powder samples were obtained from the cylinder samples of cement pastes as prepared ($\sim \phi 15 \times 45$ mm). All cylinder samples were vacuum saturated with saturated limewater and then a part of the samples were subjected to the crushing, grinding and sieving of the samples (passed through 315 μm sieve) in a carbon dioxide free chamber to avoid carbonation.

The influence of sample crushing on the porosity determination using LTC, or rather the difference between the powder and cylinder samples, was demonstrated by the calculated ice content curves, total pore volumes and pore size distribution curves. Conclusions of this study can be summarized as follows.

For the studied cement pastes, the calculated ice content curves of freezing of the powder sample differed from that of the cylinder samples, especially for the paste

CEM III. This suggests that sample crushing changes the pore connectivity. One important difference between the powder sample and the cylinder samples of the paste CEM III was that the determined maximum ice content in the powder sample was much higher compared with that determined for the cylinder samples, the relatively difference being up to 40-50%. However, this kind of marked difference was not found in the paste samples of CEM I. That is, the sample crushing could possibly result into more pores detected by LTC depending on the (porosity) properties of the studied cement paste.

The marked difference between the calculated pore volume of the powder and the cylinder samples of the paste CEM III may be attributed to some of the "isolated" pores which in the case of the cylinder samples cannot be fully filled with water in the saturation adopted before the LTC measurements start. Due to sample crushing, an important portion of the non-fully saturated "isolated" pores can then be saturated. Consequently, more pores are detected in the powder samples than that in the cylinder samples. The argument about the "isolated" pores is supported by the results of complementing investigations involving gravimetric measurements on cylinder samples and DVS measurements on powder samples.

The details of the differences between the powder and cylinder samples in terms of the resulting pore size distribution are presented in *Paper IV*.

3.2.2.6 Impact of ions present in cement pore solution on the porosity determination

As discussed earlier, the analysis of LTC data measured on cement based materials is complicated by the fact that the pore liquid is not pure water but contains many types of ionic species [Taylor 1997, Lothenbach and Winnefeld 2006]. In order to study the effect of the ionic composition on the freezing/melting behavior, an experimental attempt that one may think to clarify the impact of ions on the freezing/melting behaviors of a solution is using some model materials of simple pore structure together with artificial pore solutions. However, this approach is less relevant for cement based materials due to the fact that the present cement hydrates continuously will interact with the pore solution so as to establish new equilibrium conditions [Lothenbach and Winnefeld 2006, Lothenbach 2010, Setunge et al. 2009], meaning that cement based systems are significantly different from chemically inert model materials filled with an artificial pore solution.

Due to the experimental difficulty to directly determine the impact of ions in the pore solution of cement based materials on the freezing and melting behaviors, thermodynamic modeling in terms of chemical equilibrium calculations was used in the aim of getting further insight into the problem. The chemical equilibrium modeling was used to predict the ionic concentrations in the pore solution of cement pastes at different temperatures during freezing and melting corresponding to the conditions

used in the performed LTC measurements. That is, it is assumed that the standard thermodynamic relations and concepts can be used also for undercooled water present in the pores of the samples. The results from the model in terms of the ionic concentrations were used to determine the corresponding temperature depressions. The influence of the freezing/melting point depression caused by the ions in the pore solution of hardened cement pastes on the determined pore size distribution by LTC was investigated.

The thermodynamic modeling was performed using the program PHREEQC. The modeled results showed that the ionic strength for all investigated cement paste samples do not change to any significant level in the temperature range between 0 °C and -40 °C during the LTC measurements. Using the modeled ionic concentrations, the calculated differential pore size distributions of the studied samples, with and without considering the temperature depression caused by the ions in the pore solution, were compared. The results indicate that for the studied cement paste samples in this investigation, the temperature depression caused by the ions present in the pore solution affects the determination of the pore size distribution by LTC to a limited extent.

The details of this study are presented in *Paper V*.

Chapter 4

Moisture fixation on cement based materials

4.1 Introduction

Water can be bound into porous materials physically and chemically. Chemically bound water, loosely speaking, exists in the structure and becomes a part of the solid material; while physically bound water is the water adsorbed on the pore surfaces by van der Waals forces and that exists in the pores through capillary condensation or capillary suction. Capillary condensation takes place in small pores and other narrow spaces. Theoretically there is no upper limit in terms of the relative humidity for capillary condensation to take place. However, it is often supposed that capillary condensation is restricted to the so-called hygroscopic range, with the relative humidity ranging from some low value (above which capillary condensation is active) up to approximately 0.98. At higher relative humidities, which is normally referred to as the over hygroscopic range, capillary suction occurs [Janz and Johannesson 2001]. The behavior of the physically bound water, which includes pure adsorption on the bare material surfaces occurring at the very low relative humidity range, sorption at the hygroscopic range and suction at over hygroscopic range, is collectively referred to as the moisture fixation behavior in this description.

When a porous material is placed into an environment with a certain relative humidity, moisture exchange will happen if there is a gradient about the relative humidity between the material and the environment until the equilibrium condition is established. The relation between the moisture content and the relative humidity is usually referred to as a sorption isotherm at the hygroscopic range and a water retention curve at the over hygroscopic range. The moisture fixation behavior is closely related to important properties of the studied material, e.g., the specific surface area and pore size distribution [Sing et al. 1985, Allen 1997].

The moisture fixation behaviors of the model porous material MCM-41 and cement pastes prepared by two types of cements, i.e., CEM I 32.5 R and CEM III/B 42.5 N, were studied. By using the model material, some fundamentals behind moisture fixation method were revisited and the applicability of sorption measurements using water vapor in the context of porosity determination was expected to be validated. In this chapter, a short introduction about the measurement techniques involving moisture fixation is described. The main results and discussions involving porosity characterization using moisture fixation experiments are presented in *Paper VI* and *Paper VII*.

4.2 Measurement of sorption isotherms

4.2.1 Measurement methods

Several techniques have been developed and used to measure sorption isotherms. Due to its simplicity, the salt solution method is commonly used in this context. The "Dynamic vapor sorption (DVS)" method is a more sophisticated method which allows for arbitrary relative humidity (RH) variations and and it uses a balance with high precision. The method using pressure plate vessels makes it possible to study the moisture profiles at very high RHs (e.g., higher than 0.95, the over hygroscopic range), which is beyond the limit of the DVS method. There are also some other methods, e.g., the vacuum sorption method [Johannesson 2011c], and the calorimetric sorption method [Wadsö and Wadsö 1996, Wadsö and Markova 2000], which could also be of great interest in this context. Since only the DVS method and the pressure plate method were adopted in the experimental study of this work, details are included for these two methods in this section, along with a short description about the concept of salt solution method.

4.2.1.1 Salt solution method

The salt solution method is based on the fact that different types of salts can generate a certain RH above the surface of their saturated solutions. This method is conducted simply by storing the testing samples in chambers where over saturated salt solutions are present. Then, the mass of the samples can be checked from time to time. When the equilibrium state is reached, as indicated by the gravimetric measurements, the next measurement with a different relative humidity using another salt solution can be performed.

The salt solution method is quite simple and demands no expensive devices. However, one major shortcoming is that only discrete RHs can be obtained (based on the available salt solutions) and therefore it is difficult to obtain a general RH spectrum. Moreover, it is found that the relative pressure above the saturated salt

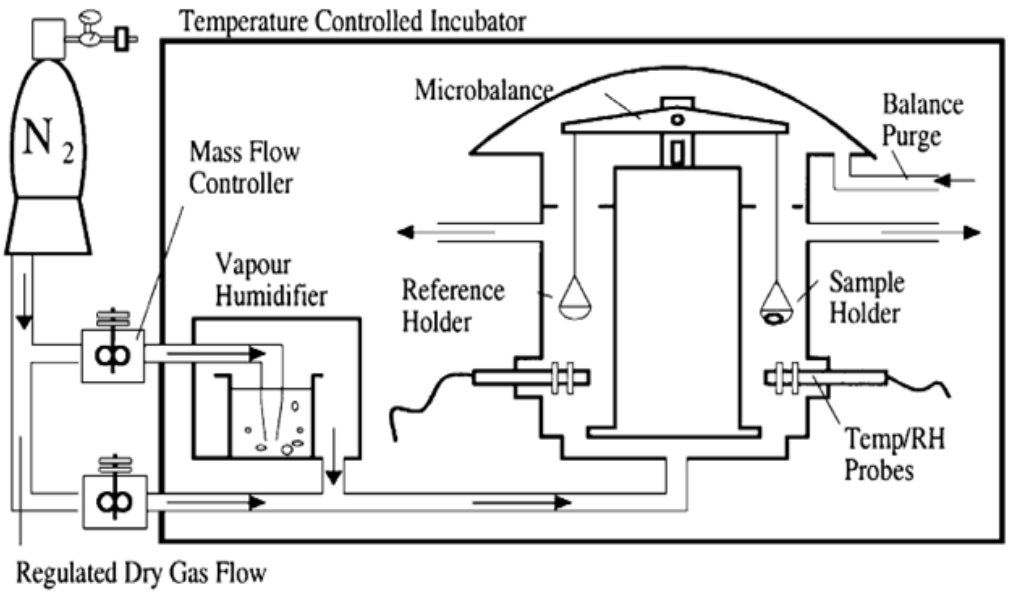

Figure 4.1: Schematic illustration of a dynamic vapor sorption (DVS) instrument. Dry and saturated air are mixed to generate the desired relative humidity and a symmetric reference holder is used to counteract the adsorption on the sample holder (after [Johannesson, 2011c]).

solution is temperature dependent. Thus, the temperature control of salt solution chamber during a measurement is very important. Additionally, it often takes a long time for the equilibrium conditions to be established at the different RHs employed and the method is usually very time-consuming.

4.2.1.2 Dynamic vapor sorption (DVS) method

The DVS measurement is conducted in a climate incubator where the temperature can be regulated and controlled. The relative humidity is generated by mixing two air flows, i.e. a totally dry (RH = 0) and a totally saturated (RH = 1) air. The proportions of the two flows can be accurately controlled by the flow regulator devices. Figure 4.1 shows the construction of the instrument schematically. The sample is placed in a sample holder at one end of a microbalance. A reference holder, which is symmetrically placed in respect to the sample holder, is used to eliminate the effect of the vapor adsorption on the surface of the sample holder.

One advantage of the DVS method is that the RH can be programmed to vary arbitrarily during a measurement. The sample size used in a DVS instrument is often very small, that is, in the order of several milligram to tens of milligrams. This enables the equilibrium conditions to be achieved rather quickly. It is also of interest to note that the generated vapor in the instrument is free of carbon dioxide, which makes this method suitable for studying cement based materials. Cement based materials are very reactive with carbon dioxide and this reaction, i.e., the carbonation, is believed

to change the porosity of the materials to a certain extent, e.g., see [Johannesson and Utgenannt 2001, Ngala and Page 1997].

As mentioned, the sample size which can be used in a DVS instrument is relatively small. This normally requires crushing the samples to be measured, in this case the cement pastes. In some cases, the representativeness of the sample could be questioned. However, it is normally possible to collect large representative samples and then divide them into a fine powder mass. One may also argue that the crushing of a sample might cause the change of the porosity. As the adsorption and capillary condensation studied in this context is at the nanometer scale, it is believed that the crushing of samples has a very limited or no effect at all in changing the nanometric porosity, e.g., as illustrated experimentally in [Baroghel-Bouny 2007, Åhs 2011].

One important limitation of using the DVS method is that it is very difficult to study the sorption behavior at high RHs, e.g., in the range of 0.95-1. The problem is mainly due to the tendency of condensation in the equipment at high RHs [Johannesson 2011c]. To overcome this limitation and to obtain the sorption behavior also at the high RH range, the method of using pressure plate vessels, or "pressure plate method", can be adopted.

4.2.1.3 Pressure plate method

The idea of using the pressure plate method is that it is possible to generate a certain RH by applying a corresponding pressure, the relation between the RH and the pressure being defined by the Kelvin-Laplace equation, which is

$$p = -\frac{RT\rho_w}{M_w}\ln(\phi) \tag{4.1}$$

where p in this case is the applied pressure in the pressure plate vessel; ϕ is the relative humidity; M_w and ρ_w is the molecular weight and the density of water; R is the universal gas constant and T is the temperature in Kelvin degree. A detailed derivation of this equation is presented in *Appendix D*.

Figure 4.2 shows an example of a pressure plate vessel schematically. A specimen is placed on top of a cloth, under which is a mixture of kaolin powder and water sitting on top of a ceramic plate. A special membrane is often used if the exerted pressure is very high. The desired pressure is applied on top of the ceramic plate and an atmospheric pressure is present under the plate. The applied pressure gradient will induce draining of the excess water in the specimen out of the system, which will be collected into a container. When there is no more water coming out of the system, the equilibrium condition is assumed to have been achieved. The equilibrated specimen can then be taken out of the vessel in order to determine its mass.

The strength of this method, as mentioned before, is that the RH in the high range can be generated with a very high accuracy, which is always problematic or

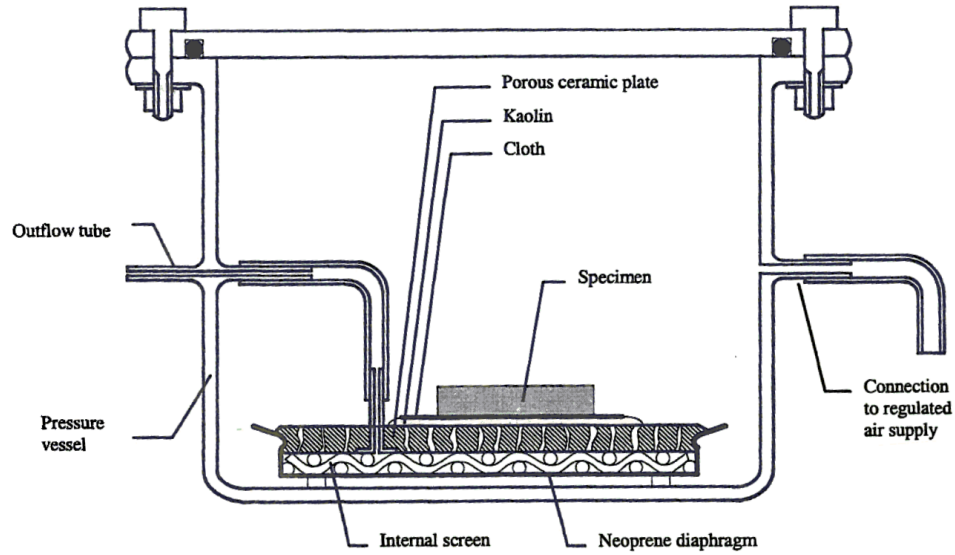

Figure 4.2: Schematic illustration of a pressure plate vessel. The pressure is applied on the top the of the ceramic plate and the atmospheric pressure is induced underneath. The excess water in the specimen will be drained out of the vessel and collected (after [Johannesson 2011c]).

inaccurate by using other methods. However, it should be noticed that it is not suitable to use this method to generate RHs lower than about 0.93, which corresponds to a pressure of higher than about 10 MPa. The reason is that the pressure vessels may not be able to hold such high pressure. Additionally, the pressure plate measurements can be very time-consuming since it typically takes weeks for the equilibrium condition to be established. It should also be remarked that the instrument is mainly used to study the desorption at the high RH range, but it is also possible to study the absorption at the high RH range through appropriate modification of the pressure vessels [Johannesson 2012].

4.2.2 Measurements on studied materials

One model porous material MCM-41 and cement pastes prepared by two types of cements, i.e., CEM I 32.5 R and CEM III/B 42.5 N, were studied. Information about the MCM-41 and the preparation of the cement paste samples, together with the DVS measurements, have been described in detail in *Paper VI* and *Paper VII*, and will not be repeated here. The details of the pressure plate measurements are described in the following.

For the MCM-41, it was demonstrated by sorption measurements (*Paper VII*) that there is almost no more capillary condensation above the RH of about 0.7. Of this reason, no pressure plate measurements were performed on the model material.

Pressure plate desorption measurements were, however, conducted on the samples of the two cement pastes, designated as CEM I and CEM III. The temperature during

Table 4.1: The values of the pressure adopted in the pressure plate measurements and the corresponding converted relative humidities.

Pressure (bar)	Relative humidity (-)
0.68	0.9995
1.4	0.9990
2.7	0.9980
5.5	0.9960
8.3	0.9939
10.9	0.9920
10.92	0.9920
27.03	0.9803
41.18	0.9701
55.12	0.9602

the measurements was 23±1 °C. A number of pressures were used and the corresponding RHs are listed in Table 4.1 (according to Eq.4.1). Small slices ($\sim \phi 15 \times 5$ mm) and cylinders ($\sim \phi 15 \times 45$ mm) were used in the measurements. Before the pressure plate experiment, the samples were curing in saturated limewater for about 6 months and then subjected to vacuum saturation. For each pressure tested in the experiment, the so called equilibrium condition, i.e., in this case when no more water was observed coming out of the plate vessel, was kept for 2-3 days before the samples were taken out to determine the mass. Pressures up to 10.9 bar were adjusted manually using the manometer connected to the pressure system and a computer monitoring and regulating system was used to control the pressures being higher than 10.9 bar, i.e., the four last pressures presented in Table 4.1. After the pressure plate measurements, the samples were subjected to oven drying at about 105 °C in order to determine the dry mass of the samples.

4.3 Summary of moisture fixation studies

4.3.1 Overview of moisture fixation studies

An overview of the conducted moisture fixation studies and the main results are shown in Table 4.2. Additionally, it also indicates in which paper (*Paper VI* and *Paper VII*) the main studies are presented.

4.3.2 Summary of moisture fixation studies

4.3.2.1 Determined sorption isotherms

For the data measured by the DVS method, a data processing procedure (curve fitting) was adopted to extrapolate the sample mass at the equilibrium condition considering the experimental settings. The details of the data extrapolation has been

Table 4.2: An overview of the moisture fixation studies.

Study	Description	In paper
Sorption isotherms	The sorption isotherms of the model material MCM-41 and the two cement pastes were presented. The results of the DVS measurements and the pressure plate measurements of the studied cement pastes were compared and discussed.	*Section 4.3.2.1
Possible pore structure changes at low relative humidities (RHs)	The possible pore structure changes at low RHs were investigated by a re-saturation study. The results show that the drying at low RHs does not cause any microstructure changes or, alternatively, if the microstructure changes does occur, the absorption process must have been able to fully restore the pore structure of hardened cement paste samples, indicating in this case that the possible microsturcture changes are reversible.	*VI*
Temperature dependent isotherms	The results of this study suggested that the differences between the sorption isotherms at different temperatures are mainly caused by the temperature dependent properties of water. The pronounced impact of temperature on desorption isotherms of cement based materials as reported in some references were not found in this study.	*VI*
Specific surface area	The calculated specific surface area was very much dependent on the choice of equations used for multilayer adsorption, indicating that the calculated specific surface area may not represent the "real" geometrical surface area.	*VII*
Pore size distribution (PSD)	The important factors influencing the analyzed PSD results using sorption data were reviewed. For the studied hardened cement pastes, three characteristic peaks were found in the calculated PSD curves from using the desorption isotherms. The peaks occurred at the radii of 1.4, 1.8 and 3.0 nm while the peak at 1.4 nm was missing in the PSD curves calculated from using the absorption isotherms. The network theory suggests that the desorption is controlled by the pore entry sizes while absorption is controlled by the interior pore sizes. The concepts behind the network theory was realized to be of great relevance in explaining the results.	*VII*

Note: * it is presented in the section rather than in the appended papers.

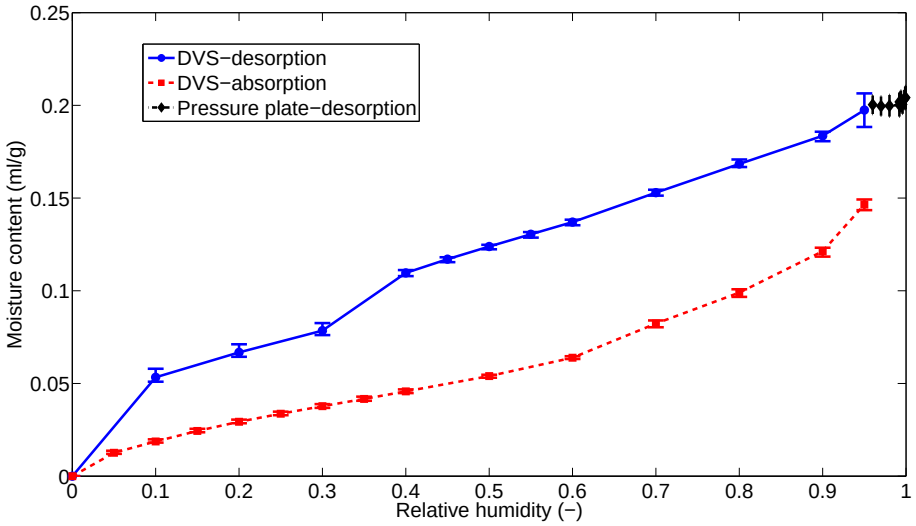

Figure 4.3: Absorption and desorption isotherms of the paste CEM I, based on the extrapolated data at equilibrium conditions (using the DVS measured data). The error bar shows the variation of three measurements.The desorption data from the pressure plate measurements are also included.

described in *Paper VI*. The determined sorption data together with the data measured by the pressure plate method for cement pastes CEM I and CEM III are shown in Figure 4.3 and Figure 4.4, respectively.

As can be seen in Figure 4.3 and Figure 4.4, very limited moisture change could be observed at the studied high RHs using the pressure plate method for both pastes CEM I and CEM. This is probably because most of the big pores are connected to some pore entries or necks whose radii are rather small, since the desorption is controlled by the pore entries or necks rather than the interior pore sizes. That is, according to the results obtained for CEM I and CEM III, the Kelvin radii of the pore entries or necks are probably smaller than that corresponding to the RH of about 0.96 which is the RH corresponding to the highest pressure in the DVS measurements. Only when the water confined in the small pore entries or necks desorbes can then the desorption of the water in the big pore bodies take place. The presented pressure plate measurement results actually emphasize the important concept of the network effect or pore connectivity in studying sorption isotherms.

It could be observed that the data from the pressure plate measurements correspond very well with the DVS desorption results for the paste CEM I (Figure 4.3) while for the paste CEM III (Figure 4.4), the moisture contents obtained from the pressure plate measurements are much lower than that from the DVS desorption results. It has not been possible to clarify this important difference and instead a short discussion of possible reasons are performed as follows.

The difference might be related to the carbonation issue irrespective of the efforts that have been taken to avoid it. According to the studies reported in [Ngala and Page

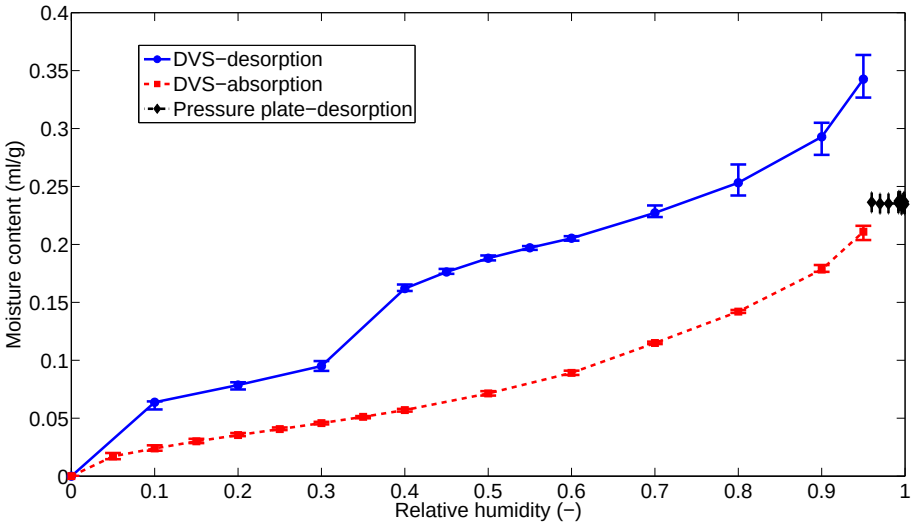

Figure 4.4: Absorption and desorption isotherms of the paste CEM III, based on the extrapolated data at equilibrium conditions (using the DVS measured data). The error bar shows the variation of three measurements. The desorption data from the pressure plate measurements are also included.

1997, Parrott 1987], the carbonation can result into the decrease of the total porosity of cementitious materials. One example of a slag cement paste with a w/c ratio of 0.4 (similar to CEM III in this study) presented in [Ngala and Page 1997] shows a porosity decrease of about 25 % (relative difference) after carbonation. However, in this study, the paste samples of CEM I and CEM III were kept almost under the same conditions. If the carbonation is considered as the only relevant factor in this context, there should be no or very limited carbonation in the paste CEM I based on the results while the paste CEM III is seriously carbonated. Then, it should imply that paste samples with high content of cementitious components would be very sensitive to carbonation. This reason, together with that precaution taken to avoid carbonation during sample preparation, makes the explanation based on carbonation mechanisms less likely. It should also be mentioned that carbonation during the pressure plate experiments is very slow because the moisture content of the samples are very high.

During the pressure plate measurements, the pores of a sample need to be saturated. However, for the paste CEM III, it seems that it could be difficult to saturate all of the pores using vacuum, especially in the case of a relatively big sample, due to the intrinsic properties, e.g., a lot of "isolated" pores and the pore system can be quite tortuous (*Paper IV*). The consequence is that the pore volume determined by the pressure plate measurements is actually smaller than the "true" value, since some of the pores are not filled by water due to insufficient preparation in terms of saturation. This is in contrast to the CEM III powder samples used in DVS measurements, in which most of the pores were concluded to be accessed by water. That is, the difference of the results between DVS and pressure plate measurements for the paste

CEM III is probably related to problems related to sample preparations in terms of achieving fully saturated conditions.

In the investigation, it appears that it was possible to fully saturate the CEM I samples but not the CEM III samples before the pressure plate measurements. Further, it is concluded that crushing seems to open up pore entries so as to make full saturation possible with the negative consequence that the "real" pore structure is changed. More discussions about the impact of sample size on the porosity characterization of cement pastes can be found in *Paper IV*.

4.3.2.2 Possible pore structure changes at low relative humidities

It has been reported in some studies, e.g., see [Feldman 1968, Atlassi 1996, Thomas and Jennings 2006, Jennings 2000, Baroghel-Bouny 2007, Jennings 2008], that changes of the pore structure of hardened cement paste samples can be expected during desorption measurements when the RH decreases to low values, e.g., below the RH of about 0.4. Some studies concluded that the pore structure changes at low RH are permanent while some other studies indicated that the changes are reversible. In the aim of clarifying the reason of the contradictory results, the possible pore structure changes at low RH were further examined in this study.

With the help of the DVS instrument, the possible pore structure changes of powdered cement paste samples at low RHs were investigated by using a re-saturation study. For the two hardened cement pastes CEM I and CEM III, firstly a desorption-absorption cycle was conducted. After this cycle, each tested sample was re-saturated with distilled water for about 3 days. The resaturation was conducted by adding several drops of distilled water on each of the tested sample in the sample holder. After the re-saturation, a second desorption-absorption cycle was applied on the samples. In this way, the changes of the pore structure at low RH were expected to be observed by comparing the obtained soprtion isotherms of the first and the second cycle, if there was any.

The results showed that the sorption isotherms after the re-saturation were almost identical to the original isotherms in all essential parts. That is, the drying at low RHs during the desorption measurement does not cause any microstructure changes or, alternatively, if the microstructure changes does occur, the absorption process must have been able to fully restore the pore structure of hardened cement paste samples, meaning the possible microsrtucture changes are reversible. The results are in agreement with the results obtained using small-angle X-ray scattering (SAXS) measurements [Winslow and Diamond 1974], small-angle neutron scattering (SANS) measurements [Pearson and Allen 1985] and the findings in [Baroghel-Bouny, 2007]. But it is carefully pointed out that it also disagrees with some other studies, e.g., [Feldman 1968, Atlassi 1996, Jennings 2000, Thomas and Jennings 2006].

It should be mentioned that the conclusion of permanent microstructure changes of cement paste samples at low RHs is often drawn based on the studies using desiccator method with saturated salt solutions, e.g., see [Feldman 1968, Atlassi 1996, Jennings 2000, Thomas and Jennings 2006]. Using the desiccator method, it often requires a long time for the equilibrium condition to be established at each RH examined. Thus, it might be reasonable to consider that the permanent microstructure changes as reported in some studies partly are related to the long time exposure at low RHs, which may enhance the aging effect as discussed by Jennings et al. [2000], meaning the so-called irreversible pore structure collapse may not be solely caused by the low RH itself, but rather due to the relatively long duration of a low RH condition. This argument is supported by the studies using methods with short RH exposure time, such as the DVS, SAXS [Winslow and Diamond 1974] and SANS [Pearson and Allen 1985], which does not show the permanent microstructure changes of cement paste samples at low RHs.

The details of low RH conditions and the effect on the pore structure of the cement based samples are presented in *Paper VI*.

4.3.2.3 Temperature dependent isotherms

The influence of temperature on the sorption isotherms of cement based materials has been reported, e.g., in [Hundt and Kantelberg 1978, Daian 1988, Radjy et al. 2003, Ishida et al. 2007, Poyet 2009, Poyet and Charles 2009]. On the other hand, the isotherms reported in studies, e.g., [Daian 1988, Radjy et al. 2003], showed hardly any temperature dependency. In the study conducted by Ishida et al. [2007], very limited differences were found between the absorption isotherms measured at different temperatures while the differences between the desorption isotherms were found to be more pronounced. The similar type of behavior was reported in [Hundt and Kantelberg 1978, Poyet 2009, Poyet and Charles 2009]. Since the reported results regarding the temperature dependent isotherms are not consistent for cement based materials, further exploration in this aspect was conducted. In this work, the sorption isotherms were measured at 25 °C, 33 °C and 40 °C.

The investigation performed here suggests suggested that the differences between the sorption isotherms at different temperatures mainly are a consequence of the temperature dependent properties of water and only to some extent due to the slight microstructure changes of the paste samples at elevated temperatures. The pronounced impact of temperature on the desorption isotherms of cement based materials as reported, e.g., in [Hundt and Kantelberg 1978, Poyet 2009, Poyet and Charles 2009], was not found in the current study.

One possible reason for the inconsistent results regarding the effect of temperature on sorption isotherms may be related to differences in the adopted measuring techniques and conditions. Desiccator method using salt solution has been adopted

in many sorption studies, e.g., in [Hundt and Kantelberg 1978, Daian 1988, Radjy et al. 2003, Ishida et al. 2007, Poyet and Charles 2009, Poyet 2009], in which the exposure time at each RH varies from several weeks to months for the equilibrium condition to be established. The different length of the exposure time at different RHs combined with the effect caused by different temperatures during measurements (especially when the measuring temperature is high) could possibly change the pore structure of the studied cement based material to a different extent. That is, the pore structure of the studied material may differ under each studied RH, due to the adopted experimental method (procedures). The argument is supported by a recent SANS study [Jennings et al. 2007], in which it was showed that elevated temperature curing can result into the changing of the porosity and extended curing at 20 °C had a similar effect. Due to the fact that the exposure time and the temperature adopted differ in studies, e.g., in [Hundt and Kantelberg 1978, Daian 1988, Radjy et al. 2003, Ishida et al. 2007, Poyet and Charles 2009, Poyet 2009], it is not surprising to see the inconsistency in the results reported. One advantage of the DVS method used in this study is that the exposure time at each RH is relatively short at controlled temperature conditions. Then, the effect due to the pore structure changes during sorption measurements is expected to be minimized.

The details of the temperature dependency of the investigated cement paste samples are presented in *Paper VI*.

4.3.2.4 Specific surface area

The specific surface area S (m^2/g) is proportional to the amount of the adsorbed moisture content on the first monolayer when it is completely covered (the monolayer capacity), with the expression given as

$$S = \frac{A_m N_A}{M_w} v_m \tag{4.2}$$

where v_m is the monolayer capacity (g/g), $N_A = 6.02 \cdot 10^{23}$ (/mol) is the Avogadro constant, $M_w = 18.0$ (g/mol) is the molar mass of water and $A_m = 10.6$ (Å^2) is the area occupied by one single water molecule. By inserting the relevant values, Eq.4.2 can be written as

$$S = 3540 \cdot v_m \tag{4.3}$$

The estimate of the monolayer capacity v_m depends on the equation considered for multilayer adsorption. A number of different types adsorption equations have been developed, e.g., see [Allen 1997], among which the representative ones including the classic BET equation [Brunauer et al. 1938], the two-layer BET equation [Brunauer et al. 1938, Johannesson 2000] and the GAB equation (being essentially the same as the Dent equation) [Dent 1977, 1980, Van den Berg 1981]. Using different adsorption

equations, the obtained monolayer capacity v_m could be different. Consequently, the calculated specific surface area could be different if different equations for multilayer adsorption are considered. In this study, the three adsorption equations mentioned above were used as a base to calculate the specific surface area for comparison purposes.

Not very surprisingly, it was concluded that the calculated specific surface area was very much sensitive to the choice of the equations considered for multilayer adsorption. For the studied materials in this investigation, the specific surface area calculated based on the two-layer BET equation was smaller than that based on the standard BET equation. The relative difference for the MCM-41 and the paste CEM I was about 26 % and 24 %, respectively. The same relative difference was calculated to be much smaller for the paste CEM III (less than 1 %). The specific surface area calculated based on the GAB equation was bigger than that obtained by the standard BET equation for the MCM-41 and the paste CEM I while the opposite relation was found for the paste CEM III.

Based on this study, it should be mentioned that the calculated specific surface area may not necessarily represent the "real" geometrical surface area, which is concluded based on the fact that the calculated specific surface area depends on the considered equation accounting for multilayer adsorption. The argument is somewhat further supported by the fact that using the same BET equation, the calculated specific surface area of a same material depend significantly on what vapor (adsorbate) is used in the experiment, as described in Section 2.5.3 (*Chapter 2*). That is, interaction forces between the adsorbate and the adsorbent most probably also affect the calculated results. Similar arguments are discussed also, e.g., in [Sing 1998, Espinosa and Franke 2006].

The details of the specific area surface estimations are presented in *Paper VII*. The detailed derivations along with the important assumptions made for the classic BET equation, the two-layer BET equation and the GAB equation are described in *Appendix C*.

4.3.2.5 Pore size distribution

The widely used BJH model [Barrett et al. 1951] was adopted in the calculation of pore size distribution (PSD) in this work. The BJH model assumes two types of water present in the pore system of a studied material, i.e., the adsorbed water and the capillary condensed water. However, the sorption measurement itself cannot distinguish between these two types of water and it only measures the total moisture content at a given RH. That is, the thickness of the adsorbed layer of water needs to be determined by some complementing approach in order to make the calculation of pore size distribution possible.

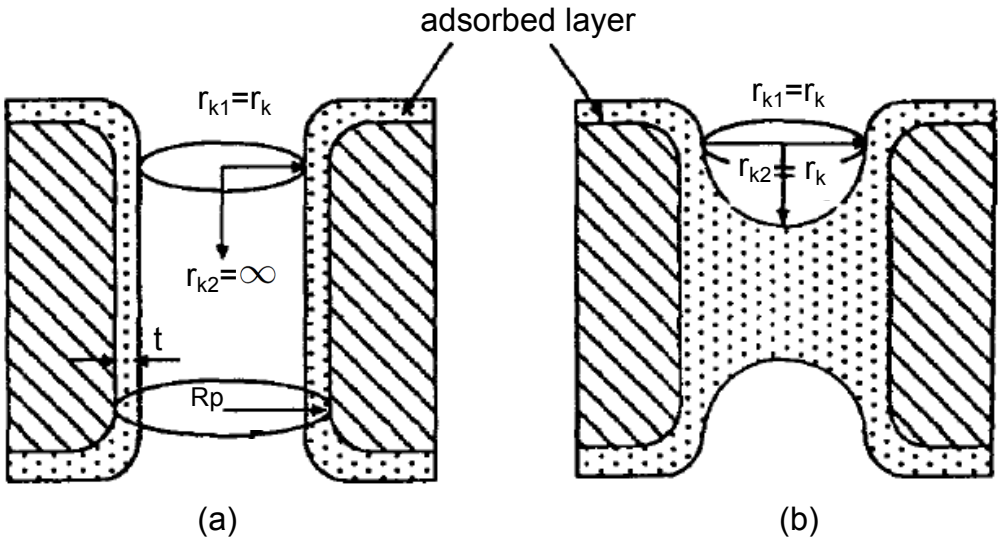

Figure 4.5: One proposed hypothesis explaining the hysteresis: different radii of the curvature during (a) absorption and (b) desorption for a cylindrical pore, slightly modified based on [Allen 1997].

It is often assumed that the statistical thickness of the adsorbed layer on a solid surface is a function of RH and the plot of this function is normally called the $t-$curve. Several $t-$curves have been proposed for water vapor. Hagymassy et al. [1969] proposed four generalized empirical $t-$curves based on the experimental studies on several types of adsorbents. Wheeler [1955] proposed the use of the empirical Halsey equation [Shull et al. 1948]. Another empirical equation was adopted by Espinosa and Franke [2006]. Johannesson [2011c] proposed an approximative method to determine the $t-$curves based on an extended BET concept. The detailed determination of the $t-$curves used in this work is presented in *Paper VII*. With the estimated $t-$curves, the pore size distribution can be calculated using the Kelvin equation among other things. The details of the adopted method to estimate the pore size distribution based on sorption measurements are discussed in *Appendix E*.

Sorption hysteresis refers to the phenomenon that the absorption isotherm follows a different path compared with that of the desorption isotherm, leaving a hysteresis loop between the two isotherms. The understanding of the underlying mechanisms of the sorption hysteresis is very important for the relevance of the assumptions made regarding the determination of pore size distribution. The origin of the hysteresis phenomenon has not been fully understood yet. It is, however, generally agreed that for most types of porous materials, the hysteresis more or less is associated with capillary condensation. One proposed explanation for the existence of sorption hysteresis is that the curvature radii of the meniscus in the same type of pore are different during the absorption and the desorption process, e.g., as discussed in [Allen 1997]. Figure 4.5 schematically shows the concept considered for a cylindrical pore. That is, the meniscus curvature (which includes two directions, i.e., $1/r_{k1} + 1/r_{k2}$) during

the absorption process is $1/r_k$ but it is $2/r_k$ during the desorption process. According to this hypothesis, the hysteresis between the absorption and desorption would be an intrinsic property of porous materials during the sorption measurements, meaning it will show up as long as the capillary condensation takes place. The idea of an intrinsic characteristics of hysteresis is challenged by different experimental studies, e.g., see [Branton et al. 1994, Ravikovitch et al. 1995, Branton et al. 1995, 1997], which did reveal that well defined reversible absorption and desorption isotherms are obtainable on a model mesoporous material MCM-41. That is, the measurements showed no hysteresis at all. Another proposed explanation for sorption hysteresis is the so-called network theory or the pore-blocking concept, which attributes the hysteresis to the inter-connectivity of the pore system, e.g., see [Seaton et al. 1989, Seaton 1991, Neimark 1991, Allen 1997, Sing 1998, 2004]. The main concept of the net work theory relies on the assumption that the the absorption isotherm reflects the pore interior size distribution while the desorption isotherm provides information about the pore entry or neck sizes and the hysteresis demonstrates the pore connectivity of a given porous material [Seaton 1991, Sing 1998, 2004]. According to the network theory, it is straightforward to explain the reversibility of the absorption isotherm and the desorption isotherm for a given porous material. No hysteresis simply indicates the absence of any pore blocking effect in the porous material. In this sense, it seems more reasonable to assume that the network theory is more relevant in explaining the hysteresis phenomenon compared with that assuming different meniscus curvature radii in absorption and desorption. This argument is also somewhat supported by the discussions in, e.g., [Sing 1998, Baroghel-Bouny 2007].

It is clearly stated in the IUPAC report dealing with sorption [Sing et al. 1985] that it is impossible to provide unequivocal recommendations in the absence of detailed knowledge about the geometry of the pores under study. But it seems to be more and more accepted that the calculation using absorption measurements may be more representative for the "true" or pore interior sizes while the calculation from the desorption is more related to the network effect (or the pore entry or neck sizes) [Sing 1998, 2001].

In this study, both desorption and absorption isotherms were measured and used in the calculation of the pore size distribution. The impact of using different $t-$curves were also studied. For the model material MCM-41, the pore radii corresponding to the peak in the calculated PSD curves, sometimes referred to as the most frequent pore radii R_{max} [Šolcová et al. 2006], using the desorption isotherm were in the range of 1.7 nm to 1.9 nm compared with 2.4 nm to 2.6 nm when using the absorption isotherm. For hardened cement pastes CEM I and CEM III, three characteristic peaks were found in the PSD curves calculated from the desorption isotherm with corresponding radii of 1.4 nm, 1.8 nm and 3.0 nm; while the peak at 1.4 nm was missing and only two peaks were found in the PSD curves calculated using the absorption isotherm.

This may indicate that, for the samples tested, 1.4 nm is an important size of the pore entries or necks. By using different $t-$curves (except the Kelvin-0 curve, see *Paper VII*), the shape of the calculated PSD curves (both from using the desorption and the absorption isotherm) for the model material MCM-41 was not seriously affected. In the case of the cement pastes, the PSD curves calculated from using the desorption isotherm were only slightly affected by the $t-$curves, but the same type of impact on the PSD curves calculated from using the absorption isotherm was more obvious. More details are presented in *Paper VII*.

It should be mentioned that the PSD curves presented in *Paper VII* assumed the same meniscus curvature during both desorption and absorption, i.e., $2/r_k$. It is noted that in literature, the curvature sometimes is assumed to be $1/r_k$ during absorption, e.g., as compared in Figure 4.5. A comparison will be made in Section 5.3 (*Chapter 5*) showing the impact of the different choices of assumed meniscus curvatures during absorption on the calculated PSD curves.

Chapter 5

Comparison of porosity results determined by low temperature calorimetry and water vapor sorption method

5.1 Introduction

Low temperature calorimetry and moisture fixation studies on the porosity of a model porous material MCM-41 and cement pastes prepared by two types of cements, i.e., CEM I 32.5 R and CEM III/B 42.5 N, have been presented in *Chapter 3* and *Chapter 4*, respectively. This chapter compares the porosity results determined by the two different methods.

5.2 General comparison

Both the LTC and the water vapor sorption (DVS) method have been used to characterize the porosity of porous materials. For cement based materials, one main advantage shared by LTC (using water as the probe liquid) and water vapor sorption method is that both methods can be applied to virgin samples without any pre-drying treatment. This is important, since the pre-drying may change the cement pore structure [Villadsen 1992, Kjeldsen and Geiker 2008]. Advantages of LTC include also the possibility of using short measurement time and the and it involves a relatively simple sample preparation procedure [Riikonen et al. 2011a]. By using the DVS instrument combined with data extrapolation processing, the measurement time for obtaining a sorption isotherm can be shortened so as to make the overall process more effective [Willems and Van Der Velden 1984, Åhs 2011].

Table 5.1: Matters of consideration of the LTC and the water vapor sorption (DVS) method for the porosity characterization of cement based materials.

Items	LTC	Water vapor sorption (DVS) method
Sample preparation	Testing samples must be fully saturated. If not, not only the pore volume but also the estimation of the the pore sizes will be misinterpreted[a].	In DVS measurements, the samples must be crushed and/or ground into powders, with consequence that the pore connectivity becomes seriously affected.
Pore size range	(1) Pores with radii smaller than that corresponding to the un-freezable water layer cannot be detected. (2) The upper limit of reliable pore radius that can be analyzed is about 40-50 nm[b].	(1) Micropores with radii of corresponding to a few water molecule's thickness may not be detected. (2) The upper limit of reliable pore radius that can be analyzed is about 30 nm[c].
Influencing factors on the measured results	(1) Supercooling and network effect influence the heat flow curves of freezing. (2) Advanced melting affects the heat flow curves of melting[d].	(1) The network effect influences the desorption curves. (2) Delayed condensation and possibly advanced absorption affect the absorption curves[e].
Factors not fully solved	(1) Temperature dependent heat of fusion. (2) The solid-liquid surface tension[f]. (3) The applicability of the thermodynamic parameters at the nanometric level[g]. (4) the thickness of the un-freezable layer, ions effect[n] and thermal lag[a].	(1) The thickness of the adsorbed layer. (2) The meniscus curvature during absorption, i.e., $1/r_k$ or $2/{r_k}^h$. (3) the computation of pore sizes, especially for the micropores[i]. (4) Applicability of the Laplace equation at the nanometric level[j].
Other issues	(1) Homogenous nucleation leads to the pore entry radii smaller than about 2.4 nm not distinguishable[k]. (2) Effects due to frost damage[l].	(1) The pore structure may change at low RHs. (2) A long waiting time for the equilibrium conditions at a RH to be established[m].

Note: (*a*). see *Paper II* and [Kjeldsen and Geiker 2008]; (*b*). after [Landry 2005, Sun and Scherer 2010, Geiker 2011]; (*c*). after [Taylor 1997, Geiker 2011]; (*d*). after [Hitchcock et al. 2011, Shiko et al. 2012]; (*e*). after [Sing 1998, 2001, Shiko et al. 2012, Sing 2004]; (*f*). see *Paper I*; (*g*). after [Setzer 2001a,b]; (*h*). see *Paper VII*; (*i*). after [Sing 1998, 2001, 2004]; (*j*). after [Beltzung and Wittmann 2005]; (*k*). after [Scherer 1993, Sun and Scherer 2010]; (*l*). see *Paper III*; (*m*). see *Paper VI;* (*n*). see *Paper V*.

It should be mentioned that there are limitations and unsolved factors for both methods, some of which are summarized and listed in Table 5.1. These limitations should be kept in mind when comparing the results determined by these two methods with that obtained by other methods, e.g., MIP, SEM, NMR. It is concluded in [Sing 2001] that in sorption studies, the analysis methods available do not give more than semi-quantitative results with respect to the pore size determination. That is, porosity results determined by the sorption method on different materials is mainly valuable for comparison purpose. Considering the factors which can influence the measured and analyzed results by using LTC as presented in Table 5.1, it may be reasonable to claim that LTC is also only a semi-quantitative method in the context of porosity determination.

5.3 Porosity results determined by LTC and water vapor sorption method

The details of the PSD calculation for the studied materials from the melting curves by LTC have been presented in *Paper IV*. The PSD curves determined by LTC and the water vapor sorption (DVS) method are compared in this section. Since the choice of water meniscus curvature during the absorption process is somewhat arguable, i.e., $1/r_k$ or $2/r_k$ (Section 4.3.2.5), both assumptions are included in the comparison.

The comparison of the determined PSD curves for the model material MCM-41 is presented in Figure 5.1. The R_{max}, i.e., the most frequently occurring pore size, determined from the LTC melting curve and the desorption isotherm is about 1.7 nm and 1.8 nm, respectively. On the other hand, the R_{max} determined from the absorption isotherm using the Hagymassy et al. $t-$curve [Hagymassy et al. 1969] is about 1.4 nm and 2.4 nm using the meniscus curvature $1/r_k$ and $2/r_k$, respectively. As has been discussed previously in *Chapter 3*, a freezing curve indicates pore entry sizes and a melting curve represents the pore interior size information. That is, the PSD curve determined from a LTC melting curve should be compared with the PSD curve determined from the absorption curve in a sorption experiment [Sing 1998, Sun and Scherer 2010]. However, for the studied MCM-41, the result is that the determined R_{max} from the LTC melting curve (1.7 nm) is significantly different from that determined from the absorption isotherm, i.e., 1.4 nm (assuming curvature as $1/r_k$) and 2.4 nm (assuming curvature as $2/r_k$). In fact, in this case, the R_{max} determined from the LTC using the melting curve is more close to the value obtained from the sorption experiment using the desorption isotherm (1.8 nm). Similar conclusions can be obtained by using other $t-$curves in analyzing the sorption data. This is because

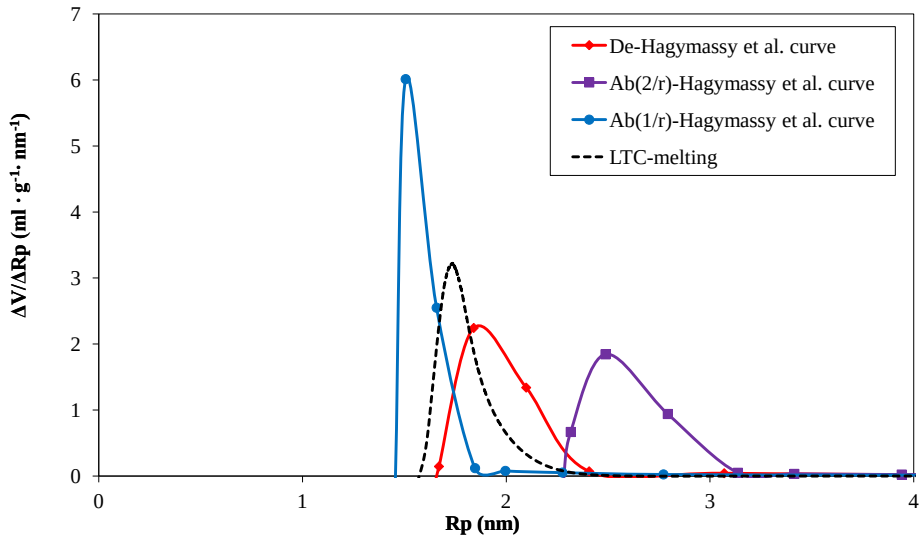

Figure 5.1: Pore size distribution (PSD) curves determined by LTC and the DVS method for the model material MCM-41. The LTC melting curve is used to calculate the PSD. The $t-$curve used in the sorption PSD calculations is the Hagymassy et al. curve [Hagymassy et al. 1969]. "De" or "Ab" indicates that either the desorption or the absorption isotherm is used in the calculation. Ab(1/r) represents that the meniscus curvature during absorption is assumed to be $1/r_k$ and Ab(2/r) represents $2/r_k$.

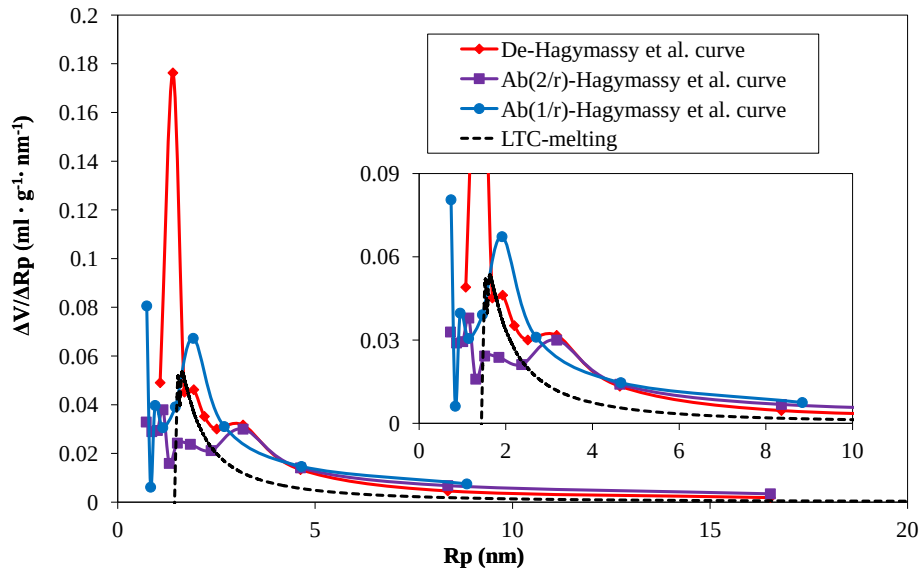

Figure 5.2: Pore size distribution (PSD) curves determined by LTC and the DVS method for the paste CEM I on powder samples. The LTC melting curve is used to calculate the PSD. The $t-$curve used in the sorption PSD calculations is the Hagymassy et al. curve [Hagymassy et al. 1969]. "De" or "Ab" indicates that either the desorption or the absorption isotherm is used in the calculation. Ab(1/r) represents that the meniscus curvature during absorption is assumed to be $1/r_k$ and Ab(2/r) represents $2/r_k$.

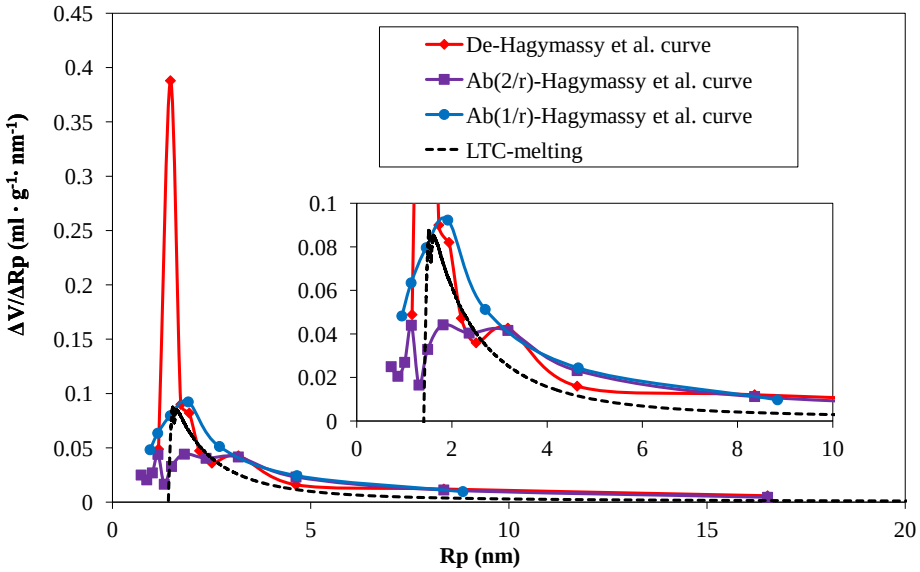

Figure 5.3: Pore size distribution (PSD) curves determined by LTC and the DVS method for the paste CEM III on powder samples. The LTC melting curve is used to calculate the PSD. The $t-$curve used in the sorption PSD calculation is the Hagymassy et al. curve [Hagymassy et al. 1969]. "De" or "Ab" indicates that either the desorption or the absorption isotherm is used in the calculation. Ab(1/r) represents that the meniscus curvature during absorption is assumed to be $1/r_k$ and Ab(2/r) represents $2/r_k$.

the calculated PSD curves for the model material MCM-41 is not very sensitive to the different considered $t-$curves as concluded in Section 4.3.2.5.

It should be mentioned that the above comparison is based on that the thickness of the un-freezable layer in the LTC study is assumed to be 0.8 nm, a typical value used in this context as proposed by Brun et al. [1973, 1977]. The un-freezable layer can not be measured directly, therefore, a normal procedure adopted in literature is to correlate the pore size of a model porous material, typically with a narrow PSD, calculated by LTC and sorption studies, e.g., see [Antoniou 1964, Brun et al. 1973, 1977, Ishikiriyama et al. 1995, Landry 2005]. That is, the value of the thickness of the un-freezable layer is obtained by fitting, e.g., by assuring that R_{max} becomes equal using the two methods. As discussed before, it has been a long debate about which isotherm (desorption or absorption) should be used in the pore size calculation in sorption studies including hysteresis. However, for many years, desorption isotherms were considered to be more thermodynamic stable and therefore it was thought to be more appropriate to use desorption isotherms to determine the pore size distribution [Sing 1998]. The drawback of this concept has been demonstrated by taking the network theory into consideration [Seaton 1991, Sing 1998], in which it is concluded that desorption isotherms only reflect the pore entry or neck sizes. It is not clearly stated in [Brun et al. 1973, 1977] that whether the adsorption or desorption isotherm was used in calculating the pore sizes in the studies. According to the results obtained

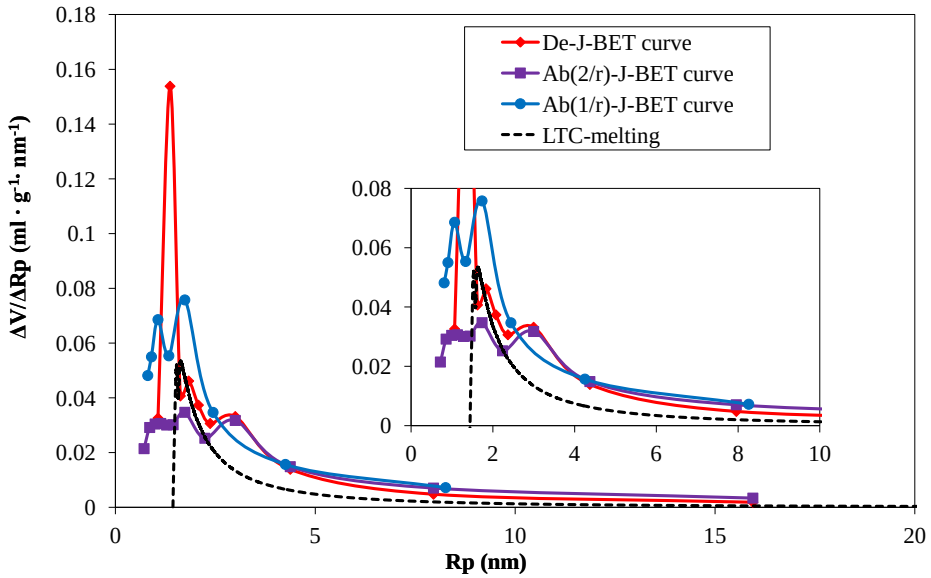

Figure 5.4: Pore size distribution (PSD) curves determined by LTC and the DVS method for the paste CEM I on powder samples. The LTC melting curve is used to calculate the PSD. The $t-$curve used in the sorption PSD calculation is the J-BET curve (*Paper VII*). "De" or "Ab" indicates that either the desorption or the absorption isotherm is used in the calculation. Ab(1/r) represents that the meniscus curvature during absorption is assumed to be $1/r_k$ and Ab(2/r) represents $2/r_k$.

in this study, it is suspected that the desorption isotherm rather than the absorption counterpart was used.

For the studied MCM-41 (Figure 5.1), the R_{max} determined from the LTC melting curve is 1.7 nm and that determined from the absorption curve, assuming meniscus curvature as $1/r_k$, is 1.4 nm. The value 1.4 nm is significantly different from the value obtained using the absorption curve assuming meniscus curvature as $2/r_k$, which results in the value of 2.4 nm. If one imposes that the R_{max} determined from a LTC melting curve should be the same as that determined from the corresponding absorption isotherm and the difference between the determined R_{max} values is solely due to that the thickness of the un-freezable layer in the LTC calculation is not correctly determined, then the value for the thickness of the un-freezable layer can be adjusted. Further discussion in this regard will be conducted later.

The comparison of the determined PSD curves for the cement pastes CEM I and CEM III are presented in Figure 5.2 and Figure 5.3, respectively. Since the sorption data were measured on powder samples, the LTC results presented here are also from powder samples (*Paper IV*). Hagymassy et al. $t-$curve [Hagymassy et al. 1969] was adopted in calculating the PSD curves using the absorption data. Compared with the results for the model material MCM-41, the most important difference is that the magnitude of PSD curve corresponding to R_{max} obtained from the desorption isotherms are much higher than that obtained from both the absorption isotherm and the LTC melting curve. The characteristics of the differences between the obtained

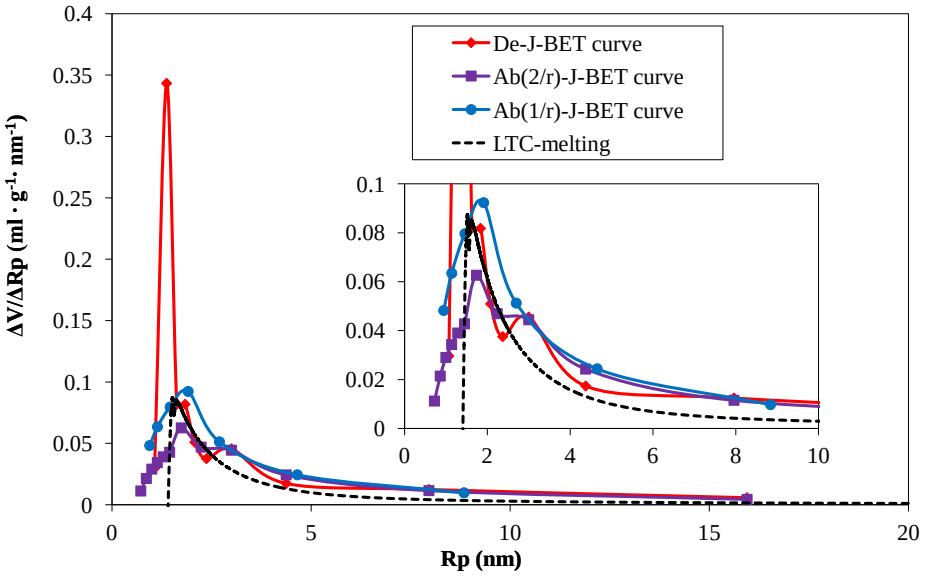

Figure 5.5: Pore size distribution (PSD) curves determined by LTC and the DVS method for the paste CEM III on powder samples. The LTC melting curve is used to calculate the PSD. The $t-$curve used in the sorption PSD calculation is the J-BET curve *(Paper VII)*. "De" or "Ab" indicates that either the desorption or the absorption isotherm is used in the calculation. Ab(1/r) represents that the meniscus curvature during absorption is assumed to be $1/r_k$ and Ab(2/r) represents $2/r_k$.

values of R_{max} for the paste CEM I are somewhat similar to that obtained for the MCM-41. That is, the R_{max} determined from the LTC melting curve (1.7 nm) is more close to that obtained from the desorption isotherm (1.4 nm) and that obtained from the absorption isotherm assuming meniscus curvature as $1/r_k$ (1.9 nm), while the value determined from the absorption isotherm assuming meniscus curvature as $2/r_k$ is about 3.2 nm. Compared with that of the MCM-41, the difference between the specific values of the R_{max}, i.e., that determined the LTC melting curve, the desorption isotherm and the absorption isotherm assuming meniscus curvature as $1/r_k$ or $2/r_k$, are different. Similar conclusions as drawn for the paste CEM I are also applicable for the paste CEM III, except that there is not a dominant peak corresponding to R_{max} for the paste CEM III when the meniscus curvature during absorption is assumed to be $2/r_k$ (Figure 5.3).

As mention in Section 4.3.2.5, the PSD curves of the cement pastes determined from the absorption data are relatively sensitive to the $t-$curves used in the calculation. Of this reason, another $t-$curve besides the Hagymassy et al. curve, i.e., the J-BET curve (*Paper VII*) was used in the calculation. This comparison of the calculated results are presented in Figure 5.4 for the paste CEM I and Figure 5.5 for the paste CEM III. By using the J-BET curve, the peak corresponding to R_{max} for the paste CEM I becomes somewhat vague compared with that obtained using the Hagymassy $t-$curve. For the case of the paste CEM III, the peak corresponding to R_{max} becomes more well defined compared with that obtained using the Hagymassy

et al. $t-$curve. Other main features of the results obtained using Hagymassy et al. $t-$curve as discussed above are also applicable to the results obtained using the J-BET $t-$curve.

Due to the limitations of currently available techniques in pore size characterization (as discussed in Section 2.5, *Chapter 2*), the exact values of the "true" (actual) pore sizes of a studied material cannot be obtained. By using different measurement techniques, as adopted here (the LTC and DVS measurements), a fitting parameter can be used, e.g., the thickness of the un-freezable layer. Such a fitting parameter can be used to match the pore size distributions obtained from the two separate measurements. However, due to the unsolved factors in sorption studies, e.g., the meniscus curvature during the absorption and the effect of the so-called delayed condensation [Findenegg et al. 1994, Sing 1998], it may make the adjustment of the thickness of the un-freezable layer little meaning. That is, it is somewhat difficult to make the pore size distribution determined by the two methods absolutely fit even for a simple model porous material. For cement based materials, the pore systems are much more complicated than that of model materials (such as the MCM-41) and more unsolved factors comes into the picture, e.g., see Table 5.1. Of this reason, it becomes even more challenging to make the pore size distribution results determined by the two methods to agree by using parameter fitting.

To sum up the discussion about the comparison study, only a certain degree of agreement can be found for the pore size distribution determined by LTC and the water vapor sorption method. It should also be mentioned that probably none of the two methods studied here can deliver the "true" (actual) pore size distribution information. That is, before the uncertainties and unsolved factors (e.g., see Table 5.1) being solved, the two methods are only semi-quantitative and meaningful for comparison purposes.

Chapter 6

Conclusions and future studies

6.1 Conclusions

This PhD study focused on using low (micro-)temperature calorimetry (LTC) and a moisture fixation method to study the pore structure of cement based materials, especially at the nanometric level. Special attention was devoted to investigating important factors influencing the analysis of measured LTC data and using LTC to characterize the pore structure of cement based materials. Besides, the moisture fixation method was selected as a comparison method for LTC by noting that both methods can be applied to virgin cement based materials without any pre-drying treatment. Attempts have been made to correlate the porosity characteristics determined by the two different techniques. The important investigations and conclusions of this PhD study can be summarized as follows:

1. Two factors are of paramount importance in the analysis of measured LTC data: (1) baseline determination of the measured heat flow; and (2) the values to be used for the the heat of fusion of the water/ice confined in pores. Two main different methods can be used to calculate the baseline. The 'J-baseline' method is a recently proposed method based on extrapolation by using the accumulated heat curves measured in the freezing and the melting process. The 'C-baseline' considers the heat capacity of both water and ice and the phase transition behavior under the different testing temperatures. Both methods can be used for baseline and ice content calculation if due attention is paid. Results obtained by the 'J-baseline' method are not affected by the uncertainties of the heat capacity of water and ice under very low temperatures and the possible fluctuations of the cooling and heating rate during testing. The 'C-baseline' can in many cases deliver accurate result due to its relatively stringent theoretical basis, provided the corrected thermodynamic parameters could be found. These two methods can be used to complement each other. The comparison study on the different values of heat of fusion commonly adopted in literature showed

that for the studied concrete samples, the relative difference of the maximum ice content determined from one freezing and melting cycle can differ up to 27 % using the 'C-baseline' method. However, using the heat of fusion of bulk water but corrected for the depressed freezing/melting temperature of the pore water results in the smallest difference between the maximum ice content calculated from the measured heat flow during freezing and melting in one cycle.

2. A careful examination of the thermodynamic background emphasized that the freezing/melting temperature of the water/ice confined in non-fully saturated pores is further depressed compared with the condition that the pores are fully saturated. The study of the experimental data measured on hardened concrete samples showed that for a same concrete mix, the total pore volume detected from the capillary saturated sample was always lower than that of the vacuum saturated sample. Compared with the vacuum saturated samples, a higher proportion of pores with small radii were found in the capillary saturated samples using the same calculation method. In addition, the observed hysteresis between the freezing and melting curves of ice content in the capillary saturated samples was more pronounced than that in the vacuum saturated samples. The major reason accounting for these phenomena could be that the pores under study cannot be fully saturated using the capillary saturation method. As the pores under study are not fully saturated, the further depression of the freezing/melting temperatures of the confined water/ice compared with that under fully saturation result in a higher proportion of small pores calculated. It is also noted that the hysteresis between the freezing and melting ice content curves was observed to be more pronounced in the capillary saturated samples than the vacuum saturated ones.

3. A mono-sized model material MCM-41 and two types of hardened cement pastes were used to study the impact of frost damage on the (meso-)porosity determination by LTC. Three continuous freezing and melting cycles were applied on the MCM-41 and two continuous cycles were applied on each of the cement paste. The measured results showed that for the model material MCM-41, the heat flow curves of freezing and melting after each cycle were more or less the same. For the two cement pastes, the heat flow curves of freezing changed after one cycle of measurement and the change was more evident in low temperature range. The heat flow curves of melting were almost not affected after one cycle of measurement. The results indicate that the pressure generated during freezing and melting has little impact on the pore structure of the powder MCM-41 samples. As for the studied cylinder paste samples, frost damage potentially takes place and it changes the pore connectivity characteristics while it had limited effect on changing the interior size distribution of the meso-pores.

4. Comparison measurements were performed on cement paste samples of the same recipe preconditioned in a small amount and a big amount of saturated limewater for a relatively long time (about 9 months). The main aim was to illustrate whether a relatively long time preconditioning (e.g., ions in cement hydrates may leach out) can change the freezing and/or melting behavior of cement pore solution compared with a case where leaching was not that dominant. The measured results showed that there is almost no difference in the heat flow curves of freezing and melting comparing the samples preconditioned in a small amount and a big amount of saturated limewater. This indicates that either the preconditioning in a big amount of limewater does not change the concentration of the pore solution very much or the leaching of ions from cement hydrates has limited influence on the freezing and melting behavior of the pore solution in the studied cement paste samples.

5. Two types of samples, i.e., in the form of powders and cylinders, were used to study the impact of sample crushing on the porosity determination using LTC. For the two types of hardened cement pastes CEM I and CEM III studied, the calculated ice content curves of freezing of the powder samples differed from that of the cylinder samples, especially for that of the paste CEM III. That is, the investigation indicates that sample crushing changes the pore connectivity. One important difference between the powder sample and the cylinder samples of the paste CEM III was that the determined maximum ice content in the powder sample was much higher compared with that in the cylinder samples, the relatively difference being as high as about 40∼50 %. However, this kind of marked difference was not found from the comparison of the paste CEM I. That is, the sample crushing can possibly result into more pores detected by LTC depending on the specific (porosity) properties of the studied paste. The marked difference between the calculated pore volume of the powder and the cylinder samples of the paste CEM III is possibly due to some of the "isolated" pores which, presumably, cannot be fully filled with water in the preparation of the cylinder samples. However, sample crushing makes it possible to saturate the pores to a greater extent if the crushing contributes to open up the "isolated" pores. Consequently, more pores are detected in the powder samples. The argument about the "isolated" pores is supported by the results of gravimetric measurements on cylinder samples and the DVS measurements on powder samples.

6. A simulation study was conducted to estimate the ionic concentrations in the pore solution of cement pastes at different temperatures during freezing and melting measurements using the LTC technique. Thermodynamic modeling using the program PHREEQC were performed. Cylinder and powder samples

of the cement pastes prepared by two different types of cements were used in the investigation. The simulated results showed that the ionic strength for each studied paste sample does not change very much at the temperature range between 0 °C and -40 °C in the LTC measurements. Using the PHREEQC simulated ionic concentrations, the calculated differential pore size distributions for the studied samples with and without considering the temperature depression caused by the ions presented in the pore solution was compared. The results indicate that for the studied cement paste samples included in this investigation, the temperature depression caused by the ions present in the pore solution affects the determination of the pore size distribution by LTC to a limited extent.

7. The possible pore structure changes at low RHs were investigated by a re-saturation study using a DVS instrument. For the studied hardened cement pastes, a desorption-absorption cycle was conducted. After this cycle, each tested sample was re-saturated with distilled water. After the re-saturation, a second desorption-absorption cycle was applied on the samples. In this way, the changes of the pore structure of the studied hardened cement paste samples at low RHs were expected to be observed by comparing the sorption isotherms of the first and the second cycle. The results showed that the sorption isotherms after the re-saturation are almost identical to the original isotherms in all essential parts. That is, the drying at low RHs during the first desorption measurement does not cause any microstructure changes according to the second cycle results. Another possibility is that if the microstructure changes do occur, the absorption process must have been able to fully restore the pore structure of the cement paste samples, meaning the possible microstructure changes are reversible.

8. The influence of the temperature on the sorption isotherms of hardened cement pastes were studied (temperature range $25 \sim 40$ °C). The results suggest that the differences between the sorption isotherms at different temperatures are mainly a consequence of the temperature dependent properties of water and only to some extent due to slight microstructure changes of the paste samples at elevated temperatures. The pronounced impact of temperature on desorption isotherms of cement based materials as reported in some references in the literature are not found in this study.

9. Three representative adsorption equations, i.e., the standard BET, the two-layer BET and the GAB equation, were used to calculate the specific surface area of the studied materials based on sorption measurement results. It was concluded that the calculated specific surface areas are very much dependent on which equation is used for describing multilayer adsorption. That is, probably none of the calculated specific surface area represent the "real" geometrical surface area.

10. Both desorption and absorption isotherms were used in the calculation of the pore size distribution (PSD). The impact of different choices of $t-$curves were also studied. For the model material MCM-41, the pore radii corresponding to the peak in the calculated PSD curves, or equally the most frequent pore radii R_{max}, using the desorption isotherm were in the range of 1.7 nm to 1.9 nm compared with 2.4 nm to 2.6 nm when using the absorption isotherm. For hardened cement pastes CEM I and CEM III, three characteristic peaks were found in the PSD curves calculated from the desorption isotherms with corresponding radii of 1.4 nm, 1.8 nm and 3.0 nm. On the other hand, the peak at 1.4 nm was missing and only two peaks were found in the PSD curves calculated using the absorption isotherms. This may indicate that 1.4 nm is an important size of the pore entries or necks to which bigger pores are connected in the investigated cement paste samples. Using different $t-$curves (except the Kelvin-0 curve, see *Paper VII*), the shape of the calculated PSD curves (using both the desorption and absorption isotherms) for the model material MCM-41 were not seriously affected. In the case of the cement pastes, the PSD curves calculated from the desorption isotherms were only slightly affected by the choice of $t-$curves, but the impact of different choices of $t-$curves on the PSD curves calculated using the absorption isotherm was more pronounced.

11. The pore size distribution determined by LTC and the water vapor sorption method were compared and only a certain degree of agreement could be found. Due to the uncertainties and many unsolved factors involved in the data analysis (e.g., see Table 5.1), probably none of these two methods could deliver the "true" (actual) pore size distribution information. That is, before the uncertainties and unsolved factors being solved, both methods are only semi-quantitative and meaningful for comparison purposes.

6.2 Future studies

An accurate characterization of the pore structure is central for the understanding of the properties and performances of cement based materials. Efforts have been made in this research work to clarify related issues of using LTC and a moisture fixation method (mainly water vapor sorption) to study cement based materials. Based on this work, several aspects can be recommended for future studies:

1. The inter-connectivity of pores is an important property of a pore system, which could affect the sorption behaviors (e.g., see [Wall and Brown 1981, Zhdanov et al. 1987, Seaton 1991, Liu et al. 1992]), the freezing/melting behaviors of a liquid in the pore system (e.g., see [Perkins et al. 2008, Hitchcock et al. 2011, Shiko et al. 2012]) and of course the properties and performances of the con-

sidered material. Unfortunately, there lacks a proper way or a parameter to stringently characterize this property. It is noted that based on the percolation theory, several attempts have been made to determine the connectivity of some model materials with relatively simple pore structure, e.g., see [Wall and Brown 1981, Zhdanov et al. 1987, Seaton 1991, Liu et al. 1992, Perkins et al. 2008]. However, the application of the percolation theory to the determination of the pore connectivity of materials with more complicated pore structure, e.g., cement based materials, is challenging. Further development of percolation theories and measuring techniques are needed to understand the pore connectivity characteristics of cement based materials.

2. Similar to LTC, NMR cryoporometry does not need to pre-dry cement based materials. Further, using NMR cryoporometry, the pore information of a studied material is also estimated by freezing/melting the pore water/ice. But the ice content is determined quite differently in the two methods. In this sense, combined NMR cryoporometry and LTC study can be of great relevance in characterizing the pore structure of cement based materials. However, it needs to be mentioned that the uncertainties and unsolved factors of each method should be carefully considered before a full comparison is made.

3. During a LTC measurement, the water filled sample is normally subjected to various combined actions, including volume expansion, crystallization pressure, hydraulic pressure, interfacical effects between the different constitutes presented in the pores, the cryo-suction process in cases that the pore system is not fully saturated and the thermomechanical coupling between the solid matrix, the liquid water and the ice crystal, e.g., see [Coussy 2005]. The general coupled behavior under such a complicated set of actions is not fully understood yet. With improved knowledge about the actual actions, the impact of freezing on the pore structure of the studied material can be better understood.

4. As indicated in Section 6.1 (item 9), it is reasonable to assume that none of the calculated specific surface areas based on the different multilayer adsorption equations represents the "real" geometrical surface area. It is of interest to get a better estimate and/or refining the whole concept so as to get better correlation between different measurement techniques and the results. If a better or more reliable estimate of the surface area could be obtained, other measurements techniques, which need information about the surface area, will also be improved. For example, in such a case, the thickness of the un-freezable water layer in LTC analysis can be determined more accurately. Further study in this regard is of great interest.

5. The temperature dependent thermodynamic parameters used for the PHREEQC calculation in this study is extrapolated from experimental data which are mainly obtained above 0 °C. In order to study the chemical equilibrium behavior of cement based materials at freezing temperatures, it is of interest to obtain the experimental data for these temperatures. It is noted that the thermodynamic parameters of some common chemical components at low temperatures can be found, e.g., in [Marion and Kargel 2008]. Further development of the existing thermodynamic databases for cement hydrates accounting for low temperatures would be of great interest in the context of, e.g., studying freezing point depression mechanisms.

6. The simulated ionic concentrations in the pore solution of cement pastes at different temperatures in LTC measurement conditions were obtained in this study by assuming thermodynamic equilibrium. However, the ionic concentrations will differ from the simulated results if the chemical equilibrium is not reached in the experimental conditions considered. Further study in this aspect is needed.

7. Further clarification about the the uncertainties and unsolved factors involved in LTC and sorption analysis (as listed in Table 5.1) helps to improve the accuracy of a pore structure characterized by the two methods.

Part II

Appendices

A A constitutive relation between the depressed freezing/melting point and the pore size

It turns out that it is extremely difficult to characterize the nanoscopic and microscopic structure of porous materials using calorimetric methods. In the approaches adopted, the most important property used to characterize a pore is the radius by assuming an idealized pore shape, e.g., sphere or cylinder are the two most common ones. The crux is that the existing thermodynamic methods need to relate the ice-water boundary surface to the volume of the ice body. Of course, such a phase boundary can have many different spatial configurations making the simplifications used questionable. Another issue is the that the energy required to change the surface area boundary is needed (basically the surface energy). This property may be subjected to very strong dependency on temperature which are almost impossible to measure directly. Further, the character of the inner solid porous walls needs to be assumed to be the same for all materials considered.

The derivation of the relation between the depressed freezing point of a liquid confined in a pore and the pore size has been discussed by many authors, e.g., in [Defay et al. 1966, Brun et al. 1977, Scherer 1993, Landry 2005]. It should be mentioned that even though the thermodynamic approach is widely used, the applicability of this method to nanoscopic systems has been questioned by, e.g., Setzer in [Setzer 2001a,b], since the thermodynamic theory used is completely macroscopic. That is, the evaluation of the smallest pore sizes using such a thermodynamic approach may be limited. However, because no nanoscopic descriptions for the present problem exists, the traditional way is followed in this description. The key related arguments for the macroscopic thermodynamic approach describing the relation between the depressed freezing/melting point and the pore size are reproduced here.

For a substance coexisting in three different phases, the balance between mechanical, thermal, and chemical potential contributions at equilibrium for a planar interfacial system upon infinitesimal changes can be described by extensive variables using the Gibbs-Duhem equations [Defay et al. 1966]:

$$S_s dT - V_s dP_s + n_s d\mu_s = 0 \tag{A.1}$$

$$S_l dT - V_l dP_l + n_l d\mu_l = 0 \tag{A.2}$$

$$S_g dT - V_g dP_g + n_g d\mu_g = 0 \tag{A.3}$$

where S_i is the entropy, T the temperature, V_i, P_i, n_i the volume, pressure and moles of the phase i. The subscripts s, l and g represent the solid phase (note: not the solid porous matrix), the liquid phase and the gas phase, respectively. Eq.A.1 to Eq.A.3 can

be supplemented by Laplace equations accounting for the curved interfaces, liquid-solid ($l-s$), liquid-gas ($l-g$) and solid-gas ($s-g$), as shown in Eq.A.4 to Eq.A.6:

$$P_l - P_g = \gamma_{lg}\frac{dA_{lg}}{dV_l} \tag{A.4}$$

$$P_g - P_s = \gamma_{gs}\frac{dA_{gs}}{dV_g} \tag{A.5}$$

$$P_s - P_l = \gamma_{sl}\frac{dA_{sl}}{dV_s} \tag{A.6}$$

where γ_{ij} is the surface tension and A_{ij} is the surface area for the curved interfaces. The equations Eq.A.4 to Eq.A.6 are the adopted constitutive equations for the pressure jump across the phase boundaries. According to the phase rule established by Defay et al. [1966], two critical interfaces dictate the equilibrium condition of a system containing three phases. Thus, we can, for example, choose to take the solid-gas and the solid-liquid interfaces as critical interfaces. Upon differentiation, Eq.A.7 and Eq.A.8 are the differentiated versions of Eq.A.5 and Eq.A.6

$$dP_g - dP_s = d(\gamma_{gs}\frac{dA_{gs}}{dV_g}) \tag{A.7}$$

$$dP_s - dP_l = d(\gamma_{sl}\frac{dA_{sl}}{dV_s}) \tag{A.8}$$

Noting that for the phases at equilibrium implying that the chemical potential of each phase is the same, that is, $d\mu_g = d\mu_s = d\mu_l$. By combining Eq.A.1 and Eq.A.3, and Eq.A.2 with Eq.A.1 and using volume V_i, entropy S_i and the the moles n_i to define the molar volume v_i ($v_i = V_i/n_i$) and the molar entropy s_i ($s_i = S_i/n_i$), we get Eq.A.9 and Eq.A.10 for the gas-solid and solid-liquid interfaces, respectively.

$$(\frac{s_g - s_s}{v_g - v_s})dT = \frac{v_g}{v_g - v_s}dP_g - \frac{v_s}{v_g - v_s}dP_s \tag{A.9}$$

$$(\frac{s_s - s_l}{v_s - v_l})dT = \frac{v_s}{v_s - v_l}dP_s - \frac{v_l}{v_s - v_l}dP_l \tag{A.10}$$

Further, by subtracting Eq.A.10 from Eq.A.9 and substituting dP_g and dP_l from Eq.A.7 and Eq.A.8, Eq.A.11 is obtained:

$$[(\frac{s_g - s_s}{v_g - v_s}) - (\frac{s_s - s_l}{v_s - v_l})]dT = \frac{v_g}{v_g - v_s}d(\gamma_{sg}\frac{dA_{sg}}{dV_g}) - \frac{v_l}{v_l - v_s}d(\gamma_{sl}\frac{dA_{sl}}{dV_l}) \tag{A.11}$$

It is demonstrated by Eq.A.11 that the freezing/melting temperature of the confined water indeed depends on the curvature of two critical interfaces, i.e., the curvature of gas-solid and solid-liquid interfaces as assumed in this case. As pointed out in [Brun et al. 1977], in order to calculate the freezing/melting temperature of the

confined liquid, it is necessary and sufficient to know the curvature dA_{ij}/dV_j of two of the three present interfaces. However, this condition can not usually be met for a porous material. But it is possible to study the particular cases where the solid-gas interface is plane, for example, a fully saturated porous material. Then the curvature dA_{sg}/dV_g is zero during the whole freezing or melting process. It is reasonable to assume $v_g \gg v_l$, thus we also have $v_g \gg v_l - v_s$. Since $dA_{sg}/dV_g = 0$ (as assumed for a fully saturated system) and $\Delta S_f = s_l - s_s$ to denote the entropy difference between the liquid and the solid phase, one obtains Eq.A.12 from Eq.A.11:

$$\Delta S_f dT - v_l d(\gamma_{sl} \frac{dA_{sl}}{dV_l}) = 0 \tag{A.12}$$

Further simplifications with respect to Eq.A.12 were adopted, e.g., in [Brun et al. 1977]. The classical assumption used for freezing is $dA_{sl}/dV_l = -2/r$ (minus sign implies the concave is toward the liquid phase) and that a different geometrical development is usually assumed for melting, i.e., $dA_{sl}/dV_l = -1/r$, corresponding to a cylindrical pore shape. With respect to a spherical pore shape, it is assumed that for both freezing and melting $dA_{sl}/dV_l = -2/r$. However, it should be mentioned that it is almost impossible to verify whether the curvature is $-1/r$ or $-2/r$ in practice. Following the classical assumptions, Eq.A.12 can be integrated and rewritten into Eq.A.13 for freezing (both cylindrical and spherical pores) and the melting of spherical pores as well and Eq.A.14 for melting of cylindrical pores, where T is the freezing/melting point of the liquid/solid confined in the pores with radii of r and T_o is that of the bulk liquid/solid. Based on Eq.A.13 and Eq.A.14, it is possible to calculate the radius of liquid/solid nucleus r since each r is explicitly related to the freezing/melting point of the liquid/solid confined in the pores. There exists a liquid layer in close contact with the pore wall, which will not undergo any phase transition during a measurement [Brun et al. 1977]. This layer is sometimes referred to as the $\delta-$layer, with a thickness denoted as δ, Thus, the pore radius R_p (pore entry radius for freezing and pore interior radius for melting) can be given as $R_p = r + \delta$.

$$\frac{2}{r} = -\frac{1}{\gamma_{ls}} \int_{T_0}^{T} \frac{\Delta S_f}{v_l} dT \tag{A.13}$$

$$\frac{1}{r} = -\frac{1}{\gamma_{ls}} \int_{T_0}^{T} \frac{\Delta S_f}{v_l} dT \tag{A.14}$$

A detailed discussion and numerical analysis of the parameters, e.g., γ_{ls} and $\triangle S_f$, for confined water can be found in [Brun et al. 1977]. It is noted that for the thickness of the $\delta-$layer, a value δ=0.8 nm for water was proposed by the same authors in their experimental study [Brun et al. 1973, 1977]. This value, which corresponds to about 2.5 layers of water molecules, is comparable to the findings in [Antoniou 1964] (less than 3 layers) and [Litvan et al. 1966] (2 layers). By using the the numerical

value for the parameters adopted in [Brun et al., 1977] and taking into account the thickness of the $\delta-$layer assumed to be δ=0.8 nm, the pore radius R_p can be expressed numerically by Eq.A.15 (based on Eq.A.13) and Eq.A.16 (based on Eq.A.14), where R_P is given in nm, freezing/melting point depression $\triangle T = T - T_0$.

$$R_p = -\frac{64.67}{\triangle T} + 0.57 \tag{A.15}$$

$$R_p = -\frac{32.33}{\triangle T} + 0.68 \tag{A.16}$$

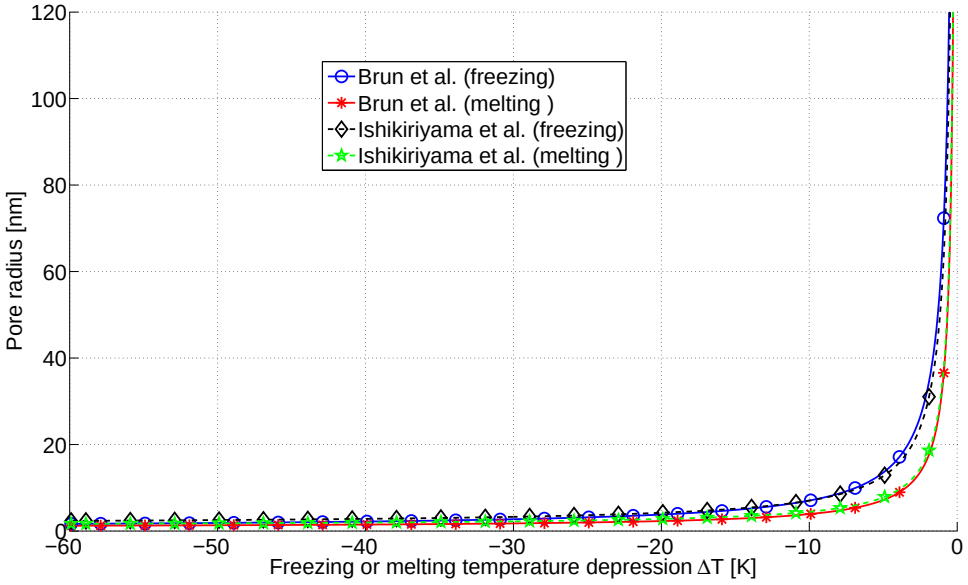

Figure A.1: Comparison of the relation between the pore radius and the freezing or melting temperature depression adopted by Brun et al. [1977] and Ishikiriyama et al. [1995]. In the relation given by Brun et al. [1977] assuming cylindrical pore shape, Eq.A.15 is for freezing and and Eq.A.16 is for melting. Then, Eq.A.15 should be compared to Eq.A.17 (for freezing and Eq.A.16) should be compared to Eq.A.18 (for melting). The thickness of the $\delta-$layer in Eq.A.17 and Eq.A.18 are also assumed to be 0.8 nm ($\delta_f = \delta_m = \delta$) as in the case of Eq.A.15 and Eq.A.16.

It is found that Eq.A.15 and Eq.A.16 are either directly cited or serve as the basis in the evaluation of pore sizes using LTC experiments, e.g., in [Quinson et al. 1987, Quinson and Brun 1988, Cuperus et al. 1992, Kloetstra et al. 1995, Hay and Laity 2000, Iza et al. 2000, Yamamoto et al. 2005, Sun and Scherer 2010].

Different from the method adopted by Brun et al. [1977] to generate the relation of the depressed freezing/melting temperature and the pore size as presented above, Ishikiriyama et al. [1995, 1995b, 1995a, 1996] utilized a somewhat sophisticated mathematical fitting and optimization process to best match the pore size distribution as derived based on LTC and nitrogen adsorption measurements using silica gels. Based on their studies, two expressions, i.e., Eq.A.17 and Eq.A.18, were suggested.

The thickness of the un-freezable layer in freezing process was assumed to be 0.5 nm $< \delta_f <$ 2.2 nm and that in melting process, 0.6 nm $< \delta_m <$ 2.8 nm. The comparisons between the results using Eq.A.17 and Eq.A.15, and Eq.A.18 and Eq.A.16 are shown in Figure A.1 assuming δ_f=δ_m=0.8 nm. It can be seen that if the pores are assumed to be cylindrical, the two different methods are in good agreement with each other both in freezing and melting. Actually in generating Eq.A.17 and Eq.A.18, no shape assumption was made, since it is based on fitting the experiments. However, the silica gel materials used by Ishikiriyama et al., represented by MCM-41, are often regarded as a model material exhibiting cylindrical pores [Kloetstra et al. 1995, Banys et al. 2005]. Thus, it is reasonable to compare the relation as derived by Ishikiriyama et al. with that by Brun et al. using the cylindrical pore shape assumption.

$$R_p = -\frac{56.36}{\triangle T} + 0.90 + \delta_f \qquad \text{for freezing} \tag{A.17}$$

$$R_p = -\frac{33.30}{\triangle T} + 0.32 + \delta_m \qquad \text{for melting} \tag{A.18}$$

It is due to mention that it is almost impossible to theoretically constitute the relation dA_{sl}/dV_l so as to represent the real action of water and ice interfaces during freezing and melting. It is noted that it is very difficult to go beyond the simple assumptions regarding hemispheres and cylinders because the microstructure and its variations are very complex. Other thermodynamic processes not considered in the analysis as described here can also be of importance for the further development of the evaluation methods discussed in this section.

B Impact of cooling and heating rate fluctuation or drifting on the ice content calculation by low temperature calorimetry

Introduction

In this section, the importance of the stability of the calorimetric measurements will be discussed in the context of ice content determination. It turns out that that certain measured calorimetric data do not allow for direct ice content determination and that fitting of data trends (or data smoothing) solves some problems if the stability performance of the instrument in question is good.

In low temperature calorimetry measurement (LTC) measurements, the target cooling or heating rate is normally set to a constant value. It has been noticed, however, that the cooling/heating rate may fluctuate or drift during a measurement. This is especially true when a measurement covers a large temperature range. In

studying cement based materials, the measuring temperature normally ranges between about 20 °C to about −80 °C or even lower to ensure that all the freezing/melting behaviors of water/ice confined in pores can be studied [Johannesson 2010].

The fluctuation and the drifting of the cooling/heating rate directly affect the measured output of heat flow (since $Q \propto q$, where Q is the measured heat flow and q is the cooling/heating rate). And consequently they have an impact on the accuracy of the determined ice content, e.g., using the "C-method" [Wu et al. 2014]. In order to analyze the ice content in a relatively stringent manner, the fluctuation and the drifting of the cooling/heating rate needs to be considered.

Three sets of data were collected and analyzed, denoted as Data I, Data II and Data III, respectively. Data I and Data III were measured at two different laboratories by the same type of SETARAM (manufacturer) calorimetric instrument (as will be described later, one instrument was "better" in terms of cooling/heating rate stability and the other one was "poorer" in terms of the stability); while Data II were measured by a TA (manufacturer) calorimetric instrument. The major difference between the two types of instruments is the testing sample size: in the SETARAM instruments, cylinder samples of size ϕ15mm × 60mm was used; and crushed samples in the order of tens of milligrams were used in the TA instrument.

Results and discussion

Analysis of Data I

The measured heat flow of Data I is shown in Figure A.2a. During the measurement, the cooling/heating rate was set to $-/+ 1.5\times10^{-3}$ °C/s (5.4 °C/h). In order to investigate the stability of the cooling/heating system of the instrument, the instant cooling/heating rate is calculated by

$$q(i+1) = \frac{T(i+1) - T(i)}{t(i+1) - t(i)} \tag{B.1}$$

where q, T and t denote the cooling/heating rate, the temperature and the time, respectively; i is the number of measuring points.

The calculated instant cooling and heating rates are shown in Figure A.2b and Figure A.2c, respectively. It can be observed that over the whole range of the freezing process, a relatively big overall drifting of the cooling rate occurs; while during a certain temperature range, the cooling rate can be regarded as stable. For the melting process, a relatively good stability of the heating rate is observed during the whole process. It may be reasonable to assume that an absolutely stable cooling/heating rate cannot be achieved during a measurement and limited fluctuation probably indicates that the instrument is under well control. That is, the calculated instant cooling or heating rate present in Figure A.2 (b and c) does not necessarily represent the true rate

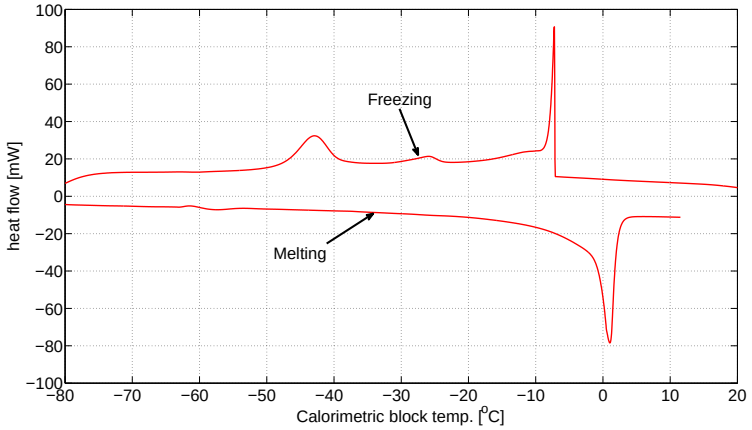

(a) Measured heat flow

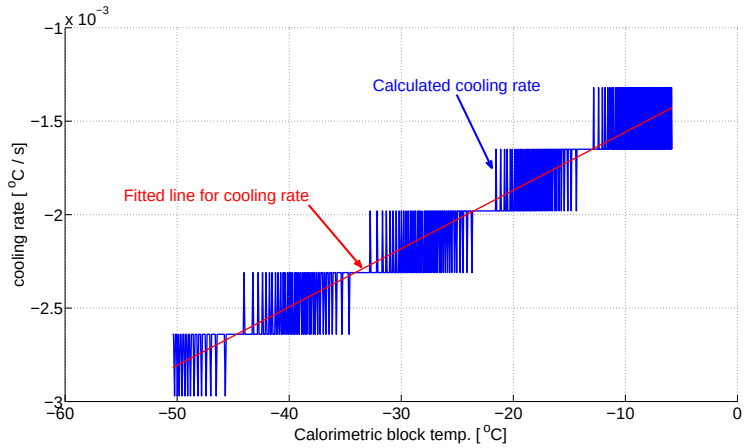

(b) Calculated and the fitted cooling rate

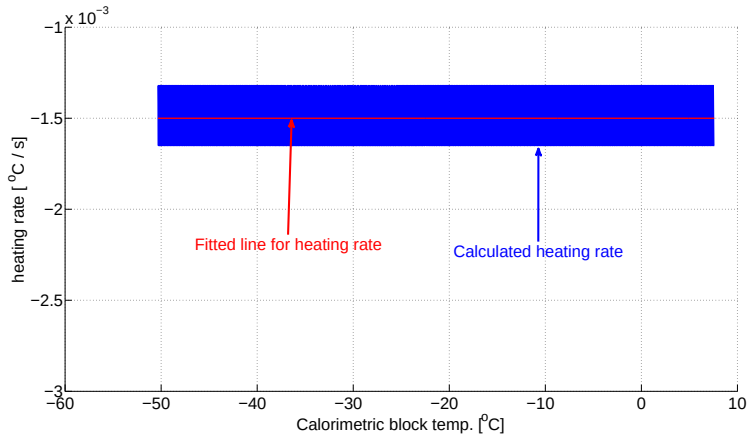

(c) Calculated and the fitted heating rate

Figure A.2: Measured heat flow and the calculated cooling and heating rate of Data I measured by a SETARAM instrument. The target cooling/heating rate was set to $-/+$ 1.5×10^{-3} °C/s (5.4 °C/h). To guide eyes, the heating rate is plotted as negative values (so as to be more easily compared to the cooling rate). A line is fitted for the cooling/heating rate and the fitted values are used as inputs to calculate the ice content at different temperatures.

during the measurement, i.e., the calculation (Eq.B.1) may magnify the fluctuation of the true rate concerning a very small drifting of the measured temperature since the time step at which recording takes place is often very short. Taking this point into consideration and based on the calculated cooling/heating rate, the drifting of the cooling/heating rate is assumed as a linear function for the sake of simplicity. The fitted line for the cooling and heating rate are shown in Figure A.2b and Figure A.2c, respectively.

The calculated ice contents using the "C-method" are shown in Figure A.3. Both the calculated and the fitted rates are considered in the calculation of the ice content. It can be observed that for the freezing process, using the calculated cooling rate results into high calculated ice content compared with that using the fitted cooling rate. While for the melting process in which the heating rate is relatively stable during the measurement (Figure A.2c), the calculated ice content curve using the calculated heating rate looks unreasonable, i.e., the ice content increases first (from about -50 °C to about -15 °C) and then decreases (from about -15 °C and above). However, the calculated ice content curve using the fitted heating rate is not subjected to the problems associated with the calculated values as discussed previously. Moreover, the maximum ice content calculated from the freezing process shows relatively good agreement with the ice content calculated from the melting process using the fitted rates. During a one cycle measurement consisting of a freezing process followed by a melting process, the maximum ice content formed during the freezing process should be equal to that melted during the melting process (mass conservation). The relatively good agreement between the calculated ice contents in the freezing and in the melting process as shown in Figure A.3 using the fitted rates may indicate that the fitted rates may be more representative for than the the fitted counterparts for the ice content calculation.

Analysis of Data II

The measured heat flow and the cooling and heating rates of Data II (crushed samples used in the TA instrument) are shown in Figure A.4. The cooling/heating rate was set to a much higher value compared with that of the Data I testing. The target values were $-/+ 8.3\times10^{-3}$ °C/s (30 °C/h).

It can be observed from the results presented in Figure A.4b and Figure A.4c that the cooling and heating rate can be regarded as relatively stable during the measurement. Compared to the SETARAM instrument used for measuring Data I, the TA instrument seems to be subjected to less drifting during the freezing measurement. Using the same method adopted for Data I, the ice contents for the freezing and the melting are calculated. Similarly, the ice content results using the calculated cooling and heating rates look unreasonable. Thus, only the ice content curves calculated using the fitted cooling and heating rate are presented here. The results are shown

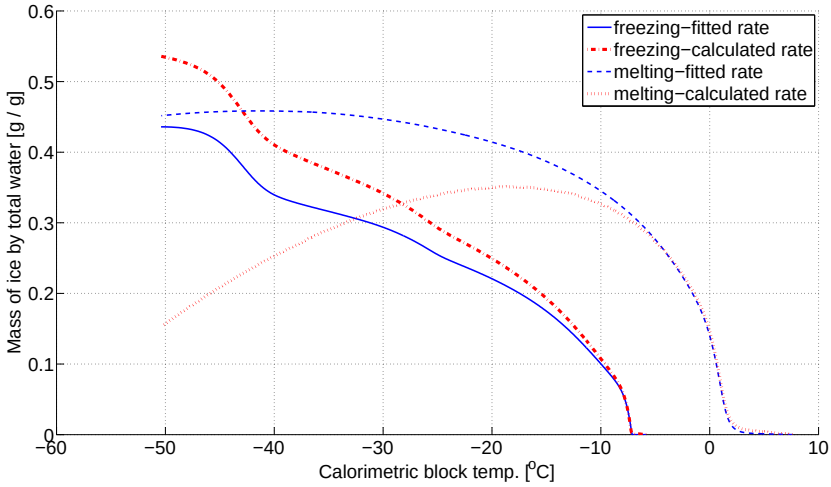

Figure A.3: The calculated ice contents of Data I using the "C-method": both the calculated and the fitted cooling and heating rates have been used in the calculation for comparison.

in Figure A.5. As can be found, a relatively good agreement is shown between the maximum ice content calculated from the freezing and that from the melting process.

Analysis of Data III

The measured heat flow and the cooling and heating rates of Data III measured by another SETARAM instrument are shown in Figure A.6. The target cooling and the heating rate were set to -9.12×10^{-4} and $+1.14\times10^{-3}$ °C/s (-3.3 and $+4.1$ °C/h), respectively.

As can be observed from Figure A.6b and Figure A.6c, the calculated cooling and heating rates of the instrument are much less stable compared with that used to obtain Data I (Figure A.2) and Data II (Figure A.4). The calculated cooling and heating rates fluctuate between negative and positive values. Using the same calculation method adopted for Data I and Data II, the calculated ice content curves using the fitted cooling and heating rates are shown in Figure A.7. As can be seen, an unreasonable melting curve is obtained, i.e., the ice content increases first and then decreases as the temperature increases.

Using the "C-method" and the fitted cooling and heating rate, the calculated ice content curves are relatively reasonable for Data I and Date II; while for Data III, it fails to obtain the similar reasonable results. Comparing Data III with Data I and Data II, the main difference is the stability characteristics of the cooling and heating rate of the measurements. The big fluctuation of the cooling/heating rate may result into that the fitted values cannot represent the detailed characteristics of the process.

In the context of ice content calculation with LTC data, essentially two methods are available. The "C-method" is considered as a relatively accurate method due to its

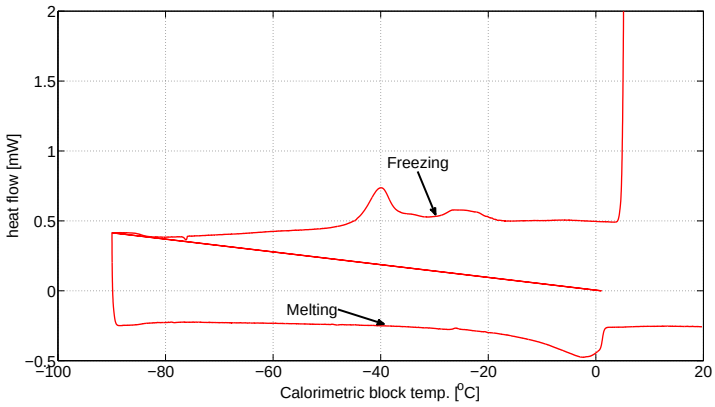

(a) Measured heat flow

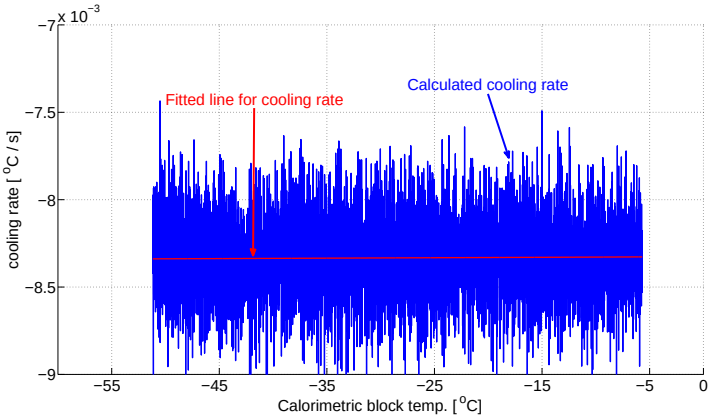

(b) Calculated and the fitted cooling rate

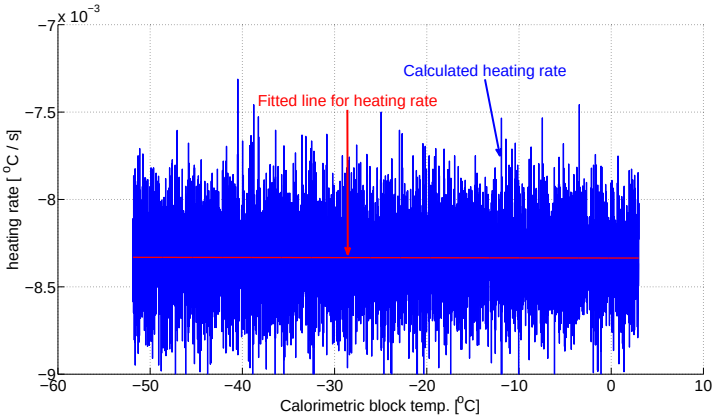

(c) Calculated and the fitted heating rate

Figure A.4: Measured heat flow and the calculated cooling and heating rate of Data II measured by the TA instrument. The line between the measured heat flow curves of freezing and melting in (a) may due to some uncertainties when changing the measuring model from the freezing to the melting process. The target cooling/heating rate was set to $-/+$ 8.3×10^{-3} °C/s (30 °C/h). To guide eyes, the heating rate is plotted as negative values (so as to be more easily compared to the cooling rate). A line is fitted for the cooling/heating rate and the fitted values are used as inputs to calculate the ice content at different temperatures.

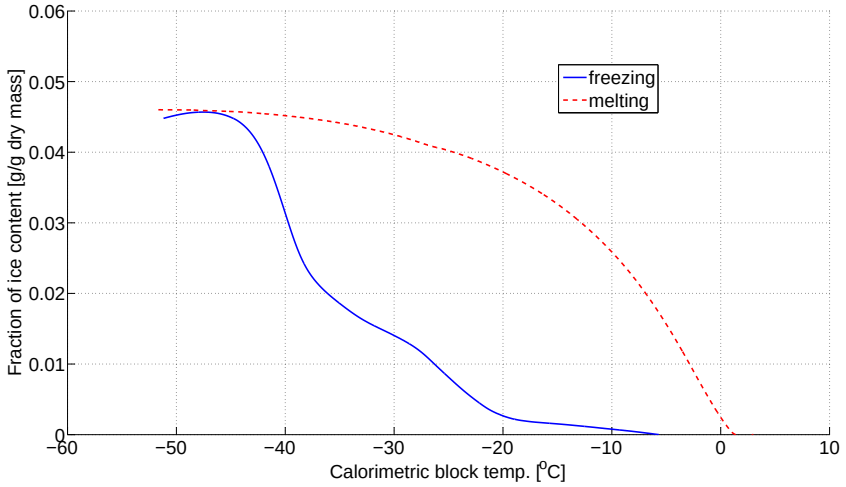

Figure A.5: The calculated ice contents of Data II using the "C-method". The fitted cooling and heating rates were used in the calculation.

stringent theoretical basis; and the "J-method" is a recently proposed extrapolation method based on explicit assumptions made regarding the measured integrated heat flows [Johannesson 2010, Wu et al. 2014]. An advantage of the "J-method" is that it is less affected by the fluctuations of the cooling and heating rate during testing compared with using the "C-method". A comparison between the "C-method" and the "J-method" for samples measured under stable cooling and heating conditions can be found in [Wu et al. 2014], in which it is demonstrated that the ice contents calculated by these two methods in principle give the same results. In order to demonstrate that the "J-method" is less sensitive to instabilities of the cooling/heating rates during a heat flow measurement, it is also applied to the Data III (measured with big fluctuation of heating and cooling rates). The calculated ice content curves using the "J-method" are shown in Figure A.8, which have significant differences compared with that calculated using the "C-method" (Figure A.7). It is not straightforward to judge the reasonableness of the calculated results using the "J-method" by comparing whether the maximum ice content calculated from the freezing is identical to that calculated from the melting process (as we do with "C-method"), because the identical maximum ice content in the freezing and melting process is an imposed assumption on the "J-method" [Wu et al. 2014]. Nevertheless, it can be found that calculated ice content curves in Figure A.8 are not smooth at all (implying literally that the ice forms and melts in a single freezing/melting process, which is definitely not the true case), indicating that the very unstable cooling/heating condition during a measurement does have an impact on the calculated results, which is not at all surprising.

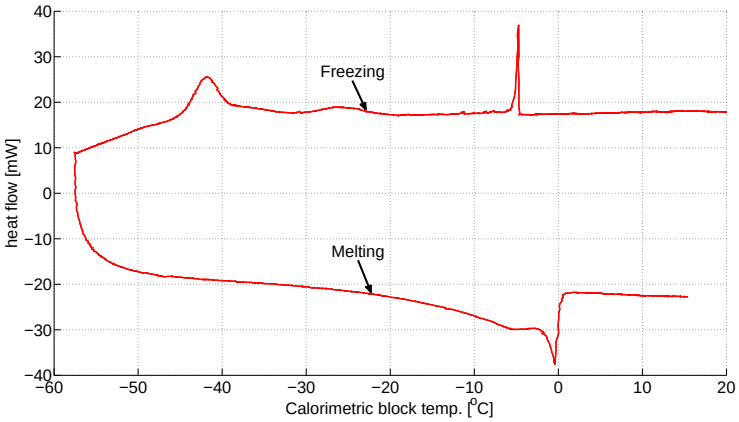

(a) Measured heat flow

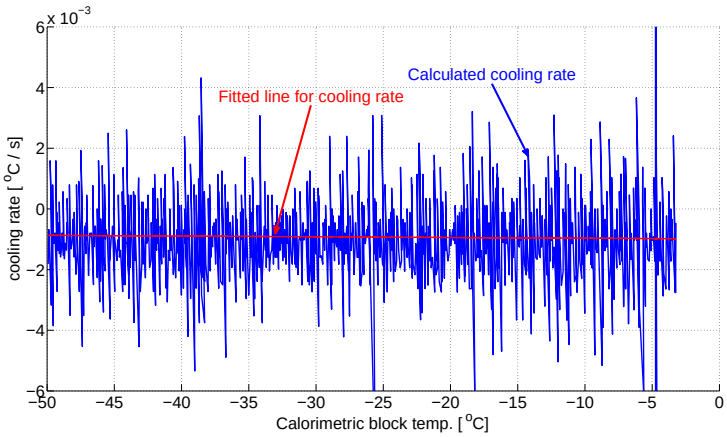

(b) Calculated and the fitted cooling rate

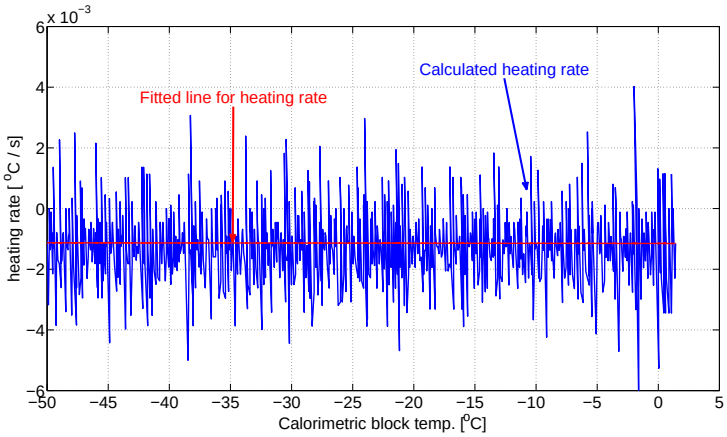

(c) Calculated and the fitted heating rate

Figure A.6: Measured heat flow and the calculated cooling and heating rate of Data III by another SETARAM instrument. The cooling and the heating rate were set to -9.17×10^{-4} and $+1.14\times10^{-3}$ °C/s (-3.3 and +4.1 °C/h), respectively. To guide eyes, the heating rate is plotted as negative values (so as to be more easily compared to the cooling rate). A line is fitted for the cooling/heating rate and the fitted values are used as inputs to calculate the ice content at different temperatures.

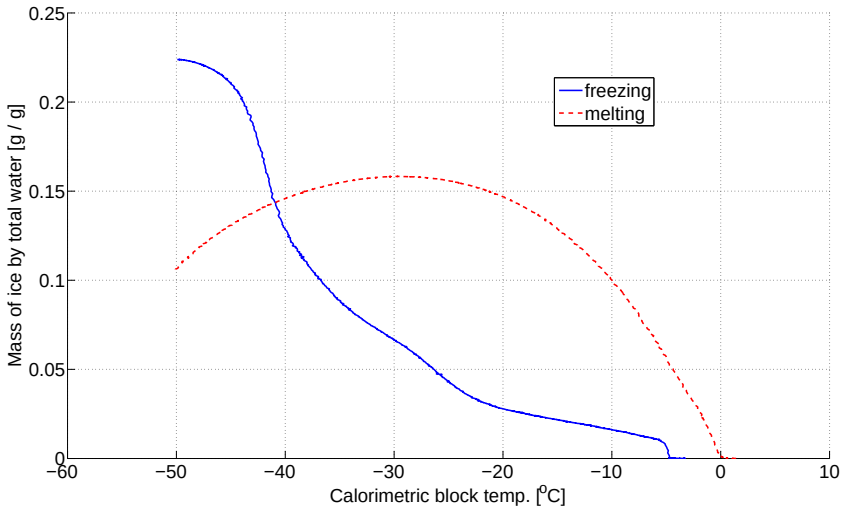

Figure A.7: The calculated ice contents of Data III using the fitted cooling and heating rates by the "C-method".

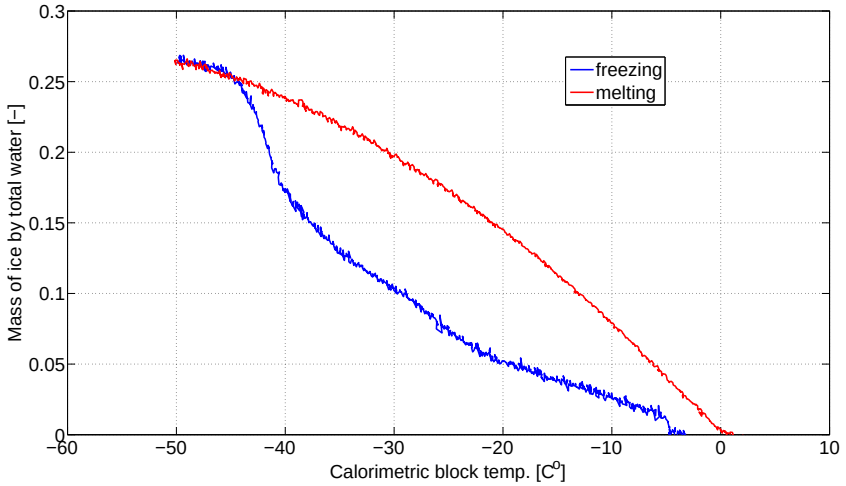

Figure A.8: The calculated ice contents of Data III by the "J-method".

Concluding remarks

Three sets of LTC data were analyzed. Two instruments recorded at stable cooling/heating conditions when subjected to a target rate and one instruments recorded at relatively big fluctuation of cooling/heating rates. The results show that reasonable freezing and melting curves of ice content can be calculated from the data measured under relatively stable cooling/heating conditions; while for the data measured under cooling/heating rates with relatively big fluctuation (e.g., varying between positive and negative values), the calculated ice content curves can be subjected to serious errors and hence considered as not relevant.

In order to calculate the ice content from the measured data in an accurate manner, it is always good practice to control the cooling and heating system under stable conditions during LTC measurements. The "J-method" gives better results than the "C-method" using data sets including important instabilities in terms of the cooling/heating rates. However, such data sets should be avoided since it always will affect the accuracy of the results negatively. The material presented here can be used as a guideline for identifying to what degree the instabilities can be accepted when calculating the ice content at different temperatures. This conclusion holds for both the "C-method" and the "J-method" discussed here.

C Equations for multilayer adsorption

In determining the pore size distribution using moisture fixation tests the effect of adsorption will be of major importance. It is believed that the capillary condensation will be formed on top of the adsorbed layers on the bare material surfaces, e.g., see [Barrett et al. 1951]. Hence, the predicted pore size is the sum of the adsorbed layer and the Kelvin radius. According to different theories, the adsorbed layer thickness changes with the relative humidity in the pores of the material. A poor prediction of the adsorbed layer thickness will also result in a poor pore size distribution. This is especially true for the small range of pores. Another important fact related to adsorption is that it puts a restriction on how small pores can be detected when adopting a moisture fixation test.

The first sound theoretical development of the relation between the amount of adsorbed vapor and the relative pressure under equilibrium is attributed to Langmuir [1916]. However, the limitation of the model is that adsorption is restricted to a monolayer. A major progress of adsorption theory was the BET multilayer adsorption method, which was initially proposed by Brunauer, Emmett and Teller [1938]. After that, a number of adsorption equations have been derived either based on the classical BET theory or by modifying some of the original assumptions. A summary of different equations with respect to adsorption can be found, e.g., in [Allen 1997].

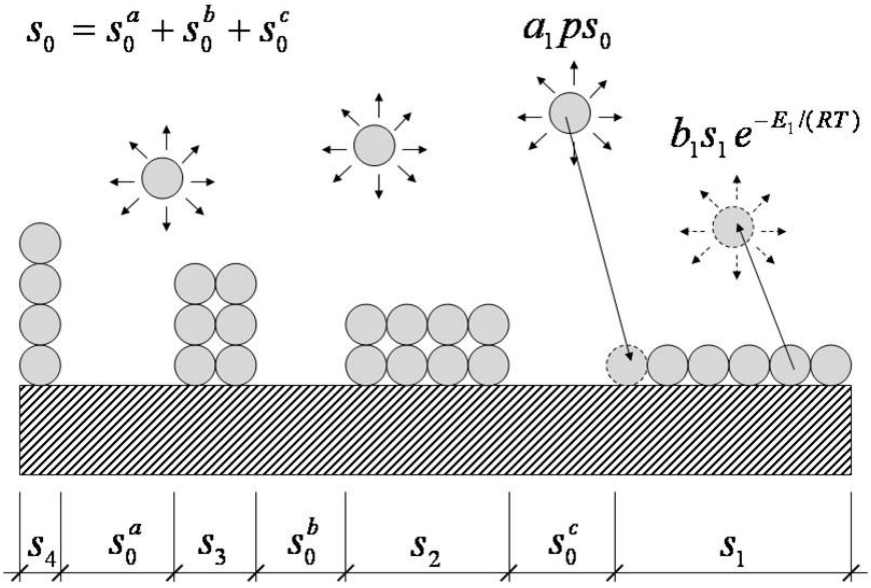

Figure A.9: Equilibrium situation for the area s_0. The arrows around the water molecules indicate that they are in "free" vapor phase. The BET theory is based on that the water molecules are piled up in a discrete manner (after [Johannesson 2011c]).

Nevertheless, the BET equation remains the most important one in studying the adsorption phenomena. In this appendix, the theoretical background and the important assumptions behind BET equation will be introduced, along with two other important equations accounting for multilayer adsorption.

Standard BET equation

To derive the standard BET equation, it is assumed that molecules in the vapor phase can only form discrete layers above a flat material surface. The surface area covered by 0, 1, 2, ... i, ... layers of adsorbed molecules is represented by s_0, s_1, s_2, ... s_i, respectively. Taking s_0 for example, at equilibrium, the rate of condensation of molecules onto the bare surface should be equal to the rate of evaporation from the first layer. The rate of condensation onto the bare surface is assumed to be given as $a_1 p s_0$ and the rate of evaporation from the first layer is assumed to be given as $b_1 s_1 e^{-E_1/(RT)}$, where p is the pressure, E_1 is the heat of adsorption of the first layer molecules, a_1 and b_1 are material constants. Hence, at equilibrium, one has

$$a_1 p s_0 = b_1 s_1 e^{-E_1/(RT)} \tag{C.1}$$

The scenario is schematically illustrated in Figure A.9.

There are four processes involved in changing the area s_1, namely: (1) condensation on the bare surface, making it belong to first layer; (2) evaporation from the first layer, changing into bare surface; (3) condensation on the first layer, changing it

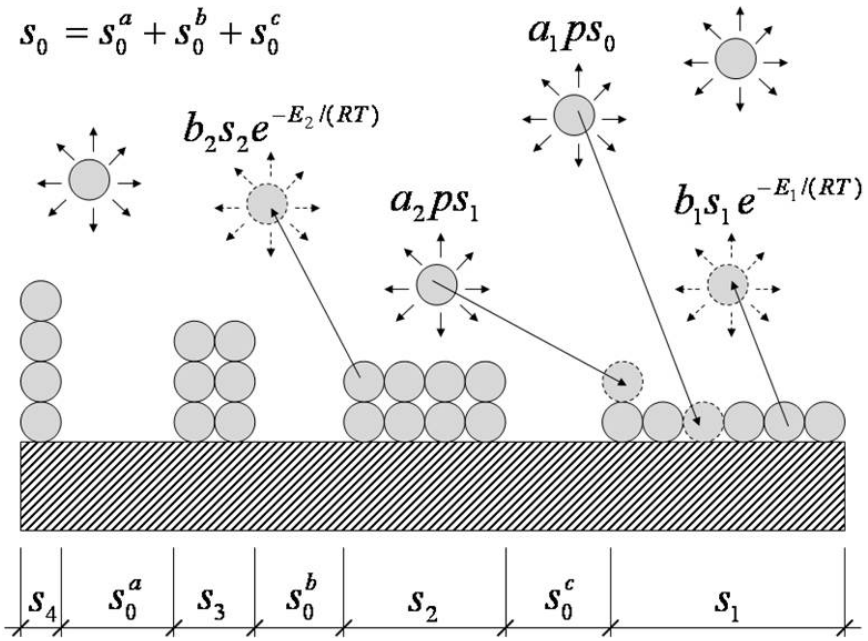

Figure A.10: Equilibrium situation for the area s_0. The arrows around the water molecules indicate that they are in "free" vapor phase. The BET theory is based on that the water molecules are piled up in a discrete manner (after [Johannesson, 2011c]).

into second layer and (4) evaporation from second layer, changing it back into the first layer. These processes are schematically illustrated in Figure A.10. At equilibrium, the surface area s_1 should also remain constant. Thus, one obtains

$$a_2 p s_1 + b_1 s_1 e^{-E_1/(RT)} = a_1 p s_0 + b_2 s_2 e^{-E_2/(RT)} \tag{C.2}$$

where a_2, b_2 and E_2 are constants for the second layer in the same manner as the constants a_1, b_1 and E_1 valid for the first layer molecules.

By inserting Eq.C.1 into Eq.C.2, one gets

$$a_2 p s_1 = b_2 s_2 e^{-E_2/(RT)} \tag{C.3}$$

That is, the rate of condensation on top of the first layer is equal to the rate of evaporation from the second layer. Proceeding with the same argument to the second and high layers, a general equation can be obtained as

$$a_i p s_{i-1} = b_i s_i e^{-E_i/(RT)} \tag{C.4}$$

where $i = 1, 2, ..., \infty$ are the the discrete layers.

The total surface area of the adsorbent can be expressed as

$$A = \sum_{i=0}^{\infty} s_i \tag{C.5}$$

and the total volume of the adsorbed vapor on the surface is

$$v = v_0 \sum_{i=0}^{\infty} i s_i \tag{C.6}$$

where v_0 is the volume of the adsorbed vapor on the adsorbent surface per unit area of the material when it is covered by a complete monolayer of molecules. Further derivation is proceeded by using Eq.C.5 and Eq.C.6 as

$$\frac{v}{Av_0} = \frac{v}{v_m} = \frac{\sum_{i=0}^{\infty} i s_i}{\sum_{i=0}^{\infty} s_i} \tag{C.7}$$

where v_m is the volume of the adsorbed vapor when the surface of the adsorbent is completely covered by a monolayer molecules.

To obtain the standard BET equation, it is assumed that only the molecules in the first layer have a condensation heat that is different from that of the normal water and the heat of condensation in the second and higher adsorbed layers are equal, which is the same as the heat of normal liquefaction E_L, i.e., $E_1 \neq E_2$ and $E_2 = E_3 = ... = E_i = E_L$. Further assumption is made that $b_2/a_2 = b_3/a_3 = ... = b_i/a_i = g$, with g being an assumed constant. By making these assumptions, the surface area s_1, s_2 can be expressed in terms of s_0:

$$s_1 = y s_0, \text{where } y = (a_1/b_1) p e^{E_1/RT} \tag{C.8}$$

$$s_2 = x s_1, \text{where } x = (p/g) e^{E_L/RT} \tag{C.9}$$

It is noted from the above discussed simplifications, for all $i > 1$, that a general equation for the s_i can be formulated as

$$s_i = x s_{i-1} = x^{i-1} s_1 = y x^{i-1} s_0 = c x^i s_0 \tag{C.10}$$

where $c = y/x = (g a_1/b_1) e^{(E_1 - E_L)/RT}$. Thus, s_1, s_2, ... s_i can all be described in terms of s_0 with the constant c and different powers of x.

By inserting Eq.C.8, Eq.C.9 and Eq.C.10 into Eq.C.7, one gets

$$\frac{v}{v_m} = \frac{c s_0 \sum_{i=1}^{\infty} i x^i}{s_0 (1 + c \sum_{i=1}^{\infty} x^i)} \tag{C.11}$$

If it is assumed that an infinite number of layers can be formed above the adsorbent surface, the summations in the denominator and the numerator of Eq.C.11 can be written as

$$\sum_{i=1}^{\infty} x^i = \frac{x}{1 - x} \tag{C.12}$$

and

$$\sum_{i=1}^{\infty} ix^i = \frac{x}{(1-x)^2} \tag{C.13}$$

where x is in the range of 0 to 1, which will be explained later.

Thus, the term v/v_m can be expressed as a function of x in the form of

$$\frac{v}{v_m} = \frac{cx}{(1-x)(1+cx-x)} \tag{C.14}$$

Eq.C.14 is the standard form of BET equation. For the adsorption on a flat surface at the saturated vapor pressure p_0, an infinite number of layers of adsorbate can build up on the adsorbent. By examining Eq.C.14, it can be found $x \to 1$ when $v \to \infty$. Thus, according to the definition of x, we have $1 = (p_0/g)e^{E_L/RT}$. Then the physical meaning of x can be identified as $x = p/p_0$, which is the relative vapor pressure (often presented as relative humidity for water vapor). In conclusion, the main assumptions in deriving Eq.C.14 are: (1) under dynamic equilibrium, the number of molecules evaporating from a layer is equal to that condensated on the layer below; (2) the condensation heat of water molecules on the second layer and higher layers are the same as that of normal bulk water, which differs from that of the first layer and (3) an infinite number of layers can be formed on the adsorbent surface. Related discussions about the assumptions behind BET theory can be found, e.g., in [Fagerlund 1973b].

Due to the assumptions made, the applicability of Eq.C.14 to describe the adsorption behavior over the whole relative humidity range in field experiments is difficult. In order to improve the accuracy, a maximum number of adsorbed layers was introduced in Brunauer et al. [1938]. That is, if the number of the adsorbed layers can not exceed a finite number, the equation should be modified by introducing the maximum number, n , of adsorbed layers, as

$$\frac{v}{v_m} = \frac{cx}{(1-x)}[\frac{1-(n+1)x^n+nx^{n+1}}{1+(c-1)x-cx^{n+1}}] \tag{C.15}$$

It is also demonstrated that if the value of x is small and the n is about 4 or 5, Eq.C.14 gives similar results as Eq.C.15. Efforts have been made to describing the adsorption behavior of vapor molecules onto solid surfaces. Most of the models developed share some of the same important assumptions as made in the standard BET model. Two alternatives to the standard BET equation will be discussed later, i.e., the two-layer BET equation and the GAB equation. More discussions about the different proposed models for adsorption can be found, e.g., in [Hailwood and Horrobin 1946, Okoh and Skaar 1980, Venkateswaran 1970, Sing et al. 1985]. However, the standard BET equation is still probably the most adopted approach to calculate the specific surface area. The possible reason could be its simplicity and straightforwardness.

It is possible to use the assumptions behind the standard BET equation to calculate the adsorbed volume present in the first layer. Based on Eq.C.6, the volume in the first layer can be described as

$$v_1 = v_0 \sum_{i=1}^{\infty} s_i \tag{C.16}$$

Thus, the relation of v_1 and v can be derived by combining the definition of s_i (Eq.C.10) and the infinite series (Eq.C.12 and Eq.C.13), as

$$\frac{v_1}{v} = \frac{cs_0 \sum_{i=1}^{\infty} x^i}{cs_0 \sum_{i=0}^{\infty} ix^i} = \frac{x/(1-x)}{x/(1-x)^2} = 1 - x \tag{C.17}$$

By replacing v in Eq.C.17 with the monolayer volume v_m according to Eq.C.14, v_1 can be related to v_m, as shown in Eq.C.18. With the monolayer volume v_m determined, the moisture content of molecules present in the first layer can be derived, as

$$v_1 = \frac{v_m cx}{1 + cx - x} \tag{C.18}$$

Similarly, the moisture content present in the second layer can be derived, as

$$v_2 = \frac{v_m cx^2}{1 + cx - x} \tag{C.19}$$

Two-layer BET equation

As described before, one of the most important assumptions made in the standard BET equation is that the condensation heat of water molecules in the second layer and higher layers are the same as that of normal bulk water and only the first layer condensations are different. Johannesson [2000] studied the assumption regarding the heat of condensation, the assumption being modified to that both the condensation heat of the water molecules in the first layer and in the second layer are different from that of the normal bulk water while the water molecules on the third and higher layers have the same condensation heat as that of bulk water. By introducing this new assumption and combining other assumptions already present in the standard BET equation, a new equation, designated as the two-layer BET equation, is obtained.

To derive the two-layer BET equation, we starts from the general equation as derived for the standard BET equation, i.e., Eq.C.4, which can be rewritten as

$$s_i = \frac{a_i}{b_i} p e^{E_i/(RT)} s_{i-1} \tag{C.20}$$

In this case, the heat of condensations have the relations $E_1 \neq E_2 \neq E_L$ and $E_3 = E_4 = ... = E_i = E_L$. Then the relation between s_i and s_{i-1} can be expressed as

$$\begin{aligned} s_1 &= ys_0 \\ s_2 &= zs_1 \\ s_3 &= xs_2 \\ s_4 &= xs_3 \\ .. &.. \quad .. \\ s_i &= xs_{i-1} \end{aligned} \tag{C.21}$$

where y, z and x are defined as

$$y = \frac{a_1}{b_1} p e^{E_1/(RT)}; \qquad z = \frac{a_2}{b_2} p e^{E_2/(RT)}; \qquad x = \frac{p}{g} e^{E_L/(RT)} \tag{C.22}$$

The constant g has the meaning of $g = b_3/a_3 = b_4/a_4 = ... = b_i/a_i$. Analogous to Eq.C.10, a general description of s_i for $i > 2$ can be expressed as

$$s_i = xs_{i-1} = x^{i-2}s_2 = zx^{i-2}s_1 = bx^{i-1}s_1 \tag{C.23}$$

where b is given as

$$b = \frac{z}{x} = \frac{a_2}{b_2} g e^{(E_2 - E_L)/(RT)} \tag{C.24}$$

The property s_1 can be related to s_0 as

$$s_1 = cxs_0 \tag{C.25}$$

where the parameter c is defined as

$$c = \frac{y}{x} = \frac{a_1}{b_1} g e^{(E_1 - E_L)/(RT)} \tag{C.26}$$

According to the above discussion, the ratio between the adsorbed volume and the monolayer capacity v/v_m established for standard BET equation, i.e., Eq.C.7, can be extended to account for a special condensation heat for second layer molecules, as

$$\frac{v}{v_m} = \frac{\sum_{i=0}^{\infty} i s_i}{\sum_{i=0}^{\infty} s_i} = \frac{s_1 + \sum_{i=2}^{\infty} i s_i}{s_0 + s_1 + \sum_{i=2}^{\infty} s_i} = \frac{cxs_0 + bcs_0 \sum_{i=2}^{\infty} i x^i}{s_0 + cxs_0 + bcs_0 \sum_{i=2}^{\infty} x^i} \tag{C.27}$$

The two summations can be calculated using the standard series of the types illustrated in Eq.C.12 and Eq.C.13, as

$$\sum_{i=2}^{\infty} ix^i = \frac{x^2(2-x)}{(1-x)^2} \tag{C.28}$$

and

$$\sum_{i=2}^{\infty} x^i = \frac{x^2}{1-x} \tag{C.29}$$

By inserting Eq.C.28 and Eq.C.29 into Eq.C.27 and together with some mathematical manipulations, it yields

$$\frac{v}{v_m} = \frac{cx[1+(b-1)(2x-x^2)]}{(1-x)[cx^2(b-1)+(c-1)x+1]} \tag{C.30}$$

This new equation describes the total adsorbed volume v as a function of the relative pressure x based on the modified assumption involving the heat of condensation in the second layer. Eq.C.30 will be referred to as the two-layer BET equation. Compared with the standard BET equation, there is one more parameter b in the two-layer BET equation. It is noted that, if the heat of condensation of the water on the second layer is the same as that of the normal water, i.e., $E_2 = E_L$, then $b = 1$ (Eq.C.24, since the term before the exponential term should be approximately equal to unity as discussed in [Johannesson 2000]). For this special case the two-layer BET equation is reduced to the standard BET equation.

The volume of molecules present in the first layer, in this case, can be calculated as

$$v_1 = v_0 \sum_{i=1}^{\infty} s_i = v_0 cs_0 x + v_0 bcs_0 \sum_{i=2}^{\infty} x^i = v_0 cs_0 x[\frac{1+x(b-1)}{1-x}] \tag{C.31}$$

And the total volume v can be found from using Eq.C.27 to obtain

$$v = s_1 + \sum_{i=2}^{\infty} is_i = v_0 cs_0 x + v_0 bcs_0 \sum_{i=2}^{\infty} ix^i = v_0 cs_0 x[\frac{(1-x)^2+bx(2-x)}{(1-x)^2}] \tag{C.32}$$

By combining Eq.C.31 and Eq.C.32, the ratio of v_1/v can be obtained. Further introducing Eq.C.30, v_1 can be expressed by the monolayer capacity v_m as

$$v_1 = \frac{v_m cx(1+(b-1)(2x-x^2))(1+x(b-1))}{[cx^2(b-1)+(c-1)x+1][(1-x)^2+bx(2-x)]} \tag{C.33}$$

Following the same methodology, the moisture content on the second layer can be derived as

$$v_2 = \frac{v_m c x^2 (1 + (b-1)(2x - x^2))}{[cx^2(b-1) + (c-1)x + 1][(1-x)^2 + bx(2-x)]} \tag{C.34}$$

With the help of a sorption calorimeter [Wadsö and Wadsö 1996, Wadsö and Markova 2000], it is possible to study the assumptions regarding the heat of condensation of the water on different layers. Johannesson [2000] conducted detailed studies by comparing the measured differential heat of adsorption and the predicted value based on the standard BET equation and the two-layer BET equation of different porous materials. Figure A.11 shows an example of the measured differential heat response during moisture uptake on a porous glass. A better agreement between the measured differential heat of adsorption and the value predicted based on the two-layer BET equation was obtained compared with that between the measured and predicted heat of adsorption based on the standard BET equation. For this specific study, it was concluded that the assumption concerning the heat of condensation according to the two-layer BET equation gave more reasonable results compared with the approach of using the standard BET equation. It is also noted that some other studies, e.g., see [Powers and Brownyard 1947, Hundt and Kantelberg 1978, Poyet 2009, Poyet and Charles 2009], pointed out that the heat of condensation of the water molecules on higher layers (higher than the second) approaches the condensation heat of normal water.

GAB equation

The heat of condensation of the molecules on different adsorbed layers is a key factor in deriving the equation for multilayer adsorption. The standard BET theory assumes that the water molecules in the first layer have a different heat of condensation but the molecules in the second and high layers have the same heat of condensation as that of normal bulk water. One way to modify the assumption of the standard BET theory is to say that the heat of condensation of the water molecules in the second and higher layers are the same but different from that of normal water, a new equation for adsorption will be the result. Guggenheim [1966], Anderson [1946] and de Boer [1968] modified the standard BET equation by taking into account the above mentioned assumption and some good agreement with the experimental data was obtained. The modified equation is the so called GAB equation [Van den Berg 1981]. Dent [1977, 1980] extended the idea further by assuming that the heat of condensation could differ for each layer, but the difference between the second and high layers tends to be small. On the other hand, the mathematical complexity would be increased considerably if each of the layer was treated differently. Thus, it was also assumed that water molecules on the second and high layers have the same condensation heat but different from that of normal water. As can be found, the equation derived by Dent, referred to as Dent equation, shares the same assumptions as that of the GAB

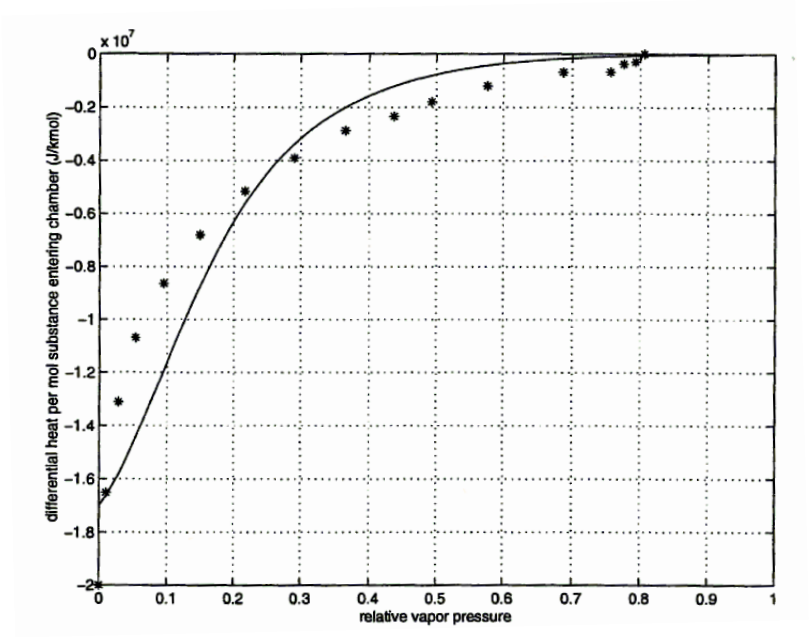

(a)

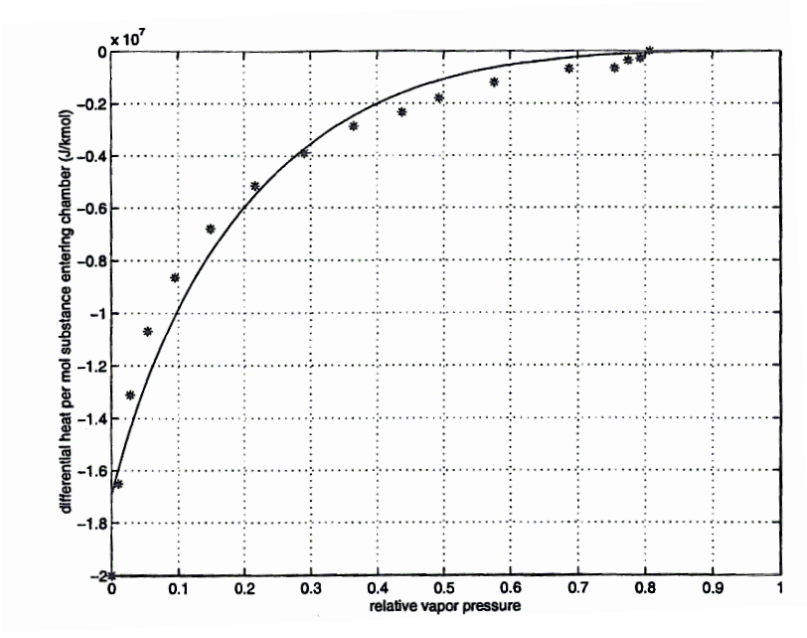

(b)

Figure A.11: Comparison of the measured differential heat response of adsorption of a porous glass with that predicted values using (a) the standard BET equation and (b) the two-layer BET equation. The stars show the measured values and the solid line represents the predicted values (after [Johannesson, 2000]).

equation. Unsurprisingly, they also share the same mathematical form and essentially they are the same.

Similar as the two-layer BET equation, the derivation of GAB equation starts with Eq.C.20 (equivalent of Eq.C.4). Considering the relation of the heat of condensation $E_1 \neq E_2$ and $E_2 = E_3 = ... = E_i = E_s \neq E_L$ (using E_s to represent the same heat of condensation of the molecules on the second and high layers), the relation between s_i and s_{i-1} then can be given as

$$\begin{aligned} s_1 &= y s_0 \\ s_2 &= z' s_1 \\ s_3 &= z' s_2 \\ .. &.. \quad .. \\ s_i &= z' s_{i-1} \end{aligned} \tag{C.35}$$

where y and x have the same meaning as defined before, which are

$$y = \frac{a_1}{b_1} p e^{E_1/(RT)}; \qquad x = \frac{p}{g} e^{E_L/(RT)} \tag{C.36}$$

While the parameter z' can be defined as

$$z' = \frac{a_2}{b_2} p e^{E_s/(RT)} \tag{C.37}$$

It should be noted here that the relation $b_2/a_2 = b_3/a_3 = ... = b_i/a_i$ holds.

Thus, a general form of s_i for $i > 1$ can be obtained as

$$s_i = z' s_{i-1} = z'^{i-1} s_1 = (kx)^{i-1} s_1 = y(kx)^{i-1} s_0 = c(kx)^i s_0 \tag{C.38}$$

where

$$k = \frac{z'}{x} = \frac{a_2}{b_2} p e^{(E_s - E_L)/(RT)}; \qquad c = \frac{a_1}{b_1} g e^{(E_1 - E_L)/(RT)} \tag{C.39}$$

Then the volume ratio of v/v_m in this case can be expressed and further derived as

$$\frac{v}{v_m} = \frac{c s_0 \sum_{i=0}^{\infty} i(kx)^i}{s_0(1 + c\sum_{i=0}^{\infty}(kx)^i)} = \frac{ckx}{(1-kx)[1+(c-1)kx]} \tag{C.40}$$

Compared with the standard BET equation, GAB equation has one more parameter k, which is a parameter accounting for the difference between the heat of condensation of the water molecules on the second and higher layers and that of the normal water. As pointed out by, e.g., Sing [1973, 1985], the upper limit of the standard BET equation is at the relative humidity range of about 0.3-0.5. Above the upper limit, there will be a typical upswing which tends to infinite in a manner not being verified by experiments. However, the GAB equation has been successfully applied

to many different adsobates and covers a much wider range of relative humidity (up to 0.9-1.0), e.g., see [Van den Berg 1984, Timmermann 2003, Blahovec and Yanniotis 2008], compared with the standard BET equation. It should be noted that the value of k is often found to be less than 1, e.g., in [Dent 1980, Timmermann 2003], which means that the heat of condensation of the water molecules on the second and high layer is smaller than that of the normal water. This is not in agreement with the obtained results as presented in, e.g., see [Powers and Brownyard 1947, Hundt and Kantelberg 1978, Poyet 2009, Poyet and Charles 2009], which does show that the condensation heat of the water molecules on the second and high layers is higher and approaches the condensation heat of normal water when reaching sufficient high layers. This fact may indicate that the GAB equation does not represent the true mechanism of adsorption at high moisture levels even though the fitting against experimental sorption isotherms matches nicely. Brunauer et al. [1969] introduced a parameter k into the standard BET equation, representing a measure of the attractive force of the adsorbent. Although the underlying assumption is different from that of the GAB model, Brunauer et al. arrived at an identical form as the GAB equation. Thus, it might be reasonable to postulate that this parameter k may be not only related to the heat of condensation but also to some other factors which are not clearly known.

The volume of the water molecules adsorbed in the first and second layer, v_1 and v_2, can according to the GAB model be calculated as

$$v_1 = \frac{v_m ckx}{1 + (c-1)kx} \tag{C.41}$$

$$v_2 = \frac{v_m c(kx)^2}{1 + (c-1)kx} \tag{C.42}$$

D Kelvin equation and Kelvin-Laplace equation

The Kelvin and the Kelvin-Laplace equations are key elements in calculating pore size distributions of materials by using moisture fixation experiments. Of this reason, the detailed description of the background of these two equations will be discussed in this appendix.

Kelvin equation

The original derivation of Kelvin equation were published as early as in late 1870s [Thomson 1871]. Some related discussions of the derivation can be found, e.g., in [Johannesson 2011c]. Part of the key arguments of the derivation will be reproduced here as follows.

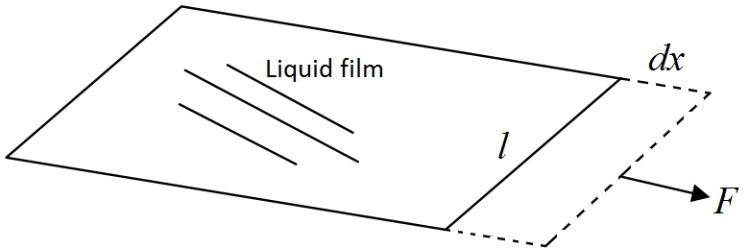

Figure A.12: An illustration of the surface tension of water γ_w through a stretched liquid film fixed in a frame. The surface tension γ_w (which is the equivalent to surface energy) represents the amount of energy needed to extend the surface by a unit area.

In order to derive the Kelvin equation, some discussions about the surface tension are necessary. The surface tension is also called surface energy, which tells how much energy is needed to extend the surface by a unit area. As shown in Figure A.12: if the surface is extended by dx in one direction, the increase in work done is then $2l\gamma_w dx$ (the factor of 2 is due to the two surfaces, i.e., at the top and the bottom side). Since the surface area is increased by $2ldx$, the definition of the surface tension γ_w can be expressed as shown in Eq.D.1. It is noted that the increase in work done is actually the increase of the Gibbs free surface energy of the water dG_w^s and if the increase in the surface area is expressed as dA_w, the surface tension γ_w can also be written as shown in Eq. D.2.

$$\gamma_w = \frac{2l\gamma_w dx}{2ldx} = \frac{\text{increase in work done}}{\text{increase in surface area}} \tag{D.1}$$

$$\gamma_w = \frac{dG_w^s}{dA_w} \tag{D.2}$$

To understand the equilibrium conditions of liquid water and its surrounding vapor phase, consider a liquid water droplet surrounded by its vapor as illustrated in Figure A.13. If the surface energy of the water droplet is higher than the energy of its surrounding vapor phase, the radius of the curvature of the liquid/vapor interface will be increased by dr to accommodate the energy difference until the equilibrium is satisfied and *vice versa*. Thus, the radius of the curvature of the interface, or rather the geometry setup, actually corresponds to the energy aspect in terms of equilibrium between the phases. Assuming the water droplet is a perfect sphere with a radius of r, Eq.D.3 can be obtained by considering the change of the surface area dA_w and the change of the radius dr.

$$A_w = 4\pi r^2; \qquad \frac{dA_w}{dr} = 8\pi r \tag{D.3}$$

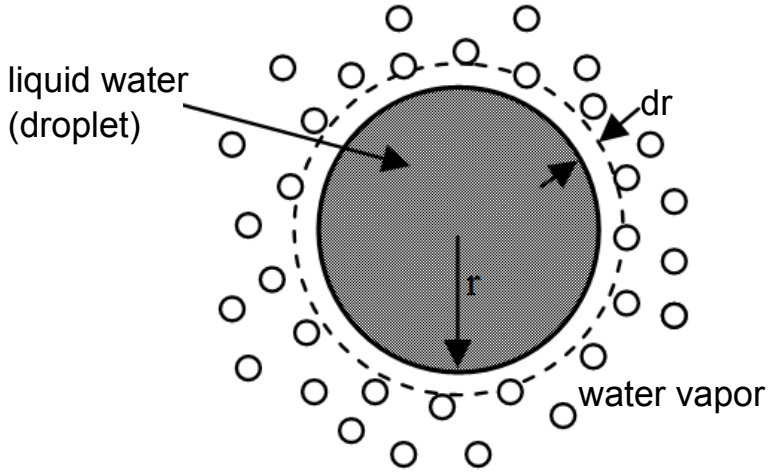

Figure A.13: If the surface energy of the liquid water droplet is not in equilibrium with energy of the surrounding vapor phase under certain relative humidity, the radius of the curvature of the liquid/vapor will be changed by dr until the equilibrium is satisfied. The curvature of the droplet is important for the equilibrium condition.

If n_w is introduced to represent the absolute number of moles in a representative volume, one obtains $n_w = \rho_w V_m / M_w$, where ρ_w and M_w are the density and molar mass of liquid water. Then by inserting the volume of the droplet, a relation between n_w and r can be developed, as

$$V_w = \frac{4}{3}\pi r^3; \qquad n_w = \frac{4}{3}\frac{\rho_w \pi r^3}{M_w}; \qquad \frac{dn_w}{dr} = \frac{4\rho_w \pi r^2}{M_w} \tag{D.4}$$

From Eq.D.2 and Eq.D.3, the change of the Gibbs free surface energy of the liquid water can be related to the radius of the droplet, as

$$\frac{dG_w^s}{dr} = \frac{dG_w^s}{dA_w} \cdot \frac{dA_w}{dr} = 8\pi r \gamma_w \tag{D.5}$$

By combining Eq.D.4 and Eq.D.5, dG_w^s can be related to n_w, as

$$\frac{dG_w^s}{dn_w} = \frac{2M_w \gamma_w}{\rho_w r} \tag{D.6}$$

Hence, Eq.D.6 describes the change of the Gibbs free energy of the liquid water (surface). With respect to that of the vapor phase surrounding the liquid, it is an experimental fact that vapors at relatively low concentrations and under constant volume and temperature, change their Gibbs free energy G_v with the number of moles of water molecules n_v in the vapor according to Eq.D.4.

$$\frac{dG_v}{dn_v} \mid_{T,V} = RT\ln(\frac{n_v}{n_v^{sat.}}) = RT\ln(\phi) \tag{D.7}$$

where R is the gas constant and T is the absolute temperature in Kelvin. This relation can be derived based on the theoretical arguments, which falls out the scope of this

discussion. However, more related information can be found, e.g., in [Johannesson 2011c].

If the liquid and the vapor phase of water are in equilibrium, the mass balance rule should hold. That is, the number of water molecules that leave/enter the water droplet must be equal to that enter/leave the vapor phase. Thus, $dn_w = -dn_v$. Furthermore, chemical equilibrium is defined as when the sum of the Gibbs free energy of the system is minimized, i.e., $dG_w^s = -dG_v$. By considering the two above mentioned conditions for the equilibrium, one gets

$$dG_w^s = -dG_v; \qquad \frac{dG_w^s}{dn_w} = -\frac{dG_v}{dn_w} = \frac{dG_v}{dn_v} \tag{D.8}$$

By combing Eq.D.6, Eq.D.7 and Eq.D.8, one obtains the Kelvin equation, which is

$$\ln(\phi) = \frac{2M_w\gamma_w}{RT\rho_w r_k} \tag{D.9}$$

It shows that under equilibrium conditions, there is a geometrical property which in this case is the radius of a droplet corresponding to a certain relative humidity, which sometimes is called Kelvin radius (r_k). The Kelvin equation can be further extended to the cases when liquid water is present in pores of a porous material or in an ideal case in a capillary tube, e.g., as shown in Figure A.14. It should be noted that if the liquid/vapor interface is concave to the liquid phase, then there should be a minus sign in front of the right hand side of Eq.D.9. For some porous media, e.g., concrete materials, the contact angle is often assumed to be zero. By performing experiments with different relative humidities on porous materials, the Kevin radii of the pores can be predicted.

Kelvin-Laplace equation

To derive the Kelvin-Laplace equation, it is appropriate to consider the equilibrium relation of the surface tension γ_w with the external forces in a segment of a curved liquid, e.g., as illustrated in Figure A.15. According to the geometry and the balance of the forces, the force dF_1 along the side s_1 can be expressed by the surface tension γ_w and the radii of the curvature r_{k1}, as

$$dF_1 = 2\gamma_w(\sin\frac{d\varphi}{2})ds_1 \approx 2\gamma_w(\frac{ds_2}{2r_{k1}})ds_1 \tag{D.10}$$

where $\sin(d\varphi/2)$ is approximated by ds_2/r_{k1} for the small incremental angle $d\varphi$. By noting that the surface area of the segment $dS = ds_1 ds_2$, the pressure exerted on the liquid-vapor interface p_1 can be expressed by rearranging Eq.D.10 to obtain

$$p_1 = \frac{dF_1}{dS} = \frac{\gamma_w}{r_{k1}} \tag{D.11}$$

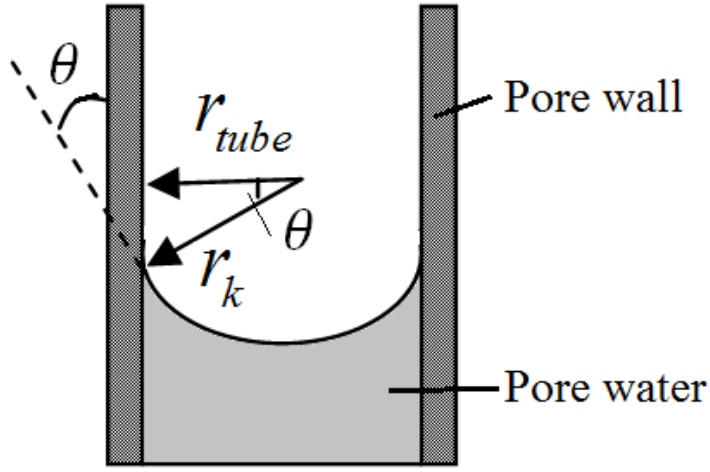

Figure A.14: Schematic illustration of the radius of the capillary tube (r_{tube}) and the Kelvin radius (r_k) with the relation being determined by the "wettability" of the liquid-wall interface in terms of the contact angle θ. The adsorbed layer is not shown in the illustration.

where p_1 is the "capillary pressure" or "suction pressure". Actually there are normally two directions for a curvature surfaces, i.e., the principal one and the normal one, thus the capillary pressure can be developed as

$$p = \gamma_w(\frac{1}{r_{k1}} + \frac{1}{r_{k2}}); \qquad p = \frac{2\gamma_w}{r_k} \quad (\text{ when } r_{k1} = r_{k2} = r_k) \tag{D.12}$$

Eq.D.12 is the Laplace equation, which shows the relation between the radii of the curvature of the liquid/vapor interface and the capillary pressure needed to keep the curvature interface in equilibrium with the surrounding vapor. By combining the Kelvin equation (Eq.D.9 with a minus sign on the right hand side for concave water liquid-vapor interface) and the Laplace equation (Eq.D.12), one obtains the Kelvin-Laplace equation, as

$$p = -\frac{RT\rho_w}{M_w}\ln(\phi) \tag{D.13}$$

The relation as shown in Eq.D.13 is, for example, used in pressure plate sorption experiments to convert an applied external pressure to a corresponding relative humidity. In this approach, relative humidities very close to 1 can be studied effectively.

E Calculation of pore size distribution

The calculation of pore size distribution, to be explained here, follows the widely used BJH model [Barrett et al. 1951]. The BJH model distinguishes between two types of water, i.e., the adsorbed water and the capillary condensed water in the studied

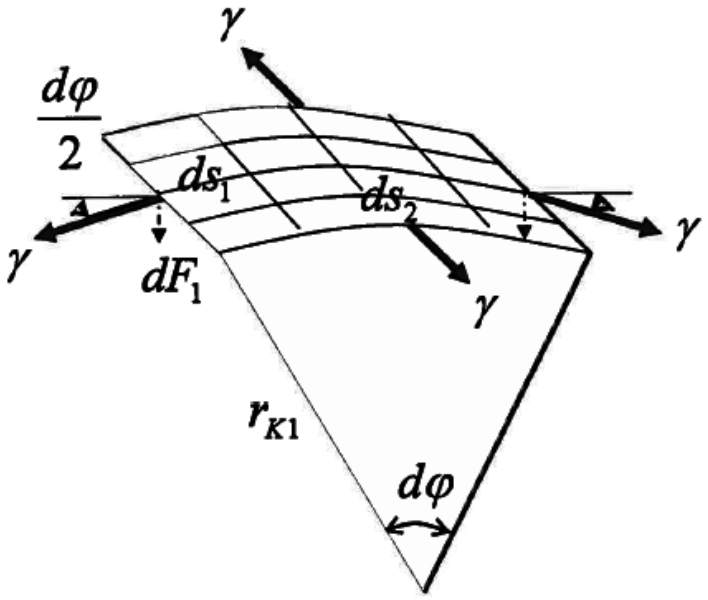

Figure A.15: The equilibrium of forces of a liquid water interface being curved in only one direction. The surface tension can be interpreted as a force integrated along a line, i.e., $dF = \gamma ds$ (after [Johannesson 2011c]).

porous material. Naturally, direct sorption measurements cannot distinguish these two types of water since only the total moisture content at a given relative pressure can be registered. With a predicted thickness of the adsorbed layer of water, the pore size distribution can be calculated using the assumption that capillary condensation is formed on top of the adsorbed layers. For a case based on cylindrical pore shape assumption, the calculation is described in a step manner with the help of an example as follows. The description of the method is based on [Barrett et al. 1951, Johannesson 2011c].

- Step 1: The measured relative humidities (ϕ) and the moisture contents (V) are listed in the first two columns of a table (Table A.1), where the moisture content is expressed in the unit of ml water per gram of the dry material.

- Step 2: Calculate the Kelvin radius r_k for each listed relative humidity according to the relation determined by Kelvin equation, i.e., Eq.E.1. The surface tension (γ_w) and density of water (ρ_w) adopted in this calculation follows Eq.E.2 (unit: N/m) [Engineeringtoolbox, b] and Eq.E.3 (unit: kg/m^3) [Engineeringtoolbox, a], respectively, where T is temperature at which the sorption measurement is performed (in Kelvin degree). The molar mass of water M_w is 0.018 (kg/mol) and the gas content $R = 8.314$ (J/(mol·K)). The wetting angle is assumed to be zero.

$$r_k = -\frac{2M_w\gamma_w}{RT\rho_w \ln(\phi)} \tag{E.1}$$

$$\gamma_w = [-0.015(T - 273.5) + 7.5669] \cdot 10^{-2} \tag{E.2}$$

Table A.1: An example to show the calculation scheme of pore size distribution, part I.

ϕ (-)	V (ml/g)	r_k (Å)	t (Å)	R_p (Å)	$\bar{r_k}$ (Å)	$\bar{R}_p$ (Å)	$\triangle t$ (Å)	$\triangle V$ (ml/g)
0.95	0.2066	206.7	6.8	213.5	160.3	153.7	0.2	0.0143
0.90	0.1923	100.6	6.6	107.2	80.4	74.1	0.4	0.0215
0.80	0.1708	47.5	6.2	53.7	44.5	38.6	0.4	0.0163
0.70	0.1545	29.7	5.7	35.4	30.7	25.2	0.5	0.0162
0.60	0.1383	20.8	5.3	26.0	24.4	19.2	0.2	0.0066
0.55	0.1317	17.7	5.0	22.8	21.4	16.5	0.2	0.0069
0.50	0.1248	15.3	4.8	20.1	18.9	14.3	0.2	0.0072
0.45	0.1176	13.3	4.5	17.8	16.8	12.4	0.3	0.0079
0.40	0.1097	11.6	4.3	15.8	14.2	10.2	0.6	0.0329
0.30	0.0768	8.8	3.7	12.5	11.1	7.7	0.7	0.0120
0.20	0.0648	6.6	3.0	9.6	8.1	5.6	1.0	0.0136
0.10	0.0512	4.6	2.1	6.7	-	-	-	-

$$\rho_w = (T-273.5)^3 \cdot 10^{-5} - 0.0057(T-273.5)^2 + 0.0089(T-273.5) + 1000.1 \quad \text{(E.3)}$$

- The calculated radii r_k will be expressed in the unit of Å (1 Å=0.1 nm) and listed in Table A.1.

- Step 3: Determine the thickness of the adsorbed layer t. The method proposed by Johannesson [2011c] combined with the standard BET equation will be used in the example, which is based on calculating the moisture content of water present in first and second layers as a function of the relative humidity using the Eq.C.18 and Eq.C.19. The predicted t values are then listed in Table A.1 in the Unit of Å.

- Step 4: The pore radius R_p corresponding to each relative humidity considered can be calculated by adding t to r_k, i.e., $R_p = r_k + t$.

- Step 5: The mean pore radii $\bar{R}_p$, mean Kelvin radii $\bar{r_k}$, the change of the thickness of the adsorbed layer $\triangle t$, and the change of the measured moisture content $\triangle V$ of two neighboring measuring points. The following equations are used:

$$\bar{R}_p = (R_p^i + R_p^{i+1})/2; \quad \bar{r_k} = (r_k^i + r_k^{i+1})/2; \quad \triangle t = t^i - t^{i+1}; \quad \triangle V = V^i - V^{i-1} \quad \text{(E.4)}$$

where the index i is the first, second and third measured values, etc., from high to low relative humidities.

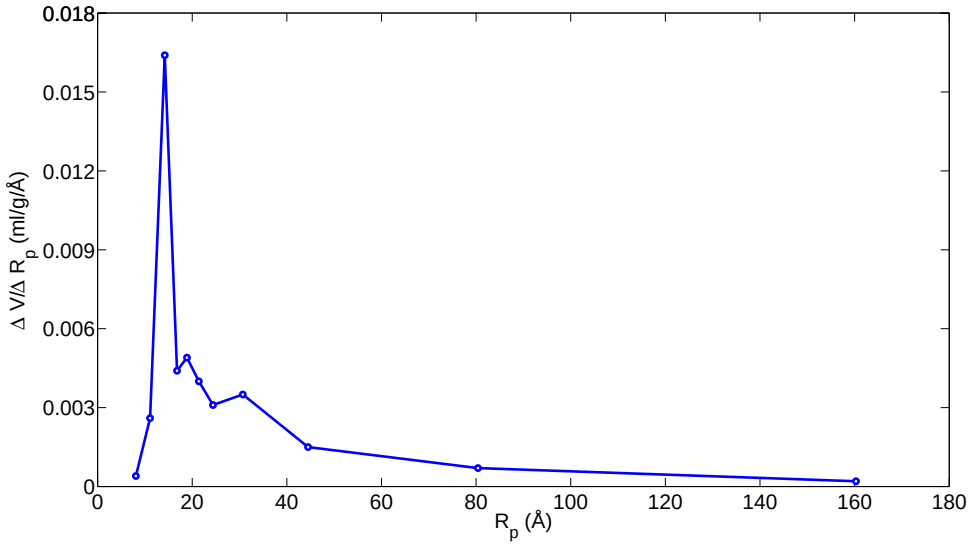

(a) Differential pore size distribution

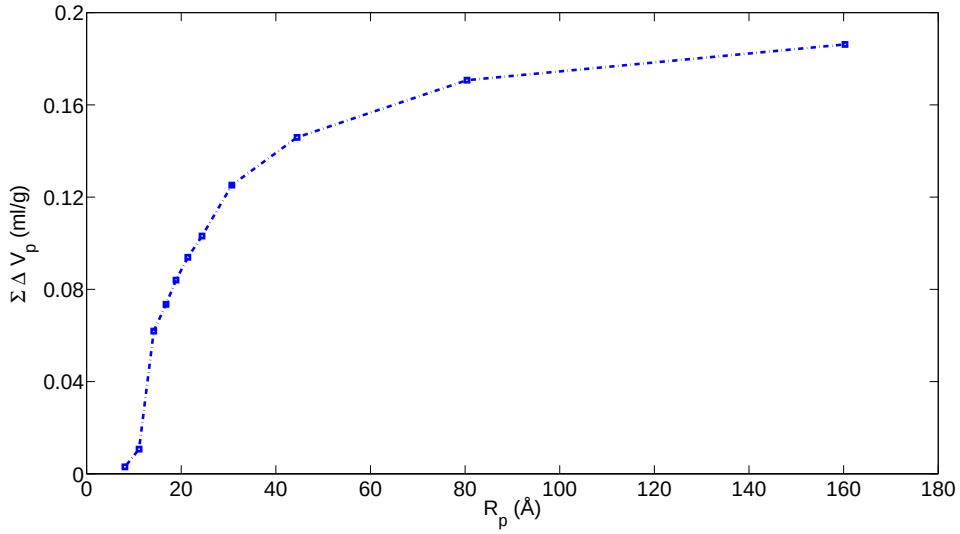

(b) Accumulated pore size distribution

Figure A.16: Differential and accumulated pore size distribution plot for the sample of the example.

Table A.2: An example to show the calculation scheme of pore size distribution, part II.

$\triangle V_p$ (ml/g)	$\triangle S_p$ (m^2/g)	$\triangle S_k$ (m^2/g)	$\sum \triangle S_p$ (m^2/g)	$\sum \triangle S_k$ (m^2/g)	$\triangle V_p/\triangle R_p$ (ml/(g·Å))	$\sum \triangle V_p$ (ml/g)
0.0155	1.93	1.85	3.93	3.85	0.0002	0.1862
0.0249	6.18	5.68	10.12	9.53	0.0007	0.1707
0.0207	9.28	8.00	19.39	17.52	0.0015	0.1459
0.0220	14.34	11.68	33.74	29.20	0.0035	0.1252
0.0093	7.61	5.97	41.35	35.17	0.0031	0.1031
0.0099	9.24	7.07	50.59	42.24	0.0040	0.0939
0.0105	11.03	8.25	61.62	50.49	0.0049	0.0840
0.0116	13.79	10.07	75.41	60.56	0.0044	0.0735
0.0513	72.27	50.46	147.68	111.03	0.0164	0.0619
0.0077	13.89	9.23	161.57	120.26	0.0026	0.0107
0.0030	7.30	4.59	168.87	124.84	0.0004	0.0030

- Step 6: The change of adsorbed moisture content $\triangle V_t$ in each step of calculation should be considered, as

$$\triangle V_t = \triangle t(\sum \triangle S_k) \cdot 10^{-4} \tag{E.5}$$

where $\triangle S_k$ is the average surface area covered by adsorbed water or in other words the surface area right outside of the Kelvin radii (the core without considering the $t-$layer). For each step of calculation, the summation of the average surface area $\sum \triangle S_k$ is the sum of the average area of unfilled pores at the relative humidity under current consideration. It can be found that actually it is still not straightforward to calculate the value of $\triangle S_k$ at each step. But on the other hand, it is possible to calculate the surface area of pores from the pore volume at each step based on the cylindrical assumption using $\triangle S_p = 2 \cdot \triangle V_p / R_p$. Furthermore, the relation between $\triangle S_p$ and $\triangle S_k$ of cylindrical pores can be expressed, as

$$\frac{S_p}{S_k} = \frac{\bar{R}_p}{\bar{r_k}} \tag{E.6}$$

Thus, Eq. E.5 can be modified to yield

$$\triangle V_t = \triangle t[\sum (\triangle S_p \cdot \bar{R}_p / \bar{r_k})] \cdot 10^{-4} \tag{E.7}$$

The initial value for this calculation is the surface area of the pores with radii larger than the highest relative humidity measured in the experiment. This value in many cases can be estimated by comparing the total surface area as determined in this BJH calculation, $\sum \triangle S_p$, with the specific surface area calculated from the standard BET equation. In studying concrete materials, Johannesson

[2011c] used the above described concept to identify the value of 2 m^2/g for the pores with Kelvin radii greater than that corresponding to the relative humidity of 0.99.

- Step 7: Calculate the pore volume $\triangle V_p$ between each measured relative humidity interval. During each relative humidity interval, the measured moisture content difference $\triangle V$ (Eq.E.4) includes both the change from the emptying of the pore cores according to Kelvin equation and that from the decreased thickness of the adsorbed layer. Thus,

$$\triangle V_p = \triangle V(\frac{\bar{R}_p}{\bar{r_k} + \triangle t})^2 \tag{E.8}$$

- Step 8: For steps with $i > 1$, the surface area $\triangle S_p$ at each relative humidity interval can be calculated as

$$\triangle S_p = 2 \cdot \triangle V_p / R_p \cdot 10^4 \tag{E.9}$$

where $\triangle S_p$ is in the unit of m^2/g, R_p is in the unit of Å.

- Step 9: Sum up the values of $\triangle S_p$, which value is needed for the calculations at the next relative humidity interval, see Table A.2.

- Step 10: When the $\triangle V_p$ is determined for each relative humidity interval, the differential and/or accumulative pore size distribution can be obtained, e.g., see the last two columns of Table A.2 and Figure A.16.

F Thermodynamic database of PHREEQC-CEMDATA07

Pore size analysis of cement based materials using the LTC may be affected by the fact that the pore solution includes a certain concentration of ions. The ionic solution may affect the surface tension of water or alter the behavior of freezing of pore water. In this latter respect, it is of interest to investigate how the ionic concentrations of the pore solution change with temperature. Such kind of investigations can be done by using thermodynamic modeling of phase assemblages in contact with water.

The thermodynamic database for the aqueous species and the mineral phases used in the PHREEQC calculation of this study is with small modifications based on the database CEMDATA07 (version 07.02) [EMPA Database]. The temperature dependence of the solubility constants is described by a three-term empirical assumption.

```
#    CEMENT PHASE DATABASE
#
#
#   Based on CEMDATA07 version 07.02 (14.08.2008)
#
#   http://www.empa.ch/plugin/template/empa/*/62204
#
#
#  Temperature dependence described by three-term analytical model
#
#
#
#
#         Thaumasite added on 28-05-2010

SOLUTION_MASTER_SPECIES


#        ATOMIC WEIGHTS

#        Naturally occuring elements: IUPAC 1993 Table 1 rounded to 0.001

#        Radioelements: Mass number of longest-lived isotope

#

#

#
#  elemen     species        alk   gfw_formula element_gfw atomic
#                                                          number
#
H               H+          -1.0        H          1.008   #   1
H(0)            H2           0.0        H                  #
H(1)            H+          -1.0        H                  #
E               e-           0.0        0.0          0.0   #
O               H2O          0.0        O         15.999   #   8
O(0)            O2           0.0        O                  #
O(-2)           H2O          0.0        O                  #
C              HCO3-         1.0        C         12.011   #   6
C(+4)          HCO3-         1.0      HCO3-                #
C(-4)           CH4          0.0       CH4                 #
Alkalinity     HCO3-         1.0      HCO3-       61.016   #
Ca             Ca+2          0.0        Ca        40.078   #  20
Si             H4SiO4        0.0        Si        28.086   #  14
K               K+           0.0        K         39.098   #  19
Mg             Mg+2          0.0        Mg        24.305   #  12
Al             Al+3          0.0        Al        26.982   #  13
S              SO4-2         0.0        S         32.067   #  16
S(-2)           HS-          1.0        HS                 #
S(2)           S2O3-2        0.0       S2O3                #
S(4)           SO3-2         0.0       SO3                 #
S(6)            SO4-2        0.0       SO4                 #
Fe             Fe+2          0.0        Fe        55.845   #  26
Fe(2)          Fe+2          0.0        Fe                 #
Fe(3)          Fe+3          0.0        Fe                 #
Br              Br-          0.0        Br        79.904   #  35
Cl              Cl-          0.0        Cl        35.453   #  17
N              NO3-          0.0        N         14.007   #   7
N(0)            N2           0.0        N2                 #
N(-3)          NH4+          0.0       NH4                 #
N(5)           NO3-          0.0       NO3                 #
Na              Na+          0.0        Na         22.99   #  11
```

```
SOLUTION_SPECIES

# PMATCH MASTER SPECIES

H+                    = H+
    log_k      0.0
    -gamma     9.00    0.064

e-                    = e-
    log_k      0.0

H2O                   = H2O
    log_k      0.0
    -gamma     0.00    0.0#64

HCO3-                 = HCO3-
    log_k      0.0
    -gamma     5.40    0.064

Ca+2                  = Ca+2
    log_k      0.0
    -gamma     4.86    0.064 # 0.01564

H4SiO4               = H4SiO4
    log_k      0.0
    -gamma     0.00    0.0#64

#b parameter not changed from here on for primary master species

Al+3                  = Al+3
    log_k      0.0
    -gamma     6.65   0.064 # 0.19

Fe+2                  = Fe+2
    log_k      0.0
    -gamma     5.08    0.064 # 0.16

K+                    = K+
    log_k      0.0
    -gamma     3.71    0.064 # 0.01

Mg+2                  = Mg+2
    log_k      0.0
    -gamma     5.46    0.064 # 0.22

SO4-2                 = SO4-2
    log_k      0.0
    -gamma     5.31   0.064 # -0.07

Br-                   = Br-
    log_k      0.0
    -gamma     3.00    0.064 # 0.00

Cl-                   = Cl-
    log_k      0.0
    -gamma     3.71    0.01

NO3-                  = NO3-
    log_k      0.0
    -gamma     3.00    0.064 # 0.00

Na+                   = Na+
    log_k      0.0
    -gamma     4.32    0.064 # 0.06
```

```
# PMATCH SECONDARY MASTER SPECIES


+1Al+3                    +1SO4-2                 = AlSO4+ ;
    -gamma      4.00    0.064   ; log_K          3.900111          ;
    -analytical_expression      -59.74759294081 0       2048.61497066133
22.9451885920   0

+1.000Al+3                +2.000SO4-2                = Al(SO4)2- ;
   -gamma      4.00    0.0640   ; log_K          5.900097          ;
   -analytical_expression       -129.37633673647        0       5505.68803129935
47.2073519666   0

 +1.000Al+3                +2.000H2O                 -2.000H+
= Al(OH)2+ ;
    -gamma      4.00    0.0640  ; log_K          -10.5937 ;
    -analytical_expression      32.53631959378  0       -6492.54044012403
-8.6321382739   0

 +1.000Al+3                +4.000H2O                 -4.000H+
= Al(OH)4- ;
    -gamma      4.00    0.0640  ; log_K          -22.8786          ;
    -analytical_expression      32.96015215706  0       -10341.60374731900
-8.5473467468   0

 +1.000Al+3                +3.000H2O                 -3.000H+
= Al(OH)3 ;
    -gamma      0.00    0.00    ; log_K          -16.4319          ;
    -analytical_expression      91.66401813525  0       -11712.97320105170
-27.8112600743  0

 +1.000Al+3                +1.000H2O                 -1.000H+
= AlOH+2 ;
    -gamma      4.00    0.0640  ; log_K          -4.95693          ;
    -analytical_expression      -34.57025049802 0       -869.70655319713
13.1464151225   0

 +1.000Al(OH)4-            +1.000H4SiO4             -1.000H2O
= Al(OH)6SiO- ;
    -gamma      4.00    0.0640  ; log_K          3.600009          ;
    -analytical_expression      0.00000000000   0       1073.39477649456
0.0000000000    0

 +1.000Al+3                +1.000SiO(OH)3-           = AlSiO(OH)3+2 ;
    -gamma      4.00    0.0640  ; log_K          7.400086          ;
    -analytical_expression      0.00000000000   0       2206.33554059029
0.0000000000    0

 +1.000Ca+2                -1.000H+                  +1.000HCO3-
= CaCO3   ;
    -gamma      0.00    0.0     ; log_K          -7.10471          ;
    -analytical_expression      18.67700851789  0       -2532.27825260820
-6.9868218332   0

 +1.000Ca+2                +1.000HCO3-               = CaHCO3+    ;
    -gamma      4.00    0.064   ; log_K          1.105633          ;
    -analytical_expression      -103.46104593645        0       4604.38192941364
36.0178771810   0

 +1.000Ca+2                +1.000SO4-2               = CaSO4 ;
    -gamma      0.00    0.0640  ; log_K          2.300088          ;
    -analytical_expression      -64.25337074408 0       2770.03421100362
23.1418327719   0

 +1.000Ca+2                +1.000H2O                 -1.000H+
= CaOH+   ;
    -gamma      4.00    0.064   ; log_K          -12.7798          ;
    -analytical_expression      14.19214642856  0       -4635.48173840128
-4.6171091261   0
```

```
 +1.000Ca+2                 +1.000SiO(OH)3-           = CaSiO(OH)3+  ;
    -gamma      4.00    0.064   ; log_K         1.200061          ;
    -analytical_expression      -88.10659232191 0       3919.11589441343
30.7796851528   0

 +1.000Ca+2                 +1.000SiO2(OH)2-2         = CaSiO2(OH)2        ;
    -gamma      0.00    0.0     ; log_K         4.600017          ;
    -analytical_expression      0.00003498360   0       1371.64549038842
-0.0000120272   0

 +1.000Fe+2                 +1.000HCO3-               -1.000H+
= FeCO3 ;
     -gamma      0.00    0.00   ; log_K         -5.94898          ;
     -analytical_expression     16.83325757655  0       -1846.89625963213
-6.7038225945   0

 +1.000Fe+2                 +1.000HCO3-               = FeHCO3+ ;
     -gamma      4.00    0.0640 ; log_K         1.999985          ;
     -analytical_expression     -104.57077896404        0       5270.65115685443
35.9245463653   0

 +1.000Fe+2                 +1.000H+                  +1.000SO4-2
= FeHSO4+ ;
     -gamma      4.00    0.0640 ; log_K         3.067952          ;
     -analytical_expression     -217.68294720087        0       9316.87298664815
76.5843086363   0

 +1.000Fe+2                 +1.000SO4-2               = FeSO4 ;
     -gamma      0.00    0.00   ; log_K         2.249983          ;
     -analytical_expression     -65.22644646497 0       2644.89637498019
23.6844985453   0

 +1.000Fe+2                 +1.000Cl-                 = FeCl+ ;
     -gamma      4.00    0.0640 ; log_K         0.139978          ;
     -analytical_expression     -84.08990370509 0       3692.01184090337
29.0358662146   0

 +1.000Fe+2                 +1.000H2O                 -1.000H+
= FeOH+ ;
     -gamma      4.00    0.0640 ; log_K         -9.49965          ;
     -analytical_expression     -7.35359137368  0       -2427.06600313247
2.4220308834    0

 +1.000H+                   +1.000SO4-2               +1.000Fe+3
= FeHSO4+2 ;
     -gamma      4.00    0.0640 ; log_K         4.468082          ;
     -analytical_expression     -268.70278991437        0       13166.04041835980
92.5513349554   0

 +1.000SO4-2                +1.000Fe+3                = FeSO4+ ;
     -gamma      4.00    0.0640 ; log_K         4.040089          ;
     -analytical_expression     -61.88124256446 0       2185.38358231463
23.6787255052   0

 +2.000SO4-2                +1.000Fe+3                = Fe(SO4)2- ;
     -gamma      4.00    0.0640 ; log_K         5.380128          ;
     -analytical_expression     -131.48050051289        0       5443.75324149227
47.9311468746   0

 +1.000Fe+2                 -1.000e-                  = Fe+3 ;
     -gamma      9.00    0.0640 ; log_K         -13.0201          ;
     -analytical_expression     6.52902464956   0       -2917.27751554918
-5.3251484453   0

 +3.000H2O                  -3.000H+                  +1.000Fe+3
= Fe(OH)3   ;
        ; log_K         -12.5594         ;
     -analytical_expression     147.12395569469 0       -13347.13553589500
-46.4423038760  0
```

```
 +2.000H2O                  -2.000H+                  +2.000Fe+3
= Fe2(OH)2+4 ;
     -gamma      4.00    0.0640 ; log_K         -2.94948         ;
     -analytical_expression     6.94584777011   0       -2950.65882826
0.0000120272    0

 +4.000H2O                  -4.000H+                  +3.000Fe+3
= Fe3(OH)4+5 ;
     -gamma      9.00    0.0640 ; log_K         -6.29892         ;
     -analytical_expression     4.18235662859   0       -3125.11656793865
0.0000240543    0

 +1.000Cl-                  +1.000Fe+3                = FeCl+2 ;
    -gamma      4.00    0.0640  ; log_K         1.480017         ;
    -analytical_expression      -72.69030177926 0       3122.83931417149
25.7418657263   0

 +2.000Cl-                  +1.000Fe+3                = FeCl2+ ;
    -gamma      4.00    0.0640  ; log_K         2.129977         ;
    -analytical_expression      -215.95223084886        0       9794.48642498307
74.8585304486   0

 +3.000Cl-                  +1.000Fe+3                = FeCl3 ;
     -gamma      0.00    0.0640 ; log_K         1.129985         ;
     -analytical_expression     -285.45375024869        0       13355.40022646740
97.7088246932   0

 +1.000H2O                  -1.000H+                  +1.000Fe+3
= FeOH+2 ;
     -gamma      4.00    0.0640 ; log_K         -2.18961         ;
     -analytical_expression     16.59946235915  0       -2732.42292291182
-3.8894655247   0

 +2.000H2O                  -2.000H+                  +1.000Fe+3
= Fe(OH)2+   ;
     -gamma      4.00    0.0640 ; log_K         -5.66961         ;
     -analytical_expression     78.23475365977  0       -7306.78682417424
-24.0049022733  0

 +4.000H2O                  -4.000H+                  +1.000Fe+3
= Fe(OH)4-   ;
     -gamma      4.00    0.0640 ; log_K         -21.5993         ;
     -analytical_expression     117.57797560593 0       -14082.57228041010
-37.1561282625  0

 +1.000Fe+3                 +1.000SiO(OH)3-           = FeSiO(OH)3+2 ;
    -gamma      4.00    0.0640  ; log_K         9.699999         ;
    -analytical_expression      0.00006996720   0       2892.15594977973
-0.0000240543   0

 +1.000K+                   +1.000SO4-2               = KSO4- ;
    -gamma      4.00    0.0640          ; log_K         0.850029         ;
    -analytical_expression      -72.97654888147 0       3150.05834400053
25.5660285453   0

 +1.000K+                   +1.000H2O                 -1.000H+
= KOH ;
    -gamma      0.00    0.00    ; log_K         -14.4597         ;
    -analytical_expression      55.77230945322  0       -5964.47470504443
-20.2983699581  0

 +1.000Mg+2                 -1.000H+                  +1.000HCO3-
= MgCO3 ;
     -gamma      0.00    0.00   ; log_K         -7.34928         ;
     -analytical_expression     17.81062888483  0       -2178.42833934954
-7.2149771905   0

 +1.000Mg+2                 +1.000HCO3-               = MgHCO3+ ;
     -gamma      4.00    0.064  ; log_K         1.068142         ;
     -analytical_expression     -107.35949477825        0       4739.07110899493
```

```
37.3957094285   0

 +1.000Mg+2                 +1.000H2O                  -1.000H+
= MgOH+ ;
    -gamma      4.00    0.0640  ; log_K         -11.4397         ;
    -analytical_expression      -27.03763638067 0       -2051.24072933459
9.0841192085    0

 +1.000Mg+2                 +1.000SO4-2                = MgSO4 ;
     -gamma      0.00    0.00   ; log_K         2.36999  ;
     -analytical_expression     -65.50267875609 0       2716.83921823504
23.7471600852   0

 +1.000Mg+2                 +1.000SiO(OH)3-            = MgSiO(OH)3+ ;
     -gamma      4.00    0.0640 ; log_K         1.499989         ;
     -analytical_expression     -92.66274049892 0       4338.36419953797
32.1739946190   0

 +1.000Mg+2                 +1.000SiO2(OH)2-2          = MgSiO2(OH)2 ;
     -gamma      0.00    0.00   ; log_K         5.700009         ;
     -analytical_expression     0.00003498360   0       1699.67075541936
-0.0000120272   0

 +1.000Na+                  -1.000H+                   +1.000HCO3-
= NaCO3- ;
    -gamma      4.00    0.0640  ; log_K         -9.05897         ;
    -analytical_expression      8.57582729935   0       -417.55748897161
-6.5608195793   0

 +1.000Na+                  +1.000HCO3-                = NaHCO3 ;
    -gamma      0.00    0.00    ; log_K         -0.25    ;
    -analytical_expression      -69.04984593286 0       3027.60721771434
23.7006149490   0

 +1.000Na+                  +1.000SO4-2                = NaSO4- ;
     -gamma      4.00    0.0640 ; log_K         0.700065         ;
     -analytical_expression     -67.94698554238 0       2908.64969369569
23.8000796198   0

 +1.000Na+                  +1.000H2O                  -1.000H+
= NaOH ;
     -gamma      0.00    0.00   ; log_K         -14.1797         ;
     -analytical_expression     40.02241563584  0       -4902.58161996995
-15.2600694449  0

 +1.000H4SiO4               -1.000H+                 = SiO(OH)3-   ;
     -gamma      4.00    0.064  ; log_K         -9.80974         ;
     -analytical_expression     67.70633238796  0       -4741.99183185177
-24.8993626804  0

 +1.000H4SiO4               -2.000H+                 = SiO2(OH)2-2  ;
     -gamma      4.00    0.064  ; log_K         -23.1397         ;
     -analytical_expression     -10.00067913457 0       -3917.49762695022
0.0000120272    0

 +1.000H+                   -1.000H2O                  +1.000HCO3-
= CO2  ;
     -gamma      0.00    0.0    ; log_K         6.351807         ;
     -analytical_expression     -118.94289041477        0       6009.06305396012
42.4908984414   0

 -1.000H+                   +1.000HCO3-              = CO3-2  ;
     -gamma      5.40    0.064  ; log_K         -10.3289         ;
     -analytical_expression     81.27367428255  0       -4731.00208183675
-30.6072155785  0

 +1.000HCO3-                +9.000H+                   +8.000e-
-3.000H2O                  = CH4     ;
    -gamma      0.00    0.0     ; log_K         27.8481  ;
    -analytical_expression      -177.87782773202        0       21721.88220712880
```

```
64.7294909742   0

 +1.000NH4+                  -1.000H+                    = NH3 ;
    -gamma      0.00    0.00    ; log_K          -9.23697          ;
    -analytical_expression      -3.59831980108  0       -2549.62881993208
1.1769785592    0

 +1.000NO3-                +10.000H+                   +8.000e-
-3.000H2O                  = NH4+ ;
    -gamma      2.50    0.0640  ; log_K          119.1361          ;
    -analytical_expression      -116.84941401789        0       46557.19607874130
43.2967186280   0

 +2.000NO3-                +12.000H+                  +10.000e-
-6.000H2O                  = N2 ;
     -gamma      0.00    0.00    ; log_K          207.2662          ;
     -analytical_expression     -275.27055430258        0       81299.07928897020
98.6135081923   0

+2.000SO4-2               +10.000H+                   +8.000e-
-5.000H2O                  = S2O3-2 ;
     -gamma      4.00    0.0640 ; log_K          38.01267          ;
     -analytical_expression     -214.77995703953        0       24017.66212043470
80.6443193886   0

 +1.000H+                   +1.000SO3-2                = HSO3- ;
     -gamma      4.00    0.0640 ; log_K          7.219989          ;
     -analytical_expression     -87.59223471343 0       3812.55224613743
33.1491573165   0


 +1.000SO4-2                +2.000H+                   +2.000e-
-1.000H2O                  = SO3-2 ;
     -gamma      4.50    0.0640 ; log_K          -3.39725          ;
     -analytical_expression     -20.01098159798 0       1624.20845779751
7.2712643319    0

+1.000H+                   +1.000SO4-2                = HSO4- ;
     -gamma      4.00    0.0640 ; log_K          1.987722          ;
     -analytical_expression     -95.44960727141 0       3428.44243310458
34.7309703157   0

 +1.000HS-                  +1.000H+                   = H2S ;
     -gamma      0.00    0.00    ; log_K          6.989962          ;
     -analytical_expression     -92.54543936710 0       5444.49694476074
32.8459524374   0

 +1.000SO4-2                +9.000H+                   +8.000e-
-4.000H2O                  = HS- ;
     -gamma      3.50    0.0640 ; log_K          33.68888          ;
     -analytical_expression     -148.49636393000        0       20433.96976138830
56.9613843750   0

 +1.000HS-                  -1.000H+                   = S-2 ;
     -gamma      5.00    0.0640 ; log_K          -19       ;
     -analytical_expression     0.00001044666   0       -5667.31548660147
0.0000000000    0

 +1.000H2O                  -1.000H+                   = OH-  ;
     -gamma     10.65    0.064  ; log_K          -13.9998          ;
     -analytical_expression     69.84779493355  0       -6215.12596863142
-25.4612719210  0

 +2.000H+                   +2.000e-                   = H2   ;
     -gamma      0.00    0.0    ; log_K          -3.10597          ;
     -analytical_expression     -55.35493262717 0       2808.32060172984
20.0675686240   0

 +2.000H2O                  -4.000H+                   -4.000e-
= O2   ;
```

```
    -gamma      0.00    0.0     ; log_K         -85.9855         ;
    -analytical_expression      -30.79426700990 0       -27925.53838584180
10.0321005086   0



PHASES

CH4(g)   ;              CH4                    =  +1.000CH4                    ;
     log_K      -2.8565  ;
     -analytical_expression     -89.63393582234  0      4440.29675525994
29.0478933816   0

CO2(g)   ;              CO2                    =  +1.000H+
-1.000H2O                  +1.000HCO3-                  ;
     log_K      -7.81956         ;
     -analytical_expression     41.87683954485  0       -1740.14204852581
-17.7229926959  0

H2(g)    ;   H2                     =  +1.000H2                          ;
    log_K       -3.10597         ;
    -analytical_expression      -52.09936672097 0       2359.52736654890
16.6015796481   0

O2(g)    ;   O2                     =  +1.000O2                          ;
    log_K       -2.8812  ;
    -analytical_expression      -76.67437063690 0       3828.93234444672
24.6329609322   0

H2S(g)   ;  H2S                      =  +1.000HS-                  +1.000H+       ;
    log_K       -8.00993         ;
    -analytical_expression      37.63799849734  0       -2225.98872774971
-15.4105293036  0

N2(g)    ; N2                      =  +1.000N2   ;
    log_K       -3.18743         ;
    -analytical_expression      -76.72711536033 0       3734.51086475577
24.6580977111   0

JenD(J2);  (CaO)1.5(SiO2)0.6666(H2O)2.5 + 3.0000 H+ = 1.5000 Ca+2 + 0.6666 H4SiO4
+ 2.6668 H2O ;
    log_k 28.713 ;      delta_h -149.267 kJ/mol ;
    -analytical_expression  0.03485     0.004238        8173.90


JenH;    (CaO)1.3333(SiO2)(H2O)2.1666 + 2.6666 H+  =  1.3333 Ca+2 + 1.0000 H4SiO4
+ 1.4999 H2O ;
     log_k 22.173 ;     delta_h -106.230 kJ/mol;
     -analytical_expression   0.6855    0.004822    5977.9

TobD(T2); (CaO)0.8333(SiO2)0.6666(H2O)1.8333 + 1.6666 H+  =  0.8333 Ca+2 + 0.6666
H4SiO4 + 1.3334 H2O ;
    log_k 13.624 ; delta_h      -64.304 kJ/mol ;
    -analytical_expression 0.48308      0.0031404       3638.8

TobH; (CaO)0.6666(SiO2)(H2O)1.5 + 1.3332 H+  =  0.6666 Ca+2 + 1.0000 H4SiO4 +
0.1666 H2O ;
   log_k  8.272 ; delta_h       -27.755 kJ/mol;
   -analytical_expression  1.2083       0.0036895       1778


SiO2(am); SiO2 + 2.0000 H2O  =  1.0000 H4SiO4;
   log_k -2.714 ;   delta_h     15.590 kJ/mol  ;
   -analytical_expression   1.5145      -0.0025038      -1037.3

C2AH8 ; Ca2Al2(OH)10:3H2O = 2Ca++ + 2Al(OH)4- + 2OH- + 3H2O     ;
   log_K        -13.5622         ;
   -analytical_expression       154.48530223981 0       -8994.12914254083
```

```
-55.7212631893  0

C2FH8 ; Ca2Fe2(OH)10:3H2O = 2Ca++ + 2Fe(OH)4- + 2OH- + 3H2O     ;
   log_K        -17.602  ;
   -analytical_expression       299.40318587869 0       -18138.64886929690
-103.5235991057 0

hydrogarnetOH  ; Ca3Al2(OH)12 = 3Ca++ + 2Al(OH)4- + 4OH-        ;
   log_K        -20.8411         ;
   -analytical_expression       291.27318390754 0       -13720.16812376770
-107.5364633634 0

hydrogarnetFe  ; Ca3Fe2(OH)12 = 3Ca++ + 2Fe(OH)4- + 4OH-        ;
   log_K        -25.158  ;
   -analytical_expression       437.20835028023 0       -23213.52271974500
-155.3909971844 0

C4AH13 ; Ca4Al2(OH)14:6H2O = 4Ca++ + 2Al(OH)4- + 6OH- + 6H2O    ;
   log_K        -25.4033         ;
   -analytical_expression       407.04628084006 0       -21037.51384617330
-146.2503502912 0

C4FH13 ; Ca4Fe2(OH)14:6H2O = 4Ca++ + 2Fe(OH)4- + 6OH- + 6H2O    ;
   log_K        -29.4028         ;
   -analytical_expression       552.15552475835 0       -30178.01620624420
-194.1184748109 0

Ettringite ; Ca6Al2(SO4)3(OH)12:26H2O = 6Ca++ + 2Al(OH)4- + 3SO4-- + 4OH- + 26H2O
;
   log_K        -44.9085         ;
   -analytical_expression       529.27779378424 0       -34439.99676380200
-185.3386429266 0

tricarboaluminate ; Ca6Al2(CO3)3(OH)12:26H2O = 6Ca++ + 2Al(OH)4- + 3CO3-- + 4OH-
+ 26H2O ;
   log_K        -46.5085         ;
   -analytical_expression       526.28378030499 0       -32615.50770370250
-187.2629896410 0

Fe-ettringite ; Ca6Fe2(SO4)3(OH)12:26H2O = 6Ca++ + 2Fe(OH)4- + 3SO4-- + 4OH- +
26H2O   ;
   log_K        -44.0084         ;
   -analytical_expression       674.03730619220 0       -42106.04906255390
-233.0864957767 0

monosulfoaluminate ; Ca4Al2(SO4)(OH)12:6H2O = 4Ca++ + 2Al(OH)4- + SO4-- + 4OH- +
6H2O    ;
   log_K        -29.2628         ;
   -analytical_expression       404.92625454716 0       -21017.60772698490
-146.9719803091 0

Fe-monosulfate ; Ca4Fe2(SO4)(OH)12:6H2O = 4Ca++ + 2Fe(OH)4- + SO4-- + 4OH- + 6H2O
;
   log_K        -33.2028         ;
   -analytical_expression       549.68566248846 0       -30126.34439200350
-194.7198331591 0

stratlingite ; Ca2Al2SiO2(OH)10:3H2O = 2Ca++ + 2Al(OH)4- + 1SiO(OH)3- + OH- +2H2O
;
   log_K        -19.7042         ;
   -analytical_expression       148.95692659946 0       -9589.95690828914
-55.1593539487  0

Fe-stratlingite ; Ca2Fe2SiO2(OH)10:3H2O = 2Ca++ + 2Fe(OH)4- + 1SiO(OH)3- + OH-
+2H2O   ;
   log_K        -23.702  ;
   -analytical_expression       293.87516007432 0       -18722.47854424510
-102.9618101367 0

hemicarboaluminate ; Ca4Al2(CO3)0.5(OH)13:5.5H2O = 4Ca++ + 2Al(OH)4- + 0.5CO3-- +
```

```
5OH- + 5.5H2O   ;
   log_K        -29.1327         ;
   -analytical_expression       411.51063104013 0       -21526.38118104660
-148.8963270235 0

Fe-hemicarbonate ; Ca4Fe2(CO3)0.5(OH)13:5.5H2O = 4Ca++ + 2Fe(OH)4- + 0.5CO3-- +
5OH- + 5.5H2O   ;
   log_K        -33.1027         ;
   -analytical_expression       556.27003898143 0       -30644.51984410740
-196.6441798735 0

monocarboaluminate ; Ca4Al2(CO3)(OH)12:5H2O = 4Ca++ + 2Al(OH)4- + CO3-- + 4OH- +
5H2O    ;
   log_K        -31.4726         ;
   -analytical_expression       419.54622572991 0       -22668.16504663430
-151.5423037557 0

Fe-monocarbonate ; Ca4Fe2(CO3)(OH)12:5H2O = 4Ca++ + 2Fe(OH)4- + CO3-- + 4OH- +
5H2O    ;
   log_K        -35.5 ;
   -analytical_expression       554.47107047792 0       -31715.13432703260
-195.43556986521        0

hydrotaliceOH ; Mg4Al2(OH)14:3H2O = 4Mg++ + 2Al(OH)4- + 6OH- + 3H2O     ;
   log_K        -56.0214         ;
   -analytical_expression       354.74992257809 0       -22738.24127204280
-135.1853566837 0

hydrotalciteFe  ; Mg4Fe2(OH)14:3H2O = 4Mg++ + 2Fe(OH)4- + 6OH- + 3H2O   ;
   log_K        -60.002  ;
   -analytical_expression       499.50943498605 0       -31856.37993510370
-182.9332095337 0

CAH10 ; CaAl2(OH)8:6H2O = Ca++ + 2Al(OH)4- + 6H2O       ;
   log_K        -7.50282         ;
   -analytical_expression       19.33995799190  0       -4170.78109558596
-5.1912860770   0

hydrogarnetSi   ; Ca3Al2(SiO4)0.8(OH)8.8 + 2.4H2O = 3Ca++ + 2Al(OH)4- + 0.8
SiO(OH)3- + 3.2OH-      ;
   log_K        -29.8707         ;
   -analytical_expression       305.23780762563 0       -16550.88410201760
-112.9922268420 0

hydrotalciteC  ; Mg4Al2(OH)12CO3:3H2O = 4Mg++ + 2Al(OH)4- + CO3-- + 4OH- + 3H2O ;
   log_K        -51.142  ;
   -analytical_expression       358.37159560480 0       -21030.32915266930
-136.9894317284 0

syngenite ; K2Ca(SO4)2H2O = 2K+ + 1Ca++ + 2SO4-- + 1H2O ;
   log_K        -7.2003  ;
   -analytical_expression       256.44664476696 0       -12598.84393306150
-89.4698545074  0

Al(OH)3am ; Al(OH)3 = Al(OH)4- - 1OH-   ;
   log_K        0.239427         ;
   -analytical_expression       -48.08001615409 0       1546.32359095493
17.4322960704   0

Fe(OH)3mic ; Fe(OH)3 = Fe(OH)4- - 1OH-  ;
   log_K        -4.60039         ;
   -analytical_expression       2.49263607431   0       -2892.86085047996
1.0555041728    0

Calcite ; CaCO3                  =  +1.000Ca+2                 -1.000H+
       +1.000HCO3-     ;
   log_K        1.84897  ;
   -analytical_expression       49.00173153277  0       -958.45338123134
-17.7571498501  0
```

```
Portlandite ; Ca(OH)2               =  +1.000Ca+2                 +2.000H2O
           -2.000H+    ;
   log_K        22.79937         ;
   -analytical_expression       -11.29923807115 0       7303.68926279255
3.8839330279    0

Anhydrite ; CaSO4                   =  +1.000Ca+2                 +1.000SO4-2    ;
   log_K        -4.35754         ;
   -analytical_expression       131.22651283827 0       -5228.78943438100
-47.7070807540  0

Gypsum ; CaSO4:2H2O             =  +1.000Ca+2                 +1.000SO4-2
       +2.000H2O        ;
   log_K        -4.58147         ;
   -analytical_expression       111.52942046684 0       -5116.92285811085
-39.9882855394  0

Hematite ; Fe2O3                  =  +3.000H2O                  -6.000H+
         +2.000Fe+3     ;
   log_K        1.118973         ;
   -analytical_expression       -11.36089784168 0       6572.14422725869
-3.8633665724   0

Brucite ; Mg(OH)2                 =  +1.000Mg+2                 +2.000H2O
        -2.000H+        ;
   log_K        16.83953         ;
   -analytical_expression       -21.32005009039 0       6781.89650685512
6.2277873260    0

Thaumasite ;  (CaSiO3)2(CaSO4)2(CaCO3)2(H2O)30= 6.000 Ca+2 + 2  SiO(OH)3- +  2
CO3-2 + 2 SO4-2 + 2 OH- + 26 H2O         ;
   log_K        -49.4078983      ;
   -analytical_expression       596.55829677308 0       -37214.18686948530
-210.5956935526 0
```

Bibliography

USGS Mineral Commodities Summary, January 2013.

M. Åhs. *Redistribution of moisture and ions in cement based materials*. PhD thesis, Division of Building Materials, Lund University, 2011.

K.K. Aligizaki. *Pore structure of cement-based materials: testing, interpretation and requirements*. Taylor & Francis, 2006.

T. Allen. *Particle size measurement: Powder sampling and particle size measurement*, volume 2. Springer, 5th edition, 1997.

R.B. Anderson. Modifications of the Brunauer, Emmett and Teller equation1. *Journal of the American Chemical Society*, 68(4):686–691, 1946.

A. A. Antoniou. Phase transformations of water in porous glass. *The Journal of Physical Chemistry*, 68(10):2754–2763, 1964.

J.A. Anzelmo. The role of XRF, inter-element corrections, and sample preparation effects in the 100-year evolution of ASTM standard test method C114. *Journal of ASTM international*, 6(2):873–881, 2009.

ASTM. Standard C150: Standard Specification for Portland Cement. Annual Book of ASTM Standards, 2007.

ASTM. Standard C114: Standard Test Methods for Chemical Analysis of Hydraulic Cement. Annual Book of ASTM Standards, 2008.

E.H. Atlassi. Influence of silica fume on the pore structure of mortar when measured by water vapour sorption isotherms. In *The Modelling of Microstructure and its Potential for Studying Transport Properties and Durability*, pages 257–270. Springer, 1996.

D.H. Bager. *Ice Formation in Hardened Cement Paste*. PhD thesis, Building Materials Laboratory, Technical University of Denmark, 1984.

D.H. Bager and E.J. Sellevold. Ice formation in hardened cement paste, Part I–room temperature cured pastes with variable moisture contents. *Cement and Concrete Research*, 16(5):709–720, 1986a.

D.H. Bager and E.J. Sellevold. Ice formation in hardened cement paste, Part II-drying and resaturation on room temperature cured pastes. *Cement and Concrete Research*, 16(6):835–844, 1986b.

J. Banys, M. Kinka, J. Macutkevic, G. Völkel, W. Böhlmann, V. Umamaheswari, M. Hartmann, and A. Pöppl. Broadband dielectric spectroscopy of water confined in MCM–41 molecular sieve materials–low-temperature freezing phenomena. *Journal of Physics: Condensed Matter*, 17:2843, 2005.

V. Baroghel-Bouny. Water vapour sorption experiments on hardened cementitious materials: Part I: Essential tool for analysis of hygral behaviour and its relation to pore structure. *Cement and Concrete Research*, 37(3):414–437, 2007.

E.P. Barrett, L.G. Joyner, and P.P. Halenda. The determination of pore volume and area distributions in porous substances. I. computations from nitrogen isotherms. *Journal of the American Chemical Society*, 73(1):373–380, 1951.

F. Beltzung and F.H. Wittmann. Role of disjoining pressure in cement based materials. *Cement and Concrete Research*, 35(12):2364–2370, 2005.

D. Bentz and P. Stutzman. Curing, hydration, and microstructure of cement paste. *ACI Materials Journal*, 103(5):348–356, 2006.

D.P. Bentz. Three-dimensional computer simulation of portland cement hydration and microstructure development. *Journal of the American Ceramic Society*, 80(1): 3–21, 1997.

J. Blahovec and S. Yanniotis. GAB generalized equation for sorption phenomena. *Food and Bioprocess Technology*, 1(1):82–90, 2008.

J.H. De Boer, editor. *The dynamical character of adsorption.* Clarendon Press, Oxford, UK, 2nd edition, 1968.

P.J. Branton, P.G. Hall, K.S.W. Sing, H. Reichert, F. Schüth, and K.K. Unger. Physisorption of argon, nitrogen and oxygen by MCM-41, a model mesoporous adsorbent. *J. Chem. Soc., Faraday Trans.*, 90(19):2965–2967, 1994.

P.J. Branton, P.G. Hall, and K.S.W. Sing. Physisorption of alcohols and water vapour by MCM-41, a model mesoporous adsorbent. *Adsorption*, 1(1):77–82, 1995.

P.J. Branton, K.S.W. Sing, and J.W. White. Adsorption of carbon tetrachloride and nitrogen by 3.4 nm pore diameter siliceous MCM-41. *J. Chem. Soc., Faraday Trans.*, 93(13):2337–2340, 1997.

M. Brun, A. Lallemand, J.F. Quinson, and C. Eyraud. Changement d'état liquid–solide dans les milieux poreux. II. Étude théorique de la solidification d'un condensate capillaire (liquid–solid change of state in porous media. II. Theoretical study of the solidification of a capillary condensate). *J.Chim.Phys.*, 6:979–989, 1973.

M. Brun, A. Lallemand, J.F. Quinson, and C. Eyraud. A new method for the simultaneous determination of the size and shape of pores: the thermoporometry. *Thermochimica Acta*, 21(1):59–88, 1977.

S. Brunauer, P.H. Emmett, and E. Teller. Adsorption of gases in multimolecular layers. *Journal of the American Chemical Society*, 60(2):309–319, 1938.

S. Brunauer, J. Skalny, and E.E. Bodor. Adsorption on nonporous solids. *Journal of Colloid and Interface Science*, 30(4):546–552, 1969.

J.W. Bullard. A three-dimensional microstructural model of reactions and transport in aqueous mineral systems. *Modelling and Simulation in Materials Science and Engineering*, 15(7):711–738, 2007.

M. Caunt. *Pore structure in blended cement pastes*. PhD thesis, Building Materials Laboratory, Technical University of Denmark, 2011.

O. Coussy. Poromechanics of freezing materials. *Journal of the Mechanics and Physics of Solids*, 53(8):1689–1718, 2005.

F.P. Cuperus, D. Bargeman, and C.A. Smolders. Critical points in the analysis of membrane pore structures by thermoporometry. *Journal of Membrane Science*, 66 (1):45–53, 1992.

J.F. Daian. Condensation and isothermal water transfer in cement mortar, Part I–pore size distribution, equilibrium water condensation and imbibition. *Transport in Porous Media*, 3(6):563–589, 1988.

D. Damidot, B. Lothenbach, D. Herfort, and F.P. Glasser. Thermodynamics and cement science. *Cement and Concrete Research*, 41(7):679–695, 2011.

R. Defay, I. Prigogine, A. Bellemans, and D.H. Everett. *Surface tension and adsorption*. Longmans London, 1966.

R. W. Dent. A multilayer theory for gas sorption. Part I: Sorption of a single gas. *Textile Research Journal*, 47(2):145–152, 1977.

R.W. Dent. A sorption theory for gas mixtures. *Polymer Engineering & Science*, 20 (4):286–289, 1980.

S. Diamond. Aspects of concrete porosity revisited. *Cement and Concrete Research*, 29(8):1181–1188, 1999.

S. Diamond and D. Bonen. Microstructure of hardened cement paste-a new interpretation. *Journal of the American Ceramic Society*, 76(12):2993–2999, 1993.

EMPA Database. Thermodynamic data for hydrated solids in portland cement system. URL `http://www.empa.ch/plugin/template/empa/*/62204`. Accessed on March 25, 2013.

Engineeringtoolbox, a. URL `http://www.engineeringtoolbox.com/water-density-specific-weight-d_595.html`. Accessed on December 13, 2012.

Engineeringtoolbox, b. URL `http://www.engineeringtoolbox.com/water-surface-tension-d_597.html`. Accessed on December 13, 2012.

R.M. Espinosa and L. Franke. Inkbottle pore-method: Prediction of hygroscopic water content in hardened cement paste at variable climatic conditions. *Cement and Concrete Research*, 36(10):1954–1968, 2006.

G. Fagerlund. Determination of pore-size distribution from freezing-point depression. *Materials and Structures*, 6(3):215–225, 1973a.

G. Fagerlund. *Methods of Characterization of Pore Structure: 3 Contributions to Rilem Committee Pore Structure and Properties of Materials*. Rapport. Lund Institute of Technology, Division of Building materials, 1973b.

G. Fagerlund. The international cooperative test of the critical degree of saturation method of assessing the freeze/thaw resistance of concrete. *Matériaux et Construction*, 10(4):231–253, 1977.

G. Fagerlund. Studies of the scaling, the water uptake and the dilation of specimens exposed to freezing and thawing in NaCl solution. In *Proceedings of RILEM committee 117 DC Freezing/thaw and de-icing resistance of concrete*, pages 37–66, Swden, 1991.

G. Fagerlund. Internal frost attack–State of the art. In *RILEM Proceedings on Frost Resistance of Concrete*, pages 321–338. Spon, London, 1997.

R. F. Feldman. The porosity and pore structure of hydrated portland cement paste. In J.P. Skalny L.R. Roberts, editor, *Pore Structure and Permeability of Cement based Materials*, volume 137, pages 59–73, Materials Research Society, Pittsburgh, PA, 1989.

R.F. Feldman. Sorption and length-change scanning isotherms of methanol and water on hydrated portland cement. In *Proc. of 5th Int. Congress on the Chemistry of Cement*, volume 3, pages 53–66. Cem. Assoc. of Japan, Tokyo, 1968.

R.F. Feldman and P.J. Sereda. A model for hydrated portland cement paste as deduced from sorption-length change and mechanical properties. *Matériaux et Construction*, 1(6):509–520, 1968.

G.H. Findenegg, S. Groβ, and Th. Michalski. Pore condensation in controlled-pore glass. an experimental test of the Saam-Cole theory. *Studies in Surface Science and Catalysis*, 87:71–80, 1994.

K. Fridh. *Internal frost damage in concrete–experimental studies of destruction mechanisms*. PhD thesis, Division of Building Materials, Lund Institute of Technology, 2005.

M. Geiker. Lecture notes on porosity development, moisture fixation, mechanisms and characterization. In the 1st training course of Nanocem MC ITN TRANSCEND, Maastricht, the Netherlands, 2011.

R.J. Good and R.S. Mikhail. The contact angle in mercury intrusion porosimetry. *Powder Technology*, 29(1):53–62, 1981.

E.A. Guggenheim. Application of statistical mechanics. Clarendon, 1966.

J. Hagymassy, S. Brunauer, and R.S. Mikhail. Pore structure analysis by water vapor adsorption: I. t-curves for water vapor. *Journal of Colloid and Interface Science*, 29(3):485–491, 1969.

A.J. Hailwood and S. Horrobin. Absorption of water by polymers: analysis in terms of a simple model. *Trans. Faraday Soc.*, 42:B084–B092, 1946.

E.W. Hansen, H.C. Gran, and E.J. Sellevold. Heat of fusion and surface tension of solids confined in porous materials derived from a combined use of NMR and calorimetry. *The Journal of Physical Chemistry B*, 101(35):7027–7032, 1997.

J.N. Hay and P.R. Laity. Observations of water migration during thermoporometry studies of cellulose films. *Polymer*, 41(16):6171–6180, 2000.

I. Hitchcock, E.M. Holt, J.P. Lowe, and S.P. Rigby. Studies of freezing–melting hysteresis in cryoporometry scanning loop experiments using NMR diffusometry and relaxometry. *Chemical Engineering Science*, 66(4):582–592, 2011.

Y. Hosokawa, K. Yamada, B. Johannesson, and L. Nilsson. Development of a multi-species mass transport model for concrete with account to thermodynamic phase equilibriums. *Materials and Structures*, 44(9):1577–1592, 2011.

J. Hundt and H. Kantelberg. Sorptionsuntersuchungen an zemestein, zementmörtel und beton (in German). *Deutscher Ausschuss für Stahlbeton*, 297:25–39, 1978.

T. Ishida, K. Maekawa, and T. Kishi. Enhanced modeling of moisture equilibrium and transport in cementitious materials under arbitrary temperature and relative humidity history. *Cement and Concrete Research*, 37(4):565–578, 2007.

K. Ishikiriyama and M. Todoki. Evaluation of water in silica pores using differential scanning calorimetry. *Thermochimica Acta*, 256(2):213–226, 1995a.

K. Ishikiriyama and M. Todoki. Pore size distribution measurements of silica gels by means of differential scanning calorimetry II. thermoporosimetry. *Journal of Colloid and Interface Science*, 171(1):103–111, 1995b.

K. Ishikiriyama, M. Todoki, and K. Motomura. Pore size distribution (PSD) measurements of silica gels by means of differential scanning calorimetry I. optimization for determination of PSD. *Journal of colloid and interface science*, 171(1):92–102, 1995.

K. Ishikiriyama, M. Todoki, K. H. Min, S. Yonemori, and M. Noshiro. Pore size distribution measurements for microporous glass using differential scanning calorimetry. *Journal of Thermal Analysis and Calorimetry*, 46(3-4):1177–1189, 1996.

M. Iza, S. Woerly, C. Danumah, S. Kaliaguine, and M. Bousmina. Determination of pore size distribution for mesoporous materials and polymeric gels by means of dsc measurements: thermoporometry. *Polymer*, 41(15):5885–5893, 2000.

M. Janz and B.F. Johannesson. Measurement of the moisture storage capacity using sorption balance and pressure extractors. *Journal of Building Physics*, 24(4):316–334, 2001.

H.M. Jennings. A model for the microstructure of calcium silicate hydrate in cement paste. *Cement and Concrete Research*, 30(1):101–116, 2000.

H.M. Jennings. Colloid model of C-S-H and implications to the problem of creep and shrinkage. *Materials and Structures*, 37(1):59–70, 2004.

H.M. Jennings. Refinements to colloid model of C–S–H in cement: CM–II. *Cement and Concrete Research*, 38(3):275–289, 2008.

H.M. Jennings and P.D. Tennis. Model for the developing microstructure in Portland cement pastes. *Journal of the American Ceramic Society*, 77(12):3161–3172, 1994.

H.M. Jennings, B.J. Dalgleish, and P.L. Pratt. Morphological development of hydrating tricalcium silicate as examined by electron microscopy techniques. *Journal of the American Ceramic Society*, 64(10):567–572, 1981.

H.M. Jennings, J.J. Thomas, D. Rothstein, and J.J. Chen. *Handbook of Porous Solids*, chapter Cement Paste as a Porous Material, pages 2971–3028. Wiley-VCH, 2002.

H.M. Jennings, J.J. Thomas, J.S. Gevrenov, G. Constantinides, and F.-J. Ulm. A multi-technique investigation of the nanoporosity of cement paste. *Cement and Concrete Research*, 37(3):329–336, 2007.

H.M. Jennings, J.W. Bullard, J.J. Thomas, J.E. Andrade, J.J. Chen, and G.W. Scherer. Characterization and modeling of pores and surfaces in cement paste. *Journal of Advanced Concrete Technology*, 6(1):5–29, 2008.

B. Johannesson. *Transport and sorption phenomena in concrete and other porous media*. PhD thesis, Division of Building Materials, Lund University, 2000.

B. Johannesson. Dimensional and ice content changes of hardened concrete at different freezing and thawing temperatures. *Cement and Concrete Composites*, 32(1):73–83, 2010.

B. Johannesson. History of cement and concrete (2A). Lecture notes for Introduction to Concrete Technology (11563), Technical University of Denmark, 2011a.

B. Johannesson. The hydration process of Portland cements (4A). Lecture notes for Introduction to Concrete Technology (11563), Technical University of Denmark, 2011b.

B. Johannesson. Moisture fixation in mature concrete and other porous materials (8A). Lecture notes for Introduction to Concrete Technology (11563), Technical University of Denmark, 2011c.

B. Johannesson, 2012. Private Communication.

B. Johannesson and P. Utgenannt. Microstructural changes caused by carbonation of cement mortar. *Cement and Concrete Research*, 31(6):925–931, 2001.

R. Kimmich. *NMR: tomography, diffusometry, relaxometry*, volume 432. Springer Berlin, 1997.

A. Kirby. *CCCC Kick the habit; A UN guide to climate neutrality.* United Nations, Environment Management Group, 2008.

A.M. Kjeldsen and M.R. Geiker. On the interpretation of low temperature calorimetry data. *Materials and Structures*, 41(1):213–224, 2008.

K.R. Kloetstra, H.W. Zandbergen, M.A. Koten, and H. Bekkum. Thermoporometry as a new tool in analyzing mesoporous MCM-41 materials. *Catalysis Letters*, 33(1): 145–156, 1995.

S.H. Kosmatka and W.C. Panarese. *Design and control of concrete mixtures*. Portland Cement Association, 2002.

W. Kuhn, E. Peterli, and H. Majer. Freezing point depression of gels produced by high polymer network. *Journal of Polymer Science*, 16(82):539–548, 1955.

D.A. Kulik. Improving the structural consistency of C-S-H solid solution thermodynamic models. *Cement and Concrete Research*, 41(5):477–495, 2011.

E.E. Lachowski and S. Diamond. Investigation of the composition and morphology of individual particles of portland cement paste: 1. C-S-H gel and calcium hydroxide particles. *Cement and Concrete Research*, 13(2):177–185, 1983.

M.R. Landry. Thermoporometry by differential scanning calorimetry: experimental considerations and applications. *Thermochimica acta*, 433(1-2):27–50, 2005.

I. Langmuir. The constitution and fundamental properties of solids and liquids. Part I. solids. *Journal of the American Chemical Society*, 38(11):2221–2295, 1916.

C.K. Lin, J.N. Chen, and C.C. Lin. An NMR, XRD and EDS study of solidification/stabilization of chromium with Portland cement and C_3S. *Journal of Hazardous Materials*, 56(1):21–34, 1997.

G.G. Litvan et al. Phase transitions of adsorbates. I. specific heat and dimensional changes of the porous glass-water system. *Canadian Journal of Chemistry*, 44(22): 2617–2622, 1966.

H. Liu, L. Zhang, and N.A. Seaton. Determination of the connectivity of porous solids from nitrogen sorption measurements–II. generalisation. *Chemical Engineering Science*, 47(17-18):4393–4404, 1992.

F.W. Locher, W. Richartz, and S. Sprung. Erstarren von Zement (in German). *Zement Kalk Gips*, 29(10):435–442, 1976.

B. Lothenbach. Thermodynamic equilibrium calculations in cementitious systems. *Materials and Structures*, 43(10):1413–1433, 2010.

B. Lothenbach and F. Winnefeld. Thermodynamic modelling of the hydration of portland cement. *Cement and Concrete Research*, 36(2):209–226, 2006.

G.M. Marion and J.S. Kargel. The FREZCHEM model. *Cold Aqueous Planetary Geochemistry with FREZCHEM: From Modeling to the Search for Life at the Limits*, pages 19–77, 2008.

P.J. McDonald, V. Rodin, and A. Valori. Characterisation of intra-and inter-C–S–H gel pore water in white cement based on an analysis of NMR signal amplitudes as a function of water content. *Cement and Concrete Research*, 40(12):1656–1663, 2010.

J.P. Mercier, W. Kurz, and G. Zambelli. *Introduction à la science des matériaux*. Traité des matériaux. Presses Polytechniques et Universitaires Romandes, 1999.

P. K. Metha and P.J.M. Monteiro. *Concrete: Microstructure, Properties, and Materials*. McGraw-Hill, 3rd edition, 2005.

S. Mindess, J.F. Young, and D. Darwin. *Concrete*. Prentice Hall, Pearson Education, 2nd edition, 2003.

J. Mitchell, J.B.W. Webber, and J.H. Strange. Nuclear magnetic resonance cryoporometry. *Physics Reports*, 461(1):1–36, 2008.

A.C.A. Muller, K.L. Scrivener, A.M. Gajewicz, and P.J. McDonald. Densification of C-S-H measured by ^{1}H NMR relaxometry. *The Journal of Physical Chemistry C*, 117(1):403–412, 2012.

A.V. Neimark. Percolation theory of capillary hysteresis phenomena and its application for characterization of porous solids. *Studies in Surface Science and Catalysis*, 62:67–74, 1991.

E.B. Nelson and D. Guillot. *Well Cementing*. Schlumberger, 2006.

A.M. Neville. *Properties of concrete*. Prentice Hall, 4th edition edition, 1995.

V.T. Ngala and C.L. Page. Effects of carbonation on pore structure and diffusional properties of hydrated cement pastes. *Cement and Concrete Research*, 27(7):995–1007, 1997.

K.I.A. Okoh and C. Skaar. Moisture sorption isotherms of the wood and inner bark of ten southern us hardwoods. *Wood and Fiber Science*, 12(2):98–111, 1980.

L.J. Parrott. *A Review of Carbonation in Reinforced Concrete*. British Cement Association, 1987.

D. Pearson and A.J. Allen. A study of ultrafine porosity in hydrated cements using small angle neutron scattering. *Journal of Materials Science*, 20(1):303–315, 1985.

E.L. Perkins, J.P. Lowe, K.J. Edler, N. Tanko, and S.P. Rigby. Determination of the percolation properties and pore connectivity for mesoporous solids using NMR cryodiffusometry. *Chemical Engineering Science*, 63(7):1929–1940, 2008.

O.V. Petrov and I. Furó. Nmr cryoporometry: Principles, applications and potential. *Prog. Nucl. Magn. Reson. Spectrosc*, 54(2):97–122, 2009.

M. Pigeon and R. Pleau. *Durability of concrete in cold climates*. Number 4. Taylor & Francis, 1995.

T.C. Powers. The air requirement of frost resistant concrete. In *Proceedings of the Highway Research Board*, volume 29, pages 184–211, 1949.

T.C. Powers. Basic considerations pertaining to freezing-and-thawing tests. In *Proceedings of the American Society for Testing and Materials*, volume 55, pages 1132–1155, 1955.

T.C. Powers. Structure and physical properties of hardened Portland cement paste. *Journal of the American Ceramic Society*, 41(1):1–6, 1958.

T.C. Powers. Physical properties of cement paste. In *Proceedings of the Fouth International Syposium on the Chemistry of Cement*, pages 577–609, Washington, D.C., 1960.

T.C. Powers and T.L. Brownyard. Studies of the physical properties of hardened portland cement paste. In *ACI Journal Proceedings*, volume 43, pages 549–602, 1947.

T.C. Powers and R.A. Helmuth. Theory of volume changes in hardened portland cement paste during freezing. In *Proceeding of Highway Research Board*, volume 32, pages 285–297, 1953.

S. Poyet. Experimental investigation of the effect of temperature on the first desorption isotherm of concrete. *Cement and Concrete Research*, 39(11):1052–1059, 2009.

S. Poyet and S. Charles. Temperature dependence of the sorption isotherms of cement-based materials: Heat of sorption and Clausius–Clapeyron formula. *Cement and Concrete Research*, 39(11):1060–1067, 2009.

J.F. Quinson and M. Brun. Progress in thermoporometry. *K. K. Unger, J. Rouquerol, K. S.W Sing and H. Kral (eds): Characterization of Porous Solids, Elsevier, Amsterdam*, page 307, 1988.

J.F. Quinson, M. Astier, and M. Brun. Determination of surface areas by thermoporometry. *Applied Catalysis*, 30(1):123–130, 1987.

F. Radjy, E.J. Sellevold, and K.K. Hansen. Isoteric vapor pressure–temperature data for water sorption in hardened cement paste: enthalpy, entropy and sorption isotherms at different temperatures. Technical Report BYG-DTU R057, Technical University of Denmark(DTU), Lyngby, Denmark, 2003.

P.I. Ravikovitch, S.C.Ó. Domhnaill, A.V. Neimark, F. Schüth, and K.K. Unger. Capillary hysteresis in nanopores: theoretical and experimental studies of nitrogen adsorption on MCM-41. *Langmuir*, 11(12):4765–4772, 1995.

L. Redler. Quantitative X-ray diffraction analysis of high alumina cements. *Cement and Concrete Research*, 21(5):873–884, 1991.

I.G. Richardson and G.W. Groves. Microstructure and microanalysis of hardened ordinary portland cement pastes. *Journal of Materials Science*, 28(1):265–277, 1993.

J. Riikonen, J. Salonen, and V.P. Lehto. Utilising thermoporometry to obtain new insights into nanostructured materials (review part 1). *Journal of Thermal Analysis and Calorimetry*, 105:811–821, 2011a.

J. Riikonen, J. Salonen, and V.P. Lehto. Utilising thermoporometry to obtain new insights into nanostructured materials (review part 2). *Journal of Thermal Analysis and Calorimetry*, 105:823–830, 2011b.

G.W. Scherer. Freezing gels. *Journal of non-crystalline solids*, 155(1):1–25, 1993.

G.W. Scherer and J.J. Valenza II. *Materials Science of Concrete*, volume VII, chapter Mechanisms of Frost Damage, pages 209–246. 2005.

G.W. Scherer, II Valenza, J. John, and G. Simmons. New methods to measure liquid permeability in porous materials. *Cement and Concrete Research*, 37(3):386–397, 2007.

K.L. Scrivener. *The development of microstructure during the hydration of Portland cement*. PhD thesis, Imperial College, London, 1984.

K.L. Scrivener. *Materials Science of Concrete*, volume 1, chapter The microstructure of concrete. American Ceramic Society, Westerville, 1989.

K.L. Scrivener. Backscattered electron imaging of cementitious microstructures: understanding and quantification. *Cement and Concrete Composites*, 26(8):935–945, 2004.

K.L. Scrivener. Lecture notes on general concepts and microstructure of cementitious materials. In the 1st training course of Nanocem MC RTN, Aalborg, Denmark, 2006.

K.L. Scrivener. Lecture notes on basic concepts, cement production, microstructural characterization methods, hydration and microstructure of cementitious materials. In the 1st training course of Nanocem MC ITN TRANSCEND, Maastricht, the Netherlands, 2011.

K.L. Scrivener, T. Füllmann, E. Gallucci, G. Walenta, and E. Bermejo. Quantitative study of portland cement hydration by X-ray diffraction/Rietveld analysis and independent methods. *Cement and Concrete Research*, 34(9):1541–1547, 2004.

N.A. Seaton. Determination of the connectivity of porous solids from nitrogen sorption measurements. *Chemical Engineering Science*, 46(8):1895–1909, 1991.

N.A. Seaton, J. Walton, et al. A new analysis method for the determination of the pore size distribution of porous carbons from nitrogen adsorption measurements. *Carbon*, 27(6):853–861, 1989.

E. Sellevold and D. Bager. Some implications of calorimetric ice formation results for frost reistance testing of concrete. *in Beton og Frost, Dansk Beton Forening*, 22: 47–74, 1985.

S. Setunge, N. Nguyen, B. Alexander, and L. Dutton. Leaching of alkali from concrete in contact with waterways. *Water, Air, & Soil Pollution: Focus*, 9(5-6):381–391, 2009.

M.J. Setzer. Mechanical stability criterion, triple-phase condition, and pressure differences of matter condensed in a porous matrix. *Journal of Colloid and Interface Science*, 235(1):170–182, 2001a.

M.J. Setzer. Micro-ice-lens formation in porous solid. *Journal of Colloid and Interface Science*, 243(1):193–201, 2001b.

E. Shiko, K.J. Edler, J.P. Lowe, and S.P. Rigby. Probing the impact of advanced melting and advanced adsorption phenomena on the accuracy of pore size distributions from cryoporometry and adsorption using NMR relaxometry and diffusometry. *Journal of Colloid and Interface Science*, 385(1):183–192, 2012.

C.G. Shull, P.B. Elkin, and L.C. Roess. Physical studies of gel microstructure. *Journal of the American Chemical Society*, 70(4):1410–1414, 1948.

K. Sing. The use of nitrogen adsorption for the characterisation of porous materials. *Colloids and Surfaces A: Physicochemical and Engineering Aspects*, 187:3–9, 2001.

K. Sing, D. Everett, R. Haul, L. Moscou, R. Pierotti, J. Rouquerol, and T. Siemieniewska. Reporting physisorption data for gas/solid systems. *Pure Appl. Chem*, 57(4):603–619, 1985.

K. S. W. Sing. *Colloid Science*, volume 1. Royal Society of Chemistry, 1973. doi: 10.1039/9781847557421-00001.

K.S.W. Sing. Adsorption methods for the characterization of porous materials. *Advances in Colloid and Interface science*, 76:3–11, 1998.

K.S.W. Sing. Characterization of porous materials: past, present and future. *Colloids and Surfaces A: Physicochemical and Engineering Aspects*, 241(1):3–7, 2004.

O. Šolcová, L. Matějová, and P. Schneider. Pore-size distributions from nitrogen adsorption revisited: Models comparison with controlled-pore glasses. *Applied Catalysis A: General*, 313(2):167–176, 2006.

J.H. Strange, J. Mitchell, and J.B.W. Webber. Pore surface exploration by NMR. *Magnetic Resonance Imaging*, 21(3-4):221–226, 2003.

L.J. Struble. Quantitative phase analysis of clinker using X-ray diffraction. *Cement, Concrete and Aggregates*, 13(2), 1991.

P.E. Stutzman. Scanning electron microscopy in concrete petrography. *Materials Science of Concrete Special Volume: Calcium Hydroxide in Concrete, Proceedings-Anna Maria Island-Floride*, pages 59–72, 2000.

Z. Sun and G.W. Scherer. Pore size and shape in mortar by thermoporometry. *Cement and Concrete Research*, 40(5):740–751, 2010.

H.F.W. Taylor. Modification of the Bogue calculation. *Advances in Cement Research*, 2(6):73–77, 1989.

H.F.W. Taylor. *Cement chemistry*. Thomas Telford, London, 2nd edition, 1997.

P.D. Tennis and H.M. Jennings. A model for two types of calcium silicate hydrate in the microstructure of portland cement pastes. *Cement and Concrete Research*, 30 (6):855–863, 2000.

J.J. Thomas and H.M. Jennings. A colloidal interpretation of chemical aging of the C-S-H gel and its effects on the properties of cement paste. *Cement and Concrete Research*, 36(1):30–38, 2006.

J.J. Thomas, H.M. Jennings, and A.J. Allen. The surface area of hardened cement paste as measured by various techniques. *Concr. Sci. Eng*, 1:45–64, 1999.

W. Thomson. On the equilibrium of vapour at a curved surface of liquid. *Philos. Mag.*, 42:448–452, 1871.

E.O. Timmermann. Multilayer sorption parameters: BET or GAB values? *Colloids and Surfaces A: Physicochemical and Engineering Aspects*, 220(1-3):235–260, 2003.

A. Valori. *Characterisation of cementitious materials by ^1H NMR*. PhD thesis, University of Surrey, 2009.

K. van Breugel. *Simulation of hydration and formation of structure in hardening cement-based materials*. PhD thesis, Delft University of Technology, 1991.

C. Van den Berg. *Vapour sorption equilibria and other water-starch interactions: a physico-chemical approach*. PhD thesis, Wageningen Agricultural University, the Netherlands, 1981.

C. Van den Berg. Description of water activity of foods for engineering purposes by means of the gab model of sorption. *Engineering and Food*, 1:311–321, 1984.

I. van Odler. *Lea's Chemistry of Cement and Concrete*, chapter Hydration, Setting, and Hardening of Portland Cement, pages 241–298. Arnold, London, U.K., 4th edition, 1998.

A. Venkateswaran. Sorption of aqueous and nonaqueous media by wood and cellulose. *Chemical Reviews*, 70(6):619–637, 1970.

J. Villadsen. Pore structure in cement based materials. Technical Report 277, Building Materials Laboratory, Technical University, Denmark, 1992.

I. Wadsö and L. Wadsö. A new method for determination of vapour sorption isotherms using a twin double microcalorimeter. *Thermochimica Acta*, 271:179–187, 1996.

L. Wadsö and N. Markova. A double twin isothermal microcalorimeter. *Thermochimica Acta*, 360(2):101–107, 2000.

G.C. Wall and R.J.C. Brown. The determination of pore-size distributions from sorption isotherms and mercury penetration in interconnected pores: The application of percolation theory. *Journal of Colloid and Interface Science*, 82(1):141–149, 1981.

MC ITN TRANSCEND Website. URL `http://www.nanocem.org/index.php?id=282`. Acessed on January 05, 2014.

A. Wheeler. Reaction rates and selectivity in catalyst pores. In P.H. Emmett, editor, *Catalysis Part II.*, page 105. Rheinhold Publ. Corp., 1955.

Wikipedia. Thermoporometry and cryoporometry. URL `http://en.wikipedia.org/wiki/Thermoporometry_and_cryoporometry`. Accessed on October 20, 2011.

H.H. Willems and K.B. Van Der Velden. A gravimetric study of water vapour sorption on hydrated cement pastes. *Thermochimica Acta*, 82(1):211–220, 1984.

D.N. Winslow and S. Diamond. Specific surface of hardened portland cement paste as determined by small-angle X-ray scattering. *Journal of the American Ceramic Society*, 57(5):193–197, 1974.

F.H. Wittmann. Trends in research on creep and shrinkage of concrete. In *The Engineering Foundation Conference, Franklin Pierce College*, pages 143–161, 1979.

Chemistry World. The concrete conundrum, March 2008.

M. Wu, B. Johannesson, and M. Geiker. Determination of ice content in hardened concrete by low temperature calorimetry: influence of baseline calculation and heat of fusion of confined water. *Journal of Thermal Analysis and Calorimetry*, 115(2): 1335–1351, 2014.

T. Yamamoto, A. Endo, Y. Inagi, T. Ohmori, and M. Nakaiwa. Evaluation of thermoporometry for characterization of mesoporous materials. *Journal of Colloid and Interface Science*, 284(2):614–620, 2005.

V.P. Zhdanov, V.B. Fenelonov, and D.K. Efremov. Determination of pore-size distribution from sorption isotherms: Application of percolation theory. *Journal of Colloid and Interface Science*, 120(1):218–223, 1987.

Part III

Appended Papers

Paper I

Determination of ice content in hardened concrete by low-temperature calorimetry: influence of baseline calculation and heat of fusion of confined water

M. Wu, B. Johannesson, M. Geiker

Published in: *Journal of Thermal Analysis and Calorimetry, 2014*

J Therm Anal Calorim (2014) 115:1335–1351
DOI 10.1007/s10973-013-3520-6

Determination of ice content in hardened concrete by low-temperature calorimetry

Influence of baseline calculation and heat of fusion of confined water

Min Wu · Björn Johannesson · Mette Geiker

Received: 16 May 2013 / Accepted: 5 November 2013 / Published online: 15 December 2013

Abstract Low-temperature calorimetry has been used to determine the ice content in concrete at different temperatures when exposed to low-temperature environments. However, the analysis of the ice content from the measured data of heat flow is not straightforward. In this study, two important factors influencing the ice content calculation are discussed. The importance of the baseline determination for the calculation of the ice content is realized. Two different methods of generating the baseline are discussed. First, the 'J-baseline' is discussed which is a recently proposed extrapolation method based on the accumulated heat curves measured in the freezing and the melting process. Second, the 'C-baseline' is discussed in which a calculated baseline is used where the heat capacity of both water and ice and the phase changing behaviour under different testing temperatures are considered. It turns out that both the 'J-baseline' method and the 'C-baseline' method can be used to calculate the approximate baseline. The heat of fusion of the water confined in small pores is another important parameter to be considered in ice content calculation. This property must be carefully analyzed in order to accurately calculate the ice contents at different temperatures in the freezing and melting process. It should be noted that there is no general agreement on how to obtain the important temperature dependence of the heat of fusion of water confined in small pores. By performing comparison studies, the present study shows the influence of the different values of the heat of fusion commonly adopted on the calculated ice content for the studied concrete samples. The importance and necessity to use an accurate value of the heat of fusion is emphasized. Based on the calculation of the baseline proposed in this work and by carefully selecting the values for the heat of fusion, the ice content in a hardened concrete sample is expected to be estimated with an acceptable accuracy.

keywords Low-temperature calorimetry (LTC) · Ice formation · Baseline calculation · Heat of fusion · Thermoporometry · Cryoporometry

Electronic supplementary material The online version of this article (doi:10.1007/s10973-013-3520-6) contains supplementary material, which is available to authorized users.

M. Wu (✉) · B. Johannesson
Department of Civil Engineering, Technical University of Denmark, Building 118, 2800 Lyngby, Denmark
e-mail: miwu@byg.dtu.dk

M. Geiker
Department of Structural Engineering, Norwegian University of Science and Technology, Trondheim, Norway

Introduction

Concrete is the most widely used construction material. As many structures have requirements to a long service life, durability is given special emphasis. In cold regions, the degradation of concrete is, among other reasons, often related to the freeze/thaw resistance (the resistance against frost damage). Concrete itself is a porous material with a rather complicated pore system, whose pore sizes can range from nanometer to millimeter [1, 2]. Due to the confinement of pores with different sizes, water present in the pores of concrete freezes at different temperatures when it is exposed to low-temperature environments. The amount of ice formed in concrete at low temperatures is an important property when studying the freeze/thaw durability [3].

Low-temperature (micro-) calorimetry (LTC), which is also known as thermoporosimetry and sometimes is

referred to as thermoporometry or cryoporometry [4], can be used to determine the ice content in concrete at different temperatures by carefully studying the freezing/melting behaviour of the confined water in the pores. The basic concept is that freezing of water is an exothermic process and the melting of ice is an endothermic process. The LTC instrument (calorimeter) records the heat flow of the sample at different testing temperatures. By analyzing the heat flow due to ice formation or melting at each temperature, the ice content in the freezing and melting process can be calculated by using the heat of fusion of the confined water/ice.

In addition to the determination of ice content, LTC is often adopted as a method to study the porosity of a material. Porosity characterization by using the measured freezing/melting temperature shift of a liquid, with which the porous material is saturated, was pioneered by researchers in a study of organic gels as early as 1950s [5]. The method was generalized and has been applied to different materials, e.g. inorganic materials [6], organic materials [7, 8, 9, 10], soil [11] and cement based materials [4, 12], etc. A detailed description of the thermodynamic basis for the derivation of the pore size distribution based on LTC measurement is attributed to Brun et al. [13]. By considering the thermodynamics, it shows that there is a unique relation between the triple point temperature of the probe liquid confined in the pores of a material and the curvature of the solid–liquid interface. Thus, by using the thermodynamic parameters of the probe liquid, i.e. surface tension, heat capacity and heat of fusion, the approximate relation between the freezing/melting temperature and the pore size can be quantified. Water is commonly chosen as a probe liquid. The advantage of using water as the probe liquid is twofold. First, water is a well-studied substance implying that the standard thermodynamic parameters are well documented; second, the specific heat capacity of water is much larger compared with that of other liquids, especially organic solutions. Thus, the measured heat flow during the freezing or melting process is comparably large and even a small amount of water undergoing phase change can be detected and recorded by the LTC instrument. However, for the determination of pore size distribution for cement-based materials, additional information is needed. For example, the solidification mechanism of the water confined in small pores must be constituted by suitable assumptions. Different assumptions about the solidification mechanisms of confined water are discussed, e.g. in [13, 14, 15, 16, 17]. The concept of un-freezable layer of water (or δ-layer) is introduced in [12, 13] and the effect of ion concentrations in the pore solution is discussed in [4, 12, 18]. It should also be mentioned that in the context of using LTC to determine pore size distribution, the thermodynamic relation between pore size and the depressed phase change temperature is often derived based on the prerequisite that the pores under study are fully saturated. That is, there is only one interface, i.e. the solid–liquid interface, in the pore system. If the pores under consideration are not fully saturated, more interfaces could exist (i.e. the vapor–liquid and the vapor–solid interface) and there are several possibilities with respect to the coexistence of the interfaces, e.g. see [6, 12, 13, 19, 20], which makes the quantitative determination of the relation between pore size and the depressed phase change temperature extremely difficult. This is of particular relevance for air-entrained cement-based materials, in which proper care should be taken to ensure fully saturation. The impact of sample saturation on the detected porosity of hardened concrete is discussed in a relatively detailed manner in [21]. Further discussions of related aspects fall outside the scope of this paper.

The study of ice formation in cement-based materials dates back to early 1970s [12, 22, 23]. Systematic study of cement-based materials using LTC was initiated in early 1980s [24, 25], in which some fundamentals for the application of the method, including the testing procedures, ice calculation method and the heat of fusion of pore confined water *versus* temperature, were explored. Following that, LTC was used to investigate important aspects of cement-based materials, e.g. the stability of the materials to temperature and drying treatment [26, 27, 28], effects of supplementary materials on the pore structure of the materials [25, 29, 30]. Other relevant studies in this regard include, e.g. [31, 32].

Although LTC has been adopted to determine the ice content in cement and concrete materials for several decades, there are some aspects that need to be further addressed. The heat flow measured by a LTC instrument at each time consists of two parts: (1) the contribution from the heat capacity of the system (including water and ice in the concrete sample, and also the concrete skeleton matrix), which will be mentioned as the 'heat flow baseline' or simply 'baseline' in our discussion; and (2) the contribution due to phase transition. In order to calculate the ice content, one needs to know how much energy goes to form or melt ice at each temperature level under consideration, indicating that the baseline should be determined. During each test, the ice in the pores of the concrete will be continuously forming/melting as the temperature decreases/increases (due to the relative wide distribution of the pores in concrete), which means that the baseline of the heat flow is continuously changing due to the change in the proportion of ice and liquid water confined in the pores. What makes it even more difficult to determine the baseline is that the heat capacities of water, ice and the solid matrix are temperature dependent. Moreover, the water under study in this case is the water confined in very small pores.

Although bulk water is a well-studied substance, some of the thermodynamic parameters, e.g. heat of fusion, of the confined water and ice still need to be further investigated.

It should be noted that LTC is not a straightforward method since: (1) the measurement provides information on the overall apparent heat capacity of the sample at different temperatures, not just that due to the water/ice phase transition; and (2) the heat of fusion of the confined water/ice needs to be known beforehand since this method itself cannot measure the temperature dependence of the heat of fusion. This study focuses on the calculation of ice content from measured data of heat flow by a LTC instrument. Comparison studies will be performed to demonstrate the impact of two different ways of calculating baseline and the different values of heat of fusion for confined water commonly adopted in literature on the calculated ice content.

Experimental data

This investigation is based on existing experimental data on micro-concrete samples with three different water-to-cement ratios (w/c = 0.4, 0.5 and 0.6) and different target air contents of 2, 4 and 6 %[1]. The details of the experimental study are presented in [33, 34, 35].

The cement content for the w/c = 0.4 concrete samples with target air contents of 2, 4 and 6 % were 515, 525 and 525 kg m^{-3}, respectively. The corresponding values for the w/c = 0.5 and w/c = 0.6 samples were 475, 480 and 480 kg m^{-3} and 340, 350 and 335 kg m^{-3}. Approximately equal amount of granite aggregates with two different size ranges, i.e. 0–3 mm and 4–8 mm, was used to prepare all the mixes. The samples were produced in 120 L batches in the laboratory. After mixing, the fresh concrete was placed into moulds. The moulds filled with fresh concrete were vibrated for a few seconds before a plastic film was placed on top to prevent evaporation. After curing under sealed condition for one day, the micro-concrete cylinders used in the calorimetric measurements were core-drilled and sawn into small cylinders with the diameter of 14 mm and the length of 60 mm. The size of the samples was chosen to fit the calorimetric device used in the investigation. Based on visual inspection it was concluded that no damage of samples was introduced by the early drilling and sawing. The samples were stored in water at about 20 °C for about four months before testing (mentioned as capillary saturated samples).

[1] In concrete technology, the freeze/thaw resistance of concrete can be improved by entraining a certain amount of high-quality air voids, typically 4–6 vol%, e.g. see [3].

A Calvet-type scanning calorimeter (SETARAM) was used for this investigation, which was calibrated and operated to work between about 20 and −130 °C. The temperature scanning consisted of a cycle starting at 20 °C and going down to about −80 °C and then back to 20 °C. The adopted cooling and heating rate was 5.4 °C h^{-1}. The samples were saturated surface dry when placed in the calorimeter. A totally dried concrete sample, of the same dimensions as the samples, was used as the reference sample in the calorimetric measurements. The same reference sample was used throughout the investigation. By using this type of reference sample, it was possible to simplify the calibration of the measurement. During the testing, the calorimeter records the calibrated heat supplied to or released from the sample. This means that the instrument measures the difference of the heat flow between the reference and the sample chamber, thus the overall heat flow response due to the confined pore water and its phase change in a sample at different temperatures can be determined. At the same time, the corresponding temperature of the sample chamber is also recorded.

The procedures of calorimetric measurements performed here differ from the 'old' ones as adopted in, e.g. [4, 28], mainly by two aspects: (1) the cooling and heating rate adopted in this work were slightly higher (which were 3.3 °C h^{-1} and 4.1 °C h^{-1}, respectively, in the 'old' procedures); (2) AgI was used as a nucleation agent in the 'old' procedures, while it was not used in this work. It is noted that in literature, there is no general agreement on the cooling and heating rate and they vary quite a lot, e.g. from about 15 °C min^{-1} to 1 °C h^{-1} [36]. The study on concrete samples [20] showed that the cooling/heating rate between 3 and about 8 °C h^{-1} does not have an important impact on the measured heat flow and further the calculated ice content. For this reason we think that the cooling/heating rate used in this work would have little impact on the ice content calculation compared with the 'old' procedures. The use of AgI helps to reduce supercooling effect. A typical water-saturated concrete sample without AgI freezes at about −8 or −9 °C [33] while it could be reduced to about −4 or −5 °C by using AgI [4]. On the other hand, the added AgI may enter into the pore water, which could possibly complicate the analysis of the freezing behaviour, e.g. affecting the freezing point and the heat of fusion, etc. Since adding AgI does not completely cancel out the supercooling effect and it may complicate the analysis of the data, it was not added in this work.

After a calorimetric measurement, the sample was dried under about 105 °C till constant mass. By doing so, the total water content of the sample was determined by the mass difference between this dried state and that before the calorimetric measurement (saturated surface dry).

More detailed explanations about the sample preparation and calorimetric measurements can be found in [33].

Interpretation of the measurement results

Baseline and ice content calculation

As discussed in Introduction, in order to calculate the ice content, the baseline of the heat flow needs to be determined. The baseline will be continuously changing during the water/ice phase transition. This is among other things due to that the heat capacity of water is about twice as large as that of the ice (e.g. compare Eq. 6 with Eq. 7). Therefore, the baseline will be moved upwards when ice transforms into water and downwards when water changes into ice, with the magnitude depending on the involved amount of water/ice that underwent phase transition. The difficulty of calculating the baseline in an exact manner is due to the continuously changing proportion of ice and water and the dependency of the heat capacities of water, ice and the concrete skeleton matrix on the temperature. This is especially true when the temperature in testing covers a large range. In the following discussion, two methods of calculating the baseline and the ice content will be presented.

'J-baseline' method

A detailed explanation of the original 'J-baseline' method is presented and discussed in [33]. Initially, the measured heat flow curves are corrected assuming a closed system, i.e. the heat developed during freezing corresponds to the heat loss during melting. After the initial calibration, the accumulated heat is integrated and shown as the solid line in Fig. 1b, from the corrected heat flow curve as shown in Fig. 1a. The first step in the analysis of the integrated heat curves according to Fig. 1b concerns the extrapolation of the initial total heat capacity of the system before freezing starts, which is shown in the curve denoted by *a* in Fig. 1b. The extrapolated heat capacity for the same system when all of the ice has been formed can be constructed in the similar manner. Hence, the curve denoted by *b* as shown in Fig. 1b can be constructed. The energy jump denoted by A in Fig. 1b is the accumulated heat difference between the extrapolated fictive energy level, given by the curve *a*, and the measured total accumulated energy level at the end of the active ice-forming stage (when the accumulated heat curve becomes linear). Similarly, the energy jump denoted by B is the heat difference between the extrapolated fictive energy level as given by the curve *b* and the true measured total accumulated energy level at the time when all of the ice is melted. It is concluded that the energy jump A is an underestimated value compared with the true energy jump caused by the solidification energy involving the formation of ice. This is because ice is continuously formed during the freezing process which will result in a continuous decrease of the baseline as more ice is formed. The decrease of the baseline is not reflected in the extrapolated baseline associated with the curve *a*. In a similar manner, the energy jump from the frozen stage to the stage when all ice is melted given by the 'distance' B in Fig. 1b overestimates the total fusion energy for the melting process.

Based on the above discussion, it is realized that the true total required energy to convert all water to ice or *vice versa* must lie somewhere in between the values indicated by the 'distances' A and B in Fig. 1b. By adopting an explicit and somewhat crude assumption that the total

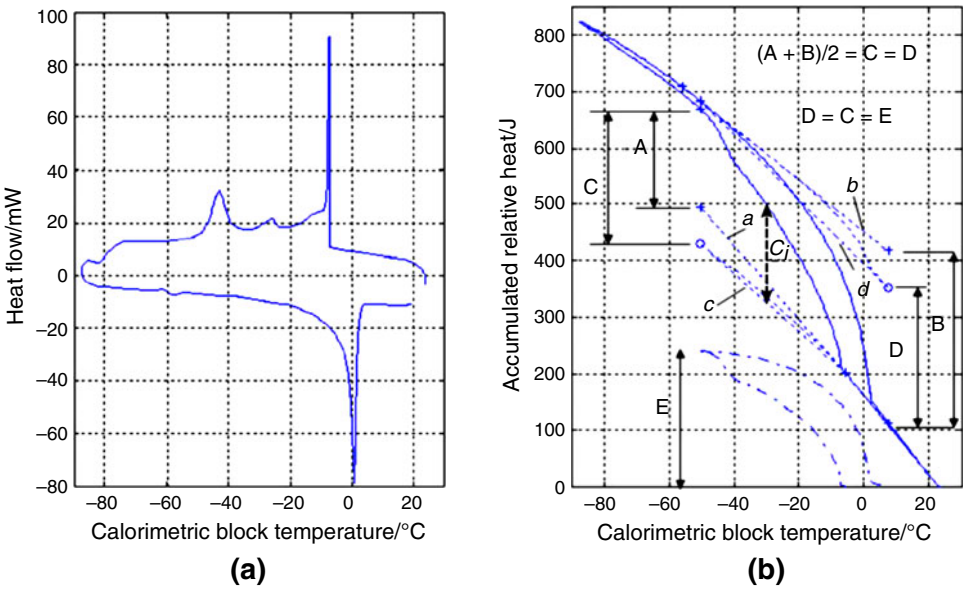

Fig. 1 An example showing how to construct the baseline using 'J-method'. **a** measured heat flow data from the calorimeter; **b** integrated values of heat responses (*solid line*) and data treatment to achieve a proper baseline (adapted from [33])

required energy to convert all water to ice or *vice versa* of the sample is the average value of A and B, i.e. (A + B)/2, a baseline can be constructed. This assumption was checked for its performance by running a calorimetric test from room temperature to about −20 °C using pure water in [20]. The results in the verification testing show a deviation of about 2 % of the tabulated heat of fusion of ice. For this reason, it is assumed that the adopted direct method performs in a manner which is acceptable. It should be remarked, however, that this type of verification does not include the varying freezing temperatures of water due to the pore confinement.

The average value of the energy jumps C = D defined by A and B, as shown in Fig. 1b, is used to determine new endpoints (marked with circles on the curves denoted by *c* and *d*). The next step in the procedure consists of making a non-linear weighting between the extreme curves *a* and *c* during the freezing process and between the extreme curves *b* and *d* during the melting process. The non-linear weighting is conducted like this: at any temperature (taking the freezing as an example), the 'distance' between the accumulated heat curve and the true baseline is calculated as the 'distance' between the accumulated heat curve and the curve *c*, denoted as C_i in Fig. 1b, multiplying by a factor of C_i /C. The same procedure is also applied to the melting curves. The two obtained weighted curves, i.e. the ones lying in between the curves *a* and *c* and in between *b* and *d*, are used as the baselines for the experiment from which the accumulated energy with respect to the ice formation can be determined. The obtained curves for accumulated energy during the ice formation and melting are also shown in the lower part of Fig. 1b. The ice content corresponding to each temperature can be calculated through dividing the accumulated heat by the heat of fusion of the confined water/ice.

It has been reported in many studies, e.g. in [7, 13, 18, 36–39], that there is a hysteresis behaviour in terms of ice content curves in the freezing and melting process, indicating that for the ice confined in the same pores, the ice formation temperature could be different from its melting temperature. As will be discussed later in "Heat of fusion of confined water/ice for ice content calculation" Section, the heat of fusion of the confined water/ice could be a temperature-dependent property. Consequently, in one measurement cycle consisting of a freezing and a melting process, the accumulated heat released in the freezing process is not necessarily equal to the heat absorbed in the melting process. Thus, the measured heat flow is not necessarily a closed system. It turns out that the initial calibration of the heat flow by assuming it is a closed system is not necessarily relevant. However, it should be noted that the maximum ice content formed in the freezing process should be equal to that melted in the melting process in one measuring cycle (mass conservation). By keeping this in mind, the curves of the accumulated energy can be further tuned by making additional assumptions concerning the temperature dependence of the heat of fusion ("Heat of fusion of confined water/ice for ice content calculation" Section) in order to give an estimate of the ice contents at different freezing and melting temperatures. The tuning is conducted by decreasing the slope of line *a* and increasing that of *b* with the same percentage (referring to Fig. 1b) if the ice calculated in the freezing is less than that in melting, and the other way around. The purpose of doing this further tuning is to ensure that the ice content determined from the freezing process is exactly the same as that from the melting process.

'C-baseline' method

As can be seen from the above discussion, the 'J-baseline' determination is an extrapolating process based on certain assumptions. Alternatively, it is possible to calculate the baseline and the ice content based on the heat capacities of ice and water by taking into account the phase changing behaviour of the confined water or ice in a sample under different temperatures in a test. The method has more theoretic basis and it will be mentioned as 'C-baseline' method in the following discussion. The 'C-baseline' method presented here is originated from a method established by Sun and Scherer in [18] with slight modification.

Before further discussion, a clarification should be made about the pore liquid in the concrete samples under this study. Actually, the liquid confined in the pores of concrete samples is not pure water, which contains certain ionic species [40, 41]. However, the pore liquid will be simply assumed as pure water first and the possible effect of the ions on the calculated results will be discussed later in "Results and discussion" Section.

The measured heat flow consists of two parts, the baseline and the heat flow due to phase transition. The baseline comprises the heat capacity of the whole system, including pore water and ice as well as the concrete skeleton matrix if no reference sample is used. The experimental data discussed in this paper were obtained using a reference sample of dried concrete with the same size as the samples tested, and we assume the concrete skeleton matrix has no influence on the measured heat flow. Thus, the overall heat capacity of the system contributed to the baseline in our testing is only attributed to the water and ice in the concrete sample. More discussion about the reference sample will be presented later.

The total heat flow into or out of a sample measured by the LTC instrument at any time is denoted by Q, while the baseline and the heat flow due to the phase transition at any time are denoted by Q_B and Q_S, respectively. Thus we have

$$Q = Q_B + Q_S \tag{1}$$

If h is used to denote the heat of the sample (not including the contribution from the phase transition) and t is the time, we have

$$Q_B = \mathrm{d}h/\mathrm{d}t \tag{2}$$

The cooling or heating rate in the testing is q and T is the temperature, then

$$q = \mathrm{d}T/\mathrm{d}t \tag{3}$$

Accordingly, the overall heat capacity of the system at any time C_p can be derived and expressed as

$$mC_p = \frac{\mathrm{d}h}{\mathrm{d}T} = \frac{\mathrm{d}h}{\mathrm{d}t} \cdot \frac{\mathrm{d}t}{\mathrm{d}T} = \frac{Q_B}{q} \tag{4}$$

where m is the total mass of the confined water and ice in the sample. In terms of the cooling/heating rate q, it should be noted that though it is often set at a constant value during a measurement, there is always a certain degree of drifting or fluctuation, big or small. As shown in Eq. 4, the baseline Q_B depends on the cooling/heating rate q, which means the drifting or fluctuation of q will affect the measured Q_B and thus the measured overall heat flow Q. Thus, it makes more sense to take into account this measured q in a testing, rather than the set constant value, especially when some important fluctuations occur. As already mentioned, since a dry sample is used in the reference chamber of the LTC instrument, the overall heat capacity is due to liquid water and ice confined in the pores of the sample, thus we have Eq. 5, where m_l is the mass of pore water and m_s is the mass of the formed ice, C_{pl} and C_{ps} are the heat capacity of water and ice, respectively.

$$mC_p = m_l C_{pl} + m_s C_{ps} \tag{5}$$

The heat capacity of water and ice are assumed to be not very sensitive to temperature according to [42, 43], as shown in Eqs. 6 and 7, where θ is the temperature in °C. So an approximation is made by treating them as constant without resulting in major errors. It is also noted that different temperature dependences about the heat capacity of water and ice are reported, e.g. in [44]. More related discussions will be conducted later.

$$C_{pl} = 4.222\left(1 - 54 \cdot 10^{-5}\theta\right) \mathrm{J\,g^{-1}\,K^{-1}} \tag{6}$$

$$C_{ps} = 2.114\left(1 + 373.7 \cdot 10^{-5}\theta\right) \mathrm{J\,g^{-1}\,K^{-1}} \tag{7}$$

Nevertheless, this approximation enables us to differentiate Eq. 5 analytically. If the initial mass of the pore liquid is m_{l0}, we have

$$m_l = m_{l0} - m_s \tag{8}$$

Thus, the change in the heat capacity is clearly related to the change of the mass of ice, as shown in Eq. 9.

$$m\frac{\mathrm{d}C_p}{\mathrm{d}t} = (C_{ps} - C_{pl})\frac{\mathrm{d}m_s}{\mathrm{d}t} \tag{9}$$

Just before the water starts to freeze (right before the first peak observed on a measured heat flow curve during freezing), the heat flow is denoted as Q_0 and the corresponding cooling/heating rate and the time are denoted as q_0 and t_0, then

$$Q_0 = q_0 m C_{p0} = q_0 m C_{pl} \tag{10}$$

The changing of the heat capacity of the system can be related to the change of the ice mass by integrating Eq. 9. The relation is shown in Eq. 11.

$$m\big(C_p(t) - C_p(t_0)\big) = (C_{ps} - C_{pl})m_s \tag{11}$$

By multiplying both sides of Eq. 11 by $q(t)$ and inserting Eq. 10, Eq. 13 can be obtained, where $Q_B(t)$ is the baseline at any proceeding time after t_0.

$$q(t) \cdot m\big(C_p(t) - C_p(t_0)\big) = q(t) \cdot (C_{ps} - C_{pl})m_s \tag{12}$$

$$Q_B(t) - Q_0\frac{q(t)}{q_0} = q(t) \cdot (C_{ps} - C_{pl})m_s \tag{13}$$

Thus, $Q_B(t)$ can be obtained by rearranging Eq. 13, which is

$$Q_B(t) = q(t) \cdot \left(\frac{Q_0}{q_0} + (C_{ps} - C_{pl})m_s\right) \tag{14}$$

The heat flow due to phase transition is given in Eq.15, where Δh is the heat of fusion of the confined water or ice, and m_s is the mass of the ice in the pores of the sample tested. As mentioned earlier, different arguments exist with respect to the determination of heat of fusion for the confined water in the freezing and melting process. Brun et al. [13] proposed that unlike the bulk water, the heat of fusion for the water confined in pores in the freezing process will be different from that in the melting process for cases in which cylindrical pore shape is assumed. The details will be further explored in the next section. Here, it should be noted that the heat of fusion in the freezing and the melting processes may differ. By using Δh_f (in freezing) or Δh_m (in melting) in the place of Δh, Equation 15 describes the case for freezing or melting, respectively.

$$Q_s(t) = \Delta h\frac{\mathrm{d}m_s}{\mathrm{d}t} \tag{15}$$

As mentioned before, the total measured heat flow $Q(t)$ is the sum of the baseline and the heat flow due to phase transition, which leads to the conclusion that

$$\begin{aligned} Q(t) &= Q_B(t) + Q_s(t) \\ &= q(t) \cdot \left(\frac{Q_0}{q_0} + (C_{ps} - C_{pl})m_s\right) + \Delta h\frac{\mathrm{d}m_s}{\mathrm{d}t} \end{aligned} \tag{16}$$

Then, Eq. 16 is rearranged to give

$$\frac{\mathrm{d}m_s}{\mathrm{d}t} + \frac{q(t)\cdot(C_{ps} - C_{pl})}{\Delta h} m_s = \frac{Q(t) - Q_0 \cdot q(t)/q_0}{\Delta h} \quad (17)$$

In a measurement, the LTC instrument will record the heat flow and the corresponding temperature of the sample chamber continuously. Thus in Eq. 16, $Q(t)$ will be given directly by the LTC instrument and $q(t)$ can be obtained by dividing the measured temperature gradient by the time interval in the calculation step. The heat of fusion Δh will be determined as an input, which will be described in the next section. So, there is only one unknown m_s. By solving Eq. 17 numerically, we will obtain the ice content at each time (corresponding to each temperature) accordingly.

It should be noted that the baseline for the freezing and the melting processes almost always are found to be different, due to the hysteresis effect in the freezing and melting process as mentioned earlier. The calculation method is, however, independent of the hysteresis and, therefore, Eq. 17 is applicable for both the freezing and the melting process. By using Δh_f in the position of Δh in Eq.17 and Q_0 representing the heat flow before ice starts to form, the mass of ice is obtained directly. As for the melting process, theoretically we could find a relatively stable region with a constant heat flow Q_0 before the ice starts to melt. However, it is in practice difficult to determine the heat flow at that temperature. There are two reasons for this: first, the formed ice will be continuously melting and the amount of the ice melted at low temperatures (approximately between −40 and −50 °C) is very small, if there is any; second, possible fluctuation of the heating rate could lead to the variations of the heat flow. A possible solution is to analyze the melting process inversely from the high to the low temperature end and treat the data similar to a 'freezing process'. The Q_0 would then be the heat flow after all of the ice has been melted, see the melting curve in Fig. 1a, which could be easily determined. By treating the melting process as a freezing process and using Δh_m in the position of Δh in Eq. 17 combined with the determined Q_0, we can also calculate the ice content corresponding to each melting temperature.

The derivations performed here are slightly different from that conducted in [18], i.e. the possible drifting or fluctuation of the cooling or heating rate is included in this study (Eq. 17). Comparison study using many sets of data [45] shows that the calculated ice content curves could be incorrect if the drifting or fluctuation of the cooling or heating rate is not considered. It is also noted that this possible drifting or fluctuation could also be very specific to the employed instrument for measurements. Moreover, compared with the experimental setup in [18], there was a reference sample used when undertaking the measurements for this study [33]. Since no reference sample was used in the experiments reported in [18], the appropriate corrections concerning the heat contribution due to the solid matrix was used in the analysis of the measured data. The assumption used in [18] is that the heat capacity of the skeleton matrix is a constant or at least it is not sensitive to temperature variation. This may be valid for some solid materials. However, the heat capacity of a material in general may vary to a certain degree under different temperatures. This variation can be further reduced by using a reference sample as described in the experiment. Additionally, the effect due to the possible uncertainties of the solid skeleton material during the freezing and melting can also be minimized by using the reference sample.

Heat of fusion of confined water/ice for ice content calculation

It has been mentioned earlier that the heat of fusion of the confined water or ice is an important parameter in calculating the ice content. However, there is no general agreement on which value should be used. The value of the heat of fusion for water confined in pores used for the analysis of LTC data can be divided into two groups: (1) as that for bulk water, but corrected based on the depressed freezing/melting temperature of the confined water, see e.g. Ishikiriyama et al. [46, 47, 48, 49]; (2) modified by taking into account important correction terms, i.e. the lowered pressure of the liquid water and the water–ice interface formation, e.g. see Brun et al. [13, 50].

Ishikiriyama et al. [46, 47, 48, 49] conducted a series of investigations and it was concluded that it is reasonable to assume that the heat of fusion of the confined water is the same as that of bulk water but with the correction based on the freezing/melting point depression of the pore water due to confinement. The value of the heat of fusion was suggested to be fitted to a polynomial as, e.g. adopted by Randall [51, 52]. The fitted heat of fusion Δh is a temperature-dependent function, which is shown in Eq. 18, where T is the temperature in Kelvin degree. As it was further pointed out in [52], the validity of Eq. 18 was verified by using an accurate absolute calorimeter and the difference between Eq. 18 and the more accurate theoretical value calculated from Kirchhoff's law was negligible. Also, Eq. 18 is used as the heat of fusion for the confined water in other LTC studies [36, 53, 54]. In the work presented in [4, 12, 24, 25, 28, 55], where Δh is expressed as a linear function of T, the absolute value of the heat of fusion used is only slightly different from the results of Eq. 18, thus the different groups of work give the same results in all essential parts. The assumption used is that the heat of fusion in the freezing and in the melting process have the same temperature dependence, i.e.

$$\Delta h = 334.1 + 2.119(T - 273.15) - 0.00783(T - 273.15)^2 \ \mathrm{J\,g^{-1}} \quad (18)$$

$$\Delta h_f = \Delta h_m = \Delta h \quad (19)$$

where Δh_f and Δh_m are to denote the heat of fusion in freezing and melting, respectively.

Brun et al. [13, 50] proposed another procedure to derive the heat of fusion of confined water or ice and its temperature dependence. It was argued that external liquid water, and/or the possible water expelled from the sample during freezing, provides a layer of ice on the outer surface, which is in equilibrium with the surrounding vapor. If the solid ice remains in thermodynamic equilibrium with the atmosphere and with the liquid water in the pores, then the liquid water, as shown in Fig. 2, must be under negative relative pressure. The pressure on the liquid water will affect the heat of fusion when it undergoes phase change. It is, further, argued by the same authors in [13, 50] that another correction term should also be added due to the formation of the solid–liquid interface in freezing and decomposition in melting. When ice forms in a pore, a solid-liquid interface is created. Thus, a portion of the energy is needed to form this ice–water interfacial surface. Accordingly, when the solid melts, the energy of this interface will be liberated. This portion of the liberated energy constitutes a positive contribution to the heat of fusion, whose magnitude depends on the surface area of the solid–liquid interface, or rather the radii of the pores where ice melts. A detailed derivation of this correction can be found in [50] and further discussion is conducted in [18].

By considering both the lowered pore pressure effect and the interfacial correction, the heat of fusion for water confined in pores in the freezing and the melting processes (mention as solidification and fusion energy in [13]) can be determined. The heat of fusion in freezing Δh_f and the heat of fusion in melting Δh_m as a function of temperature can

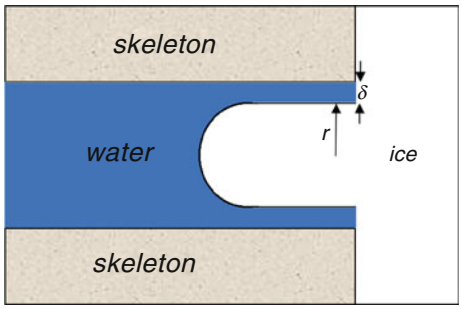

Fig. 2 According to Brun et al. [13, 50], there are two factors which influence the heat of fusion of the water confined in pores compared to its bulk state: (1) lowered pressure of the liquid water: due to that there is a layer of ice on the outer surface of the pores which is in equilibrium with its surrounding vapor (assumed), thus the liquid water confined in pores will be under negative pressure; (2) the water–ice interface formation

be calculated from the definition of Δh, as shown in Eq. 20, by using $(\Delta S_{sup})_f$ for the freezing process and $(\Delta S_{sup})_m$ for the melting process for ΔS_{sup}, respectively.

$$\Delta h = T\Delta S = T(\Delta S_f + \Delta S_{sup}) \quad (20)$$

where T is the temperature in Kelvin degree, ΔS is the overall entropy for the ice confined in pores, which consists of the solidification entropy ΔS_f and the interfacial entropy ΔS_{sup}. It is revealed that the correction terms due to the lowered pore pressure effect and the interface are important ones affecting the value of the heat of fusion [13]. Based on some simplifications, a theoretical calculation in the same paper demonstrates that in the freezing process, the effect of the lowered pressure of the pore water accounts for about 33 % of the total decreased heat of fusion at −30 °C and the interfacial correction contributes about 25 % increase to the heat of fusion when the temperature is −25 °C. By inserting the numerical values generated from the assumptions and derivations performed in [13], the heat of fusion can be expressed in numerical terms. The modified heats of fusion in the freezing and the melting were then used in a series of their subsequent work [56–60] and also cited by other authors, e.g. [61, 62, 63].

Sun and Scherer [18] followed the same procedure as adopted by Brun et al. and calculated the heat of fusion. The results showed that the correction of the interfacial energy (corresponding to the formation of the solid–liquid interface) is an important factor in the freezing process, which almost offsets the temperature dependence of Δh_f. The corrected heat of fusion in the freezing was estimated as

$$\Delta h_f = 332.4 \ \mathrm{J\,g^{-1}} \quad (21)$$

Following the approach adopted by Brun et al. [13, 18], the heat of fusion in melting process will be different compared with that of the freezing process. This is because the value of the interfacial correction depends on the curvature of the pores where ice melts. That is, the correction will be dependent on the assumption about the pore shape made. As argued, the curvature of the cylindrical pores with the same radius is only half as large as that in the freezing process and according to the calculation in [18], the corrected heat of fusion can be expressed as Eq. 22 with very small relative error. While for spherical pores, since the curvature of pores with the same radius in freezing is the same as that in melting [13], Eq. 21 works for both the freezing and the melting process [18].

$$\Delta h_m = 333.8 + 1.797(T - T_0) \quad \mathrm{J\,g^{-1}} \quad (22)$$

where T_0 is the melting point of bulk ice (freezing point of bulk water) in Kelvin degree.

According to the above discussion, it is noted that disagreement exists regarding how to obtain an expression for temperature dependence of the heat of fusion for the water

or ice confined in pores. The temperature dependence of the heat of fusion by considering correction terms accounting for interfacial effects differ from that of the more simple bulk water assumptions and the difference becomes larger as the temperature decreases, especially for the freezing process. It is somehow difficult to judge which values for the heat of fusion of the confined water is more relevant in determining the ice content. Comparison studies will be conducted to show the difference of the calculated ice content based on the different adopted values of the heat of fusion for the confined water or ice.

Results and discussion

Ice content calculated based on the two different methods

The ice content was calculated for the different samples using the 'J-baseline' method and 'C-baseline' method described previously. The heat of fusion for bulk water/ice corrected for the depressed freezing/melting temperature, i.e. Eq. 18, was used for the confined water or ice in the calculation using both 'J-baseline' method and 'C-baseline' method. The results for different samples are shown in Fig. 3. According to the melting curves in Fig. 3, it is noted that there is a portion of ice which melts above 0 °C due to the lack of equilibrium between the sample and the instrument and may also be inside the sample, despite the efforts being taken to avoid this. Compared with conventional LTC measurements in which the sample size is on the order of milligrams [7, 36], the samples used in this study are bigger. One may argue that the lack of equilibrium is probably due to the big sample size even if a very low cooling/heating rate is adopted. However, it is noted that a careful study by Landry [36] using 1–2 mg of water in conventional LTC experiments also found the extended melting above 0 °C. It should be mentioned that Riikonen et al. [7] discussed about the non-equilibrium issue and claimed that the sample during a typical LTC measurement is never in equilibrium state since it is measuring a dynamic process of freezing or melting.

By studying the freezing curves, it is found that when the temperature decreases to about −50 °C, no more ice will be formed and there is still a certain proportion of water remaining unfrozen in concrete samples as the temperature keeps decreasing. This is in agreement with the findings about mature concrete samples in [12, 24, 25, 33]. The shape of freezing curves based on 'J-baseline' and 'C-baseline' are quite similar and the ice contents calculated by the methods are in good agreement in the range of small temperature depressions. However, at larger temperature depressions, the difference between the ice content calculated by the two methods becomes bigger.

While for the melting curves as shown in Fig. 3, the results based on the 'C-baseline' method show that the ice confined in small pores starts to melt when the temperature reaches about −40 °C. This is somehow understandable if we compare the melting curve with the freezing curve. A plateau is found after about −50 °C in each of the freezing curves presented in Fig. 3, implying no more ice formation even if the temperature further decreases. As demonstrated in many studies [13, 18, 34, 35, 47, 48], the freezing point of the water confined in pores with certain pore size is lower than the melting point of the ice confined in pores with the same pore radius. Possible reasons for this phenomenon include the pore shape effect and pore connectivity. Moreover, as pointed out earlier in some studies [13, 18, 61–63], in case of cylindrical pore shape, the depression of the freezing point could be as high as double the melting point depression. Thus, it is reasonable to believe that the ice formed at −50 °C will be melted at some temperature which is higher than −50 °C. The different starting points of the melting curves of the different concrete samples as shown in Fig. 3 could be related to the porosity of the samples, such as the pore volume, pore shape or the connectivity of pores. It is also found that the melting curve according to 'J-baseline' shows certain degree of agreement with that based on 'C-baseline' despite the difference which becomes more obvious at the high depression range, i.e. the range of low temperatures. The maximum amount of ice formation calculated based on the two different methods are shown in Table 1. For the 'J-baseline' method, one of the principles is to ensure that the maximum ice formed in the freezing process is equal to ice melted in the melting process in one freezing and melting cycle, so we obtain the same value for the maximum ice content in the freezing and melting processes. While for the 'C-baseline' method, the ice content is calculated for the freezing and melting process, respectively; thus we have different values of the ice content for the freezing and melting process. It is demonstrated that the maximum amount of the ice content determined for the freezing and melting process based on 'C-baseline' is very close to each other, giving a variation about less than 3 %. It might imply the applicability of the method and Eq. 18 as the heat of fusion of the confined water in this study. The issue about the heat of fusion for confined water will be further discussed in the next section. The maximum amount of ice determined based on 'J-baseline' and 'C-baseline' differs. For our study, the largest relative difference was found for the sample C404, which was as high as 18 %; while the smallest relative difference was shown for the sample C506, which was about 8.5 %.

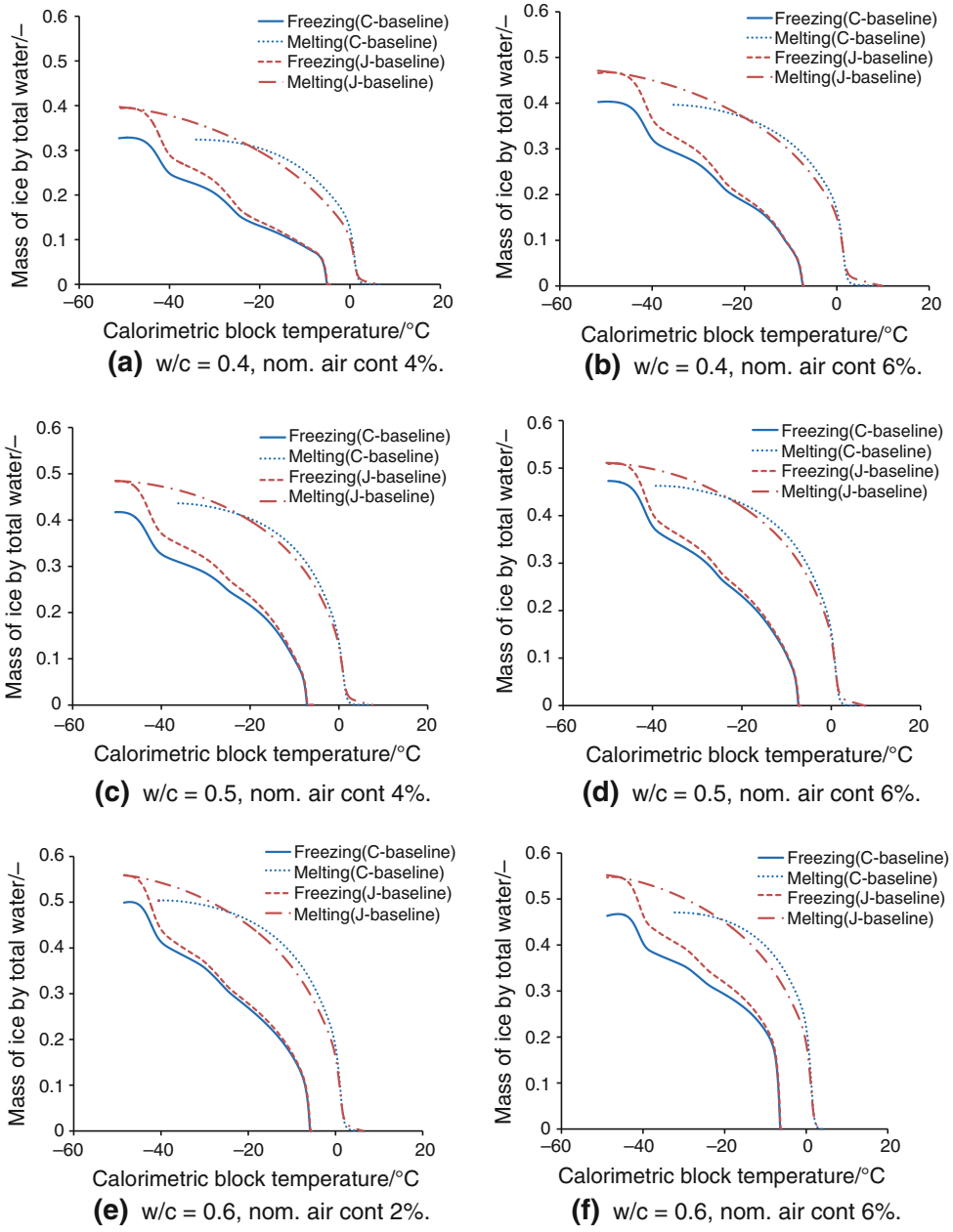

Fig. 3 Calculated mass of ice by total amount of water at different freezing and melting temperatures based on 'J-baseline' method and 'C-baseline' method. The heat of fusion and its temperature dependence for the confined water or ice is assumed as that presented in Eq. 18. Capillary saturated samples are used in the testing

Regarding the difference between the ice content calculated from 'J-baseline' method and 'C-baseline' method, possible explanations can be proposed if we look back into the calculation methods. For 'C-baseline' the calculation is based on the theoretical description of the phase changing behaviour; it should give very close information to the true value under each temperature if the parameters adopted are correct. The accuracy can be further improved by considering the temperature-dependent property of the heat capacity of water and ice combined with a careful experimental design by using a reference sample. However, it should also be noted that the temperature dependence of the heat capacity of water and ice under very low temperatures are not absolutely clear, especially for that of water. To measure the heat capacity of the water under 0 °C at atmospheric pressure, cares should be taken to keep the water under supercooled condition. This is not that easy to be achieved when the temperature is much lower compared to the freezing point of water. Under such cases, any fluctuations or uncertainties could initiate the crystallization of the liquid [44], making the direct measurement of the heat capacity extremely difficult. Different values of heat capacity of supercooled water were reviewed and reported in [44], which differ from Eq. 6 especially when the temperature is under −20 °C. Since the reported values are also in a relatively wide range, it tends to be of little meaning to study the impact of the different reported values of the heat capacity on the calculated ice content and thus the work is not conducted in this study.

Table 1 The maximum amount of ice by total water calculated from the freezing and melting process in one freezing and melting measurement cycle for the samples shown in Fig. 3.

Sample	J-baseline/%	C-baseline/%			Relative difference/%[a]
		Freezing	Melting	Average	
C404	39.7	32.7	32.4	32.6	17.9
C406	47.1	40.3	39.7	40.0	15.1
C504	48.5	41.8	43.6	42.7	11.9
C506	51.1	47.3	46.3	46.8	8.3
C602	55.9	49.9	50.4	50.2	10.2
C606	55.2	46.3	47.1	46.7	15.4

The notation for the sample C404 means that w/c = 0.40, target (nominal) air content 4 %, and likewise

[a] The relative difference is calculated by: 100(column 5–column 2)/column 2.

While for the 'J-baseline', the calculated ice content could be very sensitive to the extrapolation procedure itself. In the extrapolation, one should choose several points to determine the initial slope on the heat–temperature curve and the starting point and the ending point for a process as well. Taking the melting process for example, the initial slope is not that straightforward to be found since the changing of slope at the whole low-temperature range (till about −30 °C) is very small which is unlike the abrupt change of the initial slope for the freezing process, thus the choice of this slope is somewhat arbitrary. It is also not that straightforward to determine which temperature should be chosen as the starting point when the ice starts to melt. Assuming that a lower temperature (compared with the true value) is chosen as the starting melting point, the slope of the *b* curve tends to be smaller and then the calculated baseline *d* will be higher than its true position (referring to Fig. 1b). Consequently, the energy jump calculated accordingly will be overestimated. Since one of the principles for 'J-baseline' is to ensure that the ice calculated in the freezing process is equal to that in the melting, the overestimated melting energy will also affect the calculated ice content in the freezing process. This could possibly explain partly the difference between the two methods as shown in Fig. 3. Since it is difficult to judge the true temperature when ice just starts to melt, a temperature which is very close to the lowest ice-forming point is chosen as the starting melting point. However, according to 'C-baseline' method, the calculated starting melting temperatures of the ice are higher than the chosen points. Thus, the ice content calculated from the 'J-baseline' method is actually higher than that calculated from the 'C-baseline' method. If we move the starting point of the melting to the value as predicted by the 'C-baseline' method, it can be anticipated that both the freezing curve and the melting curve of the ice content will be in better agreement between these two methods. Figure 4 shows the results by doing the adjustment for sample C504 and C506, which does show that the ice curves are in better agreement, with still some little difference that might be due to other uncertainties, e.g. the heat capacities as aforementioned. In the verification experiment of 'J-baseline' by using water [20], which shows the estimated value varies about 2 % (relative difference) compared with the true value, it is relatively very straightforward to choose the several points as needed for the extrapolation since all the water will freeze/melt at one temperature giving very abrupt change of the slope in the accumulated energy curve. As for the case in this study, it is more complicated since the ice in concrete samples is continuously forming/melting under different temperatures. Nevertheless, an acceptable accuracy can be anticipated based on the 'J-baseline' method if special care is taken.

One advantage of the 'J-baseline' method is that the ice content calculation will not be affected by the uncertainties of the heat capacity of water and ice under very low temperatures as they are not inputs for the calculation. The calculated results can be expected in good accuracy provided a correct value of the heat of fusion ("Influence of the heat of fusion of confined water on the calculated ice content" Section) is used. Additionally, the calculation will not be affected by the fluctuation of the cooling or heating rate in testing. While for the 'C-baseline' method, the uncertainties of the heat capacity of water and ice at very low temperatures could affect the calculated results to a certain extent. Meanwhile, possible fluctuation of the cooling or heating rate should be taken into account. Bearing these in mind, actually these two methods can be used complementarily in practice.

Influence of the heat of fusion of confined water on the calculated ice content

As discussed already, different arguments exist regarding the heat of fusion for the water confined in pores. In order to study to what extend the value of the heat of fusion can affect the estimated ice content, comparison is performed by using the different values as presented in "Heat of fusion of confined water/ice for ice content calculation" Section. The heat of fusion of bulk water which freezes/melts at 0 °C, $\Delta h = 334.1\ \mathrm{J\ g^{-1}}$, is also included in the comparison. In the following study, 'C-baseline' method is adopted in calculating the ice content. To simplify the discussion, the following abbreviations are used:

– HEBT is the heat of fusion for bulk water corrected for the depressed freezing or melting temperature of the pore water (i.e. Eq. 18);

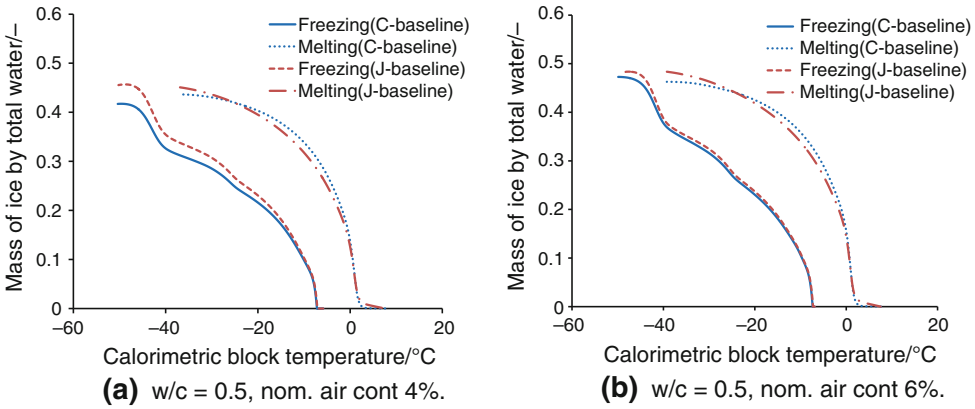

Fig. 4 Calculated mass of ice by total amount of water at different freezing and melting temperatures based on 'J-baseline' method with the starting melting point as predicted by 'C-baseline' method. Compared with the results presented in Fig. 3 c, d, the ice curves are in better agreement

- HEB is the heat of fusion of the bulk water which freezes/melts at 0 °C (i.e. $\Delta h = 334.1\,\mathrm{J\,g^{-1}}$);
- HEMC is the modified heat of fusion for cylindrical pores (i.e. Eq. 21 for freezing and Eq. 22 for melting);
- HEMS is the modified heat of fusion of water for spherical pores (i.e. Eq. 21 for both freezing and melting).

In an attempt to verify which heat of fusion of the confined water is more reasonable, a comparison study is performed on the calorimetric measurements of a mono-sized model material named SilicaV432 using distilled water as the probe liquid. The experimental data and the details were presented in [4]. Two measurements on the same material but using different heating/cooling rates were conducted, measurements denoted as M1 (cooling and heating rate 1.2 °C h^{-1}) and M2 (cooling rate 3.3 °C h^{-1} and heating rate 4.1 °C h^{-1}). The comparison results are presented in Figs. 5 and 6. It can be found that at higher temperatures, the ice curves show very good agreement while there are some differences at the low-temperature range using the different values for the heat of fusion, especially in the freezing curves. The relative differences of the maximum ice content determined from the freezing and melting process in one measurement cycle using the different heat of fusions are listed in Table 2.

According to Table 2, the relative differences between the calculated ice content from the freezing and melting process in one measurement cycle using different heat of fusions range from about −4 to −10 % for M1 and about 3 to −0.4 % for M2. It should be noted that the relative differences caused by the different heat of fusions are not significant, except that of HEMC for M1 (−9.76 %). If the average of the ice content from the freezing and the melting is taken, the biggest relative difference for both M1 and M2 using different heat of fusions are about 5 %. The very initial purpose of doing this comparison on the model material is to judge which heat of fusion makes most sense by studying the difference of the calculated ice content from the freezing and melting process in one measurement cycle, which should be very close as the ice formed should be the ice melted in one cycle, and that of the ice content using different heat of fusions. However, it is difficult to judge by looking at the small differences as presented here. Thus, all the different values of the heat of fusion as discussed were applied to the concrete samples under study anyway.

The results for sample C504 are shown in Fig. 7. According to Fig. 7a, if the heat of fusion HEB is adopted, the ice content calculated from the freezing curve will be higher than that calculated using the modified heat of fusion HEMC. The difference is small in the high-temperature range, but increases as the freezing temperature keeps decreasing. The relative difference is about 23 % when the temperature is about −50 °C. For the melting curve, the calculated ice content based on HEMC and HEB are in quite good agreement. For the same freezing and melting cycle, the maximum ice content determined from the freezing and the melting process differs significantly based on HEMC, the relative difference being as much as about 27 %, see Fig. 7a. While the ice content calculated based on HEBT in the same freezing and melting cycle only varies about 2 %. The ice contents determined from the freezing process based on HEMC and HEMS are the same, since Eq. 21 is used for the both cases. For the melting curve, the ice content deduced from HEMS is in relatively good agreement with the value calculated based on HEMC, though at the low-temperature range the value based on HEMS is smaller than that based on HEMC, showing a difference of about 3% at the lowest melting temperature for the sample (see Fig. 7a). That is, it can be concluded that the pore shape assumptions will not significantly affect the estimated ice content for a concrete sample if the modified heat of fusion is adopted.

The comparison between the ice content based on heat of fusion HEBT and HEB demonstrates some difference, as shown in Fig. 7b. In the freezing process, the maximum ice content

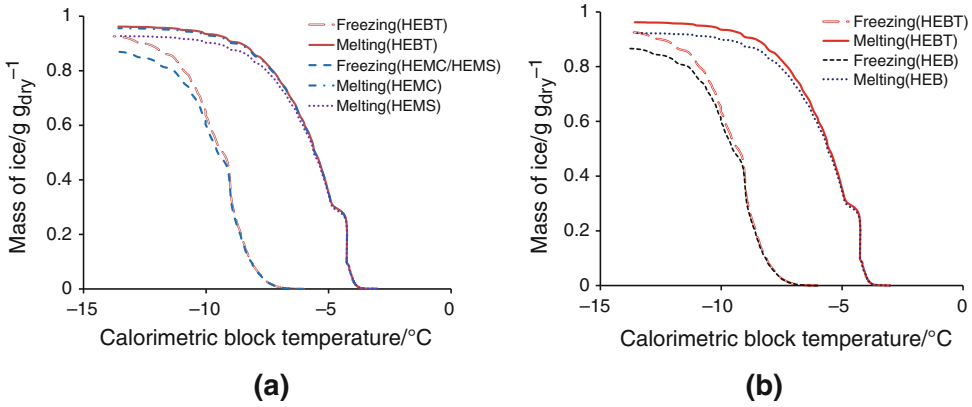

Fig. 5 Amount of ice calculated using the 'C-baseline' method and different values of the heat of fusion for M1 (cooling and heating rate 1.2 °C h^{-1}), the amount of ice presented as the ice content per unit mass of dry model material. **a** comparison between the heat of fusion HEMC, HEMS and HEBT; **b** comparison between the heat of fusion HEB and HEBT

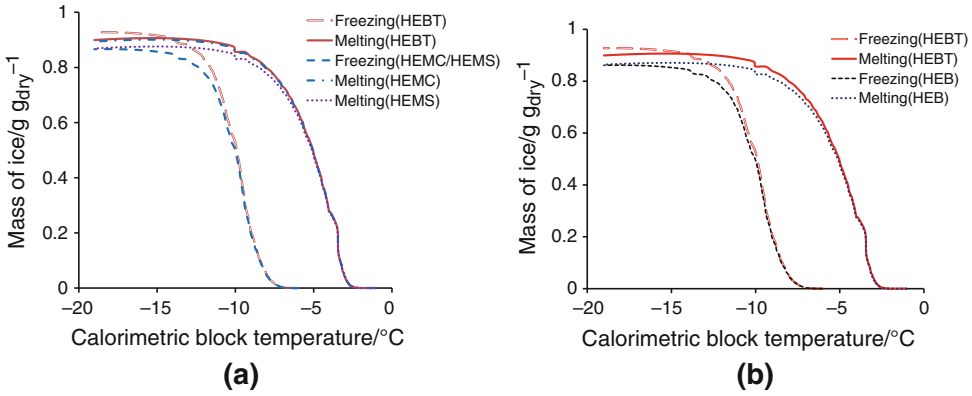

Fig. 6 Amount of ice calculated using the 'C-baseline' method and different values of the heat of fusion for M2 (cooling rate 3.3 °C h^{-1} and heating rate 4.1 °C h^{-1}), the amount of ice presented as the ice content per unit mass of dry model material. **a** comparison between the heat of fusion HEMC, HEMS and HEBT; **b** comparison between the heat of fusion HEB and HEBT

calculated based on HEBT differs from that based on HEB, the difference being increasing as the temperature decreases leading to a largest relative difference about 28 % at the lowest ice forming temperature. While for the melting, the two curves are in certain agreement especially at the high-temperature range, though a difference of 4 % is found for the maximum ice content. For the same cycle of freezing and melting, the maximum ice content based on HEB differs about 23 %, see Fig. 7b. This is in agreement with the findings discussed in [64], which show a difference about 20 % where a constant heat of fusion, i.e. HEB in our discussion, was used in the calculation.

Table 2 The relative differences of the maximum amount of ice per unit mass of dry model material calculated from the freezing and melting process in one measurement cycle using different values of the heat of fusion for the model material as presented in Figs. 5 and 6

Measurement	Heat of fusion	Mass of ice/g g_{dry}^{-1}		Relative difference/%[a]
		Freezing	Melting	
M1	HEBT	0.926	0.962	−3.89
	HEMC	0.871	0.956	−9.76
	HEMS	0.871	0.927	−6.43
	HEB	0.886	0.922	−4.06
M2	HEBT	0.927	0.899	3.02
	HEMC	0.866	0.894	−3.23
	HEMS	0.866	0.869	−0.35
	HEB	0.861	0.864	−0.35

[a] The relative difference is calculated by: 100(column 3–column 4)/column 3.

In general, as for the calculated ice content based on HEBT and HEMC, large difference is shown for the freezing process while a relatively good agreement can be found for the melting process. If the modified heat of fusion HEMC or HEMS is used, the pore shape assumptions will not have a major effect on the estimated ice content for a concrete sample. A difference of about 20 % will be observed if the heat of fusion for the normal bulk water or ice which freezes/melts at 0 °C is adopted in the calculation of the ice content between the freezing and melting process in one freezing and melting cycle.

The same trends as discussed before can be found for other samples. Figure 8 shows the comparison for the sample C506 and Fig. 9 for C602. The relative difference of the maximum ice content determined based on HEBT and HEMC can be found as about 23 and 20 % in freezing for sample C506 and C602, respectively; while for melting, they are in very good agreement with the largest variation of less than 2 %. The comparison between the values of the maximum ice content based on HEBT and HEB shows a relative difference of about 23 and 21 % in the freezing and about 5 and 4 % in the melting for sample C506 and C602, respectively.

Based on the above discussion, certain difference is found for the calculated ice content for the concrete

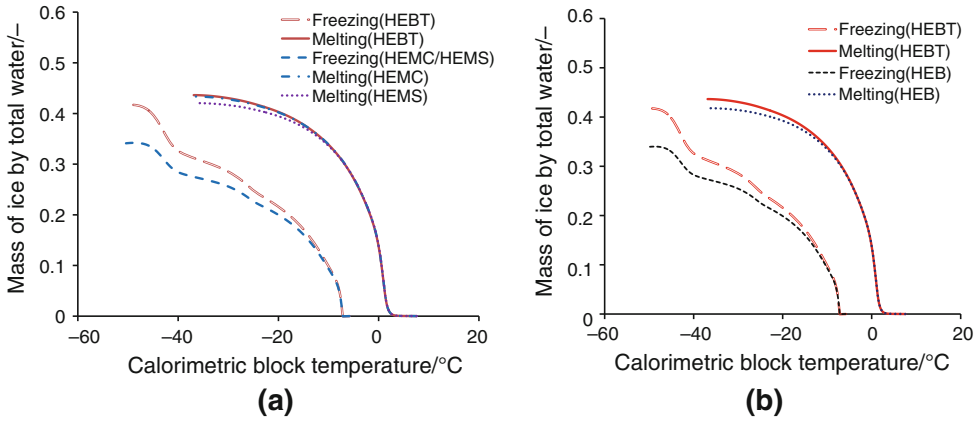

Fig. 7 Ice content calculated using the 'C-baseline' method and different values of the heat of fusion for water-saturated sample C504. **a** comparison between the heat of fusion HEMC, HEMS and HEB; **b** comparison between the heat of fusion HEB and HEBT

samples if different values of the heat of fusion of the confined water are adopted. As demonstrated already, the heat of fusion may be related to the pore shape of the sample under testing. However, it is often not that straightforward to define the pore shape in a concrete sample due to its complexity. Moreover, since we have no direct information with respect to the pore volume of the concrete samples tested, it is not possible to judge which value for the heat of fusion and its temperature dependence is most reasonable by comparing the measured pore volume and the real pore volume. During the discussion, the difference of the ice content calculated for the freezing and melting process in one freezing and melting cycle is compared from time to time. Actually, this could be a very practical criterion to judge which value of the heat of fusion and its temperature dependence makes more sense, since the maximum ice content formed in the freezing process should be equal to that melted in the melting process in one freezing and melting cycle. Accordingly, if this criterion is adopted, it seems that it makes more sense to use the heat of fusion of bulk water, but corrected for the depressed freezing/melting point of the pore water (HEBT), for the analysis.

It should be mentioned that the difference of the calculated ice contents for the monosized model material SilicaV432 are much smaller by adopting different values of the heat of fusion of the confined water, as presented before. Compared with the monosized model material, the pores inside of concrete are much more widely distributed. Thus, the freezing/melting of the pore water in concrete covers a long range of temperatures. Then the impact of the heat of fusions becomes pronounced on the calculated ice content. While the freezing/melting of the pore water in the monosized material only covers a small temperature range, the impact of the heat of fusions on the calculated ice content may be not that pronounced, as observed in Figs. 5 and 6. In this sense, it may be more appropriate to study a model material with more than one pore size (or simply a mixture of two or more model materials with different pore sizes) in order to stringently validate which heat of fusion should be adopted in this context of calculation.

In this study, the heat of fusion of pure water is used to calculate the ice content for simplicity. One may argue that the difference of the calculated maximum ice content in the freezing and melting process of one cycle might be related to the ions in the pore solution of the concrete samples, since the

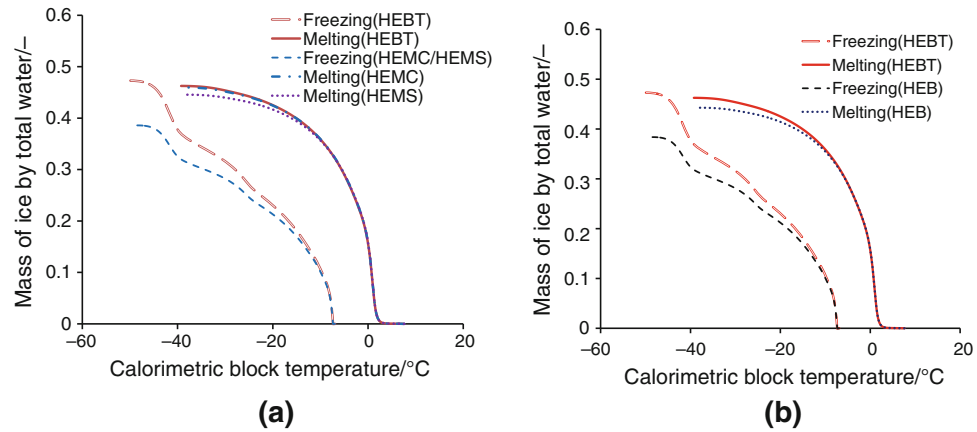

Fig. 8 Ice content calculated using the 'C-baseline' method and different values of the heat of fusion for water-saturated sample C506. **a** comparison between the heat of fusion HEMC, HEMS and HEBT; **b** comparison between the heat of fusion HEB and HEBT

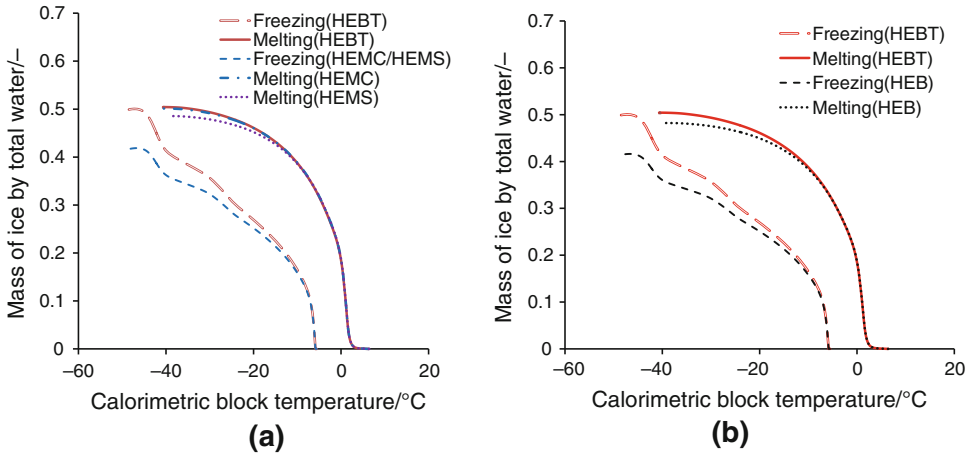

Fig. 9 Ice content calculated using the 'C-baseline' method and different values of the heat of fusion for water-saturated sample C602. **a** comparison between the heat of fusion HEMC, HEMS and HEBT; **b** comparison between the heat of fusion HEB and HEBT

heat of fusion of pore solution might differ from that of pure water. Then, it is not applicable to use the heat of fusion of pure water in the calculation. It has been noted that some authors [12, 18] suggested that the concrete pore solution could become dilute during the long-time curing in water and the pore solution can be approximated to saturated calcium hydroxide solution (the concentration is ~ 2 g L^{-1}) [18]. That is, the studied concrete pore solution in our case might be very dilute. On the other hand, there are several types of ionic species in the pore solution of a concrete sample [40, 65] and the effect of different ions on the heat of fusion of the water is also different [66]. As described in [66], there are basically two different types of ions, one of which would cause the increase of the heat of fusion of water and the other has exactly the opposite effect. Due to the complexity of the ions in the rather dilute pore solution, the heat of fusion of the pure water consequently might not be a bad approximation for the pore solution in the context of ice content predication. With the lack of further knowledge about the heat of fusion of the pore solution, the heat of fusion of pure water is used. Obviously, further study is needed to clarify related issues. A possible alternative in this context is to use NMR cryoporometry [67] as a complementary method, which follows the same concept of freezing and melting but the ice content is determined quite differently. By comparing the ice content under different freezing/melting temperatures using the two different methods, it could be possible to judge if a certain choice of the temperature-dependent function describing the heat of fusion is more reasonable than others. Further discussion in this regard falls outside the scope of this paper.

Conclusions

Low-temperature (micro-) calorimetry (LTC) has been used to determine the ice content in concrete at different temperatures by carefully studying the freezing/melting behaviour of the confined water in the pores. LTC is also widely used to investigate the porosity at nanometric level. The present study focuses on exploring the important factors influencing the analysis of LTC data with the purpose of improving the accuracy of determining the ice content.

The importance of the baseline determination for the calculation of ice content is illustrated. Two different methods of generating the baseline were discussed. The 'J-baseline' method is a recently proposed method based on extrapolation by using the accumulated heat curves measured in the freezing and the melting process. The 'C-baseline' considers the heat capacity of both water and ice and the phase changing behaviour under the different testing temperatures. Both methods can be used for baseline and ice content calculation if due attention is paid. Results obtained by the 'J-baseline' method are not affected by the uncertainties of the heat capacity of water and ice under very low temperatures and the possible fluctuations of the cooling and heating rate during testing; while the 'C-baseline' can deliver more accurate result due to its more stringent theoretical basis, provided the corrected thermodynamic parameters are used. These two methods can be used complementarily in practice.

The influence of the different values of the heat of fusion commonly adopted in literature on the calculated ice content is investigated. For the studied concrete samples, the relative difference of the maximum ice content determined from one freezing and melting cycle can differ up to 27 % due to using different values of the heat of fusion. Using the heat of fusion of bulk water, but corrected for the depressed freezing/melting temperature of the pore water, results in the smallest difference between the maximum ice content calculated from the measured heat flow during freezing and melting in one cycle.

Acknowledgements The research leading to these results has received funding from the European Union Seventh Framework Programme (FP7/2007-2013) under grant agreement 264448.

References

1. A.M. Neville.: Properties of concrete. Prentice Hall, 4th edition edition, 1995.
2. Diamond S (1999) Aspects of concrete porosity revisited. Cement Concrete Res 29(8):1181–1188.
3. M. Pigeon, R. Pleau.: Durability of concrete in cold climates. Number 4. London: Taylor & Francis; 1995.
4. Kjeldsen AM, Geiker MR (2008) On the interpretation of low temperature calorimetry data. Materials and Structures, 41(1):213–224.
5. Kuhn W, Peterli E, Majer H (1955) Freezing point depression of gels produced by high polymer network. J Polym Sci, 16(82): 539–548.
6. Blachere JR, Young JE. The freezing point of water in porous glass. J Am Ceram Soc 1972;55(6):306–308.
7. Riikonen J, Salonen J, Lehto VP (2011) Utilising thermoporometry to obtain new insights into nanostructured materials (review part 1). J Therm Anal Calorim 105:811–821.
8. Riikonen J, Salonen J, Lehto VP. Utilising thermoporometry to obtain new insights into nanostructured materials (review part 2). J Therm Anal Calorim 2011;105:823–830.
9. Majda D, Makowski W, Mańko M. Pore size distribution of micelle-templated silicas studied by thermoporosimetry using water and n-heptane. J Therm Anal Calorim 2012;109(2): 663–669.
10. Illeková E, Miklošovičová M, Šauša O, Berek D. Solidification and melting of cetane confined in the nanopores of silica gel. J Therm Anal Calorim 2012;108(2):497–503.
11. P.J. Williams.: Properties and behavior of freezing soils. Technical Report ~ 72, Norwegian Geotechnical Institute, Oslo, Norway, 1961.
12. Fagerlund G. Determination of pore-size distribution from freezing-point depression. Mater Struct 1973;6(3):215–225.
13. Brun M, Lallemand A, Quinson JF, Eyraud C. A new method for the simultaneous determination of the size and shape of pores: the thermoporometry. Thermochimica Acta 1977;21(1):59–88.
14. J.W.P. Schmelzer, editor. Nucleation Theory and Applications. WILEY-VCH, 2005.
15. Scherer GW. Freezing gels. J Non-Cryst Solids 1993;155(1): 1–25.
16. Setzer MJ. Micro-ice-lens formation in porous solid. J Colloid Interface Sci 2001;243(1):193–201.
17. Kaufmann JP. Experimental identification of ice formation in small concrete pores. Cement Concrete Res 2004;34(8):1421–1427.
18. Sun Z, Scherer GW. Pore size and shape in mortar by thermoporometry. Cement Concrete Res 2010;40(5):740–751.
19. R. Defay, I. Prigogine, A. Bellemans, D.H Everett. Surface tension and adsorption. London: Longmans; 1966.
20. K. Fridh. Internal frost damage in concrete–experimental studies of destruction mechanisms. Ph D thesis, Division of Building Materials, Lund Institute of Technology, 2005.
21. M. Wu, B. Johannesson, M. Geiker. Impact of sample saturation on the detected porosity of hardened concrete using low temperature calorimetry. Cement and Concrete Composites, submitted for publication.
22. Radjy F, Sellevoid EJ, Richards CW. Effect of freezing on the dynamic mechanical response of hardened cement paste down to −60 °C. Cement Concrete Res 1972;2(6):697–715.
23. Radjy F, Sellevold EJ. Internal friction peaks due to adsorbed and capillary water in microporous substances. Nature 1973;241(111): 133–135.
24. C. Le Sage de Fontenay. Ice formation in hardened cement paste (in Danish). Ph D thesis, Building Materials Laboratory, Technical University of Denmark, 1982.
25. D.H. Bager. Ice Formation in Hardened Cement Paste. PhD thesis, Building Materials Laboratory, Technical University of Denmark, 1984.
26. Bager DH, Sellevold EJ. Ice formation in hardened cement paste, Part I–room temperature cured pastes with variable moisture contents. Cement Concrete Res 1986;16(5):709–720.
27. Bager DH, Sellevold EJ. Ice formation in hardened cement paste, Part II-drying and resaturation on room temperature cured pastes. Cement Concrete Res 1986;16(6):835–844.
28. Bager DH, Sellevold EJ. Ice formation in hardened cement paste, Part III-slow resaturation of room temperature cured pastes. Cement Concrete Res 1987;17(1):1–11.
29. J. Villadsen. Pore structure in cement based materials. Technical Report 277, Building Materials Laboratory, Technical University, Denmark, 1992.
30. S. Jacobsen, E.J. Sellevold. Frost/salt scaling and ice formation of concrete: effect of curing temperature and silica fume on normal and high strength concrete. In J. ~ Marchand, M. ~ Pigeon, and M. ~ Setzer, editors, RILEM PROCEEDINGS 30. FREEZE-THAW DURABILITY OF CONCRETE, pages 93–105, 1997.
31. Hansen EW, Gran HC, Sellevold EJ. Heat of fusion and surface tension of solids confined in porous materials derived from a combined use of NMR and calorimetry. J Phys Chem B 1997;101(35):7027–7032.
32. F. Radjy, E.J. Sellevold, K.K. Hansen. Isoteric vapor pressure–temperature data for water sorption in hardened cement paste: enthalpy, entropy and sorption isotherms at different temperatures. Technical Report BYG-DTU R057, Technical University of Denmark(DTU), Denmark:Lyngby, 2003.
33. Johannesson B. Dimensional and ice content changes of hardened concrete at different freezing and thawing temperatures. Cement Concrete Compos 2010;32(1):73–83.
34. B. Johannesson, G. ~ Fagerlund. Concrete for the storage of liquid petroleum gas–freeze/thaw phenomena and durability at freezing to −50 °C. Report TVBM– 7174, Division of Building Materials, Lund Institute of Technology, 2003.
35. G. Fagerlund, B. Johannesson. Concrete for the storage of liquid petroleum gas, Part II: influence of very high moisture contents and extremely low temperatures, −196 °C. Report TVBM - 1851, Division of Building Materials, Lund Institute of Technology, 2005.
36. Landry MR. Thermoporometry by differential scanning calorimetry: experimental considerations and applications. Thermochimica Acta 2005;433(1-2):27–50.
37. G. Fagerlund. Studies of the scaling, the water uptake and the dilation of specimens exposed to freezing and thawing in NaCl solution. In Proceedings of RILEM committee 117 DC Freezing/thaw and deicing resistance of concrete, pages 37–66, Swden, 1991.
38. R.A. Helmuth. Capillary size-restrictions on ice-formation in hardened portland cement-pastes. In Proceedings of 4th Symposium on Chemistry of Cement, volume ~ 2, Washington DC, 1960.
39. TC Powers. Physical properties of cement paste. In Proc. Fourth Int. Symp. on the Chemistry of Cement, Washington, DC, 1960.
40. H.F.W. Taylor. Cement chemistry. London: Thomas Telford 2nd edition, 1997.
41. Lothenbach B, Winnefeld F. Thermodynamic modelling of the hydration of portland cement. Cement Concrete Res 2006;36(2):209–226.
42. C. D. Hodgman, R. C. Weast, S. M. Selby, editors. Handbook of chemistry and physics. Cleveland:The Chemical Rubber Co. 45 edition, 1965.
43. D. Gray, editor. American Institute of Physics Handbook. McGraw- Hill, New York, 2nd edition, 1963.
44. Murphy DM, Koop T. Review of the vapour pressures of ice and supercooled water for atmospheric applications. Quart J Roy Meteor Soc 2005;131(608):1539–1565.

45. M. Wu. Imapct of cooling/heating rate drifting or fluctutaion on the caculated ice content by low temperature calorimetry. Study Report, Building Materials Laboratory, Technical University of Denmark, 2011.
46. Ishikiriyama K, Todoki M, Min KH, Yonemori S, Noshiro M. Pore size distribution measurements for microporous glass using differential scanning calorimetry. J Therm Anal Calorim 1996;46(3–4):1177–1189.
47. Ishikiriyama K, Todoki M, Motomura K. Pore size distribution (PSD) measurements of silica gels by means of differential scanning calorimetry I. optimization for determination of PSD. J Colloid Interface Sci 1995;171(1):92–102.
48. Ishikiriyama K, Todoki M. Evaluation of water in silica pores using differential scanning calorimetry. Thermochimica Acta 1995; 256(2):213–226.
49. Ishikiriyama K, Todoki M. Pore size distribution measurements of silica gels by means of differential scanning calorimetry II. thermoporosimetry. J Colloid Interface Sci 1995;171(1):103–111.
50. Brun M, Lallemand A, Quinson JF, Eyraud C. Changement d'état liquid–solide dans les milieux poreux. II. Étude théorique de la solidification d'un condensate capillaire (liquid–solid change of state in porous media. II. Theoretical study of the solidification of a capillary condensate). J Chim Phys 1973;6:979–989.
51. M. Randall. International Critical Tables V–VII. New York: McGraw–Hill, 2nd edition, 1930.
52. Chen CS. Systematic calculation of thermodynamic properties of an ice-water system at subfreezing temperatures. Transac ASAE 1988;31(5):1602–1606.
53. Yamamoto T, Endo A, Inagi Y, Ohmori T, Nakaiwa M. Evaluation of thermoporometry for characterization of mesoporous materials. J Colloid Interface Sci 2005;284(2):614–620.
54. Yamamoto T, Mukai SR, Nitta K, Tamon H, Endo A, Ohmori T, Nakaiwa M. Evaluation of porous structure of resorcinol-formaldehyde hydrogels by thermoporometry. Thermochimica acta 2005;439(1):74–79.
55. Sellevold E, Bager D. Some implications of calorimetric ice formation results for frost reistance testing of concrete. in Beton og Frost, Dansk Betonforening 1985;22:47–74.
56. Quinson JF, Astier M, Brun M. Determination of surface areas by thermoporometry. Appl Catal 1987;30(1):123–130.
57. J.F. Quinson, M. Brun. Progress in thermoporometry. K. K. Unger, J. Rouquerol, K. S.W Sing and H. Kral (eds): Characterization of porous solids, Amsterdam:Elsevier, 1988. p. 307.
58. Brun M, Quinson JF, Benoist L. Determination of pore size distribution by SETARAM DSC 101 (thermoporometry). Thermochimica Acta 1981;49(1):49–52.
59. Eyraud C, Quinson JF, Brun M. The role of thermoporometry in the study of porous solids. Stud Surf Sci Catal 1988;39:295–305.
60. Van der Grift CJG, Boon AQM, Van Veldhuizen AJW, Trommar HGJ, Geus JW, Quinson JF, Brun M. Preparation and characterization of porous silica spheres containing a copper (oxide) catalyst. Appl Catal 1990;65(2):225–239.
61. M. Stöcker. Thermoporometry, in Handbook of Porous Solids. Weinheim:Wiley-VCH Verlag GmbH, 2008.
62. Hay JN, Laity PR. Observations of water migration during thermoporometry studies of cellulose films. Polymer 2000;41(16): 6171–6180.
63. Ksiazczak A, Radomski A, Zielenkiewicz T. Nitrocellulose porosity-thermoporometry. J Therm Anal Calorim 2003;74(2): 559–568.
64. Sun Z, Scherer GW. Effect of air voids on salt scaling and internal freezing. Cement Concrete Res 2010;40(2):260–270.
65. Lothenbach B. Thermodynamic equilibrium calculations in cementitious systems. Mater Struct 2010;43(10):1413–1433.
66. Mrevlishvili GM, Privalov PL. Calorimetric study of the melting of frozen aqueous solutions of electrolytes. J Struct Chem 1968; 9(1):5–7.
67. Mitchell J, Webber JBW, Strange JH. Nuclear magnetic resonance cryoporometry. Phys Reports 2008;461(1):1–36.

Supplementary material

November 16, 2013

Article title: Determination of ice content in hardened concrete by low temperature calorimetry: influence of baseline calculation and heat of fusion of confined water.

Journal name: Journal of Thermal Analysis and Calorimetry.

Authors: Min Wu[1*], Björn Johannesson[1], Mette Geiker[2].

Address: 1. Department of Civil Engineering, Building 118, Technical University of Denmark, 2800 Lyngby, Denmark; 2. Department of Structural Engineering, Norwegian University of Science and Technology, Trondheim, Norway.

[*]**E-mail:** miwu@byg.dtu.dk.

Supplementary material for paper I--ice content determiantion (Page 2)

1. Figure 1 shows the Calvet-type scanning calorimeter (SETARAM) used for this investigation.

Figure 1: Top of the SETARAM scanning calorimeter showing the liquid nitrogen supply tube and the reference and sample chamber (after [1]).

2. The comparison between the modified (adopted in this study) and the original "J-method" [1] for baseline and ice content calculation is shown in Figure 2. The comparison between the modified (adopted in this study) and the original "C-method" [2] for baseline and ice content calculation is shown in Figure 3.

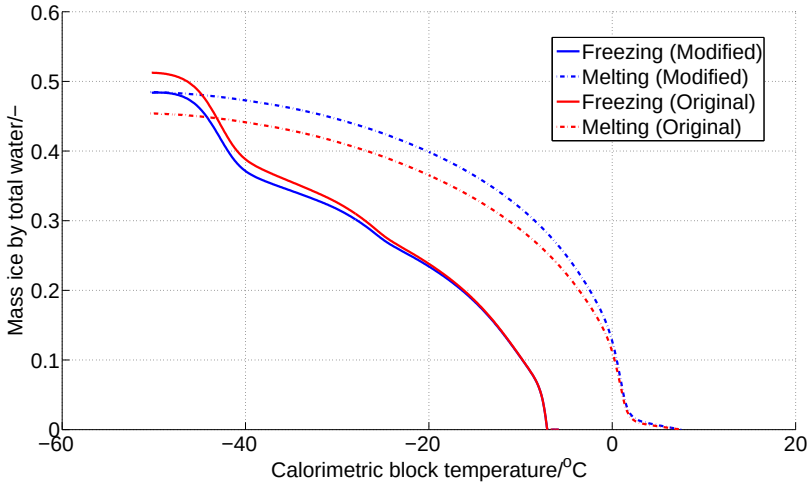

(a) w/c=0.5, nom. air cont 4%.

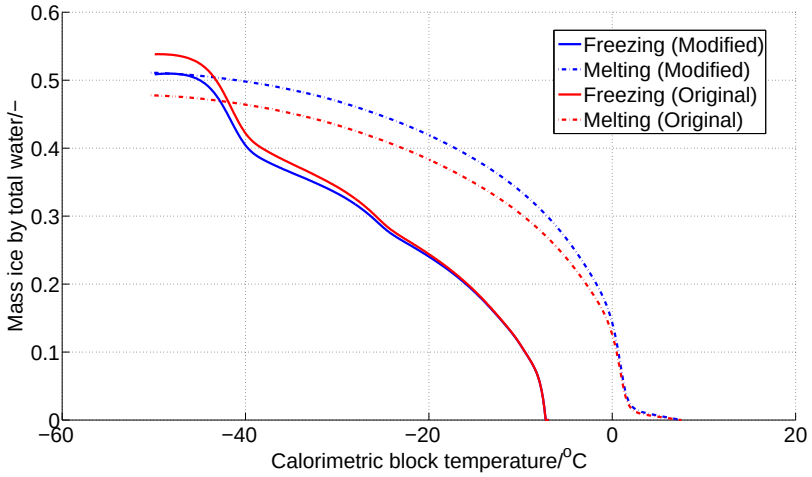

(b) w/c=0.5, nom. air cont 6%.

Figure 2: The comparison between the modified (adopted in this study) and the original "J-method" for baseline and ice content calculation for two capillary saturated concrete samples. The heat of fusion and its temperature dependence for the confined water or ice is assumed as HEBT.

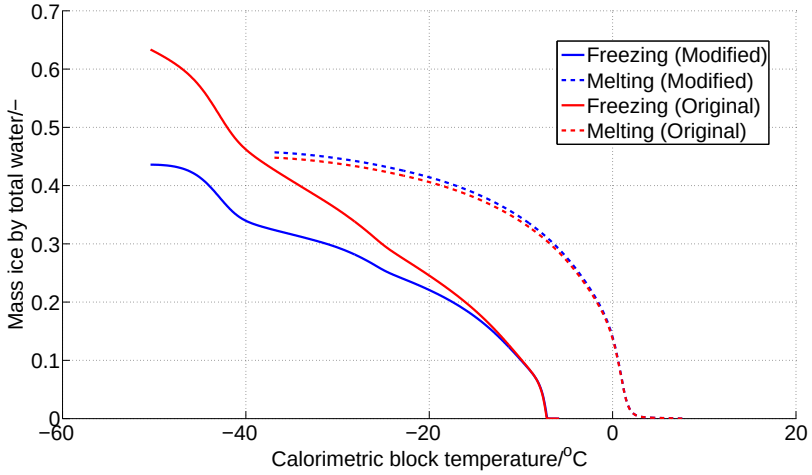

(a) w/c=0.5, nom. air cont 4%.

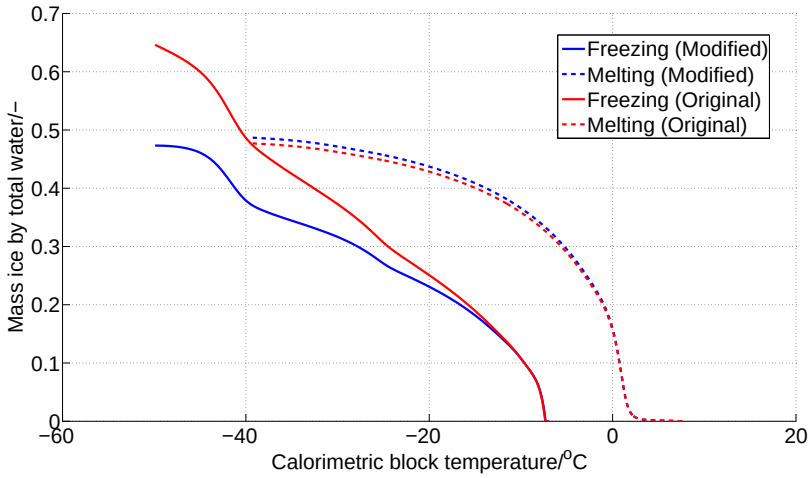

(b) w/c=0.5, nom. air cont 6%.

Figure 3: The comparison between the modified (adopted in this study) and the original "C-method" for baseline and ice content calculation for two capillary saturated concrete samples. The heat of fusion and its temperature dependence for the confined water or ice is assumed as HEBT. In the original method, the drifting of the cooling/heating rate is not taken into account.

References

[1] B. Johannesson. Dimensional and ice content changes of hardened concrete at different freezing and thawing temperatures. *Cement and Concrete Composites*, 32(1):73–83, 2010.

[2] Z. Sun and G.W. Scherer. Pore size and shape in mortar by thermoporometry. *Cement and Concrete Research*, 40(5):740–751, 2010.

Paper II

Impact of sample saturation on the detected porosity of hardened concrete using low temperature calorimetry

M. Wu, B. Johannesson

Published in: *Thermochimica Acta, 2014*

Thermochimica Acta 580 (2014) 66–78

Contents lists available at ScienceDirect

Thermochimica Acta

journal homepage: www.elsevier.com/locate/tca

Impact of sample saturation on the detected porosity of hardened concrete using low temperature calorimetry

Min Wu*, Björn Johannesson

Department of Civil Engineering, Technical University of Denmark, Building 118, 2800 Lyngby, Denmark

ARTICLE INFO

Article history:
Received 1 October 2013
Received in revised form 16 January 2014
Accepted 3 February 2014
Available online 16 February 2014

Keywords:
Concrete
Calorimetry
Freezing and thawing
Pore size distribution
Hysteresis
Thermoporometry

ABSTRACT

The present work studied the impact of sample saturation on the analysis of pore volume and pore size distribution by low temperature (micro-)calorimetry. The theoretical background was examined, which emphasizes that the freezing/melting temperature of water/ice confined in non-fully saturated pores is further depressed compared with that when the pores are fully saturated. The study of the experimental data on hardened concrete samples showed that for a same concrete mix, the total pore volume detected from the capillary saturated samples was always lower than that of the vacuum saturated samples and a higher proportion of pores with small radii were found in the capillary saturated samples. In addition, the observed hysteresis between the freezing and melting curves of ice content of the capillary saturated samples was more pronounced than that of the vacuum saturated samples. The major reason for the observed phenomena could be related to that capillary saturation cannot fully saturate the pores under study.

1. Introduction

Porosity is one of the most important characteristics of cement based materials. It is the main parameter which determines strength and influences transport properties or permeability. For this reason, it is also a major parameter determining durability. Thus considerable efforts have been devoted to the characterization of the pore structures for cement based materials.

The pore system in a cement based material is rather complicated, e.g., in terms of the pore size. There are different types of pores existing in one single cement based material. There are deliberately entrained air voids with diameters on the order of 50–100 μm for frost protection [1,2]. Mixing and casting of concrete, however, could entrap air voids whose size can reach the millimeter scale [3]. Meanwhile, there are nano-microscale "capillary pores" that are remnants of the interstitial spaces between the unhydrated cement grains [4]. Additionally, as described, e.g., in [5,6], there are interlayer spaces, or "gel pores" at the nanometric level between the primary particles of the hydration products calcium-silicate-hydrate (C-S-H). It is further argued by Sun and Scherer [7]: since the pore space in a cement based material can be fully interconnected, as indicated by the fact that the liquid can be fully exchanged by solvents, the definition of a pore size or shape is thus quite arbitrary, because there is actually only one interconnected pore with a very complicated shape.

Many methods for porosity characterization have been developed and applied to cement based materials [7–12], e.g., nitrogen adsorption/desorption (NAD), mercury intrusion porosimetry (MIP), scanning electron microscopy (SEM), scattering of X-rays or neutrons, low temperature calorimetry (LTC), nuclear magnetic resonance (NMR), moisture fixation, etc. A summarized comparison about these different methods can be found, e.g., in [7]. The measurement of NAD gives good information for mesopores (IUPAC classification) while it is not suitable to characterize capillary pores. MIP measures the pore entry radii rather than the interior pore sizes, since mercury can be intruded into some large pores through the small entrances (e.g., ink-bottle shaped pores). Optical microscopy and SEM are able to reveal the size of large pores but they are not able to resolve the mesopores. Moreover, a major disadvantage shared by NAD, MIP and SEM (including environmental SEM) is that the testing samples must be dried. For cement based materials this drying process often results in an apparent alteration of pore structure under consideration [13].

Calorimetric methods have been used to study cement based materials for a long time, e.g., see [14–18]. Low temperature (micro-)calorimetry or LTC, which is also known as thermoporosimetry and sometimes is referred to as thermoporometry or cryoporometry as well, can be applied to characterize the porosity of virgin cement based samples without any drying treatment [10,19–22]. The basic concept of LTC is that the freezing process of water is an

* Corresponding author. Tel.: +45 45251813.
E-mail address: miwu@byg.dtu.dk (M. Wu).

http://dx.doi.org/10.1016/j.tca.2014.02.002
0040-6031/

exothermic process and the melting process of ice is an endothermic one, from which the ice content can be calculated by using the heat of fusion for the confined water/ice in the freezing or the melting process and the measured heat flow with respect to ice formation or melting at different measuring temperatures. If a sample is fully saturated with water, then the volume of the ice formed/melted under different temperatures in a sense indicates the pore information of the sample under the testing. By making certain assumptions, thermodynamics demonstrate there is a unique equation showing the correspondence between the phase transition temperature of the water confined in pores and the curvature of its solid–liquid interface under the condition that the sample is fully saturated [23,24]. By studying the thermodynamic parameters of the confined water/ice, the quantitative relation of the freezing/melting temperature and the pore size can be determined.

Although LTC is often adopted as a method to study the porosity of a porous material, the analysis of the experimental data is not that straightforward. The factors which influence the accurate interpretation of the results include: the mechanism of ice formation in pores, baseline calculation, heat of fusion for water/ice confined in small pores, supercooling effect, the ions in the pore solution, the thickness of a water layer very close to the pore walls, temperature lag between the thermopile of the instrument and a testing sample, etc. It has been discussed, e.g., in [7,24–27] that there is a hysteresis behavior between the freezing and the melting process in terms of the determined ice content curves. Thus, the mechanism of ice formation in pores turns out to be very important since it would decide which process is more appropriate to be adopted to calculate the pore sizes. The mechanism of ice formation in small pores has been studied rather extensively and there are two representative assumptions in this regard, i.e., homogenous nucleation and progressive penetration following heterogeneous nucleation, e.g., in [7,24,28–30]. Homogenous nucleation indicates that the ice nuclei appear spontaneously in the liquid water and that the ice will be formed when the critical size of the nuclei (at a given temperature) is the same as that of the pore [24,28]. Brun et al. assumed in a series of work, e.g., in [24,31,32], that the ice formation process is a homogenous nucleation process. If this assumption is correct, the pore sizes detected in the freezing process is the interior (or real) sizes of the pores and then it is possible to use the freezing process to analyze the interior pore size distribution. However, studies by many authors show that the probability of homogenous nucleation governing the whole ice formation process is low and only when the temperatures is on the order of −38 °C will the homogenous nucleation become significant [29,33,34]. Thus, it is normally accepted that the freezing of water in pores should be initiated by heterogeneous nucleation and then followed by a progressive penetration of the ice front from big pores to small pores, e.g., in [7,10,15,29,35,36]. In that case, it is only possible to derive some information about the pore entry sizes, rather than the interior pore sizes, from the freezing process (some more discussions about the freezing process will be presented later combined with the measured experimental data). Then the melting process, which is assumed to reflect the interior pore sizes, is suggested to be used to calculate the pore size distribution. Based on the above discussion, probably both the freezing and the melting process should be analyzed as the freezing process may provide information about the pore entries while the melting process may reflect the interior pore size information.

There are some other topics that need to be considered in analyzing heat flow curves. The baseline calculation and the heat of fusion of pore confined water/ice are two fundamental aspects in analyzing the ice content from experimental data. The discussions about the baseline calculation can be found, e.g., in [7,17,37,38]. Many efforts have been devoted to obtaining the heat of fusion of water/ice confined in small pores, e.g., see [24,26,37,39,40]. A summarized discussion about the influence of these two aspects can be found in [41]. Supercooling refers to the phenomenon that bulk water does not freeze at 0 °C, which is often attributed to the lack of nucleation sites. If the supercooling is very pronounced, it is not possible to derive the pore entry size information corresponding to the temperatures which are higher than the freezing point of the supecooled water based on the freezing curve. In order to address this issue, two freezing and melting cycles are often adopted. Followed by the first freezing process, the sample will be heated to a temperature just below the melting point of the water in macropores. During the second freezing process, the ice crystals left in the macropores or on the exterior surface of the sample after the first melting process will serve as the nucleation sites. By doing the two cycles experiment, supercooling is expected to be avoided and then both the entry and interior sizes of the mesopores can be determined based on the measured data of the second freezing and melting process respectively. More related discussion can be found, e.g., in [7,35,36,42].

It is normally assumed that there is a portion of water which is very close to the pore walls and it will not undergo phase transition even if the temperature is very low. Banys et al. [43] estimated that the water in this layer would only freeze at a temperature between 21 and 26 K. This layer, which will be referred to as δ-layer, will definitely affect the derivation of the total pore volume and the pore size distribution. Fagerlund [15] correlated the δ-layer with the adsorbed layer in moisture fixation experiments and arrived at an equation showing the thickness of the δ-layer can be expressed as a temperature dependent function. Normally the δ-layer is treated as consisting of 2–3 layers of water molecules, which corresponds to about 0.8 nm in thickness, e.g., in [24,44,42]. Sun and Scherer [7] suggested that in mortar samples, it is more reasonable to use a value of 1.0–1.2 nm for this δ-layer due to the dissolved ions in the pore water.

The present study focuses on the impact of the sample saturation on the analysis of pore volume and pore size distribution by the LTC method. For LTC measurements, the samples to be tested need to be fully saturated with water before putting into a calorimeter. If a sample is not fully saturated, firstly the pores which are not filled with water will not be detected and as a result, the total volume of the pores will be underestimated. Furthermore, the correlation between the pore size and the depressed freezing/melting temperature in the context of pore size determination is normally based on the prerequisite that the pores under study are fully saturated, e.g. see [24,26]. However, a careful examination of the theoretical background in this study emphasizes that the thermodynamic correlation for fully saturated pores is different from that for non-fully saturated pores. Moreover, the correlation for the non-fully saturated system could be very complicated, which is extremely difficult to characterize quantitatively, if it is still possible. Under such cases, the calculated pore sizes will not be correct any more if the pores are not fully saturated while we still use the relation as derived based on the full saturation assumption. Based on the experimental data measured on hardened concrete samples conditioned by capillary saturation (samples submerged in water) and vacuum saturation, the ice content, pore volume and pore size distribution are calculated to demonstrate the impact of sample saturation on the porosity analysis.

2. Theoretical background

To illustrate the impact of sample saturation on the determined pore size distribution, the relation between the depressed freezing point of a liquid confined in a pore and the pore size should be introduced. The detailed derivation of the relation based

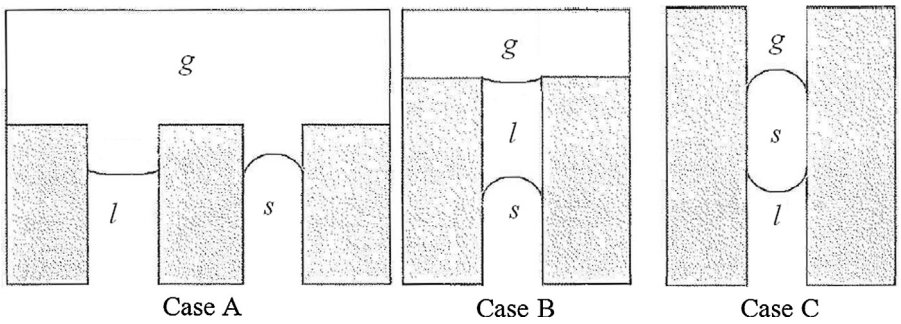

Fig. 1. Schematic illustration of the possible menisci systems found in a porous material during freezing, water being the substance confined in the pores. The illustration is based on the figure presented in [38] but with reversed curvature of solid–gas and solid–liquid interfaces.

on thermodynamics and related discussions can be found, e.g., in [23,24,29,36]. It should be mentioned that even though the thermodynamic approach is widely used, the applicability of this approach to nanoscopic systems has been questioned by, e.g., Setzer in [45,46], since the thermodynamics used are completely macroscopic. That is, the smallest pore size detected using the thermodynamic approach may be limited. However, with no more knowledge, the traditional way of using thermodynamics is followed in this work.

As pointed out by Brun et al. [24], in order to calculate the freezing/melting point of a liquid/solid confined in a pore system where the three phases (liquid, solid, gas) of the confined substance coexist, it is necessary to know two curvatures of the three interfaces (liquid–solid, liquid–gas and solid–gas). However, this condition cannot usually be met for a porous material under study. The situation will become much simpler if the porous material is fully saturated with water, which means the solid/gas interface is plane (i.e., the curvature is always zero during freezing and melting). Under such circumstances, the depressed freezing or melting temperature is only determined by the curvature of the solid/liquid interface which can be directly related to the size of the pores where the water or ice is confined. The relation can be expressed as

$$\Delta S_f dT = v_l d\left(\gamma_{sl}\frac{dA_{sl}}{dV_l}\right) \tag{1}$$

where $\Delta S_f = s_l - s_s$ is the specific entropy difference between the liquid and the solid phase; T is the temperature (in Kelvin degree); v_l is the specific volume of the liquid phase; γ_{sl} is the surface tension and dA_{sl}/dV_l is the curvature of the liquid–solid interface. It is noted that Eq. (1) is usually adopted to do the pore size analysis in the context of LTC. From the discussion, it is clear that there is a prerequisite to use Eq. (1), which is that the pores of the material under study must be fully saturated. If this condition is not met, the relation between the depressed freezing/melting point of the confined water/ice and the pore size as derived based on Eq. (1) does not hold. Still abiding by Eq. (1) to calculate the pore size distribution for a non-fully saturated pore system, the result could be in doubt.

For non-fully saturated pore systems, the possible situations for what can happen to the menisci system when water/ice freezes/melts were discussed, e.g., in [23,24]. Fridh [38] reviewed and summarized the discussion in this aspect. As shown in Fig. 1, the three possibilities of the coexisting phases include: (1) both the solid phase (s = solid) and the pore liquid (l = liquid) are exposed to the gas (g = gas) but not to each other (Case A); (2) the pore liquid is in contact with both the solid and the gas (Case B); (3) the solid phase is in contact with both the gas and the pore liquid (Case C).

For Case A, the relation between the depressed freezing point and the curvature of the interfaces can be expressed as Eq. (2); for Case B and Case C, Eqs. (3) and (4) are valid, where r_{lg}, r_{sg} and r_{ls} are the radii of the interfaces which are not necessarily equal to each other and ΔH_{fus} is the heat of fusion for the confined water; v_i is the specific volume of the phases (l, s, g); T is the freezing/melting point of the confined liquid/solid and T_o is that of the bulk liquid/solid. It should be noted that the equations (Eqs. (2)–(4)) presented here are slightly different from that presented in [38] and a reversal of the curvatures of the solid–gas and the solid–liquid remedies the differences.

By studying Eqs. (2)–(4) carefully, it can be found the relation between the depressed freezing point of the water and the curvature of the interfaces becomes much more complicated if some of the three phases coexist simultaneously. Thus, it is very difficult, if it is still possible, to quantify the relation between the pore size and the depressed freezing/melting temperature of the confined water/ice since as one lacks the knowledge about under which case(s) the pores are and how many pores there are under each case (referring to the three cases in Fig. 1). However, if a porous material is, or at least the pores under study are, fully saturated with water, the case becomes much simpler and clearer. By substituting the gas phase (g) with liquid phase (l) in Fig. 1, there will be only one interface, i.e., the liquid–solid interface. Then accordingly, the relation between the radius of the curvature and the depressed freezing point can be explicitly represented by Eq. (4) without considering the second term in the parenthesis on the right hand, or its equivalent form Eq. (1) (differential form, $\Delta H_{fus} = T\Delta S_f$), e.g., see [24,47,48].

$$\ln\frac{T}{T_0} = -\frac{2}{\Delta H_{fus}}\left(\frac{v_l\gamma_{lg}}{r_{lg}} + \frac{v_s\gamma_{sg}}{r_{sg}}\right) \tag{2}$$

$$\ln\frac{T}{T_0} = -\frac{2}{\Delta H_{fus}}\left(\frac{v_s\gamma_{ls}}{r_{ls}} + \frac{v_s - v_l}{r_{lg}}\cdot\gamma_{lg}\right) \tag{3}$$

$$\ln\frac{T}{T_0} = -\frac{2}{\Delta H_{fus}}\left(\frac{v_l\gamma_{ls}}{r_{ls}} + \frac{v_s - v_l}{r_{sg}}\cdot\gamma_{sg}\right) \tag{4}$$

With respect to water, we have $\gamma_{lg} > \gamma_{ls}$ and $v_s > v_l$ [38,47]. Then, by comparing Eq. (2) to Eq. (4) with Eq. (1), we conclude that the freezing/melting temperature of the confined water will be further depressed if the pores under study are only partially saturated compared with the fully saturated counterparts, no matter the non-fully saturated pores are under which case (i.e., the three cases in Fig. 1). The effect of the curvature of the liquid–gas interface (see Eq. (3)) and that of the solid–gas interface (see Eq. (4)) in a non-fully saturated system on the depressed freezing/melting temperatures was also discussed by Blachere and Young [49] and Williams [48] respectively. Related discussions in this aspect can also be found, e.g., in [15,23,24]. A more recent study [50] measured the melting behavior of a model pore system conditioned with different saturation degree before the freezing and it was demonstrated that the melting curves are shifted to some lower temperatures as the saturation degree lowers, in which the low saturation degree means

some of the pores are not fully saturated. This can be a very direct experimental validation supporting the argument discussed above, i.e., the further depressed freezing/melting point of the water in non-fully saturated pore systems.

It should be mentioned that due to the fact that water in very small pores does not freeze and the freezing/melting point depression of water/ice in big pores is too small, the pores that can be studied by LTC are limited mainly to mesopores with the reliable pore radii between about 2 nm and about 40 or 50 nm [7,36]. Then one may argue that to determine pore size distribution (PSD), e.g., for cement based materials, it does not matter whether the big air voids are fully saturated or not, since the concerned pores are small mesopores. As far as the small mesopores can be fully saturated by capillary saturation, which is possible considering the capillary force [51], the PSD determination should not be affected by the saturation status of the big air voids. Using the same calculation method, the calculated PSD curves for samples conditioned by capillary and vacuum saturation will be compared to illustrate the impact of sample saturation on the PSD determination.

3. Experimental data

The present investigation is based on existing experimental data. The details of the experimental study and the data can be found in [17,52,53].

The concrete samples with three different water-to-cement ratios, each with different nominal 'target' air contents were prepared. The cement content for the $w/c = 0.4$ concrete samples with nominal air contents of 2%, 4% and 6% were 515, 525 and 525 kg/m^3 respectively. And the corresponding values for the $w/c = 0.5$ and $w/c = 0.6$ samples were 475, 480 and 480 kg/m^3 and 340, 350 and 335 kg/m^3. Granite aggregate with two different size ranges, i.e., 0–3 mm and 4–8 mm, and approximately equal amount of the two fractions of the aggregate were used to prepare all the mixes. Air-entraining agent was used to produce the concrete with nominal air content 4% and 6%. The concrete samples were produced in 120L batches in the laboratory. The fresh concrete was placed into two moulds with the dimension of 200 mm × 500 mm × 500 mm and into cubic moulds with the dimension of 100 mm × 100 mm × 100 mm after mixing. The moulds filled with fresh concrete were vibrated for a few seconds, and then a plastic film was used to prevent evaporation. After curing under sealed condition for one day, the concrete was core-drilled and sawn into small cylinders with the diameter of 14 mm and the length of 60 mm. The size of the samples was chosen to fit the calorimetric device adopted in the investigation. The cylindrical samples were stored in a small bucket with about 1 l water to cure the samples at about 20 °C. And they were divided into two groups in measurement: one group of the samples were stored till about four months before testing (capillary saturation) and the other group were also water cured till about the same age but were vacuum saturated before testing (vacuum saturation).

A Calvet-type scanning calorimeter (SETARAM) was used for this investigation, as shown in Fig. 2, which was calibrated and operated to work between about 20 °C and −130 °C. The temperature scanning consisted of a cycle starting at 20 °C and going down to about −80 °C and then back to 20 °C. The adopted cooling and heating rate was 0.09 °C per minute. The samples were saturated surface dry when placed in the calorimeter. A dried (under about 105 °C till constant weight) concrete sample, of the same dimension as the testing specimen, was used as the reference sample. In the investigation, the same reference was used throughout all the tests. By using this type of reference sample, it simplifies the calibration of the measurement compared to the use of other materials such as aluminum. There are some discussions about the necessity of using a reference sample in the calorimetric experiments. Actually, the heat capacity of the solid skeleton of a porous material may vary to a certain degree under different temperatures and this variation can be further reduced if a reference sample, which is of the same size as the material used in the sample chamber but dried, is used in the experiment. More discussion in this regard can be found in [41]. During the testing, the calorimeter records the calibrated heat supplied to or released from the specimen. This means that the instrument measures the difference of the heat flow between the reference and the sample vessel, thus the heat flow due to the confined water and its phase transition in a sample at different temperatures can be determined. At the same time, the corresponding actual temperature in the sample chamber is also recorded. By using the measurement heat flow and the thermodynamic parameters for the confined water, it is possible to determine the ice content, which is an indication of the ice filled pore volume, under different temperatures.

Fig. 2. Top of the SETARAM scanning calorimeter showing the liquid nitrogen supply tube and the reference and sample chamber [17].

After a calorimetric measurement, the sample was dried under about 105 °C till constant weight. By doing so, the total water content of the sample was determined by the mass difference between this dried state and that before the calorimetric measurement (saturated surface dry). The total porosity of the concrete mixes studied were also determined through gravimetric measurements by measuring the mass of the sample both in air and submerged in water using the vacuum saturated samples.

4. Results and discussion

4.1. Volume of ice in hardened concrete samples

An accurate analysis of the measured LTC data is the basis to calculate the pore volume and pore size distribution for a porous material. Two fundamental aspects are crucial in this context, i.e., the baseline calculation of the measured heat flow and the value of the heat of fusion for the water confined in pores. The detailed discussion and the calculation scheme for determining the ice content can be found in [41].

The calculated results of the total ice volume by the total volume of the concrete sample are shown in Fig. 3. It can been found that for each concrete mix, the ice volume determined for the capillary saturated samples both in the freezing and the melting process are always smaller than that for the vacuum saturated samples. It implies that there is a portion of pores which are not filled by water in the capillary saturated samples. Since the LTC method can only

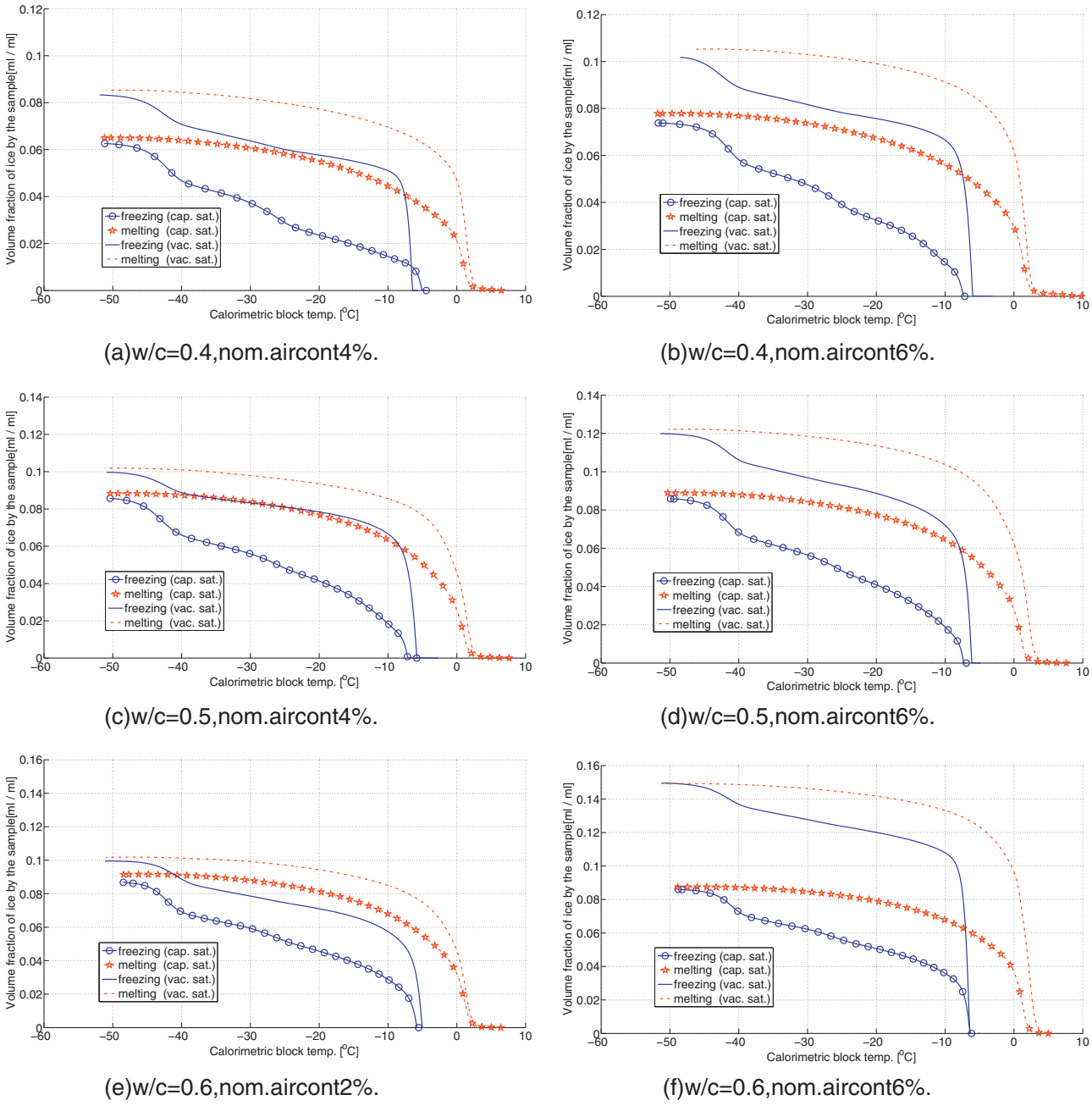

Fig. 3. Calculated fraction of the ice volume by the total volume of the sample for capillary saturated (cap. sat.) and vacuum saturated (vac. sat.) concrete samples. The nominal air content is denoted for each mix and the corresponding measured air content is shown in Table 1.

detect the pores which are filled with water, these unfilled pores will not be detected. For the concrete mixes with the same w/c under study, the difference of the total ice volume fraction between the capillary saturated sample and the vacuum saturated sample increases as the nominal air content increases. Compared with the vacuum saturated samples, the hysteresis effect, as demonstrated by the distance between the freezing curve and the melting curve at the same temperature, is more pronounced for the capillary saturated samples under most of the temperatures in testing, e.g., from $-10\,^{\circ}$C to $-40\,^{\circ}$C. This phenomenon was also pointed out in [17].

The fraction of the maximum ice volume by the total volume of the sample for the concrete mixes presented in Fig. 3 are listed in Table 1. For the calculation method adopted, there is small difference between the ice volume fraction calculated from the freezing and melting process in one cycle for each concrete sample. The result for a sample listed in Table 1 is the average value of the freezing and the melting process. With respect to the concrete mixes with $w/c = 0.4$, the maximum ice volume fraction calculated for the vacuum saturated sample and the capillary saturated sample differ by 2.1% for sample C404; while the difference becomes 3.1% for sample C406. This difference for sample C504 and C506 are 1.2% and 3.4% respectively. The trend that the difference of the maximum ice volume fraction increases as the air content increases, can also be found for the samples with $w/c = 0.6$. The difference for sample C602 is 1.2% and it increases up to 6.3% for sample C606. A possible indication of this phenomenon is that it may be difficult to saturate all of pores, especially the entrained air voids whose diameters are often on the order of 50–100 μm [1,7], with water by the capillary saturation method. However, with the vacuum saturation method, the case could be different. Taking sample C606 as an example, the

Table 1
The fraction of the maximum ice volume by the total volume of the sample for concrete samples presented in Fig. 3. The notation for the sample C404 means that $w/c = 0.40$, nominal air content 4%, and likewise for the other samples. The measured experimental data, including the approximate saturation degree of the capillary saturated samples, the measured air content and the porosity using vacuum saturated samples, are listed for the reference.

Sample	Fraction of maximum ice vol. (%)		Approx. saturation degree (cap. sat. samples)[a,b]	Measured air content (%)[a,c]	Porosity using vac. sat. samples (%)[a,b,d]
	Vac. sat.	Cap. sat.			
C404	8.5	6.4	0.93	4.2	16.8
C406	10.7	7.6	0.81	6.1	18.1
C504	9.9	8.7	0.91	3.6	18.6
C506	12.1	8.7	0.78	5.4	21.6
C602	10.0	8.8	0.88	2.6	18.1
C606	15.0	8.7	0.68	7.8	23.2

[a] Measured experimental data were given in [17].
[b] It was assumed that the samples were fully saturated by vacuum saturation method.
[c] Measured air content for the fresh concrete mixes (the measured air content for the samples C402 and C502, for which the LTC data are not analyzed here, are 2.6% and 2.0% respectively).
[d] Gravimetric measurement.

entrained air content is about 5.2% (by comparing the measured air content of sample C602 with no air-entraining agent and that of C606 with air-entraining agent); while the calculated difference of the ice volume fraction between the vacuum and capillary saturated samples is 5.0%. The difference of the ice volume is very close to the volume of the entrained air. By studying the difference of the ice volume fraction in the samples of the same w/c treated with vacuum saturation method, it is found that the difference is very close to or a little bit higher than the difference of the measured air contents. That is to say possibly after vacuum saturation all of the air voids are filled with water in the concrete samples. If the big pores, i.e., those whose pore sizes are on the same order of the entrained air voids, are filled with water, the possibility for the smaller ones (i.e., those in the nm scale) to be saturated with water is high due to the capillary suction pressure [51].

It is also noticed that RILEM [54] recommended a test method by applying vacuum to reach full saturation for concrete samples, though the applicability of this method on high strength concrete is argued and pressure saturation is proposed by some authors, e.g., see [55–57]. Since the concrete in our study is not high strength concrete and based on the above discussion of the experimental data, we tend to think that the concrete samples are almost fully saturated by vacuum saturation method. On the other hand, one main purpose of this study is to demonstrate how the thermodynamic relation can be affected by the non-fully saturated pores and hence the impact on the determination of the pore size distribution. Even if the vacuum saturation cannot absolutely fully saturate the pores in concrete samples, it would be reasonable to expect that only a small volume of pores is left unsaturated. Then the impact of the small volume of unsaturated pores is considered negligible. In this sense, the concrete samples conditioned by vacuum saturation method is mentioned as fully saturated samples anyway in this study.

4.2. Pore volume and pore size distribution

As can be found from the results shown in Fig. 3, the supercooling effect is very obvious on the freezing curves. Consequently, it is not possible to derive the pore entry sizes whose corresponding freezing temperatures are higher than the supercooled temperature. Additionally, there is a relatively large increase of ice content in the freezing curve around the temperature of about −40 °C for all the studied samples. This portion of ice is believed related to homogenous nucleation, which does not necessarily reflect the pore entry sizes, e.g., see [29,30,47]. Due to this complexity, the pore entry size information will not be analyzed in this study and we will only adopt the melting curve to do the interior pore size distribution analysis.

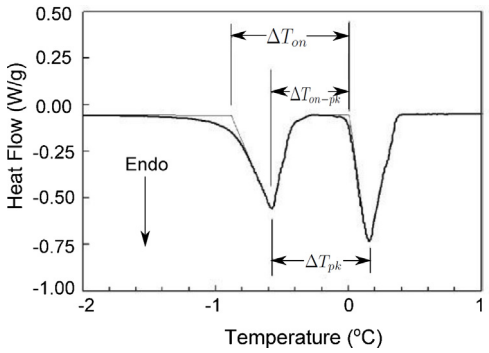

Fig. 4. Three different methods to determine the temperature depression ΔT on the LTC melting curve: the peak-difference (ΔT_{pk}), onset-difference (ΔT_{on})and onset-peak difference ($\Delta T_{on\text{-}pk}$) [36]. "Endo" denotes that the melting process is endothermic.

It can be seen in Fig. 3 that there is a portion of ice which melts above 0 °C in each concrete sample and the amount of this portion of ice is bigger in the vacuum saturated sample than that in the capillary saturated sample for the same concrete mix. This portion of the ice, most of which we believe are present in the relatively big air entrained pores in the concrete samples under our study (the surface dry samples were used in testing indicating very small amount of bulk water, if there is any), behaves like the bulk ice in terms of its heat flow characteristics. The heat flow behavior of bulk ice has been discussed, e.g., in studying the molecular sieve materials [36,42,44,58–60]. It is due to the non-equilibrium between the testing sample and the instrument even if a very small sample (on the order of milligram) is used [36]. That is, the temperature as measured by the instrument is not the same as that in the sample. Consequently, the depressed freezing/melting temperatures should be calibrated accordingly. A detailed explanation about how to calibrate the temperature depression ΔT ($\Delta T = T - T_0$) and the influence of the different determination methods, e.g., in melting process, were conducted in [36]. As shown in Fig. 4, the peak at the lower temperatures on the left side is due to the pore confinement effect and the other peak on the right side, which starts around 0 °C, is due to the surplus bulk water added to the sample. The temperature corresponding to the peak of bulk water will be influenced by the adopted scanning rate and the amount of bulk water in the experiment. Three different methods to determine a better estimate of the ΔT, i.e., the the peak-difference (ΔT_{pk}), the extrapolated onset-difference (ΔT_{on}) and the extrapolated onset-peak difference ($\Delta T_{on\text{-}pk}$), were compared for porous materials with a narrow pore size distribution. It was concluded that the onset-peak difference ($\Delta T_{on\text{-}pk}$) is most appropriate to determine the ΔT,

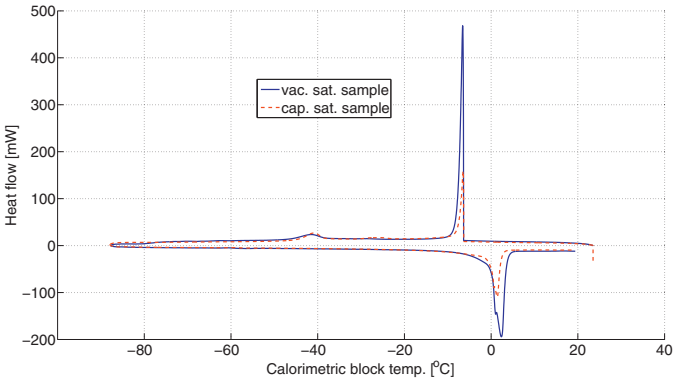

Fig. 5. Measured output data from the LTC instrument, the heat flow versus the calorimetric block temperature, for concrete mix C606. The heat flow was recorded positive in the freezing process and negative in the melting process, respectively.

which shows small sensitivity to the adopted scanning rate and the amount of the surplus bulk water [36].

A typical measured output data from the LTC instrument are plotted in Fig. 5. Unlike the porous materials with narrow pore size distribution, there is only one peak for the tested concrete samples on the melting curves, compared with the two peaks shown in Fig. 4. That is probably mainly due to that the pore sizes of the concrete samples are widely distributed and the ice confined in the pores melts continuously, as a result showing no obvious separated peaks on the melting curves. Using the same method as adopted in [36], it is possible to extrapolate an onset melting temperature on the measured melting curve for a concrete sample. But, still it is not that straightforward to determine the depressed melting temperature ΔT corresponding to each measured temperature T. Because, as we know, the onset of the melting point as determined for the concrete samples in this study should be for the ice in entrained big air voids (on the order of μm) rather than that for the bulk ice. However, the depressed melting temperatures for the ice in the μm pores are already very small, e.g., $\Delta T \approx -0.03$ K for pore radius of 1 μm and $\Delta T \approx -0.003$ K for pore radius of 10 μm (based on Eq. (5)), compared with $\Delta T \approx 0$ K for bulk ice. It makes little sense trying to distinguish the pore sizes at this small level of melting point depression. As we have no clue to which pore radius the onset melting point should correspond, it is necessary to make an assumption. Here, an assumption is made that the extrapolated onset melting point, T_{on}, is corresponding to the melting point of ice confined in the pores with the pore radius of 1 μm (since the sizes of the entrained air voids are on the order of μm), i.e., $T_{on} - T_0 = -0.03$ K. Then, the depressed melting temperature ΔT is calibrated based on the extrapolated onset melting point T_{on} and the measured melting temperature T. Actually, we can also assume the extrapolated onset melting temperature corresponds to the melting point of ice confined in the pores with radius of 500 nm, 10 μm or even to that of bulk ice. The calibrated melting point depression ΔT will not differ too much based on the different assumptions. Thus, the derived pore radii based on the calibrated ΔT (according to Eq. (6) or Eq. (5)) in the range between 2 nm and 40 or 50 nm, i.e., the reliable pore radii for this LTC method as described before, will not be sensitive to the different assumptions made.

The ions in the pore solution and the thermal lag between the instrument and the concrete sample under testing affect the freezing/melting point of the confined water/ice. It should be noted that the measurement conditions will be kept the same for all the measurements and the ions concentration in the pore solution would not differ too much for all the mixes since the same cement is used. Thus, the effects due to the ions and the thermal lag should be more or less the same for all the concrete mixes under consideration in this investigation. Meanwhile, it is also noted that the effect due to the thermal lag and that due to the ions would cancel each other out to a certain degree. As the purpose of this study is to compare the difference caused by the sample saturation on the calculated porosity, both of these factors are considered. In order to derive the pore volume and the pore size distribution, we need to assume the thickness of the δ-layer, δ. As mentioned before, there are different opinions with respect to the specific choice of the value of the δ. As the focus of this study is for comparison purpose, the δ is assumed to be 0.8 nm, as proposed by Brun et al. [24], for all the concrete samples considered. With respect to the relation between pore size and the depressed melting temperature, the numerical equations proposed by Brun et al. [24] based on Eq. (1) is used. That is, Eq. (5) is adopted for cylindrical pore assumption and Eq. (6) for spherical assumption. Based on the calculated ice volume shown in Fig. 3, the pore volume can be derived by Eq. (7), where r is the radius of the ice crystal corresponding to certain depressed melting temperature, $n = 2$ for cylindrical pores and $n = 3$ for spherical pores.

$$R_p = -\frac{32.33}{\Delta T} + 0.68 \tag{5}$$

$$R_p = -\frac{64.67}{\Delta T} + 0.57 \tag{6}$$

$$V_{pore} = V_{ice}\left(\frac{r+\delta}{r}\right)^n \tag{7}$$

The accumulated pore volume and the pore size distribution calculated for the studied concrete samples are shown in Figs. 6–8. Taking the concrete mixes with $w/c = 0.5$ as an example (Fig. 7), it is observed that the accumulated pore size distribution curve as calculated for the capillary saturated sample is below the curve for the vacuum saturated sample from 50 nm up to about 5 nm for both C504 and C506. That is to say in terms of the detected pores, a larger proportion of pores with relatively smaller pore radii is found in the capillary saturated samples than that in the vacuum saturated samples. For sample C504 (Fig. 7b), the calculated volume for the pores with radii between about 2 nm and about 9 nm in the capillary saturated sample is bigger than that in its vacuum saturated counterpart based on the cylindrical assumption; while for the spherical assumption, there are more pores with the radii between about 2 nm and about 11 nm. The similar trend can also be found for sample C506 (Fig. 7d).

Actually, the porosity of the same concrete mix should be independent of the saturation methods. With respect to the difference of the calculated pores as observed, a possible explanation could be as follows. As discussed in Section 2, the melting temperature depression ΔT for the ice confined in the non-fully-saturated pores is larger than that in the fully saturated pores. Since the relation of ΔT and R_p adopted in the calculation is based on the full saturation assumption, the pore radii derived for the non-fully saturated pores are actually underestimated. In other words, we will detect more small pores for a sample if the pores under study are not fully saturated compared with the fully saturated sample. As indicated in Fig. 7, a high proportion of small pores are found for the capillary saturated samples compared with the vacuum saturated samples. That is to say possibly the pores with the radii as shown in Fig. 7 for the capillary saturated samples may not be fully saturated. Then, one may argue that this is not relevant since we can find a portion of water present in the big air entrained pores. If the big air entrained pores have already been filled with some amount of water, the pores with radii much smaller than that of the air entrained voids should have been saturated considering the magnitude of the capillary suction pressure. A possible explanation for the non-fully saturation of the very mall pores in the capillary saturated samples could be due to the cryogenic suction or cryosuction in the freezing process, which is the effect of water from neighboring pores or from the surroundings being drawn towards ice

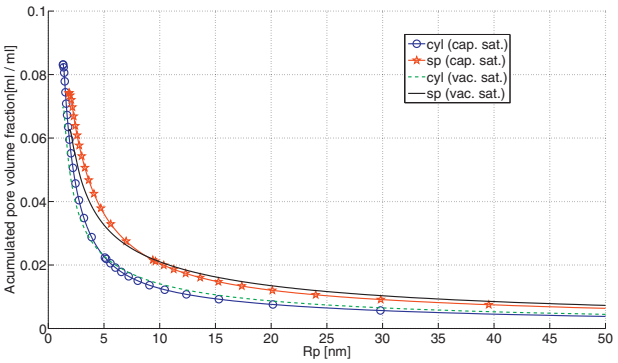

(a) Accumulated pore volume fraction for sample C404.

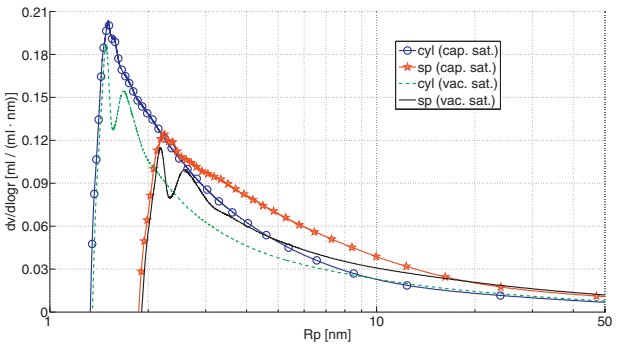

(b) Pore size distribution for sample C404.

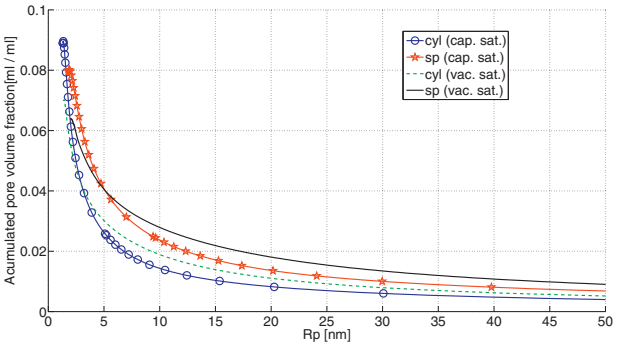

(c) Accumulated pore volume fraction for sample C406.

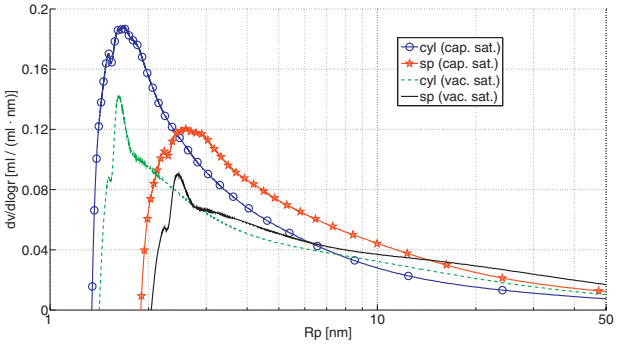

(d) Pore size distribution for sample C406.

Fig. 6. Accumulated volume fraction of the pores with radii smaller than 1 μm (assumption made) by the total volume of the sample and the pore size distribution for the concrete mixes with $w/c = 0.40$. The pore shape is assumed to be cylindrical (cyl) and spherical (sp) in the comparison.

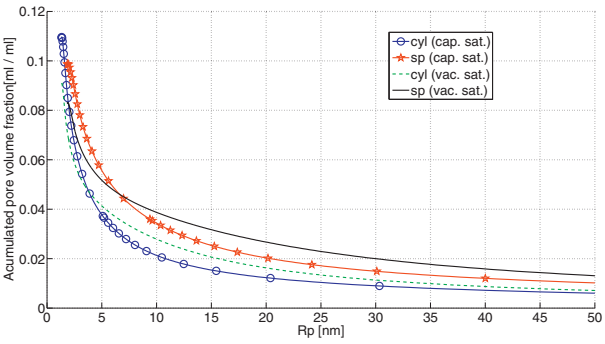

(a) Accumulated pore volume fraction for sample C504.

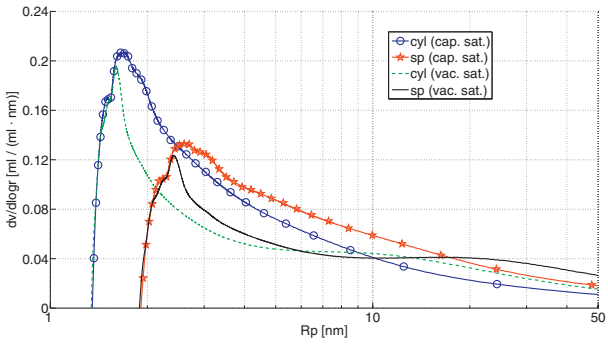

(b) Pore size distribution for sample C504.

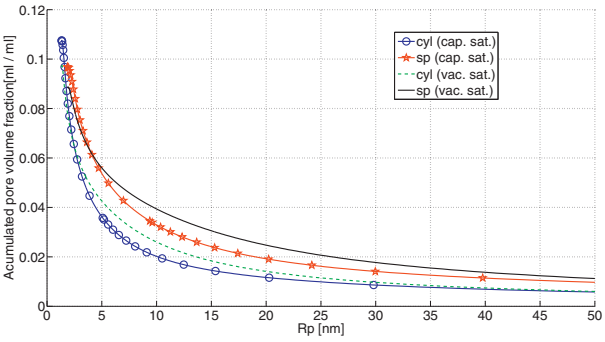

(c) Accumulated pore volume fraction for sample C506.

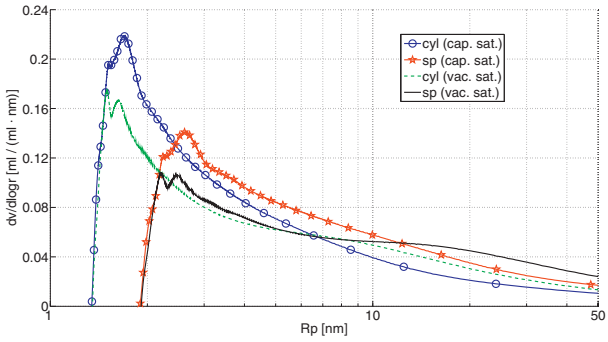

(d) Pore size distribution for sample C506.

Fig. 7. Accumulated volume fraction of the pores with radii smaller than 1 μm (assumption made) by the total volume of the sample and the pore size distribution for the concrete mixes with $w/c = 0.50$. The pore shape is assumed to be cylindrical (cyl) and spherical (sp) in the comparison.

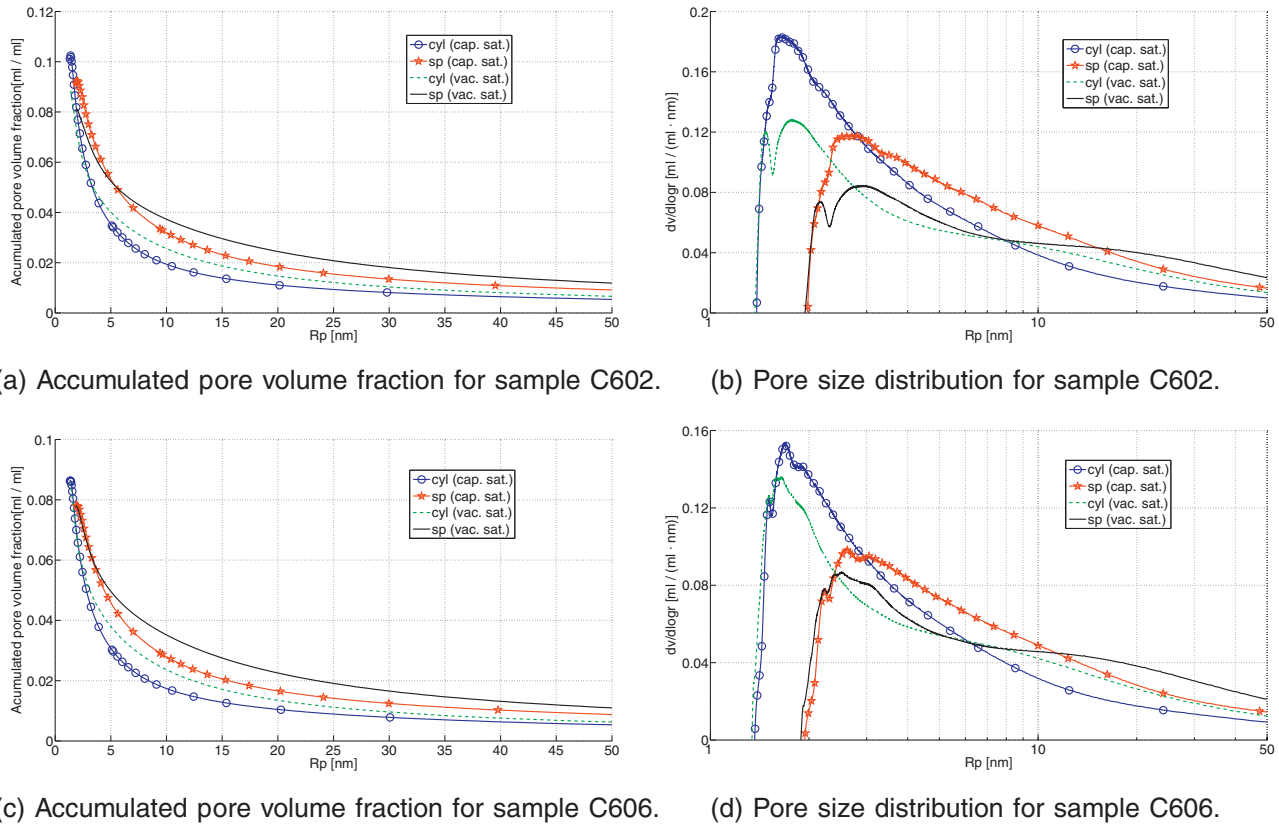

(a) Accumulated pore volume fraction for sample C602. (b) Pore size distribution for sample C602.

(c) Accumulated pore volume fraction for sample C606. (d) Pore size distribution for sample C606.

Fig. 8. Accumulated volume fraction of the pores with radii smaller than 1 μm (assumption made) by the total volume of the sample and the pore size distribution for the concrete mixes with $w/c = 0.60$. The pore shape is assumed to be cylindrical (cyl) and spherical (sp) in the comparison.

crystals already created in the pore system [29,61–64]. Since the entrained air voids are only partly filled in the capillary saturated samples and the water in these pores will freeze at higher temperatures than that in the small nm scale pores, part of the water in the small nm scale pores could possibly be drawn to the big pores, leaving the small pores in non-fully saturated condition during the freezing/melting process. While there is little or no room for this water movement for the fully saturated samples, the small pores under study will stay fully saturated.

A simplified schematic illustration about the comparison between the same pore systems under the non-fully and the fully saturated conditions during freezing are shown in Fig. 9. It should be noted that the menisci system in the drawing (corresponding to Case A in Fig. 1) is just an example and the conclusion will not be changed if the menisci system is different from the drawing. At the beginning, pore A and B can be fully saturated (due to capillary force) but pore C could be non-fully saturated under the non-fully saturated condition (left); while under the fully saturated condition (right), all of these three pores are saturated. As the temperature decreases to the point that the liquid in pore C under fully saturated condition can freeze, the water in pore C under the non-fully saturated condition will stay unfrozen due to the gas phase inside of the pore, which leads to the further depression of the freezing point of the inside water. When the temperature keeps decreasing, the liquid in pore C under the non-fully saturation (left) will freeze at a certain temperature. Meanwhile, due to the cryosuction effect, part of the water in pore A and B which are connected to the non-fully saturated pore C could be sucked out. It is noted that the water migration caused by the cryosuction could possibly take place over the whole freezing process, as far as there is still empty space. Consequently, pore A and B will be under non-fully saturated situation when the confined water freezes. Then the measured freezing/melting point of the water in the non-fully saturated pore A and B (even though they are fully saturated at the beginning) will be lower compared with their fully saturated counterparts, as illustrated in Fig. 9. The lower the freezing/melting point, the smaller the calculated pore size. Since the relation between the pore size and the measured freezing/melting point in the adopted calculation is based on the fully saturated condition, the calculated radii of the non-fully saturated pores will be smaller compared with that under fully saturation. Thus, it should be kept in mind that the high proportion of the small pores as calculated for the capillary saturated samples may not be relevant. In the context of pore size analysis using freezing/melting point depression, due to fact that it is almost impossible to derive the quantitative relation between the depressed freezing/melting point and the corresponding pore sizes as discussed in Section 2, it is not appropriate to calculate the pore size distribution for the samples whose pores under study are not fully saturated.

It is also noticed that the total accumulated pore volume as calculated (less than 1 μm by the assumption made before) for the capillary saturated samples is larger than that of the vacuum saturated samples, see Fig. 7a and c. As demonstrated before, the relation of the pore volume and the ice volume is given as Eq. (7). By taking into account the volume of the δ-layer, which could account for an important part of the total pore volume when the pore radii are very small, the pore volume as derived for the capillary saturated samples could be larger than that of the vacuum saturated samples, even if the saturation degree of the small pores in the capillary saturated samples during freezing/melting could be lower than that in the vacuum saturated samples. The reason is that the calculated pore sizes of the capillary saturated samples are smaller than that in the vacuum saturated samples (smaller pore sizes indicates more surface area), then the estimated volume of the δ-layer

Table 2
The calculated pore volume fraction detected by LTC, the volume fraction of the estimated δ-layer and the volume fraction of the pores with radii less than 0.8 nm for the concrete samples presented in Fig. 3 based on cylindrical (cyl.) and spherical (sp.) pore shape assumption. The volume fraction is the volume by the total volume of the sample. The notation for the sample C404c means that $w/c = 0.40$, nominal air content 4%, capillary saturated, and likewise ("v" indicating vacuum saturated) for the other samples. The specific surface area is also listed.

Sample	Pore vol. fraction (%)[a,b]		δ-Layer vol. fraction (%)[b]		Pore vol. fraction (%)[c,d] (R_p < 0.8 nm)		Total specific surface area (m^2/g)[e]	
	cyl.	sp.	cyl.	sp.	cyl.	sp.	cyl.	sp.
C404c	10.4	9.6	4.0	3.2	5.8	6.7	30.3	24.4
C404v	11.6	11.0	3.2	2.5	6.0	6.7	24.0	19.3
C406c	11.9	11.0	4.3	3.3	5.0	5.9	31.5	25.2
C406v	13.2	12.5	2.5	1.9	7.6	8.3	25.9	20.8
C504c	13.5	12.5	4.7	3.7	4.4	5.4	35.5	28.4
C504v	13.7	12.8	3.7	2.9	5.6	6.4	26.6	21.4
C506c	13.6	12.5	4.8	3.7	3.6	4.7	35.4	28.3
C506v	16.0	15.1	3.9	3.0	5.6	6.6	28.4	22.7
C602c	13.5	12.5	4.6	3.6	3.4	4.5	32.4	25.8
C602v	13.5	12.7	3.4	2.7	4.5	5.3	24.6	19.6
C606c	12.3	11.4	3.5	2.7	4.0	4.8	26.7	21.2
C606v	18.1	17.4	3.2	2.4	4.2	4.9	24.3	19.4

[a] The pore volume fraction detected by the LTC method.
[b] The volume of the δ-layer in the pores with radii bigger than 1 μm (assumption made) is not included.
[c] This fraction is estimated by using the measured total water content in the tested sample.
[d] It should be noted that this value might be overestimated due to the procedure adopted to measure the total water content, i.e., drying at 105 °C till constant weight.
[e] The total surface area is expressed in m^2/g dry concrete and the total specific surface area calculated does not include the contribution from the pores with radii smaller than the thickness of the δ-layer and that from the pores with radii bigger than 1 μm (assumption made).

for the capillary saturated samples could be higher than that of the vacuum saturated samples (the related volume comparison can be found in Table 2), leading to the bigger total accumulated volume as observed in the capillary saturated samples.

Similar phenomena which we have observed for the concrete mixes with $w/c = 0.5$ have also been found for the concrete mixes with $w/c = 0.4$ (Fig. 6) and $w/c = 0.6$ (Fig. 8). The proposed explanations with respect to the obtained results given for the concrete mixes with $w/c = 0.5$ are applicable to all of the concrete mixes studied.

Although it is not possible to determine the pore size distribution for the pores with radii bigger than the upper limit of the LTC method, the volume of the proportion of big pores in the concrete samples can be estimated from Fig. 3. In the previous discussion, the accumulated pore volume for the pores with radii smaller than 1 μm were calculated by making certain assumptions. For the bigger pores (radii >1 μm) in this study, the pore volume is assumed to be the same as that of the ice without considering the volume of δ-layer which is thought to be not an important part compared with the total pore volume of these big pores. By adding the volume of the big pores, i.e., the ice volume of these pores, the total accumulated pore volume detected by LTC method can be estimated. The volume of the δ-layer (in pores with radii smaller than 1 μm) can be calculated by subtracting the calculated total ice content from the calculated total pore volume. Meanwhile, it is realized that the volume of the pores with radii smaller than the thickness of the δ-layer (0.8 nm) cannot be detected by the LTC method directly because this part of water will also stay unfrozen during the testing. However, it is still possible to estimate the volume. As mentioned in Section 3, the total water content of a sample can be obtained through the gravimetric measurements. Thus the volume of the unfreezable water in the pores with radii smaller than the thickness of the δ-layer can be estimated by subtracting the volume of the total ice and the volume of the δ-layer from the volume of the total water. Furthermore, it is also possible to estimate the specific surface area from the pore volume based on the assumed pore shape. For the pores with a radii of R_p and the volume of V_{pore}, the corresponding specific surface area (S) can be calculated by Eq. (8), where $n = 2$ for cylindrical pores and $n = 3$ for spherical pores. By summing up all the specific surface area of the pores detected, the total specific surface area can be obtained. However, the total specific surface area calculated in this study does not include the contribution from the surfaces of pores with radii smaller than the thickness of the δ-layer and that from the pores with radii bigger than 1 μm. Thus, it is no more than a rough estimation. The calculated results are listed in Table 2.

$$S = \frac{n \cdot V_{pore}}{R_p} \tag{8}$$

According to Table 2, it can be seen that for the same concrete mix, the total pore volume fraction determined is normally larger in the vacuum saturated sample compared with that in the capillary saturated sample, because the saturation degree in the capillary saturated sample is lower. The calculated volume of the δ-layer is found to be larger in the capillary saturated samples compared with the vacuum saturated counterparts. The reason is that due to the further depressed phase transition point of water/ice in the capillary saturated samples, the pore radii of the capillary saturated samples are wrongly interpreted and smaller values than that in the vacuum saturated samples are obtained. For a certain pore volume, it can be imagined that the surface area of pores with smaller pore radii should be larger than that of the pores with bigger pore radii. Since the volume of the δ-layer is calculated by multiplying the calculated surface area and the thickness of the δ-layer, which is assumed to be a constant value (0.8 nm assumed in this study), larger surface area results into larger apparent volume in the δ-layer. When the pore radii are on the order of several nm, the volume of the δ-layer could be an important part of the total pore volume. As mentioned before, after adding the volume of δ-layer, the total pore volume (radii<1 μm) for the capillary saturated samples could be larger than that of the vacuum saturated ones even if the saturation degree of the pores during freezing/melting is lower in the capillary saturated samples.

As expected, the calculated total specific surface area does show that the value of the vacuum saturated samples is smaller than that of the capillary saturated samples. The reason has just been explained, i.e., the further depressed phase transition point of water/ice in the capillary saturated samples. It needs to be mentioned that the specific surface area present here is expressed in m^2/g dry concrete. The reported value for the relevant fully hydrated cement pastes in literature is between 80 and 300 m^2/g of dry paste depending on several different measuring techniques used, e.g., see [8,9,12]. A rough conversion of the unit shows that the specific surface area of the studied concrete samples is around

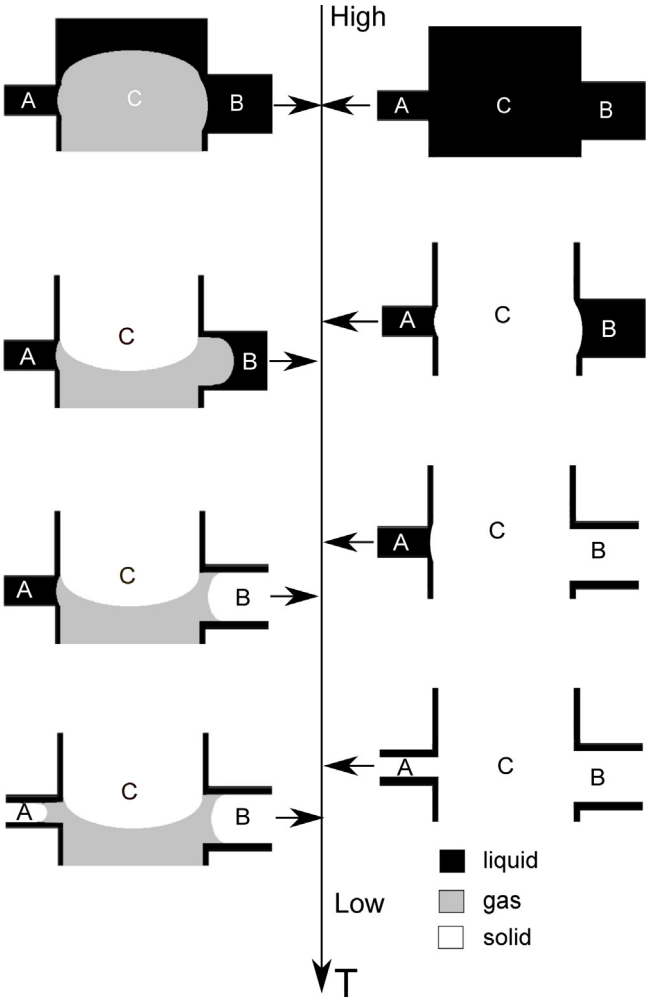

Fig. 9. A simplified schematic illustration of the comparison between the same pore systems under the non-fully saturated (left) and the fully saturated (right) conditions during freezing, pore shape being assumed to be cylindrical and the pore radius $r_C > r_B > r_A$. The three pores are not isolated and they are connected to other pores. The dark area close to the pore wall indicates liquid in the δ-layer. The temperature decreases along the line (T) from the top to the bottom. Details about the change of the liquid–gas and solid–gas curvature in the pores to meet the thermodynamic conditions as the temperature decreases are neglected in the drawing. Compared with pores under fully saturation, the calculated radii of the pores with the same radii under non-fully saturation will be smaller due to higher temperature depressions.

$100\,m^2/g$ of dry paste, which falls nicely in the reported range. Therefore, it seems that the surface area calculation might not be affected by the pores with radii smaller than the thickness of the δ-layer. This is somewhat in accordance with the argument given by Thomas et al. [9], which states the interlayer spaces (sizes comparable to the thickness of the δ-layer) within the C-S-H phase do not contribute to surface area as it is normally defined. That is, possibly the LTC method can be used in the context of surface area determination irrespective of the fact that it cannot detect the pores with radii smaller than the thickness of the δ-layer. Additionally, it should also be noted that the calculated volume of the δ-layer and the total specific surface area for the capillary saturated samples are only apparent values, which do not necessarily represent the true values due to the effect of the further depressed phase transition point of the water/ice confined in the non-fully saturated pores.

4.3. Comparison of the hysteresis

Regarding the more pronounced hysteresis effect observed in the capillary saturated samples than the vacuum saturated samples, e.g., in the temperature range of −10 °C to −40 °C, possible explanations could be proposed. Using the sample C606 as an example, the calibrated ice volume fraction diagram for the pore size distribution analysis in the study (i.e., the ice in the pores which are smaller than 1 μm by the assumption, meaning the ice in big air voids is not included) is shown in Fig. 10. It can be found that the total ice volume for the capillary saturated sample is smaller than that of the vacuum saturated one, which could be due to the lower saturation degree of the capillary saturated sample during the freezing/melting process. Under the same temperature depression ΔT_i, the distance between the freezing curve and the melting curve of the capillary saturated sample is denoted as $d1$ and that of the vacuum saturated sample is denoted as $d2$, while $d3$ denotes the distance between the two freezing curves and $d4$ for the melting curves. The lower saturation degree of the capillary saturated sample is believed to partly contribute to $d3$ and $d4$. Another contribution factor could be attributed to the fact that the freezing/melting temperature for the water/ice confined in pores with certain radius will be further depressed for the non-fully-saturated sample. Thus, a portion of water /ice which should freeze/melt at certain temperature if the pores are fully saturated will freeze/melt at a lower temperature since the pores are not fully saturated. This will result in that the freezing/melting curve of the non-fully-saturated sample will be lower than fully saturated one during certain pore radii. One may argue that the further depressed freezing/melting temperature behavior for the non-fully saturated sample should take place both in the freezing and melting process, so the contribution due to this further depression to $d3$ and $d4$ should be the same. If so, why is the hysteresis still more pronounced in the non-fully saturated sample?

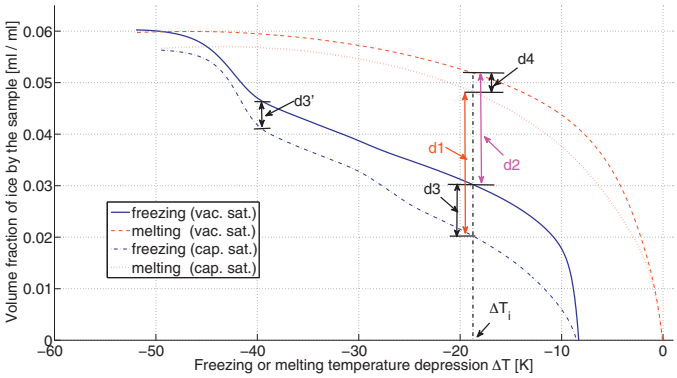

Fig. 10. The ice volume fraction of the pores with radii smaller than 1 μm (assumption made) versus the calibrated freezing/melting temperature depression for sample C606 to illustrate the more pronounced hysteresis effect found for the capillary saturated sample than the vacuum saturated sample.

According to the explanation given by Brun et al. [24], pore shape is kind of the main reason for the hysteresis. In another word, there will be hysteresis if the pore shape is cylindrical and there will not be any hysteresis at all if the pores are spherical. Since the pores are neither perfectly cylindrical nor spherical in reality, they developed a shape factor to characterize a specific pore system. Based on their arguments, it would be more appropriate to adopt the cylindrical assumption for the studied concrete samples since the hysteresis is very pronounced. As a result of this hypothesis, the pore radii corresponding to the same temperature depression ΔT in the freezing and the melting should be different. Taking the $\Delta T = -10$ °C for example, the corresponding pore radius is about 6–7 nm (Eq. (6)) in freezing and is about 3 nm (Eq. (5)) in melting. Analogously, the distance $d4$ between the melting curves in the current position in Fig. 10 should not correspond to $d3$ between the freezing curves at the same ΔT, but a position with a lower temperature whose corresponding radius is the same as that in

the melting, e.g., $d3'$. On the other hand, as can be found in Fig. 8d based on the cylindrical pore assumption, the volume of the pores predicted by the capillary saturated sample is bigger than that of the vacuum saturated sample for the pores whose radii are smaller than about 6 nm till about 2 nm. This is, the water confined in these pores in the capillary saturated sample is further depressed due to the non-fully saturated condition, with the corresponding freezing point mainly between −10 °C and −40 °C. So for the melting curve at $\Delta T = -10$ °C, the effect due to the non-fully saturated pores on the total ice volume is almost completely reflected while this effect is just starting to show on the freezing curve. As a result, $d3$ is always bigger than $d4$ at the same temperature depression during the temperature range of −10 °C to −40°C. The consequence is that $d1$ is always bigger than $d2$ for a certain ΔT during the temperature range, showing more pronounced hysteresis effect in the capillary saturated samples compared with the vacuum saturated samples. Due to the supercooling in the freezing curves, the hysteresis is not analyzed for the temperature depression less than −10 °C. When the temperature depression goes down to lower than −40 °C, the hysteresis effect tends to be the same magnitude for capillary and vacuum saturated samples and finally the hysteresis will disappear. However, it is also noted that the pore shape may not be the only reason for the hysteresis. More discussion about the origin of the hysteresis behavior, which can be found in, e.g., [7,65–67], falls outside the scope of this discussion.

5. Conclusions

Low temperature (micro-)calorimetry (LTC) is often adopted to study the pore volume and the pore size distribution of porous materials. It is noted that if the porous material under testing is not fully saturated, not only the pore volume is underestimated but also the relevance of the derived pore size distribution would be in doubt. The present study carefully examined theoretically the thermodynamic relation between the pore size and the depressed freezing/melting temperature of the confined water/ice under fully and non-fully saturated conditions and the impact of sample saturation on the analysis of the pore volume and the pore size distribution was illustrated using experimental data measured on hardened concrete samples. Some key points can be summarized as follows:

1. The thermodynamic background about the freezing/melting point of water/ice confined in a pore under fully and non-fully saturated conditions were carefully examined. It is emphasized that compared with the situation when the pore is fully saturated, the freezing/melting point of the pore water/ice is lower if the pore is not fully saturated.
2. The ice content calculated from the capillary saturated sample was lower than that from the vacuum saturated sample for the same concrete mix and the difference became bigger as the nominal air content increases. This implies that the capillary saturation may not be able to saturate all the pores, especially the entrained air voids, in the concrete samples. Then, part of the water in some of the initially saturated very small pores (at the nanometric level) before freezing starts may be sucked out by the cryo-suction force during the freezing process, leaving some of the very small pores also under non-fully saturated condition.
3. The proportion of the calculated pores with smaller radii was higher in the capillary saturated samples than that in the vacuum saturated samples using the same calculation method. The reason is probably that for the capillary saturated samples, not all of the pores under study are fully saturated during the freezing/melting process and thus the corresponding phase transition temperatures for the water/ice confined in these pores are further depressed, as illustrated in the theoretical study. Then, the pore radii would be wrongly interpreted as we still abide by the relation as derived based on the full saturation. However, since the relation for the non-fully saturated pores is extremely difficult, if it is still possible, to define, it is not appropriate to derive the pore size distribution in the context of LTC analysis using non-fully saturated samples.
4. The hysteresis behavior observed between the freezing and melting ice content curves in the capillary saturated samples was more pronounced compared with that in the vacuum saturated samples. Possibly it could also be related to the further depressed phase transition temperatures for the water/ice in the non-fully saturated pores as described in a detailed manner in the discussion.

Acknowledgment

The research leading to these results has received funding from the European Union Seventh Framework Programme (FP7/2007-2013) under Grant agreement 264448.

References

[1] T. Powers, The air requirement of frost resistant concrete, in: Proceedings of the Highway Research Board, vol. 29, 1949, pp. 184–211.
[2] M. Pigeon, R. Pleau, Durability of Concrete in Cold Climates, no. 4, Taylor & Francis, Oxford (UK), 1995.
[3] S. Kosmatka, W. Panarese, Design and Control of Concrete Mixtures, Portland Cement Association, Illinois (USA), 2002.
[4] T. Powers, T. Brownyard, Studies of the physical properties of hardened portland cement paste, in: ACI Journal Proceedings, vol. 43, 1947, pp. 549–602.
[5] H. Jennings, Refinements to colloid model of C-S-H in cement: CM-II, Cement and Concrete Research 38 (3) (2008) 275–289.
[6] P. McDonald, V. Rodin, A. Valori, Characterisation of intra- and inter-C-S-H gel pore water in white cement based on an analysis of NMR signal amplitudes as a function of water content, Cement and Concrete Research 40 (12) (2010) 1656–1663.
[7] Z. Sun, G. Scherer, Pore size and shape in mortar by thermoporometry, Cement and Concrete Research 40 (5) (2010) 740–751.
[8] R.F. Feldman, The porosity and pore structure of hydrated portland cement paste, in: J.S.L.R. Roberts (Ed.), in: Pore Structure and Permeability of Cement based Materials, vol. 137, Materials Research Society, Pittsburgh, PA, 1989, pp. 59–73.
[9] J. Thomas, H. Jennings, A. Allen, The surface area of hardened cement paste as measured by various techniques, Concrete Science and Engineering 1 (1999) 45–64.
[10] A. Kjeldsen, M. Geiker, On the interpretation of low temperature calorimetry data, Materials and Structures 41 (1) (2008) 213–224.
[11] J. Strange, J. Mitchell, J. Webber, Pore surface exploration by NMR, Magnetic Resonance Imaging 21 (3/4) (2003) 221–226.
[12] V. Baroghel-Bouny, Water vapour sorption experiments on hardened cementitious materials. Part I: essential tool for analysis of hygral behaviour and its relation to pore structure, Cement and Concrete Research 37 (3) (2007) 414–437.
[13] J. Villadsen, Pore structure in cement based materials, Tech. Rep. 277, Building Materials Laboratory, Technical University, Denmark, 1992.
[14] J. Young, A review of the mechanisms of set-retardation in portland cement pastes containing organic admixtures, Cement and Concrete Research 2 (4) (1972) 415–433.
[15] G. Fagerlund, Determination of pore-size distribution from freezing-point depression, Materials and Structures 6 (3) (1973) 215–225.
[16] Q. Xu, J. Hu, J. Ruiz, Z. Wang, K. Ge, Isothermal calorimetry tests and modeling of cement hydration parameters, Thermochimica Acta 499 (1) (2010) 91–99.
[17] B. Johannesson, Dimensional and ice content changes of hardened concrete at different freezing and thawing temperatures, Cement and Concrete Composites 32 (1) (2010) 73–83.
[18] Q. Xu, J.M. Ruiz, J. Hu, K. Wang, R. Rasmussen, Modeling hydration properties and temperature developments of early-age concrete pavement using calorimetry tests, Thermochimica Acta 512 (1) (2011) 76–85.
[19] D. Bager, Ice formation in hardened cement paste (Ph.D. thesis), Building Materials Laboratory, Technical University of Denmark, 1984.
[20] D. Bager, E. Sellevold, Ice formation in hardened cement paste. Part I: room temperature cured pastes with variable moisture contents, Cement and Concrete Research 16 (5) (1986) 709–720.
[21] D. Bager, E. Sellevold, Ice formation in hardened cement paste. Part III: slow resaturation of room temperature cured pastes, Cement and Concrete Research 17 (1) (1987) 1–11.

[22] E. Sellevold, D. Bager, Some implications of calorimetric ice formation results for frost resistance testing of concrete, in: Beton og Frost, vol. 22, Dansk Beton forening, Copenhagen (Denmark), 1985, pp. 47–74.
[23] R. Defay, I. Prigogine, A. Bellemans, D. Everett, Surface Tension and Adsorption, Longmans, London, 1966.
[24] M. Brun, A. Lallemand, J. Quinson, C. Eyraud, A new method for the simultaneous determination of the size and shape of pores: the thermoporometry, Thermochimica Acta 21 (1) (1977) 59–88.
[25] G. Fagerlund, Studies of the scaling, the water uptake and the dilation of specimens exposed to freezing and thawing in NaCl solution, in: Proceedings of RILEM Committee 117 DC Freezing/Thaw and Deicing Resistance of Concrete, Sweden, 1991, pp. 37–66.
[26] M. Brun, A. Lallemand, J. Quinson, C. Eyraud, Changement d'état liquid–solide dans les milieux poreux. II. Étude théorique de la solidification d'un condensate capillaire (liquid–solid change of state in porous media. II. Theoretical study of the solidification of a capillary condensate), Journal de Chimie Physique 6 (1973) 979–989.
[27] T. Powers, Physical properties of cement paste, in: Proc. Fourth Int. Symp. on the Chemistry of Cement, Washington, DC, 1960.
[28] J. Schmelzer (Ed.), Nucleation Theory and Applications, Wiley-VCH, Berlin-Weinheim (Germany), 2005.
[29] G. Scherer, Freezing gels, Journal of Non-crystalline Solids 155 (1) (1993) 1–25.
[30] J. Kaufmann, Experimental identification of ice formation in small concrete pores, Cement and Concrete Research 34 (8) (2004) 1421–1427.
[31] J. Quinson, M. Astier, M. Brun, Determination of surface areas by thermoporometry, Applied Catalysis 30 (1) (1987) 123–130.
[32] J. Quinson, M. Brun, Progress in thermoporometry, in: K.K. Unger, J. Rouquerol, K.S.W. Sing, H. Kral (Eds.), Characterization of Porous Solids, Elsevier, Amsterdam, 1988, p. 307.
[33] D. Rasmussen, A. MacKenzie, Clustering in supercooled water, Journal of Chemical Physics 59 (1973) 5003.
[34] H. Jellinek (Ed.), Water Structure at the Water–Polymer Interface, Plenum, New York, 1972.
[35] K. Ishikiriyama, M. Todoki, K. Min, S. Yonemori, M. Noshiro, Pore size distribution measurements for microporous glass using differential scanning calorimetry, Journal of Thermal Analysis and Calorimetry 46 (3-4) (1996) 1177–1189.
[36] M. Landry, Thermoporometry by differential scanning calorimetry: experimental considerations and applications, Thermochimica Acta 433 (1-2) (2005) 27–50.
[37] Le Sage de Fontenay, Ice formation in hardened cement paste (Ph.D. thesis), Building Materials Laboratory, Technical University of Denmark, 1982 (in Danish).
[38] K. Fridh, Internal frost damage in concrete-experimental studies of destruction mechanisms (Ph.D. thesis), Division of Building Materials, Lund Institute of Technology, 2005.
[39] E. Hansen, H. Gran, E. Sellevold, Heat of fusion and surface tension of solids confined in porous materials derived from a combined use of NMR and calorimetry, Journal of Physical Chemistry B 101 (35) (1997) 7027–7032.
[40] F. Radjy, E. Sellevold, K. Hansen, Isosteric vapor pressure-temperature data for water sorption in hardened cement paste: enthalpy, entropy and sorption isoterms at different temperatures, Tech. Rep. 57, Department of Civil Engineering, Technical University of Denmark, 2003.
[41] M. Wu, B. Johannesson, M. Geiker, Determination of ice content in hardened concrete by low temperature calorimetry: influence of baseline calculation and heat of fusion of confined water, Journal of Thermal Analysis and Calorimetry 115 (2014) 1335–1351.
[42] T. Yamamoto, A. Endo, Y. Inagi, T. Ohmori, M. Nakaiwa, Evaluation of thermoporometry for characterization of mesoporous materials, Journal of Colloid and Interface Science 284 (2) (2005) 614–620.
[43] J. Banys, M. Kinka, J. Macutkevic, G. Völkel, W. Böhlmann, V. Umamaheswari, M. Hartmann, A. Pöppl, Broadband dielectric spectroscopy of water confined in MCM-41 molecular sieve materials-low-temperature freezing phenomena, Journal of Physics: Condensed Matter 17 (2005) 2843.
[44] K. Ishikiriyama, M. Todoki, K. Motomura, Pore size distribution (PSD) measurements of silica gels by means of differential scanning calorimetry. I: optimization for determination of PSD, Journal of Colloid and Interface Science 171 (1) (1995) 92–102.
[45] M. Setzer, Mechanical stability criterion, triple-phase condition, and pressure differences of matter condensed in a porous matrix, Journal of Colloid and Interface Science 235 (1) (2001) 170–182.
[46] M. Setzer, Micro-ice-lens formation in porous solid, Journal of Colloid and Interface Science 243 (1) (2001) 193–201.
[47] G.W. Scherer, J.J. Valenza I.I., Mechanisms of Frost Damage, in: J. Skalny, F. Young (Eds.), Materials Science of Concrete, Vol. VII, American Ceramic Society, Ohio (USA), 2005, pp. 209–246.
[48] P. Williams, Properties and behavior of freezing soils, Tech. Rep. 72, Norwegian Geotechnical Institute, Oslo, Norway, 1961.
[49] J. Blachere, J. Young, The freezing point of water in porous glass, Journal of the American Ceramic Society 55 (6) (1972) 306–308.
[50] E. Shiko, K. Edler, J. Lowe, S. Rigby, Probing the impact of advanced melting and advanced adsorption phenomena on the accuracy of pore size distributions from cryoporometry and adsorption using NMR relaxometry and diffusometry, Journal of Colloid and Interface Science 385 (1) (2012) 183–192.
[51] Johannesson, Moisture fixation in mature concrete and other porous materials (8A), lecture notes for Introduction to Concrete Technology (11563), Technical University of Denmark, 2011.
[52] B. Johannesson, G. Fagerlund, Concrete for the storage of liquid petroleum gas-freeze/thaw phenomena and durability at freezing to −50 °C, Report TVBM-7174, Division of Building Materials, Lund Institute of Technology, 2003.
[53] G. Fagerlund, B. Johannesson, Concrete for the storage of liquid petroleum gas. Part II: influence of very high moisture contents and extremely low temperatures, −196 °C, Report TVBM – 1851, Division of Building Materials, Lund Institute of Technology, 2005.
[54] , in: RILEM recommendations-absorption of water by immersion under vacuum, Materials and Structures 101 (1984) 393–394.
[55] M. Geiker, P. Laugesen, in: On the effect of laboratory conditioning and freeze/thaw exposure on moisture profiles in HPC, Cement and Concrete Research 31 (12) (2001) 1831–1836.
[56] A. Henrichsen, P. Laugesen, M. Geiker, E.J. Pedersen, N. Thaulow, HETEK: method for test of the frost resistance of high performance concrete: summary, conclusions and recommendations, Tech. Rep. 97, The Danish Road Directirate, Denmark Ministry of Transport, 1997.
[57] M.I. Khan, A novel method for measuring porosity of high strength concrete, in: Proceedings of the 7th Saudi Engineering Conference (SEC7), 2007.
[58] K. Ishikiriyama, M. Todoki, in: Pore size distribution measurements of silica gels by means of differential scanning calorimetry. II. Thermoporosimetry, Journal of Colloid and Interface Science 171 (1) (1995) 103–111.
[59] K. Ishikiriyama, M. Todoki, in: Evaluation of water in silica pores using differential scanning calorimetry, Thermochimica Acta 256 (2) (1995) 213–226.
[60] M. Titulaer, J. Van Miltenburg, J. Jansen, J. Geus, in: Thermoporometry applied to hydrothermally aged silica hydrogels, Recueil des Travaux Chimiques des Pays-Bas 114 (8) (1995) 361–370.
[61] O. Coussy, T. Fen-Chong, in: Crystallization, pore relaxation and micro-cryosuction in cohesive porous materials, Comptes Rendus Mecanique 333 (6) (2005) 507–512.
[62] P. Monteiro, O. Coussy, D. Silva, in: Effect of cryo-suction and air void transition layer on hydraulic pressure of freezing concrete, ACI Materials Journal 103 (2) (2006) 136–140.
[63] A. Dupas, Effect of vertical drain barrier on road behaviour in freeze–thaw periods, in: Geotextiles, Geomembranes and Related Products, vol. 1 (out of 3 volumes): Proceedings of the 4th International Congress, The Hague, 28 May–1 June, Taylor & Francis, 1990, p. 339.
[64] P. Parker, A. Collins, in: Dehydration of flocs by freezing, Environmental Science & Technology 33 (3) (1999) 482–488.
[65] K. Morishige, K. Kawano, in: Freezing and melting of water in a single cylindrical pore: the pore-size dependence of freezing and melting behavior, Journal of Chemical Physics 110 (1999) 4867.
[66] G. Findenegg, S. Jähnert, D. Akcakayiran, A. Schreiber, in: Freezing and melting of water confined in silica nanopores, ChemPhysChem 9 (18) (2008) 2651–2659.
[67] J. Riikonen, J. Salonen, V. Lehto, in: Utilising thermoporometry to obtain new insights into nanostructured materials (review part 1), Journal of Thermal Analysis and Calorimetry 105 (2011) 811–821.

Paper III

Influence of frost damage and sample preconditioning in studying the porosity of cement based materials using low temperature calorimetry

M. Wu, K. Fridh, B. Johannesson, M. Geiker

Submitted to: *Construction and Building Materials, 2014*

Influence of frost damage and sample preconditioning on the porosity characterization of cement based materials using low temperature calorimetry

Min Wu[a], Katja Fridh[b], Björn Johannesson[a], Mette Geiker[c]

a. Department of Civil Engineering, Technical University of Denmark, Building 118, 2800 Lyngby, Denmark

b. Division of Building Materials, Lund University, Lund, Sweden

c. Department of Structural Engineering, Norwegian University of Science and Technology, Trondheim, Norway

Abstract

Low temperature calorimetry (LTC) can be used to study the meso-porosity of cement based materials. The influence of frost damage on the meso-porosity determination by LTC was investigated using a model material MCM-41 and two types of cement pastes by conducting repeated cycles of freezing and melting measurements. The results indicate that the pressure generated during freezing and melting measurements has little impact on the pore structure of the powder MCM-41 samples. As for the studied cylinder samples of cement pastes, frost damage probably takes place and it changes the pore connectivity while it has limited effects on changing the interior size distribution of the meso-pores. The analysis of the freezing and melting behavior of the pore liquid of cement based materials is complicated by the presence of ions. The freezing and melting behavior of the pore solution of cement paste samples preconditioned in either a small amount or a big amount of saturated limewater was compared. The results suggest that either the preconditioning in a big amount of limewater does not change the ionic concentration of the pore solution very much or the possible leaching of ions from cement hydrates during the preconditioning has limited influence on the freezing and melting behavior of the pore solution in the studied cement paste samples.

Keywords: Cement paste, calorimetry, freezing and thawing, frost damage, thermoporometry, cryoporometry.

1. Introduction

The freezing point of water or melting point of ice confined in pores is lower than that of bulk water or ice and the magnitude of the freezing/melting point depression depends on the size of the pores in which the freezing/melting takes place [1]. Cement based materials have a rather complicated pore system, whose pore sizes can range from nanometer to millimeter [2, 3]. Due to the confinement of pores with different sizes, water present in the pores of cement based materials freezes at different temperatures when the materials are exposed to low temperature environments. The freezing behavior of the water and/or the melting behavior of the ice confined in the pores can be used to study some important properties of the materials, e.g., the freeze/thaw durability [4, 5] and the porosity [6, 7].

Low temperature (micro-)calorimetry (LTC), which is also known as thermoporometry and sometimes is referred to as thermoporosimetry or cryoporometry [8], can be used to characterize the porosity of cement based materials. The basic concept of LTC is that the freezing process of water is an exothermic process and the melting process of ice is an endothermic process. During a measurement, the LTC instrument (calorimeter) records the heat flow of the sample at different testing temperatures. Based on the measured heat flow and using the heat of fusion for the confined water/ice, the ice content in the freezing or the melting process can be calculated. The volume of the ice formed/melted under different temperatures in a sense indicates the pore information of the sample under the testing. By introducing proper assumptions, thermodynamic studies demonstrate that there is a unique equation showing the correspondence between the phase transition temperature of the water/ice confined in pores and the curvature of its solid-liquid interface [1, 9]. The quantitative relation of the freezing/melting temperature and the pore size can be determined by adopting appropriate values for the thermodynamic parameters of the water/ice confined in the pores. LTC is an indirect method to determine porosity and special attention should be given to the measurements and the analysis of the measured data. More related discussions about using LTC to characterize cement based materials can be found, e.g., in [8, 10, 11].

Compared with traditional methods developed for porosity characterization, e.g., nitrogen adsorption/desorption (NAD), mercury intrusion porosimetry (MIP) and scanning electron microscopy (SEM), a major advantage of using LTC to characterize cement based materials is that the measurements can be conducted on virgin samples without any pre-drying treatment [7, 12–15]. This is important because the drying treatment often results in an apparent alteration of the pore structure under consideration for cement based materials [13, 14, 16]. Meanwhile, it should be mentioned that due to the fact that water in very small pores does not freeze and the freezing/melting point depression of water/ice in big pores is too small. Thus, the pores that can be

studied by LTC are limited mainly to those with radii between about 2 nm to about 40 or 50 nm [7, 17]. Water in larger pores is monitored, but the resolution is too limited to allow for determination of the actual pore size.

For water saturated porous materials, frost damage may potentially take place as the pore water freezes, especially when water in very small pores freezes [18]. The frost damage may change the pore structure of the studied materials to a certain extent. Considerable studies have been conducted to study the frost damage in cement based materials, e.g., see [19–25]. Several different mechanisms have been proposed, including the hydraulic pressure theory [20], the crystallization pressure theory [23], the closed container theory [25], etc. Even though disagreement exists with respect to the exact cause(s) of frost damage, it can be concluded that the probability of frost damage to take place is high in cement based materials with a high degree of saturation, especially when the materials are exposed to very low temperatures, e.g., in LTC measurements. Using LTC to characterize a pore size distribution, it has been explained theoretically that the pores under consideration should be fully saturated [6, 26]. An experimental study [11] has demonstrated the impact of non-fully saturated pores on the pore size determination. Thus, in practice, the samples in LTC studies are often treated with vacuum saturation with the aim to fully saturate all the accessible pores before calorimetric measurements. That is, the frost damage would be highly probable for the vacuum saturated samples of cement based materials during LTC measurements, as the lowest temperature during the measurements can be down to -80 °C or even lower to ensure all the freezable pore water can freeze [5]. In a LTC study conducted by Johannesson [5], the elastic moduli of the vacuum saturated concrete samples were measured before and after a cycle of freezing and melting measurement. The results showed that even for some of air-entrained samples, the elastic moduli decrease considerably after a cycle, indicating that the concrete samples possibly have been damaged during the measurement. Although LTC has been applied to study cement based materials for several decades, the impact of the frost damage on the porosity determination is not fully clear. Thus, one aim of the present work is to further explore the impact of frost damage on the porosity determination of cement based materials by LTC.

The pore liquid in cement based materials is another factor that should be considered in LTC studies. As we know, the pore liquid is not pure water but contains certain ionic species including calcium, sodium, potassium and hydroxide ions, etc. [27]. The presence of ionic species influences the freezing and melting behavior of the pore solution. To minimize the influence of the ions on the data analysis in LTC studies, it has been suggested to use water cured samples. The consideration is that the alkalies could leach out and then the pore liquid becomes dilute [6]. In a study conducted by Sun and Scherer [7], mortar samples ($\sim 20 \times 30 \times 100$ mm) were stored in a relatively big amount of saturated limewater ($\sim$ 48 liters) for about 6 months; and then it was

suggested that the alkalies would likely to have diffused out during the curing and the pores contained a solution very similar to saturated limewater. Since saturated limewater solution is rather dilute ($\sim$ 2 g calcium hydroxide/liter water), they further concluded that the freezing and melting behavior of the pore solution in their mortar samples could be approximated to that of pure water [7]. However, it is noted that due to a relatively big buffering capacity of the cement hydrates as demonstrated in thermodynamic modeling studies, e.g., see [28–30], the ionic concentration in the pore solution of the samples cured in big amount of saturated limewater might not necessarily be significantly changed.

In order to study the relevance of the related arguments above regarding cement pore solution, comparison measurements were performed on cement paste samples of the same recipe but preconditioned either in a small amount or in a big amount of saturated limewater (details see Section 2.1). The heat flow curves of freezing and melting of the samples preconditioned at different conditions were compared. The saturated limewater rather than pure water was used with the purpose to limit the leaching of calcium ions, since the leaching of calcium ions from cement hydrates has been demonstrated to be able to change the porosity of cement based materials to a certain extent [31, 32].

2. Experimental

2.1. Materials preparation

One mono-sized model material MCM-41 and two types of hardened cement pastes were included in this investigation. One aim of including the MCM-41 in this study was to check the instrument stability among different measurements and the homogeneity of the prepared cement paste samples, which will be further explained in Section 2.2.

MCM-41 is a silica based material and the pore structure is in the form of hexagonal arrays of uniform tubular channels of controlled width. The MCM-41 used in this study is a commercial product in powder form produced by Tianjin Chemist Scientific Ltd. The nominal pore diameter provided by the producer is 3.0 nm.

The cement paste samples were prepared by two types of cement, i.e., CEM I 32.5 R and CEM III/B 42.5 N, with the properties and the chemical composition of the cements shown in Table 1. The water-to-cement ratio was 0.4 for all the samples prepared. The fresh paste samples were mixed by a paddle mixer. After mixing, the fresh pastes were cast into cylindrical plastic vials ensuing proper compaction. The dimension of the plastic vials was about $\phi 15 \times 50$ mm. The hardened cement pastes were demoulded after one day of sealed curing at room temperature (about 20 °C) and then placed into slightly bigger plastic flasks ($\sim \phi 25 \times 60$ mm) filled with saturated limewater for curing at room temperature. After about three months, the paste samples

Table 1: Properties and the chemical composition of the two cements used in this study.

		CEM I (CEM I 32.5 R)	CEM III (CEM III/B 42.5 N)
Density	(g/cm^3)	3.06	2.90
Fineness	(cm^2/g)	2905	4635
Water demand	(%)	26.2	32.3
Initial setting time	(min)	185	270
Loss on ignition	(%)	2.1	1.4
SiO_2	(%)	20.6	29.2
Al_2O_3	(%)	5.6	8.9
Fe_2O_3	(%)	2.4	1.2
CaO	(%)	63.4	48.0
MgO	(%)	1.6	4.8
SO_3	(%)	2.9	2.6
K_2O	(%)	0.7	0.6
Na_2O	(%)	0.2	0.2
Cl	(%)	<0.1	<0.1

were divided into two groups: the first group was still left curing in the slightly bigger plastic flasks (denoted as preconditioned in a small amount of saturated limewater); and the second group was cured in a big bucket filled with saturated limewater ($\sim$ 40 liters) (i.e., denoted as preconditioned in a big amount of saturated limewater) until the date of calorimetric measurements. If it is not specially stated, the paste samples presented in this study are the samples cured in the plastic flasks (preconditioned by curing in a small amount of limewater). By using two types of cement, part of the effect due to cement types on the porosity determination by LTC is expected to be observed.

CEM I and CEM III are designated to denote the hardened cement pastes in the following description.

2.2. Calorimetric measurements

In this study, a Calvet-type scanning calorimeter (SETARAM) was used. The calorimeter was calibrated and operated to work between about 20 °C and about -130 °C. The temperature scanning of a freezing and melting cycle starts at about 20 °C and goes down to about -80 °C and then goes back to about 20 °C again. The cooling and heating rate were set to be 0.1 °C per minute.

For the easy handling of powder samples of the MCM-41 in the calorimeter, a plastic vial was chosen as a sample holder. The MCM-41 powders were placed into cylindrical plastic vials ($\sim \phi 14 \times 48$ mm) up to about half volume of the vials (the

dry weight later determined was about 0.2 g). The size of the plastic vials was chosen to fit the measuring chamber of the calorimeter. To saturate the powder samples held in the plastic vials, they were covered with distilled water and then placed under a reduced pressure ($\sim$ 40 mbar) for about 3 hours. After that, the plastic vials with saturated powder samples were put on shelf standing still for about two weeks. The apparent excess bulk water on top of the powders was removed before the calorimetric measurements. A corresponding plastic vial but empty was placed in the reference chamber of the calorimeter to counteract some uncertainties that the plastic vials may experience at low temperatures during the measurements.

The cylinder samples of cement pastes ($\sim \phi 15 \times 45$ mm) were vacuum saturated first and then the apparent water on the surface was wiped off. The paste samples were assumed to be saturated surface dry when placed in the calorimeter. A totally dry paste sample (oven drying at about 105 °C until constant weight) with the same dimension as the testing specimen was used as a reference sample. In the investigation, the same reference was used throughout all the tests. One purpose of using the reference sample is to reduce the possible uncertainties of the solid paste during the freezing and melting. More discussions about the influence and the benefits of using such a reference sample in calorimetric measurements can be found in [5, 10]. The total curing time of the cement paste samples was about one year when the calorimetric measurements were performed.

The mass of each tested vacuum saturated sample before and after calorimetric measurements were determined. The relative difference of the mass was less than about 0.15%. That is, there is almost no water loss during the calorimetric measurements. After calorimetric measurements, the samples were subjected to oven-drying at about 105 °C till constant weight and then the dry weights of the samples were determined.

In this study, calorimetric measurements were conducted on two different samples of the model material MCM-41 and three different samples of each cement paste. Through the measurements, firstly the stability of the instrument among different measurements can be validated by comparing the measured heat flow curves of the rather homogenous model material MCM-41 (as the tested samples are in powder form and were collected from a rather big batch). The heat flow curves should be quite comparable if the instrument is stable. Secondly, the homogeneity of the prepared cylinder samples of cement pastes can also be checked.

To investigate the influence of the frost damage on the applicability of using LTC to study the meso-porosity, three continuous (repeated) freezing and melting cycles were applied on a sample of the MCM-41 and two continuous cycles were applied on a sample of each cement paste studied. If the heat flow curves of freezing and melting change after each cycle, it may demonstrate the frost damage has an impact on the pore structure of a studied material and hence using the LTC method may not be able

to characterize the original or the "real" porosity accurately.

Calorimetric measurements were performed on cement paste samples of the same recipe preconditioned in a small amount and a big amount of saturated limewater. The influence of the leaching of ions from cement hydrates on the freezing and melting behaviors of the pore solution of the pastes can be studied by comparing the measured heat flow curves of the samples preconditioned at different conditions.

3. Results and discussion

3.1. Instrument stability and sample homogeneity

The measured heat flow curves of two different samples of the model material MCM-41 are shown in Figure 1. There are two distinct peaks on the heat flow curves of melting: one is around about -34 °C and the other is close at about 0 °C. Since the MCM-41 is a mono-sized material, the peak around -34 °C can be assigned to the pore water and the peak close at 0 °C should correspond to the excess bulk water in the samples.

On the heat flow curves of freezing, two groups of peaks have been observed: the first group is around about -10 °C and the second is around about -40 °C. The first group of peaks reflects the characteristics of supercooled water. Bulk water can be cooled down below 0 °C without freezing due to the energetic barrier to nucleation [33]. Supercooling is due to the uncertainties of nucleation, thus it is normally not reproducible [17]. While freezing point depression is caused by the pore confinement and it is reproducible for water freezing in the pores with the same size, which is often called undercooling [17].

For the second group peaks, there are a small peak around about -36 °C and a relatively big one around about -42 °C. The small peak is possibly related to the pore size variation along the channels of the model material MCM-41. This is suggested since studies of desorption isotherms on the same type of materials showed the same type of variations [34] (the desorption process is often considered rather comparable to the freezing process [7]). It is noted that when temperature goes down to about -38 °C, homogeneous nucleation becomes dominant and all the freezable pore water will freeze irrespective of the pore sizes [18, 35, 36]. Thus, the peak around about -42 °C on the freezing curves most likely corresponds to homogeneously nucleated pore water.

Small differences are found on the measured heat flow curves of the two different samples of the model material MCM-41 (Figure 1). That the absolute value of the measured heat flow of sample 2 is somewhat lower than that of sample 1 can be explained by the different baseline (of heat flow) of the two samples. As we know, the heat flow measured by a LTC instrument consists of two parts: (1) the contribution from the heat capacity of the system (including water, ice and the powder MCM-41

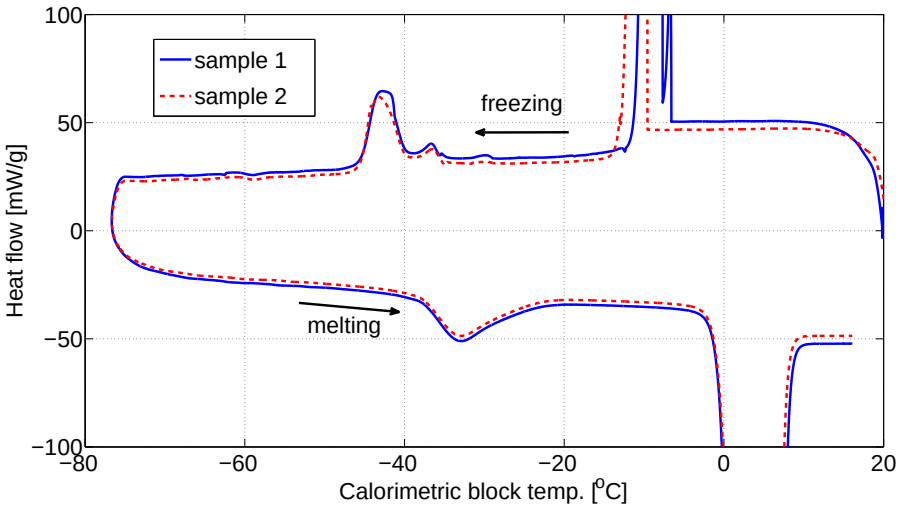

Figure 1: Measured heat flow of two different samples of the model material MCM-41. The heat flow is expressed as milliwatt (mW) per gram of dry material.

sample in this case), i.e., the baseline; and (2) the contribution due to phase transition [5, 10]. The baseline does not reflect any pore volume and should be subtracted in determining the pore volume of the studied material. For the two samples in Figure 1, the baseline of sample 2 is slightly lower than that of sample 1, i.e., due to some higher content of excess bulk water in sample 1. However, the magnitude and the position of the peaks (freezing/melting points) corresponding to the meso-pores are quite comparable for the two measurements, indicating that the pore volume of the two measured samples are comparable. It is, therefore, concluded that the stability of the instrument is satisfactory.

The measured heat flow curves of three different samples of cement pastes CEM I and CEM III are presented in Figure 2 and Figure 3, respectively. For both pastes, the first peak on the heat flow curves of freezing (observing from high to low temperatures) is believed to mainly correspond to supercooled water. Since the saturated surface dry paste samples were used in the calorimetric measurements (indicating almost no excess bulk water), the first peak is mainly contributed by the water in big pores, in which the freezing point depression of the confined water is very small, and partly contributed by the pore water with corresponding freezing point higher than that of the supercooled water. That is, the first peak on the heat flow curves of freezing mainly reflects the uncertainties of supercooling and indicates little about pore (entry) size information. The peak on the heat flow curves of freezing starting around -40 °C, similar to what has been discussed for the MCM-41, corresponds to homogeneously nucleated pore

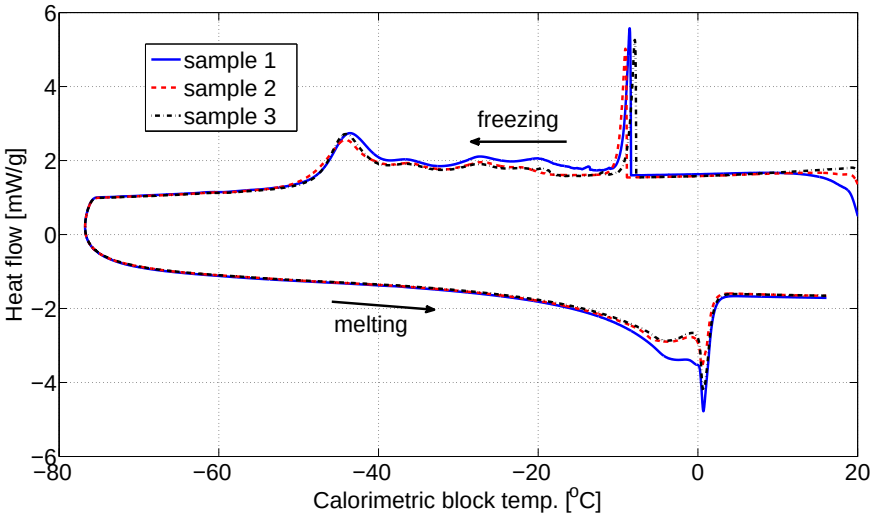

Figure 2: Measured heat flow of three different samples of the cement paste CEM I. The heat flow is expressed as milliwatt (mW) per gram of dry material.

water. On the heat flow curves of melting of the paste CEM I (observing from low to high temperatures), there are one plateau-like peak starting around -6 °C and a peak starting around 0 °C, which is extended to higher temperatures for several degrees; while on the heat flow curves of melting of the paste CEM III, besides the peak at about 0 °C, there is another peak around the temperature of about -8 °C. The peaks found on the heat flow curves of melting of the studied cement paste samples below 0 °C are contributed by the water/ice in the small pores (mainly nanometric pores) and the peak starting around about 0 °C mainly correspond to the water/ice in big pores with small temperature depression.

As can be observed from Figure 2 and Figure 3, the heat flow curves of two measured samples (sample 2 and 3) for both pastes are quite comparable except the first peak on the freezing curves. As for the model material MCM-41, the first peak is mainly related to supercooling and supercooling is normally not reproducible. For both cement pastes, the heat flow curves of sample 1 have peaks at similar locations (temperatures), but differ in magnitude of heat flow from that of the other two samples to a certain extent. One possible explanation could be an inhomogeneity of the prepared samples.

Based on the small differences as observed between the results of the measurements on the different samples of the model material MCM-41 and the relatively comparable results on the two different samples of each studied paste, it is assumed that the stability of the instrument is satisfactory. The measured differences of the cement pastes are concluded to be mainly attributed to the inhomogeneity of the prepared samples.

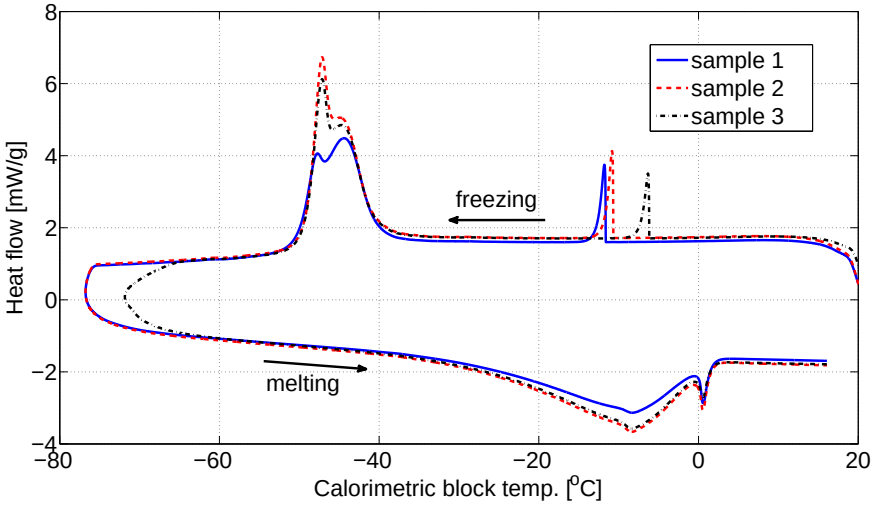

Figure 3: Measured heat flow of three different samples of the cement paste CEM III. The heat flow is expressed as milliwatt (mW) per gram of dry material.

3.2. Impact of frost damage on heat flow curves

In LTC studies, it is normally assumed that the freezing curves (after the first nucleation which is often related to supercooling) is controlled by the connectivity of a pore system, or rather the pore entry or neck sizes (assuming that the freezing process is initiated by heterogeneous nucleation followed by progressive penetration); while the melting is controlled by the pore interior sizes [7, 8, 11, 18].

3.2.1. Model material MCM-41

The measured heat flow curves of three continuous freezing and melting cycles on a sample of the model material MCM-41 is shown in Figure 4.

It can be found from Figure 4 that the heat flow curves of freezing and melting after each cycle are almost the same. The similarity between the heat flow curves of melting indicates that the effect of possible frost damage (the pressure generated during the freeing process exerted on the pore walls) probably has no or very limited impact on changing the pore interior sizes of the material MCM-41. As for the heat flow curves of freezing, one may argue that even though the freezing curves are almost the same, it is not easy to judge whether the pore entry sizes (or pore sizes variation along the channels [34]) of the MCM-41 change after each cycle of measurement. The reason for that is most probably that the pore entry sizes are too small. That is, the freezing of the pore water is dominated by homogeneous nucleation, which does not necessarily reflect pore entry sizes. However, the peak around -36 °C appears at the

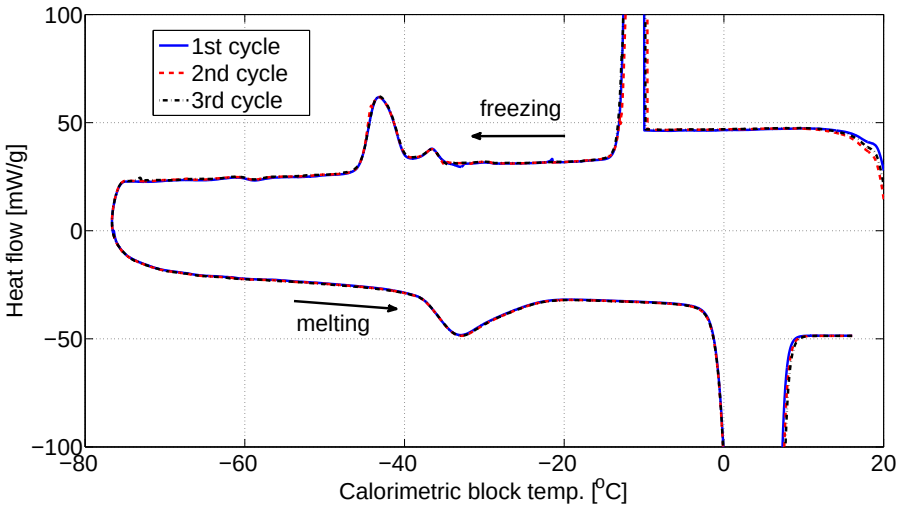

Figure 4: Measured heat flow of three continuous freezing and melting cycles on a sample of the model material MCM-41. The heat flow is expressed as milliwatt (mW) per gram of dry material. The heat flow curves of the three cycles are almost the same.

same temperature with about the same magnitude on the heat flow curves of freezing in all the three measured cycles, which somewhat demonstrates the stability of the pore structure during the three freezing cycles. That is, for the studied powder MCM-41 samples, it is assumed that the ice formed in the pore structure has limited impact on changing the porosity, including both the pore connectivity and the pore interior sizes.

3.2.2. Cement pastes

The measured heat flow curves of two freezing and melting cycles on the same cylinder sample of the cement pastes CEM I and CEM III are presented Figure 5 and Figure 6, respectively.

It can be found that for both pastes, the heat flow curves of freezing change after one cycle of measurement and the change is more evident in low temperature range. It is characterized by the shifting of the peak starting at around -40 °C (to some higher temperatures). The heat flow curves of melting are almost not affected after one cycle of measurement, except that the magnitude of the peak just above about 0 °C (i.e., mainly corresponds to the water in big pores) decreases.

3.2.2.1. Heat flow curves of freezing. The difference in the heat flow curves of the first and second freezing of the cement paste samples indicates that the pore connectivity probably has been changed, implying that frost damage may have taken place in the tested cylinder samples during the first cycle of measurement. It seems that frost

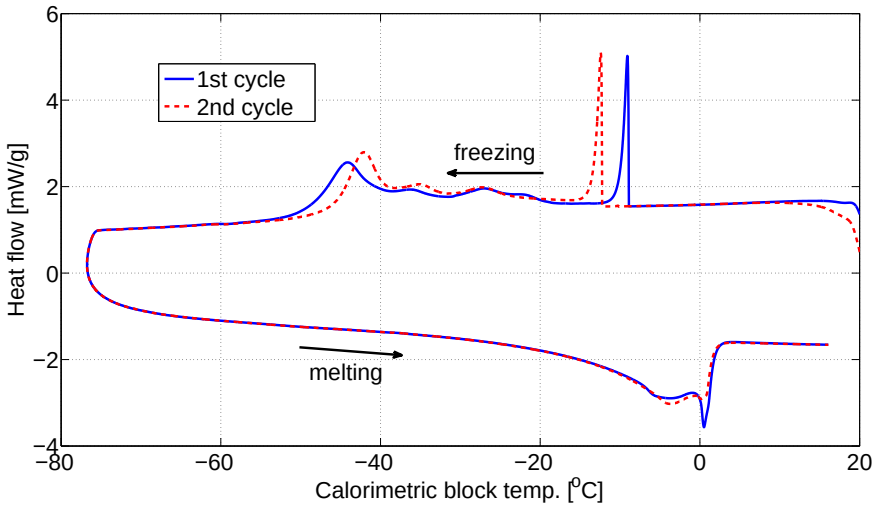

Figure 5: Measured heat flow of two continuous freezing and melting cycles on a same sample of the cement paste CEM I. The heat flow is expressed as milliwatt (mW) per gram of dry material.

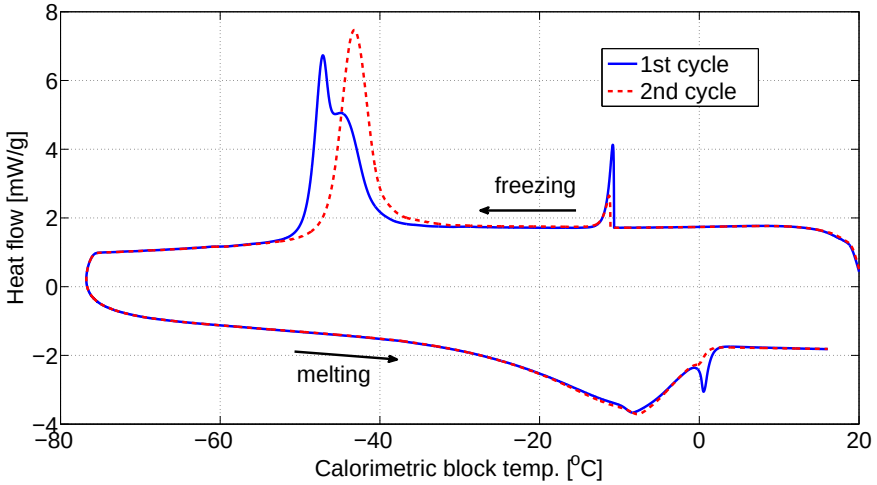

Figure 6: Measured heat flow of two continuous freezing and melting cycles on a same sample of the cement paste CEM III. The heat flow is expressed as milliwatt (mW) per gram of dry material.

damage increases the connectivity of the pore system, i.e., more pores are penetrable by ice at a certain undercooling.

The increased connectivity of the pores in the cement pastes is reflected by the relatively higher heat flow curves of freezing in the second cycle compared with that of the first cycle between the temperature from the point that the first peak finishes down till about -40 °C (see Figure 5 and Figure 6). As discussed earlier, the first peak mainly corresponds to supercooled water in big pores (in which water has small temperature depression) and the peak starting at about -40 °C is due to the homogeneously nucleated water, both of which do not necessarily reflect the pore entry sizes or the connectivity of the pore system. Thus, it is difficult to judge whether the shifting of the peak starting at around -40 °C on the heat flow curves of freezing indicates the change of the pore connectivity. However, the magnitude of the peak starting at about -40 °C can to some extent indicate the connectivity of the studied cement pastes. If the magnitude of the peak decreases after one cycle of measurement, it means that the volume of the pores in which water homogeneously nucleated decreases. The decreased volume of the (homogeneously nucleated) pores implies more pores are penetrable by the ice at higher temperatures after one cycle of measurement, which then indicates an increase of the pore connectivity. A careful evaluation (Figure 5 and Figure 6) does show that the magnitude of the peak starting at about -40 °C on the heat flow curves of freezing of the second cycle slightly decreases compared with that of the first cycle.

3.2.2.2. Heat flow curves of melting. The decreased magnitude of the peak just above about 0 °C in the heat flow curves of melting during the second cycle of the studied cement paste samples indicates that the amount of the water in relatively big pores decreases. Moreover, a close check in the curves of melting of the second cycle (Figure 5 and Figure 6) indicates a slight increase of the small pore volume compared with that of the first cycle, reflected by slightly higher (in absolute value) heat flow curves than that of the first cycle at the temperatures lower than about 0 °C. Two possible explanations could be proposed accounting for the observations.

The first explanation could be that frost damage in cement paste samples during the first cycle of measurement, e.g., in the form of micro-cracking [23, 37], can make some of the initially water inaccessible pores (e.g., as characterized by homogeneously nucleation in the freezing) accessible. When the first cycle of measurement is completed, some of the newly opened non-fully saturated pores, e.g., with relatively small pore sizes, can suck water from big pores through capillary suction, resulting in the observed changes in the heat flow curves.

This explanation is somewhat supported by the slightly decreased volume of the homogeneously nucleated pores (corresponding to the magnitude of the peak starting at about -40 °C) as observed on the heat flow curves of freezing of the second cycle compared with that of the first cycle. Following the explanation, the slight difference

between the heat flow curves of melting of the two cycles at the temperatures lower than about 0 °C (i.e., corresponding to volume of meso-pores) is not due to that the frost damage enlarges some of the small pores but that some initially homogeneously nucleated pores are opened up by the frost damage. The argument about the pore enlargement can be somewhat validated by considering that if the pore enlargement is relevant, then the small pores are more prone to be enlarged since the pressure generated during freezing in small pores is higher than that in big pores [23, 37], meaning that the volume of small pores should decrease. However, the decrease of the volume of small pores is not observed by comparing the heat flow curves of melting of the second cycle with the first cycle (Figure 5 and Figure 6).

The above explanation may be challenged by taking the cryogenic suction into consideration. Cryogenic suction, or cryosuction, is the effect of water from neighboring pores or from the surroundings being drawn towards ice crystals already created in the pore system during freezing process [18, 38–41]. If some water in the big pores are sucked into small pores which are opened by frost damage during the first cycle as argued above, then the big pores are not fully saturated during the second cycle of measurement. Following the concept of cryogenic suction, water in small pores could be drawn into the non-fully saturated big pores when ice forms in the big pores (during the second cycle). Consequently, the ice in the big pores might not decrease significantly. However, the heat flow curves of melting of the second cycle indicate that the amount of ice melted in the big pores (the peak just above about 0 °C) is smaller compared with that of the first cycle, especially for CEM III (see Figure 5 and Figure 6). The exact reasons are not clear, but it is suspected that it may be related to the very small amount of ice in the big pores of the studied cement pastes during the second cycle of measurement (which is indicated by the peak just above about 0 °C on the heat flow curves of melting). That is because for water to be able to be drawn into the big pores by cryogenic suction, ice should present in the big pores as a freezing front at the connecting points of big and small pores [18, 39, 42]. If there is only a very small amount of ice presented in a big pore, it is possible that the water in a small pore (which is connected to the big pore) can not be drawn into the big pore due to the lack of a freezing front.

The second possible explanation is that frost damage takes place and generates micro-cracks during the first cycle of measurement. The micro-cracks have small widths and are connected to big pores (e.g., air voids), directly or indirectly. After the first cycle of measurement, the micro-cracks can suck water from big pores. The consequence is that the magnitude of the measured heat flow corresponding to big pores (above about 0 °C) decreases and that corresponding to small pores (lower than about 0 °C) increases. The key of this explanation is that the generated micro-cracks must have small widths and must be connected to the big pores directly or indirectly. However, the

second explanation cannot explain the slightly decreased volume of the homogeneously nucleated pores (corresponding to the magnitude of the peak starting at about -40 °C) as observed on the heat flow curves of freezing of the second cycle compared with that of the first cycle.

The first explanation assumes that the slight increase of small pore volume is due to existing small pores in the samples (initially isolated but opened up by the frost damage); while the second explanation assumes that frost damage creates some micro-cracks which are detected as small pores during the second cycle of measurement. The first explanation may be more reasonable considering the comparison of the heat flow curves of both freezing and melting of the two measured cycles.

3.2.2.3. Influence of frost damage on pore size distribution. If frost damage takes place in cement paste samples during freezing and melting measurements, an immediate question is that whether LTC can still characterize the original or the "real" porosity of the materials. By looking at the relatively stable heat flow curves of melting of the two cycles below the temperature of about 0 °C from Figure 5 and Figure 6, it indicates that the pore (interior) size distribution (of meso-pores) is not affected to any significant degree by frost damage.

One may argue that the change of pore structure due to frost damage would have taken place during the first freezing cycle, meaning both the first and second melting measurement do not give the "real" pore size distribution. It is reasonable to consider that if the meso-pore walls of cement paste samples are not strong enough to withstand the stress generated during the measurements, the heating flow curves of melting should be shifted to higher temperatures after each cycle of measurement, e.g., as observed for some gel materials [43, 44]. This is because as long as water exists and freezes in small meso-pores, the stress generated is in the similar order. If the pore walls cannot sustain during the first cycle, they would probably also not be able to sustain during the following cycles. However, this is not the case for the studied cement paste samples. That is, the slight increase of pore volume indicated by the heat flow curve of melting of the second cycle for the cement pastes is not due to that the existing meso-pores are enlarged by frost damage. But, it is perhaps due to that the changing of some of the previous homogeneously nucleated pores slightly increases the volume of pores which is not detectable during the first cycle, since LTC can only detect pores filled with water. If the cement paste samples are free of non-penetrable pores, it may be reasonable to assume that the heat flow curves of melting of several cycles are quite comparable.

It has been revealed that a pore system with small pore entries or necks is very susceptible to frost damage. That is because the pressure generated on the pore walls during freezing in this type of pore system is very high [23]. Thus, for the studied cement paste samples, the frost damage may take place when the temperature goes down to low temperatures and the water in small pore necks freezes. The relevance of

this argument is somewhat validated by looking at the heat flow curves of freezing of the two cycles (Figure 5 and Figure 6): the main difference is below the temperature of about -30 °C. However, the relatively stable heat flow curves of melting in two consecutive cycles of measurements as obtained for the studied cement pastes may indicate that the interior sizes of the meso-pores of cement pastes may be not affected by frost damage.

Some cryoporometry studies, e.g., [45, 46], compared ice content curves of the freezing and melting between big integral and crushed samples of a same material. The results showed that the freezing curves (i.e., pore connectivity) are different while the melting curves (i.e., pore interior sizes) remain about the same, which are somewhat comparable to the results obtained in this study. That is, the effect of frost damage in cement pastes may be, to some extent, comparable to crushing big integral samples.

To sum it up, the very similar heat flow curves of freezing and melting of the MCM-41 indicate that the pressure generated during freezing has little impact on the pore structure of the powder model material. By studying the heat flow curves of freezing and melting of cement pastes, it is concluded that the frost damage probably takes place in the studied cylinder samples and it changes the pore connectivity while it has limited effect on changing the interior size distribution of the meso-pores.

3.3. Influence of sample preconditioning on freezing and melting behaviors of cement pore solution

The measured heat flow curves of the cement paste samples with the same recipe preconditioned in a small amount and a big amount of saturated limewater for CEM I and CEM III are compared in Figure 7 and Figure 8, respectively. The freezing/melting points of the peaks corresponding to pores are almost the same for the samples of each paste preconditioned in both a small amount and a big amount of saturated limewater (except the first peak on the freezing curves, which is related to supercooling and it reflects uncertainties of heterogeneous nucleation, as explained earlier), indicating that the preconditioning in different amount of limewater may not affect the freezing and melting behavior of the pore solution very much. Meanwhile, it can be found from Figure 7 that the magnitude of the peaks corresponding to pores especially on the freezing curves for the paste samples preconditioned at different conditions are also comparable (the comparability in Figure 8 is lower, which will be explained in the next paragraph). That is, if the argument given by Sun and Scherer [7] is relevant, i.e., the freezing and melting behaviors of the pore solution in cement samples cured in a big amount of limewater for a relatively long time can be approximated to that of pure water, then the approximation may be also applicable for cement samples cured in a small amount of limewater. Obviously, further study is needed to clarify the ionic concentrations in the pore solution of the paste samples preconditioned under the different conditions.

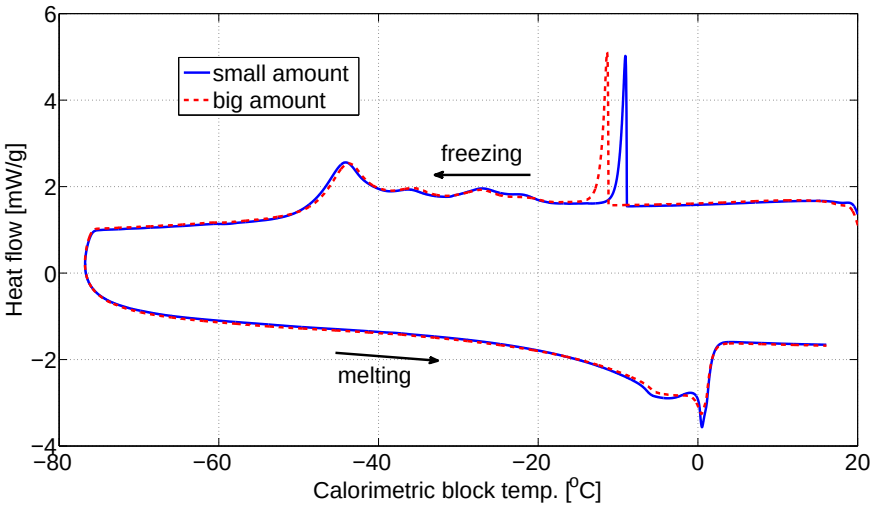

Figure 7: Measured heat flow of samples cured in a small and a big amount of saturated limewater of the cement paste CEM I. The heat flow is expressed as milliwatt (mW) per gram of dry material.

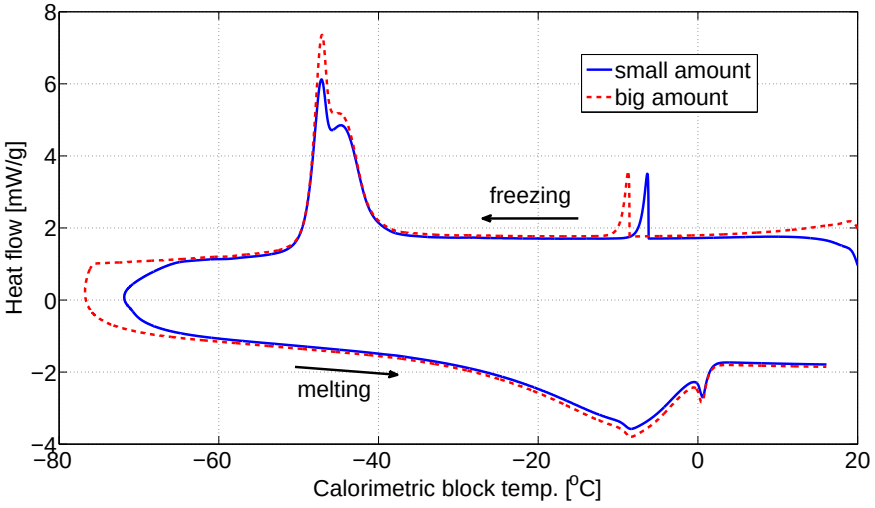

Figure 8: Measured heat flow of samples cured in a small and a big amount of saturated limewater of the cement paste CEM III. The heat flow is expressed as milliwatt (mW) per gram of dry material.

Another concern related to curing cement samples in a big amount of water is that leaching of ions from cement hydrates can possibly increase the porosity. Studies, e.g., [31, 32], have shown the effect of leaching of calcium ions from portlandite and calcium silicate hydrates on the porosity of cement based materials. For the paste CEM III (Figure 8), the heat flow curve is a little bit higher (in terms of absolute value) in the sample preconditioned in a big amount of saturated limewater, which implies somewhat higher porosity. One may argue that the somewhat higher porosity in the sample preconditioned in a big amount of saturated limewater may be related to the leaching of ions. By looking at the difference between the measured heat flow curves of different samples of the same paste CEM III (Figure 3), the difference observed in Figure 8 could also be due to the inhomogeneity of prepared paste samples since the somewhat high porosity is not observed in the paste sample of CEM I preconditioned in a big amount of saturated limewater in the comparison (Figure 7). Nevertheless, to reduce the possibility of leaching changing the porosity, it is probably a better practice to cure cement paste samples in a small amount of saturated limewater rather than in a big amount in LTC studies.

Based on this study, it can be concluded that there is almost no difference on the heat flow curves of freezing and melting between the samples preconditioned in a small amount and a big amount of saturated limewater, indicating that either the preconditioning in a big amount of limewater does not change the concentration of the pore solution very much (e.g., due to the buffering effect of the cement hydrates) or the leaching of ions from cement hydrates has limited influence on the freezing and melting behaviors of the pore solution in the studied cement paste samples.

4. Conclusions

The impact of frost damage on the characterization of the meso-porosity of a model material MCM-41 and two types of cement pastes using LTC were studied by conducting repeated freezing and melting cycles on a same sample of each studied material. The measured results showed that for the model material MCM-41, the heat flow curves of freezing and melting after each cycle were almost the same. For the two cement pastes, the heat flow curves of freezing changed after one cycle of measurement and the change was more evident in the low temperature range. The heat flow curves of melting were almost not affected after one cycle of measurement. The results indicate that the pressure generated during freezing and melting has little impact on the pore structure of the powder MCM-41 samples. As for the studied cylinder paste samples, frost damage potentially takes place and it changes the pore connectivity characteristics while it has limited effects on changing the interior size distribution of the meso-pores.

The freezing and melting behavior of the pore solution of cement paste samples preconditioned in a small amount and a big amount of saturated limewater were compar-

atively studied. The results showed that there is almost no difference in the measured heat flow curves of freezing and melting comparing the samples preconditioned in a small amount and a big amount of saturated limewater. This indicates that either the preconditioning in a big amount of limewater does not change the concentration of the pore solution very much or the leaching of ions from cement hydrates has limited influence on the freezing and melting behavior of the pore solution in the studied cement paste samples.

Acknowledgments

The research leading to these results has received funding from the European Union Seventh Framework Programme (FP7/2007-2013) under grant agreement 264448. A part of this research was funded by the Lizzy, Alfred and Valdemar Taumose's Foundation. The authors would like to thank Stefan Backe from the Division of Building Materials of Lund University for performing some of the tests.

Reference

[1] M. Brun, A. Lallemand, J.F. Quinson, and C. Eyraud. A new method for the simultaneous determination of the size and shape of pores: the thermoporometry. *Thermochimica Acta*, 21(1):59–88, 1977.

[2] A.M. Neville. *Properties of concrete*. Prentice Hall, 4th edition edition, 1995.

[3] S. Diamond. Aspects of concrete porosity revisited. *Cement and Concrete Research*, 29(8):1181–1188, 1999.

[4] M. Pigeon and R. Pleau. *Durability of concrete in cold climates*. Number 4. Taylor & Francis, 1995.

[5] B. Johannesson. Dimensional and ice content changes of hardened concrete at different freezing and thawing temperatures. *Cement and Concrete Composites*, 32(1):73–83, 2010.

[6] G. Fagerlund. Determination of pore-size distribution from freezing-point depression. *Materials and Structures*, 6(3):215–225, 1973.

[7] Z. Sun and G.W. Scherer. Pore size and shape in mortar by thermoporometry. *Cement and Concrete Research*, 40(5):740–751, 2010.

[8] A.M. Kjeldsen and M.R. Geiker. On the interpretation of low temperature calorimetry data. *Materials and Structures*, 41(1):213–224, 2008.

[9] R. Defay, I. Prigogine, A. Bellemans, and D.H. Everett. *Surface tension and adsorption*. Longmans London, 1966.

[10] M. Wu, B. Johannesson, and M. Geiker. Determination of ice content in hardened concrete by low temperature calorimetry: influence of baseline calculation and heat of fusion of confined water. *Journal of Thermal Analysis and Calorimetry*, 115(2):1335–1351, 2014.

[11] M. Wu and B. Johannesson. Impact of sample saturation on the detected porosity of hardened concrete using low temperature calorimetry. *Thermochimica Acta*, 580:66–78, 2014.

[12] D.H. Bager. *Ice Formation in Hardened Cement Paste*. PhD thesis, Building Materials Laboratory, Technical University of Denmark, 1984.

[13] D.H. Bager and E.J. Sellevold. Ice formation in hardened cement paste, Part I–room temperature cured pastes with variable moisture contents. *Cement and Concrete Research*, 16(5):709–720, 1986.

[14] E. Sellevold and D. Bager. Some implications of calorimetric ice formation results for frost reistance testing of concrete. *in Beton og Frost, Dansk Beton Forening*, 22:47–74, 1985.

[15] E.W. Hansen, H.C. Gran, and E.J. Sellevold. Heat of fusion and surface tension of solids confined in porous materials derived from a combined use of NMR and calorimetry. *The Journal of Physical Chemistry B*, 101(35):7027–7032, 1997.

[16] J. Villadsen. Pore structure in cement based materials. Technical Report 277, Building Materials Laboratory, Technical University, Denmark, 1992.

[17] M.R. Landry. Thermoporometry by differential scanning calorimetry: experimental considerations and applications. *Thermochimica acta*, 433(1-2):27–50, 2005.

[18] G.W. Scherer. Freezing gels. *Journal of non-crystalline solids*, 155(1):1–25, 1993.

[19] T.C. Powers. The air requirement of frost resistant concrete. In *Proceedings of the Highway Research Board*, volume 29, pages 184–211, 1949.

[20] T.C. Powers and R.A. Helmuth. Theory of volume changes in hardened portland cement paste during freezing. In *Proceeding of Highway Research Board*, volume 32, pages 285–297, 1953.

[21] G. Fagerlund. The international cooperative test of the critical degree of saturation method of assessing the freeze/thaw resistance of concrete. *Matériaux et Construction*, 10(4):231–253, 1977.

[22] G. Fagerlund. Studies of the scaling, the water uptake and the dilation of specimens exposed to freezing and thawing in NaCl solution. In *Proceedings of RILEM committee 117 DC Freezing/thaw and de-icing resistance of concrete*, pages 37–66, Swden, 1991.

[23] G.W. Scherer and J.J. Valenza II. *Materials Science of Concrete*, volume VII, chapter Mechanisms of Frost Damage, pages 209–246. 2005.

[24] K. Fridh. *Internal frost damage in concrete–experimental studies of destruction mechanisms*. PhD thesis, Division of Building Materials, Lund Institute of Technology, 2005.

[25] G. Fagerlund. Internal frost attack–State of the art. In *RILEM Proceedings on Frost Resistance of Concrete*, pages 321–338. Spon, London, 1997.

[26] M. Brun, A. Lallemand, J.F. Quinson, and C. Eyraud. Changement d'état liquid–solide dans les milieux poreux. II. Étude théorique de la solidification d'un condensate capillaire (liquid–solid change of state in porous media. II. Theoretical study of the solidification of a capillary condensate). *J.Chim.Phys.*, 6:979–989, 1973.

[27] H.F.W. Taylor. *Cement chemistry*. Thomas Telford, London, 2nd edition, 1997.

[28] B. Lothenbach and F. Winnefeld. Thermodynamic modelling of the hydration of portland cement. *Cement and Concrete Research*, 36(2):209–226, 2006.

[29] B. Lothenbach. Thermodynamic equilibrium calculations in cementitious systems. *Materials and Structures*, 43(10):1413–1433, 2010.

[30] S. Setunge, N. Nguyen, B. Alexander, and L. Dutton. Leaching of alkali from concrete in contact with waterways. *Water, Air, & Soil Pollution: Focus*, 9(5-6): 381–391, 2009.

[31] K. Haga, S. Sutou, M. Hironaga, S. Tanaka, and S. Nagasaki. Effects of porosity on leaching of ca from hardened ordinary portland cement paste. *Cement and Concrete Research*, 35(9):1764–1775, 2005. doi: http://dx.doi.org/10.1016/j.cemconres.2004.06.034.

[32] M. Mainguy, C. Tognazzi, J. Torrenti, and F. Adenot. Modelling of leaching in pure cement paste and mortar. *Cement and Concrete Research*, 30(1):83–90, 2000.

[33] D.M. Murphy and T. Koop. Review of the vapour pressures of ice and supercooled water for atmospheric applications. *Quarterly Journal of the Royal Meteorological Society*, 131(608):1539–1565, 2005.

[34] K. Sing. The use of nitrogen adsorption for the characterisation of porous materials. *Colloids and Surfaces A: Physicochemical and Engineering Aspects*, 187:3–9, 2001.

[35] D.H. Rasmussen and A.P. MacKenzie. Clustering in supercooled water. *The Journal of Chemical Physics*, 59:5003–5013, 1973.

[36] H.H.G. Jellinek, editor. *Water Structure at the Water-Polymer Interface*. Plenum, New York, 1972.

[37] J.J. Valenza II and G. W. Scherer. A review of salt scaling: II. mechanisms. *Cement and Concrete Research*, 37:1022–1034, 2007.

[38] O. Coussy and T. Fen-Chong. Crystallization, pore relaxation and micro-cryosuction in cohesive porous materials. *Comptes Rendus Mecanique*, 333(6): 507–512, 2005.

[39] P.J.M. Monteiro, O. Coussy, and D.A. Silva. Effect of cryo-suction and air void transition layer on hydraulic pressure of freezing concrete. *ACI Materials Journal*, 103(2):136–140, 2006.

[40] A. Dupas. Effect of vertical drain barrier on road behaviour in freeze-thaw periods. In *Geotextiles, Geomembranes and Related Products, Volume 1 (out of 3 volumes): Proceedings of the 4th International Congress, The Hague, 28 May-1 June 1990*, volume 1, page 339. Taylor & Francis, 1990.

[41] P.J. Parker and A.G. Collins. Dehydration of flocs by freezing. *Environmental Science & Technology*, 33(3):482–488, 1999.

[42] M. Hohmann. Soil freezing-the concept of soil water potential. State of the art. *Cold Regions Science and Technology*, 25(2):101–110, 1997.

[43] W. Kuhn, E. Peterli, and H. Majer. Freezing point depression of gels produced by high polymer network. *Journal of Polymer Science*, 16(82):539–548, 1955.

[44] T. Yamamoto, A. Endo, Y. Inagi, T. Ohmori, and M. Nakaiwa. Evaluation of thermoporometry for characterization of mesoporous materials. *Journal of Colloid and Interface Science*, 284(2):614–620, 2005.

[45] E.L. Perkins, J.P. Lowe, K.J. Edler, N. Tanko, and S.P. Rigby. Determination of the percolation properties and pore connectivity for mesoporous solids using NMR cryodiffusometry. *Chemical Engineering Science*, 63(7):1929–1940, 2008.

[46] E. Shiko, K.J. Edler, J.P. Lowe, and S.P. Rigby. Probing the impact of advanced melting and advanced adsorption phenomena on the accuracy of pore size distributions from cryoporometry and adsorption using NMR relaxometry and diffusometry. *Journal of Colloid and Interface Science*, 385(1):183–192, 2012.

Paper IV

Impact of sample crushing on porosity characterization of hardened cement pastes by low temperature calorimetry: comparison of powder and cylinder samples

M. Wu, K. Fridh, B. Johannesson, M. Geiker

Submitted to: *Journal of Thermal Analysis and Calorimetry, 2014*

Noname manuscript No.
(will be inserted by the editor)

Impact of sample crushing on porosity characterization of hardened cement pastes by low temperature calorimetry: comparison of powder and cylinder samples

Min Wu · Katja Fridh
Björn Johannesson · Mette Geiker

Received: date / Accepted: date

Abstract The impact of sample crushing on the detected porosity of hardened cement pastes by low temperature calorimetry (LTC) was studied using powder and cylinder samples. Two types of cements, CEM I and CEM III, were used to prepare the pastes. A model porous material, MCM-41, was also used in order to investigate some aspects of the measurement and the evaluation approach. The powder and cylinder samples of the cement pastes were compared in terms of the calculated ice content curves, total pore volumes and pore size distribution curves. For the two studied cement pastes, the calculated ice content curves of freezing of the powder sample differed from that of the cylinder samples, especially for the paste CEM III. The results indicate that sample crushing changed the pore connectivity as compared to non-crushed samples. One important difference between the powder sample and the cylinder samples of the paste CEM III was that the determined maximum ice content in the powder sample was much higher than that in the cylinder samples, the relatively difference being about 40-50%. However, this kind of marked difference was not found in the paste CEM I. The observed difference between the calculated pore volume of the powder and the cylinder samples of the paste CEM III is possibly due to some of the "isolated" pores which, presumably, cannot be fully filled with water in the preparation of the cylinder samples. However, sample crushing makes it possible to saturate the pores to a greater extent if the crushing contributes to open up the "isolated" pores. Consequently, more pores are detected in the powder samples. The argument that the "isolated" pores have a tendency to be opened up by the crushing process is supported by results using gravimetric measurements and "dynamic (water) vapor sorption" measurements on powder samples.

Keywords Low temperature calorimetry, cement paste, freezing and thawing, pore size distribution, thermoporometry, cryoporometry

Min Wu · Björn Johannesson
Department of Civil Engineering, Building 118
Technical University of Denmark, 2800 Lyngby, Denmark
E-mail: miwu@byg.dtu.dk

Katja Fridh
Division of Building Materials
Lund University, Lund, Sweden

Mette Geiker
Department of Structural Engineering,
Norwegian University of Science and Technology, Trondheim, Norway

1 Introduction

The pore system in a cement based material is very complicated and the pore sizes can range from millimeter scale [1] to nanometric level [2, 3]. The porosity at the nanometric level is of paramount importance in studying properties of cement based materials. It is the main parameter which influences, e.g., the strength, the shrinkage, the transport properties and the durability [4]. Moreover, the properties of the nanometric pores are quite essential in the modeling of some important processes of cement based materials, e.g., moisture transport [5, 6], drying shrinkage [7] and carbonation [8, 9]. Thus, the accuracy of the pore structure characterization of cement based materials is crucial.

Low temperature (micro-)calorimetry or LTC, also known as thermoporometry and sometimes referred to as thermoporosimetry or cryoporometry [10], is one of the used methods to investigate the porosity of materials, especially pores at the meso-level, i.e., pores with widths between 2 and 50 nm, according to the IUPAC definition [11, 12]. LTC has been used extensively to study the porosity of cement based materials, e.g., in [10, 13–15]. Compared with the traditional methods developed for porosity characterization, e.g., mercury intrusion porosimetry (MIP), nitrogen adsorption/desorption (NAD) and scanning electron microscopy (SEM), a major advantage of using LTC on cement based materials is that the measurements can be conducted on virgin samples without any drying treatment [10, 15–17], as the drying treatment in many cases results in an alteration of the pore structure of cement based materials [18, 19].

As for most of the techniques, LTC is an indirect method for porosity determination. The analysis of the measured data is not straightforward and special care should be taken in the data analysis. In LTC studies, e.g., using water as the probe liquid, the instrument records the heat flow during the freezing and melting process. Based on the measured heat flow, the ice content in a sample at different temperatures can be calculated. To calculate the ice content, the baseline must be determined carefully and appropriate values of the heat of fusion of the water/ice confined in small pores at different temperatures must be specified. The impact of the two factors, i.e., the baseline determination and the values of the heat of fusion of confined water/ice, on the calculated ice content has been presented in an earlier study [20]. To calculate the pore size distribution, the relation between the pore size and the depressed freezing/melting point must be known. Under certain basic assumptions, thermodynamic considerations demonstrate that there is a unique equation between the phase transition temperature of the water/ice confined in pores and the curvature of its solid-liquid interface [21, 22]. The quantitative relation of the freezing/melting point and the pore size can be principally determined by adopting appropriate values for the thermodynamic parameters of the confined water/ice. However, there is no generally consensus on which values should be used for the thermodynamic parameters of water confined in pores, especially at low temperatures, e.g., the surface tension, the heat of fusion and the heat capacity of water and ice [11, 22, 23]. This makes the quantitative determination of the relation between the freezing/melting point and the pore size difficult. Additionally, it should be mentioned that the samples to be tested in LTC studies need to be fully saturated by the probe liquid. If the samples are not fully saturated, the total pore volume will be underestimated since the LTC method can only detect the pores filled with the probe liquid. Moreover, the relation between the depressed freezing/melting temperature and the pore size in this context is normally derived based on the prerequisite that the pores under study are fully saturated. It has been shown that the needed thermodynamic relations to be used for fully saturated pores are different from that for non-fully saturated pores [24]. The needed thermodynamic relations for a non-fully saturated pore system are very complicated, and therefore difficult to determine quantitatively, if it is still possible at all. The impact of using the thermodynamic relations as derived based on fully saturation for non-fully saturated system on the determined pore size distribution is discussed in [24].

In LTC studies, the freezing of pore water is normally assumed to be a process initiated by heterogeneous nucleation and then followed by progressive penetration [25, 26]. That is, the freezing process after the heterogeneous nucleation, i.e., the ice penetration process, is controlled by the pore entry or neck sizes; while the melting process is controlled by the pore interior sizes [15, 27]. For this reason, the freezing process indicates the pore connectivity and the melting process reflects the pore interior size distribution. It is noted that in some LTC studies on cement based materials, the sample size is either relatively small (with the mass on the order of tens of milligrams), e.g., see [28], or relatively big (with

the mass on the order of several grams), e.g, see [10], depending on the instrument adopted. For LTC measurements on samples with relatively small size, crushing and sometimes even grinding is needed in sample preparation. The procedure of sample crushing and/or grinding is also needed in sorption studies using a "Dynamic water vapor sorption (DVS)" instrument due to the small sample holder. In sorption studies, it is normally pre-assumed that the crushing and/or grinding of the cement paste samples do not change the pore structure at the nanometric level, e.g., see [29, 30]. However, it should be mentioned that there are NMR cryoporometry studies, e.g., see [31, 32], which compares the measurements on the same material but in different forms, i.e., big integral and crushed samples. The results show that the pore connectivity is changed by the sample crushing even though the pore interior size distribution remains about the same. The impact of sample crushing, i.e., using different size of samples, in LTC studies on the determined porosity of hardened cement pastes is, however, not fully clear and needs to be further examined.

In this investigation, using LTC to characterize the porosity of hardened cement pastes prepared by two different types of cements is discussed. For each hardened cement paste, two types of samples, i.e., in the form of powders and cylinders, are used. The impact of sample crushing on the detected porosity of the studied hardened cement pastes is demonstrated and some possible explanations are proposed for the observed differences.

2 Experimental

2.1 Materials preparation

One mono-sized model material MCM-41 and two hardened cement pastes were studied in this investigation. The primary consideration of including the model material is to validate the applicability of using LTC in the context of porosity determination.

2.1.1 Model material MCM-41

MCM-41 is a silica based material and the pore structure is in the form of hexagonal arrays of uniform tubular channels of controlled width, which has been widely used as a model material in the context of porosity characterization [33–36]. The MCM-41 used in this study is in the powder form and is produced by Tianjin Chemist Scientific Ltd. The nominal pore diameter and the total pore volume reported by the producer are 3.0 nm and $\geq$ 0.70 mL g^{-1}, respectively.

In order to handle powders more easily in the instrument during calorimetric measurements (Section 2.2), a cylindrical plastic vial was used as a sample holder the powder sample. The size of the plastic vials ($\sim \phi 14 \times 48$ mm) was chosen to fit the measuring chamber of the calorimeter. The MCM-41 powders were placed into the plastic vials up to about half the volume (the dry mass was about 0.2 g) and then covered with distilled water. In order to saturate the samples, the plastic vials containing powders covered with distilled water were placed under a reduced pressure ($\sim$ 40 mbar) for about 3 hours. After that, the apparent excess bulk water on top of the powders was removed and the samples were stored in closed containers for two to three weeks before calorimetric measurements.

2.1.2 Cement pastes

Two types of cements, i.e., CEM I 32.5 R and CEM III/B 42.5 N, were used to prepare paste samples in this study. The properties and the chemical composition of the cements are shown in Table 1. The water-to-cement ratio of the prepared paste samples was 0.4. A paddle mixer was used to mix the fresh pastes. After mixing, the fresh pastes were cast into cylindrical plastic vials followed by proper compaction. The dimension of the plastic vials is about $\phi 15 \times 50$ mm. The hardened cement pastes were demoulded after one day of sealed curing at room temperature (about 20 °C). Following the demoulding, the paste samples were placed into slightly bigger plastic flasks ($\sim \phi 25 \times 60$ mm) filled with saturated limewater for curing at room temperature.

Table 1: Properties and the chemical composition of the two cements used in this study.

	CEM I (CEM I 32.5 R)	CEM III (CEM III/B 42.5 N)
Density/g cm^{-3}	3.06	2.90
Fineness/cm^2 g^{-1}	2905	4635
Water demand/%	26.2	32.3
Initial setting time/min	185	270
Loss on ignition/%	2.1	1.4
SiO_2/%	20.6	29.2
Al_2O_3/%	5.6	8.9
Fe_2O_3/%	2.4	1.2
CaO/%	63.4	48.0
MgO/%	1.6	4.8
SO_3/%	2.9	2.6
K_2O/%	0.7	0.6
Na_2O/%	0.2	0.2
Cl/%	<0.1	<0.1

The cylinder samples of the hardened cement pastes were used to obtain powder samples. The cylinders were firstly vacuum saturated with saturated limewater and then the crushing and grinding of the samples were conducted in a carbon dioxide free chamber to avoid carbonation. After that, the ground paste powders (passed through 315 μm sieve) were placed into the plastic vials up to about half the volume and then covered with saturated limewater. This procedure was also conducted in the carbon dioxide free chamber. Following that, the plastic vials containing cement paste powders were placed under reduced pressure for saturation purpose (as did for the MCM-41 powders in Section 2.1.1). After the saturation, the apparent excess bulk water on top of the powders was removed and the samples were stored in closed containers for two to three weeks before calorimetric measurements (after calorimetric measurements, the dry mass of cement paste powders and the total water content in each plastic vial were determined as about 1:1).

For cylinder samples of the cement pastes, they were vacuum saturated and then the apparent bulk water on the surface of cylinders was wiped off before calorimetric measurements.

When calorimetric measurements were performed, the total curing time of the cylinder and powder samples of the studied cement pastes were about 1 year and 1.5 years, respectively.

By using two types of cements, part of the effect due to cement types on the porosity determination by LTC is expected to be observed. The hardened cement pastes are designated as CEM I and CEM III in the following discussion.

2.2 Calorimetric measurements

A Calvet-type scanning calorimeter (SETARAM) was used in this investigation. The calorimeter was calibrated and operated to work between about 20 °C down to about -130 °C. The cooling and heating rate were set to be 0.1 °C min^{-1}. A freezing and melting cycle consists the temperature scanning starting from about 20 °C and going down to about -80 °C and then back to about 20 °C again.

In the measurements of the powder samples, a plastic vial same as the sample holder but empty was placed in the reference chamber of the calorimeter. The purpose was to counteract the effects due to some uncertainties that the plastic vial may experience during freezing and melting measurements. In the measurements of the cylinder cement paste samples, a totally dry paste sample (oven drying at about 105 °C until constant mass) of the same dimension as the testing specimen was used as a reference sample in the LTC instrument. One purpose of using the reference sample is to reduce the possible uncertainties of the solid paste during the freezing and melting measurements. More discussions about the influence and the benefits of using such a reference sample in calorimetric measurements can be found in [20, 37].

Due to the energetic barrier to nucleation, bulk water can be cooled down below 0 °C without freezing, i.e., the supercooling behavior [23]. Due to the supercooling, it is then not possible to derive any pore

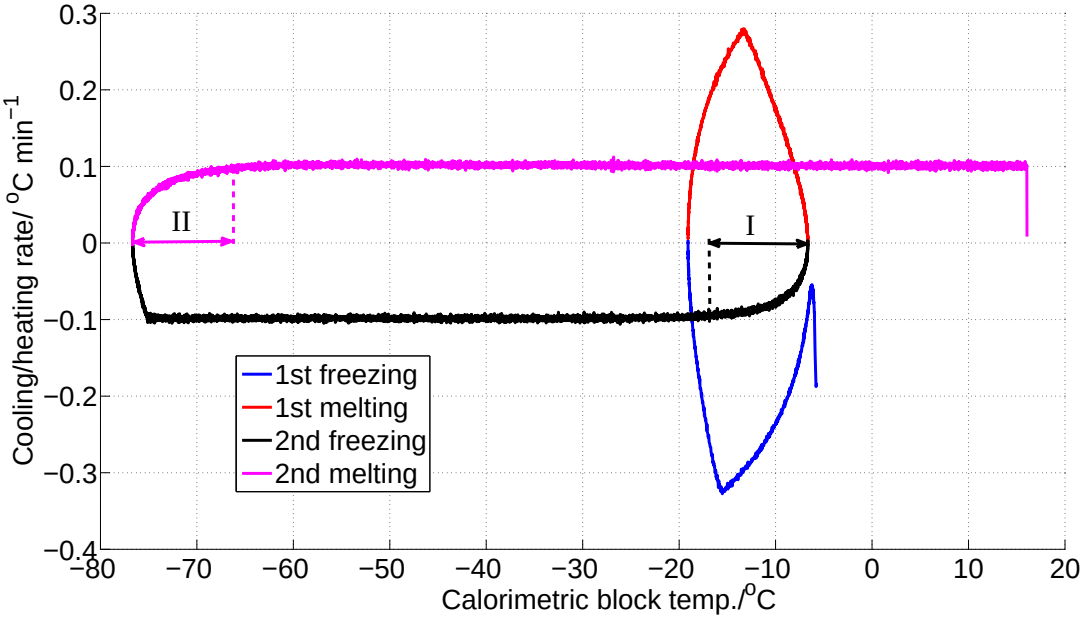

Fig. 1: The cooling/heating rates during a trial run of two cycles of freezing and melting using the employed instrument.

entry information from the freezing curves during the temperature range between 0 °C and the point when the supercooling terminates (the initial nucleation starts). In order to suppress the supercooling of water during freezing and to derive more information from the freezing process in LTC studies, two cycles of freezing and melting measurements have been suggested, e.g, see [12, 15, 38]. The first freezing process is to create some ice crystals and the first melting process is run up to just below the melting point of macroscopic ice (i.e., the ice in big air voids or on the external surfaces of the testing sample), e.g., that the samples were heated to -0.05 °C in [15] and about -0.5 °C in [38]. The macroscopic ice formed in the first freezing process, which serves as the ice front, then penetrates through the pore network of the sample during the second freezing process. By adopting the two cycles procedure, the pore entry and interior sizes can be obtained from the second freezing and melting process, respectively.

A trial run of a two cycles of freezing and melting using the employed instrument was conducted. The first cycle was run on a relatively high cooling/heating rate, as suggested in [12, 15, 38], since the main purpose is just to create some macroscopic ice to be used in the second cycle. The second cycle was run on the set cooling/heating rate for measurements, i.e., 0.1 °C per minute. The cooling/heating rates during the trial run are calculated and shown in Figure 1. It is found that it would take about 10 °C for the cooling/heating rate to be stabilized when the process is changed from cooling to heating and *vice versa* (as indicated by notation I and II in Figure 1). The importance of the stability of the cooling/heating rate during measurements in the ice content determination has been discussed in [20]. That is, the ice content during the temperatures with unstable cooling/heating rate may not be calculated properly. Assuming the testing samples are successfully heated up to just slightly lower than 0 °C in the first melting process and then the samples are cooled down immediately, the ice content of the second freezing during the temperature from about 0°C to about -10 °C may not be obtained properly, due to the unstable cooling rate during the temperature range. As will be shown later, measurements on the cylinder samples of cement pastes using one freezing and melting cycle show that the supercooling also terminates at around -10 °C (see Figure 3 and Figure 4). Similar to the two cycles of measurement, the ice content of the freezing process during the temperature from about 0°C to about -10 °C also cannot be obtained. That is, using two cycles cannot provide more pore entry information (derived from the ice content curve of

the freezing process) compared with that using one cycle. Thus, only one freezing and melting cycle was used for all the measurements.

The mass of the tested vacuum saturated samples before and after calorimetric measurements were determined. The relative difference of the mass is less than about 0.15%. That is, there is almost no water loss during the calorimetric measurements. After calorimetric measurements, the tested samples were oven-dried at about 105 °C until constant mass to obtain the dry masses. The total water content of each sample was obtained by the mass difference between the dry state and the state before the calorimetric measurement.

For the model material MCM-41, calorimetric measurements were performed on two samples of the same kind. By doing this, the stability of the instrument was expected to be validated (assuming the MCM-41 powders are homogenous as they were collected from a rather big batch). For the cylinder samples of each cement paste, three different samples were measured with the purpose to check the homogeneity of the prepared cylinder samples. The powder samples of each investigated cement paste were collected from two cylinders and the homogeneity was not further checked. That is, only one calorimetric measurement was conducted on the powder samples of each studied cement paste.

Additionally, using vacuum saturated samples, the total porosity of the cylinder samples of the two studied cement pastes were also determined through gravimetric measurements by recording the mass of the samples both in air and submerged in water.

3 Results and discussion

3.1 Ice content

The ice content calculation based on the measured data of heat flow is central for pore volume and pore size distribution determination in LTC studies. Special care should be taken in determining the baseline of heat flow and choosing the appropriate values for the thermodynamic parameters of water/ice confined in pores, i.e., surface tension, heat capacity and heat of fusion. A detailed discussion in this context and the methods for ice content calculation can be found in [20]. The "C-method" together with the values chosen for the relevant parameters as discussed in [20], which has been demonstrated suitable to calculate the ice content, is used in this study.

3.1.1 Model material MCM-41

The calculated ice content curves of the two measured samples of the model material MCM-41 are shown in Figure 2. It can be found that the difference between the ice content curves (both freezing and melting) of the two samples is small. That is, the stability of the instrument is concluded to be satisfactory.

3.1.2 Cement pastes

For the cement pastes CEM I and CEM III, the calculated ice content curves for the measured three cylinder samples and one powder sample of each paste are presented in Figure 3 and Figure 4, respectively. It should be mentioned that the presented ice content does not include the "bulk" ice, which is determined by calculating the ice content corresponding to the peak above 0 °C from the heat flow curve of melting. For the cylinder samples, the "bulk" ice is mainly the ice in big pores (with small temperature depression, e.g., air voids) since saturated surface dry samples were used; while for the powder samples, the "bulk" ice should contain both the ice in big pores and the excess bulk water since there is still a portion of excess water in the powder samples as determined.

As can be found from Figure 3, for the paste CEM I, the calculated ice content curves of two of the measured three cylinder samples (cylinder 2 and cylinder 3) are quite comparable; while the ice content curves of one sample (cylinder 1) differ from that of the other two to a certain extent. Since the instrument is rather stable (according to the measurements on the MCM-41, see Figure 2), the difference between the ice content curves as determined for the cylinder samples is attributed to the

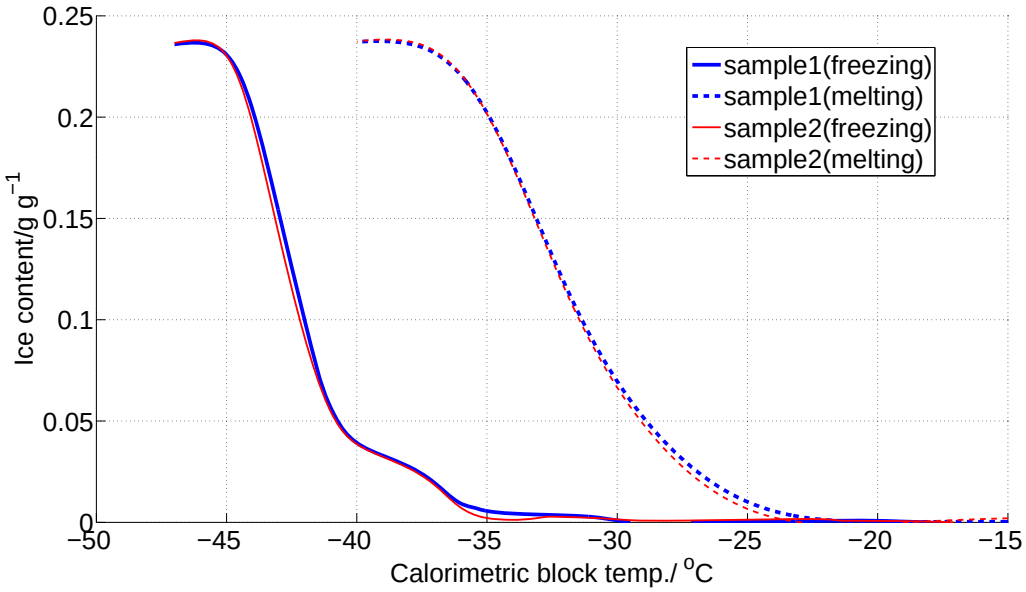

Fig. 2: Calculated ice content curves of the two measured samples of the model material MCM-41 (with excess bulk ice subtracted). The ice content is expressed as gram per gram of dry material.

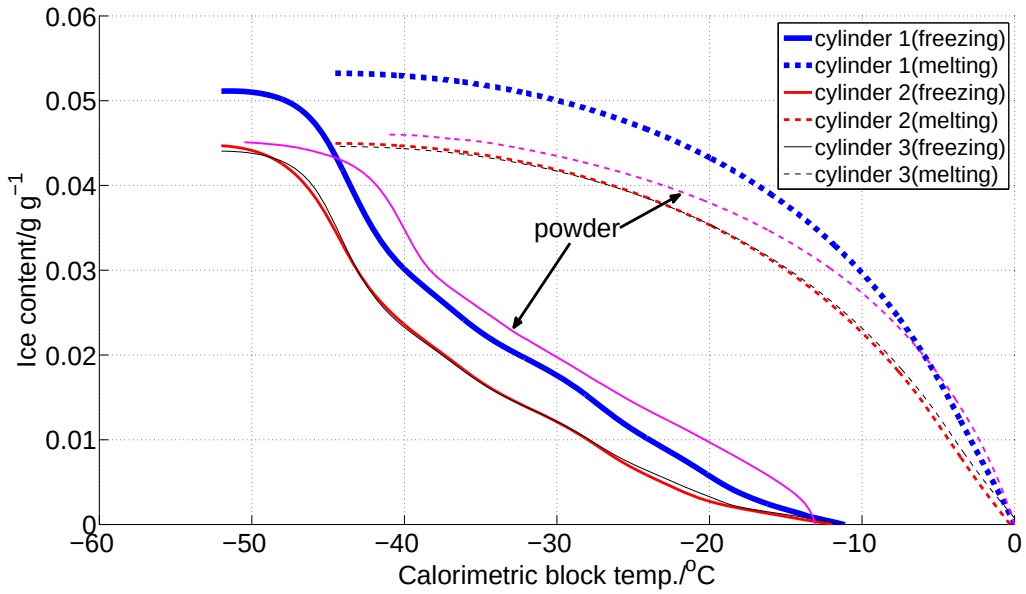

Fig. 3: Calculated ice content curves of cylinder and powder samples of the cement paste CEM I (with "bulk" ice subtracted). The content of "bulk" ice in each sample is determined by calculating the ice content corresponding to the peak above 0 °C from the heat flow curve of melting. The ice content is expressed as gram per gram of dry material.

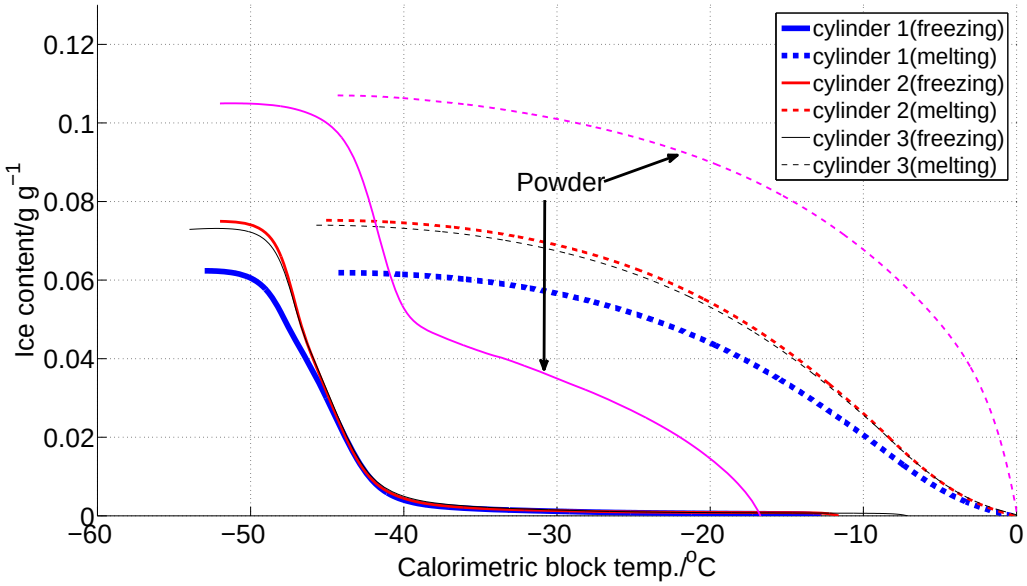

Fig. 4: Calculated ice content curves of cylinder and powder samples of the cement paste CEM III (with "bulk" ice subtracted). The content of "bulk" ice in each sample is determined by calculating the ice content corresponding to the peak above 0 °C from the heat flow curve of melting. The ice content is expressed as gram per gram of dry material.

inhomogeneity of the prepared samples. For the powder sample of the paste CEM I, the ice content curve during melting is higher than that of cylinder 2 and cylinder 3 at a same temperature while it is generally lower compared with that of the cylinder 1 (except during the temperature range between -7 °C and about 0 °C). There are two main differences between the ice content curves of freezing of the powder sample and the cylinder samples. Firstly, the ice content curve of freezing of the powder sample starts at a somewhat lower temperature than that of the cylinders. That is because the starting point of the ice content curve of freezing reflects the heterogeneous nucleation temperature (of supercooled water) and it generally decreases as the sample size decreases [39]. Secondly, the ice content curve of freezing of the powder sample is higher than that of all the three cylinders at a same temperature. The more ice content detected at a same temperature during freezing indicates that the connectivity of the pores in the powder sample is increased compared with that of the cylinders, i.e., more pores are penetrable by ice at a same temperature. The increased connectivity of the powder sample is more obvious by comparing the ice content curve of freezing of the powder sample with that of cylinder 1. Even though cylinder 1 has a higher pore volume than the powder sample (i.e., reflected by a higher maximum ice content), the ice content curve of freezing of the powder sample is still higher than that of the cylinder sample at a same temperature. The results may indicate that the crushing of cylinder samples into powders increases the pore connectivity.

Some differences as found between the powder sample and the cylinder samples for the paste CEM I are also found for the paste CEM III (Figure 4), e.g., the inhomogeneity of the prepared cylinder samples and the increased pore connectivity in the powder sample than that in the cylinder samples. There are also some new features. The difference between the ice content curve of freezing of the powder sample and that of the cylinder samples for the paste CEM III is more significant compared with that of the paste CEM I. From the ice content curves of freezing of the paste CEM III (Figure 4), it should be mentioned that the freezing behavior of the water in cylinder samples is quite different from that in the powder sample. When the temperature goes down to about -40 °C, very limited amount of ice is formed in the cylinder samples while about half of the total ice is formed in the powder sample. As we know, the freezing process is an ice penetration process (after the initial heterogeneous nucleation)

controlled by pore entry sizes. That is, the pore entry sizes in cylinder samples of the paste CEM III can be very small and ice cannot penetrate through the small pore entries. Only when the temperature goes down to a very low point when homogenous nucleation becomes significant (e.g., about -40 °C) , will the pore water then freeze irrespective of pore sizes. While for the powder sample, ice has already penetrated into the sample and occupied about half of the total pore volume when the temperature goes down to about -40 °C. The comparison of the ice content curves of freezing between the powder sample and cylinder samples of the paste CEM III indicates that the crushing of cylinder samples into powders may significantly change the pore connectivity.

Another important difference between the powder sample and the cylinder samples of the paste CEM III is that the determined maximum ice content in the powder sample is much higher compared with that in the cylinder samples. The relatively difference is up to about 40-50%. However, the marked difference is not found from the comparison of the paste CEM I (Figure 3).

The marked difference of the determined maximum ice content between the cylinder and powder samples of the paste CEM III (indicating more pores detected in the powder sample) may be related to the "isolated" pores. It should be mentioned that in LTC studies on cement based materials, there is normally a peak starting at around -40 °C (and it is extended to lower temperatures) on the measured freezing heat flow curves and this peak is often associated with the so-called "isolated" pores, e.g., see [10, 27, 40]. Then two types of "isolated" pores can be envisaged: (1) totally isolated pores (which may form due to, e.g., self-desiccation during the hydration); (2) pores connected to very small pore entries in which water does not freeze above about -40 °C, i.e., pores "isolated" by small pore entries. It could be that some of the "isolated" pores in the cylinder samples cannot be fully saturated with water during vacuum saturation due to a very complicated pore structure, e.g., of which pores are less connected and the whole pore system is quite tortuous; while in the powder sample, due to the increased pore connectivity as a result of the sample crushing, some of the initially "isolated" pores can be opened and then they are able to be filled with water during vacuum saturation. Consequently, the overall saturation degree of the "isolated" pores in the powder sample after vacuum saturation could be much higher compared with that in the cylinder samples. Since LTC detects only the water filled pores, it is not surprising that more pores are detected in the powder sample, as observed in Figure 4. The impact of sample crushing on the "isolated" pores is schematically illustrated in Figure 5 (the small amount of water in the "isolated" pores, i.e., pore A and pore B in Figure 5a and pore C in Figure 5b, is schematic, which may come from, e.g., diffusion and/or unreacted mixing water).

The much more marked difference of the ice content between the powder and cylinder samples as found in the paste CEM III (Figure 4) compared with that in the paste CEM I (Figure 3) may indicate that there are probably more "isolated" pores in the paste CEM III than that in the paste CEM I. Combined with the calculated total pore volume, more discussions about the impact of the sample crushing on the detected porosity will be conducted in Section 3.2.

From the comparison of the ice content curves for the powder and cylinder samples of the studied cement pastes, it can be concluded that the crushing of a sample into powders increases the pore connectivity. Another important consequence of sample crushing is that it could possibly result into more pores detected by LTC in the crushed powders than that in a big sample, with one possible reason being that the saturation degree of the "isolated" pores in a big sample can be greatly increased after the crushing during saturation.

3.2 Total pore volume

The total content of pore water (more accurately, it is ice and the unfreezable water in pores) in each LTC studied sample is calculated by subtracting the content of "bulk" ice (as explained in Section 3.1) from the determined total water content. Further assuming the density of pore ice/water as 1.0 g mL^{-1}, the total pore volume of each LTC studied sample is estimated[1]. For the materials measured more than

[1] The density of ice is temperature dependent [41], see Eq.3. But the temperature dependence is not considered here for simplicity purposes. As the density of ice is less than 1.0 g mL^{-1} [41] and maybe for unfreezable pore water as well [42], this assumption probably results into somewhat underestimation of the pore volume.

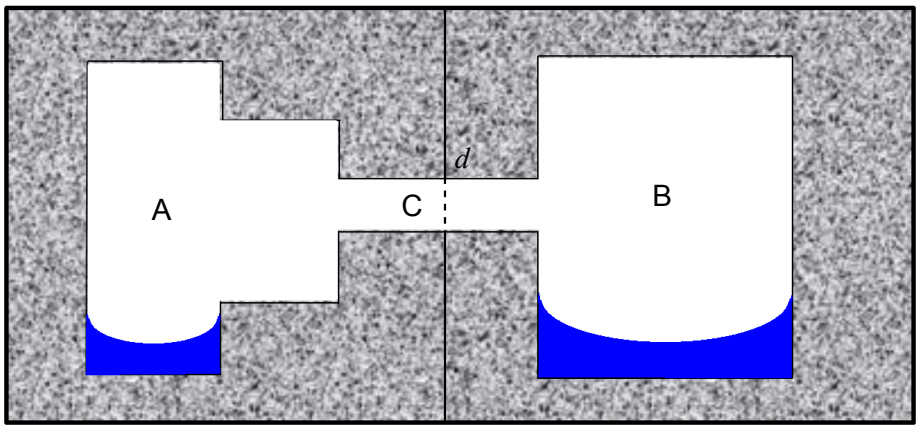

(a)

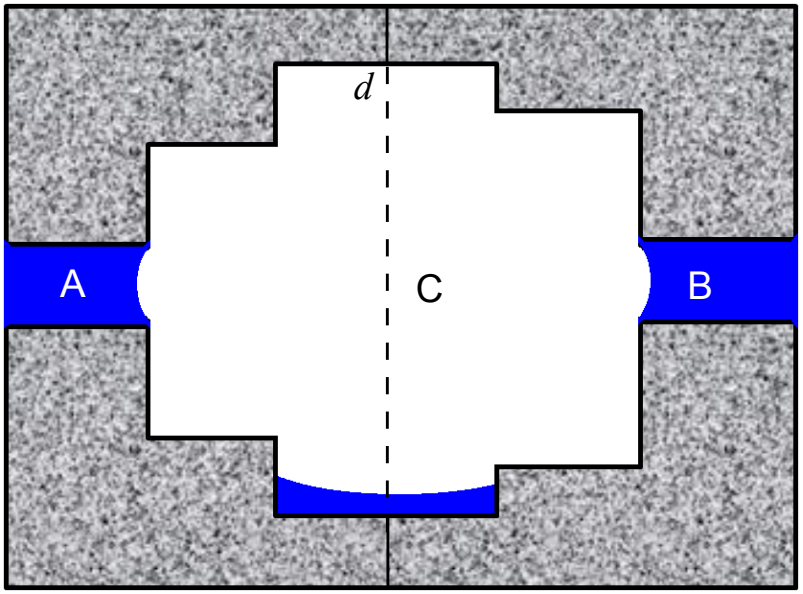

(b)

Fig. 5: A schematic illustration of "isolated" pores. (a) pore A, pore B and pore C are three connected but totally isolated pores; (b) pore C is connected to but kind of "isolated" by pore A and pore B with very small sizes. The "isolated" pores are inside of a rather big hardened cement paste (e.g., a cylinder sample). During vacuum saturation, water may have no access to the totally isolated pores, e.g., in (a) and probably small pore entries may block or prevent water from penetrating into the "isolated" pores, e.g., in (b). However, if the sample is crushed along any line between pore A and pore B, e.g., the line d, then all the "isolated" pores are more easily to be filled with water during saturation (corresponding to powder samples).

Table 2: Total pore volume of the MCM-41 and the pastes CEM I and CEM III obtained from different methods. The values are expressed in the unit of milliliter per gram dry material/mL g^{-1}.

		LTC[a]	Gravimetric measurement[b]	DVS[b,c,d]
MCM-41		0.72	-	0.77
CEM I	cylinder	0.20	0.21	-
	powder	0.21	-	0.20
CEM III	cylinder	0.23	0.23	-
	powder	0.29	-	0.35

Note: (a). the volume of the big pores (e.g., air voids, as explained in Section 3.1) in the cement pastes is not included. From the calculation on the cylinder samples, the volume of the the big pores in pastes CEM I and CEM III is about 0.007 and 0.003 mL g^{-1}, respectively; (b). density of pore water is assumed to be 1.0 g mL^{-1}; (c). moisture content determined during desorption at the RH of 0.95 which is almost the upper limit that the instrument can work with; d). the age of the cement pastes is about 6-8 months when measured.

once in this study, the total pore volume is obtained by averaging that of the several measurements. The total pore volume of the LTC studied samples are listed in Table 2. The porosity of the model material MCM-41 and the pastes CEM I and CEM III were also studied by the Dynamic (water) Vapor Sorption (DVS) measurement [43]. The DVS results, together with that of the gravimetric measurements, are also listed in Table 2.

As can be seen from the results presented in Table 2, the total pore volume of the paste CEM I obtained from different methods are comparable. For the paste CEM III, the total pore volume determined from the gravimetric measurements is comparable to that of the cylinder samples by LTC; while the total pore volume determined from DVS, which is much higher than that of the cylinder samples by LTC, is more comparable to that of the powder sample by LTC. The comparison between the results obtained from the gravimetric and the DVS measurement for the cement paste CEM III is in agreement with that of the results obtained from LTC studies on the powder and cylinder samples, i.e., the sample crushing is concluded to have an impact on the detectable pore volume. However, by noting that the differences between the results found for the paste CEM III using different samples are not observed on the paste CEM I, it should be mentioned that the effect of the sample crushing is probably dependent on the (porosity) properties of the studied material.

3.3 Pore size distribution

Based on different pore shape assumption and the process (either freezing or melting), Brun et al. [22] proposed two equations accounting for the relation between the pore size and the freezing/melting depression. The two equations are used in this study, i.e.,

$$R_p = -\frac{64.67}{T - T_0} + 0.57 \tag{1}$$

$$R_p = -\frac{32.33}{T - T_0} + 0.68 \tag{2}$$

where R_p (nm) is the pore size; T and T_0 is the freezing/melting point of pore water/ice and bulk water/ice, respectively. For the cylindrical pore assumption, Eq.1 is used for the freezing process and Eq.2 is used for the melting process; while for spherical pore assumption, Eq.1 is used for both the freezing and the melting process. The density of ice adopted in the pore size distribution calculation is a temperature dependent function, which is [41]

$$\rho_{ice} \approx 0.9167 - 2.053 \cdot 10^{-4}\theta - 1.357 \cdot 10^{-6}\theta^2 \qquad \text{g mL}^{-1} \tag{3}$$

where θ is the temperature in Celsius degree. More discussions with respect to the pore size distribution calculation is presented in [24].

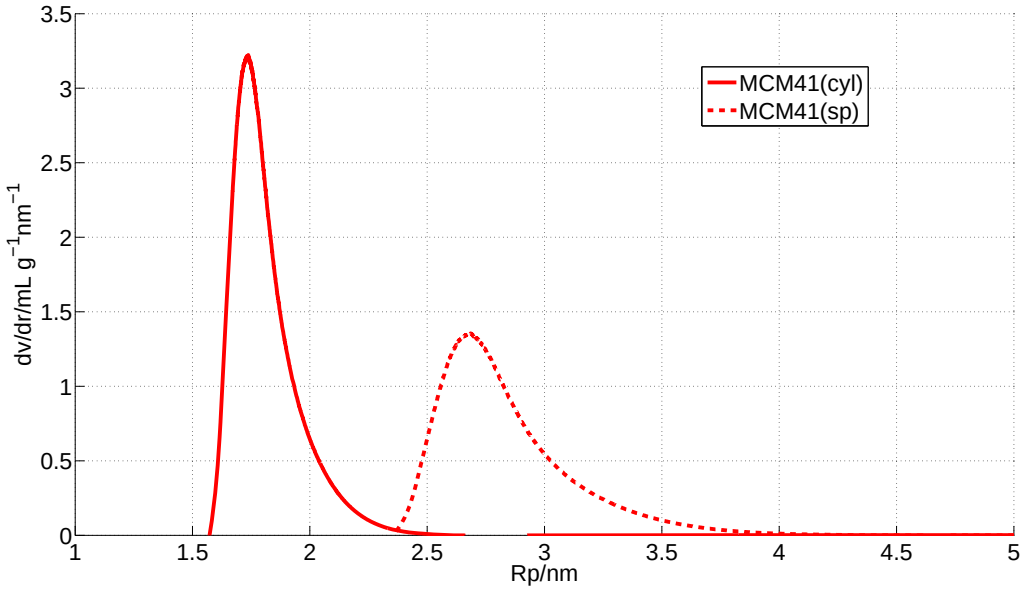

Fig. 6: Calculated differential pore size distribution of the model material MCM-41 based on the cylindrical (cyl) and the spherical (sp) pore assumption.

With the obtained ice content curves of the freezing and the melting process, it is possible to calculate both the pore entry size and the pore interior size distribution of the studied material. However, for the measured samples in this study, it should be mentioned that the meaningful temperature range of the freezing curves that can be used to calculate the pore entry sizes is only from around -10 °C to about -40 °C. The pores with entry sizes bigger than that corresponding to a temperature depression of about -10 °C are not detected because of supercooling. That is, no ice has been formed before reaching about -10°C and hence no calculation can be made. When the temperature goes down to about -40 °C, the homogenous nucleation becomes significant [25, 26, 44] and all the freezable pore water would freeze independent of the pore (entry) sizes. That is, the ice formed around the homogenous nucleation temperature does not indicate any pore size information. For the MCM-41, the pore (entry) size is too small to be obtained from the freezing curve as the main ice content is formed below about -40 °C. For the studied cement pastes, the pore entry radii that can be obtained are between about 2.4 nm to about 5-6 nm (using Eq.1). As the obtained pore (entry) size range is quite limited from the ice content curves of freezing of the cement pastes, the results are not presented. In the following, only the ice content curves of melting are used to calculate the pore interior size distribution.

3.3.1 Model material MCM-41

For the model material MCM-41, the mean ice content of the two measured samples (melting curves) as presented in Figure 2 is used for the calculation of the pore size distribution. The thermal lag between the calorimetric block and a tested sample is assumed to be negligible. The calculated pore size distribution (PSD) curves of the MCM-41 are presented in Figure 6. The pore radius corresponding to the peak in the calculated PSD curves, sometimes referred to as the most frequent pore radius R_{max} [45], is about 1.7 nm and 2.7 nm assuming cylindrical and spherical pores, respectively. It should be mentioned that the pores of MCM-41 products are often assumed to be very close to cylindrical shape [33, 34, 36, 46]. Including the spherical shape assumption in the calculation is for comparison purpose only. The R_{max} of 1.7 nm based on the cylindrical pore assumption is close to the value provided by the producer, i.e., the diameter of 3.0 nm.

3.3.2 Cement pastes

For the cylinder samples of each cement paste, the representative ice content is calculated by averaging the results of the three cylinder samples (melting curves) of each paste (Figure 3 and Figure 4). One may argue that the thermal lag for the cylinder samples might be different from that for the powder sample. If the thermal lag is different, it should be more obvious at very low temperatures. For all the measured cement paste samples, there is a characteristic peak corresponding to homogenous nucleation, which starts around -40 °C and is extended to several degrees lower, on the heat flow curves of freezing [40, 47]. By comparing the starting temperature of the characteristic peak due to homogenous nucleation on the heating flow curves of freezing, it is concluded that the thermal lag for the cylinder samples and the powder sample are close, if there is any. One may also argue that the ionic concentration in the pore solution might be different, since the water content in the powder sample is higher than that in the cylinder samples. A study [47] indicates that the amount of curing water has very limited effect in changing the freezing and melting behaviors of the cement pore solution. In this study, it is therefore assumed that the impact of the ions on the freezing and melting point depression for the cylinder samples and the powder sample are more or less the same. In this investigation, both the thermal lag and the effect due to ions are not considered.

The calculated accumulated and differential PSD curves for the pastes CEM I and CEM III are shown in Figure 7 and Figure 8, respectively. It can be found that the calculated accumulated PSD curves of the powder sample are generally higher than that of the cylinder sample, especially for the paste CEM III (Figure 8a), indicating that the volume of the relatively big pores is higher in the powder sample. However, from the calculated differential PSD curves, it is found that the portion of small pores, i.e., with the radii between about 2 to 10 nm for the paste CEM I and the radii between about 2 to 5-6 nm (depending on the pore shape assumption) for the paste CEM III, is relatively higher in the cylinder sample.

More big pores found in the powder sample compared to the cylindrical ones may attribute to that the sample crushing opens some “isolated” pores which may be not fully filled with water before crushing but can be fully saturated after crushing (Section 3.1). Thus, more pores are detected using the powder sample. For the more small pores in the cylinder samples observed from the calculated differential PSD curves, it is possibly related to the so-called advanced melting phenomenon [32, 48]. It is normally assumed that for cylindrical pores, the melting would take place in a radical direction [32], or melting from the side (the direction perpendicular to the diameter) [15]. However, melting could also take place from the end (the direction parallel to the diameter), depending on the pore size and connectivity [15, 32]. If melting initiates from the end, it is the so-called advanced melting. The concept of advanced melting is schematically shown in 9. Since the sample crushing changes the connectivity of the pores, the impact of advanced melting on the powder and the cylinder samples may be different. One consequence of the advanced melting on the pore size distribution determination is that big pores may be wrongly calculated as small pores [32], which can somewhat explain the difference between the calculated volume of small pores in the powder and the cylinder samples. Additionally, some of the “isolated” pores in cylinder samples may be not fully saturated as mentioned earlier (Section 3.1). It has been demonstrated in [24] that the freezing/melting point of the water/ice confined in the non-fully saturated pores will be further depressed compared with the condition that the pores are fully saturated. The effect is that the calculated sizes of the pores under non-fully saturation are underestimated. Thus, it could also explain that there are more (calculated or apparent) small pores in the powder sample than what found in the cylinder sample as observed for the studied pastes.

4 Conclusions

Two types of samples, i.e., in the form of powder and cylinder, were used to study the impact of sample crushing on the detected porosity of hardened cement pastes by low temperature calorimetry (LTC). The studied cement pastes were prepared by two types of cements. The difference between the powder

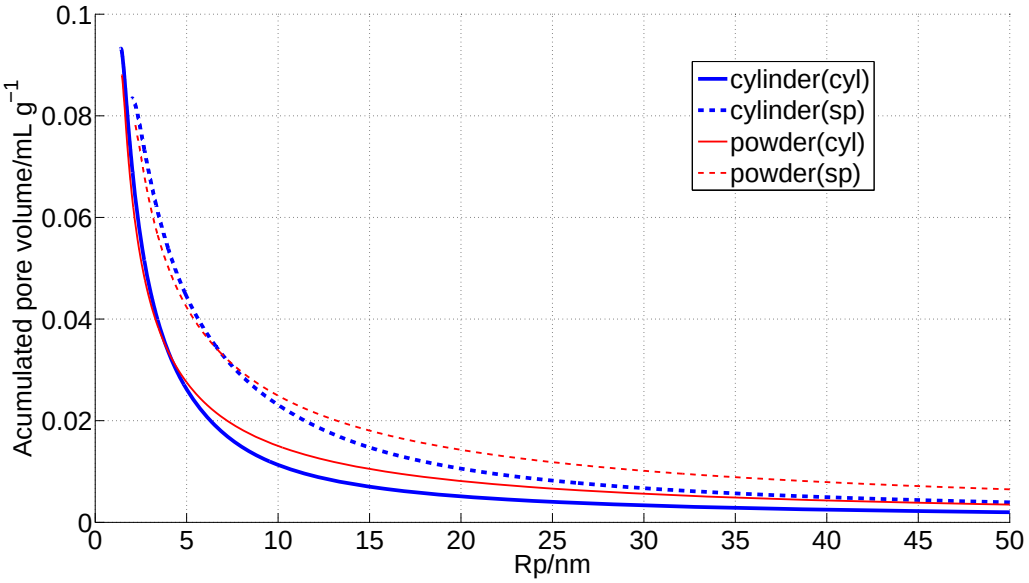

(a) Accumulated pore size distribution

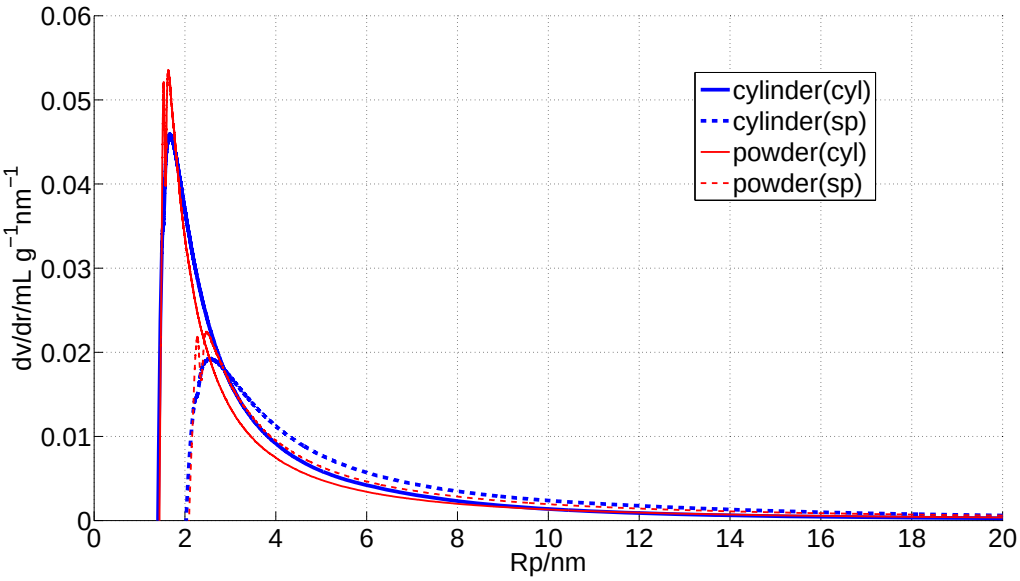

(b) Differential pore size distribution

Fig. 7: Calculated accumulated and differential pore size distribution curves of cylinder and powder samples of the cement paste CEM I. The pore shape is assumed to be cylindrical (cyl) or spherical (sp).

and cylinder samples was compared in terms of the calculated ice content curves, total pore volumes and pore size distribution curves.

For the studied cement pastes, the calculated ice content curves of freezing of the powder sample differed from that of the cylinder samples, especially for the paste CEM III. It indicated that sample crushing changed the pore connectivity. Another important difference between the powder sample and the cylinder samples of the paste CEM III was that the determined maximum ice content in the powder sample was much higher compared with that in the cylinder samples, the relatively difference being about

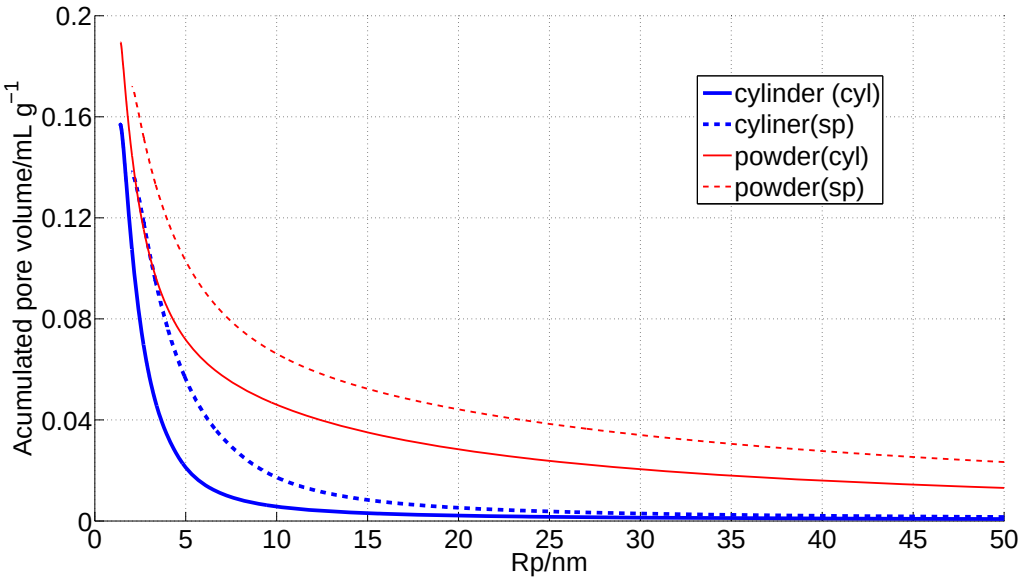

(a) Accumulated pore size distribution

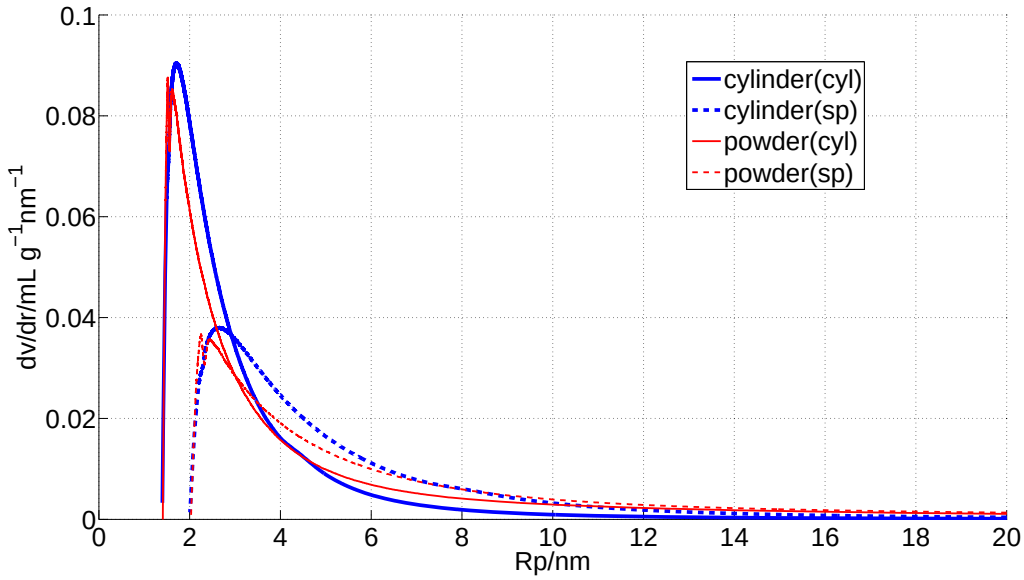

(b) Differential pore size distribution

Fig. 8: Calculated accumulated and differential pore size distribution curves of cylinder and powder samples of the cement paste CEM III. The pore shape is assumed to be cylindrical (cyl) or spherical (sp).

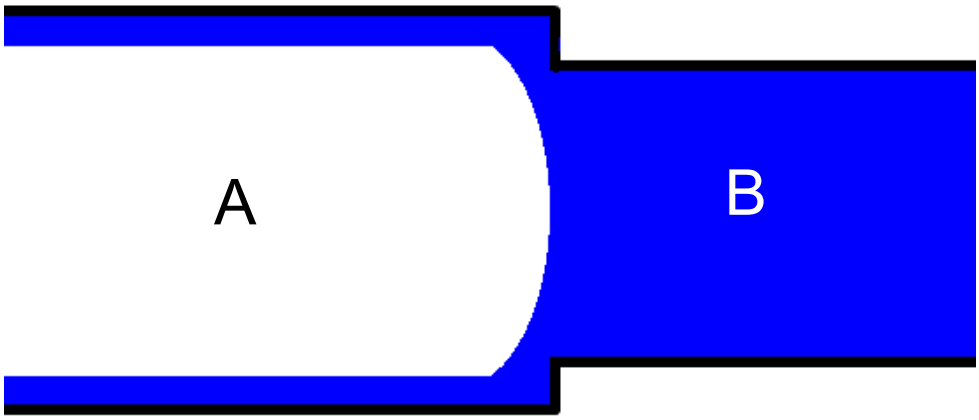

Fig. 9: A schematic illustration of the concept of advanced melting, based on the description from [15, 32]. Pore A and B are two cylindrical pores and connected co-axially, with radii $R_A > R_B$. If the melting initiates from the side (the direction from left to right in the drawing), the ice in pore B will melt at a temperature corresponding to $1/(R_B - \delta)$ and then in pore A at a temperature corresponding to $1/(R_A - \delta)$, where δ is the thickness of the unfreezable layer close to the pore wall. That is, the ice in pore A will melt at a higher temperature compared with the ice in pore B (the smaller the curvature, the higher the melting point). But as pore A and B are connected, the melting point of the ice in pore A also depends on the size relation of the two pores. Considering the case when the ice in pore B melts, the water in pore B is in equilibrium with a ice/water interface having a curvature infinitesimally smaller than $1/(R_B - \delta)$. The ice in pore A terminates in a hemispherical cap with a curvature of $2/(R_A - \delta)$. If $2/(R_A - \delta) \geq 1/(R_B - \delta) = 2/[2(R_B - \delta)]$, i.e., approximately $R_A < 2R_B$ (assuming δ is smaller than R_A and R_B), then the ice hemispherical cap is not thermodynamically stable in pore A and the ice in pore A will melt from the end (the direction from top to bottom in the drawing). That is, due to the connectivity of the two pores and if $R_B < R_A < 2R_B$, the ice in pore A could melt from the end rather than from the side. This is the so-called advanced melting phenomenon. In such a case, the melting point of the ice in pore A from the end (corresponding to the curvature of pore B melting, $1/(R_B - \delta)$) is lower than that from the side (corresponding to the curvature of pore A melting, $1/(R_A - \delta)$). Using the same calculation (Eq.2, which assumes melting from the side), some big pores may be wrongly calculated as small pores due to the advanced melting.

40-50%. However, this kind of marked difference was not found from the comparison of the powder and cylinder samples ofthe paste CEM I. That is, sample crushing could possibly result into more pores detected by LTC depending on the (porosity) characteristic properties of the studied paste.

About the marked difference between the calculated pore volume of the powder and the cylinder samples of the paste CEM III, one possible reason could be that some of the “isolated” pores which, presumably, cannot be fully filled with water in the preparation of the cylinder samples. However, sample crushing makes it possible to saturate the pores to a greater extent if the crushing contributes to open up the “isolated” pores. Consequently, more pores can be detected in the powder samples. The argument about the “isolated” pores is supported by the results of gravimetric measurements on cylinder samples and that of DVS measurements on powder samples.

Acknowledgments

The research leading to these results has received funding from the European Union Seventh Framework Programme (FP7/2007-2013) under grant agreement 264448. A part of this research was funded by the Lizzy, Alfred and Valdemar Taumose’s Foundation. The authors would like to thank Stefan Backe from the Division of Building Materials of Lund University for performing some of the tests.

References

1. S.H. Kosmatka and W.C. Panarese. *Design and control of concrete mixtures*. Portland Cement Association, 2002.
2. H.M. Jennings. Refinements to colloid model of C–S–H in cement: CM–II. *Cement and Concrete Research*, 38(3):275–289, 2008.
3. P.J. McDonald, V. Rodin, and A. Valori. Characterisation of intra-and inter-C–S–H gel pore water in white cement based on an analysis of NMR signal amplitudes as a function of water content. *Cement and Concrete Research*, 40(12):1656–1663, 2010.
4. H.F.W. Taylor. *Cement chemistry*. Thomas Telford, London, 2nd edition, 1997.
5. V. Baroghel-Bouny. Water vapour sorption experiments on hardened cementitious materials. Part II: Essential tool for assessment of transport properties and for durability prediction. *Cement and Concrete Research*, 37(3):438–454, 2007.
6. V. Baroghel-Bouny, M. Mainguy, and O. Coussy. Isothermal drying process in weakly permeable cementitious materials- assessment of water permeability. In *International Conference on Ion and Mass Transport in Cement-Based Materials*, pages 59–80, 1999.
7. V. Baroghel-Bouny, M. Mainguy, T. Lassabatere, and O. Coussy. Characterization and identification of equilibrium and transfer moisture properties for ordinary and high-performance cementitious materials. *Cement and Concrete Research*, 29(8):1225–1238, 1999.
8. M. Thiery, V. Baroghel-Bouny, G. Villain, and P. Dangla. Numerical modeling of concrete carbonation based on durability indicators. In V.M. Malhotra, editor, *Proceedings of the 7th CANMET/ACI International Conference on Durability of Concrete*, pages 765–780, 2006.
9. B. Bary and A. Sellier. Coupled moisture–carbon dioxide–calcium transfer model for carbonation of concrete. *Cement and Concrete Research*, 34(10):1859–1872, 2004.
10. A.M. Kjeldsen and M.R. Geiker. On the interpretation of low temperature calorimetry data. *Materials and Structures*, 41(1):213–224, 2008.
11. K. Ishikiriyama and M. Todoki. Pore size distribution measurements of silica gels by means of differential scanning calorimetry II. thermoporosimetry. *Journal of Colloid and Interface Science*, 171(1):103–111, 1995.
12. M.R. Landry. Thermoporometry by differential scanning calorimetry: experimental considerations and applications. *Thermochimica Acta*, 433(1-2):27–50, 2005.
13. D.H. Bager. *Ice Formation in Hardened Cement Paste*. PhD thesis, Building Materials Laboratory, Technical University of Denmark, 1984.
14. D.H. Bager and E.J. Sellevold. Ice formation in hardened cement paste, Part III-slow resaturation of room temperature cured pastes. *Cement and Concrete Research*, 17(1):1–11, 1987.
15. Z. Sun and G.W. Scherer. Pore size and shape in mortar by thermoporometry. *Cement and Concrete Research*, 40(5):740–751, 2010.
16. D.H. Bager and E.J. Sellevold. Ice formation in hardened cement paste, Part I–room temperature cured pastes with variable moisture contents. *Cement and Concrete Research*, 16(5):709–720, 1986.
17. E. Sellevold and D. Bager. Some implications of calorimetric ice formation results for frost reistance testing of concrete. *in Beton og Frost, Dansk Beton Forening*, 22:47–74, 1985.
18. J. Villadsen. Pore structure in cement based materials. Technical Report 277, Building Materials Laboratory, Technical University, Denmark, 1992.
19. R. Espinosa and L. Franke. Influence of the age and drying process on pore structure and sorption isotherms of hardened cement paste. *Cement and Concrete Research*, 36(10):1969–1984, 2006.
20. M. Wu, B. Johannesson, and M. Geiker. Determination of ice content in hardened concrete by low temperature calorimetry: influence of baseline calculation and heat of fusion of confined water. *Journal of Thermal Analysis and Calorimetry*, 115(2):1335–1351, 2014.
21. R. Defay, I. Prigogine, A. Bellemans, and D.H Everett. *Surface tension and adsorption*. Longmans London, 1966.
22. M. Brun, A. Lallemand, J.F. Quinson, and C. Eyraud. A new method for the simultaneous determination of the size and shape of pores: the thermoporometry. *Thermochimica Acta*, 21(1):59–88, 1977.

23. D.M. Murphy and T. Koop. Review of the vapour pressures of ice and supercooled water for atmospheric applications. *Quarterly Journal of the Royal Meteorological Society*, 131(608):1539–1565, 2005.
24. M. Wu and B. Johannesson. Impact of sample saturation on the detected porosity of hardened concrete using low temperature calorimetry. *Thermochimica Acta*, 580:66–78, 2014.
25. G.W. Scherer. Freezing gels. *Journal of non-crystalline solids*, 155(1):1–25, 1993.
26. D.H. Rasmussen and A.P. MacKenzie. Clustering in supercooled water. *The Journal of Chemical Physics*, 59:5003, 1973.
27. G. Fagerlund. Determination of pore-size distribution from freezing-point depression. *Materials and Structures*, 6(3):215–225, 1973.
28. D. Bentz and P. Stutzman. Curing, hydration, and microstructure of cement paste. *ACI Materials Journal*, 103(5):348–356, 2006.
29. M. Åhs. *Redistribution of moisture and ions in cement based materials*. PhD thesis, Division of Building Materials, Lund University, 2011.
30. V. Baroghel-Bouny. Water vapour sorption experiments on hardened cementitious materials: Part I: Essential tool for analysis of hygral behaviour and its relation to pore structure. *Cement and Concrete Research*, 37(3):414–437, 2007.
31. E.L. Perkins, J.P. Lowe, K.J. Edler, N. Tanko, and S.P. Rigby. Determination of the percolation properties and pore connectivity for mesoporous solids using NMR cryodiffusometry. *Chemical Engineering Science*, 63(7):1929–1940, 2008.
32. E. Shiko, K.J. Edler, J.P. Lowe, and S.P. Rigby. Probing the impact of advanced melting and advanced adsorption phenomena on the accuracy of pore size distributions from cryoporometry and adsorption using NMR relaxometry and diffusometry. *Journal of Colloid and Interface Science*, 385 (1):183–192, 2012.
33. P.J. Branton, P.G. Hall, K.S.W. Sing, H. Reichert, F. Schüth, and K.K. Unger. Physisorption of argon, nitrogen and oxygen by MCM-41, a model mesoporous adsorbent. *J. Chem. Soc., Faraday Trans.*, 90(19):2965–2967, 1994.
34. P.J. Branton, P.G. Hall, and K.S.W. Sing. Physisorption of alcohols and water vapour by MCM-41, a model mesoporous adsorbent. *Adsorption*, 1(1):77–82, 1995.
35. P.I. Ravikovitch, S.C.Ó. Domhnaill, A.V. Neimark, F. Schüth, and K.K. Unger. Capillary hysteresis in nanopores: theoretical and experimental studies of nitrogen adsorption on MCM-41. *Langmuir*, 11(12):4765–4772, 1995.
36. J. Banys, M. Kinka, J. Macutkevic, G. Völkel, W. Böhlmann, V. Umamaheswari, M. Hartmann, and A. Pöppl. Broadband dielectric spectroscopy of water confined in MCM–41 molecular sieve materials–low-temperature freezing phenomena. *Journal of Physics: Condensed Matter*, 17:2843, 2005.
37. B. Johannesson. Dimensional and ice content changes of hardened concrete at different freezing and thawing temperatures. *Cement and Concrete Composites*, 32(1):73–83, 2010.
38. K. Ishikiriyama, M. Todoki, and K. Motomura. Pore size distribution (PSD) measurements of silica gels by means of differential scanning calorimetry I. optimization for determination of PSD. *Journal of Colloid and Interface Science*, 171(1):92–102, 1995.
39. Z. Sun and G.W. Scherer. Effect of air voids on salt scaling and internal freezing. *Cement and Concrete Research*, 40(2):260–270, 2010.
40. J.P. Kaufmann. Experimental identification of ice formation in small concrete pores. *Cement and Concrete Research*, 34(8):1421–1427, 2004.
41. R. L. David, editor. *CRC Handbook of Chemistry and Physics*. CRC Press, 83rd edition, 2002.
42. K. Ishikiriyama and M. Todoki. Evaluation of water in silica pores using differential scanning calorimetry. *Thermochimica Acta*, 256(2):213–226, 1995.
43. M. Wu, B. Johannesson, and M. Geiker. Application of water vapor sorption measurement for porosity characterization of hardened cement pastes. Construction and Building Materials, Submitted for publication, .
44. H.H.G. Jellinek, editor. *Water Structure at the Water-Polymer Interface*. Plenum, New York, 1972.

45. O. Šolcová, L. Matějová, and P. Schneider. Pore-size distributions from nitrogen adsorption revisited: Models comparison with controlled-pore glasses. *Applied Catalysis A: General*, 313(2):167–176, 2006.
46. P.J. Branton, K.S.W. Sing, and J.W. White. Adsorption of carbon tetrachloride and nitrogen by 3.4 nm pore diameter siliceous MCM-41. *J. Chem. Soc., Faraday Trans.*, 93(13):2337–2340, 1997.
47. M. Wu, K. Fridh, B. Johannesson, and M. Geiker. Influence of frost damage and sample preconditioning on the porosity characterization of cement based materials using low temperature calorimetry. Construction and Building Materials, Submitted for publication, .
48. I. Hitchcock, E.M. Holt, J.P. Lowe, and S.P. Rigby. Studies of freezing–melting hysteresis in cryoporometry scanning loop experiments using NMR diffusometry and relaxometry. *Chemical Engineering Science*, 66(4):582–592, 2011.

Paper V

A preliminary study of the influence of ions in the pore solution of hardened cement pastes on the porosity determination by low temperature calorimetry

M. Wu, B. Johannesson, M. Geiker

Published in: *Thermochimica Acta, 2014*

Thermochimica Acta 589 (2014) 215–225

Contents lists available at ScienceDirect

Thermochimica Acta

journal homepage: www.elsevier.com/locate/tca

A preliminary study of the influence of ions in the pore solution of hardened cement pastes on the porosity determination by low temperature calorimetry

Min Wu [a,*], Björn Johannesson [a], Mette Geiker [b]

[a] Department of Civil Engineering, Technical University of Denmark, Building 118, 2800 Lyngby, Denmark
[b] Department of Structural Engineering, Norwegian University of Science and Technology, Trondheim, Norway

ARTICLE INFO

Article history:
Received 25 March 2014
Received in revised form 21 May 2014
Accepted 23 May 2014

Keywords:
Cement paste
Low temperature calorimetry
PHREEQC
Ionic strength
Pore size distribution
Thermoporometry

ABSTRACT

Thermodynamic modeling was used to predict the ionic concentrations in the pore solution of cement pastes at different temperatures during a freezing and melting measurement in low temperature calorimetry (LTC) studies. By using the predicted ionic concentrations, the temperature depressions caused by the ions presented in the pore solution were determined. The influence of the freezing/melting point depression caused by the ions on the determined pore size distribution by LTC was demonstrated. Thermodynamic modeling using the program PHREEQC was performed on the cylinder and powder samples of cement pastes prepared by two types of cements, i.e., CEM I 32.5 R and CEM III/B 42.5 N. Using the modeled ionic concentrations, the calculated differential pore size distributions for the studied samples with and without considering the temperature depression caused by the ions in the pore solution were compared. The results indicate that for the studied cement paste samples, the influence of the temperature depression caused by the presence of the ions in the pore solution on the determination of the pore size distribution by LTC is limited.

1. Introduction

Water confined in small pores freeze at lower temperatures compared with that of bulk water. The depressed freezing/melting point of water/ice due to pore confinement is related to the size of the pores [1]. Taking a porous material saturated with water as an example, the water confined in the material will gradually freeze accordingly to the pore sizes (assuming the material has several different pore sizes) as the temperature decreases. Similarly, the ice confined in the pores of the material will gradually melt as the temperature increases. As the freezing of water is an exothermic process and the melting of ice is an endothermic process, the heat flow evolution during the freezing and melting process can be recorded by calorimetric devices. Hence, the ice content can be estimated from the recorded heat flow in such a measurement. With the calculated ice content and the thermodynamic relation between pore size and the depressed freezing/melting point combined with other important assumptions, it is possible to determine the pore size distribution for the studied material. This is the principal concept of a method for porosity characterization, i.e., low temperature (micro-)calorimetry or LTC (also known as thermoporometry) [2]. This method was pioneered by researchers in a study of organic gels as early as in the 1950s [3] and later the method was generalized and proposed to be used for different materials, e.g., soil [4] and inorganic materials [5]. In recent years, LTC has experienced further development and it has been used to study many different types of porous materials [6].

The pore system in cement based materials is rather complicated, with the pore sizes ranging from nanometers to millimeters [7,8]. Porosity is an important parameter for cement based materials, because it influences, e.g., the strength, the shrinkage, the transport properties or permeability and the durability [9] of the materials. Moreover, the characteristics and properties of the pores are important in the modeling and understanding of some important processes for cement based materials, e.g., drying shrinkage [10], carbonation [11,12] and moisture transport [13,14]. For these reasons, an accurate characterization of the porosity for cement based materials is of great importance. LTC has been used to study cement based materials, e.g., in [15,2,16]. A major advantage of using LTC to characterize cement based materials, compared with the traditional methods developed for porosity characterization, e.g., mercury intrusion porosimetry (MIP), nitrogen

* Corresponding author. Tel.: +45 45251813.
E-mail address: miwu@byg.dtu.dk (M. Wu).

http://dx.doi.org/10.1016/j.tca.2014.05.027
0040-6031/

adsorption/desorption (NAD) and scanning electron microscopy (SEM), is that the measurements can be conducted on virgin samples without any drying treatment [16–18]. The drying treatment often results in an alteration of the pore structure for cement based materials [19,20]. It should be mentioned that due to the fact that the liquid present in very small pores does not freeze and that the freezing/melting point depression of liquid in big pores is too small, the pores that can be studied by LTC are limited mainly to those with radii from about 2 nm to about 40 or 50 nm [21,16]. Water in larger pores is monitored, but the resolution is too limited to allow for determination of the actual pore size. Meanwhile, as an indirect method to study porosity, the analysis of the measured LTC data is not that straightforward. More related discussions can be found, e.g., in [22,23].

Extensive studies have been conducted with respect to the analysis of LTC data using pure water as the probe liquid, e.g., see [1,24–26,21]. However, the analysis of LTC data measured on cement based materials is complicated due to the fact that the pore liquid is not pure water but contains different types of ionic species [9,27]. Compared with the freezing/melting of pure water/ice, the presence of ionic species in a pore liquid may mainly cause two effects which would have important impact on the analysis of LTC data. Firstly, the freezing/melting point will be further depressed, depending on the ionic concentration of the pore solution. The temperature depression caused by ions can be predicted if the ionic concentration of the pore solution is known, e.g., see [28,29]. Secondly, the heat of fusion of the pore solution might be different from that of pure water. It has been demonstrated that the heat of fusion of a pore solution depends on the ionic concentration and the types of ionic species but the exact relation is not clear, e.g., see [30]. That is, even if the ionic concentration and the ionic species of a pore solution are known, the heat of fusion of the pore solution still might not be predictable. The main purpose of this work is to try to study the impact of ions present in cement pore solution on the porosity determination by the LTC method.

One may argue that the impact of ions on the freezing and melting behaviors of the pore solution of cement based materials can be studied by using a model material with a simple pore structure. An artificial cement pore solution can be prepared and used to saturate the model material. By comparing the freezing and melting behaviors of pure water and an artificial pore solution in the same type of model material, the impact of the ions can be studied. However, it should be mentioned that an important characteristic of the pore solution of cement based materials is that the pore walls (cement hydrates) have a great buffering capacity as demonstrated in thermodynamic modeling studies, e.g., see [27,31,32], i.e., ions will precipitate when the concentrations in the pore solution are higher than saturation for the considered reactions and ions will diffuse from the cement hydrates into the pore solution if the concentrations are lower than the saturation of the reactions considered. The implication is that the freezing of a pore solution of cement based materials may not be able to be represented or related to the freezing of an artificial cement pore solution in a model material. There is no buffering effect, as described above between pore walls of a model material, e.g., the mostly used silica gels or porous glass, and the artificial pore solution. The artificial cement pore solution in a model material will become more and more concentrated as water freezes out, since the salts are not likely to be included into ice crystals [33,34], while the ionic concentration of pore solution of cement based materials might not change that much during freezing depending on the chemical interaction with the cement hydrates. Consequently, the ionic concentration of the artificial pore solution in a model material may differ significantly from the pore solution as more water freezes out in the case of cement based materials, even though the initial concentrations are about the same. Thus, studying the freezing behavior of an artificial cement pore solution in model materials may not necessarily give useful information in the process of understanding the impact of ions on the freezing behavior of the pore solution in cement based materials.

It is noted that in order to minimize the influence of the ions in the analysis of LTC studies, the preconditioning of cement based samples by curing them in a big amount of (lime)water for a relatively long time has been suggested, e.g., see [15,16]. In this approach it is assumed that the alkalies leach out of the sample and then allowing the pore liquid to be approximated to be dilute. Consequently the freezing of the diluted pore solution could be assumed as that of pure water [16]. However, a LTC experimental study compared the freezing and melting behaviors of the pore solution of cement paste samples preconditioned in a big amount of saturated limewater for a relatively long time and in a small amount of limewater [35]. The results showed limited difference. That is, it is questionable whether the preconditioning is effective enough. It should also be remarked that the leaching process may result in some changes of the porosity of the studied cement based materials, e.g., see [36,37].

The difficulty to directly determine the impact of ions in cement pore solution on the freezing and melting behaviors by experiments is realized. Thermodynamic modeling is a very useful tool and it has been applied to cement science very successfully, e.g., see [38,27,39,31,40,41]. In this work, a preliminary study is conducted to explore the ionic concentrations in the pore solution of cement pastes at different temperatures during freezing and melting measurements in LTC studies. By assuming chemical equilibrium and using experimental LTC data, thermodynamic modeling is used to predict the ionic concentrations in the pore solution of cement pastes. With the predicted ionic concentrations, the temperature depressions caused by the ions can then be determined. The main focus of this work is to demonstrate the influence of the freezing/melting point depression caused by the ions in the pore solution of hardened cement pastes and how this affects the determined pore size distribution.

2. LTC study and results

2.1. Materials and calorimetric measurements

Two types of cement, i.e., CEM I 32.5 R and CEM III/B 42.5 N, were used to prepare the cement paste samples used in this study. The chemical composition of the cements are shown in Table 1. The water-to-cement ratio was 0.4 for all the pastes prepared. The fresh paste samples were mixed by a paddle mixer. After mixing, the fresh pastes were cast into cylindrical plastic vials ensuing proper compaction. The dimension of the plastic vials was about ϕ15 mm × 50 mm. The hardened cement paste samples were demolded after one day of sealed curing at room temperature (about 20 °C) and then placed into slightly bigger plastic flasks (~ϕ25 mm × 60 mm) filled with saturated limewater for curing at room temperature. CEM I and CEM III are designated to describe the hardened cement pastes in the following description.

Both cylinder and powder samples of the cement pastes were studied. To obtain the powder samples, the cylinder samples as prepared were used. The cylinders of cement pastes were firstly vacuum saturated with saturated limewater and then the crushing and grinding of the samples was conducted in a carbon dioxide free chamber to avoid carbonation. After that, the ground paste powders (passed through a 315 μm sieve) were placed into the plastic vials (with dimension of ϕ15 mm × 50 mm as mentioned earlier, which are used as sample holders) till about half the volume and then saturated limewater was added to immerse the powders. This procedure was also conducted in the carbon dioxide free chamber. In

Table 1
Chemical composition of cements (mass%).

Cement	Ig. loss	SiO_2	Al_2O_3	Fe_2O_3	CaO	MgO	SO_3	Na_2O	K_2O
CEM I (32.5 R)	2.1	20.6	5.6	2.4	63.4	1.6	2.9	0.2	0.7
CEM III (/B 42.5 N)	1.4	29.2	8.9	1.2	48.0	4.8	2.6	0.2	0.6

order to saturate the powder samples, the sample holders containing powders covered with saturated limewater were placed under a reduced pressure (~40 mbar) for about 3 h. After that, the apparent excess bulk water on top of the powders was removed. Then the sample holders with saturated powders were kept standing still for two to three weeks before calorimetric measurements. The cylinder samples used for calorimetric measurements were vacuum saturated first and then the bulk water on the surface of cylinders was wiped off. The total curing time for the cylinder and powder samples was about 1 year and 1.5 years, respectively, before the calorimetric measurements were conducted.

A Calvet-type scanning calorimeter (SETARAM) was used to study the cement pastes. The calorimeter was calibrated and operated to work between about 20 °C and about −130 °C. The cooling and heating rates were set to be 0.1 °C per minute. In the adopted freezing and melting cycle, the temperature scanning started from about 20 °C and went down to about −80 °C and then back to about 20 °C again.

The mass of the tested vacuum saturated samples before calorimetric measurements were measured. After calorimetric measurements, the tested samples were oven-dried at about 105 °C till constant weights. The total water content in each sample was measured by the mass difference between the dry state and the state before the calorimetric measurement. More details about the materials and the measurements can be found in [42].

2.2. Calculated ice content

Based on the measured calorimetric heat flow curves, the ice content in the studied paste samples at different temperatures can be calculated. The results of the calculated ice content for the pastes CEM I and CEM III are presented in Figs. 1 and 2, respectively. It should be mentioned that the presented ice content does not include the "bulk" ice, which is determined by calculating the ice content corresponding to the peak above 0 °C from the heat flow curve of melting. For the cylinder samples, the "bulk" ice is mainly the ice in big pores (e.g., air voids) since saturated surface dry samples were used (since the bulk water on the surface of cylinders was wiped off), while for the powder samples, the "bulk" ice should contain both the ice in big air voids and the excess bulk water since there is still a portion of excess water in the powder samples as determined. Detailed discussion concerning the underlying assumptions behind the calculation can be found in [22]. The difference of the calculated ice content between the powder and cylinder samples has been discussed in [42].

As will be described in the next section, the water content in the sample under consideration is an input parameter for predicting the ionic concentration in the pore solution. The calculated ice content curves will be used to determine the remaining water content in the studied samples at different temperatures during LTC measurements. Details will be presented later.

3. Modeling the ionic concentration

The freezing of the pore water in cement based materials (due to the relatively wide pore size distribution) typically takes place at a wide range of temperatures. Normally, for ions presented in a certain amount of water, the concentration of the solution would increase as the pore water gradually freezes out [2,43]. However, the concentration of a cement pore solution may change differently due to the relatively big buffering capacity of cement hydrates as mentioned earlier. The concentrations of different ions in a cement pore solution depend on the equilibrium constants of the involved chemical reactions. The equilibrium constants are normally temperature dependent. It is, therefore, necessary to consider the temperature dependence of the equilibrium constants included in the model to predict the ionic concentration of a cement pore solution. In this work, the thermodynamic phase equilibrium program PHREEQC [44] is used.

In this section, the essential aspects of using the PHREEQC program to predict the ionic concentrations of the pore solution of cement based materials at different temperatures are discussed. It is noted that in the following the hydrated cement minerals are simply referred to as "hydrates" and a chemical reaction is referred to as "dissolution" or "precipitation" depending on the direction of the reaction.

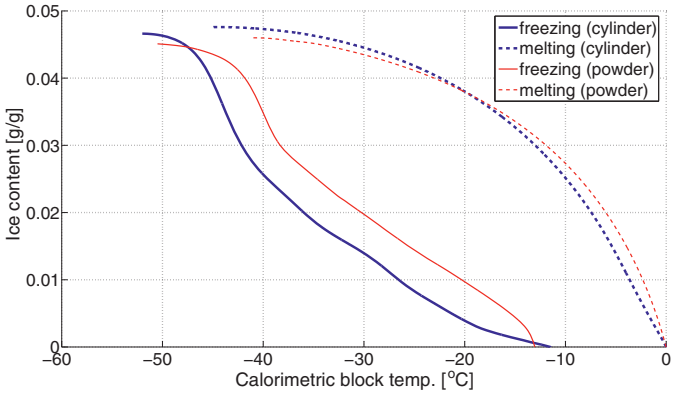

Fig. 1. Calculated ice content curves of cylinder and powder samples of the cement paste CEM I (with "bulk" ice subtracted). The content of "bulk" ice in each sample is determined by calculating the ice content corresponding to the peak above 0 °C from the heat flow curve of melting. The ice content is expressed as gram per gram of dry material (g/g). The "bulk" ice determined in the cylinder and the powder sample are about 0.007 and 0.65 g/g, respectively.

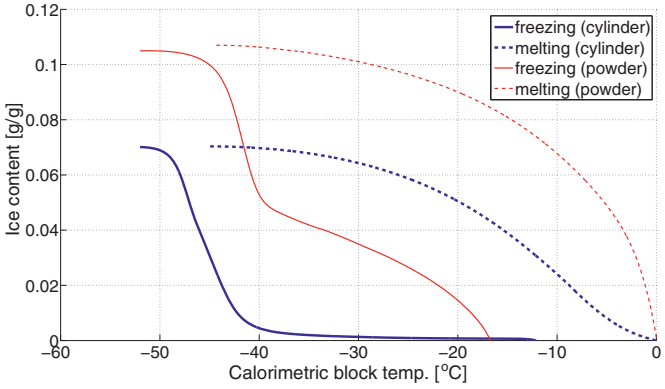

Fig. 2. Calculated ice content curves of cylinder and powder samples of the cement paste CEM III (with "bulk" ice subtracted). The content of "bulk" ice in each sample is determined by calculating the ice content corresponding to the peak above 0 °C from the heat flow curve of melting. The ice content is expressed as gram per gram of dry material (g/g). The "bulk" ice determined in the cylinder and the powder sample are about 0.003 and 0.91 g/g, respectively.

3.1. General description of the PHREEQC program

The PHREEQC program can be used to calculate a solution composition and the solid phase assemblages under equilibrium. This is carried out by solving simultaneously the mass conservation law of master species, law of charge balance and mass-action equations which describe the constitutive relations of aqueous species and hydrates [45].

Equilibrium between the aqueous species and the solid phase assemblages is described by mass-action equations. The mass-action equations can be expressed as

$$K_{a,p} = \prod_i (\gamma_i c_i)^{n_{i,p}} \tag{1}$$

where $K_{a,p}$ is the thermodynamic equilibrium constant of the hydrate p ($p = 1, 2, \ldots, g$; g is the total number of considered hydrates); γ_i and c_i are the activity coefficient and the concentration of ion i, respectively; $n_{i,p}$ is the stoichiometric coefficient of the ion i in hydrate p. The values for $n_{i,p}$ may be positive or negative. In PHREEQC, terms on the left-hand side of a dissolution reaction are assigned negative coefficients and terms on the right-hand side are assigned positive coefficients.

Activity coefficients of aqueous species are estimated by the Davies equation:

$$\log \gamma_i = -Az_i^2 \left(\frac{\sqrt{\mu}}{1+\sqrt{\mu}} - 0.3\mu \right) \tag{2}$$

or optionally the extended or WATEQ Debye–Hückel equation:

$$\log \gamma_i = -\frac{Az_i^2\sqrt{\mu}}{1+Ba_i^0\sqrt{\mu}} + b_i\mu \tag{3}$$

where z_i is the ionic charge of aqueous species i; A and B are constants that depend only on temperature; μ is the ionic strength of the solution. For Eq. (3), it is the extended Debye–Hückel equation if b_i is equal to zero; and it is the WATEQ Debye–Hückel equation if b_i is not equal to zero [46]. In the extended Debye–Hückel equation, a_i^0 is the ion size parameter, while in the WATEQ Debye–Hückel equation, a_i^0 and b_i are ion-specific parameters fitted from mean-salt activity-coefficient data [45]. Unless otherwise specified in the database file or the input data set, the Davies equation is used for charged species in this work.

The thermodynamic database for the aqueous species and the mineral phases used in this study is CEMDATA07 (version 07.02) [47], which is developed with a special focus on cement based systems, e.g., see [39,40,27].

It should be noted that more involved constitutive assumptions than that illustrated in Eq. (1) are assumed in describing the equilibrium conditions for some cement hydrates. Due to the mineralogical and chemical complexity of some cement hydrates, an adequate description of all the phases involved in cement hydration is not yet possible. Thus, different assumptions exist for certain types of hydrates, e.g., the C-S-H phase [48,49,41] and the AFm phase [27,38]. More discussions about different chemical models for the solid phases of cement hydrates can be found, e.g., in [50]. For the C-S-H phase, Hydrogarnet phase, Stratlingite phase, Ettringite (AFt) and calcium aluminate monosulfate (AFm) phase, a solid solution method is used in this study. The main precipitation/dissolution reactions considered for cement hydration in this study are listed in Appendix A.

The equilibria of a solid solution phase can be written as in terms of the end members constituting the solid solution, as [45]

$$K_{a,p_{ss}} = \frac{\prod_i (\gamma_i c_i)^{n_{i,p_{ss}}}}{\lambda_{p_{ss}} x_{p_{ss}}} \tag{4}$$

where $K_{a,p_{ss}}$ is the equilibrium (solubility) constant of component p in pure form; $n_{i,p_{ss}}$ is the stoichiometric coefficient of species i in the dissolution reaction for component p in solid solution ss; $x_{p_{ss}}$ is the mole fraction of component p in the solid solution ss; and $\lambda_{p_{ss}}$ is the activity coefficient. The mole fraction of a component in a solid solution is defined as [45]

$$x_{p_{ss}} = \frac{n_{p_{ss}}}{\sum_{p_{ss}}^{N_{ss}} n_{p_{ss}}} \tag{5}$$

where N_{ss} is the number of end members in the solid solution ss. For an ideal solid solution, the activity coefficient $\lambda_{p_{ss}}$ is 1.0.

In short, two types of inputs are essential to calculate the composition of the pore solution of a hardened cement sample using the PHREEQC program, i.e., the initial chemical composition and the solubility constants of involved chemical reactions. The determination of the initial chemical composition of a hardened cement sample and the consideration of the temperature dependent property of solubility constants are presented as follows.

3.2. Chemical composition of a hardened cement sample

The chemical composition of a hardened cement sample involving degree of hydration as an input for the equilibrium calculation using the PHREEQC program can be determined from the characteristic values of cement minerals, i.e., the chemical composition, the hydration degree and the mass concentration.

If there are M kinds of oxides and N kinds of minerals in a cement, the initial chemical composition of a hardened cement to be used in the equilibrium calculation, denoted as a vector $\mathbf{c}$, can be calculated as

$$\begin{pmatrix} c_1 \\ \vdots \\ c_M \end{pmatrix} = \begin{pmatrix} R_{11} & \cdots & R_{1N} \\ \vdots & \ddots & \vdots \\ R_{M1} & \cdots & R_{MN} \end{pmatrix} \begin{pmatrix} \alpha_1 x_1 \\ \vdots \\ \alpha_N x_N \end{pmatrix} = \begin{pmatrix} R_{11} & \cdots & R_{1N} \\ \vdots & \ddots & \vdots \\ R_{M1} & \cdots & R_{MN} \end{pmatrix} \begin{pmatrix} \alpha_1 & & 0 \\ & \ddots & \\ 0 & & \alpha_N \end{pmatrix} \begin{pmatrix} x_1 \\ \vdots \\ x_N \end{pmatrix} \tag{6}$$

where c_m ($m = 1, \ldots, M$) is the content of the mth oxide in a hydrated cement, x_n ($n = 1, \ldots, N$) is the content of the nth mineral in the cement, α_n is the hydration degree of the nth mineral and R_{mn} is the content of the mth oxide in the nth mineral. The matrix $\mathbf{R}$ (with the elements of R_{mn}) can be determined theoretically from the composition formula of pure minerals (refer to the classical Bogue calculation, e.g., see [51]). When matrix $\mathbf{R}$ is invertible, i.e., $M = N$, the mineral content vector $\mathbf{x}$ consisting of the elements x_n can be calculated by $\mathbf{x} = \mathbf{R}^{-1}\mathbf{p}$, in which $\mathbf{p}$ is the vector containing the mass concentration of the different oxides in the cement. Thus, the input of the initial chemical composition to be used in the equilibrium calculation can be written as

$$\mathbf{c} = \mathbf{R}\,\mathrm{diag}(\alpha_1, \ldots, \alpha_N)\mathbf{R}^{-1}\mathbf{p} \tag{7}$$

where the diagonal matrix $\mathrm{diag}(\alpha_1, \ldots, \alpha_N)$ includes the hydration degrees of the different minerals, i.e., $\alpha_1, \ldots, \alpha_N$.

3.3. Temperature dependent solubility constant K_a

In PHREEQC, there are two ways to describe the temperature dependent property of the solubility constant K_a for a chemical reaction. If the standard enthalpy of a reaction $\Delta_r H^{\ominus}_{298}$ (at 25 °C)

is an input, the temperature dependence of K_a will be considered according to the van't Hoff equation, which is

$$\ln(K_{aT}) \approx \ln(K_{a298}) - \frac{\Delta_r H^{\ominus}_{298}}{R}\left(\frac{1}{T} - \frac{1}{298}\right) \quad (8)$$

where K_{aT} is the approximated solubility constant at temperature T (in Kelvin degree) from the solubility constant K_a at temperature 298 K (25 °C); R is the gas constant. With the van't Hoff equation and the known solubility constant at one temperature, it is possible to extrapolate the solubility constants at other temperatures. It should be noted that Eq. (8) is based on the assumption that the enthalpy of a reaction $\Delta H^{\ominus}_T$ is a constant (i.e., without temperature dependence), which is not necessarily true. Thus, the accuracy of the predicted solubility constants is very much restricted by this assumption. Nevertheless, without further knowledge about the thermodynamic properties at a desired temperature, Eq. (8) can provide a rough approximation. The detailed derivation of the temperature dependence of solubility constant K_a and related discussions are presented in Appendix B.

The temperature dependence of K_a can also be defined by an explicit empirical expression in PHREEQC, which is in the form of

$$\log_{10}(K_a) = A_1 + A_2 T + \frac{A_3}{T} + A_4 \log_{10}(T) + \frac{A_5}{T^2} \quad (9)$$

where A_1–A_5 are five different fitting parameters (constants). If the standard enthalpy and the five constants of the empirical expression are both given as inputs, the empirical expression will be used in preference in the PHREEQC calculation.

The temperature dependence of the solubility constants in terms of the five constants A_1–A_5 presented in the database CEMDATA07 (version 07.02) [47] is used in this study. No verifications of the validity of the data at freezing temperatures have been made. With no further knowledge about the thermodynamic data, the temperature dependent property of the solubility constants included in the database CEMDATA07 (version 07.02) is used in this work to study the freezing behavior of cement pore solution.

3.4. Input parameters for calculation

To calculate the change of the ionic concentration of a cement pore solution during LTC measurements, the following input parameters are needed:

- Chemical composition of the cement
- Cement content and water content in the sample
- Hydration degree of cement minerals
- Temperature

With the above input parameters, the ionic concentrations of a cement pore solution at different temperatures (with no ice present) can be calculated with the experimentally determined total water content. In order to calculate the ionic concentrations of the pore solution at different temperatures during LTC measurements in the presence of ice, the water content in the studied sample is adjusted by subtracting the corresponding calculated ice content (see Figs. 1 and 2) from the total water content.

Parrot and Killoh [52] proposed a set of empirical expressions to predict the hydration degree of cement minerals in OPC, which are

$$R_t = \frac{K_1}{N_1}(1-\alpha_t)(-\ln(1-\alpha_t))^{(1-N_1)} \quad (10)$$

$$R_t = \frac{K_2(1-\alpha_t)^{2/3}}{1-(1-\alpha_t)^{1/3}} \quad (11)$$

$$R_t = K_3(1-\alpha_t)^{N_3} \quad (12)$$

Table 2
Parameters used to calculate the hydration degree of cement (clinker) minerals as a function of time, data from Parrot and Killoh [52].

Parameters	Cement minerals			
	C_3S	C_2S	C_3A	C_4AF
K_1	1.5	0.5	1.0	0.37
N_1	0.7	1.0	0.85	0.7
K_2	0.05	0.006	0.04	0.015
K_3	1.1	0.2	1.0	0.4
N_3	3.3	5.0	3.2	3.7

where R_t and α_t are the rate and degree of hydration at time t, respectively; K_1, N_1, K_2, K_3, and N_3 are constant parameters and the values for cement minerals are listed in Table 2. Eq. (10) is for nucleation and growth; Eq. (11) or (12) is for diffusion controlled hydration. The lowest value of R_t is considered as the rate controlling step. The degree of hydration α_t at time t (in days) is then expressed as $\alpha_t = \alpha_{t-1} + \Delta t \cdot R_{t-1}$. Lothenbach and Winnefeld [27] found reasonable agreement between the predicted hydration degrees using the empirical expressions (Eqs. (10)–(12)) together with the parameter values presented in Table 2 and the results based on the XRD semi-quantitative analysis. For the cylinder and powder samples of the cement pastes under consideration, the hydration degree of the minerals are mainly estimated according to the empirical expressions and parameter values proposed by Parrot and Killoh [52] (i.e., Eq. (10)–(12) and Table 2). The calculated values are listed in Table 3. It is assumed that the hydration degree of cement minerals in both CEM I and CEM III are the same in this study.

4. Modeling results

In LTC studies, the ice content curves of melting processes are normally used to calculate the pore interior size distribution, as freezing processes would only indicate the pore entry or neck sizes [21,16]. Since the main purpose of this study is to demonstrate the influence of ions on the calculated pore (interior) size distribution, the results presented here, therefore, only focus on the melting processes.

The modeled ionic strength for the cement pastes CEM I and CEM III at different temperatures during the melting process are presented in Fig. 3. It can be found that for each cement paste (both the cylinder and powder samples), the modeled ionic strength does not change very much during the temperature range between 0 °C and −40 °C. The modeled ionic strength for the pastes CEM I and CEM III are around 0.5 mol/kg water and 0.7 mol/kg water, respectively.

The modeled ionic strength results at different temperatures will be used to calculate the temperature depression caused by the ions. Then the influence of the ions in the pore solution of the studied cement paste samples on the determination of the pore size distribution will be demonstrated by comparing the calculated pore size distribution with and without considering the temperature depression caused by the presence of ions in the pore solution.

Table 3
Assumed hydration degree of cement minerals in the samples of cement paste CEM I and CEM III. The age of the cylinder and power samples is 1 year and 1.5 years, respectively.

Sample	C_3S	C_2S	C_3A	C_4AF	$CaSO_4$[a]
Cylinder	0.95	0.76	1.00	0.89	1.00
Powder	0.96	0.78	1.00	0.91	1.00

[a] The hydration degree is not calculated from the equations proposed by Parrot and Killoh [52] but following the suggestion given in [41].

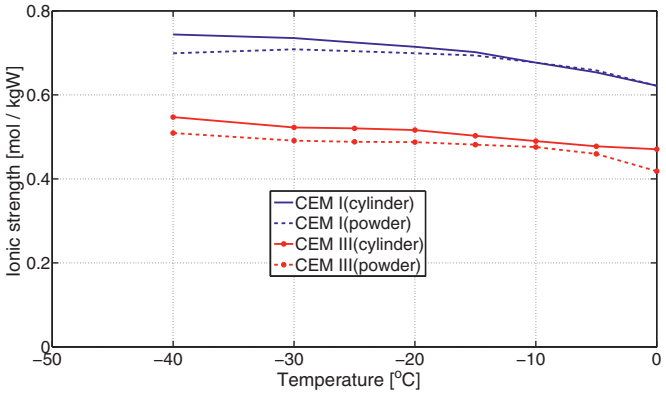

Fig. 3. Modeled ionic strength for the cement pastes CEM I and CEM III at different temperatures during the melting process. The ionic strength is expressed as mole per kilogram of water.

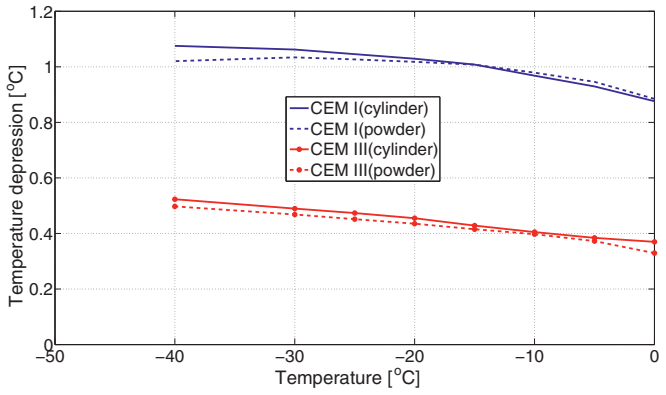

Fig. 4. Calculated temperature depression using the predicted ionic concentrations (Fig. 3) for the cement pastes CEM I and CEM III at different temperatures during the melting process.

5. Influence of the ions on the calculated pore size distribution

5.1. Calculated freezing/melting point depression by the ions

The freezing/melting point depression caused by ions in the pore solution of the cement paste samples can be estimated by using the following equation [28,29]

$$\Delta T \approx -\left(\frac{RT_0^2}{\Delta H_A^{fus}}\right) X_B \gamma \tag{13}$$

where ΔT is the temperature depression, i.e., the difference between the freezing/melting point of the ionic solution and that of pure water T_0; ΔH_A^{fus} is the heat of fusion of water; X_B is the mole fraction of the solute and γ is the activity coefficient of the solution. For a solution with several types of ions (e.g., cement pore solutions in our case), the activity coefficient γ can be calculated as

$$\gamma = \frac{\sum_{i=1}^{N} n_i \gamma_i}{\sum_{i=1}^{N} n_i} \tag{14}$$

where n_i the mole concentration of the ith ion in the solution; N is the total number of the ions considered. The detailed derivation of Eq. (13) is presented in Appendix C. More discussions about the activity coefficient γ_i and γ can be found, e.g., in [28,29,53].

The mole concentration n_i and the activity coefficient of each ionic species γ_i are outputs from a PHREEQC calculation. With the obtained n_i and γ_i, the activity coefficient of a cement pore solution γ can be calculated using Eq. (14). The ionic strength μ of a solution in PHREEQC is calculated using [45]

$$\mu = \frac{1}{2}\sum_{i=1}^{N} z_i^2 \frac{n_i}{W_{aq}} \tag{15}$$

where W_{aq} is the mass of the solvent water in the solution. It is noted that the modeled ionic species in a cement pore solution are rather complicated with several different charges. However, to obtain the X_B for a cement pore solution from the modeled ionic strength μ in this study, it is assumed that the ionic charges for the species are ± 1. As can be found from Eq. (15), the assumption would result into higher X_B than the true value if the species with charges (absolute value) higher than 1 are important in a solution. That is, the estimated X_B in this study somehow corresponds to the upper limit of the more general case.

With the modeled ionic strength results (presented in Section 4), the temperature depressions caused by the ions in the studied cement paste samples are calculated and shown in Fig. 4. The calculated temperature depression for each studied cement paste sample has a relatively small variation during the considered temperature range (between 0 °C and −40 °C). The variation is about 0.9–1.1 °C for the paste CEM I and about 0.4–0.5 °C for the paste CEM III. The temperature depression caused by the ions will be considered in calculating the pore size distribution.

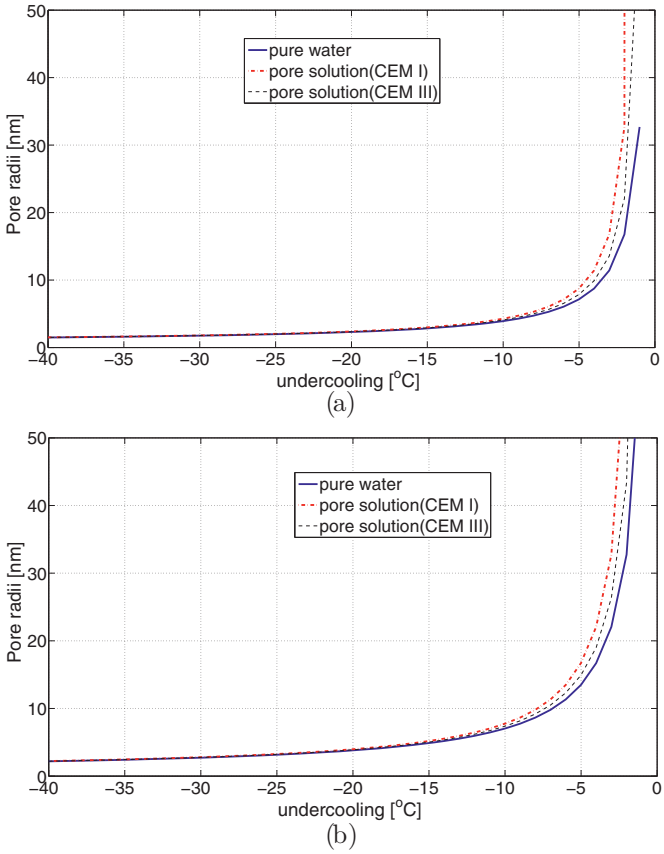

Fig. 5. Comparison of the relation between the pore radii and the undercooling (in melting) with and without considering the temperature depression caused by the ions in the pore solution of the cement pastes CEM I and CEM III (cylinder samples). The pore shape is assumed to be (a) cylindrical and (b) spherical.

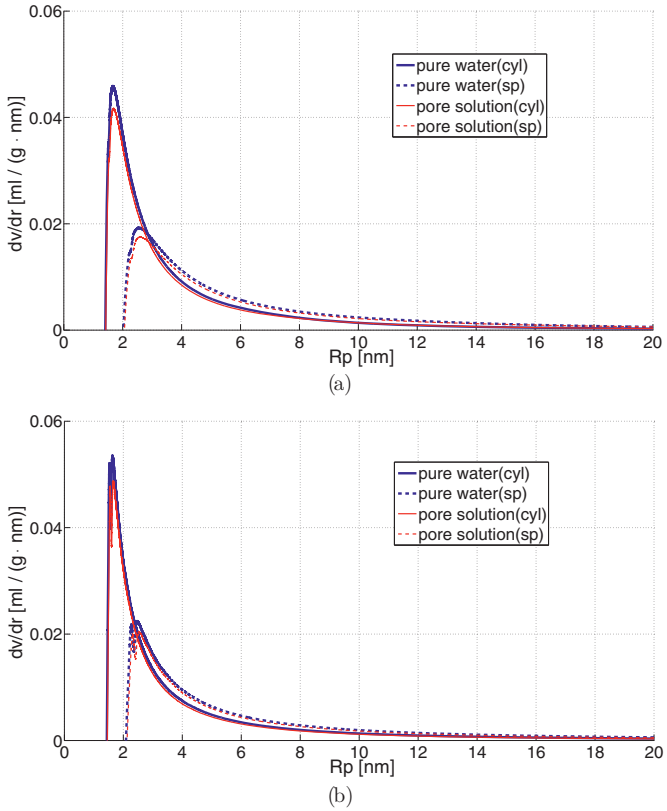

Fig. 6. Calculated differential pore size distribution for the CEM I sample considering the pore liquid as pure water or as an ionic pore solution based on cylindrical (cyl) and spherical (sp) pore assumptions: (a) for the cylinder sample and (b) for the powder sample.

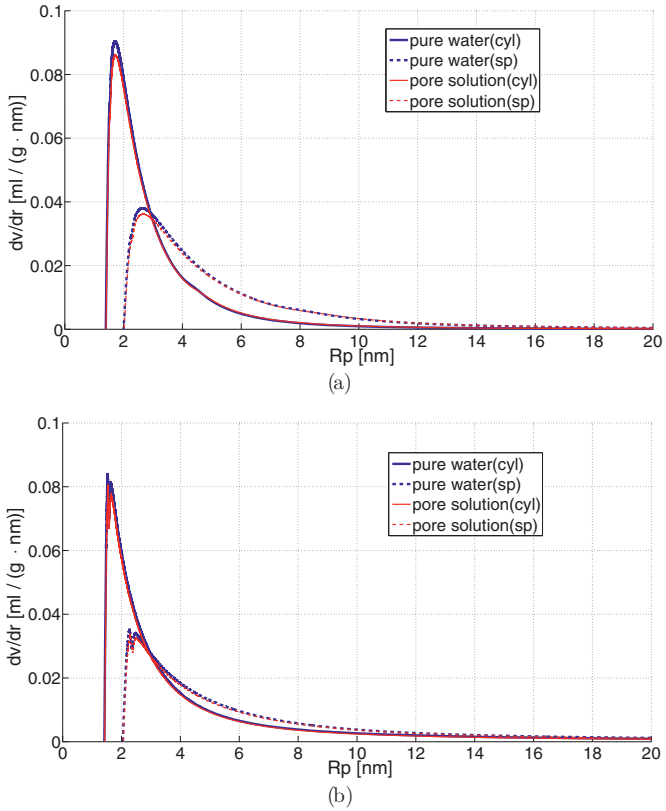

Fig. 7. Calculated differential pore size distribution for the CEM III sample considering the pore liquid as pure water or as an ionic pore solution based on cylindrical (cyl) and spherical (sp) pore assumptions: (a) for the cylinder sample and (b) for the powder sample.

5.2. *Influence of the ions on the calculated pore size distribution*

For pure water/ice, the relation between the freezing/melting point depression (or undercooling) caused by the pore confinement and the pore size is assumed to follow the equations proposed by Brun et al. [1], which are

$$R_p = -\frac{32.33}{T - T_0} + 0.68 \tag{16}$$

$$R_p = -\frac{64.67}{T - T_0} + 0.57 \tag{17}$$

where R_p(nm) is the pore size; t is the depressed freezing/melting point of pore water/ice. For melting processes, Eq. (16) is used for the cylindrical pore shape assumption and Eq. (17) is used for the spherical pore shape assumption. Before further discussion, a clarification is made here about the temperature depression (or undercooling) which is defined as $T - T_0$ in this work.

The relation between the pore radii and the undercooling (in melting) with and without considering the temperature depression caused by the ions in the pore solution of the cylinder samples of the cement pastes CEM I and CEM III are compared in Fig. 5. By considering the pore solution as pure water, Eq. (16) or (17) is used to calculate the pore radii (according to the assumed pore shape). By considering the pore solution as an ionic solution, the contribution of the temperature depression caused by the ions (Fig. 4) to a measured undercooling is excluded when calculating the pore radii using Eq. (16) or (17). It can be found that for undercoolings, e.g., higher than about −10 °C, there is some noticeable difference between the calculated pore radii with and without considering the effect caused by the presence of the ions, while for undercoolings lower than about −10 °C, very limited difference is found between the calculated pore radii. This conclusion also holds for the powder samples, since the temperature depression caused by the ions in the powder and the cylinder samples for each cement paste are almost the same.

The calculated differential pore size distribution considering the pore liquid as pure water or as an ionic solution for the cement pastes CEM I and CEM III is compared in Figs. 6 and 7, respectively. There is only some slight difference between the calculated differential pore size distributions for each cement paste sample with and without considering the temperature depression caused by the ions in the pore solution. That is, using the modeled ionic concentrations for the pore solution of the studied cement paste samples, the resulting influence of the temperature depression caused by the ions in the pore solution on the pore size distribution determination by LTC is limited.

6. Conclusions

Thermodynamic modeling was used to predict the ionic concentrations in the pore solution of cement pastes at different temperatures during a freezing and melting measurement in LTC studies. That is, it was assumed that the standard thermodynamic relations and concepts can be used also for undercooled water present in the pores of the paste samples. The modeled ionic concentrations were used to determine the temperature depressions caused by the ions presented in the pore solution. The influence of the freezing/melting point depression caused by the ions in the pore solution of hardened cement pastes on the determined pore size distribution by LTC was investigated.

Thermodynamic modeling using the program PHREEQC was performed on the cylinder and powder samples of the cement

pastes prepared by two different types of cements. The results showed that the ionic strength for each studied paste sample does not change very much at the temperature range between 0 °C and −40 °C during the LTC measurements. Using the modeled ionic concentrations, the calculated differential pore size distributions for the studied samples with and without considering the temperature depression caused by the ions presented in the pore solution were compared. The results indicate that for the studied cement paste samples in this investigation, the temperature depression caused by the ions present in the pore solution affects the determination of the pore size distribution by LTC to a limited extent.

Acknowledgment

The research leading to these results has received funding from the European Union Seventh Framework Programme (FP7/2007–2013) under grant agreement 264448.

Appendix A. Dissolution/precipitation reactions for cement hydrates

The dissolution/precipitation reactions considered for the cement hydrates in this study are listed in Table 4. The table is mainly based on the chemical models proposed by Kulik [49] and Lothenbach and Winnefeld [27] and it is compiled from a summary prepared by Jensen et al. [50].

Appendix B. Temperature dependence of solubility constant K_a

The chemical equilibrium of a reaction is defined by the Gibbs free energy. Each component participated in a chemical reaction has its own Gibbs free energy relative to a fixed reference, which can be expressed as

$$G_i = G_i^{\ominus} + RT\ln(a_i) \tag{18}$$

where a_i is the activity ($a_i = \gamma_i c_i$), G_i is the molar Gibbs free energy for component i and $G_i^{\ominus}$ is the standard reference value. Due to the minimization of the total Gibbs free energy of a reaction at equilibrium, the change of the standard reference values of the Gibbs free energy of a chemical reaction, $\Delta_r G_T^{\ominus}$, can be expressed as [54]

$$\Delta_r G_T^{\ominus} = -RT\ln(K_a) \tag{19}$$

According to the relation between Gibbs free energy, enthalpy and entropy, i.e., $G = H - TS$, the same relation also holds for the properties with the standard reference values, which can be written as

$$\Delta_r G_T^{\ominus} = \Delta_r H_T^{\ominus} - T\,\Delta_r S_T^{\ominus} \tag{20}$$

This relation can be regarded as the relation between the Gibbs free energy, enthalpy and entropy for a specific chemical reaction. The entropy property is not always that straightforwardly measurable. However, through mathematical derivations, it is possible to replace the entropy with some other property which can be measured more easily. Under constant pressure, the definition of entropy is $S = -(dG/dT)_P$. In a similar reasoning as used to obtain Eq. (20), one can obtain

$$\Delta_r S_T^{\ominus} = -\frac{d(\Delta_r G_T^{\ominus})}{dT} \tag{21}$$

By inserting Eq. (21) into Eq. (20), one obtains

$$\frac{d(\Delta_r G_T^{\ominus})}{dT} = \frac{\Delta_r G_T^{\ominus} - \Delta_r H_T^{\ominus}}{T} \tag{22}$$

Table 4
Dissolution/precipitation reactions for cement hydrates.

	Reactions[a]
Pure phases	
Portlandite	$Ca(OH)_2 + 2H^+ \leftrightarrow Ca^{2+} + 2H_2O$
Brucite	$Mg(OH)_2 + 2H^+ \leftrightarrow Mg^{2+} + 2H_2O$
Syngenite	$K_2Ca(SO_4)_2H_2O \leftrightarrow Ca^{2+} + 2K^+ + 2SO_4^{2-} + H_2O$
Gypsum	$CaSO_4 \cdot 2H_2O \leftrightarrow Ca^{2+} + SO_4^{2-} + 2H_2O$
Anhydrite	$CaSO_4 \leftrightarrow Ca^{2+} + SO_4^{2-}$
Silica (am)	$SiO_2 + 2H_2O \leftrightarrow H_4SiO_4$
$Al(OH)_3$(am)	$Al(OH)_3 + OH^- \leftrightarrow Al(OH)_4^-$
CAH_{10}	$CaAl_2(OH)_8 \cdot 6H_2O \leftrightarrow Ca^{2+} + 2Al(OH)_4^- + 6H_2O$
Solid solutions	
	C-S-H
TobH	$(CaO)_{0.66}(SiO_2)(H_2O)_{1.5} + 1.32H^+ \leftrightarrow 0.66Ca^{2+} + H_4SiO_4 + 0.16H_2O$
TobD	$(CaO)_{0.83}(SiO_2)_{0.66}(H_2O)_{1.83} + 1.66H^+ \leftrightarrow 0.83Ca^{2+} + 0.66H_4SiO_4 + 1.34H_2O$
JenH	$(CaO)_{1.33}(SiO_2)(H_2O)_{2.16} + 2.66H^+ \leftrightarrow 1.33Ca^{2+} + H_4SiO_4 + 1.49H_2O$
JenD	$(CaO)_{1.5}(SiO_2)_{0.66}(H_2O)_{2.5} + 3.00H^+ \leftrightarrow 0.66Ca^{2+} + H_4SiO_4 + 0.16H_2O$
	AFm(1)
C_2AH_8	$Ca_2Al_2(OH)_{10} \cdot 3H_2O \leftrightarrow 2Ca^{2+} + 2Al(OH)_4^- + 2OH^- + 3H_2O$
C_2FH_8	$Ca_2Fe_2(OH)_{10} \cdot 3H_2O \leftrightarrow 2Ca^{2+} + 2Fe(OH)_4^- + 2OH^- + 3H_2O$
	AFm(2)
C_4AH_{13}	$Ca_4Al_2(OH)_{14} \cdot 6H_2O \leftrightarrow 4Ca^{2+} + 2Al(OH)_4^- + 6OH^- + 6H_2O$
C_4FH_{13}	$Ca_4Fe2(OH)_{14} \cdot 6H_2O \leftrightarrow 4Ca^{2+} + 2Fe(OH)_4^- + 6OH^- + 6H_2O$
	AFm(3)
C_2ASH_8	$(CaO)_2Al_2O_3SiO_2 \cdot 8H_2O \leftrightarrow 2Ca^{2+} + 2Al(OH)_4^- + H_3SiO_4^- + OH^- + 2H_2O$
C_2FSH_8	$(CaO)_2Fe_2O_3SiO_2 \cdot 8H_2O \leftrightarrow 2Ca^{2+} + 2Fe(OH)_4^- + H_3SiO_4^- + OH^- + 2H_2O$
	AFm(4)
$C_4A\bar{S}H_{12}$	$(CaO)_3Al_2O_3(CaSO_4) \cdot 12H_2O \leftrightarrow 4Ca^{2+} + 2Al(OH)_4^- + SO_4^{2-} + 4OH^- + 6H_2O$
$C_4F\bar{S}H_{12}$	$(CaO)_3Fe_2O_3(CaSO_4) \cdot 12H_2O \leftrightarrow 4Ca^{2+} + 2Fe(OH)_4^- + SO_4^{2-} + 4OH^- + 6H_2O$
	Hydrogarnet
C_3AH_6	$(CaO)_3Al_2O_3 \cdot 6H_2O \leftrightarrow 3Ca^{2+} + 2Al(OH)_4^- + 4OH^-$
C_3FH_6	$(CaO)_3Fe_2O_3 \cdot 6H_2O \leftrightarrow 3Ca^{2+} + 2Fe(OH)_4^- + 4OH^-$
	AFt
Al-Ettringite	$Ca_6Al_2(SO_4)_3(OH)_{12} \cdot 26H_2O \leftrightarrow 6Ca^{2+} + 2Al(OH)_4^- + 3SO_4^{2-} + 4OH^- + 26H_2O$
Fe-Ettringite	$Ca_6Fe_2(SO_4)_3(OH)_{12} \cdot 26H_2O \leftrightarrow 6Ca^{2+} + 2Fe(OH)_4^- + 3SO_4^{2-} + 4OH^- + 26H_2O$
	Strätlingite
Al-Strätlingite	$Ca_2Al_2SiO_2(OH)_{10} \cdot 3H_2O \leftrightarrow 2Ca^{2+} + 2Al(OH)_4^- + SiO(OH)_3^- + OH^- + 2H_2O$
Fe-Strätlingite	$Ca_2Fe_2SiO_2(OH)_{10} \cdot 3H_2O \leftrightarrow 2Ca^{2+} + 2Fe(OH)_4^- + SiO(OH)_3^- + OH^- + 2H_2O$

[a] Reactions involving carbon dioxide is not included in the calculation considering the samples were always cured under saturated limewater.

By using a mathematical manipulation, the Gibbs–Helmholtz equation can be obtained, that is

$$\begin{aligned}\frac{d}{dT}\left(\frac{\Delta_r G_T^{\ominus}}{T}\right)_P &= \Delta_r G_T^{\ominus}\left(\frac{d}{dT}\left(\frac{1}{T}\right)\right)_P + \frac{1}{T}\left(\frac{d(\Delta_r G_T^{\ominus})}{dT}\right)_P \\ &= -\frac{\Delta_r G_T^{\ominus}}{T^2} + \frac{1}{T}\left(\frac{d(\Delta_r G_T^{\ominus})}{dT}\right)_P \\ &= \frac{1}{T}\left(\left(\frac{d(\Delta_r G_T^{\ominus})}{dT}\right)_P - \frac{\Delta_r G_T^{\ominus}}{T}\right)\end{aligned} \tag{23}$$

Combining Eqs. (23) and (22), the Gibbs–Helmholtz equation is obtained, as

$$\frac{d}{dT}\left(\frac{\Delta_r G_T^{\ominus}}{T}\right)_P = -\frac{\Delta_r H_T^{\ominus}}{T^2} \tag{24}$$

Then, assuming $\Delta_r G_T^{\ominus}$ and K_a to be temperature dependent functions and applying differentiation on both sides of Eq. (19) followed by rearrangement gives

$$\frac{d\ln(K_a)}{dT} = -\frac{1}{R}\frac{d}{dT}\left(\frac{\Delta_r G_T^{\ominus}}{T}\right) \tag{25}$$

Combining Eq. (24) and (25), the result is

$$\frac{d\ln(K_a)}{dT} = -\frac{\Delta_r H_T^{\ominus}}{RT^2} \tag{26}$$

For a system under constant pressure, the change of enthalpy ΔH against temperature t is related by the change of heat capacity $\Delta C_p^{\ominus}$, which is $(d(\Delta H)/dT)_P = \Delta C_p$. Thus, for a chemical reaction, the change of enthalpy (the standard reference value) $\Delta_r H_T^{\ominus}$ at temperature T can be expressed as

$$\Delta_r H_T^{\ominus} = \Delta_r H_{T_0}^{\ominus} + \int T_0{}^T \Delta_r C_p \, dT \tag{27}$$

where $\Delta_r H_{T_0}^{\ominus}$ is the change of enthalpy of the chemical reaction at the temperature T_0, which is normally a constant reference with a known value.

By assuming different temperature dependencies of the heat capacity, C_p, the dependence of the solubility constant K_a on the temperature can be obtained as follows.

1. Assuming $C_p = a_1 + a_2T + a_3T^{-2} + a_4\sqrt{T} + a_5T^2$ (a_1, a_2, …, a_5 are fitting parameters) and inserting it into Eq. (27), an analytical expression of $\Delta_r H_T^{\ominus}$ is obtained. Inserting the obtained analytical expression of $\Delta_r H_T^{\ominus}$ into Eq. (26) followed by integration, K_a is obtained and it can be expressed as [55,56]

$$\log_{10}(K_a) = A_1' + A_2'T + \frac{A_3'}{T} + A_4'\ln(T) + \frac{A_5'}{T^2} + A_6'T^2 + A_7'\sqrt{T} \tag{28}$$

where $A_1', A_2', \ldots, A_7'$ are constants. If the entropy ($S^{\ominus}$), the enthalpy ($H^{\ominus}$) and the coefficients of the heat capacity equation (a_1, a_2, …, a_5) for the components in reaction are known, the constants $A_1', A_2', \ldots, A_7'$ can be directly calculated [57,58]. Otherwise, the constants can be obtained by fitting available experimental data to Eq. (28). It should be mentioned that the analytical expression for the temperature dependence of K_a adopted in PHREEQC (Eq. (9)) is based on five terms, which is slightly different from the expression including seven terms as derived above. The difference is due to that the heat capacity C_p is assumed to be represented with three fitting parameters as, $C_p = a_1' + a_2'T + a_3'T^{-2}$, in the approach adopted in PHREEQC.
2. Assuming the heat capacity of the chemical reaction $\Delta_r C_p$ is a constant in the considered temperature range, the temperature dependence of K_a can be reduced to an approximation including three fitting parameters as [38]

$$\log_{10}(K_a) = A_1' + \frac{A_3'}{T} + A_4'\ln(T) \tag{29}$$

3. Assuming the heat capacity of the chemical reaction $\Delta_r C_p = 0$, i.e., the enthalpy $\Delta_r H_T^{\ominus}$ in the considered temperature range is a constant, the temperature dependence of K_a can be expressed as

$$\log_{10}(K_a) = A_1' + \frac{A_3'}{T} \tag{30}$$

It is noted that Eq. (30) is of the same format as the van't Hoff equation described before, i.e., Eq. (8).

More discussions about the extrapolation of the temperature dependent solubility constant K_a can be found, e.g., in [55,56]. Using the extrapolated temperature dependence of solubility constants to study cement based materials can be found, e.g., in [38,27,39,31,58–60].

Appendix C. Freezing/melting point depression by ions

The thermodynamic basics describing the freezing point depression caused by ions are discussed in this section. The thermodynamic background for this kind of problem can be found in general physical chemistry books, e.g., in [28,29].

Under equilibrium condition, the relation between infinitesimal change of the temperature, the pressure and the chemical potential of the solvent (pure water in our case) in a pore solution can be expressed by Gibbs–Duhem equations [61], which is

$$S_A^l\,dT - V_A^l\,dP_A^l + n_A^l\,d\mu_A^l = 0 \tag{31}$$

where S is the entropy, t is the temperature in Kelvin degree, V, p, μ and n are the volume, pressure, chemical potential and moles of the solvent A in liquid phase l, respectively. Assuming constant temperature, i.e., dT=0, Eq. (31) reduces to

$$n_A^l\,d\mu_A^l = V_A^l\,dP_A^l \tag{32}$$

By further assuming that the ideal gas law applies, which means

$$V_A^l = \frac{n_A^l RT}{P_A^l} \tag{33}$$

where R is the gas constant. Inserting Eq. (33) into Eq. (32) and differentiating yields

$$\int_{\mu=\mu_A^{l0}}^{\mu=\mu_A^l} d\mu_A^l = \int_{P=P_A^{l0}}^{P=P_A^l} \frac{RT}{P_A^l}\,dP_A^l; \quad \mu_A^l = \mu_A^{l0} + RT\ln\left(\frac{P_A^l}{P_A^{l0}}\right) \tag{34}$$

where μ_A^{l0} is the reference chemical potential of the pure water and P_A^{l0} is its corresponding reference pressure.

The effect of the composition of a solution on its chemical potential can be assessed by introducing Rault's law which states that the partial pressure of a component is proportional to its mole fraction in the solution, i.e.,

$$X_A = \frac{P_A^l}{P_A^{l0}} \tag{35}$$

where X_A is the mole fraction of the solvent A in the solution. Taking Rault's law into consideration, the difference between the chemical potential of pure water and the water containing ions can according to Eq. (34) be expressed as

$$\mu_A^l = \mu_A^{l0} + RT\ln(X_A) \tag{36}$$

At the temperature when the water freezes, the three phases of the water, i.e., liquid (l), solid (s) and gas (g), are under equilibrium, indicating their chemical potentials are equal. That is, $\mu_A^l = \mu_A^s$, where μ_A^s is the chemical potential of solid ice. It should be noted that the ice crystals formed in a pore solution are no different from that formed from pure water, since the ions will be expelled out and will not be included into the crystalline structure of ice during freezing, e.g., see [33]. By introducing $X_B = 1 - X_A$, where X_B is the mole fraction of the dissolved solutes in the solution, and replacing μ_A^l with μ_A^s in Eq. (36), one obtains

$$\ln(1 - X_B) = \frac{\mu_A^s - \mu_A^{l0}}{RT} \tag{37}$$

According to classical thermodynamics, the difference between the chemical potentials μ_A^s and $\mu_A^{l^0}$ can be regarded as the molar Gibbs free energy, that is

$$\mu_A^s - \mu_A^{l^0} = \Delta G_A^{l-s} = \Delta G_A^{fus} \tag{38}$$

Similarly, the difference between the entropies (S) and the enthalpies (H) of the liquid and the solid phase is denoted as

$$S_A^s - S_A^{l^0} = \Delta S_A^{fus}; \qquad H_A^s - H_A^{l^0} = \Delta H_A^{fus} \tag{39}$$

Since $G = H - TS$, Eqs. (38) and (39) can be combined to obtain

$$\Delta G_A^{fus} = \Delta H_A^{fus} - T\Delta S_A^{fus} \tag{40}$$

Further inserting Eq. (40) into Eq. (37), it gives

$$\ln(1 - X_B) = \frac{\Delta H_A^{fus}}{RT} - \frac{\Delta S_A^{fus}}{R} \tag{41}$$

Considering $X_B = 0$, i.e., the case of pure water, Eq. (41) becomes

$$\frac{\Delta H_A^{fus}}{RT_0} - \frac{\Delta S_A^{fus}}{R} = 0 \tag{42}$$

where T_0 is the freezing point of pure water. Inserting Eq. (42) into Eq. (41), the relation between the freezing point of the water containing ions with a mole fraction of X_B (T) and that of the pure water (T_0) can be established as

$$\ln(1 - X_B) = \frac{\Delta H_A^{fus}}{R}\left(\frac{1}{T} - \frac{1}{T_0}\right) \tag{43}$$

Further simplification of Eq. (43) can be made by assuming that the solution is weak, i.e., $X_B \ll 1$, and that the depressed freezing point is not significantly different from that of the pure water, i.e., $T \approx T_0$. That is to say,

$$\ln(1 - X_B) \approx -X_B; \qquad \frac{1}{T} - \frac{1}{T_0} = \frac{T - T_0}{TT_0} \approx \frac{\Delta T}{T_0^2} \tag{44}$$

where $\Delta T = T - T_0$, i.e., the freezing point depression. Thus, Eq. (43) can be approximated as

$$X_B \approx -\frac{\Delta H_A^{fus}\,\Delta T}{RT_0^2} \tag{45}$$

Rearrangement of Eq. (45) gives

$$\Delta T \approx -\left(\frac{RT_0^2}{\Delta H_A^{fus}}\right) X_B \tag{46}$$

It is noted that the prediction by Eq. (46) has been confirmed by experimental results for solutions with relatively low concentrations [28]. The derivation of Eq. (46) is based on an ideal solution. When the concentrations of a solution is high, the solution could be far from ideal and the freezing point depression could differ greatly from what is predicted by Eq. (46), e.g., as pointed out in [53]. Normally, the activity coefficient γ is introduced in order to account for non-ideal solutions. The equation used is

$$\Delta T \approx -\left(\frac{RT_0^2}{\Delta H_A^{fus}}\right) X_B \gamma \tag{47}$$

More discussions about the validity of the proposed equations and the determination of the involved parameters can be found, e.g., in [28,29,53].

References

[1] M. Brun, A. Lallemand, J. Quinson, C. Eyraud, A new method for the simultaneous determination of the size and shape of pores: the thermoporometry, Thermochim. Acta 21 (1) (1977) 59–88.
[2] A. Kjeldsen, M. Geiker, On the interpretation of low temperature calorimetry data, Mater. Struct. 41 (1) (2008) 213–224.
[3] W. Kuhn, E. Peterli, H. Majer, Freezing point depression of gels produced by high polymer network, J. Polym. Sci. 16 (82) (1955) 539–548.
[4] P. Williams, Properties and behavior of freezing soils. Tech. Rep. 72, Norwegian Geotechnical Institute, Oslo, Norway, 1961.
[5] J. Blachere, J. Young, The freezing point of water in porous glass, J. Am. Ceram. Soc. 55 (6) (1972) 306–308.
[6] J. Riikonen, J. Salonen, V. Lehto, Utilising thermoporometry to obtain new insights into nanostructured materials (review part 1), J. Therm. Anal. Calorim. 105 (2011) 811–821.
[7] A. Neville, Properties of Concrete, 4th edition, Longman, Essex, UK, 1995.
[8] S. Diamond, Aspects of concrete porosity revisited, Cement Concr. Res. 29 (8) (1999) 1181–1188.
[9] H. Taylor, Cement Chemistry, 2nd edition, Thomas Telford, London, 1997.
[10] V. Baroghel-Bouny, M. Mainguy, T. Lassabatere, O. Coussy, Characterization and identification of equilibrium and transfer moisture properties for ordinary and high-performance cementitious materials, Cement Concr. Res. 29 (8) (1999) 1225–1238.
[11] M. Thiery, V. Baroghel-Bouny, G. Villain, P. Dangla, Numerical modeling of concrete carbonation based on durability indicators, in: V. Malhotra (Ed.), Proceedings of the 7th CANMET/ACI International Conference on Durability of Concrete, 2006, pp. 765–780.
[12] B. Bary, A. Sellier, Coupled moisture–carbon dioxide–calcium transfer model for carbonation of concrete, Cement Concr. Res. 34 (10) (2004) 1859–1872.
[13] V. Baroghel-Bouny, Water vapour sorption experiments on hardened cementitious materials. Part II: Essential tool for assessment of transport properties and for durability prediction, Cement Concr. Res. 37 (3) (2007) 438–454.
[14] V. Baroghel-Bouny, M. Mainguy, O. Coussy, Isothermal drying process in weakly permeable cementitious materials – assessment of water permeability, in: International Conference on Ion and Mass Transport in Cement-Based Materials, 1999, pp. 59–80.
[15] G. Fagerlund, Determination of pore-size distribution from freezing-point depression, Mater. Struct. 6 (3) (1973) 215–225.
[16] Z. Sun, G. Scherer, Pore size and shape in mortar by thermoporometry, Cement Concr. Res. 40 (5) (2010) 740–751.
[17] R.F. Feldman, The porosity and pore structure of hydrated portland cement paste, in: J.S.L.R. Roberts (Ed.), in: Pore Structure and Permeability of Cement Based Materials, vol. 137, Materials Research Society, Pittsburgh, PA, 1989, pp. 59–73.
[18] J. Thomas, H. Jennings, A. Allen, The surface area of hardened cement paste as measured by various techniques, Concr. Sci. Eng. 1 (1999) 45–64.
[19] J. Villadsen, Pore structure in cement based materials. Tech. Rep. 277, Building Materials Laboratory, Technical University, Denmark, 1992.
[20] R. Espinosa, L. Franke, Influence of the age and drying process on pore structure and sorption isotherms of hardened cement paste, Cement Concr. Res. 36 (10) (2006) 1969–1984.
[21] M. Landry, Thermoporometry by differential scanning calorimetry: experimental considerations and applications, Thermochim. Acta 433 (1/2) (2005) 27–50.
[22] M. Wu, B. Johannesson, M. Geiker, Determination of ice content in hardened concrete by low temperature calorimetry: influence of baseline calculation and heat of fusion of confined water, J. Therm. Anal. Calorim. 115 (2) (2014) 1335–1351.
[23] M. Wu, B. Johannesson, Impact of sample saturation on the detected porosity of hardened concrete using low temperature calorimetry, Thermochim. Acta 580 (2014) 66–78.
[24] K. Ishikiriyama, M. Todoki, K. Motomura, Pore size distribution (PSD) measurements of silica gels by means of differential scanning calorimetry. I. Optimization for determination of PSD, J. Colloid Interface Sci. 171 (1) (1995) 92–102.
[25] K. Ishikiriyama, M. Todoki, Pore size distribution measurements of silica gels by means of differential scanning calorimetry. II. Thermoporosimetry, J. Colloid Interface Sci. 171 (1) (1995) 103–111.
[26] K. Morishige, K. Kawano, Freezing and melting of water in a single cylindrical pore: the pore-size dependence of freezing and melting behavior, J. Chem. Phys. 110 (1999) 4867.
[27] B. Lothenbach, F. Winnefeld, Thermodynamic modelling of the hydration of portland cement, Cement Concr. Res. 36 (2) (2006) 209–226.
[28] P. Atkins, J. De Paula, Physical Chemistry, 8th edition, Oxford University Press, Oxford, UK, 2006.
[29] K. Laidler, J. Meiser, Physical Chemistry, 3rd edition, Houghton Mifflin Company, Boston, 1999.
[30] G. Mrevlishvili, P. Privalov, Calorimetric study of the melting of frozen aqueous solutions of electrolytes, J. Struct. Chem. 9 (1) (1968) 5–7.
[31] B. Lothenbach, Thermodynamic equilibrium calculations in cementitious systems, Mater. Struct. 43 (10) (2010) 1413–1433.
[32] S. Setunge, N. Nguyen, B. Alexander, L. Dutton, Leaching of alkali from concrete in contact with waterways, Water, Air, Soil Pollut.: Focus 9 (5-6) (2009) 381–391.
[33] G. Scherer, Freezing gels, J. Non-Cryst. Solids 155 (1) (1993) 1–25.

[34] J. Kaufmann, Experimental identification of ice formation in small concrete pores, Cement Concr. Res. 34 (8) (2004) 1421–1427.
[35] M. Wu, K. Fridh, B. Johannesson, M. Geiker, Influence of frost damage and sample preconditioning on the porosity characterization of cement based materials using low temperature calorimetry, Microporous Mesoporous Mater. (2014) (submitted for publication).
[36] K. Haga, S. Sutou, M. Hironaga, S. Tanaka, S. Nagasaki, Effects of porosity on leaching of ca from hardened ordinary portland cement paste, Cement Concr. Res. 35 (9) (2005) 1764–1775, http://dx.doi.org/10.1016/j.cemconres.2004.06.034.
[37] M. Mainguy, C. Tognazzi, J. Torrenti, F. Adenot, Modelling of leaching in pure cement paste and mortar, Cement Concr. Res. 30 (1) (2000) 83–90.
[38] D. Damidot, B. Lothenbach, D. Herfort, F. Glasser, Thermodynamics and cement science, Cement Concr. Res. 41 (7) (2011) 679–695.
[39] B. Lothenbach, T. Matschei, G. Möschner, F. Glasser, Thermodynamic modelling of the effect of temperature on the hydration and porosity of portland cement, Cement Concr. Res. 38 (1) (2008) 1–18.
[40] T. Schmidt, B. Lothenbach, M. Romer, K. Scrivener, D. Rentsch, R. Figi, A thermodynamic and experimental study of the conditions of thaumasite formation, Cement Concr. Res. 38 (3) (2008) 337–349.
[41] Y. Hosokawa, K. Yamada, B. Johannesson, L. Nilsson, Development of a multi-species mass transport model for concrete with account to thermodynamic phase equilibriums, Mater. Struct. 44 (9) (2011) 1577–1592.
[42] M. Wu, K. Fridh, B. Johannesson, M. Geiker, Impact of sample crushing on the porosity characterization of hardened cement pastes by low temperature calorimetry: comparison of powder and cylinder samples, J. Therm. Anal. Calorim. (2014) (submitted for publication).
[43] Z. Sun, G. Scherer, Effect of air voids on salt scaling and internal freezing, Cement Concr. Res. 40 (2) (2010) 260–270.
[44] P. Parker, A. Collins, Dehydration of flocs by freezing, Environ. Sci. Technol. 33 (3) (1999) 482–488.
[45] D.L. Parkhurst, C. Appelo, User's Guide to PHREEQC (Version 2): A Computer Program for Speciation, Batch-Reaction, One-Dimensional Transport, and Inverse Geochemical Calculations, US Geological Survey, Denver, 1999.
[46] A. Truesdell, B. Jones, WATEQ, a computer program for calculating chemical equilibria of natural waters, J. Res. U.S. Geol. Surv. 2 (1974) 233–274.
[47] EMPA Database, Thermodynamic Data for Hydrated Solids in Portland Cement System, 2008, accessed on 25.03.13, http://www.empa.ch/plugin/template/empa/*/62204
[48] A. Nonat, The structure and stoichiometry of C-S-H, Cement Concr. Res. 34 (9) (2004) 1521–1528.
[49] D. Kulik, Improving the structural consistency of C-S-H solid solution thermodynamic models, Cement Concr. Res. 41 (5) (2011) 477–495.
[50] M.M. Jensen, B. Johannesson, M.R. Geiker, Framework for reactive mass transport: phase change modeling of concrete by a coupled mass transport and chemical equilibrium model, Comput. Mater. Sci. (2014) (in press).
[51] B. Johannesson, Cement Clinker Composition and Phases 3B, Lecture Notes for Introduction to Concrete Technology (11563), Technical University of Denmark, Kgs. Lyngby, Denmark, 2011.
[52] L. Parrot, D. Killoh, Prediction of cement hydration, in: Proc. Br. Ceram. Soc., No. 35, 1984, pp. 41–53.
[53] B. Johannesson, Classical Thermodynamics and Its Use in Understanding Freezing and Thawing of Concrete 12A(A), Lecture Notes for Introduction to Concrete Technology (11563), Technical University of Denmark, Kgs. Lyngby, Denmark, 2011.
[54] B. Johannesson, Chemical Equilibrium of Cement-Based Materials 5A(B), Lecture Notes for Introduction to Concrete Technology (11563), Technical University of Denmark, Kgs. Lyngby, Denmark, 2011.
[55] G. Anderson, D. Crerar, Thermodynamics in Geochemistry: The Equilibrium Model, vol. 588, Oxford University Press, New York, 1993.
[56] J. Munoz, D. Nordstrom, Geochemical Thermodynamics, 2nd edition, Blackwell, Boston, 1994.
[57] J. Ederová, V. Šatava, Heat capacities of C_3AH_6, C_4ASH_{12} and $C_6AS_3H_{32}$, Thermochim. Acta 31 (1) (1979) 126–128.
[58] D. Damidot, F. Glasser, Thermodynamic investigation of the $CaO–Al_2O_3–CaSO_4–H_2O$ system at 50 °C and 85 °C, Cement Concr. Res. 22 (6) (1992) 1179–1191.
[59] D. Kulik, Minimising uncertainty induced by temperature extrapolations of thermodynamic data: a pragmatic view on the integration of thermodynamic databases into geochemical computer codes, in: The Use of Thermodynamic Databases in Performance Assessment, OECD, Barcelona, 2002, pp. 125–137.
[60] T. Matschei, B. Lothenbach, F. Glasser, Thermodynamic properties of Portland cement hydrates in the system $CaO–Al_2O_3–SiO_2–CaSO_4–CaCO_3–H_2O$, Cement Concr. Res. 37 (10) (2007) 1379–1410.
[61] R. Defay, I. Prigogine, A. Bellemans, D. Everett, Surface Tension and Adsorption, Longmans, London, 1966.

Paper VI

A study of the water vapor sorption isotherms of hardened cement pastes: possible pore structure changes at low relative humidity and the impact of temperature on isotherms

M. Wu, B. Johannesson, M. Geiker

Published in: *Cement and Concrete Research, 2014*

Cement and Concrete Research 56 (2014) 97–105

Contents lists available at ScienceDirect

Cement and Concrete Research

journal homepage: http://ees.elsevier.com/CEMCON/default.asp

A study of the water vapor sorption isotherms of hardened cement pastes: Possible pore structure changes at low relative humidity and the impact of temperature on isotherms

Min Wu [a,*], Björn Johannesson [a], Mette Geiker [b]

[a] Department of Civil Engineering, Building 118, Technical University of Denmark, 2800 Lyngby, Denmark
[b] Department of Structural Engineering, Norwegian University of Science and Technology, Trondheim, Norway

ARTICLE INFO

Article history:
Received 26 August 2013
Accepted 21 November 2013

Keywords:
Adsorption (C)
cement paste (D)
microstructure (B)
temperature (A)
isotherms

ABSTRACT

Using water vapor sorption isotherms measured by the "dynamic vapor sorption" (DVS) method, a resaturation study was conducted to investigate possible pore structure changes of hardened cement paste samples caused by the drying at low relative humidity during desorption measurements. The results indicate that either the relatively short term drying does not cause any microstructure changes or the pore structure of the hardened cement paste samples can be restored during the absorption process. Additionally, the temperature dependency of sorption isotherms was investigated using both hardened cement paste samples and a model material MCM-41. The pronounced impact of temperature on desorption isotherms of cement based materials as reported in literature was not found in this investigation. The results suggest that the differences between the sorption isotherms measured at different temperatures are mainly caused by the temperature dependent properties of water.

1. Introduction

Water vapor sorption isotherms of a porous material are the graphic representation of the water content against the relative humidity (RH) of the environment at equilibrium condition, i.e., the RH inside of the material is equal to that of the external. Based on the determined water vapor isotherms, it is possible to derive important properties of the material under study. For hardened cement pastes, the properties including, e.g., the bulk porosity accessible to water vapor, the porosity and the amount of the hydration products—calcium silicate hydrate (C-S-H) gel, the specific surface area, the pore size distribution as well as the connectivity of the pores, can be studied [1,2]. Moreover, the transport properties, such as the permeability and the diffusion coefficients of the hardened paste can also be obtained from studying the sorption isotherms [3]. Additionally, the derived properties from the water vapor sorption isotherms are quite essential in the modeling of some important processes, e.g., moisture transport [3,4], drying shrinkage [5] and carbonation [6,7]. A clarification is made here about the terminology "adsorption" and "absorption". In many cases, e.g., see [8], "adsorption" is used in describing the process of the liquid uptake, including both the adsorbed and the capillary condensed liquid. While some other authors, e.g., see [9,10], use "absorption" to describe exactly the same content, i.e., including both types of liquid uptake. In this work, the word "absorption" will be used to describe the combined effect of both the adsorption and the capillary condensation while "adsorption" simply refers to the liquid fixed due to multilayer adsorption.

It has been reported in some studies, e.g., see [1,11–15], that changes of the pore structure of hardened cement paste samples can be expected during desorption measurements when the RH decreases to low values, e.g., below the RH of about 0.4. It has been argued by Jennings et al. [12–14] that drying below the RH at about 0.4 results into the restructure, or more precisely the collapse of the low density (LD) C-S-H products. Additionally, it is argued in [12–14] that the loose-packed C-S-H will be converted into LD C-S-H at very low RHs. Based on a colloid description of the C-S-H structure, an explanation was proposed by the same authors, which is that the drying enhances the chemical aging, i.e., the increase of the polymerization degree of the silicate chains in the C-S-H particles over time. This kind of irreversible chemical aging will change the C-S-H particles into stiffer, stronger and denser ones. Baroghel-Bouny [1] studied the first and second desorption isotherms of several different hardened cement paste samples and concluded that microstructure changes occurred in some of the studied samples, represented by higher water contents measured during the second desorption isotherm in the low RH range (especially for RH between 0.33–0.12). Some other studies, e.g., in [11], reported that the pore structure of hardened cement paste samples was coarsened by the so-called drying effect at low RHs. Thus, it should be mentioned that for the same behavior of pore structure changes in this context, contradictory results have been reported, e.g., the results in [1] demonstrate the increase of small pores while that in [11] indicate the coarsening of the pore structure. Due to the instability caused by the drying involved in the desorption process, the first and the second desorption isotherm

* Corresponding author.
E-mail address: miwu@byg.dtu.dk (M. Wu).

0008-8846/$ – see front matter © 2013 Elsevier Ltd. All rights reserved.
http://dx.doi.org/10.1016/j.cemconres.2013.11.008

cycles have been studied rather extensively. It has been suggested that the second desorption is more stable and thus it should be more representative for a pore structure analysis [15]. However, based on some experimental evidence, Baroghel-Bouny [1] also pointed out that the microstructure changes of cement pastes caused by the drying at low RHs are reversible, which is different from the permanent changes as reported and discussed by Jennings et al. [12–14].

The influence of temperature on the sorption isotherms of cement based materials has been reported, e.g., in [16–21]. The absorption isotherms measured by Daian [19] between 20 °C and 55 °C demonstrated that the higher the temperature, the less the amount of the absorbed water at a certain RH. However, the differences between the absorption isotherms measured under different temperatures were rather small. Similar results were also reported in the study conducted by Radjy et al. [20]. The authors measured the absorption isotherms between 0 °C and 60 °C and the desorption isotherms between 0 °C and 40 °C on mature hardened cement paste samples, and the results showed hardly any temperature dependent property. Ishida et al. [21] investigated the absorption and desorption isotherms for an 80-day water cured hardened cement paste samples under 20 °C, 40 °C and 60 °C. Very limited differences were found in the absorption isotherms in that study, however, the differences in the desorption isotherms were found to be more pronounced. As the temperature increases, not only the amount of water adsorbed decreased but the shape of the isotherms was also concluded to be modified [21]. Similar behavior, i.e., rather significant differences of the desorption isotherms under different temperatures, was reported in [16–18]. The temperature dependence of sorption isotherms of cement based materials can be attributed to two different mechanisms [22,23]: (1) the coarsening of pore structure, e.g., ettringite dissolution and C-S-H alteration; and (2) the temperature dependence of water properties. Poyet et al. [16,17] pointed out that yet another factor may be involved in influencing the sorption isotherms at different temperatures. They assumed that the isotherm evolution is purely due to the so-called “thermal desorption”, which is to say that the shift of the adsorbed water content on the desorption isotherms at different temperatures is induced only by the temperature effect while the potential microstructure changes are considered as negligible. Based on these assumptions and the Clausius–Clapeyron formula, they developed a method to predict the desorption isotherms under different temperatures using a desorption isotherm measured at one temperature as a reference state. If the rather pronounced differences between desorption isotherms measured at different temperatures are due to the thermal effect as argued by, e.g., Poyet et al. [16,17], similar differences should be observed also on absorption curves measured at different temperatures while little difference is reported [16,17]. Since the reported results regarding the temperature dependent isotherms are not consistent for cement based materials, further exploration in this aspect is needed.

In the present work, possible changes of the pore structure of hardened cement paste samples at low RHs will be investigated through a resaturation method. Following a first desorption–absorption cycle, where the desorption goes down to RH = 0, the tested samples will be resaturated with distilled water. After that, a second desorption–absorption cycle will be conducted on the resaturated samples. In this way, the changes of the pore structure of the studied hardened cement paste samples at low RHs are expected to be observed by comparing the sorption isotherms of the first and the second cycle, if there is any. Moreover, the sorption isotherms will be measured under different temperatures to study important influencing factors with respect to the temperature dependence of the sorption isotherms of hardened cement pastes.

2. Experimental

2.1. Materials preparation

Three materials were studied in this investigation: one model porous material named MCM-41 and hardened cement pastes prepared by two types of cement. By including the model material MCM-41, whose pore structure is considered stable during the studied temperature range (25–40 °C), it can provide reference information in the study of the temperature dependent isotherms in which the factor of the changing of pore structure caused by temperature can be excluded.

MCM-41 is a silica based material whose pore structure is in the form of hexagonal arrays of uniform tubular channels of controlled width, which is often used as a model material in porosity studies. The MCM-41 used in this study is produced by Tianjin Chemist Scientific Ltd. The information provided by the producer concerning the pore diameter, the specific surface area and the total pore volume is 3.0 nm, $\geq$800 m^2/g and $\geq$0.70 ml/g, respectively.

CEM I 32.5 R and CEM III/B 42.5 N were the two types of cement used to prepare the paste samples, see Table 1. The W/C ratio for all cement paste samples was 0.4. The paste samples were mixed using a paddle mixer. After mixing, the pastes were cast into plastic vials with a diameter of about 15 mm and a length of about 50 mm followed by proper compaction. After the sealed curing at room temperature (about 20 °C) in the plastic vials for about one day, the hardened paste samples were demoulded. Then, each paste sample was placed into a slightly bigger plastic flask filled with saturated limewater to cure at room temperature until the desired age for experiments was reached. In the following description, the hardened cement pastes will be denoted as CEM I and CEM III.

The cement paste samples were cured for about 6 months before testing. Before sorption measurements, the prepared cylinder samples of the hardened cement pastes were vacuum saturated with saturated limewater and then the crushing and grinding of the samples was conducted in a carbon dioxide free chamber since very small sample size was needed (Section 2.2). To avoid possible drying during the process, the RH inside of the chamber was set at 1 (the measured RH was about 0.90–0.95) and the sample crushing and grinding was conducted rather quickly (in 30–40 min) for each paste. Immediately after that, the ground powder was placed into plastic flasks containing saturated limewater with the amount just to cover the powders (for about a week) before the sorption experiments. This procedure was also conducted in a carbon dioxide free chamber.

One concern with respect to the sample preparation of cement pastes is that the powder samples might not be fully saturated by submerging in limewater, even though a vacuum saturation was performed before the sample crushing. To check the saturation situation, powder samples were subjected to reduced pressure (~40 mbar) for about 3 h followed by 24 h of standing still. After that, the total (lime) water contents were determined. Compared with the samples submerged in limewater, the relative difference of the total (lime) water content was less than about 5%. In this sense, we think it is acceptable to submerge the powder samples in limewater for the purpose of sorption measurements.

Another concern is that drying might have already taken place during the sample preparation of cement pastes, even if special care was

Table 1
Properties and the chemical composition of the two cements used in this study.

		CEM I (CEM I 32.5 R)	CEM III (CEM III/B 42.5 N)
Density	(g/cm^3)	3.06	2.90
Fineness	(cm^2/g)	2905	4635
Water demand	(%)	26.2	32.3
Initial setting time	(min)	185	270
Loss on ignition	(%)	2.1	1.4
SiO_2	(%)	20.6	29.2
Al_2O_3	(%)	5.6	8.9
Fe_2O_3	(%)	2.4	1.2
CaO	(%)	63.4	48.0
MgO	(%)	1.6	4.8
SO_3	(%)	2.9	2.6
K_2O	(%)	0.7	0.6
Na_2O	(%)	0.2	0.2
Cl	(%)	<0.1	<0.1

taken. To see the extent of water loss during the sample crushing, the desorption curve of a powder sample of CEM I paste measured by the DVS instrument was checked. It is because the first step of the desorption measurement (with RH set at 0.95) can be approximated to what takes place during the sample crushing in the carbon dioxide free chamber. The initial mass of the sample (after taking out from the sample vial covered by limewater, which includes some bulk water adhered to the sample surface) was about 16 mg; the dry mass later determined at RH = 0 was about 8 mg and the water loss during the first half hour of the measurement was about 1 mg. That is, during the first half hour, most of the water lost is the bulk water adhered to the sample surface (since the total pore water later determined at the RH = 0.95 from the desorption was about 21% of the dry mass, i.e., about 1.6 mg). In this sense, the drying effect during sample crushing is considered limited.

More importantly, as will be shown later, some arguments of this study are mainly drawn based on the comparison of the results obtained by the DVS method and that by the traditional desiccator method using salt solutions. It often takes long time, e.g., several weeks to months, to measure a sorption data at one RH using the desiccator method [11,12,15]. That is, the drying effect of the samples using desiccator method should be much more pronounced compared with that in the DVS method used here. If the desiccator method can catch the first sorption isotherms (which is often assumed so in literature, e.g., see [1]), it is then reasonable to think that the DVS method for sure can also catch the first sorption isotherms.

2.2. Sorption measurements

The "dynamic vapor sorption" (DVS) method was used to measure the sorption behaviors of the materials in this investigation. The sorption measurements were conducted in a climate incubator in which the temperature can be accurately regulated and controlled. The desired relative humidity can be generated by mixing two air flows, i.e., a totally dry (RH = 0) and a totally saturated (RH = 1) air in various proportions. The proportion of the two flows is controlled by the input settings of the instrument. Fig. 1 is a schematic illustration of a DVS instrument. More detailed descriptions of the instrument can be found in [24].

It should be noted that it can take very long time for the equilibrium condition to be established at a given pre-set relative humidity. Consequently, it is almost practically impossible to wait for the establishment of the equilibrium condition at each relative humidity in a sorption measurement. The duration time of each relative humidity in the DVS instrument can be controlled by either setting the mass change ratio against time, *dm*/*dt*, or by setting the duration time directly. Once the set conditions are met, the instrument will directly go to the next step of the pre-set relative humidities. In this study, the *dm*/*dt* criterion is set to 0.002% and the shortest and the longest duration time for each RH step is set to be 0.5 and 24 h, respectively. Then, the equilibrium moisture content corresponding to each generated relative humidity step will be extrapolated from the measured data. The details about the extrapolation will be presented later. The temperature of the measurements was 25 °C except when it is specifically stated.

The sorption measurement for the model material MCM-41 started from an absorption (RH from 0 to 0.95) followed by a desorption (RH from 0.95 to 0) measurement. Considering the possible effect of drying at low RHs on the microstructure as discussed earlier, the experiments with hardened cement paste samples started from the desorption and then followed by the absorption. By adopting this procedure, the possible effect caused by the so-called drying damage at low RHs is expected to be reduced.

For each material under study, sorption measurements were conducted three times using different samples. The total sorption experimental study lasted for about four months and the three sets of measurements were undertaken at the beginning, the middle and the end of the total measuring time. By doing this, firstly the stability of the instrument can be validated as the model material MCM-41 has a stable pore structure which will not change against time; and secondly the possible evolution of the pore structure against time of the hardened cement paste samples can be checked since further hydration might take place in cement based materials even though some relatively mature samples are used.

Concerning the resaturation study of the two hardened cement pastes, firstly a desorption–absorption cycle was conducted. After this cycle, each tested sample was resaturated with distilled water for about 3 days. The resaturation was conducted by adding several drops of distilled water on each of the tested sample in the sample holder (see Fig. 1). After the resaturation, a second desorption–absorption cycle was applied on the samples. Immediately after the second desorption–absorption cycle, a scanning desorption curve starting from RH = 0.95 to RH = 0 was measured on each sample.

3. Results and discussion

3.1. Instrument and sample stability

The results of the three sorption measurements for the model material MCM-41 are presented in Fig. 2. Generally, the measured results on the three samples are rather comparable, especially on the desorption isotherms. If we compare the three desorption measurements in RHs lower than about 0.45, they are observed to be almost identical. For the point at RH = 0.5, the small difference observed might be related to the homogeneity of the sample since very small sample (less than 10 mg in this case) was used. Another possible reason for the differences might be due to the instrument setting with regard to the equilibrium condition. It can be found in Fig. 2 that the major desorption occurs

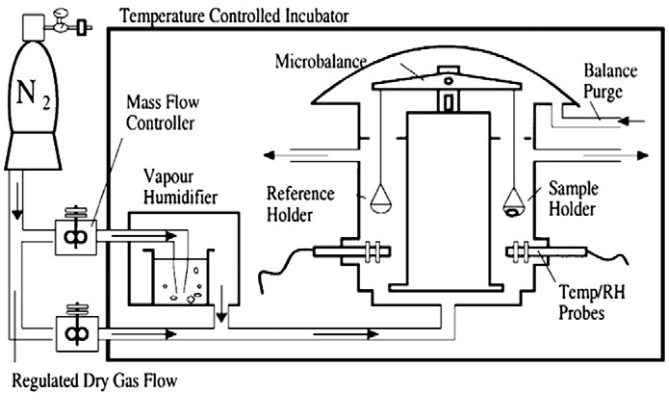

Fig. 1. Schematic illustration of a dynamic vapor sorption (DVS) instrument. Dry and saturated air are mixed to generate the desired relative humidity and a symmetric reference holder is used to counteract the adsorption on the sample holder (after [24]).

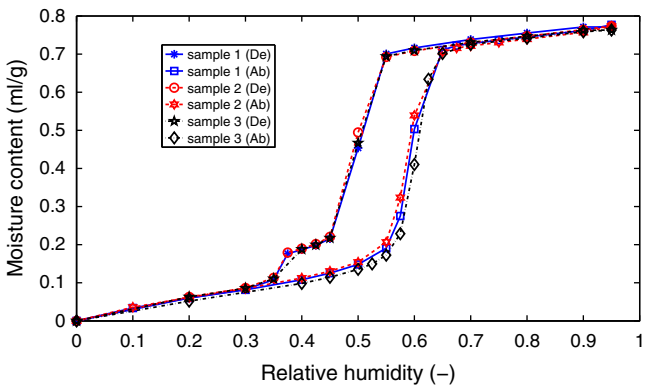

Fig. 2. Three sorption measurements for the model material MCM-41. "De" and "Ab" denote desorption and absorption, respectively. The moisture content is expressed as ml water per gram of dry sample and the mass of the dry sample is determined at the point where RH = 0.

between the RH of 0.45 to 0.55. That is, there is a possibility that the equilibrium condition was not established at RH = 0.5 during the pre-set duration time of each RH step (24 h), e.g., see the desorption isotherm of sample 2, which shows a slightly higher value than other measurements. The similar trend of non-equilibrium as observed in the desorption isotherms can also be found in the absorption curves. Concerning the absorption isotherms, the agreement is, however, quite satisfactory both at high (>0.7) and low RH (<0.4) ranges with some differences found only at the middle RH range (0.4–0.7). The same arguments as presented for the desorption isotherms are also applicable for the absorption isotherms.

The measured sorption isotherms for the two hardened cement pastes CEM I and CEM III are shown in Figs. 3 and 4. As can be observed, a fairly good comparability is found in the absorption isotherms for both CEM I and CEM III in the whole RH range while there are some differences in the desorption isotherms. The differences in CEM I (Fig. 3) lie in high RHs and RH < 0.4 while the differences in CEM III (Fig. 4) are mainly at high RHs (0.8–0.95). The differences measured at the high RHs can be attributed to that the equilibrium condition is not established, which is similar to what has been discussed for the MCM-41 in the same context but with some additional differences. Here, however, the main reason causing the equilibrium condition not being achieved is due to the adopted experimental procedure. As mentioned earlier, in order to avoid any possible carbonation and pre-drying, the cement paste samples need to be cured in saturated limewater before the desorption measurement started. That is, there was some surplus water adhered to the outer surfaces of the hardened cement pastes. This water might not be able to be desorbed during the pre-defined 24 h for each step at the very high RHs. This is especially true for the first step of a desorption, i.e., at RH = 0.95. The original measured data confirmed the relevance of the above mentioned argument, i.e., the dm/dt was still higher than the pre-set value at some of the high RH points shown in Figs. 3 and 4 when it went to the next RH step. As will be presented later, a procedure will be introduced to extrapolate the sample mass under equilibrium conditions. The main differences between a measured isotherm and the corresponding corrected isotherm (with the extrapolated data) are at very high RHs. That is, most of the differences at the high RHs will be canceled out by adopting the proposed extrapolation procedure.

By looking at the data measured for CEM I at RH < 0.4 (Fig. 3), the desorption of measurement 1 shows higher moisture content than that of sample 2 and sample 3 while the desorption isotherms of sample 2 and sample 3 are almost identical in the considered RH range. It may be suspected that it is the continuing hydration process which has altered the porosity of the material. However, it should be noticed that firstly the total porosity (demonstrated by the maximum moisture content) of sample 2 and sample 3 are not reduced; and secondly the

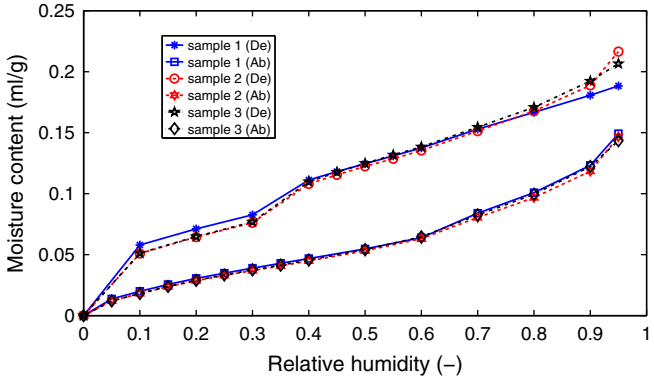

Fig. 3. Three sorption measurements for the hardened cement paste CEM I. "De" and "Ab" denote desorption and absorption, respectively. The moisture content is expressed as ml water per gram of dry sample and the mass of the dry sample is determined at the point where RH = 0.

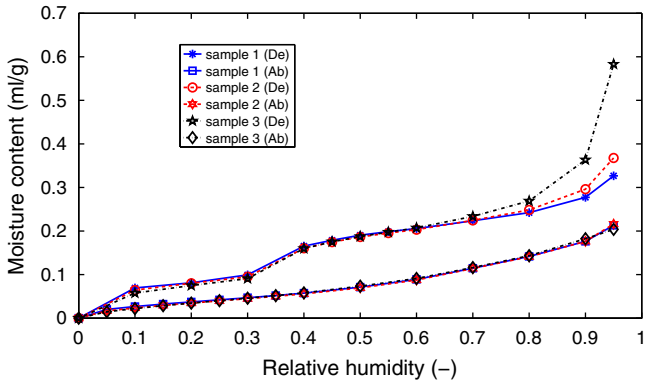

Fig. 4. Three sorption measurements for the hardened cement paste CEM III. "De" and "Ab" denote desorption and absorption, respectively. The moisture content is expressed as ml water per gram of dry sample and the mass of the dry sample is determined at the point where RH = 0.

difference is not found for sample CEM III (Fig. 4). Compared with CEM I, CEM III includes much more supplementary cementitious component (ground granulated blast furnace slag). That is, the continuing hydration would be more likely in sample CEM III than in CEM I given the same hydration age while this is not the case in this study. Additionally, the same type of difference is not observable in the measured absorption isotherms. Therefore, it is assumed that the samples used are old enough and that the change of the pore structure due to further hydration during the measurement period is presumably low. The relatively small difference observed at RH < 0.4 for CEM I comparing the three measurements might instead be related to some unknown uncertainties during the desorption measurement of sample 1.

3.2. Extrapolation of sorption data

As mentioned in Section 2.2, it is almost practically impossible to wait for the establishment of equilibrium condition at each studied RH step. Therefore, a data processing procedure (curve fitting) is adopted to extrapolate the sample mass to its equilibrium condition. It has been proposed that the sample mass against time in a sorption measurement follows the equation [25,26]

$$m(t) = m_f - \left(m_f - m_0\right)\mathrm{e}^{-k(t-t_0)} \quad (1)$$

where $m(t)$ is the sample mass at the time t, m_0 is the initial mass and t_0 is the initial time of the curving fitting, m_f is the fitted asymptotic sample mass at the equilibrium condition for the studied RH and k is a curve fitting constant. Fig. 5 gives an illustration of a data extrapolation. The solid line is the measured experimental data; the dash–dot line represents the fitted curve and the dot line shows the extrapolated

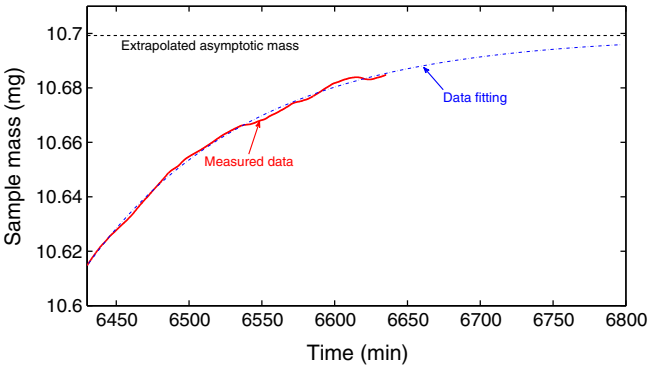

Fig. 5. An example showing the data processing procedure to extrapolate the asymptotic sample mass at the equilibrium conditions.

asymptotic sample mass at the assumed equilibrium condition for the considered RH step.

Using the extrapolated data, the corrected isotherms under the assumed equilibrium conditions can be plotted. For the model material MCM-41(besides the point at RH = 0), the point with important difference between the extrapolated and the measured isotherms is found at RH = 0.5 in desorption and at a RH around 0.6 in absorption in which moisture desorbs/condenses rather drastically. For the studied hardened cement pastes CEM I and CEM III, the point at RH = 0 is a point with relatively big difference between the extrapolated and the measured isotherms, which indeed is similar to the results of the MCM-41. However, more points with important difference are found at the high RHs (0.95, 0.9 and sometimes 0.8) of the studied hardened cement paste samples, especially between the extrapolated and the measured desorption isotherms. The reason has been discussed already, i.e., related to the experimental procedure and the pre-setting in the instrument. For other RH points than the ones discussed above, the relative difference of the moisture content between the extrapolated and measured data are no more than about 0.3%.

With the extrapolated data, the corrected sorption isotherms of the three studied materials were constructed and they are presented in Figs. 6, 7 and 8.

3.3. Resaturation of hardened cement paste samples

Considering the comparable results obtained on different samples in the sorption measurements as discussed in Section 3.1, each measurement for the resaturation study was conducted only once. The sorption isotherms (after data extrapolation to equilibrium) are shown in Figs. 9 and 10. It can be observed that there is actually no major difference between the first absorption isotherm (denoted as the "original" isotherm) and the second after resaturation (denoted as the "resaturated" isotherm) for both cement pastes the CEM I and CEM III. Comparing the first desorption isotherm with the one after resaturation, one can conclude that they follow about the same path but the isotherm after resaturation is slightly lower than the original one. The difference between the two desorption isotherms becomes smaller as the RH decreases. It would be reasonable to argue that the difference in the measured response is due to the fact that the adopted resaturation procedure cannot fully saturate all of the pores, especially the big pores, rather than the change of the pore structure. The relevance of this argument can be motivated by looking at the desorption scanning curve started from the point RH = 0.95 following the absorption measurement of the resaturated sample. The difference between the original desorption isotherm and the scanning curve also follows about the similar trend as observed for that between the original desorption isotherm and the isotherm after the resaturation, but the difference is much bigger, especially at high RHs. This is reasonable because for the scanning curve, the pores whose Kelvin radii are larger than that corresponding to the RH of 0.95 are empty when the desorption starts. While for the original desorption at RH = 0.95, these pores with pore entry radii (Kelvin radii) smaller than that corresponding to the RH of 0.95 but bigger interior radii (bearing in mind the simplified "ink-bottle" pore model and the desorption is controlled by the pore entry or neck sizes [2]) are still filled with water. This explains why higher moisture content at the same RH is observed on the original isotherm compared with that of the scanning curve. As the RH decreases, the volume of the moisture content which stays undesorbed in the relatively big pores but with small pore entries (or the "ink-bottle" pores for simplicity) also decreases, resulting into smaller and smaller difference between the original desorption isotherm and the scanning curve. That is, the difference is probably mainly caused by the unfilled "ink-bottle" pores. Therefore, if the resaturation can fully saturate all the big pores, it can be expected that there should be no difference between the original desorption isotherm and the one of the resaturated sample.

By looking at the desorption isotherms, it can be found that there is a somewhat significant change in terms of the moisture content at the RH of about 0.4. It might indicate that something possibly occurs around the RH at this level, e.g., the possible conversion of the loose-packed C-S-H particles as discussed by Jennings et al. [12–14]. If this is the case, it can be expected that no permanent changes of the pore structure takes place since the desorption isotherm after resaturation is almost identical to the original isotherm in all essential parts. If the microstructure changes due to the drying at low RHs are relevant in this context, the results in this study tend to support the statement given by Baroghel-Bouny [1] which claims that the reversibility of the microstructure changes, while they are not in accordance with the argument saying that the drying at low RHs changes the microstructure permanently. Additionally, it is also noticed that studies of hardened cement

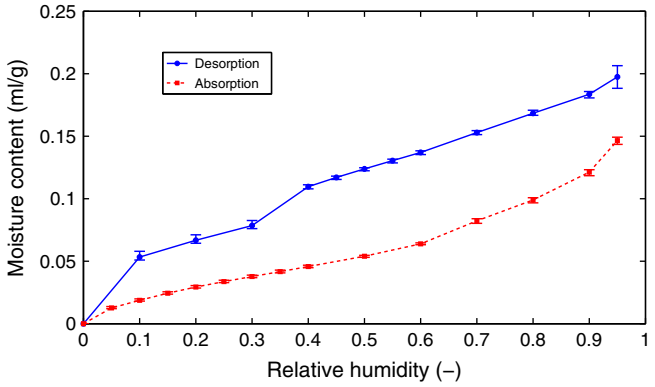

Fig. 7. The sorption isotherms for CEM I based on the extrapolated data. The error bar shows the variation of three repetitive measurements as presented earlier.

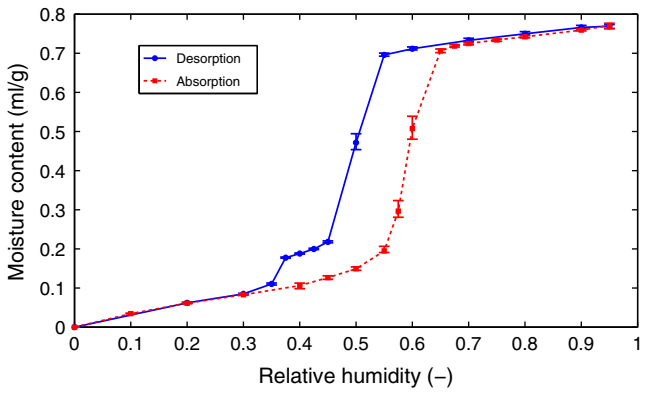

Fig. 6. The sorption isotherms for MCM-41based on the extrapolated data. The error bar shows the variation of three repetitive measurements as presented earlier.

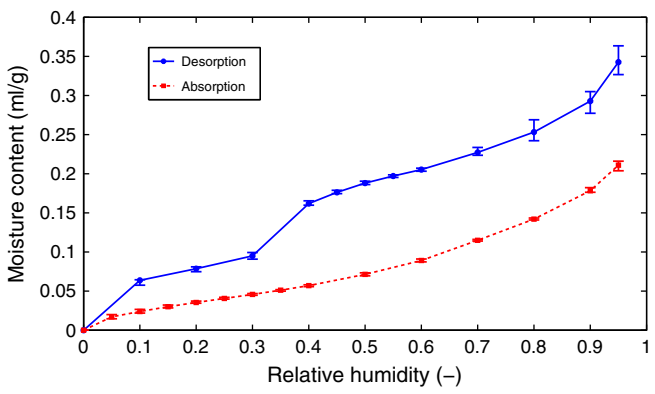

Fig. 8. The sorption isotherms for CEM III based on the extrapolated data. The error bar shows the variation of three repetitive measurements as presented earlier.

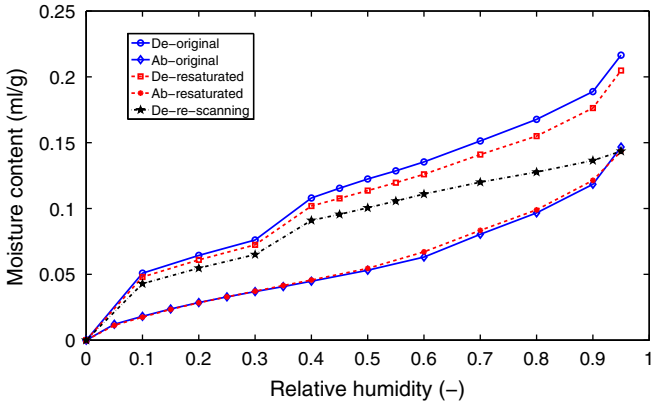

Fig. 9. The sorption isotherms (after data extrapolation) for the hardened cement paste sample CEM I. The 'De-original' and 'Ab-original' isotherms are from the first desorption–absorption cycle. The 'De-resaturated' and 'Ab-resaturated' isotherms are the measurements following the sample resaturation. The 'De-re-scanning' is a desorption scanning curve from RH = 0.95 following the 'Ab-resaturated' isotherm.

pastes using both small-angle X-ray scattering (SAXS) [27] and small-angle neutron scattering (SANS) [28] indicate that the surface area and the C-S-H gel structure can be fully recovered upon the rewetting of a D-dried specimen. It should be mentioned that the conclusion of permanent microstructure changes of cement paste samples at low RHs is often drawn based on the studies using desiccator method with saturated salt solutions, e.g., see [11,12,15]. Using the desiccator method, it often takes long time for the equilibrium to be established at one RH. Thus, it might be reasonable to consider that the permanent microstructure changes as reported in some studies are related to the long time exposure at low RHs, which may enhance the aging effect as discussed by Jennings et al. [12], meaning the so-called irreversible pore structure collapse may not be solely caused by the drying effect at low RHs itself. This argument is supported by the studies using methods with short RH exposure time, such as the DVS, SAXS [27] and SANS [28], which do not show the permanent microstructure changes of cement paste samples at low RHs. To further validate the argument, DVS measurements can be applied to cement paste samples which have been exposed to a certain (low) RH, e.g., 0.30 or 0.40, for relatively a long time (on the order of several months). By comparing the results of the "undried" and 'dried" samples, the effect of drying at low RHs for relatively extended period of time can be obtained.

The study indicates that either the drying at low RHs during the desorption measurement does not cause any microstructure changes or if the microstructure changes do occur, the absorption process must have been able to restore the pore structure of hardened cement paste samples, meaning the possible microstructure changes are reversible.

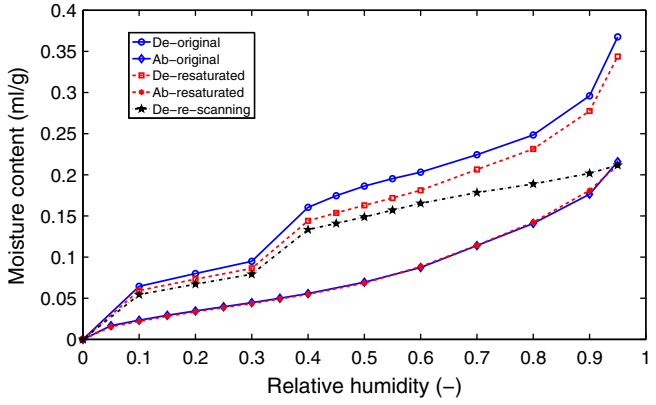

Fig. 10. The sorption isotherms (after data extrapolation) for the hardened cement paste sample CEM III. The 'De-original' and 'Ab-original' isotherms are from the first desorption–absorption cycle. The 'De-resaturated' and 'Ab-resaturated' isotherms are the measurements following the sample resaturation. The 'De-re-scanning' is a desorption scanning curve from RH = 0.95 following the 'Ab-resaturated' isotherm.

3.4. Temperature dependent sorption isotherms

Three different temperatures, 25 °C, 33 °C and 40 °C, were considered in this study. Same as the resaturation study, each measurement was conducted only once. The absorption and the desorption isotherms (after data extrapolation to equilibrium) for the MCM-41, CEM I and CEM III are shown in Figs. 11, 12 and 13, respectively. The general trend as reported in the literature is also found for the three materials studied, i.e., the higher the temperature, the less the amount of absorbed water. For MCM-41 (Fig. 11), the difference between the isotherms at different temperatures is mainly in the RH range of 0.3–0.7. For hardened cement pastes (Figs. 12 and 13), the difference is mainly observed below the RH of about 0.7 in the desorption isotherms while some small difference can be found above the RH of about 0.5–0.6 in the absorption isotherms. The pronounced differences in the desorption isotherms obtained for well hydrated concrete as reported in [16–18] were not observed in this study.

To study the influence of the temperature dependent properties of water on the sorption isotherms, the isotherms at the temperature of 33 °C and 40 °C can be roughly extrapolated from the measured isotherm (absorption or desorption) under 25 °C by assuming all water to be capillary condensed water and using the Kelvin equation which is [8]

$$\frac{1}{r_{k1}}+\frac{1}{r_{k2}}=-\frac{RT\rho_w}{M_w\gamma_w}\ln(\phi) \tag{2}$$

where M_w, γ_w and ρ_w is the molecular weight, surface tension of the liquid–gas interface and the density of water, respectively; ϕ is the RH, R the gas constant and T the temperature in Kelvin degree; r_{k1} and r_{k2} denote the two principal radii of the curvature of the liquid meniscus and the contact angle is assumed as zero. The temperature dependence of the surface tension and density of water are considered following Eq. (3) (in the unit of N/m) [29] and Eq. (4) (in the unit of kg/m^3) [30], respectively.

$$\gamma_w=(-0.0167t+7.598)\cdot 10^{-2} \tag{3}$$

$$\rho_w=2\cdot 10^{-5}t^3-0.006t^2+0.0227t+999.94 \tag{4}$$

where $t=T-273.15$ $(0<t<100)$. For the same radius of a curvature, the corresponding relative humidity will be changed according to

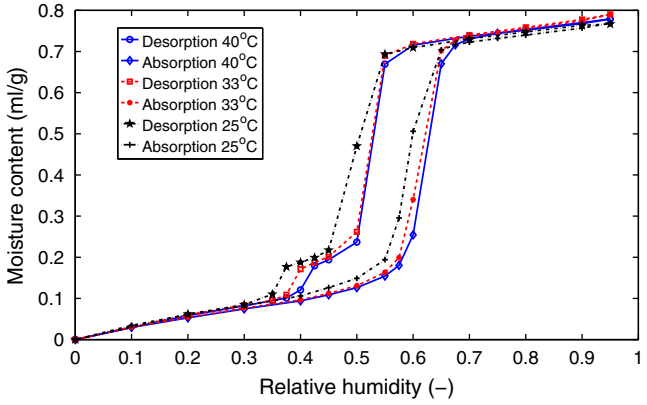

Fig. 11. The temperature dependent sorption isotherms for MCM-41 measured at 25 °C, 33 °C and 40 °C. The moisture content is expressed as gram water per gram of dry material and the mass of the dry sample is determined at the point where RH = 0.

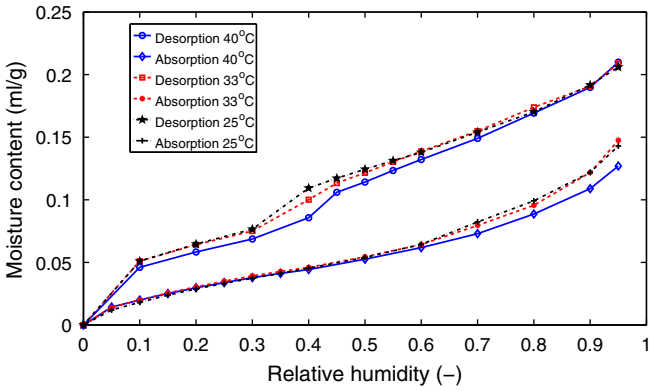

Fig. 12. The temperature dependent sorption isotherms for CEM I measured at 25 °C, 33 °C and 40 °C. The moisture content is expressed as gram water per gram of dry material and the mass of the dry sample is determined at the point where RH = 0.

the Kelvin equation Eq. (2) at different temperatures. The shift of the relative humidity can be expressed as

$$\ln(\phi_2) = \frac{T_1 \rho_{w1} \gamma_{w2}}{T_2 \rho_{w2} \gamma_{w1}} \ln(\phi_1) \tag{5}$$

where the indices 1 and 2 indicate the properties under two different temperatures. By plotting the moisture content measured under T_1 (corresponding to 25 °C in this case) against the calculated relative humidity ϕ_2 (corresponding to 33 °C or 40 °C in this case), the impact of the temperature dependent properties of water on the sorption isotherms can be estimated. It should be mentioned that this extrapolation does not distinguish the adsorbed water and capillary condensed water and assumes all the water is capillary condensed, thus it is just an approximation.

The comparison between the measured and the extrapolated isotherms (based on the isotherm measured at 25 °C) at the temperature 33 °C and 40 °C for MCM-41 are shown in Fig. 14 (absorption) and Fig. 15 (desorption). It can be observed that the temperature dependent properties of water can account for most of the observed temperature effect on the measured sorption isotherms. For the two hardened cement pastes, the measured and the extrapolated desorption isotherms are shown in Fig. 16 (for CEM I) and Fig. 17 (for CEM III), respectively. Again the temperature dependent properties of water can account for some of the observed temperature effect on the measured sorption isotherms. However, there are still some differences between the measured and the extrapolated desorption isotherms, especially when the RH is in the range of 0.3–0.5, indicating that solely taking into account the temperature dependent properties of water might not be able to explain all the differences. It should be noted that the remaining differences may be due to the adsorbed layer which is not considered in the

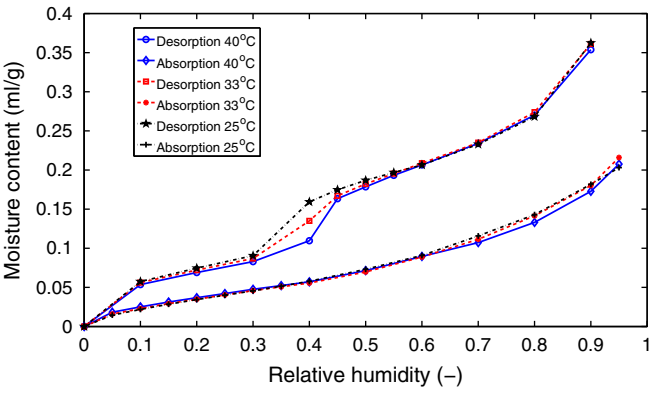

Fig. 13. The temperature dependent sorption isotherms for CEM III measured at 25 °C, 33 °C and 40 °C. The moisture content is expressed as gram water per gram of dry material and the mass of the dry sample is determined at the point where RH = 0.

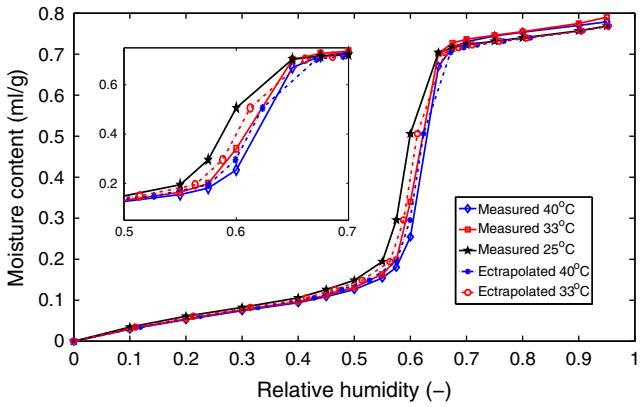

Fig. 14. The comparison between the measured and the temperature extrapolated absorption isotherms for MCM-41 under the temperature 33 °C and 40 °C. The extrapolation is based on the isotherm measured at 25 °C according to Eq. (5).

extrapolation as mentioned earlier. Compared with the results for MCM-41 in which limited differences are found between extrapolated and measured isotherms (silica gel is considered as temperature resistant with respect to the pore volumes and shape at the adopted measuring temperatures), it tends to motivate that may be the elevated temperature slightly change the microstructure of the studied hardened cement paste samples, as discussed in [22,23]. The extrapolations on the absorption isotherms for the two hardened cement pastes are not presented here. However, a close check of Figs. 12 and 13 shows that the moisture contents measured at 33 °C and 40 °C below the RH of about 0.5 are slightly higher than that measured at 25 °C. This is not in accordance with what is predicted by considering the temperature effect, which is that lower moisture content should be measured at a higher temperature. Hence, the volume of the pores whose corresponding capillary condensation relative pressures are lower than 0.5 might be increased slightly at the elevated measuring temperatures, which is somewhat similar to the effect caused by the drying as reported in [1].

The current study regarding the influence of the temperature on the sorption isotherms of hardened cement pastes suggests that the differences in the sorption isotherms at different temperatures are mainly caused by the temperature dependent properties of water and to some extent due to slight microstructure changes of the paste samples at elevated temperatures. The pronounced impact of temperature on desorption isotherms of cement based materials as reported in [16–18] are not found in this study.

It should be mentioned that the exact reasons for the relatively inconsistent results with respect to the impact of temperature on sorption isotherms of cement based materials as reported in literature are not

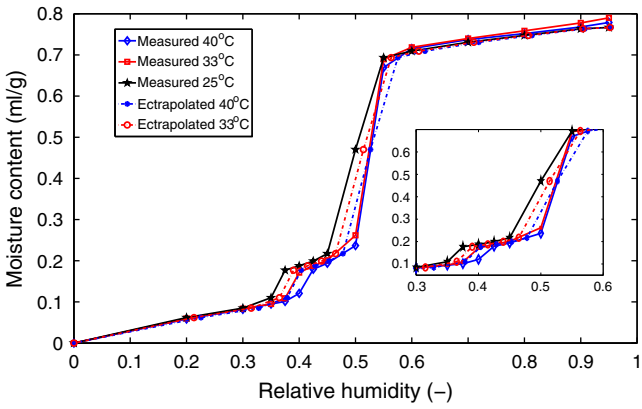

Fig. 15. The comparison between the measured and the temperature extrapolated desorption isotherms for MCM-41 under the temperature 33 °C and 40 °C. The extrapolation is based on the isotherm measured at 25 °C according to Eq. (5).

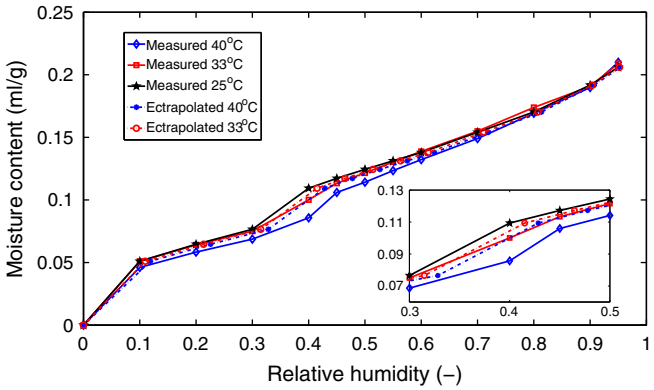

Fig. 16. The comparison between the measured and the temperature extrapolated desorption isotherms for CEM I under the temperature 33 °C and 40 °C. The extrapolation is based on the isotherm measured at 25 °C according to Eq. (5).

clear. However, it might possibly be related to the measurement method adopted. As mentioned before, desiccator method using salt solution has been adopted in many sorption studies, e.g., in [16–21], in which the exposure time at each RH varies from several weeks to months for the equilibrium condition to be established. The different length of the exposure time at different RHs combined with the effect caused by different temperatures during measurements (especially when the measuring temperature is high) could possibly change the pore structure of the studied cement based material to a different extent. That is, the pore structure of the studied material may differ under each studied RH, due to the adopted experimental method (procedures). The argument is supported by a recent SANS study [31] which showed that curing at elevated temperature could result into the changing of the pore structure and extended curing at 20 °C had a similar effect. Since the exposure time and the temperature differ in studies, e.g., in [16–21], it is somewhat not surprising to see the inconsistent results as reported. One advantage of the DVS method used in this study is that the exposure time at each RH is relatively short. Then, the effect due to the pore structure changes during sorption measurements is expected to be minimized.

4. Conclusions

Water vapor sorption isotherms measured by the "dynamic vapor sorption" (DVS) method were used to investigate the possible changes of the pore structure of hardened cement pastes (CEM I and CEM III) subjected to low relative humidities. In addition, the temperature dependency of the sorption isotherms was investigated. Some key points of this investigation can be summarized as follows.

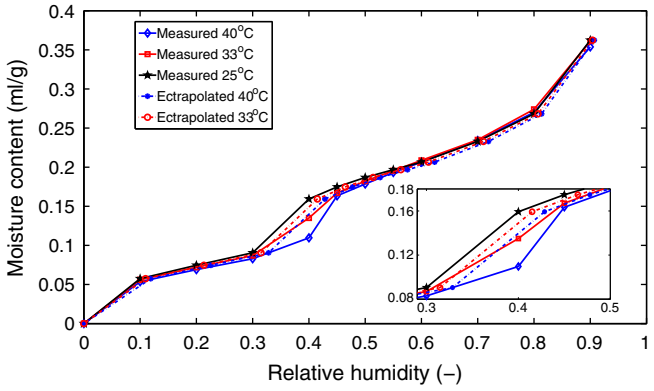

Fig. 17. The comparison between the measured and the temperature extrapolated desorption isotherms for CEM III under the temperature 33 °C and 40 °C. The extrapolation is based on the isotherm measured at 25 °C according to Eq. (5).

1. Small differences were observed between the sorption measurements on a model material MCM-41using different samples. Similarly, only small differences were observed for the investigated hardened cement pastes which indicate that the hardened cement paste samples only to a very limited extent hydrated further during the period of the investigation (about 3–4 months).
2. A resaturation study on the hardened cement paste samples was conducted in order to investigate the possible microstructure changes caused by the drying at low RHs during desorption measurements. Following the first original desorption–absorption cycle, the samples were resaturated and a second desorption measurement was performed. The measurement results show that the second desorption isotherm was in all essential parts similar to the first one. That is, either the drying did not cause any microstructure changes during the desorption at low RHs or if the microstructure changes did occur, the absorption process must have been able to restore the pore structure of hardened cement paste samples. The latter is in agreement with the results obtained using small-angle X-ray scattering measurements [27], small-angle neutron scattering measurements [28] and the findings in [1]. But it also disagrees with some other studies, e.g., [11–13,15]
3. The influence of temperature on the sorption isotherms was studied. Only limited impact was observed and the results suggest that the differences between sorption isotherms under different temperatures are mainly caused by the temperature dependent properties of water. The pronounced impact of temperature on desorption isotherms of cement based materials as reported in [16–18] was not found.

Acknowledgment

The research leading to these results has received funding from the European Union Seventh Framework Programme (FP7/2007-2013) under grant agreement 264448.

References

[1] V. Baroghel-Bouny, Water vapour sorption experiments on hardened cementitious materials: part I: essential tool for analysis of hygral behaviour and its relation to pore structure, Cem. Concr. Res. 37 (3) (2007) 414–437.
[2] N.A. Seaton, Determination of the connectivity of porous solids from nitrogen sorption measurements, Chem. Eng. Sci. 46 (8) (1991) 1895–1909.
[3] V. Baroghel-Bouny, Water vapour sorption experiments on hardened cementitious materials. Part II: essential tool for assessment of transport properties and for durability prediction, Cem. Concr. Res. 37 (3) (2007) 438–454.
[4] V. Baroghel-Bouny, M. Mainguy, O. Coussy, Isothermal drying process in weakly permeable cementitious materials—assessment of water permeability, International Conference on Ion and Mass Transport in Cement-Based Materials, 1999, pp. 59–80.
[5] V. Baroghel-Bouny, M. Mainguy, T. Lassabatere, O. Coussy, Characterization and identification of equilibrium and transfer moisture properties for ordinary and high-performance cementitious materials, Cem. Concr. Res. 29 (8) (1999) 1225–1238.
[6] M. Thiery, V. Baroghel-Bouny, G. Villain, P. Dangla, Numerical modeling of concrete carbonation based on durability indicators, in: V.M. Malhotra (Ed.), Proceedings of the 7th CANMET/ACI International Conference on Durability of Concrete, 2006, pp. 765–780.
[7] B. Bary, A. Sellier, Coupled moisture–carbon dioxide–calcium transfer model for carbonation of concrete, Cem. Concr. Res. 34 (10) (2004) 1859–1872.
[8] K. Sing, D. Everett, R. Haul, L. Moscou, R. Pierotti, J. Rouquerol, T. Siemieniewska, Reporting physisorption data for gas/solid systems, Pure Appl. Chem. 57 (4) (1985) 603–619.
[9] M. Janz, B.F. Johannesson, Measurement of the moisture storage capacity using sorption balance and pressure extractors, J. Build. Phys. 24 (4) (2001) 316–334.
[10] V. Kocherbitov, L. Wadsö, A desorption calorimetric method for use at high water activities, Thermochim. Acta 411 (1) (2004) 31–36.
[11] R.F. Feldman, Sorption and length-change scanning isotherms of methanol and water on hydrated Portland cement, Proc. of 5th Int. Congress on the Chemistry of Cement, vol. 3, Cem. Assoc. of Japan, Tokyo, 1968, pp. 53–66.
[12] H.M. Jennings, A model for the microstructure of calcium silicate hydrate in cement paste, Cem. Concr. Res. 30 (1) (2000) 101–116.
[13] J.J. Thomas, H.M. Jennings, A colloidal interpretation of chemical aging of the C-S-H gel and its effects on the properties of cement paste, Cem. Concr. Res. 36 (1) (2006) 30–38.
[14] H.M. Jennings, Refinements to colloid model of C-S-H in cement: CEM-II, Cem. Concr. Res. 38 (3) (2008) 275–289.

[15] E.H. Atlassi, Influence of silica fume on the pore structure of mortar when measured by water vapour sorption isotherms, The Modelling of Microstructure and its Potential for Studying Transport Properties and Durability, Springer, 1996, pp. 257–270.
[16] S. Poyet, Experimental investigation of the effect of temperature on the first desorption isotherm of concrete, Cem. Concr. Res. 39 (11) (2009) 1052–1059.
[17] S. Poyet, S. Charles, Temperature dependence of the sorption isotherms of cement-based materials: heat of sorption and Clausius–Clapeyron formula, Cem. Concr. Res. 39 (11) (2009) 1060–1067.
[18] J. Hundt, H. Kantelberg, Sorptionsuntersuchungen an zemestein, zementmörtel und beton (in German), Dtsch. Aussch. Stahlbeton 297 (1978) 25–39.
[19] J.F. Daian, Condensation and isothermal water transfer in cement mortar, Part I—pore size distribution, equilibrium water condensation and imbibition, Transp. Porous Media 3 (6) (1988) 563–589.
[20] F. Radjy, E.J. Sellevold, K.K. Hansen, Isoteric vapor pressure–temperature data for water sorption in hardened cement paste: enthalpy, entropy and sorption isotherms at different temperatures, Technical Report BYG-DTU R057, Technical University of Denmark (DTU), Lyngby, Denmark, 2003.
[21] T. Ishida, K. Maekawa, T. Kishi, Enhanced modeling of moisture equilibrium and transport in cementitious materials under arbitrary temperature and relative humidity history, Cem. Concr. Res. 37 (4) (2007) 565–578.
[22] Z.P. Bazant, W. Thonguthai, Pore pressure and drying of concrete at high temperature, J. Eng. Mech. Div. 104 (5) (1978) 1059–1079.
[23] B. Bary, A polydispersed particle system representation of the porosity for non-saturated cementitious materials, Cem. Concr. Res. 36 (11) (2006) 2061–2073.
[24] B. Johannesson, Moisture fixation in mature concrete and other porous materials (8A), Lecture notes for Introduction to Concrete Technology (11563), Technical University of Denmark, 2011.
[25] H.H. Willems, K.B. Van Der Velden, A gravimetric study of water vapour sorption on hydrated cement pastes, Thermochim. Acta 82 (1) (1984) 211–220.
[26] M. Åhs, Redistribution of moisture and ions in cement based materials, PhD thesis Division of Building Materials, Lund University, 2011.
[27] D.N. Winslow, S. Diamond, Specific surface of hardened Portland cement paste as determined by small-angle X-ray scattering, J. Am. Ceram. Soc. 57 (5) (1974) 193–197.
[28] D. Pearson, A.J. Allen, A study of ultrafine porosity in hydrated cements using small angle neutron scattering, J. Mater. Sci. 20 (1) (1985) 303–315.
[29] Engineering toolbox, URL http://www.engineeringtoolbox.com/water-surface-tension-d_597.html(Accessed on December 13, 2012).
[30] Engineering toolbox, URL http://www.engineeringtoolbox.com/water-density-specific-weight-d_595.html(Accessed on December 13, 2012).
[31] H.M. Jennings, J.J. Thomas, J.S. Gevrenov, G. Constantinides, F.-J. Ulm, A multi-technique investigation of the nanoporosity of cement paste, Cem. Concr. Res. 37 (3) (2007) 329–336.

Paper VII

Application of water vapor sorption measurement for porosity characterization of hardened cement pastes

M. Wu, B. Johannesson, M. Geiker

Accepted by: *Construction and Building Materials, 2014*

Application of water vapor sorption measurement for porosity characterization of hardened cement pastes

Min Wu[a], Björn Johannesson[a], and Mette Geiker[b]

a. Department of Civil Engineering, Building 118, Technical University of Denmark, 2800 Lyngby, Denmark

b. Department of Structural Engineering, Norwegian University of Science and Technology, Trondheim, Norway

Abstract

Water vapor sorption can be used to study important properties of porous materials including specific surface area and pore size distribution (PSD). However, the data analysis is somewhat inconsistent in literature. In this work, the important factors influencing the analyzed results using sorption data were reviewed. Water vapor sorption measurements were then applied to two hardened cement pastes and one model porous material MCM-41. The specific surface area was calculated based on different equations accounting for multilayer adsorption and the PSD was analyzed from both the absorption and the desorption isotherms for comparison. The calculated specific surface area was quite dependent on which equation is considered for multilayer adsorption. For the studied hardened cement pastes, three characteristic peaks were found in the calculated PSD curves from the desorption isotherms with corresponding radii of 1.4, 1.8 and 3.0 nm while the peak at 1.4 nm was missing in the PSD curves calculated from the absorption isotherm. The network theory, suggesting desorption is controlled by the pore entry sizes while absorption is controlled by the interior pore sizes, tends to be of great relevance in explaining the results.

Keywords: Microstructure, specific surface area; pore size distribution; adsorption; cement paste; network theory.

1. Introduction

Porosity is one of the most important characteristics of cement based materials. Vapor sorption measurement has been widely used to determine the specific surface area and the pore size distribution of porous materials [1, 2]. The calculation of specific surface area is normally based on the classical BET theory [3]. With respect to the pore size distribution, the method proposed by Barret, Joyner and Halenda (the BJH model) [4] is widely adopted. The BJH model is based on the assumption that there are two types of liquid existing simultaneously in the pores of a material due to different binding mechanisms, i.e., adsorption and capillary condensation. This assumption allows the determination of the pore size distribution for pores in the meso-size and micro-size range (following the classification of International Union of Pure and Applied Chemistry (IUPAC) [2]). For clarification purpose, a note is made here about the terminology "adsorption" and "absorption". In many cases, e.g., see [2], "adsorption" is used in describing the process of the liquid uptake, including both the adsorbed and the capillary condensed liquid. Other authors, e.g., see [5, 6], use "absorption" to describe exactly the same content, i.e., including both types of liquid uptake. Since the BJH model will be used throughout this study and to avoid any confusion, the expression "absorption" will be used to describe the combined

effect of both multilayer adsorption and capillary condensation while "adsorption" simply refers to the liquid fixed due to multilayer adsorption.

Sorption measurement using nitrogen is perhaps the most common technique adopted in the context of porosity characterization and it has been studied rather extensively, e.g., see [1, 7, 8]. However, a comparison study performed by Hagymassy et al. [9] using both nitrogen and water vapor in characterizing hardened cement paste samples has demonstrated that both the total calculated pore volume and the calculated surface area using water vapor data are much larger compared with that using nitrogen data. The main reason was explained by the fact that the nitrogen cannot penetrate into the entire pore system of hardened cement pastes due to the relatively big molecular size. It was, further, pointed out by the same authors that the use of nitrogen will result in that not only the smallest pores but also many big pores, which are the so-called ink-bottle pores with small entry or neck sizes but big interior sizes, are left out of consideration in the measurement using nitrogen. That is the smallest pore entries or necks constraint the penetration of nitrogen molecules into the body of ink-bottle pores. Consequently, the pore structure analysis using nitrogen was concluded to be of little value in studying the porous materials of complex pore structure with wide distribution of pore sizes, e.g., the hardened cement pastes. As the main purpose of this work is to study hardened cement pastes, water vapor is considered more suitable than nitrogen in the context of the porosity characterization. Another reason for using water vapor in studying cement based materials is that the pre-drying of the samples can be avoided compared with that using nitrogen since the drying process in some cases results in certain alteration of the pore structure of hardened cement pastes [10].

Sorption behavior of water vapor on porous materials can be used to study important characteristics of the materials, e.g., the specific surface area and the pore size distribution. As an indirect method, some important factors which influence the analyzed results using sorption data need to be considered.

1.1. Equations accounting for multilayer adsorption

The calculation of the specific surface area is based on the equation considered for multilayer adsorption. A number of equations have been developed and the most representative ones are discussed as follows. It should be noted that the calculated specific surface area of a material for most cases would be different if different equations accounting for multilayer adsorption are considered.

The first sound theoretical development of the relation between the amount of adsorbed vapor and the relative pressure under equilibrium is attributed to Langmuir [11]. However, the limitation of the Langmuir model is that adsorption is restricted to the monolayer. A major step in the understanding of adsorption is the development of the BET multilayer adsorption theory Brunauer et al. [3]. After the development of the BET theory, a number of adsorption equations have been developed using the similar concepts. A summary of different equations with respect to multilayer adsorption can be found, e.g., in [1]. However, the standard BET equation remains the most important one. The standard BET equation is

$$\frac{v}{v_m} = \frac{cx}{(1-x)(1+cx-x)} \tag{1}$$

where v is the adsorbed moisture content (in the case of water vapor), v_m is the so-called monolayer capacity (the moisture content corresponding to that the first layer of the material surface is fully occupied), c is a constant related to the energy of adsorption and x is the relative pressure (humidity). To derive the standard BET equation, it is assumed that only the molecules in the first layer have a condensation heat that is different from that of the bulk water and that the heat of condensation in the second and higher adsorbed layers are equal, which is the same as the heat of liquefaction [3, 12]. Johannesson [13] further studied the assumption regarding the heat of condensation, the assumption

being modified so that both the condensation heat of the water molecules on the first layer and second layer are different from that of the normal bulk water while the water molecules on the third and higher layers have the same condensation heat as that of bulk water. By introducing this new assumption and combining other assumptions which are also made in obtaining the standard BET equation, a new equation, designated as the two-layer BET equation, can be obtained as

$$\frac{v}{v_m} = \frac{cx[1 + (b-1)(2x - x^2)]}{(1-x)[cx^2(b-1) + (c-1)x + 1]} \tag{2}$$

where there is one more constant parameter b accounting for the modified assumption concerning the condensation heat compared with the standard BET equation. With the help of a so-called sorption calorimeter [14, 15], it is possible to study the assumptions regarding the heat of condensation of the water on different layers. Johannesson [13] conducted detailed studies by comparing the measured differential heat of adsorption and the predicted value based on the standard BET equation and the two-layer BET equation for different porous materials. The results showed a better agreement between the measured differential heat of adsorption and the value predicted based on two-layer BET equation compared with that obtained by using the standard BET equation. It was concluded that the assumptions about heat of condensation behind the two-layer BET equation is more adequate compared with that using the standard BET equation.

Guggenheim [16], Anderson [17] and de Boer [18] modified the standard BET equation by assuming that the heat of condensation of the water molecules on the second and all the higher layers are the same, but different from that of bulk water, and a good agreement was found between the experimental data and the modified equation on different tested adsorbates. The modified equation is the so called GAB equation [19], which is

$$\frac{v}{v_m} = \frac{ckx}{(1-kx)[1 + (c-1)kx]} \tag{3}$$

Similar to the two-layer BET equation, there is one more constant, k, as compared to the standard BET equation. The property k is related to the modified assumption about the condensation heat compared with the standard BET equation.

Dent [20, 21] conducted some related studies and further discussed that the heat of condensation could actually differ for each layer, but the difference between the second and higher layers tends to be small. In addition, the mathematical complexity would be increased considerably if each of the layer was treated differently. Thus, for simplicity it was assumed that water molecules on the second and all the higher layers have the same condensation heat but different from that of bulk water. The Dent equation is based on the same principles as the GAB equation and also has the same mathematical form. It should be mentioned that Brunauer et al. [22] introduced an extension of the BET equation using a parameter k, whose value represents a measure of the attraction force of the adsorbent. Although the basis is quite different, Brunauer et al. arrived at an equation identical to the GAB equation. Thus, it might be reasonable to think that the parameter k may not only be related to the heat of condensation but also to other factors , e.g., the attractive forces.

1.2. The thickness of the adsorbed layer

In order to calculate the pore size distribution according to the BJH model, it is necessary to know the thickness of the adsorbed layer. As we know, the BJH model assumes two types of water, i.e., the adsorbed water and the capillary condensed water [4]. However, the sorption measurement itself cannot distinguish the two types of water and only measures the total moisture content at a given

relative humidity (RH). That is, the thickness of the adsorbed layer of water needs to be determined beforehand in the calculation of a pore size distribution.

It is often assumed that the statistical thickness of the adsorbed layer on a solid surface is a function of the relative humidity and the plot of this function is normally called the $t-$curve. The $t-$curve can be obtained by using the volume of the moisture adsorbed on the surface of an adsorbent divided by the surface area as

$$t = (V_{ad}/S) \cdot 10^{-3} \tag{4}$$

where t is the statistical thickness of the adsorbed layer in nm, V_{ad} is the adsorbed volume on the surface in $\mathrm{cm}^3 \cdot \mathrm{g}^{-1}$ and S is the surface area in $\mathrm{m}^2 \cdot \mathrm{g}^{-1}$. There is no direct means to obtain the exact surface area S of a material, and normally the BET specific surface area is used instead due to its wide application, e.g., in [23, 24]. It should also be noted that there are some discussions on to which extent the BET specific surface area represents the true geometrical surface area of a studied material [25]. More related discussions regarding this will be presented in Section 3. As mentioned earlier, the moisture content measured on a porous material during an absorption experiment at a relatively high RH contains both the adsorbed and the capillary condensed water and therefore it is not possible to obtain the V_{ad} directly from the measured data. For most cases, the standard BET equation predicts too high moisture content for adsorption at high RHs (as will be demonstrated later, the two-layer BET equation and the GAB equation have the similar weakness), thus it is not relevant to use this kind of prediction in the whole relative humidity range. Therefore, $t-$curves are often determined experimentally from nonporous adsorbents, where the capillary condensation is considered absent. Initially it was argued that a universal $t-$curve existed for all nonporous materials. This argument was later revised and it was proposed that the $t-$curve should be a function of the physicochemical and thermodynamic nature of the sample surface which can be interpreted in terms of the constant c obtained from analyzing the standard BET equation, e.g., in [23].

Numerous $t-$curves have been proposed for nitrogen adsorption and a review in this aspect can be found, e.g., in [1, 26]. As far as water vapor is concerned, Hagymassy et al. [9] studied the adsorption behavior on several types of adsorbents, such as silica gel, rutile and quartz and generalized four $t-$curves based on the different calculated energy constants c using the standard BET calculation. These types of $t-$curves are commonly used for determining the pore size distribution using water vapor. Apart from the $t-$curves proposed by Hagymassy et al., there are some other suggestions. The empirical Halsey equation has been used, e.g., see [27, 28]

$$t = -d(\frac{A}{\ln\phi})^B \tag{5}$$

where d is the thickness of a monolayer water molecules, ϕ is the relative humidity, A and B are constants. Espinosa and Franke [25] adopted an empirical equation accounting for the $t-$curve as

$$t = 0.395 - 0.189\ln(-\ln\phi) \tag{6}$$

By noting the commonly occurring overestimation of the adsorbed moisture content as predicted by the standard BET equation at high relative humidities (the predicted moisture content often ends up with infinity), Johannesson [12], in the context of pore size distribution calculations, assumed that only the water molecules in the first and second layer are considered in calculating the thickness of the adsorbed layer. Following this concept, the moisture contents in the first and second layer can be calculated based on the equations accounting for multilayer adsorption, e.g., using the standard or the two-layer BET equation, and then they can be used to calculate the $t-$curves using

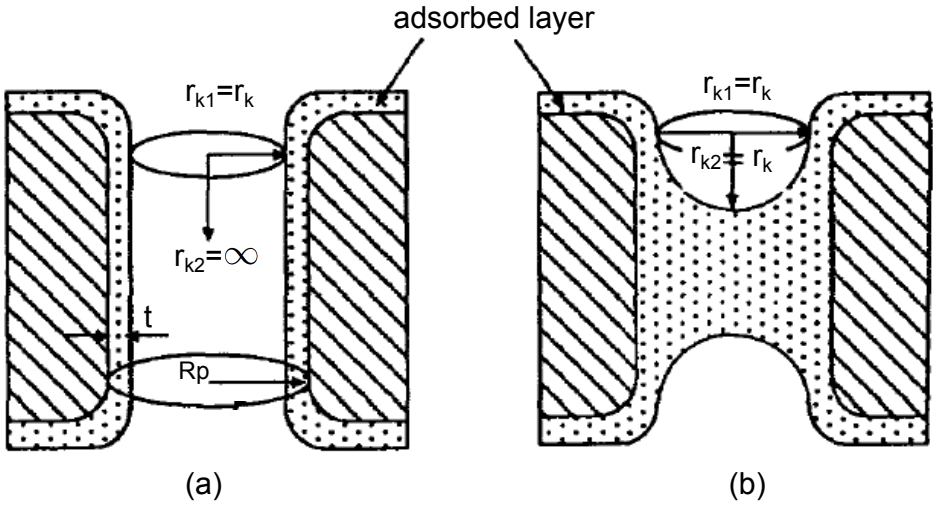

Figure 1: One proposed hypothesis explaining the hysteresis: different radii of the curvature during absorption (a) and desorption (b) for a cylindrical pore, slightly modified based on [1].

$$t = d \cdot \frac{v_1 + v_2}{v_m} \tag{7}$$

where v_1, v_2 and v_m are the calculated moisture content in the first layer, the second layer and the monolayer capacity, d is the thickness of a monolayer water molecules. The thickness of the first two layers are to be added to the calculated Kelvin radii at a certain relative humidity to obtain the radii of the studied pores. It should be mentioned that the calculation of the $t-$curves using this method is a somewhat crude approximation, but it has the advantage that the $t-$curves for an adsorbate on an adsorbent can be determined directly from the measured absorption data without considering any additional reference data. This is of interest since the adsorption behavior could be unique for an adsorbate combined with a certain adsorbent. The comparisons of different adopted $t-$curves for the studied materials will be presented later.

1.3. Sorption hysteresis

Sorption hysteresis refers to the phenomenon that the absorption isotherm follows a different path compared with the desorption isotherm, leaving a hysteresis loop between the two isotherms. The hysteresis phenomenon has attracted significant attention, e.g., see [1, 2, 29–31], and some recent progress can be found, e.g., in [32, 33]. The origin of the hysteresis phenomenon has not been fully understood yet. It is, however, generally agreed that the hysteresis is associated with capillary condensation [2]. The detailed discussion of the origin of the hysteresis phenomenon is beyond the scope of this work, with only two representative explanations which would have an important impact on the pore size distribution determination being introduced.

One proposed explanation for the hysteresis is based on the hypothesis that the curvature radii of the same pore are different during the absorption and the desorption, e.g., see [1]. The Kelvin equation is used to determine the radius of a curvature of capillary condensation and it can be related to the

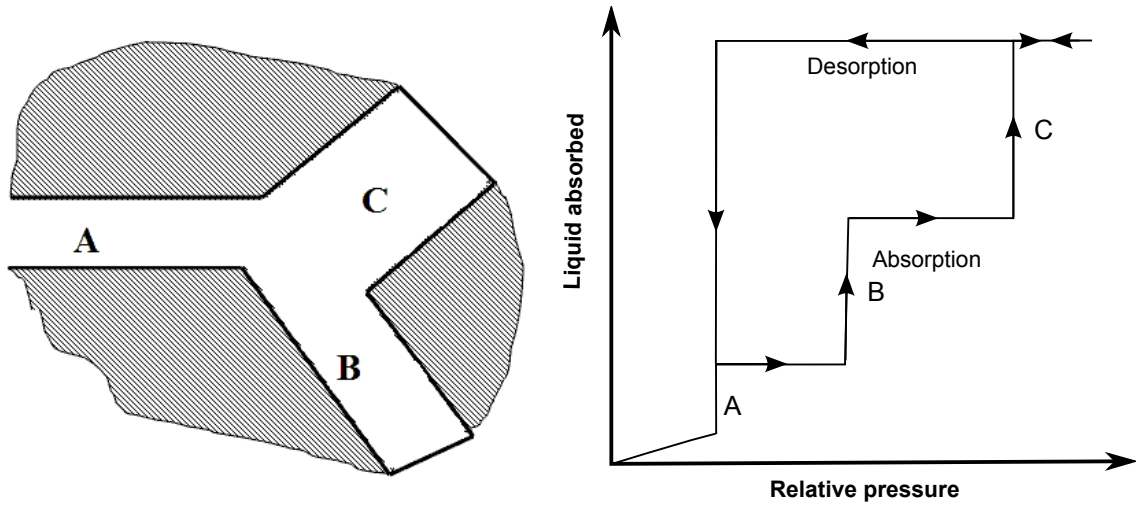

(a) (b)

Figure 2: An illustration of the proposed pore network concept accounting for hysteresis: (a) a pore system of three pores forming a network in a porous material, slightly modified based on [38] and (b) the corresponding schematic absorption and desorption isotherms, where the desorption isotherm is always higher than the absorption during the relative pressure range of capillary condensation of the three pores.

radii at the two principal directions r_{k1} and r_{k2}, which can be written as

$$\frac{1}{r_{k1}} + \frac{1}{r_{k2}} = -\frac{RT\rho_w}{M_w\gamma_w}\ln(\phi) \tag{8}$$

where M_w, γ_w and ρ_w is the molecular weight, surface tension of the liquid-gas interface and the density of water respectively, R is the gas constant and T is the temperature in Kelvin degree. Figure 1 schematically shows the concept considered for a cylindrical pore. According to this hypothesis, during absorption $r_{k1} = r_k$ and $r_{k2} = \infty$; while during the desorption, $r_{k1} = r_{k2} = r_k$. By inserting these relations into Eq.8, one obtains that the relative humidity for capillary condensed water in absorption (denoted as ϕ_A) and in desorption (denoted as ϕ_D) are different in the same pore, the relation being $\phi_D = \phi_A^2$. That is to say, for the same amount of moisture content, $\phi_D < \phi_A$. Thus, the desorption curve is by the model predicted to be above the the absorption curve during a hysteresis loop. The author [1] further extended the applicability of the same concept to other pore shape assumptions, including ink-bottle pores, parallel plate (slit) pores and wedge shaped pores. It was concluded that the relation as derived, i.e., $\phi_D = \phi_A^2$, also holds for the different pore models.

Following the concept of the above explained model, the hysteresis between the absorption and desorption curves would be an intrinsic property of porous materials during the sorption measurements, meaning it will show up as long as capillary condensation takes place. However, it must be noted that there are some studies [34–37] which did reveal that well defined reversible Type IV isotherms (IUPAC classification) are obtainable on a model mesoporous material MCM-41, without showing any hysteresis at all. Taking into account the reversibility of the absorption and the desorption isotherms for mesoporous materials, it seems that the hypothesis assuming different radii of the meniscus curvature in the absorption and desorption is not applicable in explaining the hysteresis phenomenon.

Another proposed approach which is called network theory or pore-blocking concept attributes the

hysteresis to the inter-connectivity of the pore system, e.g., see [1, 38]. An illustration of this model can be given by looking at a simplified pore system with three pores forming a network as shown in Figure 2a. The pore size of the three pores decreases in the sequence of pore C, pore B and pore A. Pore B and pore C are closed at one end. During the absorption, the vapor will enter and condensate in the pores in the sequence of pore A, pore B and pore C. Even though the small pores are filled first, they do not block off what is happening in the internal big pores closed at one end and the big pores can be filled through evaporation from the end connecting with small pores [1]. When the absorption process is finished at a certain relative pressure, all the three pores are filled with the liquid. During desorption, as the relative pressure decreases, theoretically the liquid in pore C should be vaporized and emptied first and after this, pore B and pore A will be emptied, which is the opposite process of the absorption process described previously. However, the liquid in pore B and pore C cannot vaporize at their condensation pressure because the liquid is not in contact with the vapor phase and the liquid in pore B and pore C will be under a metastable condition. When the relative pressure decreases to the condensation pressure of pore A, the liquid in pore A will vaporize and the liquid in both pore B and pore C will also vaporize at this point since they are no longer blocked by the liquid in pore A. That is, during desorption, the liquid in the three pores will vaporize at the same relative pressure, i.e., the condensation pressure for pore A in this case. This will result into that the moisture content measured during the desorption at the relative pressures higher than that of the condensation pressure of pore A will always be higher than the moisture content measured during the absorption, i.e., resulting into a hysteresis loop, the isotherms being schematically shown in Figure 2b. The network effect is also mentioned sometimes as the pore blocking effect, e.g., in [31, 39]. The controlling pore size of the network, e.g., pore A in this case, can be referred to as the entry or neck size [40, 41] in the context of porosity description. It should be mentioned that it is not appropriate to treat this network effect absolutely the same as that caused by the so called "ink-bottle" pores, since the network effect depicts the complex pore structure in the three dimensional space while the concept of "ink-bottle" pores provides a too simplified picture in this regard as discussed by, e.g., Sing et al. [2].

With the above mentioned network hypothesis, it is straightforward to explain the reversibility of the absorption isotherm and the desorption isotherm for a given porous material, which cannot be explained by the previously described hypothesis assuming different radii of the meniscus curvature in the absorption and the desorption, as illustrated in Figure 1. No hysteresis simply indicates the absence of any pore blocking effect in the porous material. In this sense, it seems more reasonable to assume that the network theory is more relevant in explaining the hysteresis phenomenon compared with that assuming different meniscus curvature radii in absorption and desorption. This argument is somewhat supported by the discussions in, e.g., [24, 39], claiming that the sorption hysteresis is only a "short term" phenomenon and it will disappear given a long enough time.

Porosity characterization using water vapor measurements has been studied for a while. However, the analysis of sorption data is somewhat inconsistent in literature due to some non-fully solved factors, e.g., the ones discussed above. In this work, the impact of using different equations proposed for multilayer adsorption on the calculated specific surface area will be studied. The influence of the different $t-$curves on the derived pore size distribution will also be discussed and the pore size distribution will be derived from both the absorption and the desorption isotherms. Additionally, the network theory will be demonstrated as a concept of particular interest in explaining the differences found between the absorption and desorption measurements and the properties derived from the absorption and the desorption isotherm of the studied porous materials.

Table 1: Properties and the chemical composition of the two cements used in this study.

		CEM I (CEM I 32.5 R)	CEM III (CEM III/B 42.5 N)
Density	(g/cm^3)	3.06	2.90
Fineness	(cm^2/g)	2905	4635
Water demand	(%)	26.2	32.3
Initial setting time	(min)	185	270
Loss on ignition	(%)	2.1	1.4
SiO_2	(%)	20.6	29.2
Al_2O_3	(%)	5.6	8.9
Fe_2O_3	(%)	2.4	1.2
CaO	(%)	63.4	48.0
MgO	(%)	1.6	4.8
SO_3	(%)	2.9	2.6
K_2O	(%)	0.7	0.6
Na_2O	(%)	0.2	0.2
Cl	(%)	<0.1	<0.1

2. Experimental

2.1. Materials

Three materials were studied in this investigation: one model mesoporous material MCM-41 and two types of hardened cement pastes. The primary purpose of including the model material in this investigation is to validate the applicability of sorption measurement using water vapor in the context of surface area and porosity determination.

MCM-41 is a silica based material and its pore structure is in the form of hexagonal arrays of uniform tubular channels of controlled width. Of this reason, MCM-41 is often used as a model material in porosity studies. The MCM-41 used in this study is produced by Tianjin Chemist Scientific Ltd. The nominal pore diameter provided by the producer is 3.0 nm and the nominal specific surface area and the total pore volume is reported to be $\geq$ 800 m^2/g, $\geq$ 0.70 ml/g respectively.

Two different cements, i.e., CEM I 32.5 R and CEM III/B 42.5 N, were used to prepare the paste samples with a W/C ratio of 0.4. Table 1 shows the properties and the chemical composition of the two cements used. A paddle mixer was used for the mixing of the fresh samples. After mixing, the pastes were cast into plastic vials with a diameter of about 15 mm and a length of about 50 mm with proper compaction. After one day of sealed curing at room temperature (about 20 °C) in the plastic vials, the paste samples were demoulded. Then, each paste sample was placed into a bigger self-sealable plastic flask filled with saturated lime water for curing at room temperature till the desired age for experiments.

The hardened cement paste samples were cured for about 6 months before the sorption measurements. The "dynamic vapor sorption" (DVS) method was used to do the sorption measurements (Section 2.2). Since the sample size which can be used in a DVS instrument is relatively small, it normally means that the hardened cement paste samples need to be crushed and/or even grinding. In some cases, the representativeness of the sample can be questioned. However, it is normally possible to collect a large representative sample and then divide them into a fine powder-like mass. One may also argue that the crushing of a sample might cause the change of the porosity. As the adsorption and capillary condensation studied in this context is at the nanometric scale, it is believed that the

crushing of samples has very little or no effect at all in changing the nanometer porosity, e.g., as illustrated experimentally in [24, 42].

The cylinder samples of the hardened cement pastes were firstly vacuum saturated with saturated lime water and then the crushing and grinding of the samples was conducted in a carbon dioxide free chamber to avoid carbonation. Meanwhile, to avoid possible drying of the samples during the preparation process, the RH inside of the chamber was set at 1 (the measured RH was about 0.90–0.95) and the sample crushing and grinding was conducted rather quickly (in 30–40 min) for each paste. Immediately after that, the ground sample powders were placed into plastic flasks containing saturated lime water with the amount just to cover the powders (for about a week) before the sorption experiments. This procedure was also conducted in the carbon dioxide free chamber. More discussions about the sample preparation can be found in [43].

The hardened cement pastes will be shortly designated as CEM I and CEM III in the following description.

2.2. Sorption measurements

The DVS method was used to study the sorption behaviors of the three porous materials under consideration. The measurements were conducted in a climate incubator where the temperature can be regulated and controlled. The relative humidity was generated into desired proportions by mixing two air flows, i.e., a totally dry (RH = 0) and a totally saturated (RH = 1) air. The proportions of the two flows can be accurately controlled by the flow regulator devices. Figure 3 shows the instrument schematically. The sample was placed into a sample holder at one end of a microbalance. A reference holder, which is symmetrically connected to the sample holder on the other end of the microbalance, was used with the purpose to eliminate the effect of the vapor adsorption on the surface of the sample holder.

One advantage of the DVS method is that the RH can be programmed to vary arbitrarily during a measurement. Additionally, the sample size used in a DVS instrument is often very small, which is on the order of several to tens of milligram (mg). This enables the equilibrium conditions to be achieved rather quickly. It is also of interest to note that the mixed vapor is free of carbon dioxide, which makes this method suitable to study cement based materials, e.g., see [44, 45].

It should be noted that it could take a very long time for the equilibrium condition to be established at a given RH. Actually, it is practically impossible to wait for the establishment of the exact equilibrium condition at each RH in a sorption measurement. The duration time of each RH in the DVS instrument can be controlled by either setting the mass change ratio against time, dm/dt, or setting the duration time directly. Once the set conditions are met, the instrument will directly go to the next step of the set RH scheme. In this study, the dm/dt is set as 0.002% and the shortest and the longest duration time for each step is set to be 0.5 and 24 hours, respectively. The moisture content corresponding to each measured RH will be then extrapolated from the measured data and the details will be presented later. The temperature of the measurements was 25 °C.

The sorption measurement for the model material MCM-41 (as received) in this study started from an absorption (RH from 0 to 0.95) followed by a desorption process (RH from 0.95 to 0). Discussions concerning the possible damage of cement samples when the RH decreases to some low values (typically 0.3-0.4) can be found, e.g., in [24, 46]. Due to this, the experiments with hardened cement paste samples started from the desorption and then followed by the absorption. The purpose of the above described approach is trying to reduce the possible effect caused by the so-called drying damage at low RHs. A more detailed discussion in this aspect will be conducted later combined with the measured experimental data.

The same type of sorption measurement was conducted three times using different samples on the model material MCM-41 and the two hardened cement pastes in this study. The total experimental

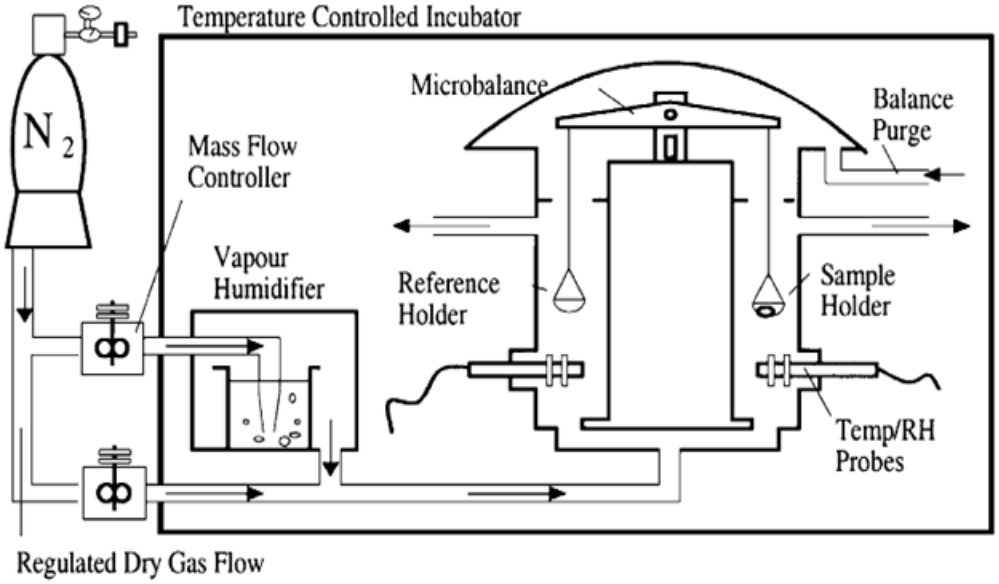

Figure 3: Schematic illustration of a dynamic vapor sorption (DVS) instrument. Dry and saturated air are mixed to generate the desired relative humidity and a symmetric reference holder is used to counteract the adsorption on the sample holder [12].

sorption study lasted for about four months and the sampling of the three measurements were chosen in the beginning, the middle and the end of the total measuring time. By doing so, firstly the repeatability of the instrument can be tested as the model material MCM-41 has a stable pore structure (which will not change against time); and secondly the possible evolution of the pore structure against time for the hardened cement paste samples can also be checked since further hydration might take place in cement based materials in the presence of moisture even though some relatively old samples are used. A more detailed discussion about the measurements of the materials under study is presented elsewhere [43].

3. Results and discussion

3.1. Sorption isotherms

As discussed before, it is practically impossible to wait for the establishment of the exact equilibrium condition at each studied RH step. Therefore, a data processing procedure (curve fitting) is adopted to extrapolate the sample mass so as to represent the equilibrium condition. The sample mass against time in a sorption measurement has been proposed following the equation [47, 48]

$$m(t) = m_f - (m_f - m_0)\mathrm{e}^{-k(t-t_0)} \tag{9}$$

where $m(t)$ is the sample mass at the time t, m_0 represents the initial mass and t_0 is the initial time of the curving fitting, m_f is the fitted asymptotic sample mass at the equilibrium condition for the studied RH and k is a curve fitting constant. Figure 4 shows an example of the extrapolation. The solid line represents the measured data in the experiment, and the dash-dot line is the fitted curve

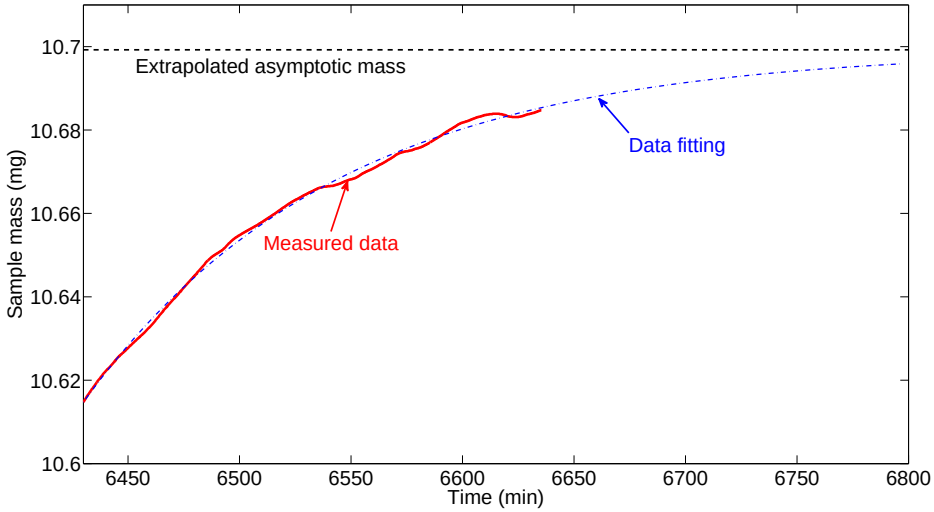

Figure 4: An example showing the data processing procedure to extrapolate the asymptotic sample mass at the equilibrium condition.

and the dot line shows the final extrapolated asymptotic sample mass at the equilibrium condition for the RH step considered.

With the extrapolated data, the corrected isotherms under equilibrium conditions can be constructed. For the sample MCM-41, besides the point at RH = 0, the point with some difference between the extrapolated and the measured isotherms is found at RH = 0.5 in desorption and RH around 0.6 in absorption where moisture condenses/desorbs drastically. For the hardened cement paste samples CEM I and CEM III, the point at RH = 0 is also a point with rather significant difference between the extrapolated and the measured isotherms, which is similar to the sample MCM-41. Additionally, more points with important difference between the extrapolated and the measured desorption isotherms are found at the very high RHs (0.95, 0.9 and sometimes 0.8) of the studied hardened cement paste samples. The reason has been discussed already, i.e., due to the experimental procedure and the pre-setting in the instrument. For the other RH points, the relative difference of the moisture content between the extrapolated and measured data are no more than about 0.5%.

The corrected sorption isotherms of the three studied materials are presented from Figure 5 to Figure 7. Compared with the corrected sorption isotherms of the model material MCM-41, the hysteresis at low RHs is found for the two hardened cement paste samples. The hysteresis at low RHs was reviewed and shortly discussed in [8], arguing that this hysteresis is due to the fact that the thermodynamic equilibrium is still not established at low RHs during absorption. Since the extrapolation process is adopted and the absence of the hysteresis at low RHs in the corrected isotherms of the sample MCM-41, it may indicate that the non-equilibrium assumption is not relevant in this context. However, the hysteresis at low RHs can be better explained if the network theory is considered, which is that higher moisture content measured during the desorption compared with that during absorption is caused by the aforementioned pore-blocking effect. The comparison between the model material MCM-41 and the hardened cement paste samples indicates that the pore-blocking effect may disappear in the MCM-41 at low RHs, while it lasts almost for the whole measured RHs for the hardened

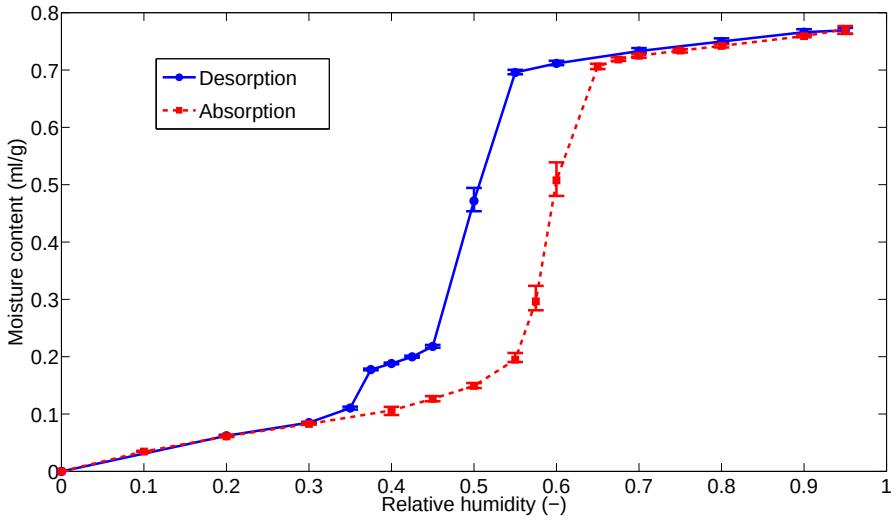

Figure 5: The sorption isotherms for the MCM-41based on the extrapolated data at equilibrium conditions and the error bar shows the variation of three different measurements. The moisture content is expressed as ml water per gram of dry sample and the mass of the dry sample is determined at the point where RH = 0.

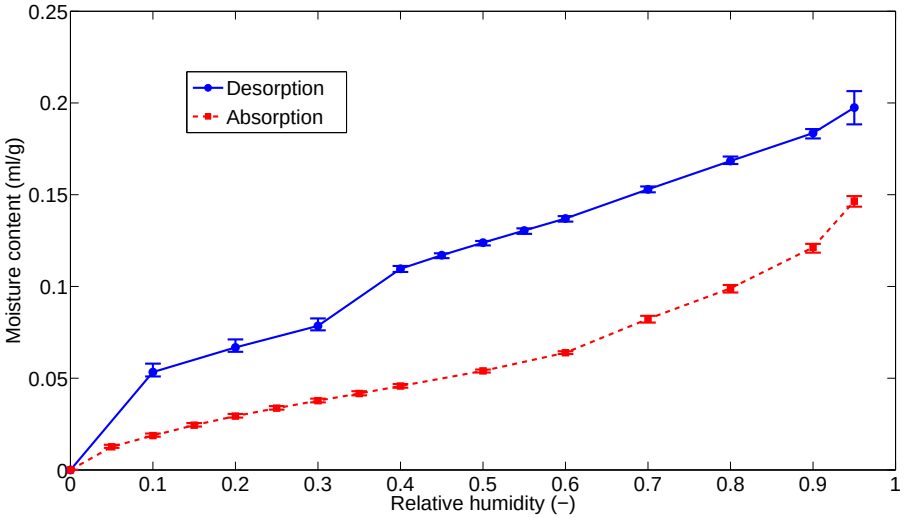

Figure 6: The sorption isotherms for the paste CEM I based on the extrapolated data at equilibrium conditions and the error bar shows the variation of three different measurements. The moisture content is expressed as ml water per gram of dry sample and the mass of the dry sample is determined at the point where RH = 0.

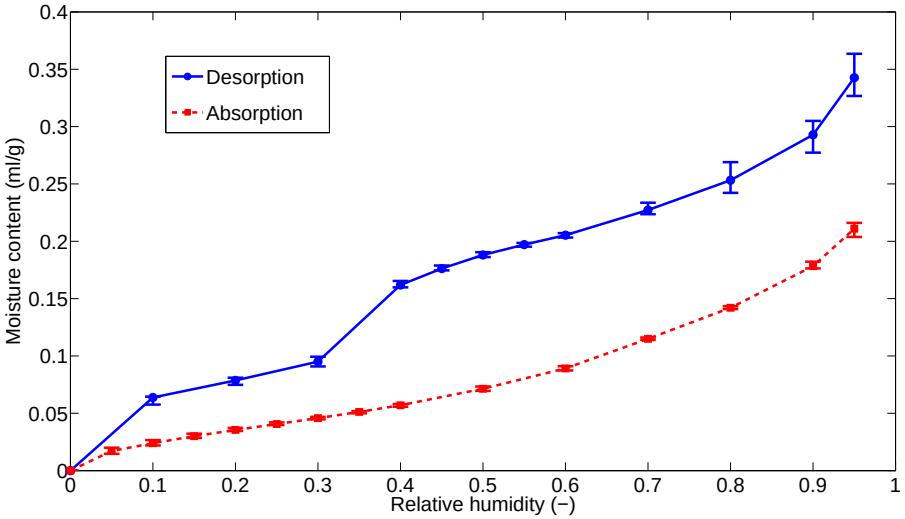

Figure 7: The sorption isotherms for the paste CEM III based on the extrapolated data at equilibrium conditions and the error bar shows the variation of three different measurements. The moisture content is expressed as ml water per gram of dry sample and the mass of the dry sample is determined at the point where RH = 0.

cement paste samples, which might possibly imply a much more complex pore structure including pore-blocking effect in the hardened cement paste samples.

3.2. Specific surface area of the studied materials

The specific surface area S (m^2/g) is proportional to the amount of the adsorbed moisture on the first monolayer when it is completely covered, with the expression given as

$$S = \frac{A_m N_A}{M_w} v_m \tag{10}$$

where v_m is the monolayer capacity (g/g), $N_A = 6.02 \cdot 10^{23}$ (mol^{-1}) is the Avogadro constant, $M_w = 18.0$ (g/mol) is the molar mass of water and $A_m = 10.6$ (Å^2) is the area occupied by one water molecule [9] . By inserting these values, Eq.10 can be written as

$$S = 3540 \cdot v_m \tag{11}$$

As has been discussed earlier, several different equations have been developed to describe the multilayer adsorption. If different types of equations accounting for multilayer adsorption are used, the calculated specific surface area could be different. In this section, the standard BET equation, the two-layer BET equation and the GAB equation will be used to calculate the specific surface area. The absorption data from Figure 5 to Figure 7 in the RH range ≤ 0.4 are used to do the necessary curve fitting to obtain the important parameters.

The curve fitting results are shown from Figure 8 to Figure 10. It can be observed that for the MCM-41 (Figure 8), the predicted amount of the adsorbed moisture content decreases in the sequence of the standard BET equation, the two-layer BET equation and the GAB equation and the predicted isotherms all lie below the measured moisture content at the RH between 0.5 to 0.9. For the hardened

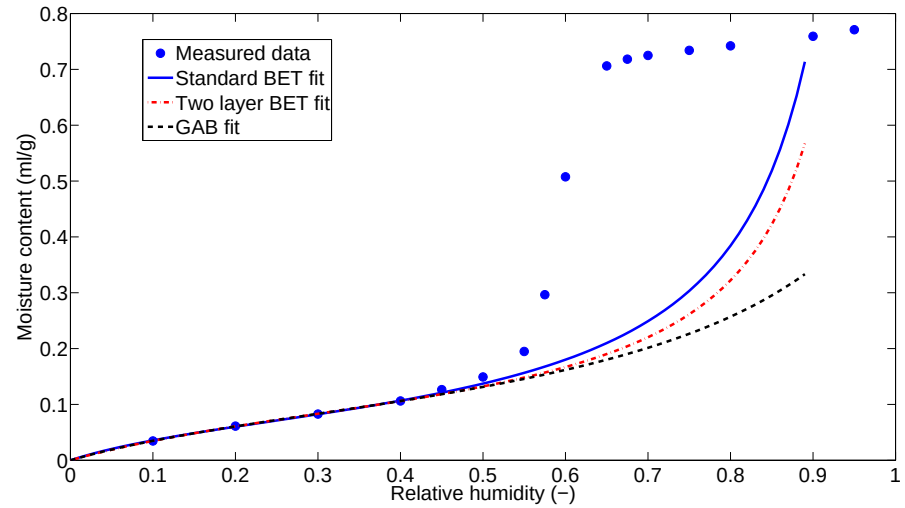

Figure 8: The curve fitting for the MCM-41 using the standard BET equation, the two-layer BET equation and the GAB equation accounting for multilayer adsorption.

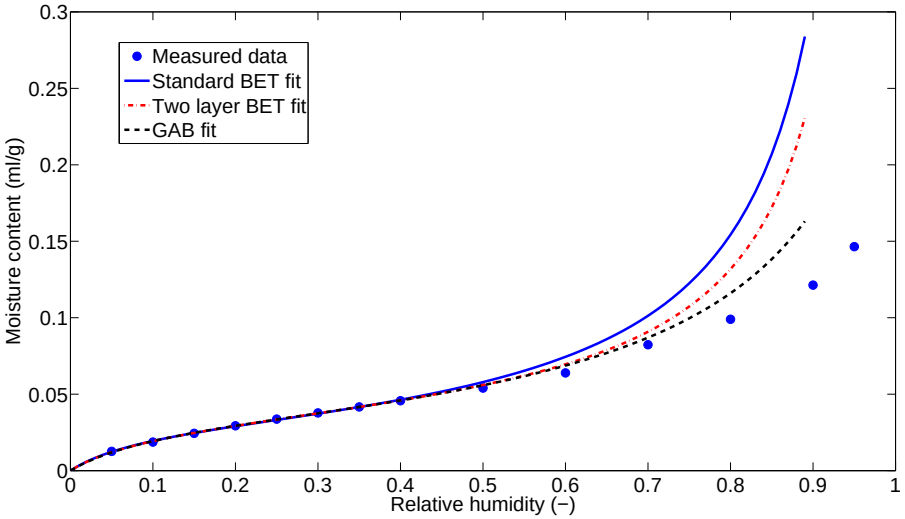

Figure 9: The curve fitting for the paste CEM I using the standard BET equation, the two-layer BET equation and the GAB equation accounting for multilayer adsorption.

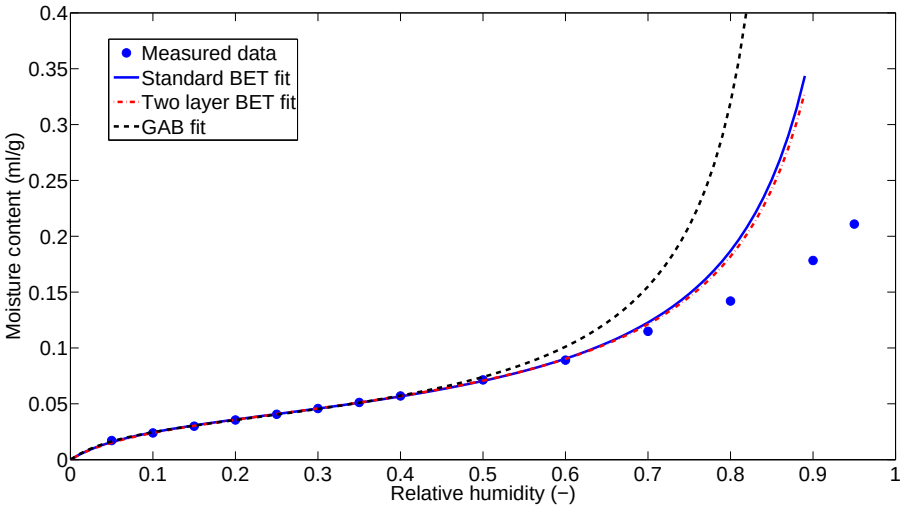

Figure 10: The curve fitting for the paste CEM III using the standard BET equation, the two-layer BET equation and the GAB equation accounting for multilayer adsorption.

cement paste sample CEM I (Figure 9), the predicted amount of the adsorbed moisture content decreases in the same sequence as that of the MCM-41 but all of the predicted adsorption isotherms are higher than the measured absorption isotherms at the RH $>$ 0.5. As introduced before, the measured absorption isotherm contains both the moisture uptake from the multilayer adsorption and the capillary condensation. Thus, the moisture content through multilayer adsorption should always be lower than the measured absorption data. Therefore, all the three equations for multilayer adsorption tend to overestimate the adsorbed moisture content at the RH $>$ 0.5. The similar overestimation of the adsorbed moisture content at high RHs is also observed for sample CEM III (Figure 10). However, for CEM III, the GAB fit results in the highest isotherm which is different compared with the results obtained for the sample MCM-41 and CEM I. This is related to the nature of the GAB fitting parameters k. The calculated specific surface area based on the three different equations and the fitted parameters are shown in Table 2.

According to results presented in Table 2, it can be found the calculated specific surface area based on the two-layer BET equation is normally smaller than that based on the standard BET equation. The relative difference for the MCM-41 and the paste CEM I are 26% and 24% respectively, while the relative difference is much smaller for the paste CEM III (less than 1%). The specific surface area calculated from the GAB equation is bigger than that from the standard BET equation for the MCM-41 and the paste CEM I while the opposite relation is found for the paste CEM III. This is associated with the best fitted GAB parameter k. The k value for both MCM-41 and CEM I are less than 1 while the value for CEM III is larger than 1. It has also been noticed that the values for k in literature is often reported to be less than 1, e.g., see [21, 49]. Thus, unsurprisingly it can be concluded that the calculated specific surface area is very sensitive to which equation (model) is used for multilayer adsorption. It should be noted that it has been claimed that the calculated specific surface area actually does not represent the real geometrical surface area [25], because it also depends on the interaction forces between the adsorbate and the adsorbent, which are reflected in the values of the parameters like c, b and k as presented in Table 2.

Table 2: The fitted parameters and the calculated specific surface area for the studied materials based on different equations accounting for multilayer adsorption.

	MCM-41			CEM I			CEM III		
	BET[a]	TBET[a]	GAB	BET[a]	TBET[a]	GAB	BET[a]	TBET[a]	GAB
v_m	0.0800	0.0591	0.0994	0.0315	0.0239	0.0346	0.0381	0.0357	0.0346
c	6.04	7.12	5.40	11.17	14.37	10.51	12.24	12.60	13.61
b	-	2.45	-	-	2.51	-	-	1.28	-
k	-	-	0.81	-	-	0.89	-	-	1.12[b]
surf. area (m^2/g)	283	209	352	112	85	123	135	126	123

Note: (a) BET and TBET represent the standard BET equation and the two-layer BET equation respectively; (b) the k value is often reported as less than 1.

3.3. Pore size distribution of the studied materials

3.3.1 The thickness of the adsorbed layer

Different models to calculate the thickness of the adsorbed layer of water vapor, or the $t-$curves, have been discussed previously. The impact of the model selected on the calculated thickness of the adsorbed layer is discussed in the following. The Halsey equation and the empirical equation Eq.6 are two types of $t-$curves for water vapor, which are independent of the adsorbents under consideration. The $t-$curves proposed by Hagymassy et al. [9] for water vapor depends on the standard BET constant c. The BET constant c values for the proposed four generalized $t-$curves are c =10−14.5, c =50−200, c =5.2 and c =23. Three other $t-$curves are also included following the assumption made by Johannesson [12] for comparison purpose, i.e. only the water molecules in the first and second layer as calculated will be considered to account for the thickness of the adsorbed layer (referring to Eq.7), based on the standard BET equation, the two-layer BET equation and the GAB equation. They are denoted as J-BET, J-TBET and J-GAB, respectively.

The comparison between the different $t-$curves for the studied materials MCM-41, CEM I and CEM III are shown in Figure 11, Figure 12 and Figure 13. The standard BET constant c calculated for the MCM-41 is about 6 (Table 2), thus the Hagymassy et al. $t-$curve with $c = 5.2$ is considered as the most relevant. The standard BET constant c calculated for the CEM I and CEM III are about 11 and 12 (Table 2), respectively. Therefore, the Hagymassy et al. curve with c =10∼14.5 is used for both CEM I and CEM III. Of all the $t-$curves considered, the Halsey equation predicts the highest values at low RHs (<0.4) and generally the Hagymassy et al. curve gives the highest values at high RHs. The three other $t-$curves, i.e., the J-BET, J-TBET and J-GAB, basically predict lower values compared to other $t-$curves especially when the RH is higher than 0.4. Since only the water in the first two layers as calculated based on the equations accounting for multilayer adsorption is considered to calculate the thickness of the adsorbed water and even though the equations tend to overestimate the moisture contents at high RHs, it is not surprising that the predicted thickness of the adsorbed layer from these three $t-$curves (J-BET, J-TBET and J-GAB) are relatively smaller compared with other $t-$curves considered in this study.

In order to demonstrate the impact of the assumed thickness of the adsorbed layer on the determined pore size distribution, the application of Kelvin equation without considering any adsorbed layer at all, i.e., $t \equiv 0$, will also be included in this study. The $t-$curves considered in the calculation of pore size distribution are listed in Table 3.

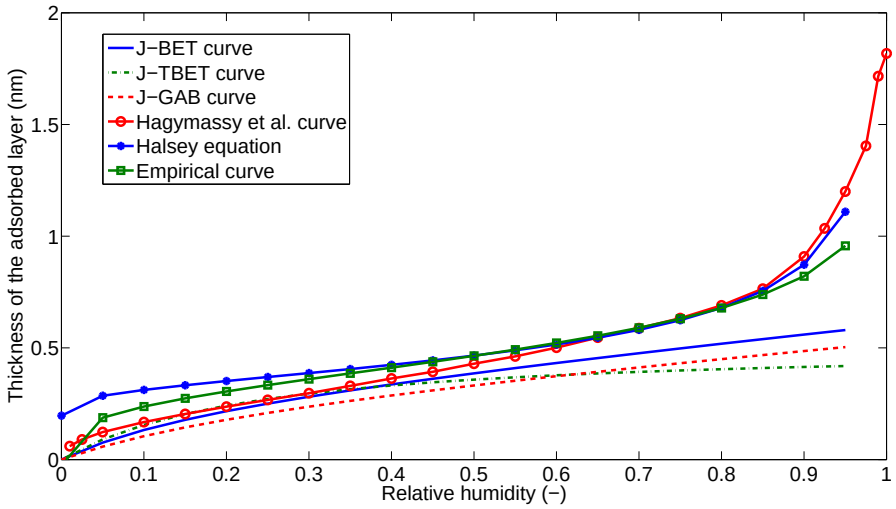

Figure 11: Different $t-$curves considered for the model material MCM-41.

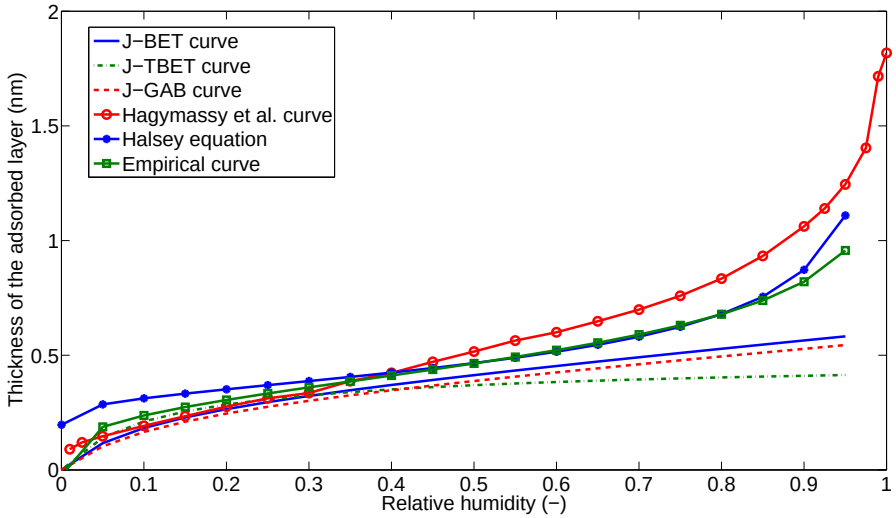

Figure 12: Different $t-$curves considered for the paste CEM I.

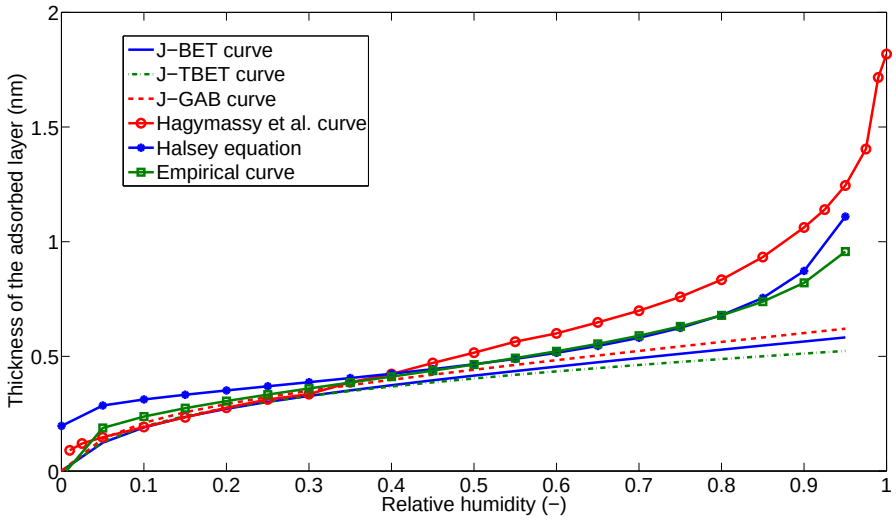

Figure 13: Different $t-$curves considered for the paste CEM III.

Table 3: The different $t-$curves considered in calculating the pore size distribution.

$t-$curves	Thickness t (nm)	Ref.
Kelvin-0 curve	$t \equiv 0$	-
Empirical curve	$t = 0.395 - 0.189\ln(-\ln\phi)$	[25]
Halsey equation	$t = -0.3(1.63/\ln\phi)^{1/3}$	[50]
Hagymassy et al. curve	Figure 11 to Figure 13	[9]
J-BET curve	Figure 11 to Figure 13	-
J-TBET curve	Figure 11 to Figure 13	-
J-GAB curve	Figure 11 to Figure 13	-

3.3.2 Pore size distribution

Following the BJH model, the pore volume of a studied material can be calculated using the moisture content data from high RH to low RH step by step. Thus, the total calculated pore volume depends on that to which RH value the calculation is executed. The lower the RH limit considered in the calculation, the bigger the calculated total pore volume. There is a possibility that the calculated pore volume will be bigger than the maximum measured moisture content if the lowest RH limit considered in the calculation is too low. That is because the calculation of pore size distribution using the Kelvin equation could only be applied in the RH range where capillary condensation takes place. At a certain low RH, capillary condensation could be absent for a studied material and the measured moisture content is merely due to multilayer adsorption. There is no general agreement on what is the limiting RH for capillary condensation in this type of calculations [8] and it has been indicated by some studies that the corresponding limiting pore size (width) may be as high as 7.5 nm [51, 52]. Normally, the closure point of the hysteresis is taken as the lower limit of capillary condensation [53]. However, the sorption data of the two hardened cement paste samples in this study show no obvious closure of the hysteresis. Therefore, from a practical perspective, the limiting pore size (the corresponding RH) in this study is determined by comparing the calculated total pore volume with the maximum moisture content measured. When these two values get sufficiently close to each other, the calculation is then terminated. In this manner, an indication of the lowest allowable RH is estimated. It should be noted that the estimated lowest allowable RH depends on the $t-$curve used in the calculation. The pore volume calculation also depends on the assumption concerning the pore shape. Cylindrical pores are assumed in the calculation described in this paper.

The calculated pore size distribution also depends on which isotherm is used as input data, i.e., desorption or absorption. There is no consensus about which isotherm should be adopted to calculate the pore size distribution. It is clearly stated in the IUPAC report dealing with sorption [2] that it is impossible to provide unequivocal recommendations in the absence of detailed knowledge about the geometry of the pores under study. But it seems to be more and more accepted that the calculation using absorption measurements may be more representative for the true pore size distribution while the calculation from the desorption perhaps is more related to the network effect (referring to the pore entry or neck sizes discussed before or the more simplified conventional "ink-bottle" model) [8, 39]. In this study, the pore size distribution will be calculated from both the absorption and desorption isotherms for comparison. It has been mentioned earlier that there is a hypothesis assuming different radii of the meniscus curvature for the same pore during the absorption and desorption, e.g., see Figure 1. However, this is considered as irrelevant for our purposes since it fails to explain the reversibility of the absorption and the desorption isotherms for mesoporous materials. Therefore, a hemispherical meniscus will be assumed in both desorption and absorption (referring to Figure 1b, $r_{k1} = r_{k2} = r_k$).

The calculated differential pore size distribution (PSD) curves of the MCM-41 from the desorption and the absorption isotherm using different $t-$curves are shown in Figure 14. It can be seen that the PSD curves calculated from the desorption isotherm using different $t-$curves (Figure 14a) basically have the similar shape with only one peak, except the one using Kelvin-0 $t-$curve which shows two peaks. The pore radii corresponding to the peak in the calculated PSD curves (except that using the Kelvin-0 $t-$curve), sometimes referred to as the most frequent pore radii R_{max} [26], are in the range of 1.7 nm to 1.9 nm, with the one using Halsey equation as the $t-$curve giving the biggest value and the one using the J-GAB $t-$curve giving the smallest. The two peaks in the pore size distribution curve using the Kelvin-0 $t-$curve corresponds to pore radii at about 1 nm and 1.4 nm. Similar trends are also found in the PSD curves calculated from the absorption isotherm using the six different $t-$curves (except that using the Kelvin-0 $t-$curve), as presented in Figure 14b, but the pore radii R_{max} are bigger than that calculated from the desorption isotherm (Figure 14a), which are in the range of 2.4

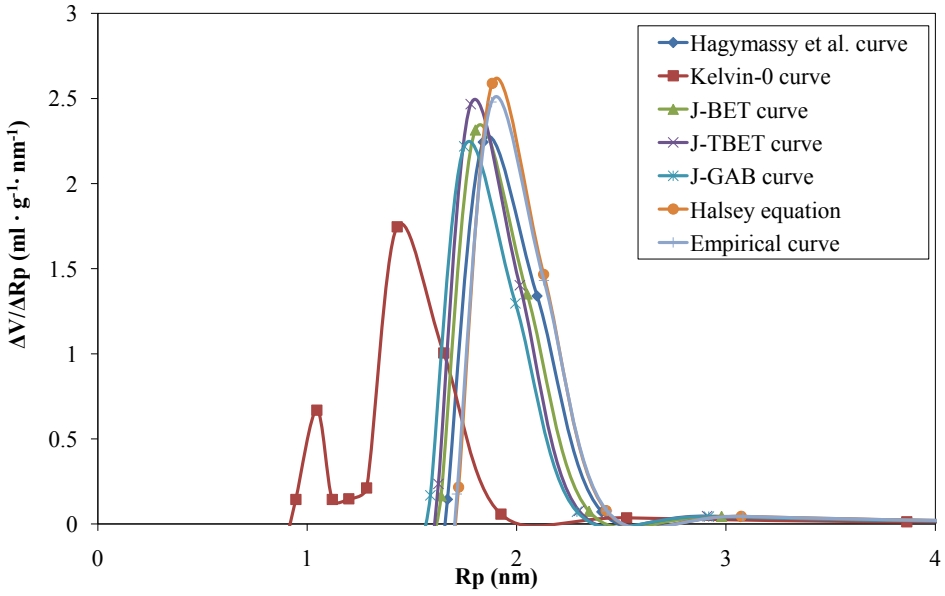

(a)

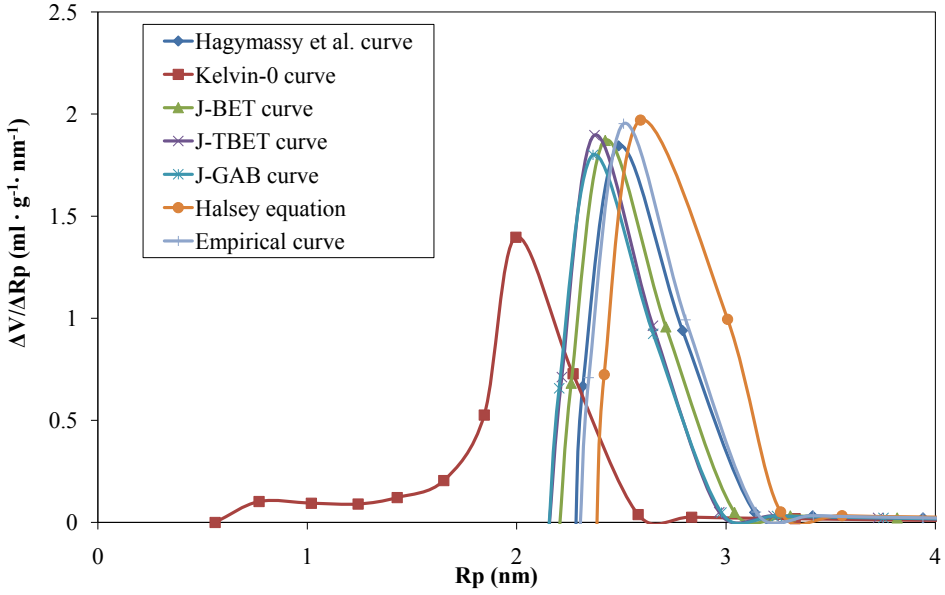

(b)

Figure 14: Differential pore size distribution of the MCM-41 calculated from (a) the desorption isotherm and (b) the absorption isotherm using different $t-$curves.

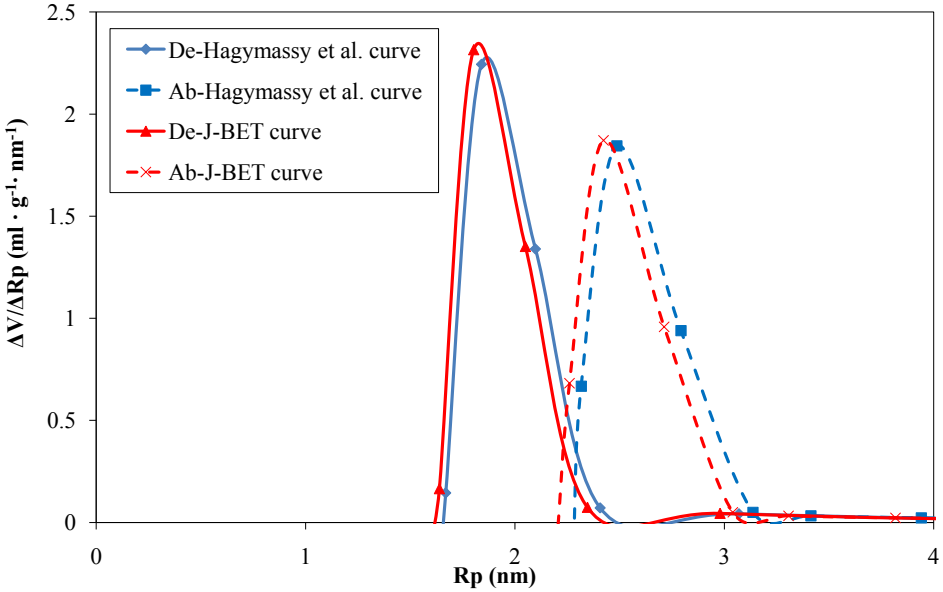

Figure 15: Comparison of the differential pore size distribution of the MCM-41 calculated from the desorption and absorption isotherms using Hagymassy et al. and J-BET $t-$curves.

nm to 2.6 nm. However, the PSD curves calculated from the absorption isotherm using the Kelvin-0 $t-$curve also shows one peak, whose corresponding pore radii is about 2 nm, but it has a relatively broad tail around the pore radii of about 1 nm.

Additionally, the PSD curves calculated from the absorption isotherm are slightly broader than those calculated from the desorption isotherm. A more representative comparison about the difference between the PSD curves calculated from the absorption and the desorption isotherms using Hagymassy et al. $t-$curve and J-BET $t-$curve is presented in Figure 15.

The influence of the assumed thickness of the adsorbed layer ($t-$curves) on the calculated pore size distribution can be summarized as follows: the thinner the layer is assumed, the smaller the pore size will be calculated. This becomes more evident by comparing the PSD curves calculated using either of the six other $t-$curves with that using the Kelvin-0 $t-$curve, see Figure 14.

Due to the restriction on the total pore volume adopted, the calculation of the PSD curves is terminated, e.g., when the pore radii are around 1.5-1.6 nm using the desorption isotherm (not considering that using the Kelvin-0 $t-$curve). That is because the calculated total pore volume is already equal to the maximum measured moisture content at the pore radii of 1.5-1.6 nm (corresponding to RH of around 0.4). The indication of this calculation can be understood as that the limiting RH (at the low end) for capillary condensation is about 0.4 for the model material MCM-41, and the moisture content measured under the RH of 0.4 is probably due to multilayer adsorption. However, the PSD calculation using the Kelvin-0 $t-$curve still continues under the pore radii (1.5-1.6 nm) since the total calculated pore volume is still much less than the maximum measured moisture content (as it does not account for the adsorbed water). It can be imagined that the adsorbed water is actually treated as the capillary condensed water in the very small pores when the Kelvin-0 $t-$curve is used, which causes the overestimation of the volume of the very small pores. This tends to motivate the statement that if the thickness of the adsorbed layer is underestimated, then the volume of the very small pores

Table 4: The calculated BJH surface area and the BET specific surface area for the MCM-41. The most frequent pore radii R_{max} with different $t-$curves are also presented.

Items		Surface area (m^2/g)		R_{max} (nm)	
		absorption	desorption	absorption	desorption
BJH	Hagymassy et al. curve	617	814	2.5	1.8
	Kelvin-0 curve	843	982	2.0	1.4
	J-BET curve	615	817	2.4	1.8
	J-TBET curve	613	834	2.4	1.8
	J-GAB curve	603	800	2.4	1.7
	Halsey equation	631	857	2.6	1.9
	Empirical curve	631	845	2.5	1.9
BET		283		-	

becomes overestimated, as clearly illustrated by the PSD curve using the Kelvin-0 $t-$curve compared with that using the other $t-$curves in Figure 14a.

It is of interest to compare the original measured desorption isotherm of the MCM-41 in Figure 5 with the obtained PSD curves (Figure 14a). There is a relatively sharp decrease or a shoulder after the RH at about 0.4 before the closure of the hysteresis. The peak around 1 nm in the determined PSD curve using the Kelvin-0 $t-$curve corresponds to this shoulder. However, if one looks into other PSD curves using a suitable $t-$curves, the calculation is actually terminated before this sharp decrease. Thus, it can be concluded that the peak around 1 nm in the PSD curve using the Kelvin-0 $t-$curve is just a calculation defect caused by not considering the adsorbed layer properly, which does not necessarily indicate the presence of another group of pores with radii around 1 nm in the MCM-41. The PSD curve calculated from the absorption isotherm using the Kelvin-0 $t-$curve (Figure 14b) results in no peak around 1 nm, which motivates the above statement.

One possible explanation for the existence of the shoulder before the closure of the hysteresis on the desorption isotherm as shown in Figure 5 is the hydrophobicity of the surfaces of the silica gel based MCM-41. Related discussions about the hydrophobicity of the surfaces of silica gels can be found, e.g., in [9, 23, 54]. The hydrophobic surfaces of the MCM-41 is confirmed by checking the specific surface area calculated using the standard BET equation from the absorption isotherm and that from the BJH calculation, which results in that the calculated BET specific surface area is much smaller compared with that from the BJH calculation (either using the absorption or the desorption isotherm). The results of the BET specific surface area and BJH surface area of the MCM-41 sample in this study are shown in Table 4. During adsorption, the hydrophobic property of the MCM-41 surfaces makes water molecules difficult to adsorb to the hydrophobic sites at low RHs. Hence, a considerable high RH is needed to trigger the water adsorption on these sites [9, 23, 55]. While during desorption, it can be assumed that all the capillary condensed water is almost desorbed when the RH decreases to about 0.4. The reason which motivates this statement is that the porosity calculation is terminated at RH about 0.4 as discussed before, indicating that the volume of all the pores has been calculated. Hence, the moisture content measured at the RH of about 0.4 is attributed to the adsorbed water on the material surfaces. Since some sites of the MCM-41 surfaces are hydrophobic, further decreasing the RH below 0.4, the water molecules attached on these hydrophobic sites of the MCM-41 at high RHs are not stable and tend to leave the surfaces as the RH decreases. After the water on the hydrophobic sites leaves, the absorption and desorption isotherms converge at the RH around 0.3.

It can be found from Table 4 that the BJH surface area calculated from the desorption is often larger than that from the absorption (about 200 m^2/g in this case). It is because the PSD calculated

from the desorption tends to overestimate the volume of small pores since desorption only measures the pore entry or neck sizes, leading to a higher surface area compared with that calculated from the absorption. As expected, the BJH surface area calculated using the Kelvin-0 $t-$curve either from absorption or desorption is much higher compared with that using other $t-$curves. The most frequent pore radii R_{max} calculated from the absorption is larger than that from the desorption by about 0.6-0.7 nm for the different $t-$curves considered.

The differential and accumulated PSD curves calculated from the desorption isotherm for the paste CEM I are shown in Figure 16. Similar to the sample MCM-41, the PSD curves calculated from the six different $t-$curves (except that from the Kelvin-0 $t-$curve) are in relatively good agreement with each other, showing one major peak around the pore radii of 1.4 nm and two relatively small shoulders around 1.8 nm and 3.0 nm. There are also three peaks in the pore size distribution calculated using the Kelvin-0 $t-$curve, the corresponding pore radii are 1.0 nm, 1.4 nm and 2.5 nm, which are smaller compared with that using other $t-$curves. The underestimation of the pore sizes and the overestimation of the volume of small pores using the Kelvin-0 $t-$curve are more obvious in the calculated accumulate PSD curves, as shown in Figure 16b.

The differential and accumulated PSD curves calculated from the absorption isotherm for the sample CEM I are shown in Figure 17. It turns out that the different $t-$curves used affect the PSD curves calculated from the absorption isotherm in a relatively more pronounced manner compared with that calculated from the desorption isotherm, especially at the very small pore sizes. However, the two shoulders found in the pore size distribution curves using the six different $t-$curves (except that from the Kelvin-0 $t-$curve) from the desorption isotherm corresponding to the pore radii of 1.8 nm and 3 nm are also observed in the curves calculated from the absorption. The magnitude of the peak around the pore radii of 3.0 nm is comparable with the PSD curves calculated from the desorption and the absorption. A more direct comparison about the difference between the PSD curves calculated from the desorption and the absorption isotherm is shown in Figure 18. The major difference between the PSD curves calculated from the desorption and the absorption is that the most pronounced peak found from that using the desorption isotherm with the pore radii corresponding to about 1.4 nm is not found in the PSD curves calculated from the absorption. Even though it seems that there does exist one peak (or even more than one) in the calculated PSD curves using the absorption isotherm below the pore radii of 1 nm, especially in the curves using the Kelvin-0 and Halsey $t-$curves. Of this reason, it is reasonable to assume that the peak(s) may be related to the uncertainties arising from the different thickness assumed for the adsorbed layer, which might not represent the true pore size information.

The differential and accumulated PSD curves calculated from the desorption and absorption isotherm for the sample CEM III are shown from Figure 19 and Figure 20, respectively. In Figure 21, a direct comparison of the PSD curves calculated from the desorption and the absorption isotherm is shown. Similar results with respect to the peaks and the comparison between the calculated PSD curves from the absorption and desorption as found for the sample CEM I are also observed for the sample CEM III. A more direct comparison about the difference between the pore size distribution of CEM I and CEM III can be found in Figure 22a (calculated from the desorption isotherm) and Figure 22b (calculated from the absorption isotherm). It can be found that the pore radii of the peaks correspond very well in the sample CEM I and CEM III, but there are much more small pores observed in the sample CEM III, especially those pores with radii less than about 5 nm. This results are in agreement with the findings in literature, that is, the pore structure generally becomes finer with the introduction of supplementary cementitious materials, e.g. see [56–58].

The missing peak around 1.4 nm in the PSD curves calculated from the absorption isotherm compared with that calculated from the desorption isotherm deserves further discussions. Since 1.4

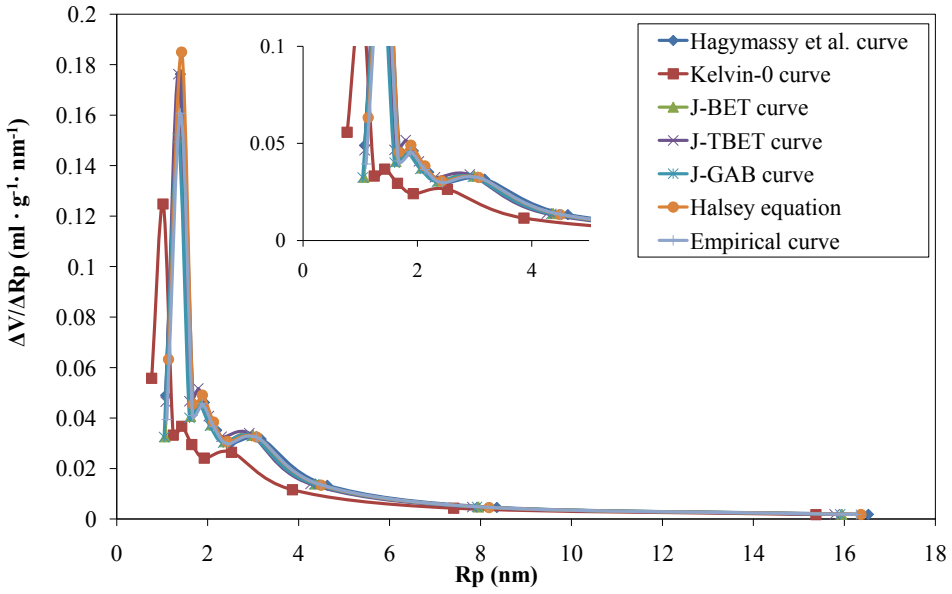

(a)

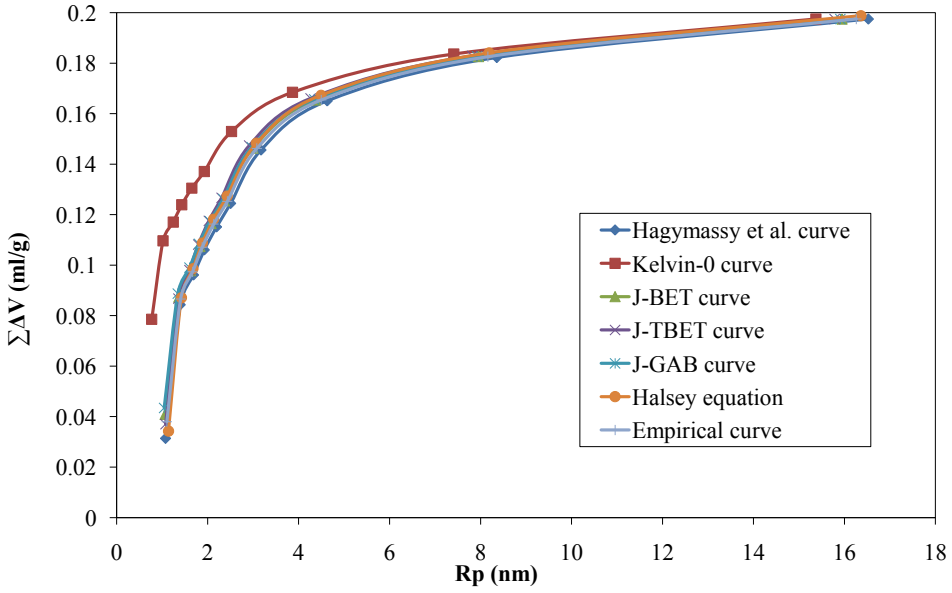

(b)

Figure 16: Pore size distribution curves of the paste CEM I calculated from the desorption isotherm using different $t-$curves: (a) differential PSD; (b) accumulated PSD.

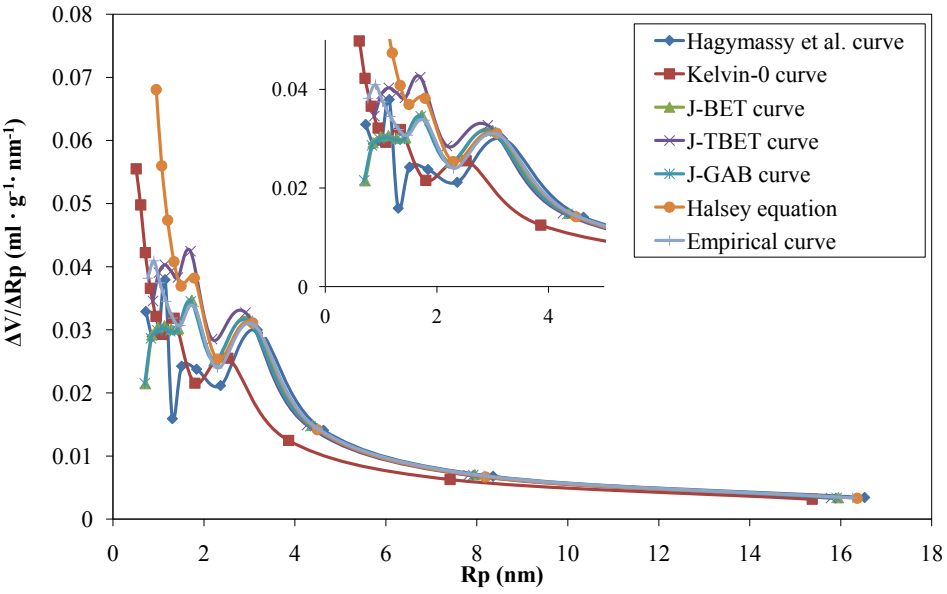

(a)

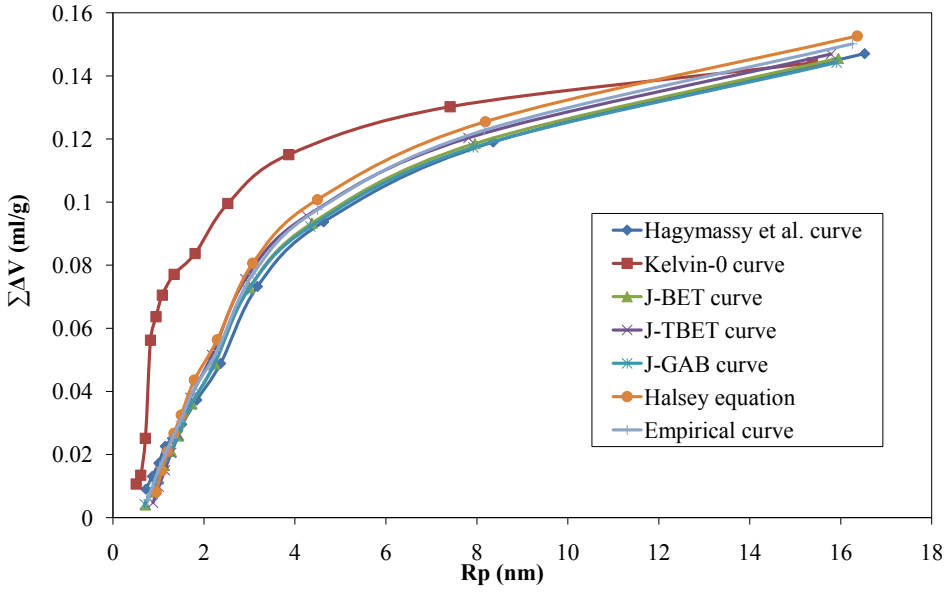

(b)

Figure 17: Pore size distribution curves of the paste CEM I calculated from the absorption isotherm using different $t-$curves: (a) differential PSD; (b) accumulated PSD.

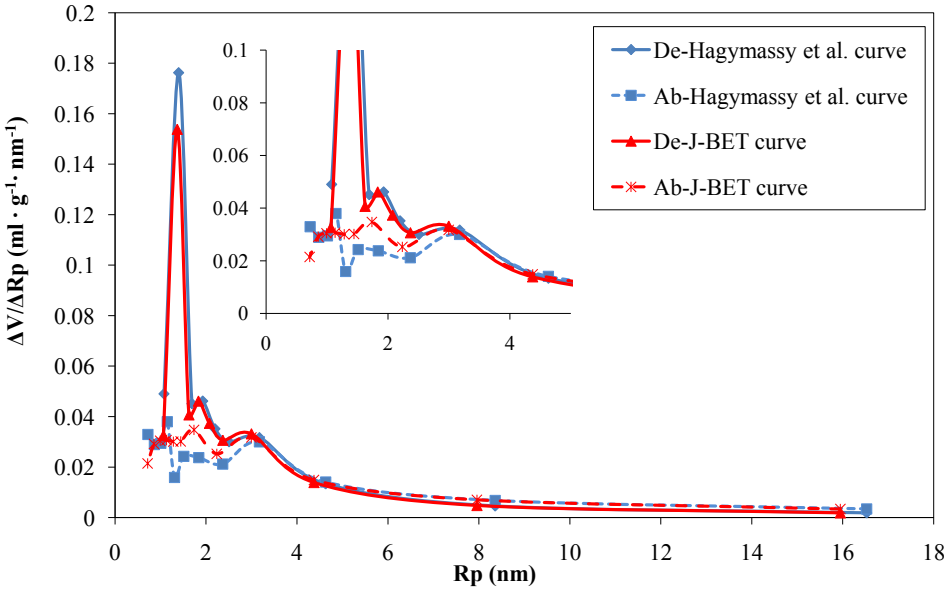

Figure 18: Comparison of the differential pore size distribution of the paste CEM I calculated from the desorption and absorption isotherms using Hagymassy et al. and J-BET $t-$curves.

nm corresponds to the RH about 0.4, one may argue the pore size peak at 1.4 nm may be related to microstructure changes (or pore structure collapse) caused by the drying effect when the RH is at this low level as discussed, e.g. in Jennings et al. [59–61], reflected by a relatively large change of the moisture content in the measured desorption isotherms. Therefore, the peak at 1.4 nm on the PSD curves calculated from the desorption isotherm should only reflect the collapse of the pore structure and should not be relevant in terms of the true pore size information. To check the relevance of the argument regarding the pore structure collapse of the studied cement pastes, a resaturation study was conducted [43]. The resaturation study went as follows: firstly a desorption-absorption cycle was applied, where the RH went down to 0 during the desorption. After that, each tested paste sample was resaturated with distilled water. Following that, a second desorption-absorption cycle was applied on the resaturated samples. The sorption isotherms (both desorption and absorption) of the resaturated samples were concluded to be identical to what was measured during the first desorption-absorption cycle. That is to say, if the microstructure changes caused by the so-called drying at low RHs take place, the resaturation of the sample after a desorption measurement must be able to fully restore the pore structure. However, if the microstructure changes are assumed relevant in this context, it seems difficult to understand when and how the restoration of the pore structure takes place in the absorption. Obviously the restoration does not take place around the RH of 0.4 (as the peak around this RH is missing in absorption curves), but it will be restored anyway (as discussed in the resaturation study). Thus, it turns out to be difficult to find convincing evidence to attribute the peak around 1.4 nm purely to the microstructure changes which might occur during the desorption. However, if the network effect is taken into consideration, the peak around 1.4 nm observed on the PSD curves calculated from the desorption isotherm can be better explained. According to the concept of the network effect, one can assume that this 1.4 nm should correspond to the radii of pore entries or necks which are probably connected to many pores with bigger interior sizes. During desorption, water in

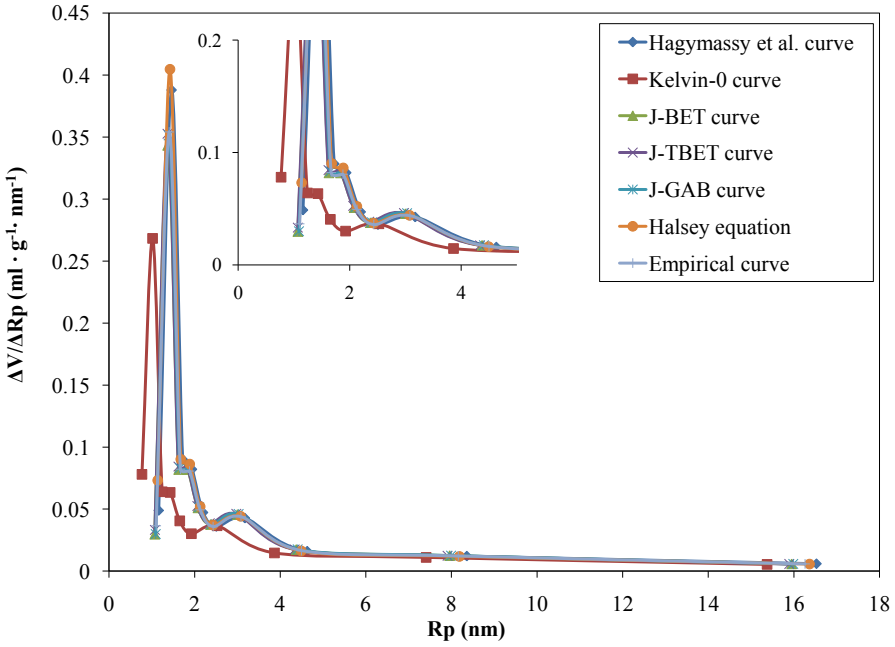

(a)

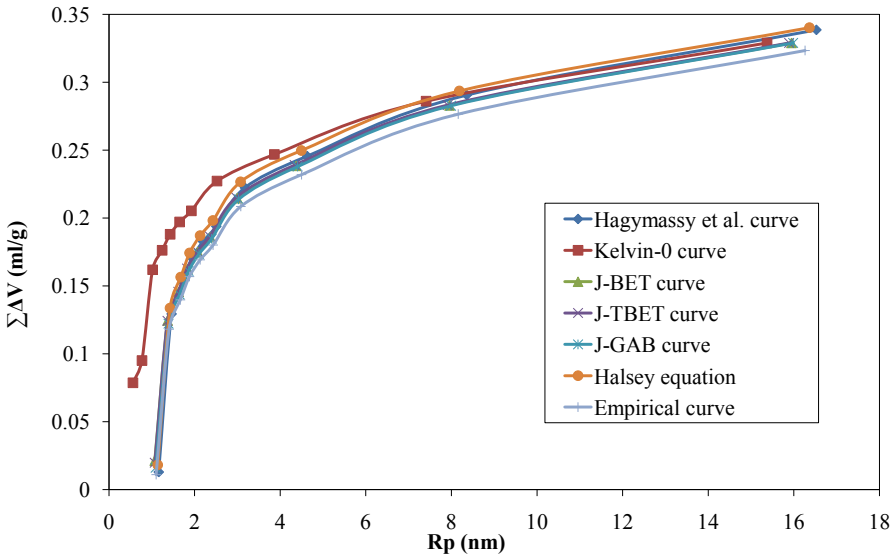

(b)

Figure 19: Pore size distribution curves of the paste CEM III calculated from the desorption isotherm using different $t-$curves: (a) differential PSD; (b) accumulated PSD.

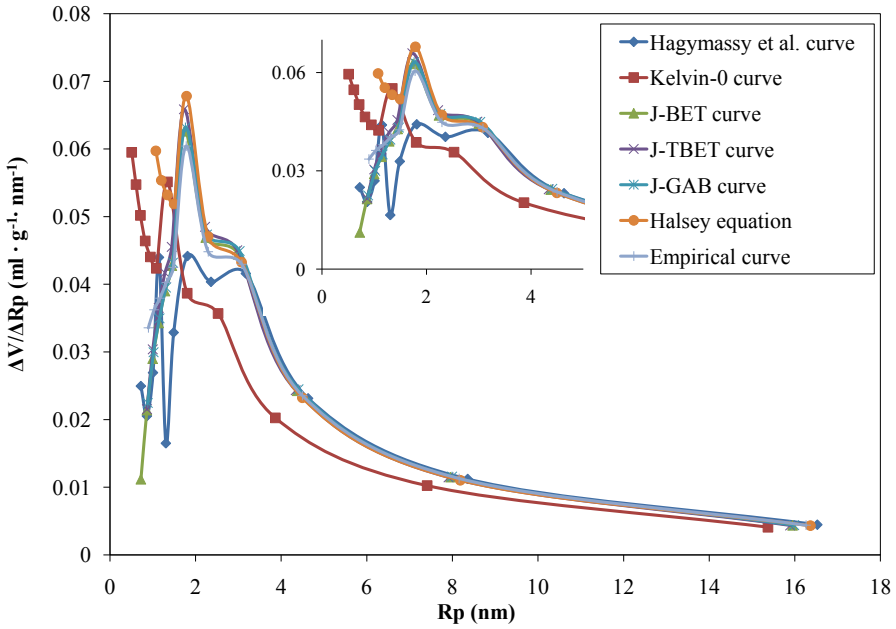

(a)

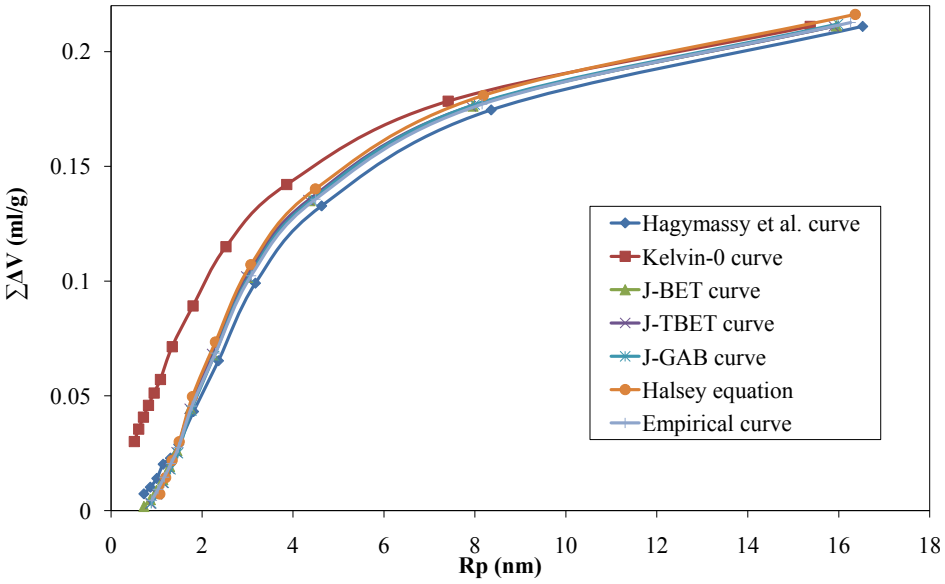

(b)

Figure 20: Pore size distribution curves of the paste CEM III calculated from the absorption isotherm using different $t-$curves: (a) differential PSD; (b) accumulated PSD.

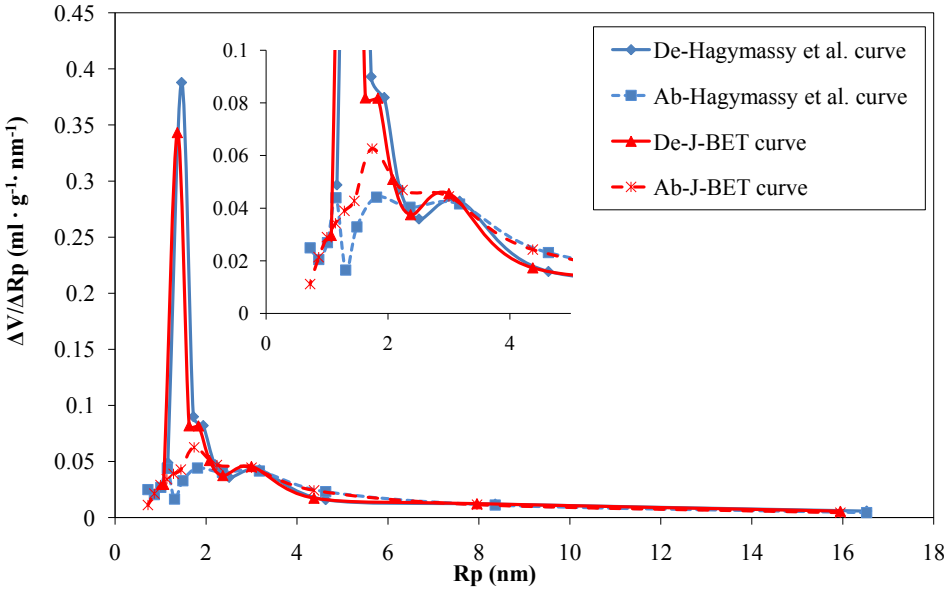

Figure 21: Comparison of the differential pore size distribution of the paste CEM III calculated from the desorption and absorption isotherms using Hagymassy et al. and J-BET $t-$curves.

these bigger pores can only be emptied when the water in the entries and necks has been desorbed. This effect might be the reason for why the calculated relatively big peak around 1.4 nm is observed on desorption curves. While during absorption, the pores are gradually filled at the RHs corresponding to their interior sizes as determined by the Kelvin equation. The implication of the comparison between the PSD results calculated from the desorption and the absorption isotherm to a large extent can be understood as that 1.4 nm is an important size of the pore entries or necks to which big pores are connected in the cement paste samples.

The BET specific surface area and the surface area calculated from the BJH method for the pastes CEM I and CEM III are listed in Table 5. Similar to what has been found for the MCM-41, the BJH surface area calculated from the desorption isotherm is much bigger than that from the absorption isotherm. It is also noticed that the calculated BJH surface area from absorption fits very well with the BET specific surface area, except that using the Kelvin-0 $t-$curve. The relatively higher BJH surface area using the Kelvin-0 $t-$curve can be attributed to the overestimation of the small pores as discussed before. With respect to the difference between the BJH surface area calculated from the desorption and absorption isotherm, a reasonable explanation can be formulated by taking into account the network theory, which is that the desorption measurement only reflects the pore entry or neck sizes rather than the interior sizes of the pores. Following this concept, it can be imagined that the calculation using the desorption data actually overestimates the volume of small pores, resulting into a higher surface area compared with the BET value, which is in accordance with what is shown in Table 5. The agreement between the BJH surface area calculated from the absorption and the BET specific surface area in this study might indicate that it is actually more reasonable to use the absorption isotherm to calculate the pore size distribution, as recommended in [8, 31, 38, 39]. On the other hand, since the desorption isotherm also can provide information about the network effect, a combined study of both the desorption and the absorption isotherms may give a more detailed picture

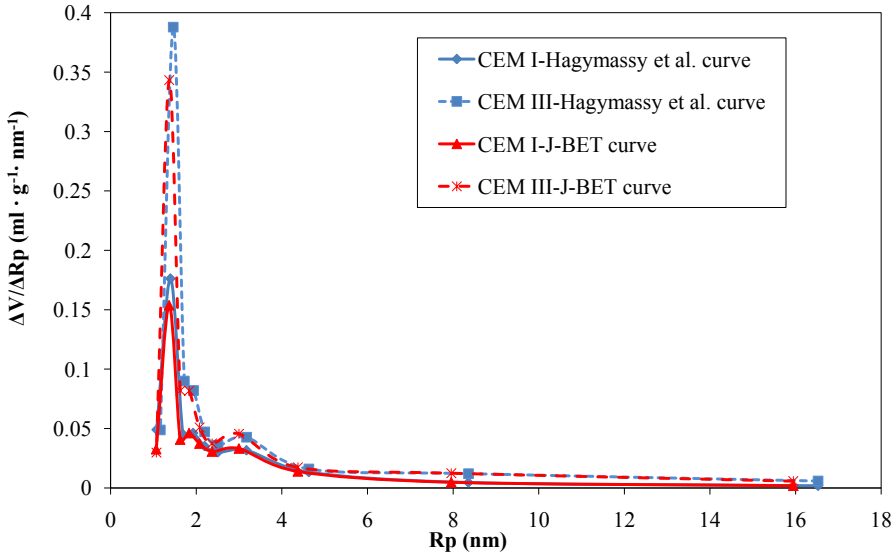

(a)

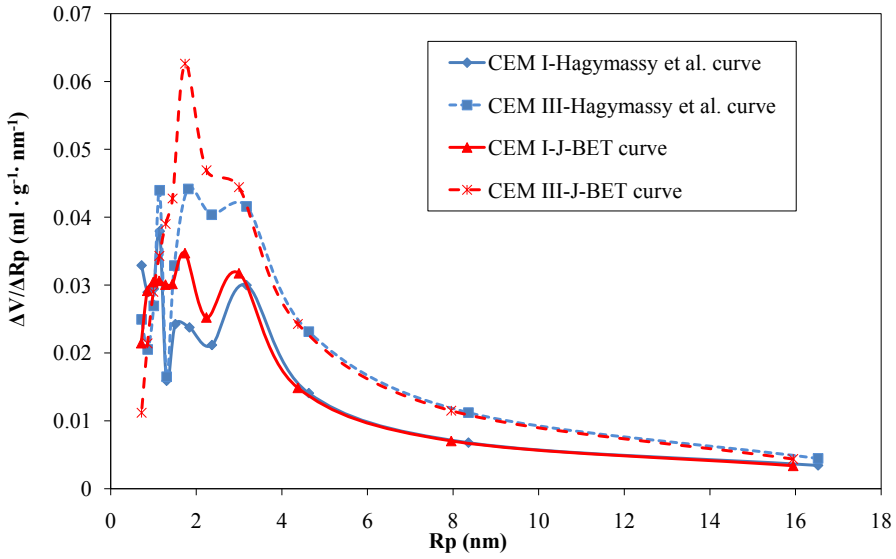

(b)

Figure 22: Comparison of the differential pore size distribution curves of the pastes CEM I and CEM III calculated from (a) the desorption isotherm and (b) the absorption isotherm using Hagymassy et al. and J-BET $t-$curves.

Table 5: The calculated BJH surface area and the BET specific surface area (m^2/g) for the two hardened cement pastes CEM I and CEM III.

Items		CEM I		CEM III	
		absorption	desorption	absorption	desorption
BJH	Hagymassy et al. curve	119	196	146	294
	Kelvin-0 curve	164	204	183	331
	J-BET curve	111	169	138	281
	J-TBET curve	110	185	141	286
	J-GAB curve	112	169	139	282
	Halsey equation	116	214	143	308
	Empirical curve	117	181	140	285
BET		112		135	

about the porosity characteristics of the material under study.

4. Conclusions

Sorption behavior of water vapor on a porous material can be used to study important characteristics of the material, e.g., the specific surface area and the pore size distribution. In this work, the specific surface area was calculated based on different equations accounting for multilayer adsorption and the pore size distribution was derived from both the absorption and the desorption isotherms using different $t-$curves for two hardened cement pastes (CEM I and CEM III) and one model porous material (MCM-41). Some important points of this investigation can be summarized as follows.

1. The calculated specific surface area is very much dependent on the equations considered for multilayer adsorption. For the studied materials, the specific surface area calculated based on the two-layer BET equation was smaller than that based on the standard BET equation. The relative difference for sample MCM-41 and CEM I wass about 26% and 24%, respectively; while the relative difference was much smaller for the paste CEM III (less than 1%). The specific surface area calculated from the GAB equation was bigger than that obtained by the standard BET equation for sample MCM-41 and sample CEM I while the opposite relation was found for the paste CEM III. These somewhat inconsistent results were suspected to be due to the fitted GAB parameter k. The best fitted k value for both the MCM-41 and the CEM I were less than 1 while the value obtained for CEM III was larger than 1.
2. Various $t-$curves were assumed accounting for the thickness of the adsorbed layer in calculating the pore size distribution. Except the Kelvin-0 $t-$curve, which assumes 0 thickness for the adsorbed layer, the pore size distribution calculated from either the desorption or the absorption isotherm shows reasonable agreement. For the model material MCM-41, the most frequent pore radii R_{max} found using the desorption isotherm is in the range of 1.7 nm to 1.9 nm compared with 2.4 nm to 2.6 nm when using the absorption counterpart. For the hardened cement pastes CEM I and CEM III, three characteristic peaks are found in the PSD curves calculated from the desorption isotherm with corresponding radii of 1.4 nm, 1.8 nm and 3.0 nm while the peak at 1.4 nm is missing and only two peaks are found in the PSD curves calculated using the absorption isotherm. This may indicate that 1.4 nm is an important size of the pore entries or necks to which bigger pores are connected in the investigated cement paste samples.
3. For the model material MCM-41, the calculated BJH surface area (using either the absorption or the desorption isotherm) was much bigger than the calculated BET specific surface area.

The reason for this could probably be related to the hydrophobic properties of its surface. Additionally, the BJH surface area calculated from the desorption isotherm was also bigger than that calculated from the absorption isotherm, which could be explained by that fact that the calculation using the desorption isotherm overestimates the volume of small pores, leading to a relatively high calculated surface area. The same conclusion holds for the hardened cement pastes in terms of the difference observed between the BJH surface area calculated using the desorption and the absorption isotherms. However, since the surface of hardened cement paste samples is hydrophilic, the BJH surface area, especially that calculated from the absorption isotherm, was much closer to the BET specific surface area for the two studied hardened cement pastes.

4. The network theory, which states that the desorption is controlled by the pore entry or neck sizes while the absorption is controlled by the real pore sizes, tends to be of great relevance in explaining some of the results, including the hysteresis behavior, the difference between the calculated pore size distribution curves and the difference in the BJH surface areas calculated from the desorption and the absorption isotherms.

Acknowledgment

The research leading to these results has received funding from the European Union Seventh Framework Programme (FP7/2007-2013) under grant agreement 264448.

References

[1] T. Allen. *Particle size measurement: Powder sampling and particle size measurement*, volume 2. Springer, 5th edition, 1997.

[2] K. Sing, D. Everett, R. Haul, L. Moscou, R. Pierotti, J. Rouquerol, and T. Siemieniewska. Reporting physisorption data for gas/solid systems. *Pure Appl. Chem*, 57(4):603–619, 1985.

[3] S. Brunauer, P.H. Emmett, and E. Teller. Adsorption of gases in multimolecular layers. *Journal of the American Chemical Society*, 60(2):309–319, 1938.

[4] E.P. Barrett, L.G. Joyner, and P.P. Halenda. The determination of pore volume and area distributions in porous substances. I. computations from nitrogen isotherms. *Journal of the American Chemical Society*, 73(1):373–380, 1951.

[5] M. Janz and B.F. Johannesson. Measurement of the moisture storage capacity using sorption balance and pressure extractors. *Journal of Building Physics*, 24(4):316–334, 2001.

[6] V. Kocherbitov and L. Wadsö. A desorption calorimetric method for use at high water activities. *Thermochimica Acta*, 411(1):31–36, 2004.

[7] K. S. W. Sing. *Colloid Science*, volume 1. Royal Society of Chemistry, 1973. doi: 10.1039/9781847557421-00001.

[8] K. Sing. The use of nitrogen adsorption for the characterisation of porous materials. *Colloids and Surfaces A: Physicochemical and Engineering Aspects*, 187:3–9, 2001.

[9] J. Hagymassy, S. Brunauer, and R.S. Mikhail. Pore structure analysis by water vapor adsorption: I. t-curves for water vapor. *Journal of Colloid and Interface Science*, 29(3):485–491, 1969.

[10] J. Villadsen. Pore structure in cement based materials. Technical Report 277, Building Materials Laboratory, Technical University, Denmark, 1992.

[11] I. Langmuir. The constitution and fundamental properties of solids and liquids. Part I. solids. *Journal of the American Chemical Society*, 38(11):2221–2295, 1916.

[12] B. Johannesson. Moisture fixation in mature concrete and other porous materials (8A). Lecture notes for Introduction to Concrete Technology (11563), Technical University of Denmark, 2011.

[13] B. Johannesson. *Transport and sorption phenomena in concrete and other porous media.* PhD thesis, Division of Building Materials, Lund University, 2000.

[14] I. Wadsö and L. Wadsö. A new method for determination of vapour sorption isotherms using a twin double microcalorimeter. *Thermochimica Acta*, 271:179–187, 1996.

[15] L. Wadsö and N. Markova. A double twin isothermal microcalorimeter. *Thermochimica Acta*, 360(2):101–107, 2000.

[16] E.A. Guggenheim. Application of statistical mechanics. Clarendon, 1966.

[17] R.B. Anderson. Modifications of the Brunauer, Emmett and Teller equation1. *Journal of the American Chemical Society*, 68(4):686–691, 1946.

[18] J.H. De Boer, editor. *The dynamical character of adsorption.* Clarendon Press, Oxford, UK, 2nd edition, 1968.

[19] C. Van den Berg. *Vapour sorption equilibria and other water-starch interactions: a physico-chemical approach.* PhD thesis, Wageningen Agricultural University, the Netherlands, 1981.

[20] R. W. Dent. A multilayer theory for gas sorption. Part I: Sorption of a single gas. *Textile Research Journal*, 47(2):145–152, 1977.

[21] R.W. Dent. A sorption theory for gas mixtures. *Polymer Engineering & Science*, 20(4):286–289, 1980.

[22] S. Brunauer, J. Skalny, and E.E. Bodor. Adsorption on nonporous solids. *Journal of Colloid and Interface Science*, 30(4):546–552, 1969.

[23] A. Raoof, J.P. Guilbaud, H. Van Damme, P. Porion, and P. Levitz. Analysis of the multilayer thickness relationship for water vapor and nitrogen adsorption. *Journal of Colloid and Interface Science*, 206(1):1–9, 1998.

[24] V. Baroghel-Bouny. Water vapour sorption experiments on hardened cementitious materials: Part I: Essential tool for analysis of hygral behaviour and its relation to pore structure. *Cement and Concrete Research*, 37(3):414–437, 2007.

[25] R.M. Espinosa and L. Franke. Inkbottle pore-method: Prediction of hygroscopic water content in hardened cement paste at variable climatic conditions. *Cement and Concrete Research*, 36(10): 1954–1968, 2006.

[26] O. Šolcová, L. Matějová, and P. Schneider. Pore-size distributions from nitrogen adsorption revisited: Models comparison with controlled-pore glasses. *Applied Catalysis A: General*, 313(2): 167–176, 2006.

[27] C.G. Shull, P.B. Elkin, and L.C. Roess. Physical studies of gel microstructure. *Journal of the American Chemical Society*, 70(4):1410–1414, 1948.

[28] A. Wheeler. Reaction rates and selectivity in catalyst pores. In P.H. Emmett, editor, *Catalysis Part II.*, page 105. Rheinhold Publ. Corp., 1955.

[29] D.H. Everett and W.I. Whitton. A general approach to hysteresis. *Transactions of the Faraday Society*, 48:749–757, 1952.

[30] J.H. De Boer. *The Structure and properties of porous materials*. Proceedings of the Symposium of the Colston Research Society. Butterworths, 1958.

[31] K.S.W. Sing. Characterization of porous materials: past, present and future. *Colloids and Surfaces A: Physicochemical and Engineering Aspects*, 241(1):3–7, 2004.

[32] Z.P. Bažant and M.Z. Bazant. Theory of sorption hysteresis in nanoporous solids: Part I snap-through instabilities. *Journal of the Mechanics and Physics of Solids*, 60(9):1644–1659, 2012.

[33] M.Z. Bazant and Z.P. Bažant. Theory of sorption hysteresis in nanoporous solids: Part II molecular condensation. *Journal of the Mechanics and Physics of Solids*, 60(9):1660–1675, 2012.

[34] P.J. Branton, P.G. Hall, K.S.W. Sing, H. Reichert, F. Schüth, and K.K. Unger. Physisorption of argon, nitrogen and oxygen by MCM-41, a model mesoporous adsorbent. *J. Chem. Soc., Faraday Trans.*, 90(19):2965–2967, 1994.

[35] P.I. Ravikovitch, S.C.Ó. Domhnaill, A.V. Neimark, F. Schüth, and K.K. Unger. Capillary hysteresis in nanopores: theoretical and experimental studies of nitrogen adsorption on MCM-41. *Langmuir*, 11(12):4765–4772, 1995.

[36] P.J. Branton, P.G. Hall, and K.S.W. Sing. Physisorption of alcohols and water vapour by MCM-41, a model mesoporous adsorbent. *Adsorption*, 1(1):77–82, 1995.

[37] P.J. Branton, K.S.W. Sing, and J.W. White. Adsorption of carbon tetrachloride and nitrogen by 3.4 nm pore diameter siliceous MCM-41. *J. Chem. Soc., Faraday Trans.*, 93(13):2337–2340, 1997.

[38] N.A. Seaton. Determination of the connectivity of porous solids from nitrogen sorption measurements. *Chemical Engineering Science*, 46(8):1895–1909, 1991.

[39] K.S.W. Sing. Adsorption methods for the characterization of porous materials. *Advances in Colloid and Interface science*, 76:3–11, 1998.

[40] G.C. Wall and R.J.C. Brown. The determination of pore-size distributions from sorption isotherms and mercury penetration in interconnected pores: The application of percolation theory. *Journal of Colloid and Interface Science*, 82(1):141–149, 1981.

[41] V.P. Zhdanov, V.B. Fenelonov, and D.K. Efremov. Determination of pore-size distribution from sorption isotherms: Application of percolation theory. *Journal of Colloid and Interface Science*, 120(1):218–223, 1987.

[42] E.L. Perkins, J.P. Lowe, K.J. Edler, N. Tanko, and S.P. Rigby. Determination of the percolation properties and pore connectivity for mesoporous solids using NMR cryodiffusometry. *Chemical Engineering Science*, 63(7):1929–1940, 2008.

[43] M. Wu, B. Johannesson, and M. Geiker. A study of the water vapor sorption isotherms of hardened cement pastes: possible pore structure changes at low relative humidity and the impact of temperature on isotherms. *Cement and Concrete Research*, 56:97–105, 2014.

[44] B. Johannesson and P. Utgenannt. Microstructural changes caused by carbonation of cement mortar. *Cement and Concrete Research*, 31(6):925–931, 2001.

[45] V.T. Ngala and C.L. Page. Effects of carbonation on pore structure and diffusional properties of hydrated cement pastes. *Cement and Concrete Research*, 27(7):995–1007, 1997.

[46] J.J. Thomas, H.M. Jennings, and A.J. Allen. The surface area of hardened cement paste as measured by various techniques. *Concr. Sci. Eng*, 1:45–64, 1999.

[47] H.H. Willems and K.B. Van Der Velden. A gravimetric study of water vapour sorption on hydrated cement pastes. *Thermochimica Acta*, 82(1):211–220, 1984.

[48] M. Åhs. *Redistribution of moisture and ions in cement based materials.* PhD thesis, Division of Building Materials, Lund University, 2011.

[49] E.O. Timmermann. Multilayer sorption parameters: BET or GAB values? *Colloids and Surfaces A: Physicochemical and Engineering Aspects*, 220(1-3):235–260, 2003.

[50] T. Sneck, L. Kinnunen, and H. Oinonen. *Measurements of Pore Size Distribution of Porous Materials: Interim Report.* State Institute for Technical Research, Helsinki, Finland, 1966.

[51] C.M. Lastoskie and K.E. Gubbins. Characterization of porous materials using density functional theory and molecular simulation. *Studies in Surface Science and Catalysis*, 128:41–50, 2000.

[52] P.I. Ravikovitch and A.V. Neimark. Characterization of nanoporous materials from adsorption and desorption isotherms. *Colloids and Surfaces A: Physicochemical and Engineering Aspects*, 187:11–21, 2001.

[53] S.J. Gregg and K.S.W. Sing. *Adsorption, surface area, and porosity.* Academic Press, London, 2 edition, 1982.

[54] F.A. Shebl, M. Abd El-Khalik, and F.M. Helmy. Theoretical studies on the standard but misleading adsorption isotherm I: True adsorption isotherm. *Surface technology*, 19(4):321–334, 1983.

[55] V. Kocherbitov and V. Alfredsson. Hydration of MCM-41 studied by sorption calorimetry. *The Journal of Physical Chemistry C*, 111(35):12906–12913, 2007.

[56] R.D. Hooton. Permeability and pore structure of cement pastes containing fly ash, slag, and silica fume. *Blended Cements, ASTM STP*, 897:128–143, 1986.

[57] V.M. Malhotra. *Supplementary cementing materials for concrete.* Special publication / Canada Centre for Mineral and Energy Technology ; SP86-8E. Energy, Mines, and Resources Canada, Canada Centre for Mineral and Energy Technology, 1987.

[58] A.M. Neville. *Properties of concrete.* Prentice Hall, 4th edition edition, 1995.

[59] H.M. Jennings. A model for the microstructure of calcium silicate hydrate in cement paste. *Cement and Concrete Research*, 30(1):101–116, 2000.

[60] J.J. Thomas and H.M. Jennings. A colloidal interpretation of chemical aging of the C-S-H gel and its effects on the properties of cement paste. *Cement and Concrete Research*, 36(1):30–38, 2006.

[61] H.M. Jennings. Refinements to colloid model of C–S–H in cement: CM–II. *Cement and Concrete Research*, 38(3):275–289, 2008.